Digital Image Analysis Study of Bubbling, Solids Mixing and Segregation in Fluidized Beds.

by

Kok Seng Lim

Thesis submitted for the degree of

Doctor of Philosophy

in

The University of Adelaide

(Faculty of Engineering)

(August 1992)

Declaration

This work contains no material which has been accepted for the award of any other degree or diploma in any university or other tertiary institution and, to the best of my knowledge and belief, contains no material previously published or written by another person, except where due reference has been made in the text.

I give consent to this copy of my thesis, when deposited in the University Library being available for loan and photocopying.

Kok S.T Lim

25th - August - 1992

ACKNOWLEDGEMENTS

The author wishes to express his earnest thanks to the following people and institutional organizations for their continual support and assistance throughout this work.

Special thanks are due to Associate Professor Pradeep Agarwal, the immediate supervisor, for his unremitting encouragement, motivation, guidance and optimism. Thanks are also to be extended to Dr. B.K. O'Neill for his assistance when Associate Professor Pradeep Agarwal was on study leaves.

The supports provided by the academics staff of the Department of Chemical Engineering, especially Professor J.B. Agnew, are greatly appreciated.

The author wishes to thank all the technical staff, Ted Jones and Colin Tipper in particular, for the construction of the equipments, and Bruce Ide and Andrew Wright for technical support and maintenance, David Atkinson and Sanh Tran for computing support and advice.

Many thanks to Carl Minerd for his ingenious design and construction of the 'opto-coupler' which provided the 'edge' to this novel experimental studies.

Thanks are to be conveyed to V.S. Gururajan for sharing his expertise and knowledge on the work of mathematical modelling.

The author also like to thank the Australian Research Councils for providing the financial funding necessary to perform this investigation and the University of Adelaide for the scholarship which enabled him pursue this study.

The author also wish to thank the post-graduate students of this Department, Ashley Hull in particular, for their constructive suggestions and discussions. Contributions and assistance from the graduates students especially L.Z. Hui and J.M.L Chee, are also acknowledged.

Many thanks to Mary Barrow and Elain Minerd for assisting in the preparation of the manuscripts.

Personal thanks are to be extended to the friends in Australia, Dennis Coleman, late Pat Pietsch, and daugthers, Mary Ann and Jenny, and Hazel and Brian Coleman for their friendship and support and close friend, Xiao Ming Zhang for her compassion and comfort.

Lastly, the authors wish to convey his appreciation to his parents and members of the family for their support and encouragement throughout his study in Australia.

TABLE OF CONTENTS

CONTENT	PAGE
Chapter 1 INTRODUCTION	1
Chapter 2 LITERATURE REVIEW	6
2.1 BUBBLE SIZE DISTRIBUTIONS	6
2.2 CONVERSION OF BUBBLE PIERCED LENGTH TO BUBBLE SIZE	13
2.3 INFLUENCE OF THE ANGLE OF BUBBLE RISE ON THE INTERPRETATION OF SUBMERSIBLE PROBE SIGNALS	17
2.4 MIXING OF UNIFORM SOLIDS	19
2.5 SEGREGATION IN BINARY FLUIDIZED SYSTEMS	26
2.6 MOTION OF A LARGE AND LIGHTER PARTICLE IN A FLUIDIZED BED OF SMALLER PARTICLES	37
Chapter 3 EXPERIMENTAL	39
3.1 EXPERIMENTAL SYSTEM	39
3.1.1 Apparatus	39
3.1.2 Imaging System	41
3.1.3 Equipment Configuration	44
3.2 EXPERIMENTAL TECHNIQUE	47
3.2.1 Measurement of Bubble Size Distributions	47
3.2.1.1 Experimental procedure	47
3.2.1.2 Measurement method	47
3.2.2 Measurement of Bubble Pierced Length at an 'Imaginary' Probe	59
3.2.2.1 Experimental procedure	59
3.2.2.2 Measurement method	59
3.2.3 Measurement of the Angle of Bubble Rise and Bubble Velocity	63
3.2.3.1 Experimental procedure	63
3.2.3.2 Measurement method	63
3.2.4 Measurement of Tracer Concentration in the Mixing of Uniform Solids	68
3.2.4.1 Experimental procedure	68
3.2.4.2 Measurement method	70
3.2.5 Measurement of Jetsam Concentration in Segregating Binary Fluidized Systems	83
3.2.5.1 Experimental procedure	83
3.2.5.2 Measurement method	83

3.2.6 Measurement of the Circulation Patterns of Large and Lighter (or 'Active') Particle 91

3.2.6.1 Experimental procedure 91

3.2.6.2 Measurement methods 93

Chapter 4 RESULTS and DISCUSSION: BUBBLE HYDRODYNAMICS 97

4.1 DISTRIBUTIONS OF BUBBLE SIZE PARAMETERS 97

4.1.1 Theoretical Models 98

4.1.2 Comparison of Model Calculations with Experimental Data 101

4.1.3 Conclusions 118

4.2 CONVERSION OF BUBBLE PIERCED LENGTH TO BUBBLE SIZE 119

4.2.1 Theoretical Analysis 119

4.2.2 Computational Procedures 122

4.2.3 Distributions of Bubble Size Parameters 129

4.2.4 Overall Statistical Analysis 133

4.2.5 Approximate Relation between Bubble Pierced Length and Bubble Diameter Distributions 134

4.2.6 Requirements for Refinements in Theory 143

4.2.7 Conclusions 146

4.3 THE ANGLE OF BUBBLE RISE AND SUBMERSIBLE PROBE SIGNAL INTERPRETATION METHODS 148

4.3.1 Theoretical Analysis 148

4.3.2 Bubble Deformation 151

4.3.3 Measurements of Bubble Velocity 155

4.3.4 Effect of Non-Vertical Bubble Rise on Measurements using Two-element Probes 155

4.3.5 Effect of Bubble Selection Criteria on Multiple-tipped Probe Measurements 159

4.3.6 Relationship Between Bubble Velocity and Size 163

4.3.7 Effect of Bubble Shape on Velocity 165

4.3.8 Conclusions 170

171

Chapter 5 RESULTS and DISCUSSION: SOLIDS MIXING and SEGREGATION 171

5.1 MIXING OF UNIFORM SOLIDS 171

5.1.1 Theory 172

5.1.2 Model Parameters 176
5.1.3 Results of Model Comparison with Experimental Data 185
5.1.4 Discussion 205
5.1.5 Conclusions 208
5.2 SEGREGATION IN BINARY FLUIDIZED SYSTEMS 210
5.2.1 Theory 210
5.2.2 Model Parameters 218
5.2.3 Parametric Studies 220
5.2.4 Comparison with Experimental Results 240
5.2.5 Conclusions 265
5.3 MOTION OF A LARGE PARTICLE 270
5.3.1 Particle Motion and Circulation Pattern 270
5.3.1.1 Particle motion in one circulation 270
5.3.1.2 Overall circulation pattern 275
5.3.1.3 Theory for 'active' particle velocity 279
5.3.2 Phase Residence Probability 294
5.3.2.1 Experimental measurements 294
5.3.2.2 Theory for residence phase probability 296
5.3.2.3 Conclusions 299
Chapter 6 CONCLUSIONS AND RECOMMENDATIONS 300
NOMENCLATURE 308
REEFERENCE 315
APPENDIX A PARTICLE SIZE DISTRIBUTION 327
APPENDIX B MINIMUM FLUIDIZATION VELOCITY 330
APPENDIX C DERIVATION OF BUBBLE GROWTH MODEL OF DARTON (1977) IN 2-D SYSTEM 333
APPENDIX D COMPUTER PROGRAMS AND CODES 335

LIST OF FIGURES

		PAGE
FIGURE 3.1.1:	(a)Experimental setup for digital image analysis, (b) Schematic of the two-dimensional fluidized bed.	40
FIGURE 3.1.2:	The structure of a PCVISION frame grabber.	43
FIGURE 3.1.3:	(a) On-line measurement system; (b) Off-line measurement system.	45
FIGURE 3.2.1:	Histogram of grey scale value for an image consisting of emulsion and bubble phase with the peak on the left I_E represents the emulsion phase and the right I_B, represents the bubble phase. A threshold I_{TH} is selected to distinguish these phases.	48
FIGURE 3.2.2:	A block diagram showing the logic of the software for the measurement of bubble parameters by digital image analysis technique.	51
FIGURE 3.2.3:	Schematic of a small bubble used in reconstituation of the true bubble size	53
FIGURE 3.2.4a:	Typical distribution of bubble diameter showing the effect of correction for the undersized bubbles	56
FIGURE 3.2.4b:	Distribution of shape factor *S*;	57
FIGURE 3.2.4c:	Distribution of bubble aspect ration a.	58
FIGURE 3.2.5:	A schematic showing the position of an 'imaginary' probe, X.	62
FIGURE 3.2.6:	*Local* cumulative distributions for the bubble dimensions y, d_H, d_V and d_E measured from the experiments.	63
FIGURE 3.2.7:	Measurement of bubble velocity and angle of incidence utilizing 1 : 2 interlaced image scanning feature.	66
FIGURE 3.2.8:	Relationship between the reflected light intensity (grey scale) and concentration (volume fraction) of the coloured traces particles.	72
FIGURE 3.2.9:	Normalized calibration curves for tracer concentration for different types of coloured tracer particles.	74
FIGURE 3.2.10:	The continuously changing of threshold value for the bubble edge detection as a result of changing image intensity distribution.	75

FIGURE 3.2.11: A schematic of the analysis of tracer concentration in square cells along a horizontal plane in a fluidized bed. 78

FIGURE 3.2.12: A typical temporal response of (a) Concentration of solids tracer: (b) Bubble fraction across the bed width at height $Z/H_E = 0.254$. 79

FIGURE 3.2.13: Anomalous result in tracer concentration measurement at height near the initial tracer location 80

FIGURE 3.2.14: The sequence of images showing the distortion of tracer layer during the initial introduction of gas bubble into the bed. 81

FIGURE 3.2.15: Minimum fluidization velocity of mixture determined from fast defluidization procedure. 86

FIGURE 3.2.16: The fit of intensity change with composition of tracer concentration using exponential decay function. 87

FIGURE 3.2.17: Surface plot of jetsam concentration in a binary fluidized bed 89

FIGURE 3.2.18: Subdivision of search area and analysis of the region (one particle size) in the neighbourhood of the 'active' particle 95

FIGURE 3.2.19: The movement of an 'active' particle measured in a two-dimensional bubbling fluidized bed. 96

FIGURE 4.1.1a: Comparison of the model prediction for the bubble diameter density distribution with experimental data at different gas velocities
Curve A: d_0 by equation 4.1.18
Curve B: d_0 by equation 4.1.15 103

FIGURE 4.1.1b: Comparison of model prediction with experimental data 104

FIGURE 4.1.2a: Comparison of the model prediction for the bubble diameter distribution with experimental data at various bed heights.
Curve A: d_0 by equation 4.1.18
Curve B: d_0 by equation 4.1.15 105

FIGURE 4.1.2b: Comparison of model prediction with experimental data. 106

FIGURE 4.1.2c: Comparison of model prediction with experimental data. 107

FIGURE 4.1.2d: Comparison of model prediction with experimental data. 108

FIGURE 4.1.3a: Comparison of model prediction for the cumulative distribution of bubble size with experimental data at various bed heights.
Curve A: d_0 by equation 4.1.18
Curve B: d_0 by equation 4.1.15 111

FIGURE 4.1.3b: Comparison of model prediction with experimental data 112

FIGURE 4.1.4a: Comparison of average bubble size $\bar{d}_B$ with various empirical correlations as a function of bed height.
Curves A: by Agarwal (1987): B: Chiba et al (1975); C: Rowe and Yocono (1975); D: Werther (1978); E: Mori and Wen (1975). 113

FIGURE 4.1.4b: Comparison of experimental data with empirical correlations for average bubble size. 114

FIGURE 4.1.5: Comparison of average bubble size $\bar{d}_B$ with various empirical correlations as a function of gas velocity:
Curves A: by Agarwal (1987). d_0 by equation 4.1.18: B: Agarwal (1987) d_0 by equation 4.1.15; C: Chiba et al (1975); D: Rowe and Yocono (1975); E: Werther (1978); F: Mori and Wen (1975). 116

FIGURE 4.1.6: The plot of average bubble shape factor and aspect ratio with different bed heights. 117

FIGURE 4.2.1: Geometry of a probe in a cylindrical bed. 121

FIGURE 4.2.2: Geometry for the greater section of an ellipsoid 126

FIGURE 4.2.3a: Comparison of the predicted distributions of various bubble parameters (d_H, d_V, d_E, C_P) with experimental data at lower bed height using various bubble shape models.
a: spherical; b: ellipsoidal, a = 0.77; c: spherical cap, $\theta_w = 120°$; d: hemispherical and e: ellipsoidal, a = 0.77, Werthers method. $d_p = 2.12 \times 10^{-4}$ m, Z = 0.1 m, $U_0 = 0.101$ m/s, $2 L_{pr}/D_T = 0.0$ 130

FIGURE 4.2.3b: Comparisons of predicted distributions with experimental data. 130

FIGURE 4.2.3c: Comparison of predicted distributions with experimental data 131

FIGURE 4.2.3d: Comparison of predicted distributions with experimental data 131

FIGURE 4.2.4: Comparison of predicted (a) mean and (b) standard deviation of bubble horizontal dimension, d_H, using various bubble shape models, with the experimental data 136

FIGURE 4.2.5: Comparison of predicted (a) mean and (b) standard deviation of bubble vertical dimension, d_V, using various bubble shape models, with the experimental data 137

FIGURE 4.2.6: Comparisons of the predicted (a) mean and (b) standard deviation of bubble equivalent diameter, d_E, using various bubble shape models, with the experimental data. 138

FIGURE 4.2.7: Comparisons of the predicted (a) mean and (b) standard deviation of bubble equivalent circumference, C_P, using various bubble shape models, with the experimental data. 139

FIGURE 4.2.8: Comparisons between the mean values of different bubble dimensions (d_H, d_V, d_E) and mean bubble pierced length, y. 142

FIGURE 4.2.9: Experimental cumulative distributions for (a) pierced length, y, and (b) vertical dimension d_V measured at different lateral positions, $2L_{pr}/D_T$ in the bed 144

FIGURE 4.3.1: (a) Interpretation of probed signal for bubble moving at an angle θ_B

(b) Geometrical relationship of signals measured by the upper and lower probe. 149

FIGURE 4.3.2: Typical parametric results (for b = 10) on the ratio of inferred and actual velocity ($V_{B,m}/V_{B,\theta}$) as a function of angle of incidence, θ_B, and off-centre distance, $\tau = r/R$. 152

FIGURE 4.3.3: Extent of change and deformation for local bubble size (d_E), aspect ratio (a) and shape factor (S) between two image fields 1/50 s apart; experimental conditions: $Z/H_F = 0.55$, $2L_{pr}/W = 0.0$, $U_o/U_{mf} = 2.84$ 154

FIGURE 4.3.4a: Cumulative distributions of bubble velocity at different bed heights; experimental conditions: $2L_{pr}/W = 0.0$, $U_o/U_{mf} = 2.84$ 156

FIGURE 4.3.4b: Cumulative distributions of bubble velocity at different superficial gas velocities; experimental conditions: $Z/H_F = 0.55$, $2L_{pr}/W = 0.0$, $U_o/U_{mf} = 2.84$ 157

FIGURE 4.3.4c: Cumulative distributions of bubble velocity at different lateral bed positions; experimental conditions: $Z/H_F = 0.55$, $U_o/U_{mf} = 2.84$ 158

FIGURE 4.3.5: Distribution of the angle of incidence q_B of the rising bubbles measured at various experimental conditions and compared with the experimental results of Gunn and Al-Doori (1987)* 160

FIGURE 4.3.6: (a) Size and (b) velocity distribution for the entire population and those rising vertically at different gas velocity ($Z/H_F = 0.55$, $2 L_{pr}/W = 0.0$) 161

FIGURE 4.3.6: (c) Size and (d) velocity distribution for the entire population and those rising vertically at different heights ($U_o/U_{mf} = 2.84$) 162

FIGURE 4.3.7a: Distribution of the coefficient of bubble rise velocity K_B (based on d_V) for bubble swarms and injected bubbles (continuous and single) calculated from the simple bubble velocity and size relationship, equation (4.3.5) 164

FIGURE 4.3.7b: Distribution of the coefficient of rise velocity K_B (based on d_V) for bubble swarms calculated from equation 4.3.6 with the inclusion of $(U_o - U_{mf})$ and compared with the K_B obtained for a single bubble injection experimental calculated from (4.3.5) 166

FIGURE 4.3.8a: Distribution of the coefficient of bubble velocity $V_{B,S}$ for bubbles having different aspect ratio 168

FIGURE 4.3.8b: Scatter plot velocity $V_{B,S}$ and size d_V for different aspect ratio α; bubble swarms: (o : $\alpha < 1$; ▲ : $\alpha > 1$) ; single injection (* : $\alpha < 1$; ■: $\alpha > 1$) 169

FIGURE 5.1.1: Material balance on the tracer in (a) the upward moving wake (and drift) phase; (b) in the downward moving dense phase. 174

FIGURE 5.1.2: Comparison of experimentally measured bubble size with prediction using equation (5.1.13). 177

FIGURE 5.1.3a: Time averages of the experimentally measured bubble throughflow factor as a function of bed height. 179

FIGURE 5.1.3b: Probability density function of $(1 + f_W - K_T)$ inferred from experimentally measured time-averaged bubble fraction at different heights, superficial velocities and particles sizes. 180

FIGURE 5.1.4a: Predictions of axial concentration response of solids tracer using values of exchange coefficient calculated by various solids exchange models and comparison with the experimental data. 183

FIGURE 5.1.4b: Predictions of axial concentration response of solids tracer using values of exchange coefficient calculated by various solids exchange models and comparison with the experimental data. 184

FIGURE 5.1.5a Comparison of model predictions with experimental data for $d_p = 2.40 \times 10^{-4}$ m and $U_o/U_{mf} = 1.91$. 186

FIGURE 5.1.5b Comparison of model predictions with experimental data for $d_p = 2.40 \times 10^{-4}$ m and $U_o/U_{mf} = 2.21$. 187

FIGURE 5.1.5c Comparison of model predictions with experimental data for $d_p = 2.40 \times 10^{-4}$ m and $U_o/U_{mf} = 2.50$. 188

FIGURE 5.1.5d Comparison of model predictions with experimental data for $d_p = 2.40 \times 10^{-4}$ m and $U_o/U_{mf} = 4.63$ 189

FIGURE 5.1.6: Comparison of model prediction with experimental data for $d_p = 5.12 \times 10^{-4}$ m and $U_o/U_{mf} = 2.2$. 191

FIGURE 5.1.7: Comparison of model prediction with experimental data for $d_p = 7.25 \times 10^{-4}$ m and $U_o/U_{mf} = 1.75$ 192

FIGURE 5.1.8a: Comparison of model prediction with experimental data: influence of intitial tracer location; $d_p = 2.4 \times 10^{-4}$ m and $U_o/U_{mf} = 2.21$; $q = 0.0$. 193

FIGURE 5.1.8b: Comparison of model prediction with experimental data: influence of intitial tracer location; $d_p = 2.4 \times 10^{-4}$ m and $U_o/U_{mf} = 2.21$; $q = 0.4$. 194

FIGURE 5.1.9a: Replicate tests 198

FIGURE 5.1.9b: Replicate tests 199

FIGURE 5.1.10a: Estimation of the average downward solids velocity, $\bar{U}_S$, from tracer arrival (break-through) time measurement: $d_p = 2.4 \times 10^{-4}$ m 200

FIGURE 5.1.10b: Estimation of the average downward solids velocity, $\bar{U}_S$, from tracer arrival (break-through) time measurement: $d_p = 5.12 \times 10^{-4}$ m 201

FIGURE 5.1.10c: Estimation of the average downward solids velocity, $\bar{U}_S$, from tracer arrival (break-through) time measurement: $d_p = 7.25 \times 10^{-4}$ m 202

FIGURE 5.1.11: Comparison of the measured average dense phase solids velocity $\bar{U}_S$ with model calculation by equation (5.1.16). 203

FIGURE 5.1.12: Plots of the estimated exchange constant A_{WE} with U_O/U_{mf} for different bed particle sizes. 204

FIGURE 5.1.13: Plots of exchange coefficient k_W estimated from the present model analysis as a function of bubble size d_B and compared with the values calculated from solids exchange models by (Chiba and Kobayashi, 1977; and Yoshida and Kunii, 1968). 206

FIGURE 5.2.1: Material balance on the jestam in (a) the upward moving wake (and drift) phase; (b) in the downward moving dense phase. 212

FIGURE 5.2.2a: Simulated response of (i) jetsam concentration; (ii) bubble size and (iii) bubble fraction as a function of time at different bed heights using G-R model (model parameters: $U_O = 0.15$m/s; $d_J/d_F = 3.0$; $\rho_J/\rho_F = 1.0$, $U_{mf,J}/U_{mf,F} = 5.6$, $Y_{GR} = 0.65$, $f_w = 0.35$) 221

FIGURE 5.2.2b: Simulated response of jetsam concentration as a function of height within the bed at different times using G-R model (model parameters: $U_O = 0.15$m/s; $d_J/d_F = 3.0$; $\rho_J/\rho_F = 1.0$, $U_{mf,J}/U_{mf,F} = 5.6$, $Y_{GR} = 0.65$, $f_w = 0.35$) 223

FIGURE 5.2.2c: Predicted height of the defluidized layer as a function of time using G-R model (model parameters: $U_O = 0.15$m/s; $d_J/d_F = 3.0$; $\rho_J/\rho_F = 1.0$, $U_{mf,J}/U_{mf,F} = 5.6$, $Y_{GR} = 0.65$, $f_w = 0.35$) 224

FIGURE 5.2.3a: Simulated response of (i) jetsam concentration; (ii) bubble size and (iii) bubble fraction as a function of time at different bed heights using Yoshida model (model parameters: U_o = 0.15m/s; d_J/d_F = 3.0; ρ_J/ρ_F = 1.0, $U_{mf,J}/U_{mf,F}$ = 5.6, Y_Y = 0.6, f_w = 0.35) 225

FIGURE 5.2.3b: Simulated response of jetsam concentration as a function of height within the bed at different times using Yoshida model (model parameters: U_o = 0.15m/s; d_J/d_F = 3.0; ρ_J/ρ_F = 1.0, $U_{mf,J}/U_{mf,F}$ = 5.6, Y_Y = 0.6, f_w = 0.35) 226

FIGURE 5.2.4a: Influence of superficial gas velocity on the transient response of jetsam concentration at Z = 0.05m using G-R model (model parameters: U_o = variable; d_J/d_F = 3.0; ρ_J/ρ_F = 1.0, $U_{mf,J}/$ = 5.6, = 0.65, f_w = 0.35) 228

FIGURE 5.2.4b: Influence of superficial gas velocity on the axial jetsam concentration profile at t = 60s using G-R model (model parameters: U_o = variable; d_J/d_F = 3.0; ρ_J/ρ_F = 1.0, $U_{mf,J}/U_{mf,F}$ = 5.6, Y_{GR} = 0.65, f_w = 0.35) 229

FIGURE 5.2.4c: Influence of superficial gas velocity on the predicted height of the defluidized layer as a function of time using G-R model (model parameters: U_o = variable; d_J/d_F = 3.0; ρ_J/ρ_F = 1.0, $U_{mf,J}/$ = 5.6, Y_{GR} = 0.65, f_w = 0.35) 230

FIGURE 5.2.5a: Influence of superficial gas velocity on the transient response of jetsam concentration at Z = 0.05m using Yoshida model (model parameters: U_o = variable; d_J/d_F = 3.0; ρ_J/ρ_F = 1.0, $U_{mf,J}/U_{mf,F}$ = 5.6, Y_Y = 0.6, f_w = 0.35) 231

FIGURE 5.2.5b: Influence of superficial gas velocity on the axial jetsam concentration profile at t = 60s using Yoshida model (model parameters: U_o = variable; d_J/d_F = 3.0; ρ_J/ρ_F = 1.0, $U_{mf,J}/$ = 5.6, Y_Y = 0.6, f_w = 0.35) 232

FIGURE 5.2.5c: Influence of superficial gas velocity on the predicted height of the defluidized layer as a function of time using Yoshida model (model parameters: U_o =

variable; d_J/d_F = 3.0; ρ_J/ρ_F = 1.0, $U_{mf,J}/U_{mf,F}$ = 5.6, Y_Y = 0.6, f_w = 0.35) 233

FIGURE 5.2.6a: Influence of segregation rate parameter on the transient response of jetsam concentration at Z = 0.05m using G-R model (model parameters: U_o = 0.15m/s; d_J/d_F = 3.0; ρ_J/ρ_F = 1.0, $U_{mf,J}/U_{mf,F}$ = 5.6, Y_{GR} = variable, f_w = 0.35) 234

FIGURE 5.2.6b: Influence of segregation rate parameter on the axial jetsam concentration profile at t = 60s using G-R model (model parameters: U_o = 0.15m/s; d_J/d_F = 3.0; ρ_J/ρ_F = 1.0, $U_{mf,J}/U_{mf,F}$ = 5.6, Y_{GR} = variable, f_w = 0.35) 235

FIGURE 5.2.6c: Influence of segregation rate parameter on the predicted height of the defluidized layer as a function of time using G-R model (model parameters: U_o = 0.15m/s; d_J/d_F = 3.0; ρ_J/ρ_F = 1.0, $U_{mf,J}/$ = 5.6, Y_{GR} = variable, f_w = 0.35) 236

FIGURE 5.2.7a: Influence of segregation rate parameter on the transient response of jetsam concentration at Z = 0.05m using Yoshida model (model parameters: U_o = 0.15m/s; d_J/d_F = 3.0; ρ_J/ρ_F = 1.0, $U_{mf,J}/U_{mf,F}$ = 5.6, Y_Y = variable, f_w = 0.35) 237

FIGURE 5.2.7b: Influence of segregation rate parameter on the axial jetsam concentration profile at t = 60s using Yoshida model (model parameters: U_o = 0.15m/s; d_J/d_F = 3.0; ρ_J/ρ_F = 1.0, $U_{mf,J}/U_{mf,F}$ = 5.6, Y_Y =variable, f_w = 0.35) 238

FIGURE 5.2.7c: Influence of segregation rate parameter on the predicted height of the defluidized layer as a function of time using Yoshida model (model parameters: U_o = 0.15m/s; d_J/d_F = 3.0; ρ_J/ρ_F = 1.0, $U_{mf,J}/U_{mf,F}$ = 5.6, Y_Y = variable, f_w = 0.35) 239

FIGURE 5.2.8a: Experimentally measured minimum fluidization velocity as a function of jetsam mass fraction in binary mixtures of equi-density particles

(set A): $d_J/d_F = 3.02$; $\rho_J/\rho_F = 1.0$
(set B): $d_J/d_F = 2.14$; $\rho_J/\rho_F = 1.0$ 241

FIGURE 5.2.8b: Experimentally measured minimum fluidization velocity as a function of jetsam mass fraction in binary mixtures of particles of differing densities and sizes

(set C): $d_J/d_F = 1.73$; $\rho_J/\rho_F = 1.43$
(set D): $d_J/d_F = 1.26$; $\rho_J/\rho_F = 1.43$ 242

FIGURE 5.2.9a: Experimental response of jetsam concentration as a function of time at different bed heights for U_o = 0.155m/s; particle properties (set A): $d_J/d_F = 3.02$; $\rho_J/\rho_F = 1.0$, $U_{mf,J}/ = 5.6$ 244

FIGURE 5.2.9b: Experimental response of bubble fraction as a function of time at different bed heights for U_o = 0.155m/s; particle properties (set A): $d_J/d_F = 3.02$; $\rho_J/\rho_F = 1.0$, $U_{mf,J}/U_{mf,F} = 5.6$ 245

FIGURE 5.2.9c: Experimental axial jetsam concentration profile at different times for U_o = 0.155m/s; particle properties (set A): $d_J/d_F = 3.02$; $\rho_J/\rho_F = 1.0$, $U_{mf,J}/U_{mf,F} = 5.6$ 246

FIGURE 5.2.10a: Experimental response of jetsam concentration as a function of time at different bed heights for U_o = 0.152m/s; particle properties (set C): $d_J/d_F = 1.73$; $\rho_J/\rho_F = 1.43$, $U_{mf,J}/U_{mf,F} = 4.7$ 247

FIGURE 5.2.10b: Experimental response of bubble fraction as a function of time at different bed heights for U_o = 0.152m/s; particle properties (set C): $d_J/d_F = 1.73$; $\rho_J/\rho_F = 1.43$, $U_{mf,J}/U_{mf,F} = 4.7$ 248

FIGURE 5.2.10c: Experimental axial jetsam concentration profile at different times for U_o = 0.152m/s; particle properties (set C): $d_J/d_F = 1.73$; $\rho_J/\rho_F = 1.43$, $U_{mf,J}/U_{mf,F} = 4.7$ 249

FIGURE 5.2.11a: Experimental response of jetsam concentration as a function of time for different superficial velocities at Z = 0.02m; particle properties (set A): $d_J/d_F = 3.02$; $\rho_J/\rho_F = 1.0$, $U_{mf,J}/U_{mf,F} = 5.6$ 250

FIGURE 5.2.11b: Experimental axial jetsam concentration profile for different superficial velocities at t=60s particle properties (set A): d_J/d_F = 3.02; ρ_J/ρ_F = 1.0, $U_{mf,J}/U_{mf,F}$ = 5.6 251

FIGURE 5.2.12a: Experimental response of jetsam concentration as a function of time for different superficial velocities at Z = 0.019m; particle properties (set C): d_J/d_F = 1.73; ρ_J/ρ_F = 1.43, $U_{mf,J}/U_{mf,F}$ = 4.7 253

FIGURE 5.2.12b: Experimental axial jetsam concentration profile for different superficial velocities at t=40s particle properties (set C): d_J/d_F = 1.73; ρ_J/ρ_F = 1.43, $U_{mf,J}/U_{mf,F}$ = 4.7 254

FIGURE 5.2.13a: Experimental response of jetsam concentration as a function of time for different superficial velocities at Z = 0.02m; particle properties (set D): d_J/d_F = 1.26; ρ_J/ρ_F = 1.43, $U_{mf,J}/U_{mf,F}$ = 2.45 255

FIGURE 5.2.13b: Experimental axial jetsam concentration profile for different superficial velocities at t=60s particle properties (set D): d_J/d_F = 1.26; ρ_J/ρ_F = 1.43, $U_{mf,J}/U_{mf,F}$ = 2.45 256

FIGURE 5.2.14a: Experimental response of jetsam concentration as a function of time at different bed heights for U_O = 0.166m/s; particle properties (set B): d_J/d_F = 2.14; ρ_J/ρ_F = 1.0, $U_{mf,J}/U_{mf,F}$ = 3.23 257

FIGURE 5.2.14b: Experimental axial jetsam concentration profile at different times for U_O = 0.166m/s; particle properties (set B): d_J/d_F = 2.14; ρ_J/ρ_F = 1.0, $U_{mf,J}/U_{mf,F}$ = 3.23 258

FIGURE 5.2.15a: Dimensionless height of the defluidized layer, Z*, as a function of dimensionless time, t*, for Set A (d_J/d_F = 3.02; ρ_J/ρ_F = 1.0, $U_{mf,J}/U_{mf,F}$ = 5.6) particles. 261

FIGURE 5.2.15b: Dimensionless height of the defluidized layer, Z*, as a function of dimensionless time, t*, for Set B (d_J/d_F = 2.14; ρ_J/ρ_F = 1.0, $U_{mf,J}/U_{mf,F}$ = 3.23) particles. 262

FIGURE 5.2.15c: Dimensionless height of the defluidized layer, Z*, as a function of dimensionless time, t*, for Set C (d_J/d_F = 1.73; ρ_J/ρ_F = 1.43, $U_{mf,J}/U_{mf,F}$ = 4.7) particles. 263

FIGURE 5.2.15d: Dimensionless height of the defluidized layer, Z*, as a function of dimensionless time, t*, for Set D (d_J/d_F = 1.26; ρ_J/ρ_F = 1.43, $U_{mf,J}/U_{mf,F}$ = 2.45) particles. 264

FIGURE 5.2.16: Time to reach the equilibrium defluidized layer height, $t_{P,S}$, as a function of the modified excess gas velocity, $(Uo-U^*_{mf,C})$, for Set A (d_J/d_F = 3.02; ρ_J/ρ_F = 1.0, $U_{mf,J}/U_{mf,F}$ = 5.6) and Set C (d_J/d_F = 1.73; r_J/r_F = 1.43, $U_{mf,J}/U_{mf,F}$ = 4.7) particles. 266

FIGURE 5.2.17: The equilibrium defluidized layer height, $Z_{P,S}$, as a function of the modified excess gas velocity, $(Uo-U^*_{mf,C})$, for Set A (d_J/d_F = 3.02; ρ_J/ρ_F = 1.0, $U_{mf,J}/U_{mf,F}$ = 5.6) and Set C (d_J/d_F = 1.73; r_J/r_F = 1.43, $U_{mf,J}/U_{mf,F}$ = 4.7) particles. 267

FIGURE 5.2.18: The equilibrium defluidized layer height, C as a function of the time required to reach equilibrium height, $t_{,P,S}$, for Set A (d_J/d_F = 3.02; r_J/r_F = 1.0, $U_{mf,J}/U_{mf,F}$ = 5.6) and Set C (d_J/d_F = 1.73; ρ_J/ρ_F = 1.43, $U_{mf,J}/U_{mf,F}$ = 4.7) particles. 268

FIGURE 5.3.1: (a) Lateral position of the 'active' particle as a function of time
(b) Velocity component in the x-direction, $V_{A,x}$ as a function of time. 272

FIGURE 5.3.1: (c) Vertical position of the 'active' particle as a function of time
(d) Velocity component in the y-direction, $V_{A,y}$ as a function of time. 273

FIGURE 5.3.1: (e) Resultant velocity of the 'active' particle as a function of time
(f) Bubble-particle interaction as a function of time 274

FIGURE 5.3.2: Circulation pattern of an 'active' particle in the fluidized bed 275

FIGURE 5.3.3a: Angular direction of 'active' particle motion. 276

FIGURE 5.3.3b:	Magnitude of 'active' particle velocity in various regions of the bed.	278
FIGURE 5.3.4a:	Height-averaged velocity of the 'active' particle at different lateral positions.	280
FIGURE 5.3.4b:	The cumulative distributions of the height-averaged absolute particle velocity in different regions of the bed.	281
FIGURE 5.3.5a:	The downward velocity of the 'active' particle in the wall region, $V_{A,DW}$, as a function of height: Comparison of experiment with theory.	283
FIGURE 5.3.5b:	Height-averaged velocity of the 'active' particles in two different regions of the bed as a function of excess gas velocity.	284
FIGURE 5.3.6:	Plot of $V_{A,UC}$ and U_B as a function of $V_{A,DC}$	287
FIGURE 5.3.7:	Comparison of the experimental data of Nienow et al. (1978) with calculations using equation (5.3.3)	289
FIGURE 5.3.9:	Schematic diagram of 'active' particle motion around a bubble.	293
FIGURE 5.3.8:	Downward velocity of the active particle in the central region, $V_{A,DC}$, and the wake exchange constant, A_{WE}, as a function of U_o/U_{mf}	291
FIGURE 5.3.10:	Cumulative faction of events as a function of the number cells surrounding the 'active' particle in the bubble void.	295
FIGURE 5.3.11:	Dense phase residence probability as a function of excess gas velocity. Comparison of theory with experiment.	298
FIGURE A1:	Cumulative size distribution for glass ballotini type AB	328
FIGURE A2:	Cumulative size distribution for glass ballotini type C	328
FIGURE A3:	Cumulative size distribution for glass ballotini type B	329
FIGURE A4:	Cumulative size distribution for glass ballotini type A	329
FIGURE B1:	Minimum fluidization velocity determination for glass ballotini of one batch under classification type AB.	331

FIGURE B1: Minimum fluidization velocity determination for glass ballotini of another batch under classification type AB. 331

FIGURE B1: Minimum fluidization velocity determination for glass ballotini for type B. 332

FIGURE B1: Minimum fluidization velocity determination for glass ballotini for type A. 332

LIST OF TABLES

	PAGE
TABLE 2.1. SUMMARY OF BUBBLE HYDRODYNAMIC MEASUREMENT TECHNIQUES	9
TABLE 2.2. RELATIONSHIP BETWEEN AVERAGE BUBBLE PIERCED LENGHT AND DIAMETER	16
TABLE 2.3. A REVIEW OF THE STUDIES ON MIXING OF UNIFORM SOLIDS	22
TABLE 2.4. A REVIEW OF STUDIES ON SEGREGATION IN FLUIDIZED BED	30
TABLE 3.1. EXPERIMENTAL OPERATING CONDITIONS FOR MEASUREMENTS ON BUBBLE PIERCED LENGTHS	60
TABLE 3.2. EXPERIMENTAL OPERATING CONDITIONS FOR BUBBLE VELOCITY MEASUREMENTS	64
TABLE 3.3. EXPERIMENTAL CONDITIONS FOR STUDIES ON MIXING OF UNIFORM SOLIDS	69
TABLE 3.4. PHYSICAL PROPERTIES OF PARTICLES USED IN SEGREGATION STUDIES	84
TABLE 3.5. EXPERIMENTAL CONDITIONS FOR SEGREGATION STUDIES	85
TABLE 3.6. EXPERIMENTAL CONDITIONS FOR THE STUDY OF LARGE PARTICLE MOTION AND DENSE PHASE RESIDENCE PROBABILITY MEASUREMENT	92
TABLE 4.1. EMPIRICAL CORRELATIONS FOR AVERAGE BUBBLE SIZE.	110
TABLE 4.2. GEOMETRICAL RELATIONSHIPS FOR VARIOUS SHAPES.	125
TABLE 4.3. BUBBLE SHAPES AND SHAPE PARAMETERS	127
TABLE 4.4a. OVERALL ERRORS ANALYSIS ON THE MEAN VALUES.	135
TABLE 4.4b. OVERALL ERRORS ANALYSIS ON THE STANDARD DEVIATION.	135
TABLE 4.5. CORRELATION BETWEEN THE EXPERIMENTAL MEAN AND STANDARD DEVIATION OF VARIOUS BUBBLE DIMENSIONS.	141
TABLE 5.1 SUMMARY OF MODELLING RESULTS ON MIXING OF UNIFORM SOLIDS	196

SUMMARY

In the design of bubbling fluidized-bed reactors, a good understanding of the bubbling phenomena is required. It has been well recognized that the bubble hydrodynamics influence the solids mixing and segregation in the fluidized bed. Although the mechanisms for solids mixing and segregation have been reasonably well studied and characterized, detailed modelling and experimental verification of the behaviour of the fluidized bed still remains a challenge. The key limitation lies in the scarcity of experimental data on simultaneous characterization of bubble flow and solids mixing.

In this study, novel techniques utilising digital image analysis have been developed for quantitative measurement of bubbling phenomenon with the presence of both bubble and dense phases in a two-dimensional fluidized bed.

The development of the experimental techniques for the measurement of the gas bubble parameters, concentration of coloured solids tracer in homogeneous and binary particle systems will be described. In addition, a unique experimental method for the tracking of the larger and lighter particles circulating in the fluidized bed will also be presented. The measurement and analysis methods are objective and fully automated, hence, eliminating all subjective determination and tedious manual effort on data acquisition and analysis.

In the study of the bubble hydrodynamics, distributions of bubble size, shape, velocity in a two-dimensional bed have been measured for various bed heights, particle sizes and operating conditions. In addition, pierced length and several size measures of bubbles intercepted at an 'imaginary' probe in a thin two-dimensional fluidized bed were measured. Prediction of bubble size from measurements on bubble pierced lengths

using the geometrical probability approach and bubble shape assumptions has been assessed and discussed. Measurement of the bubble size/shape, velocity and the angle of rise also enable experimental assessment of the limitations of dual-tipped probes commonly used in three-dimensional beds.

In the solids mixing study, the course of mixing of uniform solids in two-dimensional bubbling fluidized beds has been followed. In this investigation, experimental data have been obtained on the axial mixing of uniform solids. Oscillations in the concentration response, resulting from the gross circulation of the solids, have been observed experimentally. These oscillations become increasingly more prominent as the bed particle size increases. These measurements have been used to evaluate the three-phase counter-current back-mixing model. The bubble parameters required for the model were obtained from independent experiments conducted as a part of this investigation; the exchange coefficient, however, was found by parameter estimation using the solids mixing data. With this choice of parameters, the counter-current flow model has been found to predict the experimental trends reasonably well. The estimated values for the exchange coefficient do not compare favourably with the predictions of the models available in the literature. These models predict that the wake exchange coefficient should increase with increase in the minimum fluidization velocity of the bed particles. Our results, on the other hand, show that the wake exchange coefficient increases with U_O/U_{mf} for $U_O/U_{mf} < 3$ and the values, in this region, are independent of the particle size.

The technique used for the study of mixing of uniform particles was extended to the study of segregation phenomenon resulting from size or density differences. Unsteady material balance equations from the Gilibaro-Rowe (1974) and Yoshida (1980) models for segregating fluidized beds were solved numerically. The possibility of the formation of a defluidized layer at the bottom of the bed was taken into account.

Comparison of model predictions with data indicated that though these models did reflect some features of the experiment, the influence of the superficial velocity on the temporal variation of the concentration at any specific height within the bed was not predicted. In fact, a trend completely opposite to that predicted was observed experimentally. If these models are to be used, then the segregation rate parameter must have a dependence on superficial velocity substantially different to that currently available in the literature. Further work in this direction is recommended. The influence of jetsam concentration was not explored in this experimental study; such measurements are recommended as well.

Some preliminary empirical relations were established for the movement of the defluidized layer with time. In particular, a promising new indicator for segregation propensity was proposed from analogy with vapour-liquid equilibrium data representation methods. Additional data are necessary before further generalization can be attempted.

Finally, a specific aspect of bubbling beds which has important significance, especially in the area of coal combustion, has been investigated. In bubbling fluidized bed combustion, large coal particles - comprising about 1% of the total bed inventory - are fluidized along with smaller sulphur-sorbent particles. The density of the coal particles is less than that of the bed particles. This combination of the concentration, size and density for coal and bed particles results in the setting up of circulation pattern for the coal particles. The motion of a larger and lighter particle circulating in a fluidized bed has been determined. The larger particle was found to move downward near the wall region and travel up in the central core of the fluidized bed in a jerky manner. The characteristic particle velocities in both regions have been measured. The present

experimental technique enables, for the first time, the determination of the phase residence probability of the particles associating with the dense phase. A simple model has been proposed for the prediction of this quantity as a function of excess gas velocity.

Chapter 1

INTRODUCTION

The first large-scale, commerically significant fluidized bed commenced smooth operation in 1926. The process, known as the Winkler gas generator, involved the gasification of powdered coal. The Winkler gas generator may be considered inefficient by today's standards because of its high oxygen consumption and its large carbon loss through entrainment.

The application of fluidized bed technology to commercial processes has grown phenomenally over the decades since the Winkler gas generator was state-of-the-art. Examples of current commerical applications are in the production of ethylene, alkyl chloride, phthalic anhydride and polypropylene. Processes using fluidized bed technology include catalytic cracking; catalytic reforming and coking; coal drying; combustion and gasification; calcination and nuclear fuel preparation.

It is well known that gas flow in excess of that required to maintain minimum fluidization conditions flows through the bed in the form of gas pockets or bubbles. These bubbles are responsible for the behaviour of the fluidized bed in terms of its

mixing, heat/mass transfer and reactant conversion capabilities. Consequently, much research has been directed towards linking the behaviour of bubbles to the performance of a fluidized bed.

A bubbling fluidized bed is a two-phase reactor. In the study of the hydrodynamics of such beds, most experimental techniques reported in the literature measure the characteristics of one of the phases in isolation of the other. For example, several probes have been developed which measure only bubble characteristics. Solids mixing studies, on the other hand, are ofter carried out by sectioning slumped beds or monitoring the movement of tracer particles - such studies ignore bubble behaviour.

It would be preferable, if possible, to study the behaviour of the bubble and solid phases simultaneously - unwarranted assumptions could then be avoided. Currently, the only possibility in this direction is the use of two-dimensional (or thin) beds made of transparent walls which permit non-intrusive and direct viewing of what is happening inside.

Such beds have been used very often in the past to obtain qualitative and quantitative information on bubble characteristics. However, photographic techniques employed to extract quantitative information on bubbles are laborious and require subjective interpretation in the delineation of bubble-solid phase boundaries. The labour-intensive effort reduces the motivation for obtaining sufficient data for making reasonable statistical inferences.

Two-dimensional beds have also been used to study the influence of bubble motion on the motion of solids in the bed. The aim of these studies was to obtain an understanding of the underlying mechanisms. Extraction of quntitative information has remained extremely difficult especially under freely bubbling conditions.

In this research, novel, non-intrusive digital image analysis methods have been developed and used to study the behaviour of bubbles and solid phases in two-dimensional beds. These procedures provide several key advantages which make them extremely attractive for simultaneous measurements of the two phases. A high level of automation is introduced into the acquisition, processing and analysis of digitized images. The laborious manual effort and consequent tedium of previous studies have been dramatically alleviated. Automation of the analysis procedure means that a large number of images are captured for any data set. This should improve the statistical accuracy of any ensemble estimates produced. The use of these techniques also improves the reliability of delineation of the phase boundaries as edge detection is objective and consistent.

In the research reported in this thesis, digital image analysis techniques have been used on two-dimensional fluidized beds to tackle the following problems :

- measurement of bubble size distributions;
- evaluation of geometrical probability methods for interpretation of pierced length signals obtained from dual-tipped submersible probes frequently employed for bubble characterization in three-dimensional beds;
- evaluation of the influence of non-vertical bubble rise on the interpretation methods, and designs, of submersible probes used in three-dimensionsal fluidized beds;
- measurement and interpretation of tracer concentration profiles in fluidized beds of uniform particles;
- measurement and interpretation of jetsam concentration profiles in segregating binary fluidized beds; and

• tracking of a larger and lighter (or 'active') particle in fluidized beds of smaller and heavier particles.

In the literature reservations have been expressed regarding the use of two-dimensional beds to obtain quantitative information applicable to large beds. In a sense, the same objection can be raised against the frequently used small diameter cylidrical beds since they are likely to slug even for comparatively low excess gas velocities. Whether the measurements made in the two-dimensional beds apply quantitatively to large scale beds can be debated. Nevertheless, the studies made relating to the calibration of submersible probes will be of assistance in developing improved submersible probe designs. Bubble properties measured in the two-dimesional bed are used in the interpretation of data on solids mixing and segregation. In principle, this offers an opportunity to evaluate the detailed models for the behaviour of solids in fluidized beds reported in the literature.

In **Chapter 2** a brief literature review is presented for the topics examined in the research programme. Much has been published about fluidized beds in the past four decades and many excellent reviews are available. The emphasis in this chapter has been placed on providing a summary in tabular form; the reviews have been referred to for details.

Details of the experimental apparatus and procedures employed are provided in **Chapter 3**. The configurations of the imaging hardware used in the measurements are described. The principles of the algorithms developed for the measurements made are also presented.

Results relating to the bubble phase, measurements as well as theory, are given and discussed in **Chapter 4**.

Chapter 5 presents the experimental and theoretical results on the behaviour of solids in fluidized beds.

Conclusions from this work and recommendations for further work are outlined in **Chapter 6**.

Chapter 2

LITERATURE REVIEW

Much has been written about bubbling fluidization in the past four decades. It is not proposed to review the entire literature in this section. This would be ambitious and, in view of the several excellent reviews on this important subject, unnecessary. The literature review presented here, therefore, provides what might be termed as introductory notes and remarks which form the basis for the research; reviews available in the literature have been referred to for details.

2.1 BUBBLE SIZE DISTRIBUTIONS

Bubble characteristics strongly influence the hydrodynamics of fluidized beds and determine the performance of fluidized bed reactors and combustors. The extent of gas-solid mixing, heat and mass transfer as well as conversion are governed by the number, size and motion of bubbles passing through the bed. In a bubbling bed, bubbles rise from the distributor in swarm and grow in size as they travel up the bed. The principal mechanism of growth is bubble coalescence. Earlier researchers (Yasui and Johanson, 1958; Kato and Yen, 1969; Geldart, 1969; Chiba et al., 1973; Mori and Wen, 1975; Darton et al., 1977; Rowe, 1976) attempted to describe the process of bubble growth and proposed a variety of semi-empirical correlations for the

estimation of variation of the mean bubble diameter with bed height. Very few workers (Chiba, et al. 1975; Rowe and Yocono, 1975; Burgess and Calderbank, 1975; Werther, 1974; Sung and Burgess, 1987; Glicksman, et al., 1987) have reported the longitudinal as well as lateral distribution of bubble sizes. In a detailed design of a fluidized bed reactor or combustor, the importance of the lateral distribution of the bubble sizes should not be overlooked.

Recently, mathematical models based on the population balance approach to describe bubble growth in fluidized beds have been developed (Argyriou, 1971; Shah et al., 1977; Agarwal, 1985, 1987; Fox and Fan, 1987).

In particular, analytic expressions were derived for the distribution of key bubble characteristics such as velocity, diameter and volume by Agarwal (1985). However, verification of these models has been seriously disadvantaged by the lack of relevant experimental data.

Several experimental techniques have been employed for the measurement of bubble parameters. The work has been conducted in either two- or three-dimensional beds. In general, the measurement techniques can be classified into two catagories depending on the nature of the sensors contacting the bubble phase. Miniature capacitance/resistance probes (Burgess and Calderbank, 1975; Geldart and Kelsey, 1972; Werther and Molerus, 1973a, b), optical probes (Glicksman et al., 1987) and static pressure probes (Atkinson and Clark, 1988) are classified as internal sensors. Such sensors make direct contact with the bubbles. The intrusive nature of these submersible probes is expected to alter the local fluidization conditions. Moreover, the characterization of the bubble sizes and shapes from the measurement of the bubble pierced lengths requires extensive data interpretation and calibration. External sensors include the X-ray (Rowe and Everett, 1972), γ-ray (Weimer et al., 1985),

laser (Sung and Burgess, 1987) and photographic methods(Chiba et al., 1975; Saxena et al., 1984). All except for X-ray and γ-ray techniques are performed in two-dimensional beds. These techniques provide good visual observation thereby improving qualitative understanding of bubble behaviour. Unfortunately, the collection of quantitative data necessitates subsequent frame-by-frame analysis of the images. This can be time consuming and laborious. A brief summary adapted from Cheremisinoff (1986) of the experimental techniques is presented in **Table 2.1**. The need for an automated technique which permits rapid collection of reliable data on bubble is evident.

In this research digital image analysis methods have been developed for measuring bubble size distributions. The tasks of data collection and analysis have been automated. Large sample sizes enable more accurate statistical analysis.

TABLE 2.1. SUMMARY OF BUBBLE HYDRODYNAMIC MEASUREMENT TECHNIQUES

General measurement basis	Detailed measurement basis	Distribution of mean	Sensor installation	Disadvantages / Difficulties	Advantages	Reference
Photographic	Still photography	no	External to test section	1. only provides record of wall conditions 2. requires large number of stills to obtain size distribution	1. very simple equipment 2. nondisturbing flow field	Rowe (1971)
	Cine photography (high speed (>80 frames/s) and related photographic methods)	yes (size, shape, and rise velocity)	same	1. same as for still photography 2. data abstraction tedious 3. errors in data abstraction-subjective 4. high-quality photographs needed for automatiac/semi-automatic data abstraction 5. depth of field and special lighting arrangement to be considered	1. same as still photography	Rowe (1971)
X-rays	X-ray detection through vessel walls	yes (size and shape)	External to test section	1. difficult to use in large beds 2. penetration limitation of 0.15 cm 3. high cost 4. best resolution of data limited to single jet bubbling phenomena	1. can scan over column height 2. nondisturbing to flow field	Rowe and Partridge (1965), Rowe and Everett (1972), Rowe (1971)
Optical	Light obscuraction (detector counting of nonobscured light ray) also lasers	yes (equivalent size, rise velocity	External to test section or *in situ*	1. uses absolute intensity measurement 2. problems of coincidence and edge effects 3. assumes spherical bubbles - inaccuracies in size	1. nondisturbing to some flow fields	Yasui and Johanson (1958), Yoshida et al. (1978a)

TABLE 2.1. SUMMARY OF BUBBLE HYDRODYNAMIC MEASUREMENT TECHNIQUES (continued)

General measurement basis	Detailed measurement basis	Distribution of mean	Sensor installation	Disadvantages / Difficulties	Advantages	Reference
	Fibre optics	yes (equivalent size, rise velocity	*in situ*	1. same as light transmission 2. limited to low temperature measurements - material problem (LED and photocell, epoxy resin, etc, selection)	1. same	Okhi and Shirai (1978)
Pressure fluctuations	Uses pressure difference between bubble and emulsion phases	no (mean size, rise velocity for slugging beds only)	Sensor exposed to flow at wall	1. difficult to calibrate 2. signal analysis most reliable for slugging beds 3. no information on bubble shape 4. no information on spatial distribution of bubbles across column	1. nondisturbing to flow field 2. simple technique/low cost 3. can provide slug rise velocity and av slug length by cross-correlation of transducer signals over column height 4. provides qualitative identification of fluidizing regime and quantitative data on dominant bed frequency	Littman and Homolka (1970)
Electromagnetic waves	γ–*rays* transmission	no (mean bed voidage)	External to test section	1. uses absolute intensity measurement 2. sphericalbubble assumption applied to mean voidage measurement in obtaining size 3. does not provide rise velocity 4. costly	1. simple arrangement 2. nondisturbing to flow field	Wiemer (1985)

TABLE 2.1. SUMMARY OF BUBBLE HYDRODYNAMIC MEASUREMENT TECHNIQUES (continued)

General measurement basis	Detailed measurement basis	Distribution of mean	Sensor installation	Disadvantages / Difficulties	Advantages	Reference
	microwaves	no (mean bed surface velocity)	Transmitter above bed surface	1. information on bed surface behaviour only 2. subjective signal interpretation 3. not fully demonstrated	1. simple arrangement/low cost 2. nondisturbing to flow field 3. can deduce slug rise velocity from measurement of bed surface velocity	El-Sayed et al (1983)
	ultrasonics	no (mean voidage)	External to test section or *in situ*	1. not demonstrated in gas - solid fluidization 2. calibration difficult 3. significant signal loss in wall transmission 4. subjective signal	1. non - disturbing to flow field 2. inexpensive/simple system	Yosef et al., (1975)
Electroresistivity properties	capacitance/resistance probes	yes (pierced length, bubble width and rise velocity)	*in situ*	1. conductor limited in length to avoid noise in probe response restricts applicability to large or deep beds 2. extensive calibration and signal processing required 3. three-dimensional probe configuration needed for size determination 4. sensor material problems in high temperature tests 5. disturbs flow field	1. spatial distributions obtainable through sequential sensor sampling arrangement 2. readily automated for time-averaged data acquisition	Park et al. (1969), Burgess and Calderbank (1975), Calderbank et al. (1976), Whittmann et al. (1978), Yoshida et al. (1982)

TABLE 2.1. SUMMARY OF BUBBLE HYDRODYNAMIC MEASUREMENT TECHNIQUES (continued)

General measurement basis	Detailed measurement basis	Distribution of mean	Sensor installation	Disadvantages / Difficulties	Advantages	Reference
	inductance	yes	*in situ*	1. conductor limited in length to avoid noise in probe response restricts applicability to large or deep beds 2. requires bed seeding of ferromagnetic particles which may fluidize differently than remainder of bed 3. measurement sensitivity not as good as capacitance/resistivity probes	1. same as capacitance probes	Cranfield (1972)
	impedance	yes (pierced length, bubble width and rise velocity)		1, conductor limited in length to avoid noise in probe response restricts applicability to large or deep beds	1. applicable to three-phase fluidization	Linneweber and Blass (1983)
	electric discharge	yes (pierced length and rise velocity)	*in situ*	1. sensor materials of construction require careful consideration - effected by oxidation reactions 2. problems with electric discharge in emulsion phase 3. same as capacitance probes	1. applicable to high-temperature tests (~ 1000 C)	Yoshida, et al. (1982)
thermal	thermistor probe	yes (rise velocity)	*in situ*	1. self-heating - probe not sensitive at high temperatures (200 C<) 2. disturbs flow field 3. sensor calibration tedious	1. provides data on instantaneous fluctuations of local heat transfer coefficients 2. can provide rises velocity by cross-correlation of two sensor signals	Wen et al., 1978

2.2 CONVERSION OF BUBBLE PIERCED LENGTH TO BUBBLE SIZE

Submersible probes are effective tools for the study and measurement of the local properties of multiphase systems. Probes based on the local variation of the electrical properties (for example, capacitance and resistance), transmission/dispersion of electromagnetic waves (for example, fiber-optic, laser, X-rays) and the hydrostatic pressure (pneumatic) have been described in the literature, **Table 2.1**.

In bubbling fluidized beds, these probes have been used to detect the characteristics of gas bubbles. The emphasis has been on the determination of a mean bubble size though it is clear that bubble coalescence produces distributions in size both laterally as well as vertically. This mean size is then used in the determination of the extent of heat/mass transfer and chemical reaction (Kunii and Levenspiel, 1969). The simple dual-tip probe measures only the pierced length of a bubble. The mean bubble size is generally assumed to be proportional to the mean value of pierced length measured by the probe; representative examples are given in **Table 2.2**. Since the probes do not always intersect the bubble at its centre, the distribution of bubble sizes can not be deduced simply from the pierced length distribution (Werther, 1974a, b; Clark and Turton, 1988). The development of more sophisticated models for heat/mass transfer and chemical reaction will require inclusion of details of bubble size distributions. It is clear that novel probe designs or more sophisticated methods for interpretation of dual-tip probe signals will be necessary to generate the required information on bubble size distributions.

Probes with multiple tips or sensors to detect and reject the bubbles whose central axes are not vertically aligned with the probe have been developed (Burgess and Calderbank, 1975; Sung and Burgess, 1987). The optimal design and the bubble selection algorithm for such probes, however, requires knowledge of the shape of the bubbles. Any particular design would be unable to cope with the possibility of different bubbles having different shapes. Alternatively, Atkinson and Clark (1988) have developed a selection algorithm based on the fact that the coefficient

$$K_B = \frac{U_B}{\sqrt{g\,y}} \tag{2.2.1}$$

of bubble rise velocity, U_B, will be minimum for the bubbles which rise centrally past the probe, where y is the pierced length in equation (2.2.1). The *a priori* choice of a minimum coefficient applicable to all bubble shapes and sizes, however, appears to be difficult.

Geometrical probability (Kendall and Moran, 1963) concepts offer an elegant solution to the conversion of the distribution of pierced lengths to that of bubble sizes. This possibility has been explored in some depth by Werther (1974a, b) and, more recently, by Clark and Turton (1988). Both works assume horizontally uniform bubbling and a uniform shape for the entire bubble population. In Werther's model the bubbles were assumed to be ellipsoids characterised by a vertical diameter and a constant aspect ratio; Clark and Turton permit the bubble populations to have other shapes. These methods, however, presume that the entire bubble population is characterised only in terms of a single size measure - the horizontal dimension, d_H, of individual bubbles. Only a spherical shape is completely specified by one single size variable; at least one other size characteristic is required for all other bubble shapes. Consequently, though Clark and Turton tabulated results for several bubble

shapes, additional size parameters (for example, the aspect ratio as used by Werther) would have to be specified for generating a solution. Experimental data are necessary for the determination of these parameters. The major limitation in developing and refining procedures for the transformation of the measured pierced length to bubble size remains the lack of an experimental technique for the verification of the proposed methods.

In this work, digital image analysis techniques have been used for the simultaneous measurement of the pierced length, maximum horizontal and vertical dimensions, circumference and cross-sectional area for individual bubbles that would be intercepted at a probe in the two-dimensional bed for several operating conditions. Computer based data acquisition and analysis have permitted large number of measurements enabling statistically more reliable inferences. Theoretical results are obtained in terms of the local bubble size density functions so that, in principle, non-uniformity in bubbling can also be taken into account. The theory is adapted for application to thin two-dimensional beds. Several assumptions regarding the shape of bubbles in gas fluid beds have been made in the literature. The experimental data on pierced lengths along with assumed bubble shapes are used in the theory to predict the distributions of the horizontal and vertical dimensions, equivalent diameter and circumference of the bubbles. These predictions are then compared with the experimentally obtained data.

TABLE 2.2. RELATIONSHIP BETWEEN AVERAGE BUBBLE PIERCED LENGTH AND DIAMETER

Reference	Expression	Comments
Gunn et al (1985)	$\overline{d}_E = \frac{4}{\pi}\frac{\overline{y}}{\sqrt{\alpha}}$ $= 1.41\overline{y}$	1. Ellipsoidal bubble with α=0.813. 2. Integrated over all possible y due to off-center effect. $\overline{y} = \frac{1}{d_H}\int_{-d_H/2}^{d_H/2} y\,dx$
Rowe et al (1981)	$\overline{d}_B = 1.20\overline{y}$	1. Spherical bubble with bubble wake volume, equals 1/3 bubble volume
Chan et al (1987)	$\overline{d}_E = 1.43\overline{y}$	1. Equivalent bubble diameter. 2. Determined from the average bubble pierced length and bubble rise velocity.
Weimer et al (1985)	$\overline{d}_B = \frac{4}{\pi}\overline{y}$ $= 1.27\overline{y}$	1. Spherical bubble. 2. Integrated over all possible y.

2.3 INFLUENCE OF THE ANGLE OF BUBBLE RISE ON THE INTERPRETATION OF SUBMERSIBLE PROBE SIGNALS

Submerged probes have been used extensively for the study of local bubbling characteristics in three-dimensional gas fluidized beds, **Table 2.1;** however, several limitations remain in the interpretation of signals recorded from such probes.

Dual-tipped probes have been used most often. There are two limitations specific to such probes. Firstly, the axis of the probe need not be aligned with the axes of the rising bubbles; consequently, these probes measure the pierced length rather than the diameter of the bubble. Geometrical probability has been advanced as a possible method for converting the measured distributions of pierced lengths to those of bubble diameters, **section 2.2.** Secondly, the signal interpretation procedures employed for dual-element probes also assume that the bubbles rise vertically past the probe. However, observations made in two-dimensional beds show that the rising bubbles follow an intricate pattern, influenced by other bubbles in the vicinity as well as the local solids flow. The implication of non-vertical bubble rise on the measurement of bubble characteristics using two-element submerged probes does not appear to have been examined though Gunn and Al-Doori (1987) have reported limited measurements for the angle of bubble rise in a two-dimensional fluidized bed (glass ballotini : 5×10^{-4} m; $U_{mf} = 0.3$ m/s) operated at 1.7 U_{mf}.

Three-element probes have been used (Burgess et al., 1981; Chiba et al., 1975; Sung and Burgess, 1987) in two-dimensional beds and five-element probes by Burgess and Calderbank (1975) in three-dimensional beds. The additional elements

were included to detect and reject non-vertically rising bubbles. Though the collection and processing of signals from such probes is more complex in comparison with two-element probe signal analysis, the availability of digital processing systems ensures that this task can be accomplished. However, the influence of the selection methods on the statistics of bubble populations does not appear to have been investigated.

In this work, it is first shown theoretically that the discrepancy between the actual and inferred (assuming vertically rising bubbles) velocity can be quite substantial depending on the angle of bubble incidence at a dual-tipped probe and the distance of the bubble center from the probe. Digital image analysis methods have then been developed to measure the velocity and the angle of bubble rise. Further, the data collected using image analysis methods were analysed to determine whether the rejection of the non-vertically rising bubbles leads to discrepancies between the actual bubble characteristics and those measured by multiple-element probes. Simultaneous measurements afforded by image analysis permit the determination of the relationships between the bubble size/shape and velocity. Additional experiments have been performed to compare such relationships for bubble swarms in a freely bubbling fluidized bed with those for single bubbles and bubble chains injected in an incipiently fluidized bed.

2.4 MIXING OF UNIFORM SOLIDS

It is well recognized that the mixing of solids in gas fluidized beds is induced by the motion of bubbles: solids, in the form of bubble wakes, are carried up by bubbles, and the dense phase solids are simultaneously displaced downwards elsewhere. Periodic disposal and replenishment of wake fragments as the bubble rises through the bed also occur (Rowe et al., 1965).

Various mathematical models have been proposed in the literature represent the solids mixing phenomena in terms of (Verloop et al., 1968):

- a combination of perfect mixing, short-circuiting, piston flow and the like;
- a combination of a number of perfect mixers;
- diffusivity or mixing coefficient;
- circulation patterns; and
- existence of different layers with different flow characteristics.

Models in the first two categories do not recognize the physical behaviour of fluidized beds; the parameters obtained from data fitting may, then, be of limited value. Based on the observation of periodic disposal and replenishment of wake fragments, solids motion has been characterized by diffusivity or mixing coefficients; a strong advantage of this approach is the ease in applying available mathematical results for data interpretation. Oscillations measured in tracer experiments (de Groot, 1967), however, limit the applicability of this model. Two- and three-phase counter-current back-mixing models require numerical solution of hyperbolic partial differential equations; their assessment and determination of model parameters are limited by the scarcity of experimental data on simultaneous characterization of bubble flow

and solids mixing. These issues have been discussed in several reviews (Kunii and Levenspiel, 1969; Potter, 1971; van Deemter, 1985); a summary of representative studies is given in **Table 2.3**.

Two approaches have been employed to follow solids movement in a fluidized bed experimentally (Bellgardt and Werther, 1986):

- local investigation of the motion of individual particles; and
- gross behaviour of solids mixing using tracer techniques.

For such experiments, the tracer particles must possess a distinctive property which enables measurement of their motion (for the first approach) or concentration (for the second approach). The first approach has most often relied on the use of radio-active particle particles. Investigations on the gross mixing behaviour have employed several types of tracer particles including

- radio-active (May, 1959);
- coloured (Sutherland, 1961; Singh et al., 1972);
- magnetic (Sutherland, 1961; Avidan and Yerushalmi, 1985);
- chemically different (Talmor and Benenati, 1963; Berruti et al., 1986);
- subliming (for lateral mixing : Bellgardt and Werther, 1986); and
- heated (Lewis et al., 1962; Valenzuela and Glicksman, 1984).

In general, the first four techniques can only be used for a single short transient experiment after which the bed must be sectioned for analysis, or in the case of radio-active tracer, allowed to decay. Data collection and analysis from sectioning of a slumped bed is generally laborious. Further, for rapid solids mixing rates, the results may be distorted during the bed slumping transient. In an interesting variation, Avidan and Yerushalmi (1985) used magnetic particles as tracer and measured their inductance. This technique and those based on subliming or heated tracer particles

permit more continuous data collection; however, additional analysis or assumptions are required to relate the measurements (for example, inductance or temperature profiles) with tracer concentrations. Moreover, such measurements may yield only local data on the variation of tracer concentration with time. Interpretation of the local response data requires care since model parameters determined from data fitting may not accurately reflect mixing characteristics at other locations in the bed. An ideal measurement technique would, therefore, possess the following characteristics : (a) a fast response; (b) ability to measure the tracer concentration while the bed is fluidized (without the need of slumping); and (c) ability to measure, simultaneously, the mixing behaviour at different locations in the bed to enable unambiguous determination of model parameters.

In this work digital image analysis have been used to follow the course of axial mixing of uniform solid particles. This technique satisfies the three criteria suggested above; however, it is applicable only to two-dimensional fluidized beds. The experimental data obtained for a range of operating conditions have been used to evaluate the three-phase counter-current back-mixing model (Gwyn et al., 1970).

TABLE 2.3. A REVIEW OF THE STUDIES ON MIXING OF UNIFORM SOLIDS

Reference	Experimental		Theoretical model
	Technique	Results	
Avidan and Yerushalmi (1985)	• non-intrusive induction probe • tracer : ferromagnetic coated particles • bed : FCC particles (d_P=4.9x10^{-6}m)	• transient C = f(Z,t) • dispersion coefficient	• Dispersion model • limitation of countercurrent flow model at high gas velocity was discussed • the solution technique using the method of characteristics appears to be incorrect.
Babu et al. (1973)	• bed-sectioning • dissolving salt particle • tracer : glass beads (d_P = 4.70x10^{-6} m, ρ_P = 2480 kg/m^3) • bed : gannular sodium tripolyphosphate (d_P = 4.48x10^{-6} m, ρ_P = 2500 kg/m^3)	• C vs Z • estimation of exchange coefficient	• three phases - bubble, wake and dense - wee considered • Laplace transform technique was used to solve model equation assuming an infinite bed
Bailie (1967)			• multi-phase model - upward and downnward phase with cross flow was proposed • finite difference stepwise stop-and-go procedure with N compartments was used to solve the equations • model parameters were not related to bubble parameters

TABLE 2.3. A REVIEW OF THE STUDIES ON MIXING OF UNIFORM SOLIDS (continued)

Reference	Experimental		Theoretical model
	Technique	Results	
Bellgardt and Werther (1986)	• measurements of local bed temperature to determine the spatial tracer distribution. • measurement of the concentration of the gaseous sublimation product CO_2 and yield quantitative information about the local tracer concentration	• temperature profiles - axial mixing larger order of magnitude than lateral mixing • correlation for the lateral dispersion coefficient	• lateral dispersion model
Esin and Altun (1984)	• bed sectioning by shovel • size analysis • bed : ($d_P = 8.46 \times 10^{-4}$ m, $\rho_P = 1521$ kg/m^3) • tracer : ($d_P = 6.45 \times 10^{-6}$ m, $\rho_P = 1521$ kg/m^3)	• C = f(Z,t) • large time interval - data limited • dispersion coefficient	• Dispersion model • correlation
Fan and Chang (1979)	• visual counting • coloured balls • bed : ($d_P = 3.65 \times 10^{-2}$ m, white) • tracer : d_P = same, yellow)	• transient: C = f(Z,t)	• non-stationary random walk model
Gwyn et al. (1970)			• Three-phase countercurrent back-mixing model - bubble, wake and dense - model was proposed • numerical methods were used to solve the general material balance equations for gas and solid

TABLE 2.3. A REVIEW OF THE STUDIES ON MIXING OF UNIFORM SOLIDS (continued)

Reference	Experimental		Theoretical model
	Technique	Results	
Ishida and Wen (1973)			• bubble assemblage model • steady state solution
Kozanoglu and Levy (1991)	• bed sectioning • counting coloured particles	transient: C = f(Z,t)	• multi-phase model with four wake phases • numerical solution
Lakshamaman and Potter (1987,90)		• data from Sitnai (1981) used for comparison with model	• multi-phase - wake, dense and wall phase - 'Cinematic' model. • used Sitnai's (1981) data for comparison • discussed problems associated with inversion of Laplace transform
Liu and Gidaspow (1981)		• data from May (1959) used for comparison with model	• hydrodynamic approach • Laplace transforms (infinite bed) and method of image (finite bed) were used for solving the equations
May (1959)	• scintillation counter • radioactive tracer (d_P = 2.0x10^{-6} - 1.5x10^{-4}m)	• transient: C = f(Z,t)	• Diffusion model

TABLE 2.3. A REVIEW OF THE STUDIES ON MIXING OF UNIFORM SOLIDS (continued)

Reference	Experimental		Theoretical model
	Technique	Results	
Sitnai (1981)	• sampling tubes • used magnetic separation • tracer : iron ore (d_P = 6.70x10^{-4} m, ρ_P = 3870 kg/m^3) bed : silica sand (d_P = 7.00x10^{-4} m, ρ_P = 2580 kg/m^3)	• investigated in bed with horizontal tubes • C = f(Z,t) • exchange coefficients estimated	• model wih wake, dense and wall phase • numerical solutions
Tailby and Cocquerel (1961)	• bed-sectioning • analysis of colour of the dyed particles dissolved in chloroform by spectrophotometer.	• F-diagram: residence time of solids in continuous feed system	• combination of perfect mixing, short-circuting, piston flow and the like
van Deemter (1967)		• data from de Groot (1967) used for comparison with model	• multiphase - counter-cuurrent flow model • Laplace transform solution for large times • simulation of solids mixing response with different values of material exchange relative to circulation (indicated oscillation)

2.5 SEGREGATION IN BINARY FLUIDIZED SYSTEMS

When particles of differing size and/or densities are fluidized together, segregation can occur. In a binary system, one particle species (flotsam) tends to migrate towards the upper end of the fluidized bed and the other prefers to occupy the lower section of the bed (jetsam). Which species forms the jetsam (or the flotsam) depends on both the relative sizes as well as the densities of the fluidized particles (Chiba et al., 1980; Nienow and Chiba, 1985). Experimental studies on segregation in fluidized beds usually aim to measure the variation of the concentration of the tracer particle with respect to height above the distributor. The tracer particles can be well mixed or in the form of a separate layer at the beginning of the experiment. The bed is fluidized at the required operating conditions. At the end of the run - most often after steady state conditions have been achieved - the bed is slumped and the particles are aspirated layer by layer (for example, Beeckmans et al., 1984; Rice and Brainovich,1986).

A more elaborate approach in which the solids at different heights above the distributor were isolated by the simultaneous introduction of several horizontal plates has also been reported (Garcia-Ochoa et al, 1989); the advantage of this technique being that more information on the bed voidage becomes available compared to the conventional bed slumping procedure. The tracer particles are then separated from the solids collected from different horizontal levels - most often by sieving or, in the case of frequently used iron-based tracer, magnetically. The results from such experiments have usually been interpreted, at the macroscopic level, in terms of a mixing index that varies between 0 (complete segregation) and 1 (complete mixing).

The mixing index is related to the superficial gas velocity by a logistic equation which requires the specification of a parameter termed the takeover velocity. Empirical correlations for the takeover velocity include the influence of particle size, shape and densities; the relative proportion of jetsam and flotsam, and the bed aspect ratio. The mixing index approach has been reviewed in detail by Nienow and Chiba (1985) and, more recently, by Daw and Frazier (1988).

More detailed approaches have also been used in which mechanisms for mixing and segregation have been taken into account. It is well recognised that mixing in bubbling fluidized bed is caused solely by bubbles (Rowe et al., 1965). The three-phase countercurrent backmixing model, perhaps the most advanced approach available to describe mixing of gas as well as solids in a bed of uniform particles, views the bed to be made of three - bubble, emulsion (dense), and the wake - phases. The bubble phase is considered to be free of solids; hence, the description of solids mixing requires the solution of coupled material balance equations written for the wake (in which solids move up) and the dense (where solids move down) phases. Besides the gross circulation of solids, a lateral exchange of solids between these phases is also included (Gwyn et al., 1970; van Deemter, 1985). Segregation, which competes with mixing, is also a consequence of bubble motion (Rowe et al., 1972a, b). An approach similar to that used for solids mixing can thus be adopted to model solids motion in a segregating fluidized bed by including an additional term describing the segregation propensity. There is, however, some uncertainty as to which of the phases the segregation term is associated with: Gibilaro and Rowe (1974) prefer to include it in the dense phase, whereas Yoshida (1980) considers it more likely in the wake phase. Thus, there are three rate parameters which require specification in order to obtain concentration profiles of jetsam (or flotsam) in bubbling fluidized beds of

binary solids: a gross circulation rate; lateral exchange rate; and a segregation rate (either in the dense or in the wake phase). Gibilaro and Rowe (1974), in their steady state formation, also include an axial dispersion term in the dense phase material balance. Though Daw and Frazier (1988) advocate its retention, this term has often been considered unnecessary (Nienow and Chiba, 1985). There are other second order effects in low concentration jetsam systems and an additional mechanism of overlayering in cases of high jetsam concentration systems.

In the approaches of Gibilaro and Rowe (1974) and Yoshida (1980), the variation of bubble properties with height above the distributor was not considered. This short coming, in context of the Gibilaro-Rowe model, was addressed by Naimer et al. (1982). Their calculation procedure, however, cannot cope with the possibility of the formation of a defluidized layer at the bottom of the bed; a mechanism for segregation which has been considered to be important (Chiba and Nienow, 1983; Beeckmans, 1984). Their use of the empirical results of Tanimoto et al. (1980) in the estimation of the segregation rate parameter has been criticised by Beeckmans who argued that the segregation velocity predicted is significantly higher than the experimental values measured.

Much effort has been placed on experiments and modelling relating to the steady state concentration profiles. Beeckmans (1984) notes that transient behaviour has been almost but not entirely neglected. Yang and Keairns (1982) have reported data on segregation in a dolomite - acrylic binary system. They observed the formation of a defluidized layer rich in the jetsam in the lower regions of the bed. A two-compartment model with interchange of particles was proposed. Yoshida et al. (1980) presented experimental data on segregation of equi-density particles of different sizes. The experiment was compared with the predictions of their model in

which bubble properties were assumed to be constant. Beeckmans and Stahl (1987) presented data on strongly segregating system (glass and iron particles with the same U_{mf}); a model which assumed the presence of pure jetsam in the region above the distributor was proposed. Burgess et al (1977) reported a model in which bubble wake was assumed to consist of a stagnant and a well mixed region. Segregation was assumed to occur by falling of the jetsam particle through the bubble void. This idea of the wake consisting of several regions has been considered in greater detail recently by Kozanoglu and Levy (1992) who have postulated the existence of four regions in the bubble wake. Representative work reported in the literature has been summarized in **Table 2.4**.

In this work, results of a theoretical and experimental study on the transient mixing/segregation behaviour of binary solids in a bubbling fluidized bed are presented. The temporal variation of the axial concentration profile has been followed experimentally using digital image analysis techniques. In the modelling study, unsteady state solutions of the Gibilaro-Rowe and Yoshida models have been generated numerically. The variation of bubble properties with height above the distributor has been taken into account. Further, the possibility of the formation of a defluidized region above the distributor has been taken into account.

TABLE 2.4 A REVIEW OF STUDIES ON SEGREGATION IN FLUIDIZED BED

Reference	Theoretical		Experimental			Comment
	Model	Result	System and Method	Experimental variable	Result	
Beeckmans and Stahl (1987)	• kinetic model for rate of approach to steady state	• prediction of C in upper strata	• id = 0.137m • bed-sectioning • magnetic separation	• d_J/d_F=0.70 • ρ_J/ρ_F=2.84 • $U_{mf,J}/U_{mf,F}$=1.0 • glass, iron	• determined upward velocities of jetsam particles	• jetsam velocities much lower than Tanimoto et al. (1980)
Beeckmans et al. (1985)			• 3-D: id = 0.279m • 2-D: thickness = 0.013m • bed-sectioning • magnetic and sieve separation	• d_J/d_F= 1 - 2.7 • ρ_J/ρ_F= 1.6-2.9 • $U_{mf,J}/U_{mf,F}$= 1 • magnetite, steel, coal, sand		• negligible jetsam transport in wakes above the interface
Beeckmans et al. (1984)			• id = 0.279m • double tracer technique • layer by layer suction • separation by screening and magnetic	• d_J/d_F= 0.27-2.3 • ρ_J/ρ_F= 1 - 3.7 • $U_{mf,J}/U_{mf,F}$= 0.31-6.5 • charcoal, limestone,sand, maganetite salt	• measure settling velocity of jetsam	• presence of defluidized layer noted • jetsam velocities much lower than Tanimoto et al. (1980)
Bilbao et al. (1988)	• modified G-R model • 2 circulation terms • use bubble model • criteria for defluidization	• steady state: C = f(Z)	• id = 0.08m • bed-sectioning • separation by screening	• d_J/d_F= 0.12-0.68 • ρ_J/ρ_F= 5.7 • $U_{mf,J}/U_{mf,F}$= 0.07-0.39 • $\bar{x}_J$=0.125-0.54 • sand, straw	• steady state: C = f(Z)	• use different exchange parameters for fluidized and defluidized regions. • circulation parameter accounts for particular characteristics of straw

id: internal diameter of the fluidized bed; 3D: three-dimensional; 2D: two-dimensional

TABLE 2.4 A REVIEW OF STUDIES ON SEGREGATION IN FLUIDIZED BED (continued)

Reference	Theoretical		Experimental			Comment
	Model	Result	System and Method	Experimental variable	Result	
Bilbao et al. (1991)	• modified G-R model	• transient: C = f(Z,t)	• id = 0.08m • bed-sectionin • separation by screening	• d_J/d_F= 0.12-0.32 • ρ_J/ρ_F=5.71 • $U_{mf,J}/U_{mf,F}$= 0.07-0.17 • $\bar{x}_J$= 0.14-0.33 • sand, straw	• mixing index • transient: C = f(Z,t)	• see Bilbao et al. (1988)
Chen and Kearns (1975)			• id = 0.114m • sampling port • sieving, vacuum suction for density separation	• d_J/d_F= 1.4-7.2 • ρ_J/ρ_F= up to 3.8 • $U_{mf,J}/U_{mf,F}$= up to 6.15 • $\bar{x}_J$= a range • binary, and particle species system	• transient: C = f(Z,t) • phase diagram of U vs C	• segregation at low velocity was found to be rapid
Chiba et al. (1979)			• id = 0.05, 0.1m	• d_J/d_F= up to 6.7 • ρ_J/ρ_F= up to 59 • $U_{mf,J}/U_{mf,F}$= up to 23 • copper shot, glass bead, hollow char, silica balloons	• pressure drop profile • correlation for U_{mf} for mixture	
Chiba et al. (1980)			• id = 0.05m • bed-sectioning	• d_J/d_F= 0.17 - 0.6 • ρ_J/ρ_F= 2.3 • $U_{mf,J}/U_{mf,F}$= 0.07-0.85 • $\bar{x}_J$= 0.15 • hollow char, glass bead	• steady state: C = f(Z) • mixing index • pressure drop profile	• tabulated criteria for jetsam • dense material can be flotsam if size ratio < 0.35 and $\bar{x}_J$ < 0.15

id: internal diameter of the fluidized bed; 3D: three-dimensional; 2D: two-dimensional

TABLE 2.4 A REVIEW OF STUDIES ON SEGREGATION IN FLUIDIZED BED (continued)

Reference	Theoretical		Experimental			Comment
	Model	Result	System and Method	Experimental variable	Result	
Daw and Frazier (1988)		• segregation index	• id = 0.102m • bed-sectioning • magnetic, manual separation	• d_J/d_F= 1.03-1.92 • ρ_J/ρ_F= 1.0-3.3 • $U_{mf,J}/U_{mf,F}$= 1.02-2.3 • coal, limestone, acrylic, polypropylene glass, steel shot	• steady state: C = f(Z)	• Segregation index related toG-R model with circulation, segregation and axial diffusion mechanisms
Ekinci et al. (1990)			• id = 0.1, 0.2m • on-line temperature detection	• d_J/d_F= up to 10 • ρ_J/ρ_F= up to 2.2 • lignite, dolomite, sand, quartz	• transient temperature profile	• extent of segregation deduced from temperature profile
Garcia-Ochoa et al. (1989)	• G-R model	• steady state: C = f(Z)	• id = 0.114m • bed-sectioning while fluidized	• d_J/d_F=1.0 • ρ_J/ρ_F=1.5-2.39 • $U_{mf,J}/U_{mf,F}$= 0.25-0.75 • $\bar{x}_J$• polyethene, glass, alumina	• steady state: C = f(Z)	• wake fractions estimated are too small • many combinations of parameter possible • poor fit if axial diffusion not included in G-R model
Gibilaro and Rowe (1974) (G-R model)	• steady-state model with segregation in dense phase • mechanisms considered: circulation, exchange, segregation and axial diffusion	• analytic results for steady state: C = f(Z)				• possibility of a defluidized layer not considered. • the model parameters not related to bubble parameters. • model parameters were considered to be independent of height

id: internal diameter of the fluidized bed; 3D: three-dimensional; 2D: two-dimensional

TABLE 2.4 A REVIEW OF STUDIES ON SEGREGATION IN FLUIDIZED BED (continued)

Reference	Theoretical		Experimental			Comment
	Model	Result	System and Method	Experimental variable	Result	
Hemati et al. (1990)			• id = 0.1m • divide bed into slices • concentration determined from weight loss from burning of sawdust	• d_J/d_F= up to 7.5 • ρ_J/ρ_F= up to 5.2 • sawdust, coal sand, alumina	• mixing index	• strong segregation at lower velocity
Kozanoglu and Levy (1992)	• G-R model with modified 4 wake phases • used bubble model	• Transient: C = f(Z,t)	• id = 0.152m • bed-sectioning • manual separation	• d_J/d_F=0.93 • ρ_J/ρ_F=2.14 • $U_{mf,J}/U_{mf,F}$= 1.94 • $\bar{x}_J$= a range • glass, plastic	• transient: C = f(Z,t) • measured segregation coefficient	• defluidized layer considered • segregation parameters related to bubble characteristics
Naimer et al. (1982)	• G-R model	• mixing index • steady state: C = f(Z)				• related segregation rate to bubble parameter and separation distance from Tanimoto et al. (1980) • not applicable for jetsam rich system • defluidized layer not accounted for
Nienow and Cheesman (1980)			• X-ray cineph otography, and bed-sectioning	• large particles of different shape • ρ_J/ρ_F= 0.55-3.9 • foam rubber, aluminium foil, cardboard, alumina	• the effect of particle shape • mixing index • steady state: C = f(Z)	

id: internal diameter of the fluidized bed; 3D: three-dimensional; 2D: two-dimensional

TABLE 2.4 A REVIEW OF STUDIES ON SEGREGATION IN FLUIDIZED BED (continued)

Reference	Theoretical		Experimental			Comment
	Model	Result	System and Method	Experimental variable	Result	
Nienow et al. (1987)			• id = 0.15m • different distributors • bed-sectioning • separation by sieving	• d_J/d_F= up to 35 • ρ_J/ρ_F= 1 $U_{mf,J}/U_{mf,F}$= large range • ballotini, polystyrene, alumina, steel shot	• steady state: C = f(Z) • binary and multi-species systems • modified mixing index using Sauter mean diameter	• defluidization encountered
Nienow et al. (1978)			• id = 0.141, 0.222m • bed-sectioning	• d_J/d_F= 0.127-2.38 • ρ_J/ρ_F= 1.19-8.44 • $U_{mf,J}/U_{mf,F}$=1 - 10.4 • $\bar{x}_J$0.064-0.7	• mixing index • effect of size, density, gas velocity, shape, concentration studied	
Rice and Brainovich (1986)			• 3-D: id = 0.273m • 2-D thickness = 0.28x0.025m • bed-sectioning• photographic and techniques• separation by sieving	• d_J/d_F= 1.89-3.9 • ρ_J/ρ_F= 1 • $\bar{x}_J$= 0.356 • glass beads	• steady state: C = f(Z) • modified mixing index	

id: internal diameter of the fluidized bed; 3D: three-dimensional; 2D: two-dimensional

TABLE 2.4 A REVIEW OF STUDIES ON SEGREGATION IN FLUIDIZED BED (continued)

Reference	Theoretical		Experimental			Comment
	Model	Result	System and Method	Experimental variable	Result	
Rowe et al. (1972a, b)			• 2-D bed • 3-D bed • photographic, sectioning	• d_J/d_F= 1.67-6.67 • ρ_J/ρ_F= 1-8.4 • $U_{mf,J}/U_{mf,F}$= wide range	• steady state: C = f(Z) • mixing index • visual segregation patterns	• segregation mechanisms identified
Seo and Gidspow (1987)			• rectangular bed 0.4 x 0.038m • X-rays, γ-*rays* and radio-active tracer particle	• d_J/d_F= 1.2-3.4 • ρ_J/ρ_F= 1.2-1.9 • $U_{mf,J}/U_{mf,F}$= 1.5-8.3 • glass bead, lead glass, pyrite, coal	• Time-averaged spatial distribution of tracer concentraction	
Tanimoto et al. (1980)			• 2-D: 0.01x0.3x1.0m • cinephotography	• d_J/d_F= 0.25 - 3.9 • ρ_J/ρ_F= 3.5 - 4.5 • used aggregates of glass bead, copper shot, lead shot	• measure segregation distance	• single bubble injection
Tanimoto et al.(1981)	• use G-R model • estimation of segration rate	• steady state: C = f(Z)	• id = 0.19, 0.50m • bed-sectioning	• d_J/d_F= 0.25-3.9 • ρ_J/ρ_F= 3.5-4.5 • $U_{mf,J}/U_{mf,F}$= 0.245-49.2 • glass, copper shot, lead shot		
Yang and Keairns (1982)	• two fulidized beds with interchange of particles	• Transient: C = f(Z,t)	• id = 0.07m • bed-sectioning • separation by screening	• d_J/d_F= 2.23 • ρ_J/ρ_F= 2.35 • $\bar{x}_J$= 0.2-0.8 • acrylic, dolomite	• transient: C = f(Z,t)	• presence of entrapment zone

id: internal diameter of the fluidized bed; 3D: three-dimensional; 2D: two-dimensional

TABLE 2.4 A REVIEW OF STUDIES ON SEGREGATION IN FLUIDIZED BED (continued)

Reference	Theoretical		Experimental			Comment
	Model	Result	System and Method	Experimental variable	Result	
Yoshida et al. (1980) (Yoshida model)	• mechanisms • segregation by exchange • circulation	• Transient: C = f(Z,t)	• id = 0.1m • bed-section-ing • separation by screening	• d_J/d_F= 1.5-12.4 • ρ_J/ρ_F= 1.0 • $U_{mf,J}/U_{mf,F}$= 2.0-36.0 • glass	• Transient: C = f(Z,t)	• bubble properties considered to be indenpendent of height

id: internal diameter of the fluidized bed; 3D: three-dimensional; 2D: two-dimensional

2.6 MOTION OF A LARGE AND LIGHTER PARTICLE IN A FLUIDIZED BED OF SMALLER PARTICLES

In bubbling fluidized bed combustion, large coal particles - comprising about 1% of the total bed inventory - are fluidized along with smaller sulphur-sorbent particles. The density of the coal particles is less than that of the bed particles. This combination of the concentration, size and density results in the setting up of circulation pattern for a coal particle within the bed: a jerky upward movement under the influence of rising bubbles and a downward motion when associated with the dense phase (Nienow et al., 1978). Based on these experimental observations, Agarwal (1987) estimated that the char particle could be associated with the bubble phase of the fluidized for as much as 20% of its time in the bed whereas earlier models for fluidized bed combustion assumed that the char resided only in the dense phase. In view of the different properties of the two phases of the bubbling bed, the motion of the 'active' particle - represented in terms of a phase residence probability - is of importance in modelling heat and mass transfer for such particles (Agarwal and La Nauze, 1989; Linjewile and Agarwal, 1990). Recent experimental investigations indicate that the combustion of volatile species in the immediate vicinity of a devolatilizing coal particle is inhibited in the dense phase and takes place preferentially when the coal particle is associated with the bubble phase (Agarwal, 1986; Prins et al., 1989). The above studies have dealt with single char particles in the fluidized bed. Recently Hesketh and Davidson (1991) found from experiment that particle motion will influence the batch burn-out time of char introduced into the fluidized

bed. The importance of the determination, experimental as well as theoretical, of the characteristics of the motion of an 'active' particle in modelling fluidized bed combustion is evident.

It appears necessary to detect not only the particle's position within the bed but also the nature of its association with the two phases of the bubbling fluidized bed. Rios et al. (1986) measured the local velocity of an 'active' particle using radioactive tracer. The interpretation of the measurements in terms of an axial presence probability, however, could not provide a complete picture of the circulation pattern of the particle and the nature of its interaction with the bubble and dense phases. The only alternatives currently available are visual inspection or the use of photographic techniques on a two-dimensional bed. The tracking of the 'active' particle and the determination of its interaction with the bubble and dense phases by the naked eye is not possible because of the fast and apparently erratic movements of these particles in the bed though qualitative features can still be extracted (Nienow et al., 1978). A manual analysis on a sequence of image frames from a pre-recorded film is feasible (Tanimoto et al., 1980); however, such analyses are tedious, subjective and laborious.

In this work, digital image analysis techniques have been used to measure the circulation patterns and the local velocities of the 'active' particle resulting from bubble/particle interactions for a range of 'active' particle densities and fluidizing gas velocities. The technique has also been used to measure the phase residence probability.

Chapter 3

EXPERIMENTAL

3.1 EXPERIMENTAL SYSTEM

3.1.1 Apparatus

The experimental apparatus is illustrated in **Figure 3.1.1**. A two-dimensional fluidized bed of dimensions 1.00 x 0.20 x 0.009 m was constructed from transparent perspex. A porous plate served as a distributor. The solids in the bed were fluidized by compressed air supplied from the mains. Sufficient pressure drop across the calming section prior to the gas distributor ensured uniform distribution of gas through the distributor and the bed. The flow rate of the gas was monitored and measured by rotameters. Two types of rotameters were installed to measure flow rates ranging from 1.2 l/min to 120 l/min. A pressure probe (made of fine stainless steel tube) attached to the adjacent manometer was inserted into the bed from the top to enable pressure drop measurements. Minimum fluidization velocities of the various types of particles used were determined from the pressure-drop and superficial gas velocity plots. Additionally, a gas injector was installed to generate single bubbles in beds maintained at incipient fluidization conditions.

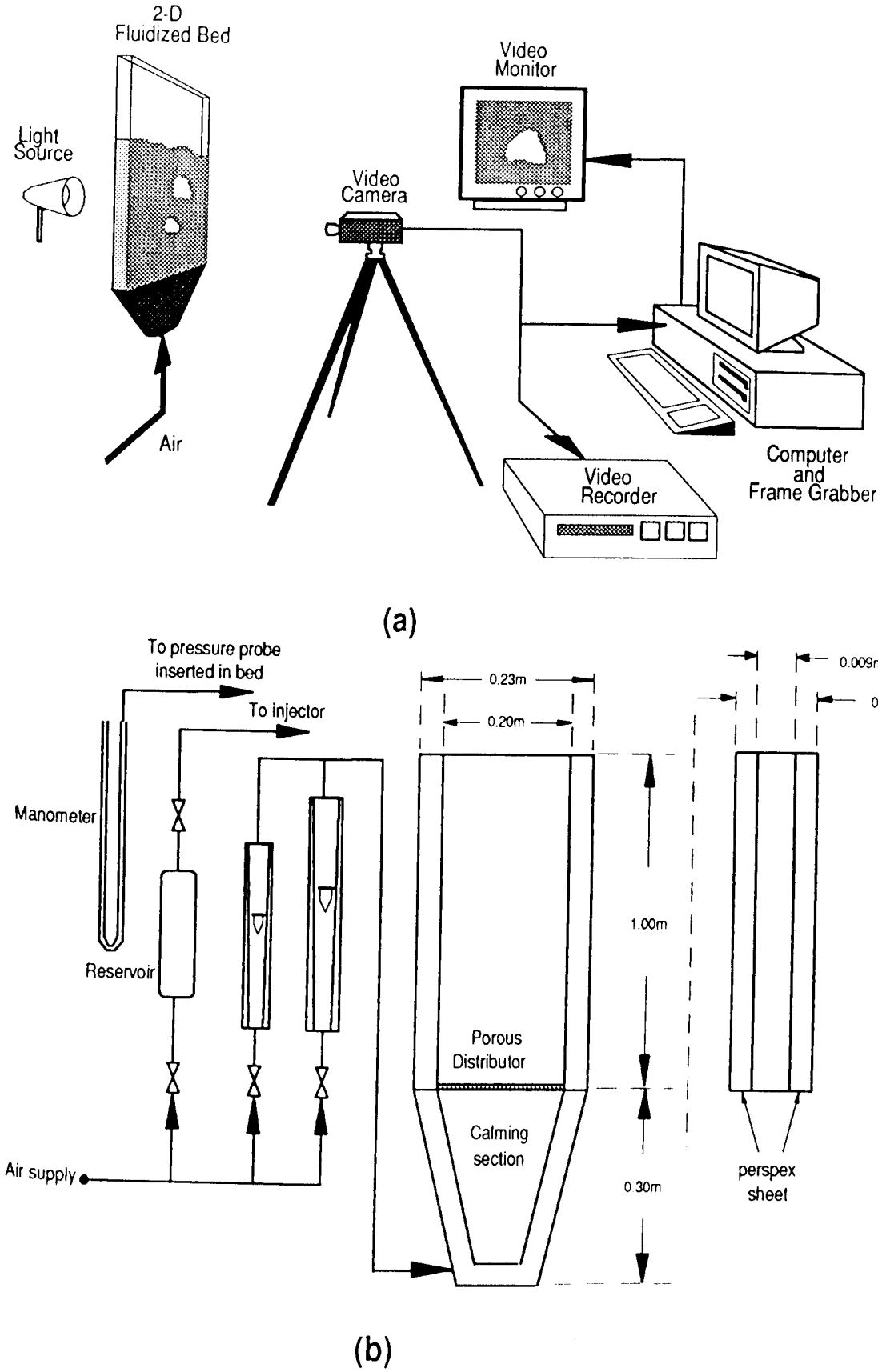

FIGURE 3.1.1: (a) Experimental setup for digital image analysis, (b) Schematic of the two-dimensional fluidized bed.

The bed was uniformly illuminated by light sources to eliminate undesirable shadows and intensity gradients. The lighting condition depended on the nature of the investigation. If only the bubble phase was of interest, then a back-lighting condition was adequate where bright images of the bubble void could be observed through the transparent perspex sheets and the solids phase remained, in comparison, opaque to visible light. However, if both the solids and bubble phase were to be observed, the bed must be exposed to both front- and back-lighting conditions.

Images from the bed (bubble or solids) were captured using a CCD (charge-coupled device) video camera. The analog image signals from the video camera were digitized by an image digitizer (frame-grabber). The digitized image was subsequently displayed on the video monitor. A sequence of the images could also be recorded on tape using a video cassette recorder. Computer software was developed to automate the procedures for image acquisition, data processing and analysis.

3.1.2 Imaging System

The digital image analysis system included the following components:

Frame grabber: A PCVISION™ frame grabber from Imaging Technology Inc. was installed in the system for digitizing (through an A/D converter) the analog image signals from the video (camera or recorder). The digitization process involved two steps: the division of images into 512x512 picture elements (pixels) and subsequent quantification of brightness level of each pixel to a gray scale value. The digital brightness level ranges from 0 (minimum) to 255 (maximum). The pixel values were stored in the frame memory. Display logic on the frame-grabber converted the pixels in the frame memory back to an analog RS-170 format

signal for display on the video monitor. The digital data stored in the frame memory can be accessed by the host computer through the PC-Bus interface. The elementary structure of a frame-grabber is shown in **Figure 3.1.2.**

Video camera : Two models of CCD cameras have been used in the experimental studies. Both types display monochrome (or black and white) images. One of the models (Sony XC/77RR-CE) possessed several additional features including a variable shutter speed ($2x10^{-2}$ to $1x10^{-4}$ s) and auto/manual gain control. The high shutter speed feature was essential for capturing fast moving images without a 'blurring' or 'tailing' effect, especially in measurements related to particle motion in the fluidized bed. The auto-gain feature in the video camera enabled self-adjustment of the illumination level under the influence of the background or surrounding brightness. Auto-gain has its advantages in certain areas of study but is undesirable in quantification of intensities required, for example, in determination of concentration from intensity levels in studies on solids mixing and segregation. For most general purpose experiments, an ordinary video camera can suffice.

Video equipment : Video equipment, including a video monitor and a video cassette recorder (VCR), was available for the visual study of the behaviour of the fluidized bed and for the recording of the experimental runs for subsequent analysis. The VCR was modified so that it was coupled with the computer using an opto-coupler device through a serial port. This enabled control of the key operating functions of the VCR (for example *play, pause, stop frame advance*). A video mixer WJ-MX10 (Panasonic) was utilised for combining different video

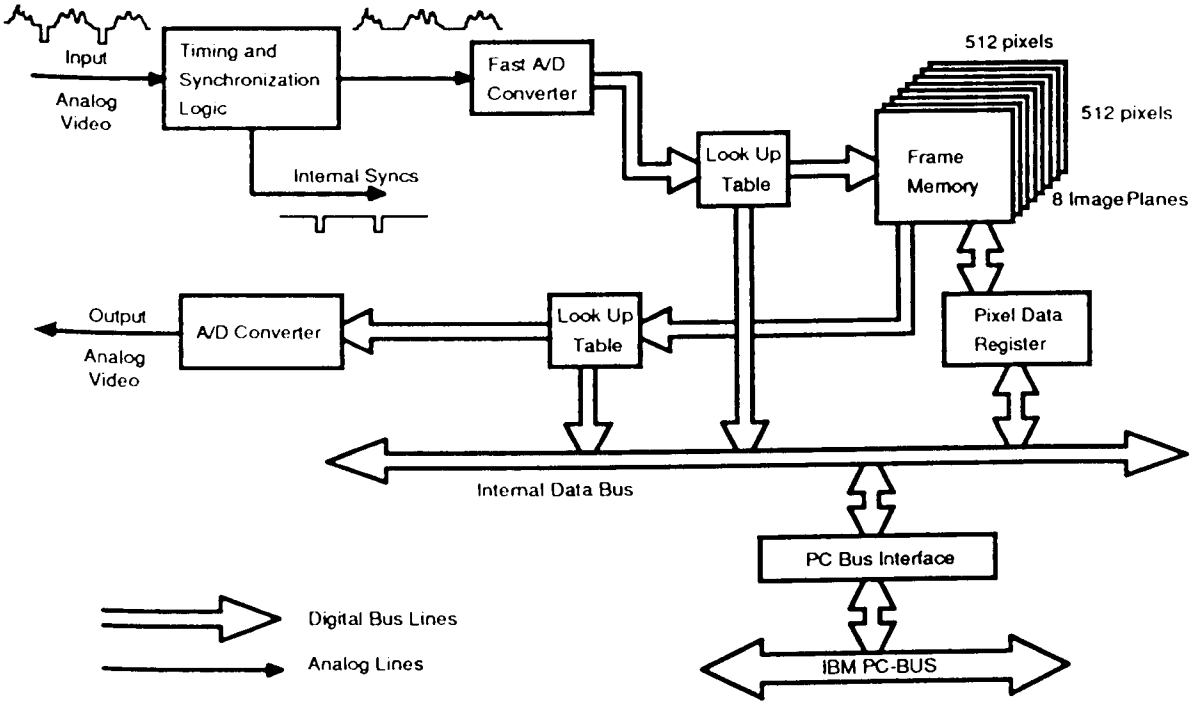

FIGURE 3.1.2: The structure of a PCVISION frame grabber.

signals and eliminating synchronisation problems in the video signals. The video mixer formed an integral part of the imaging system and at the same time performed useful graphic functions.

3.1.3 Equipment Configuration

The experimental and imaging system used in this work has evolved and has been upgraded with time. A range of configurations and setups were used in the various parts of the study. The basic configurations used in the studies, however, can be classified under two general categories.

On-line measurement system : The on-line measurement system for digital image analysis is shown **Figure 3.1.3a**. The image of the bed was captured by the camera and immediately digitized by the frame-grabber. This image was then processed and analysed with the use of appropriate software. The data were stored on the hard disk in the computer before the next image was snapped. The entire routine was fully automated, and data could be collected for pre-specified times and the time-averaged properties could be computed at the end of each run. This arrangement was suitable for the study of statistically meaningful parameters. This approach was used in the measurement of bubble size, velocity and related bubble parameters and the phase residence probability of the 'active' particle in the fluidized bed.

Off-line measurement system : **Figure 3.1.3b** shows the configuration of the off-line measurement method. This method was adopted if the temporal variationof the measured quanatity was of interest. This included the tracking of particle motion and the studies on the rate of solids mixing and segregation. This method also provided a feasible means of studying processes which could not be analysed in real-time. The sequence of events was first recorded on tape. A

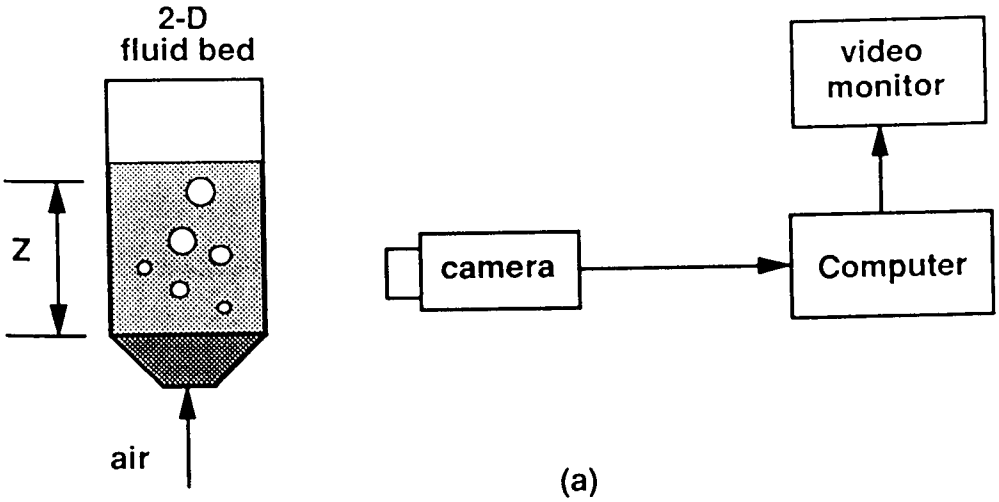

(a)

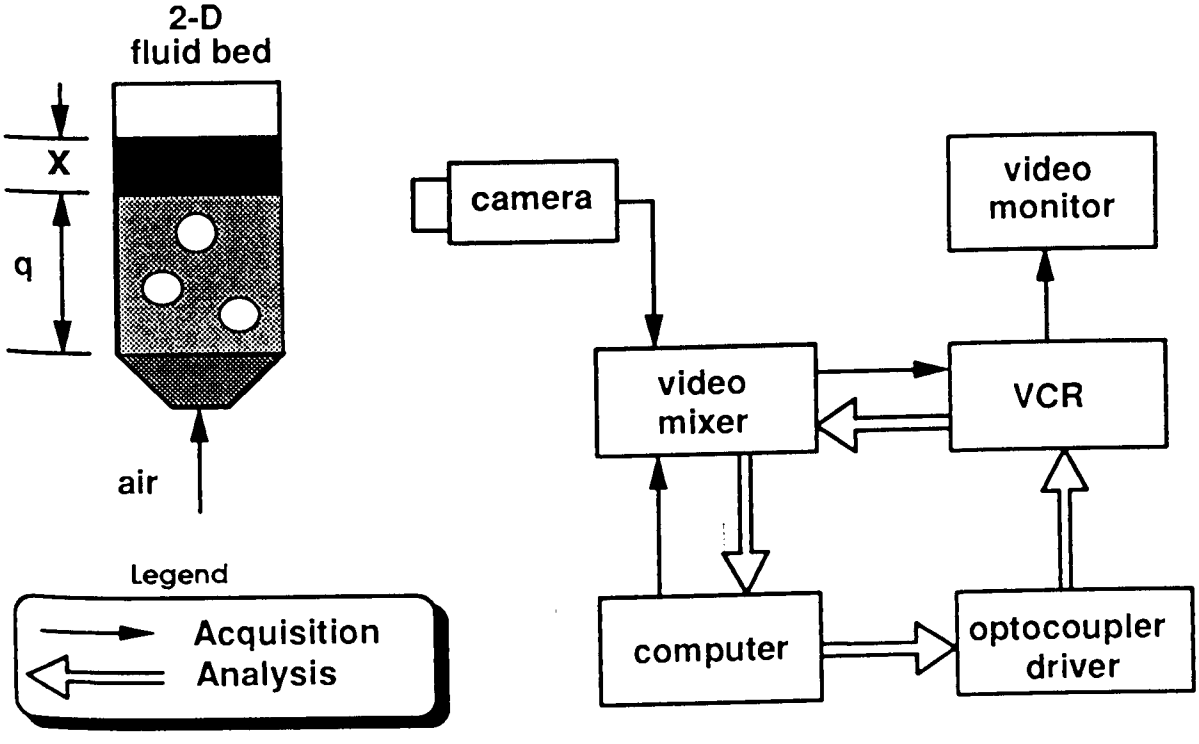

(b)

FIGURE 3.1.3: (a) On-line measurement system;
(b) Off-line measurement system.

computer routine was developed for the generation of the encoding signals from which a set of bar codes denoting the frame number was generated. The signals from the video camera and the image frame encoding signals from the PC were then combined at the digital video mixer and combined signals were recorded by the VCR. The encoding process required precise synchronization with the rate of standard video frame (that is, 25 frames/s) as poor synchronization led to incomplete and incorrect frame number transcription. The frame encoding feature allowed the tracking of time and was utilised for a fully automated frame-by-frame analysis of the video tape. During data analyses, the images were displayed back from the tape in slow advance mode. The image of the frame was then anaylsed using appropriate software. The frame number was interpreted so that the exact time was known. After the completion of the data analyses, the computer advanced the VCR to the next frame through the use of an opto-coupler driver and the same routine was executed again. The time interval between two successive frames is 0.04 s. For some slower processes, the image data were analysed between several frames.

3.2 EXPERIMENTAL TECHNIQUE

3.2.1 Measurement of Bubble Size Distributions

3.2.1.1 Experimental procedure

The setup used for measurements of bubble size is shown schematically in **Figure 3.1.3a**. Two different sizes of glass ballotini were employed in the experiments. The geometric mean of particle sizes were 2.09×10^{-4} and 2.50×10^{-4} m and the corresponding minimum fluidization velocities were 0.031 m s^{-1} and 0.068 m s^{-1} respectively. The distributions of the bubble properties were analysed at various heights ranging from 0.05 m to 0.4 m. The effects of the variation of gas fluidizing flowrates on the bubble parameters were also studied. The range of superficial velocities of the air varied from 1.6 to 5 times the minimum fluidization velocity.

3.2.1.2 Measurement method

Thresholding : The initial step in data processing involves discrimination of bubbles from the emulsion phase. The general procedure for this identification involves examination of the histogram of the gray scale values for an image consisting of both phases. A typical histogram of such an image is presented in **Figure 3.2.1**. The gray scale distribution is normally bimodal and the separation of the two peaks is large provided the image contrast is sufficient. The peak at a lower gray scale level corresponds to the background or the emulsion phase whilst the other peak represents the bubble phase. These two phases may be distinguished by assigning a threshold value (or cut-off level) somewhere between these two modal values. In practice, the threshold value may either be chosen from a gray scale value whose frequency is at a

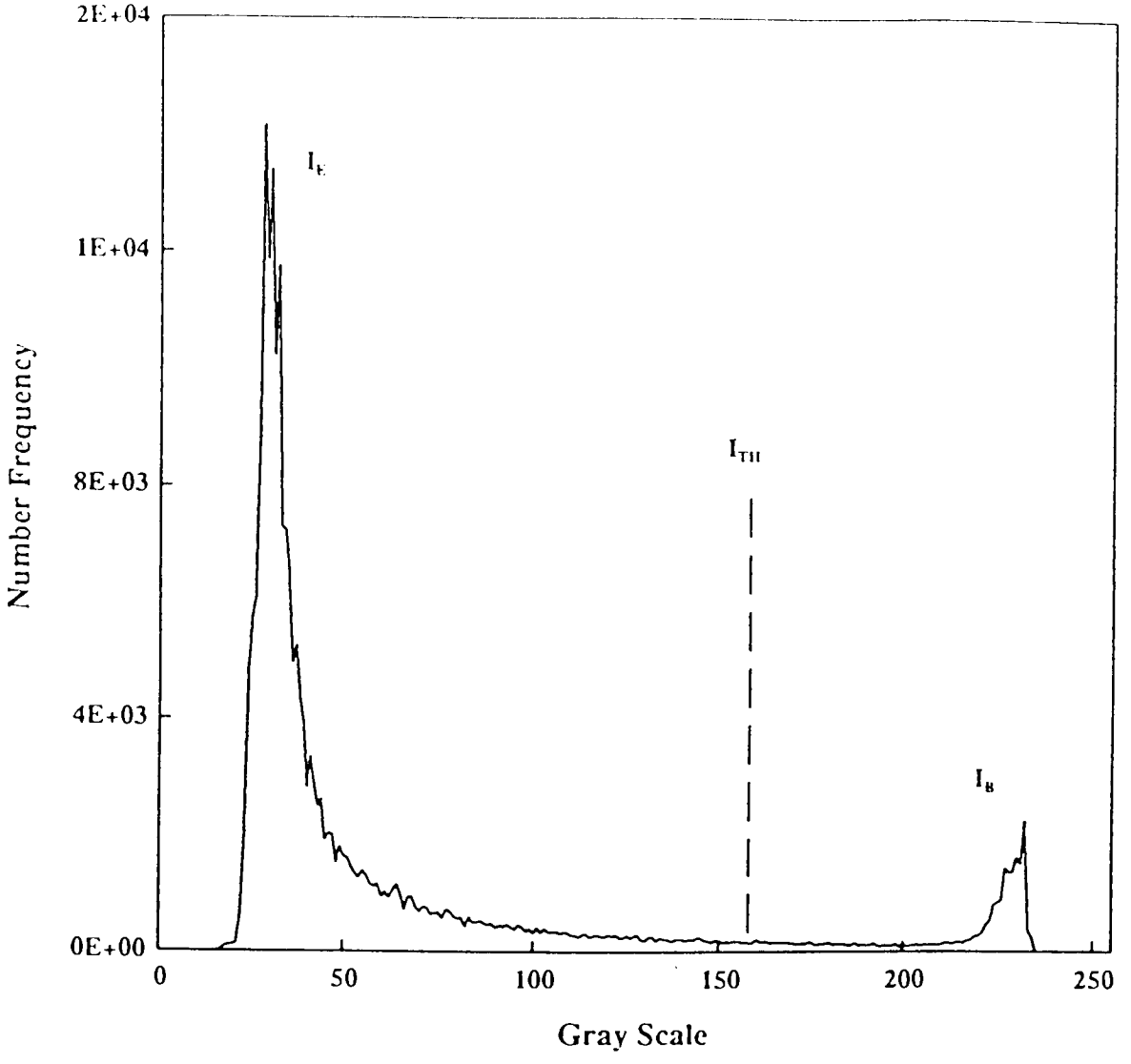

FIGURE 3.2.1: Histogram of grey scale value for an image consisting of emulsion and bubble phase with the peak on the left I_E represents the emulsion phase and the right I_B, represents the bubble phase. A threshold I_{TH} is selected to distinguish these phases.

minimum or at midway between the modal values (Castleman, 1976; Gonzalez and Wintz, 1987). This threshold value is then used for the detection of the bubble boundary. The area possessing a gray scale greater than the threshold value is identified as bubble phase. A global threshold value may be applied provided lighting conditions are reasonably uniform.

Image contrast was normally high. Thus, the delineation of the bubble boundary with high accuracy is possible using the global thresholding method. However, as noted, this method of thresholding is subject to some limitations. The detection of very small bubbles, where excessive solid interference occurs, produces problems as a consequence of the light attenuation in the emulsion phase. If there exists a high proportion of bubbles possessing a size smaller than the critical value, then the computed distribution of the bubble size is not truly representative of the entire bubble population. Consequently, the bubble size distribution measured at lower heights, where the smaller bubbles predominate, will require correction and is therefore not as reliable as data gathered higher up in the bed.

Edge detection and automatic bubble measurement procedure : The detection and measurement of the bubble parameters have been automated by employing a series of systematic edge searching routines. The initial step of the routine detects the numbers of the bubbles intersecting a line positioned at some height above the distributor. For every bubble detected, further scanning across the image is performed in both horizontal and vertical directions so that the complete boundary of the bubble may be delineated. Various geometrical properties of the bubble are readily evaluated during this process. The measured bubble parameters are the projected area of the bubble, A, the

perimeter (or circumference), C_P, vertical and horizontal extremities, d_V and d_H, and the approximate location of the bubble centre, $(\bar{x}, \bar{y})$. From these measurements, other size parameters for the bubbles can be inferred. Bubble size, expressed as an area-equivalent diameter, d_E, can be readily calculated as follows

$$d_E = \sqrt{4\frac{A}{\pi}} \tag{3.2.1}$$

where A is the area of the bubble as projected in a two-dimensional plane. A shape factor, S, may be defined to compare the shape of the bubble to the circular form. Thus,

$$S = \frac{\pi d_E}{C_P} \qquad 0 < S \leq 1 \tag{3.2.2}$$

where C_P is the bubble perimeter evaluated from the experiment. S is unity for the perfectly circular or spherical bubble. The orientation of the bubble may be characterized by the aspect ratio, α, where

$$\alpha = \frac{d_V}{d_H} \tag{3.2.3}$$

and d_V and d_H are the vertical and horizontal extremities of the bubble dimensions.

This logic for edge detection is repeated for the subsequent frames. The procedures of the routines are summarized in block diagram form as **Figure 3.2.2**. Generally, a total of about 2000 to 5000 frames of images are analysed for each experiment.

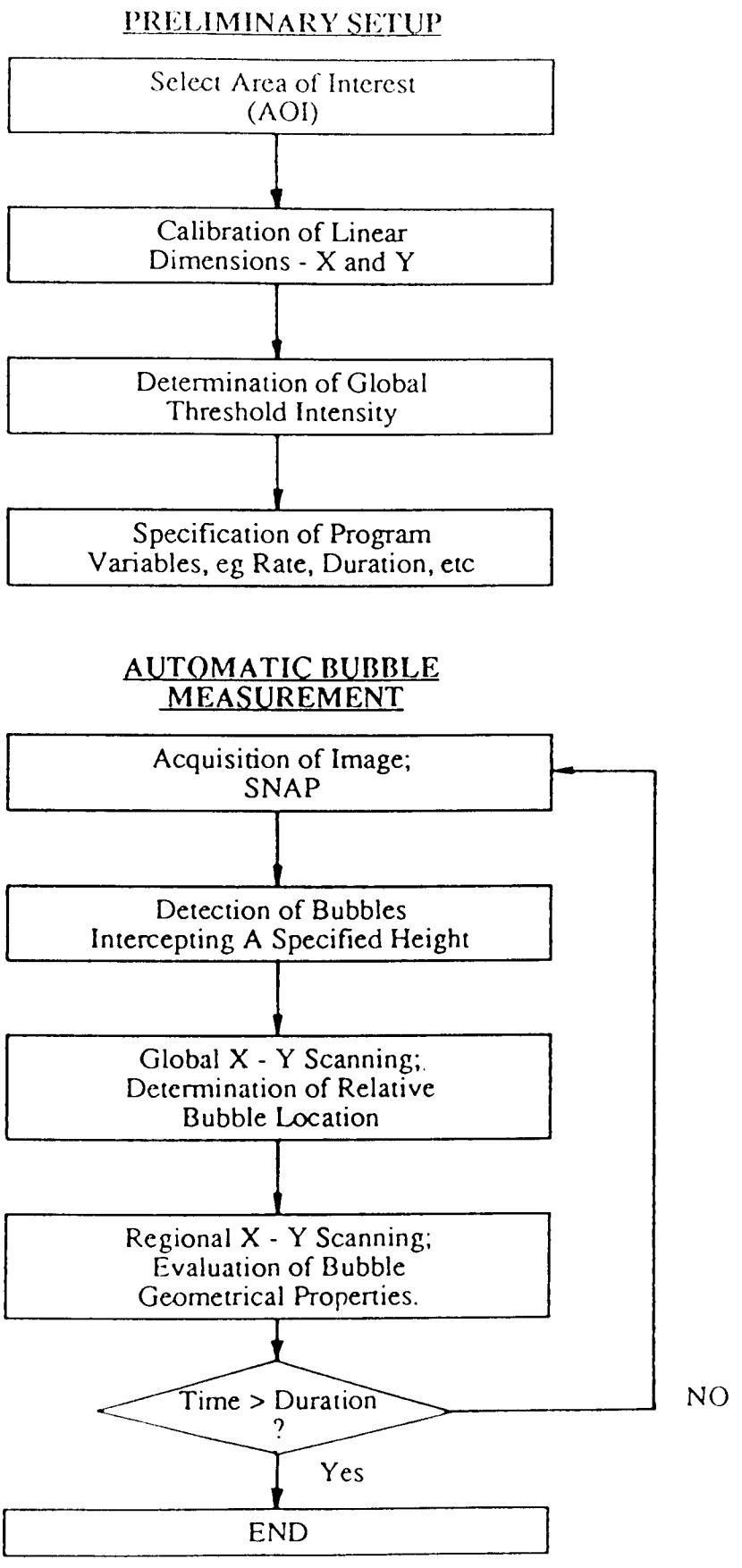

FIGURE 3.2.2: A block diagram showing the logic of the software for the measurement of bubble parameters by digital image analysis technique.

Reconstitution of the true bubble size : As the edge detection is both objective and consistent, bubble parameters can be accurately measured. However, it has been observed that this technique underestimates the sizes of bubbles having diameters comparable to the bed thickness. These bubbles are partially embedded in the solid phase and the interference of this solid leads to minor absorption of the light energy. A more rigorous method of thresholding and edge detection should be adopted, for example, the adaptive thresholding technique (Gonzalez and Wintz, 1987) with the value of threshold varying from one region of image to the other. Unfortunately, the application of this technique is not practicable because a substantial computational time is required for the evaluation of different threshold values in each region. To overcome the deficiency, a simple model has been developed to reconstruct the true bubble sizes from the measured quantities.

The model is based upon an assumption of bubble shape, viz spherical or ellipsoidal. The following analysis considers an ideal spherical bubble. Envisage such a bubble of radius R which is small in comparison to the bed thickness, t_T with the bubble's centre aligned with the central axis, **Figure 3.2.3a**. The bubble will be surrounded by a solid phase of thickness δ. If, as a first approximation, the extent of absorption of the light energy in the solid phase is assumed to be proportional to the thickness of this solid layer, δ, then the following relationship is readily derived.

$$\frac{I_B - I_{TH}}{I_B - I_E} = K_R \frac{2\delta}{t_T} = C_R \qquad (3.2.4)$$

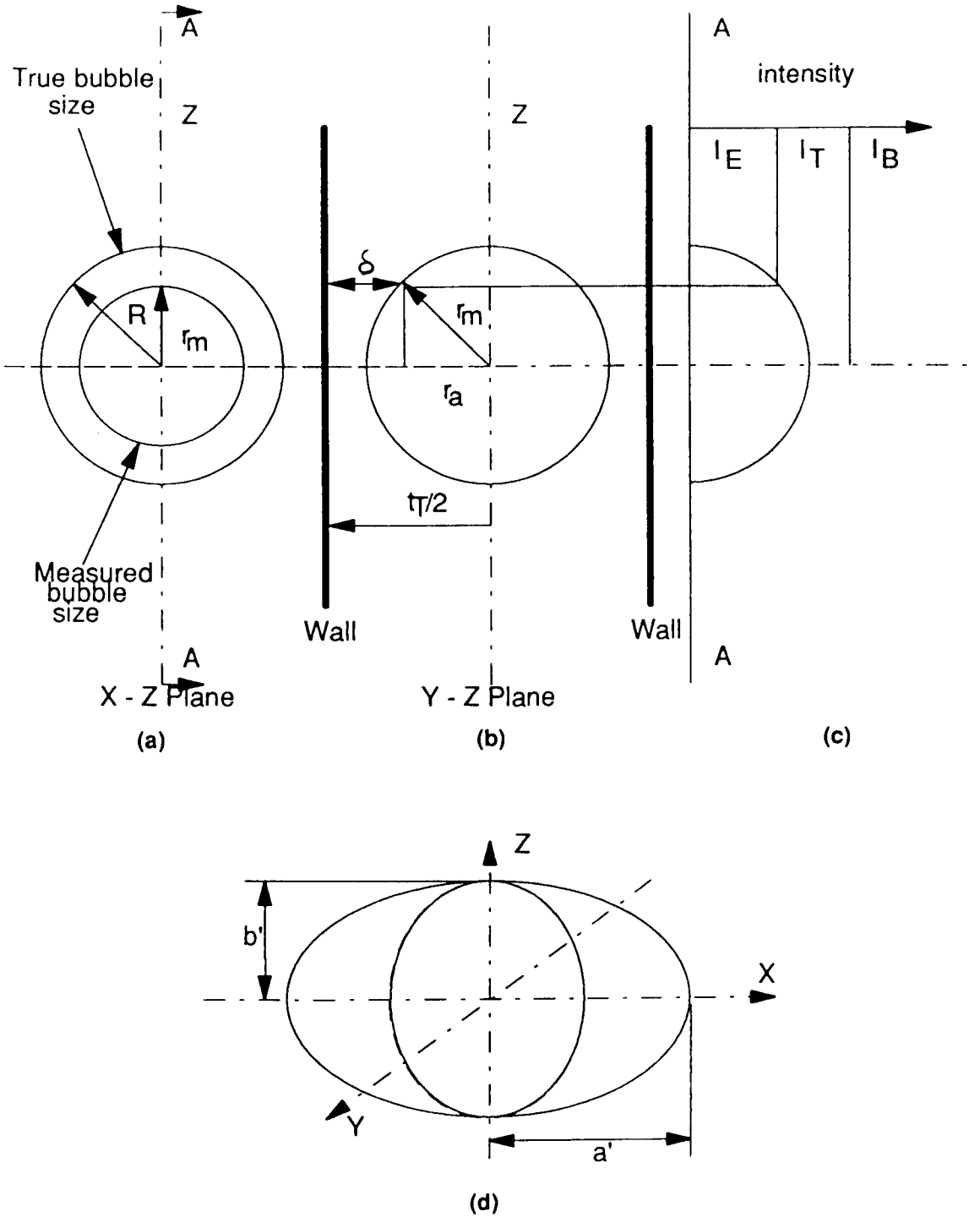

FIGURE 3.2.3: Schematic of a small bubble used in reconstitution of the true bubble size

Here $0 < C_R \leq 1.0$ and K_R is assumed to be unity. I_E is set as the intensity of the background or the emulsion phase, I_B as the intensity level for an unobstructed light path and I_{TH} as the threshold level selected for the distinction of the bubble and emulsion phase. Clearly, I_{TH} defines the measured bubble radius,r_m.

For this small spherical bubble located at the bed centre, **Figure 3.2.3b**, the true radius R can be related to the measured radius r_m by simple geometric consideration as

$$R^2 = r_a^2 + r_m^2 \tag{3.2.5}$$

also

$$r_a = \frac{t_T}{2} - \delta \tag{3.2.6}$$

Combining equations (3.2.4) and (3.2.6) yields

$$r_a = \frac{t_T}{2}(1 - C_R) \tag{3.2.7}$$

Substitution of the value of r_a from equation (3.2.7) into equation (3.2.5) yields

$$R^2 = r_m^2 + \left[\frac{t_T}{2}(1 - C_R)\right]^2 \tag{3.2.8}$$

With the true bubble area, A, defined as $A = \pi R^2$ and the measured bubble area , A_m, defined as $A_m = \pi r_m^2$ equation (3.2.8) may be written as

$$A = A_m + \pi\left[\frac{t_t}{2}(1 - C_R)\right]^2 \tag{3.2.9}$$

It is clear that the second term on the right hand size of equation (3.2.9) represents the correction factor for the undersized bubbles. The effect of

correction factor is negligible for larger bubbles where $A_m \gg \pi[t_t/2(1-C_R)]^2$. Equivalent expressions for bubble shapes other than the spherical form, such as ellipsoidal (**Figure 3.2.3d**), can be derived by employing similar reasoning. The results are presented below.

$$A = A_m + \eta\pi\left[\frac{t_T}{2}(1-C_R)\right]^2 \quad where \quad \eta = \frac{1}{\alpha} \quad , \quad \alpha \leq 1$$

$$\eta = \alpha \quad , \quad \alpha > 1 \qquad (3.2.10)$$

The lateral distributions of the key bubble parameters (size, shape factor and aspect ratio) were determined for all the bubbles having their centres distributed within a region 0.01 m high across the bed width at some specified height, Z, above the distributor plate. The typical distributions of the bubble parameters are presented in **Figure 3.2.4**. The result presented in **Figure 3.2.4a** shows the distribution of bubble size in radial (lateral) position, consistent with the observation reported by Chiba et al. (1975). Furthermore, the bubbles are roughly spherical with a high proportion of bubble possessing shape factors within 0.85 and 1, **Figure 3.2.4b**. Likewise, the aspect ratio of the bubbles appears to be approximately normally distributed with the mean value close to unity, **Figure 3.2.4c**.

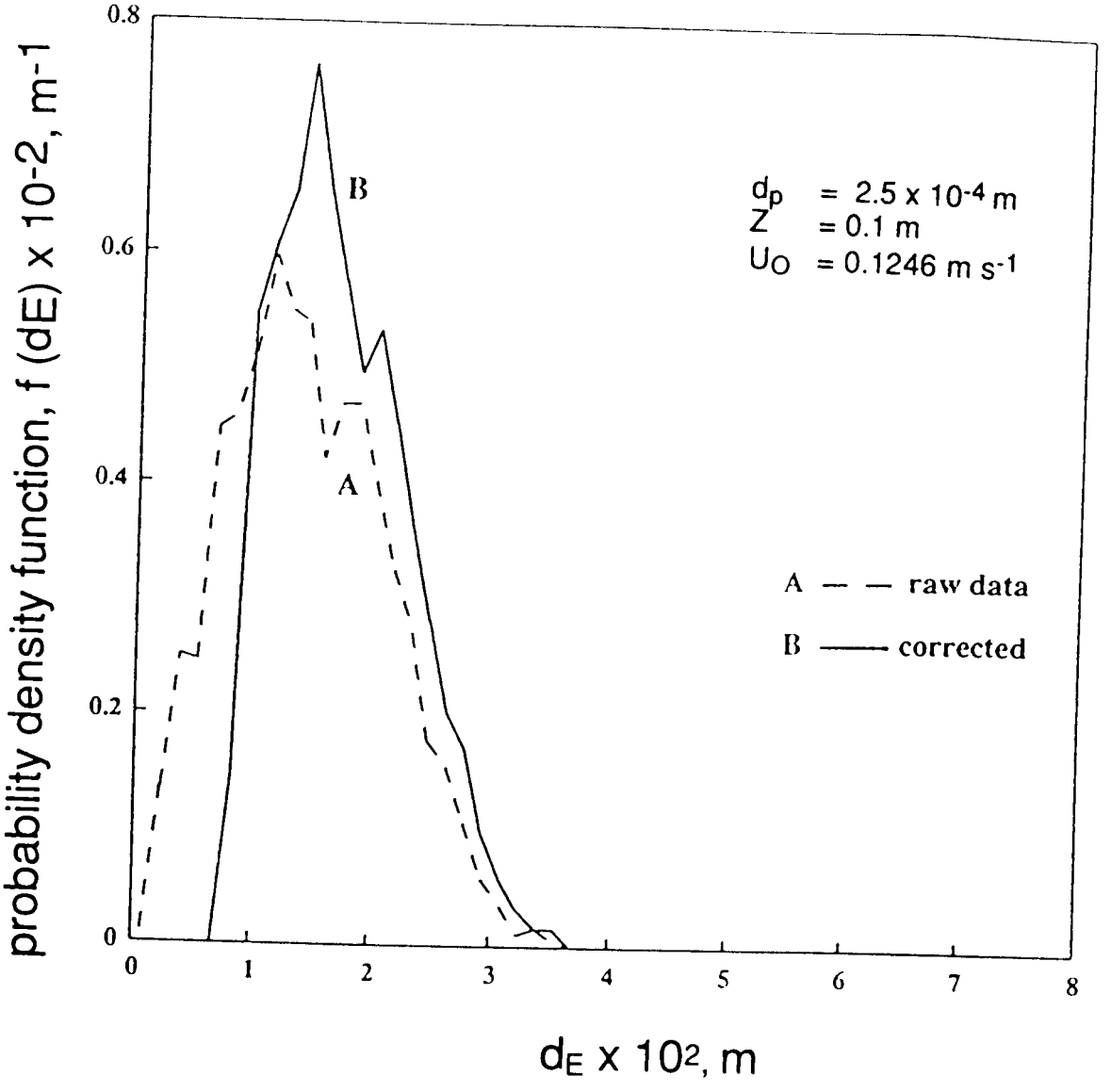

FIGURE 3.2.4a: Typical distribution of bubble diameter showing the effect of correction for the undersized bubbles

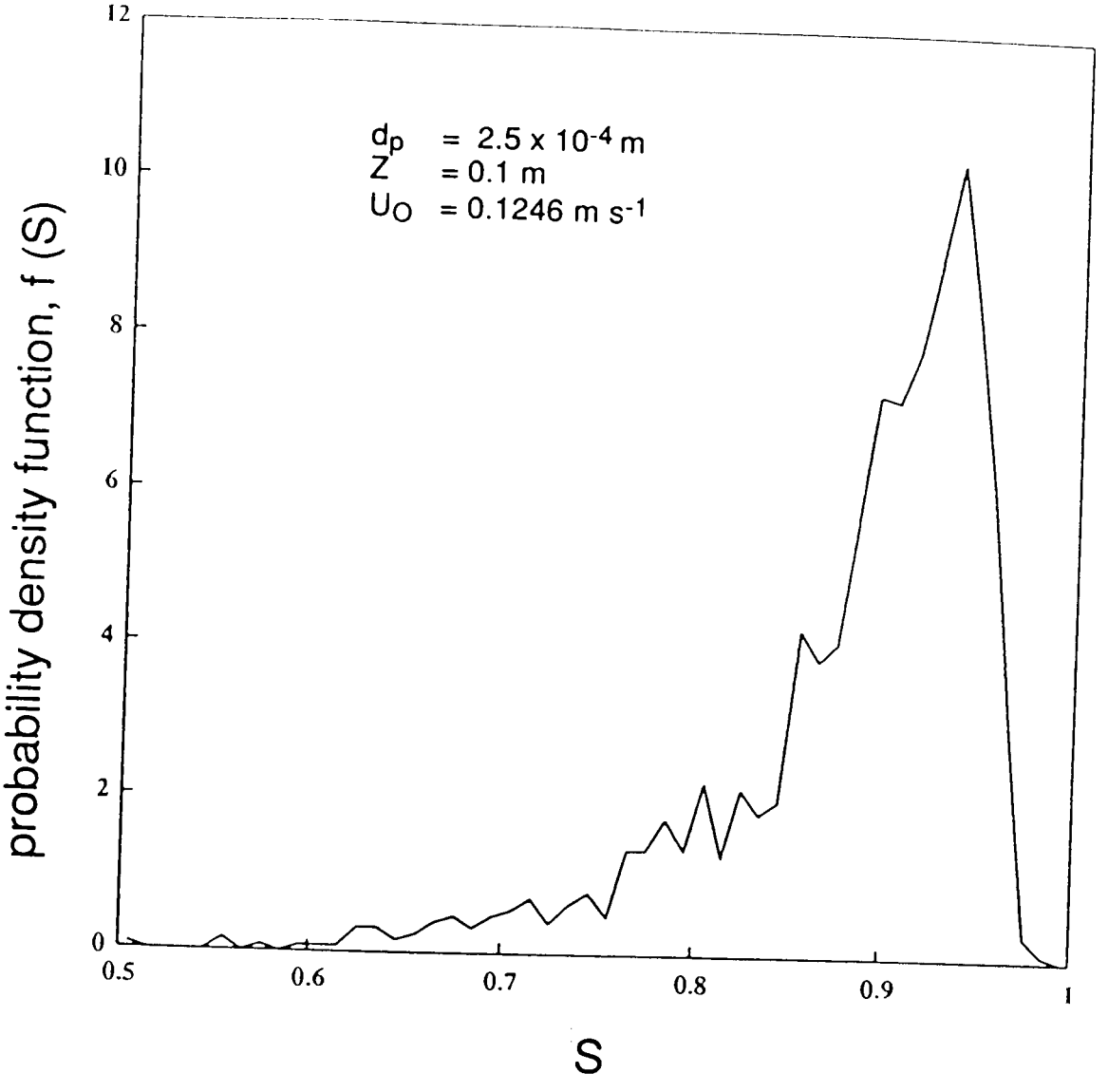

FIGURE 3.2.4b: Distribution of shape factor S

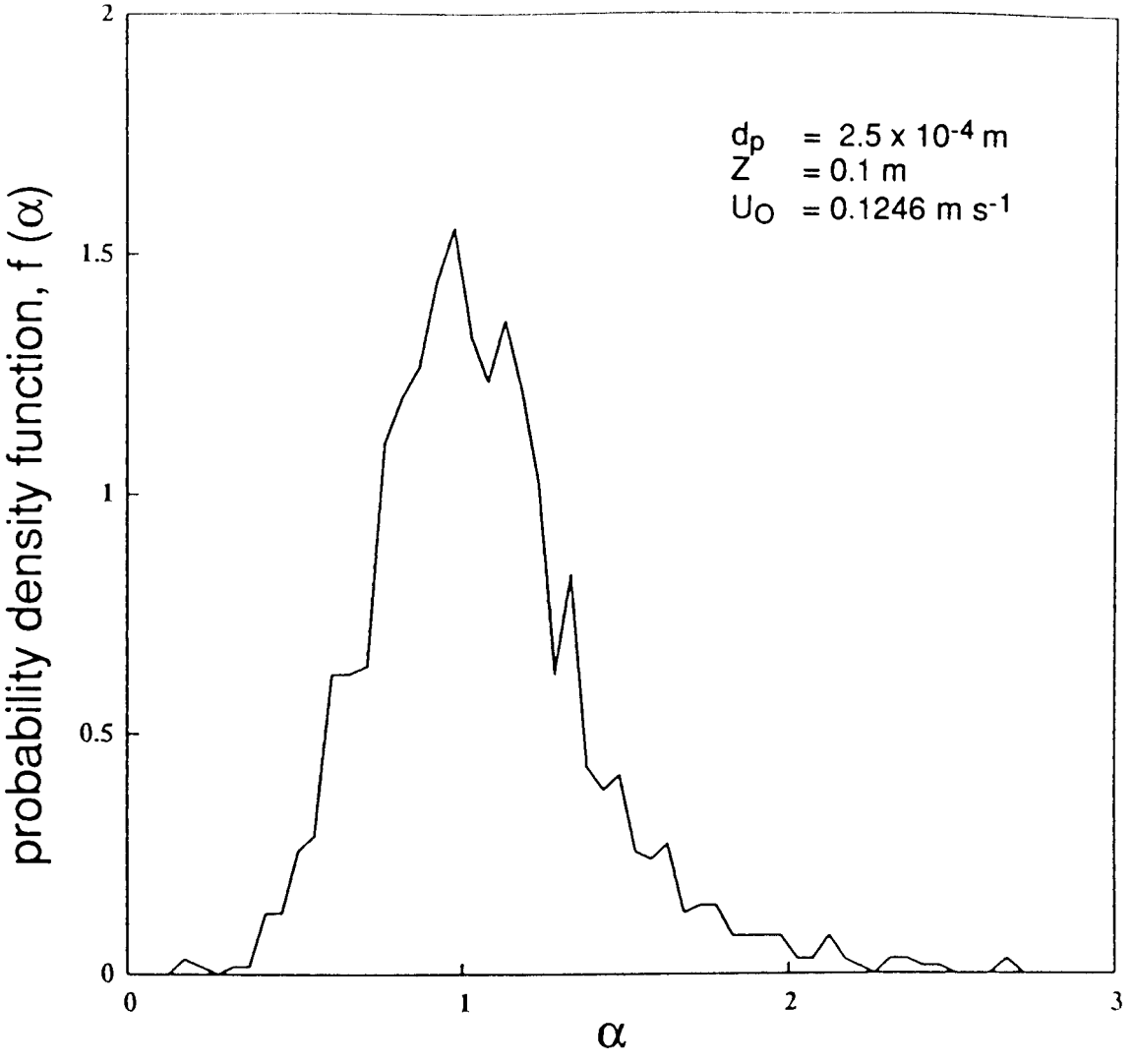

FIGURE 3.2.4c: Distribution of bubble aspect ration α

3.2.2 Measurement of Bubble Pierced Length at an 'Imaginary' Probe

3.2.2.1 Experimental procedure

The experimental set-up used for measurement of bubble pierced lengths is shown **Figure 3.1.3a**. Two size fractions of glass ballotini (2.1×10^{-4}m and 2.5×10^{-4}m) were used as bed material and the corresponding minimum fluidization velocities were 0.031 m/s and 0.068 m/s respectively. Experiments were performed under different fluidizing conditions and at various 'imaginary' probe positions within the bed. The operating conditions employed are summarized in **Table 3.1**

3.2.2.2 Measurement method

The operation of an in-bed probe is simulated by specifying its 'imaginary' position, X, within the bed, **Figure 3.2.5**. One frame of the image is captured and analysed at a time. The parameters of a bubble are measured only if the bubble intercepts the specified probe position, that is, if X lies within the bubble. For each detected bubble, the vertical chord drawn through X to the boundary of the bubble was taken as its pierced length, y. In addition, size measures (maximum vertical and horizontal lengths, d_V and d_H respectively), projected area, A, and circumference, C_P, were also measured. Measurements of these parameters were performed by scanning the image in both horizontal and vertical directions. Several hundreds of bubbles were analysed and the distributions of various bubble properties are generated.

It must be emphasized that this approach measures the temporal size distribution of the bubbles at the 'imaginary' probe position. Hence, this approach must be distinguished from a photographic analysis which measures

TABLE 3.1. EXPERIMENTAL OPERATING CONDITIONS FOR MEASUREMENTS ON BUBBLE PIERCED LENGTHS

	Powder size ($x10^4, m$)	
	2.1 (U_{mf} = 0.031 m/s)	2.5 (U_{mf} = 0.068 m/s)
Fluidising velocity $x10^2, m/s$	10.13	8.40, 12.46, 13.3
Bed heights $x10^2, m$	10, 20	5, 10, 20, 25
Probe position ($2L_{pr}/D_T$)	0	0, 0.2, 0.4, 0.6, 0.8

the size distribution of bubbles in the entire frame - that is, the spatial size distribution. If the spatial size distributions are measured, it is necessary to convert them to the temporal size distribution taking bubble velocity into account.

Typical results obtained from the experiments are shown in **Figure 3.2.6** where the cumulative distributions of y, $d_H$and d_V have been plotted. The measured projected area data were converted to the area equivalent diameter, d_E, using $d_E = \sqrt{4A/\pi}$, equation (3.2.1); the cumulative distribution of d_E has also been plotted in **Figure 3.2.6**.

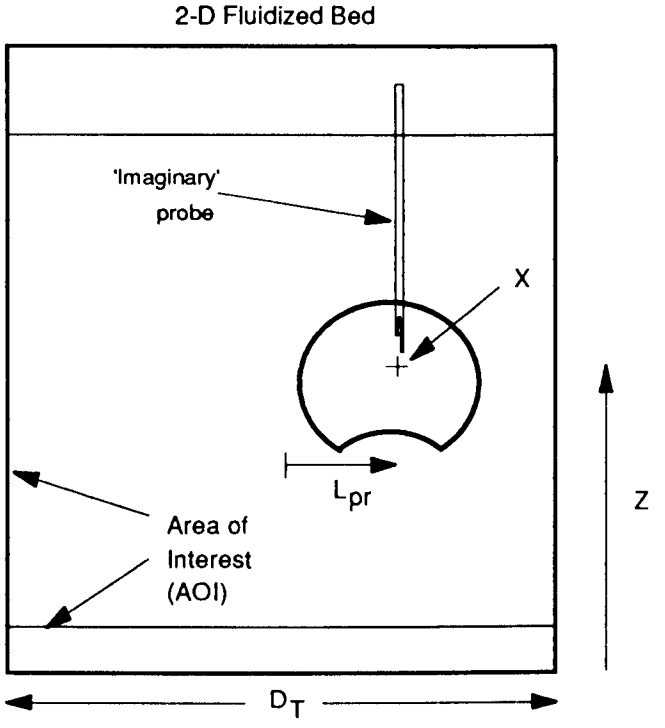

FIGURE 3.2.5: A schematic showing the position of an 'imaginary' probe, X.

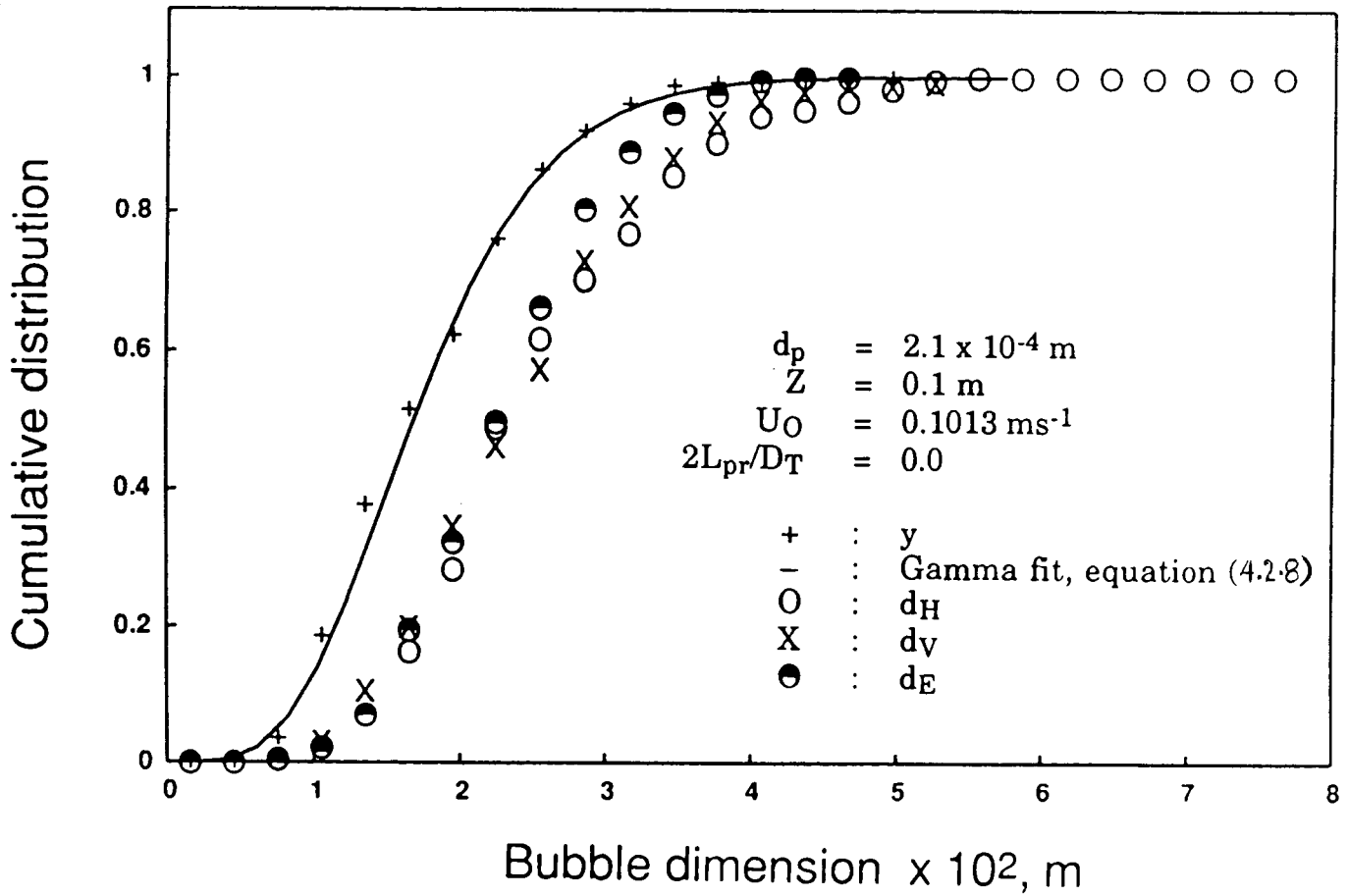

FIGURE 3.2.6: *Local* cumulative distributions for the bubble dimensions y, d_H, d_V and d_E measured from the experiments.

3.2.3 Measurement of the Angle of Bubble Rise and Bubble Velocity

3.2.3.1 Experimental procedure

For bubble velocity measurements, both on-line and off-line measurement methods - **Figures 3.1.3a** and **b**, were used. The local characteristics of the bubbles were measured for a fluidized bed of glass ballotini of size 2.4×10^{-4}m (U_{mf} = 0.0528 m/s). The static bed height, H_F, was 0.36 m in all experiments. Measurements of bubble size/shape, velocity and the angle of incidence were performed for several fluidizing gas velocities. To determine the effect of spatial location on the measured variables, experiments were conducted at several lateral positions - L_{pr} denoting the distance of the imaginary probe from the central vertical axis of the bed of width W - at different heights, Z, above the distributor. The experimental conditions used are summarized in **Table 3.2**.

Additional experiments were performed to compare the bubble size/shape and velocity relationships for bubble swarms formed at the porous distributor with those from a single nozzle ($\phi = 2mm$), J-shaped injector operated to produce single bubbles or a continuous chain of bubbles. For these experiments, the bed was maintained at minimum fluidization conditions with gas flow through the porous distributor. A fixed volume reservoir (cylindrical tube of diameter 0.125 m and length 0.330 m) maintained at variable gauge pressure was used to generate bubbles; the experimental conditions are summarized also in **Table 3.3.**

TABLE 3.2. EXPERIMENTAL OPERATING CONDITIONS FOR BUBBLE VELOCITY MEASUREMENTS

FREELY BUBBLING FLUIDIZED BED			
particle size	probe location		U_O/U_{mf}
$x10^6, m$	$2L_{pr}/W$	Z/H_F	$U_{mf} = 0.0528 m/s$
180-300	0.0	0.55	1.4, 1.75, 2.28, 2.84
	0.0, 0.5	0.55	2.84
	0.0, 0.25, 0.5	0.28	2.84

CONTINUOUS INJECTION OF BUBBLES IN INCIPIENTLY FLUIDIZED BED (Injector located at bed central axis and 0.03 m above the distributor)			
particle size	probe location		volumetric rate
$x10^6, m$	$2L_{pr}/W$	Z	l/min (69 kPa g)
180-300	0.0	0.78	1.0, 1.5, 2.0, 3.0, 4.0, 6.0

SINGLE INJECTED BUBBLES IN INCIPIENTLY FLUIDIZED BED (Injector located at bed central axis and 0.03 m above the distributor)		
particle size $x10^6$, m	dimension of cylindrical reservoir	reservoir pressure kPa g
180-300	ϕ = 0.125 m, L = 0.33 m	103.4, 137.8, 172.3

3.2.3.2 Measurement method

An 'imaginary' probe was assigned at a specified position in the bed. Bubble properties were measured if a bubble was found to be intercepted by this 'imaginary' probe in any given image frame.

The novel technique for the measurement of the instantaneous velocity of the bubble and the angle of bubble rise (or the angle of incidence at the vertical probe) utilizes the 1-2 interlace image scanning feature which is intrinsic to most standard video imaging systems. A full image is composed of two half images - an odd field and an even field. While the camera acquires one field, the other field is sent to the digitizer board or frame grabber. There is a short time period - known as the vertical blanking time - between the end of the acquisition of one field and the beginning of the acquisition of the next field. However, this time interval is negligible in comparison with the total acquisition time (1/25 s) for a frame. Therefore, the time delay between the odd and even fields is 1/50 s. For measurements, the two image fields were separated from a single image frame and analysed, **Figure 3.2.7**, to determine the location of the bubble centroid in each image field. The instantaneous bubble velocity was determined from the translation of the bubble centroid over the time interval (1/50 sec) between the image fields. The absolute bubble velocity, $V_{B,S}$, was calculated using

$$V_{B,S} = \sqrt{V_{B,x}^2 + V_{B,y}^2} \qquad (3.2.11a)$$

where $V_{B,x}$ and $V_{B,y}$ are the measured velocity components in the x and y directions respectively. Further, the angle of incidence, θ_B, was deduced from

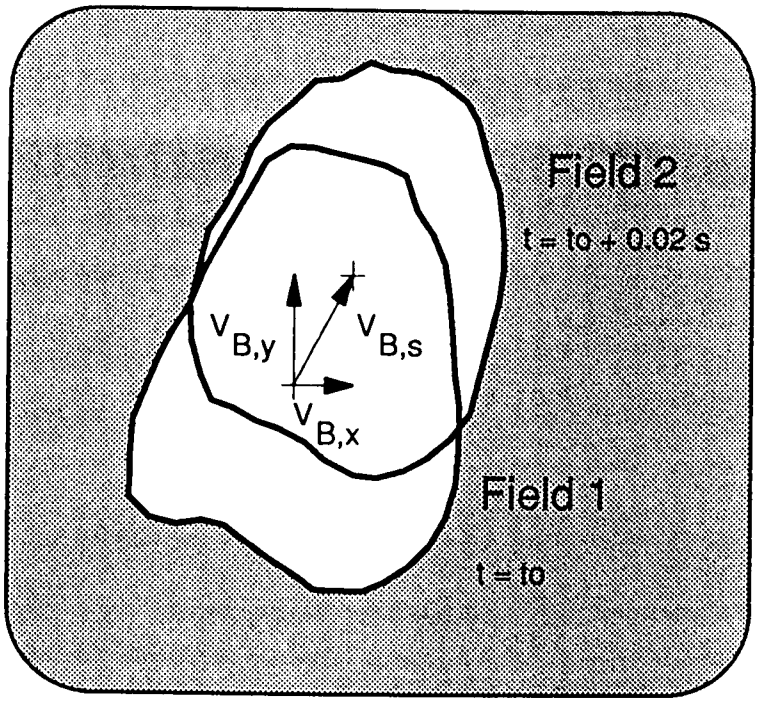

FIGURE 3.2.7: Measurement of bubble velocity and angle of incidence utilizing 1 : 2 interlaced image scanning feature.

$$\theta_B = \tan^{-1}\left(\frac{V_{B,x}}{V_{B,y}}\right) \qquad (3.2.11b)$$

The global intensity thresholding method, described in **section 3.2.1**, was utilized for the bubble edge detection and the measurement of bubble size parameters (area A, perimeter C_P, area - equivalent diameter d_E, vertical d_V and horizontal d_H diameters) and shape (aspect ratio α, shape factor S) in each image field.

3.2.4 Measurement of Tracer Concentration in the Mixing of Uniform Solids

3.2.4.1 Experimental procedure

The experimental set-up for the solids mixing experiments is shown in **Figure 3.1.3b**. A layer of tracer particles, comprising a fraction x of the total bed volume, was introduced as a horizontal plane at location q (defined as relative position to the total fixed bed height, H_F). The total height of the fixed bed was 0.25 m. The bed was then fluidized at a pre-determined superficial gas velocity, U_O.

The measurements of the solids mixing behaviour were performed for the bed fluidized at various superficial gas velocities and with three different particle sizes. Additionally, the effect of initial conditions (amount and position of the tracer) on the solids mixing patterns were also investigated. A summary of the experimental conditions employed in this investigation is presented in **Table 3.3**.

Tracer particles for the experiments were prepared by dyeing ballotini using the method patented by Hyde (1940) and as described by Selim et al. (1983). Particles were treated with a 3% solution of ferrous sulfate at 358 K for about 30 minutes with occasional stirring. Subsequently they were treated with a warm 1 % solution of potassium ferrocyanide acidified with HCl to colour them Prussian blue. This colour was selected for the solid tracer because it gave maximum contrast with the uncoloured glass ballotini. Minimum fluidization velocity of the tracer particles prepared from each of three size fractions were determined experimentally; the colouring process had no significant effect upon the results, **Table 3.3**.

TABLE 3.3. EXPERIMENTAL CONDITIONS FOR STUDIES ON MIXING OF UNIFORM SOLIDS

Particle Size d_p**(m)**	**Total tracer concentration, x**	**Initial tracer position, q**	U_o/U_{mf}
2.40×10^{-4} (Bulk U_{mf}= 0.068 m/s) (Tracer U_{mf} = 0.067 m/s)	0.1, 0.2, 0.3, 0.5	0.0, 0.4, 0.5, 0.7, 0.8, 0.9	1.63, 1.91, 2.20, 2.50, 3.56, 4.64, 6.91
5.12×10^{-4} (Bulk U_{mf}= 0.240 m/s) (Tracer U_{mf} = 0.235 m/s)	0.2	0.8	1.43, 1.68, 1.94, 2.21, 2.25
7.25×10^{-4} (Bulk U_{mf} = 0.350 m/s) (Tracer U_{mf} = 0.339 m/s)	0.2	0.8	1.35, 1.54, 1.75, 2.00, 2.23

3.2.4.2 Measurement method

The mixing behaviour of the solids tracer in the bed was observed through the CCD video camera. The bed was illuminated with front and back lighting to permit distinction of the bubble phase from the dense phase; and, at the same time, to provide sufficient contrast for the coloured tracer and the bulk material.

Independent measurements of bubble size, d_B, bubble velocity, U_B, and the expanded bed height, H_E, were also carried out. Bubble size and velocity were measured using the techniques described in **sections 3.2.1** and **3.2.3**.

Intensity and Concentration Relationship : The principle for the measurement of the tracer concentration is based on the fact that the frame grabber digitizes each of the 512 x 512 pixels (picture elements) comprising a frame into gray scale values from 0 to 255. The dark tracer (dyed in Prussian blue) would then acquire lower gray scale values in contrast with the uncoloured bulk bed material. These two pure constituents should possess gray scale values at the opposing extremes of the gray scale spectrum; for a mixture consisting of the dyed tracer and undyed bed material, the gray scale value should lie between these limits. Ideally, the gray scale value of a sample consisting of any amount of the tracer should vary linearly with concentration. Preliminary tests showed that there was a unique and monotonic relationship between the tracer concentration and gray scale value, but the relationship was not linear. This could be an intrinsic characteristic of the photo-sensitivity in the video camera or the reflective and transmittive properties of the glass beads. Nonetheless, the relationship between the tracer concentration and gray scale intensity could still be established if samples of known concentrations were used for calibration.

The calibration of tracer concentration, defined in terms of volume fraction (or weight fraction if tracer particles and the bulk material have the same density), was conducted by mixing a known quantity of tracer material in a fluidized bed containing the bulk material. The measured intensity distribution of the well-mixed sample was found to follow a Normal Distribution. The mean was then taken as the characteristic gray scale value representing the sample concentration. Similar tests were conducted for different quantities of tracer and plots of the intensity values with respect to the tracer concentration are shown in **Figure 3.2.8**. The results showed that the intensity became less sensitive to concentration at higher tracer concentrations. The tracer used in the experiments was, therefore, diluted to a concentration C_C (shown in **Figure 3.2.8**) to ensure operation in the region where intensity varied strongly with tracer concentration.

The functional relationship between the concentration and the *absolute* gray scale value established at one background lighting condition can not be applied to experiments conducted at other conditions. To overcome such difficulties, the measured absolute values were normalized with respect to the gray scale values of the unmixed (or pure) components; the normalized gray scale parameter, I_{nor}, was defined as

$$I_{nor} = \frac{I - I_{\min}}{I_{\max} - I_{\min}} \tag{3.2.12}$$

where I, $I_{\min}$ and $I_{\max}$ represent the absolute gray scale intensity for the mixture, the unmixed components having darker (the tracer) and lighter (the bulk) colours respectively.

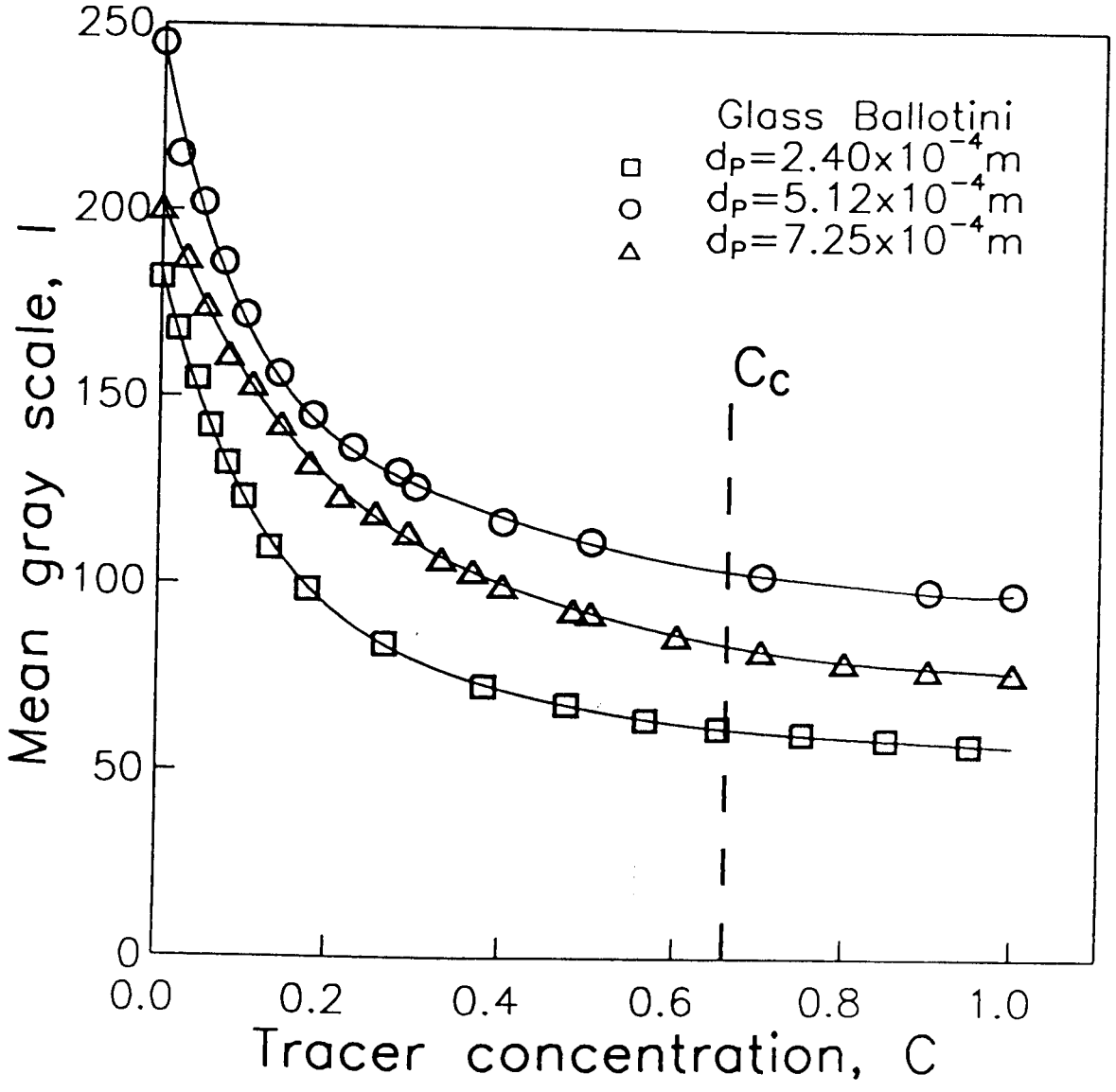

FIGURE 3.2.8: Relationship between the reflected light intensity (grey scale) and concentration (volume fraction) of the coloured tracer particles.

A normalized functional relationship between C_{nor} (where C_{nor} = 1.0 at C_C) and I_{nor} was established and was plotted, **Figure 3.2.9**. This normalization procedure eliminated the local variability when the tracer particles were used at different background conditions. The relationship was expressed as an n-order polynomial equation and readily evaluated by computer in the automated data analysis routine. Different correlations were obtained for the different types of glass ballotini used. In the absence of a physical model, generality can not be claimed for these calibration results. Since the above correlation was derived from a statistical method, the results are not exact. Evidently, some degree of uncertainty is associated with the method of concentration measurement using this approach; however, error analysis indicated that the extent of uncertainty in the concentration was ±5%which, in practice, is reasonable.

Data Analysis : The data analysis routine is divided into two stages.

In the first step, the bubble phase was distinguished from the dense phase by thresholding techniques. This can be accomplished readily as the bubble phase possesses higher intensity values in comparison to the dense phase. However, preliminary tests showed that as the mixing of the coloured tracer progressed, the detection of the bubble/dense phase boundary, using the pre-determined global threshold, was becoming unsatisfactory and the bubble void area was consistently underestimated. This occurred due to the continuous change of the intensity distribution of the image as the initially uncoloured bulk of the solids progressively mixed with the darker tracer, turning the bulk phase to a slightly darker mixture; measurements confirming this change are shown in **Figure 3.2.10**. This problem necessitated the use of adaptive

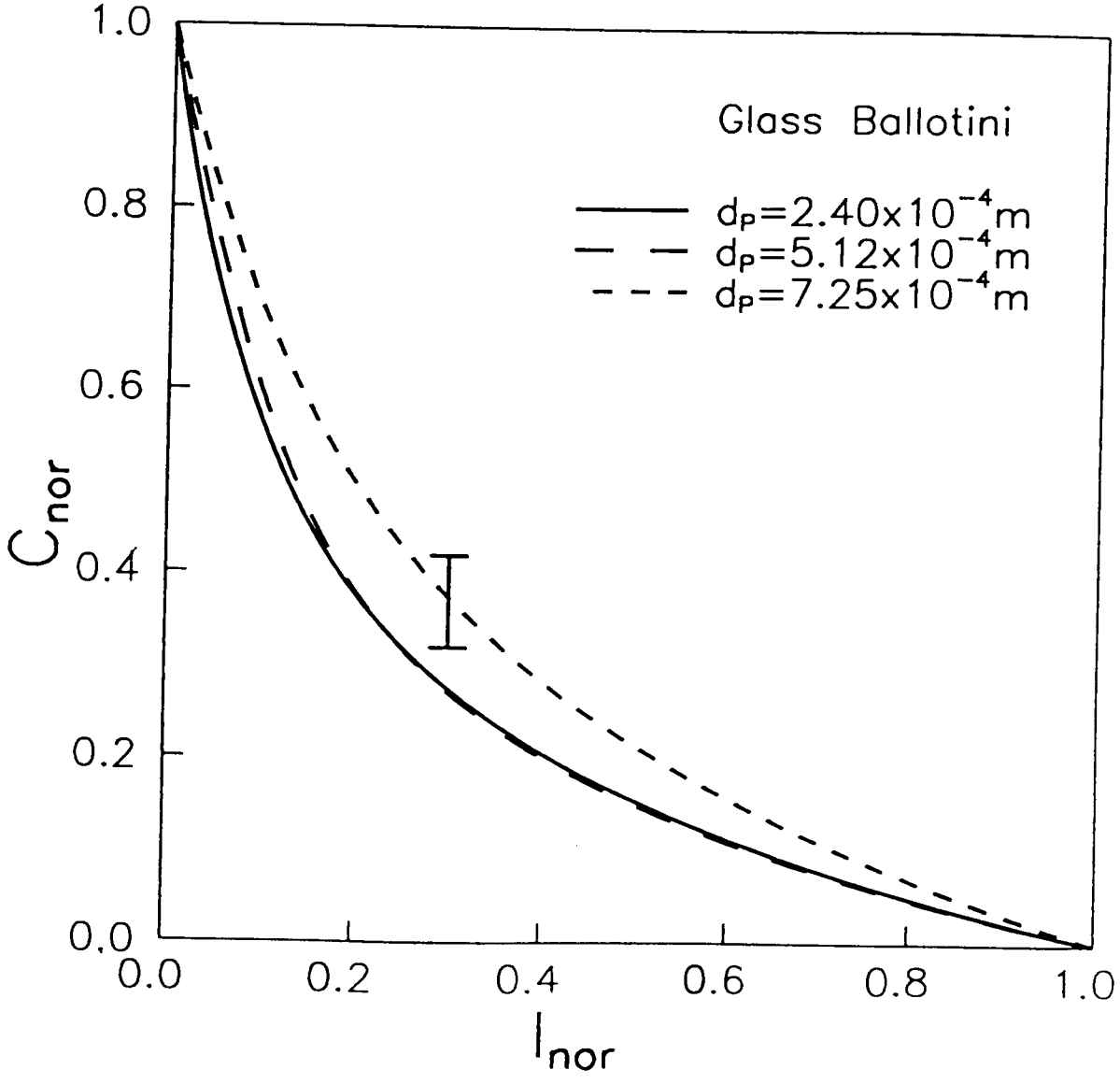

FIGURE 3.2.9: Normalized calibration curves for tracer concentration for different types of coloured tracer particles.

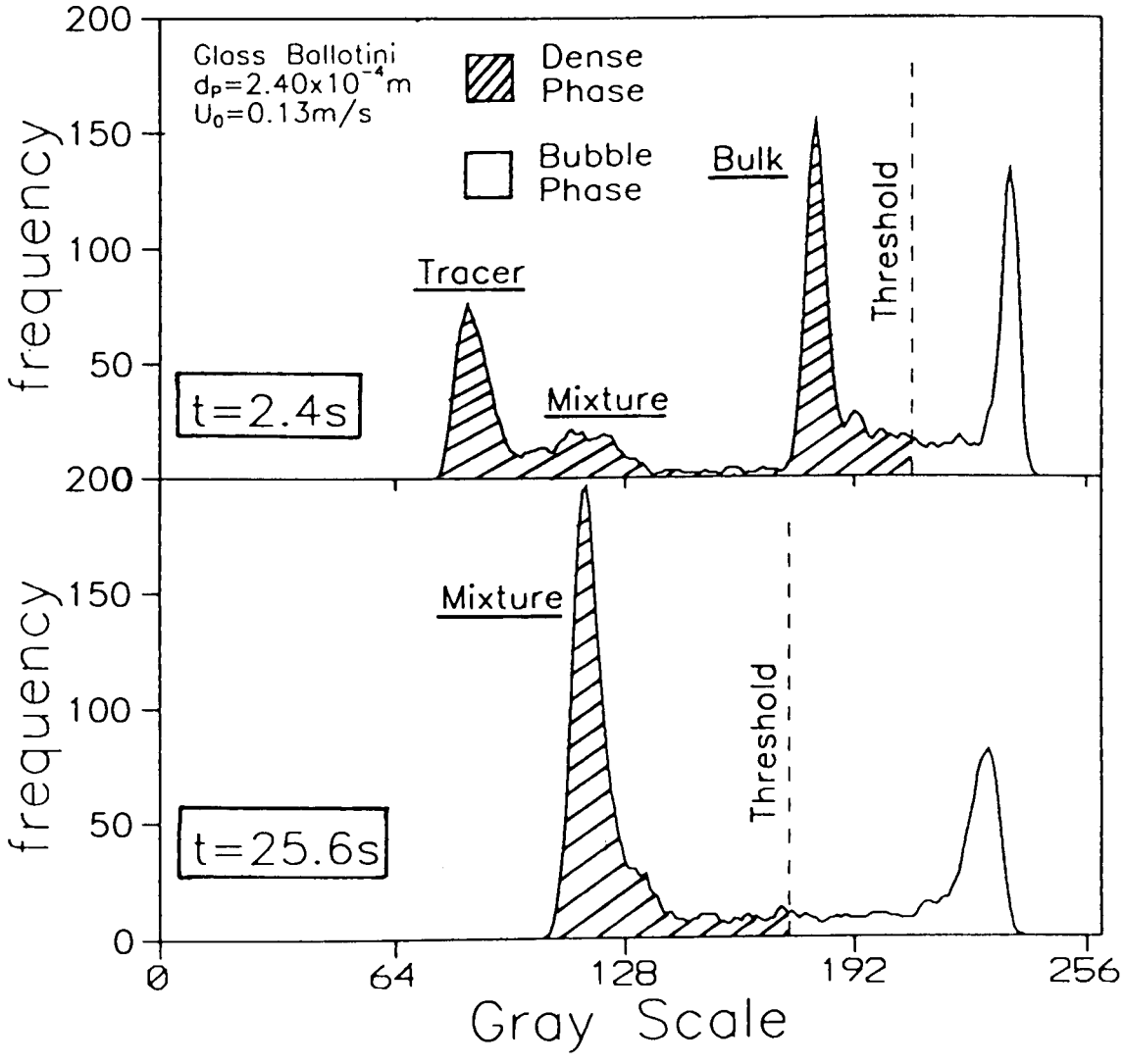

FIGURE 3.2.10: The continuously changing of threshold value for the bubble edge detection as a result of changing image intensity distribution.

thresholding methods and a scheme for an automated determination of the varying threshold values was also incorporated in the procedures for boundary detection. Visual inspection, on the video monitor, of the images being analysed confirmed that such refinement improved the operation of the phase identification and separation routines.

In the second stage, the tracer concentration of each cell, $C_{i,j}$ consisting of 0.01 x 0.01 m^2 cell size at a given location in the bed, was determined from the mean intensity (or gray scale) of the cell excluding the bubble phase and then inferred from the concentration/intensity calibration curve. The temporal volume fraction or concentration $C(Z,t)$ of the solids tracer at a given a horizontal plane above the distributor plate, $i = Z$, was determined by summing the tracer fraction in each cell across the horizontal plane, namely

$$C(Z,t) = \frac{\sum_{j=1}^{N} \Delta A_{i,j} C_{i,j}}{\sum_{j=1}^{N} \Delta A_{i,j}} \qquad (3.2.13a)$$

where $\Delta A_{i,j}$ is the incremental cell area excluding the bubble phase in *ith* row and *jth* column depicted in a two-dimensional M x N matrix. Similarly, the temporal bubble fraction, $\varepsilon_B(Z,t)$, was defined as

$$\varepsilon_B(Z,t) = 1 - \frac{\sum_{j=1}^{N} \Delta A_{i,j}}{W \Delta Z} \qquad (3.2.13b)$$

where W and ΔZ denote the bed width and size of incremental bed height. A schematic diagram depicting the procedure used for the analysis of concen-

tration is shown in **Figure 3.2.11**. Typical measurements of the total tracer concentration, $C(Z,t)$, and bubble fraction, $\varepsilon_B(Z,t)$, at a given height are shown in **Figure 3.2.12a** and **b**.

It was observed that the axial concentration measured at heights near the region where the tracer was located initially was lower than its expected value towards the start of the run. This anomalous result is shown in **Figure 3.2.13** where the tracer concentration was expected to be close to 1 for $t \sim 0$ whereas the measurements were significantly lower. A little thought revealed that this anomaly arose from the severe distortion and deformation experienced by the tracer layer during bed expansion immediately after the injection of the fluidizing gas at the distributor. Images dumped to the printer from the videotape, **Figure 3.2.14**, illustrate the progression of events for the run corresponding to the measurements plotted in **Figure 3.2.13**. An estimate for the time duration of the anomalous result is expected to be of the order of the height of the tracer layer divided by the velocity of the initial bubble; for all cases considered in this investigation, the anomaly is expected to last less than a second. Measurements at locations other than the immediate vicinity of the tracer layer will not show this behaviour. In addition, the sequence of events shown in **Figure 3.2.14** also establishes that the temporal fluctuation in the measurements of tracer concentration as well as bubble fraction (**Figure 3.2.12a** and **b**) is mainly due to the passage of the bubbles. For the purpose of model comparison with the experimental data in **section 5.1**, such temporal fluctuations in the measurements were smoothed by averaging a number of data

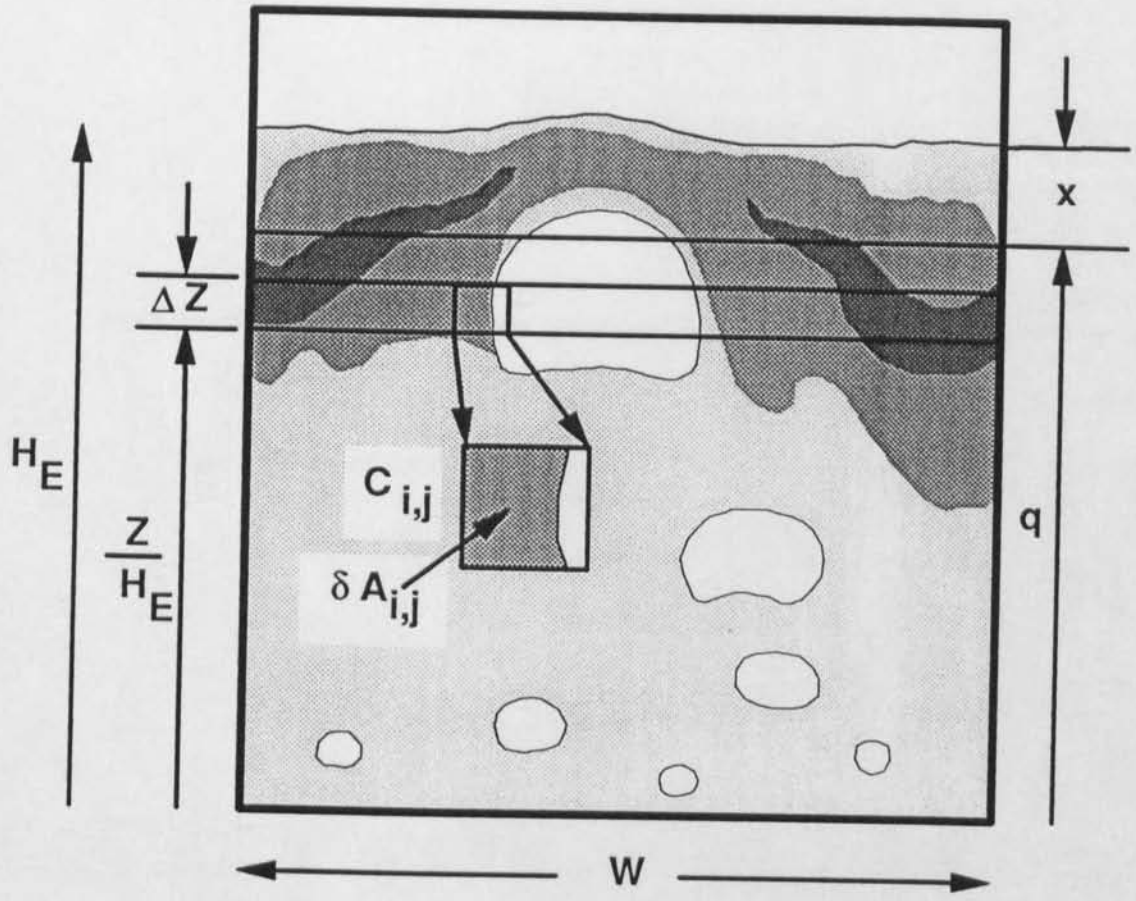

FIGURE 3.2.11: A schematic of the analysis of tracer concentration in square cells along a horizontal plane in a fluidized bed.

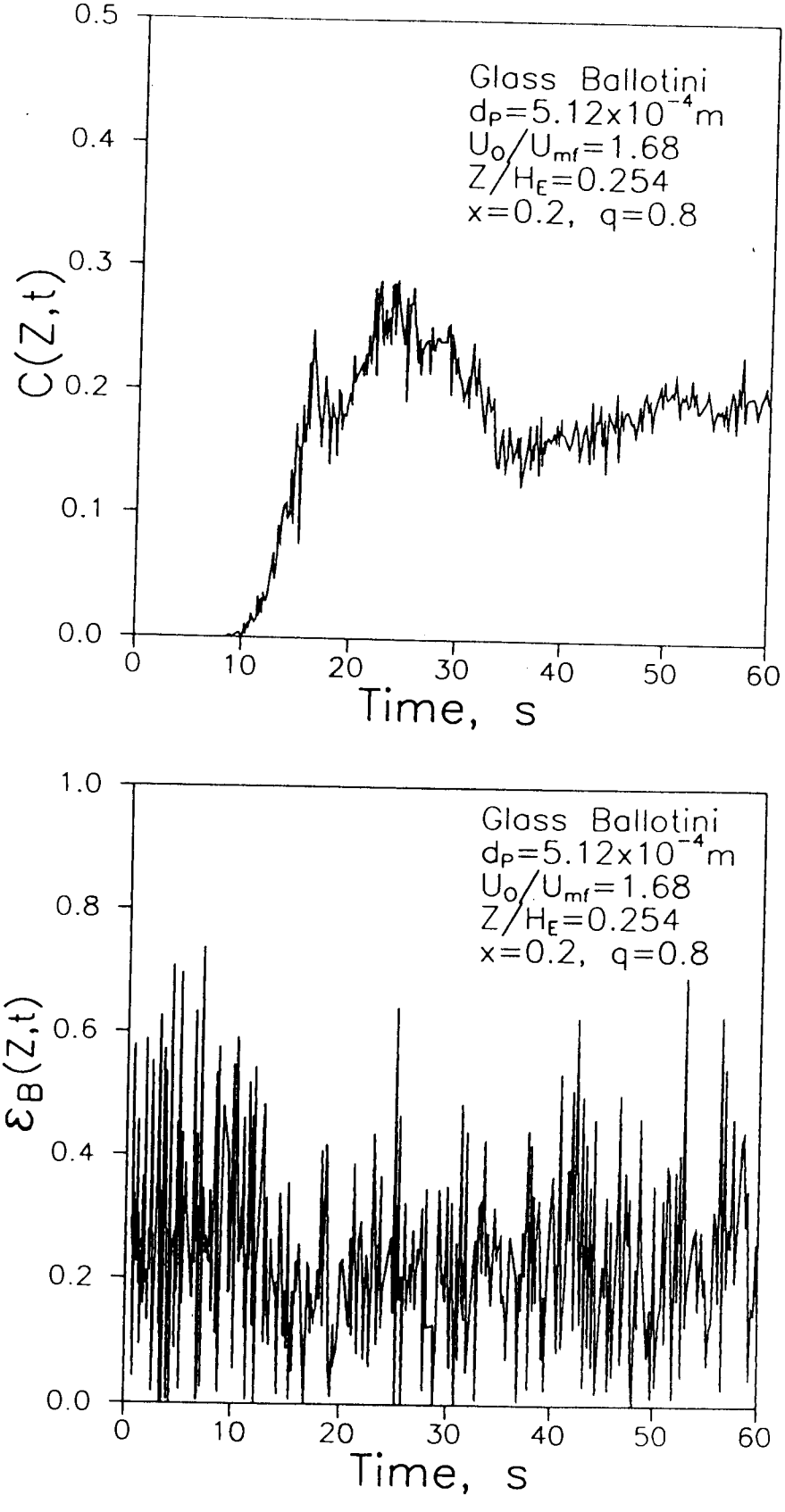

FIGURE 3.2.12: A typical temporal response of (a) Concentration of solids tracer: (b) Bubble fraction across the bed width at height $Z/H_E = 0.254$.

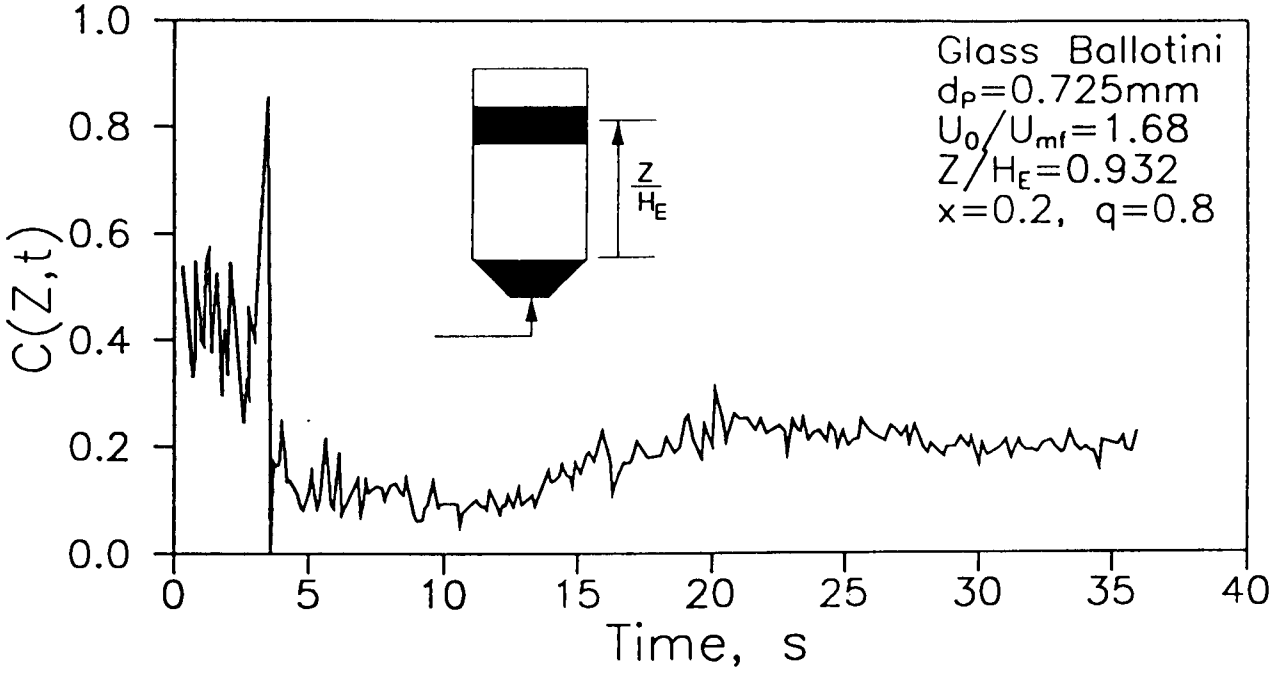

FIGURE 3.2.13: Anomalous result in tracer concentration measurement at height near the initial tracer location

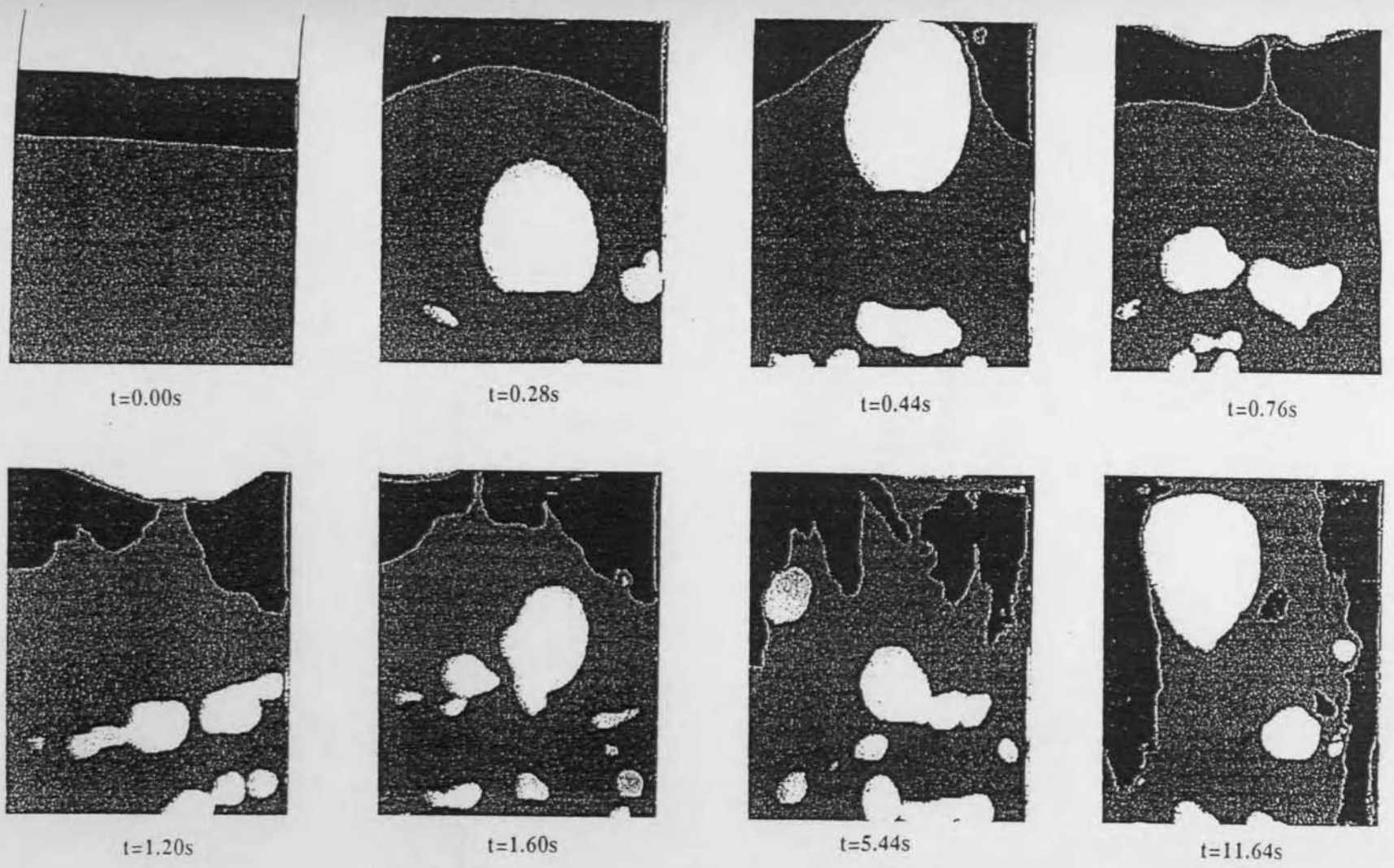

FIGURE 3.2.14: The sequence of images showing the distortion of tracer layer during the initial introduction of gas bubble into the bed.

points within a specified time interval. The smoothing procedures were performed with care so that the gross solids mixing patterns were not severely distorted.

3.2.5 Measurement of Jetsam Concentration in Segregating Binary Fluidized Systems

3.2.5.1 Experimental procedure

The rate of segregation of binary-particle system as a result of of density or size difference was investigated in the two-dimensional bed shown in **Figure 3.1.3b**. The process of segregation occurring when the initially well-mixed bed was fluidized at a gas velocity was observed using a CCD video camera and recorded on tape. A fully-mixed bed was achieved by fluidizing the mixture at gas velocity slightly higher than the minimum fluidization velocity of the heavier or larger component, $U_{mf,J}$ for several minutes. A mixture containing 0.2-0.25 weight fraction of the jetsam was used. The total height of the fixed bed was around 0.2-0.25m. The types of particles used in these studies are show in **Table 3.4.** The bed particles consisted of glass ballotini which possessed a lighter color. The solids (jetsam) of darker color were chosen as tracer particles. Tracer particles made from larger glass ballotini were also dyed according to the procedure discussed in section 3.2.4. The effect of fluidizing velocity on the solids mixing and segregation was also studied. The range of gas velocity used is show in **Table 3.5**. The minimum fluidization velocities of the mixtures as a function of composition were also measured using the fast defluidization procedures described by Nienow and Chiba (1985); a typical result is shown in **Figure 3.2.15**.

3.2.5.2 Measurement method

Calibration of jetsam concentration : The concentration of the tracer material was inferred from the intensity of the mixture as described in **section 3.2.4**. A calibration curve was charted out for each type of the binary mixture

TABLE 3.4 PHYSICAL PROPERTIES OF PARTICLES USED IN SEGREGATION STUDIES

Particle Type	Size d_p (m)	Density ρ_P(kg/m^3)	Minimum fluidisation velocity U_{mf} (m/s)
Glass Ballotini	2.40×10^{-4} +	2482	0.068
	5.12×10^{-4} +,*		0.22
	7.25×10^{-4} *		0.38
Aluminium oxide	4.14×10^{-4} *	3557	0.32
	5.18×10^{-4} *		0.40
	6.45×10^{-4} *		0.38

+ Bulk (Flotsam)

* Tracer (Jetsam)

TABLE 3.5 EXPERIMENTAL CONDITIONS FOR SEGREGATION STUDIES

Set	Size ratio d_J/d_F	Density ratio ρ_J/ρ_F	U_{mf} ratio $U_{mf,J}/U_{mf,F}$	Gas velocity U_O(m/s)	Jetsam mass fraction, x_J
A	3.02	1	5.60	0.14 - 0.464	0.2
B	2.14	1	3.23	0.85 - 0.206	0.2
C	1.73	1.43	4.70	0.134 - 0.401	0.25
D	1.26	1.43	2.45	0.342 - 0.602	0.25

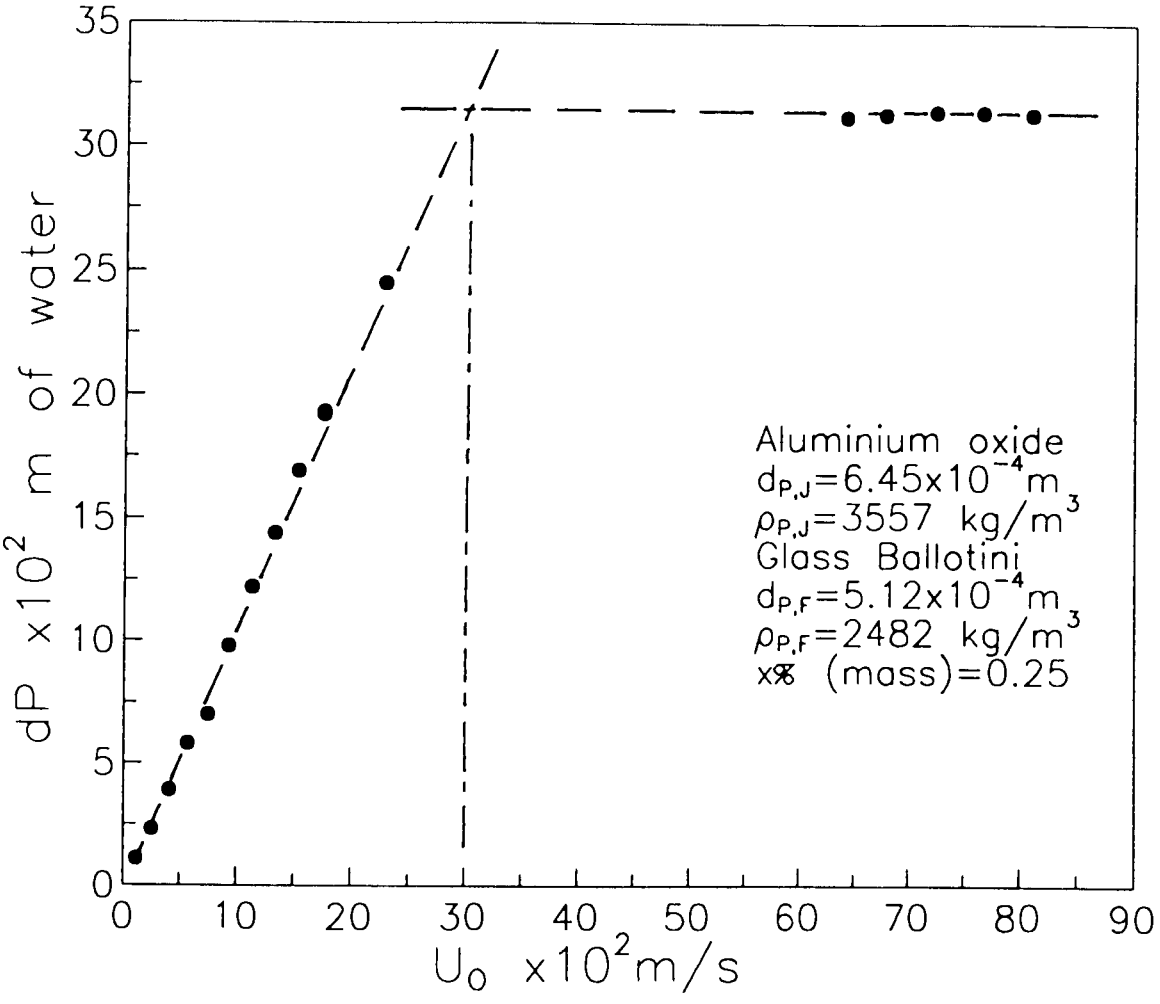

FIGURE 3.2.15: Minimum fluidization velocity of mixture determined from fast defluidization procedure.

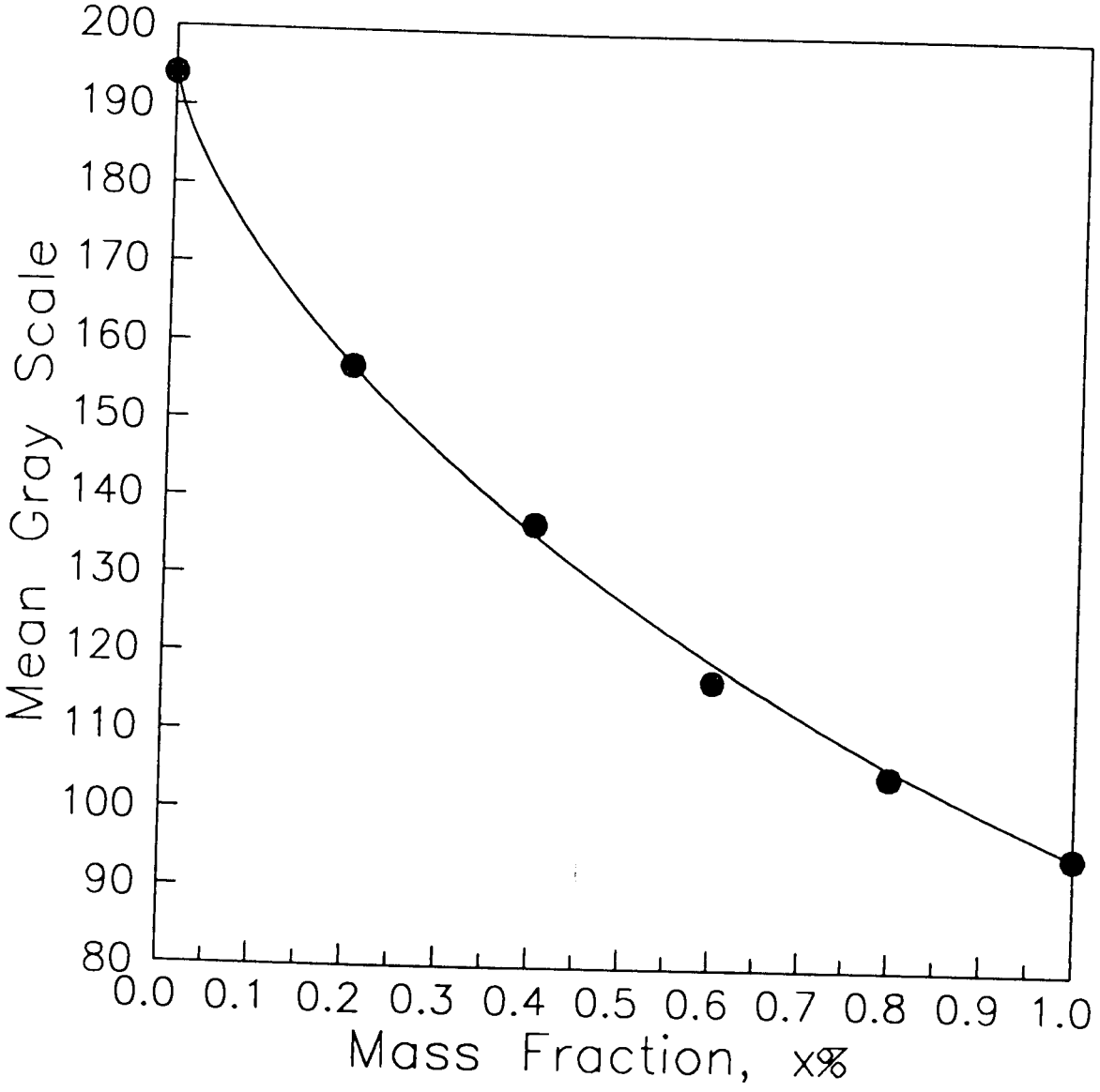

FIGURE 3.2.16: The fit of intensity change with composition of tracer concentration using exponential decay function.

used. In the course of this investigation, it was ascertained that the change of the intensity with the concentration of the tracer followed a functional relationship which could be uniquely described by an exponential decay function similar to the Beer's law

$$I = I_O \exp(-\kappa C^{\eta}) \qquad (3.2.14)$$

The corresponding constants I_O, κ and η can be determined readily by solving the above equation from three independent intensity-concentration data sets. The validity of the equation (3.2.14) for describing the the change of intensity with concentration is shown in **Figure 3.2.16** where each data point was determined explicitly from sample mixtures of known concentrations. This method provided a very convenient method for the determination of concentration of coloured tracer materials in binary mixtures used in this work. The procedure used was to first measure the intensity values of both the pure tracer and bulk material before they were mixed in the fluidized bed. The intensity of the mixture was then measured following fluidization at a high velocity to achieve a well mixed condition. These three data points permitted the calculation of the three unknowns in equation (3.2.14). Thus a single calibration effort was required if all experiments were conducted using the same binary system.

Analysis procedure : The analysis procedure for the determination of jetsam concentration in the bed was similar to that described in **section 3.2.4** and illustrated in **Figure 3.2.11**. Adaptive thresholding was used to distinguish the gas bubbles from the solids phase. The intensity in a cell of 1×10^{-4} m^2 in the bed was measured and the jetsam concentration was inferred from the

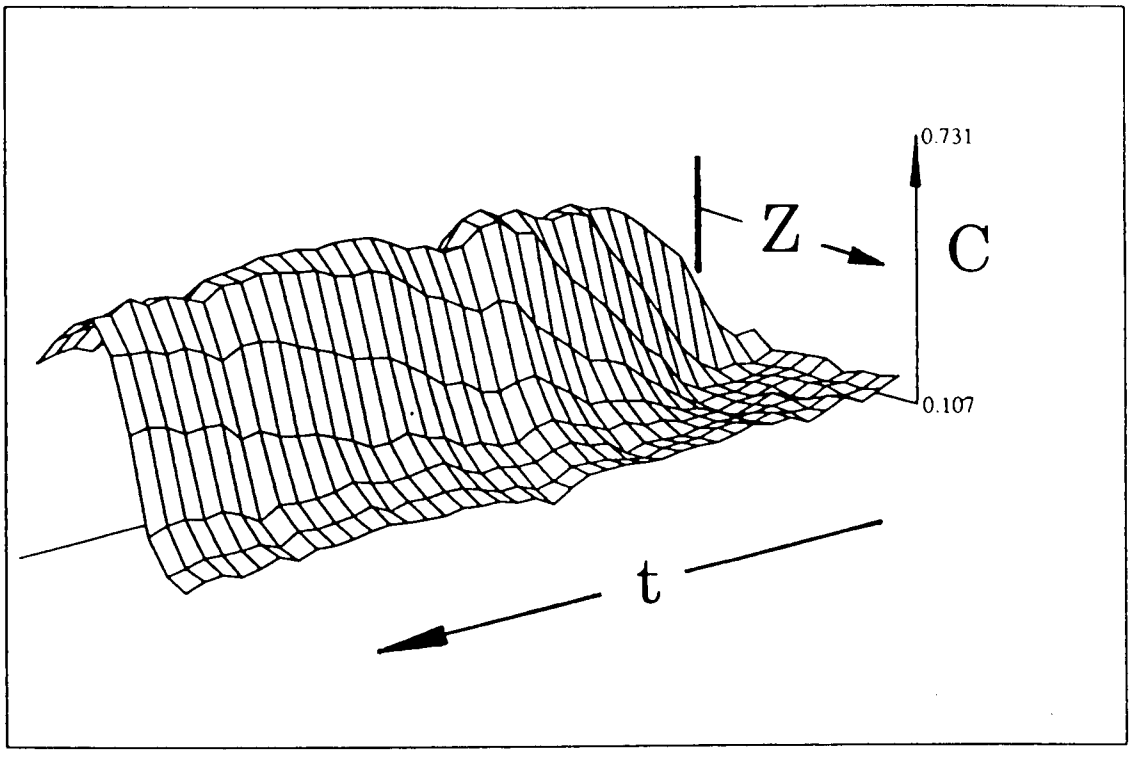

CZT

FIGURE 3.2.17: Surface plot of jetsam concentration in a binary fluidized bed

calibration curve. The average axial composition of the bed was calculated subsequently. Typical results are shown in **Figure 3.2.17** where a surface plot of the variation of the jetsam concentration with time is shown at different heights within the bed. Accumulation of the jetsam tracer in the lower regions of the bed with time is evident.

3.2.6 Measurement of the Circulation Patterns of Large and Lighter (or 'Active') Particle

3.2.6.1 Experimental procedure

For particle detection and tracking experiments, both off- and on-line measurement systems - **Figure 3.1.3a** and **b**, were employed.

The diameter of the 'active' particles used in this investigation was chosen as $7x10^{-3}$ m; such particles were large enough to permit easy detection and small enough to permit free movement in the bed with minimum interference from wall surfaces which are $9x10^{-3}$ m apart. 'Active' particles of different density were then prepared by impregnating plastic spheres of this size with materials of different densities or with an air cavity. Additional experiments were performed with coal particles of this size. Particle motion characteristics were measured in beds of glass ballotini (bed particle size : $7.12x10^{-4}$ m) operated at different superficial gas velocities. The physical properties of the bed and 'active' particles, and the fluidization conditions used in the experimental program are summarized in **Table 3.6.**

The motion of an 'active' particle (prepared from plastic or coal) was observed using a variable shutter speed ($2x10^{-2}$ to $1x10^{-4}$ s) CCD video camera (Sony XC/77RR-CE) capturing images at a rate of 25 frames per second.

In the first part of the investigation, the circulatory pattern of the 'active' particle motion in the bubbling bed was determined. The movement of particle was traced by performing the automated frame-by-frame analysis of images pre-recorded on the video tape, that is the off-line measurement system. With the knowledge of time and particle displacement, the velocity of the particle was calculated.

TABLE 3.6. EXPERIMENTAL CONDITIONS FOR THE STUDY OF LARGE PARTICLE MOTION AND DENSE PHASE RESIDENCE PROBABILITY MEASUREMENT

Bed particles			
d_P = 7.25 x 10^{-4}m, ρ_P = 2482 kg/m^3, U_{mf} = 0.38 m/s			
'Active' particle			
(d_A = 0.007 m)		U_O **(m/s)**	
Type	ρ_A **(kg/m^3)**	**Particle tracking experiment**	**Particle dense phase residence probability experiment**
plastic	947	0.565, 0.605, 0.687	0.565, 0.605, 0640, 0681, 0.721, 0.767, 0.81
	1141	0.604, 0.687, 0.774	0.681, 0.721, 0.767, 0.822, 0.870
	1309	0.774	0.681, 0.721, 0.766, 0.850
coal	1016	0.566, 0.602, 0.639, 0.680, 0.720, 0.764, 0.807	

In the second part of the study, the phase residence probability of the 'active' particle in a fluidized bed was measured. For such experiments - performed on-line - a number of frames were captured at random for a given duration (for example, an experimental run of 1.5 - 2 hours totalled to about 300-500 frames). The position of the particle and its association with either phases of the fluidized bed were determined for every frame. The time-averaged data were computed at the end of each run.

3.2.6.2 Measurement methods

Particle search and recognition : Since the particle may be present either in bubble or dense phase, a method for phase separation and identification is required. The interface between the bubble and dense phase could be distinguished without great difficulty by using intensity thresholding method. The value of the threshold could be obtained by examining the intensity histogram of the image (Lim et al., 1990). Though the 'active' particle is opaque, the intensity of the particle is not always constant and lower than that of dense phase. The relative intensity of the particle with respect to the dense phase was found to vary with the local intensity level of the surrounding region. For example, the particle would appear to be brighter closer to the bubble than when it was totally submerged in the dense phase. Hence, the 'active' particle can not be identified with simple thresholding method as that used for bubble-dense phase distinction. Interference from bed particles adjacent to the edge of the bubble further complicated the problem. Therefore, the measurement approach adopted additional identification logics as discussed in the following.

The key feature for the search method was to assume the particle always appeared slightly darker that its surroundings. However, due to the variation of particle intensity and background intensity throughout the bed area, an absolute minimum intensity of the whole bed area may not necessarily represent the 'active' particle. This problem was overcome by searching for the location of minimum intensity in a smaller sub-area or viewing area. Given all the possible 'active' particle positions (the darkest spot in each sub-area), the true position needs to be located. Image intensities in the regions neighbouring a probable position - represented as a 3 by 3 array of square cells, each of the size of the 'active' particle with the probable particle located on the central cell $A_{2,2}$ as shown in **Figure 3.2.18** - were evaluated. An algorithm consisting of a series of statistical evaluations of intensity values of the neighbouring cells and combined with a set of logics which compared the pattern of the cell intensity variations in horizontal, vertical and diagonal directions was implemented for the verification of the true particle location. In case none of the probable particle positions satisfied the criteria, a null decision was realised. Visual observations confirmed that the implemented algorithms were substantially successful in tracking the particle. Results of data analysis indicated that the percentage of null decisions ranged from 5 to 15%. It was assumed that the results of the analyses were not influenced by the undetected particle positions. In practice, experiments with high fraction of the undetected events were excluded. A typical result showing the motion of the active particle is given in **Figure 3.2.19**.

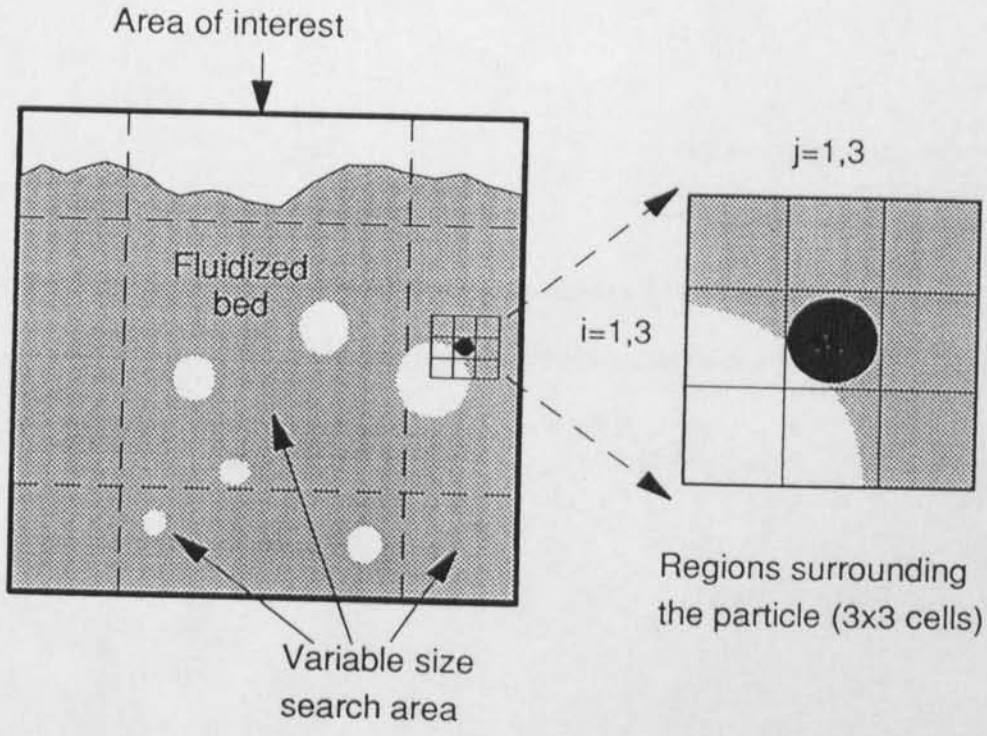

FIGURE 3.2.18: Subdivision of search area and analysis of the region (one particle size) in the neighbourhood of the 'active' particle

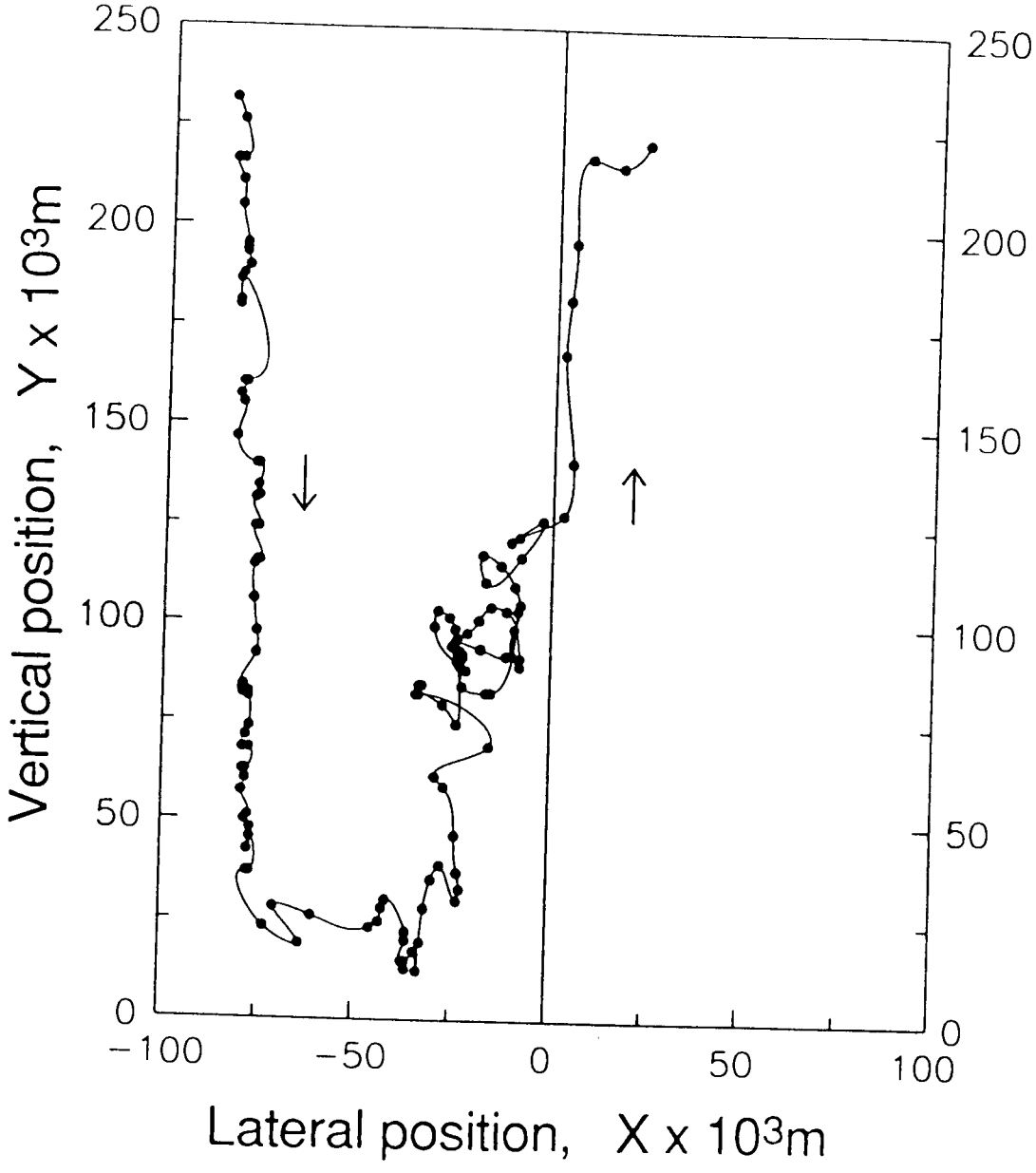

FIGURE 3.2.19: The movement of an 'active' particle measured in a two-dimensional bubbling fluidized bed.

Chapter 4

RESULTS and DISCUSSION:

BUBBLE HYDRODYNAMICS

4.1 DISTRIBUTIONS OF BUBBLE SIZE PARAMETERS

Recognition of its importance in controlling the behaviour of the fluidized bed has led to substantial research effort, both theoretical as well as experimental, directed towards estimation of the size of bubbles. Most of this effort has been aimed towards determination of an average bubble size. However, coalescence (and splitting) of the rising bubbles will inevitably lead to distributions of bubble sizes at different lateral and horizontal positions within the bed. This section describes the results of the measurements made in the two-dimensional bed; the experimental results are compared with predictions of a model for bubble size distributions reported by Agarwal (1985, 1987).

4.1.1 Theoretical Models

The population balance based approach developed by Agarwal (1985, 1987) considered coalescence as the dominant growth mechanism. Collision frequency was assumed to depend on the velocity difference between two coalescing bubbles. Analytic expressions were reported for prediction of the distribution of the bubble characteristics. The density function for the bubble diameter, d'_B, for an unconstrained growth in a large diameter bed was expressed as follows

$$f(d'_B) = \frac{1}{2} \frac{\Gamma(m+1)^{(m-1)/2}}{\Gamma(m+1)^{(m+1)/2}} \cdot \frac{x^{m+1}}{y^{m+2} d'^{1/2}_B} \cdot \exp\left(-\left\{\frac{\Gamma(m+1)}{\Gamma(m-1)}\right\}^{1/2} \cdot \frac{x}{y}\right) \tag{4.1.1}$$

where

$$x = \left(\bar{d}'_B - \frac{d_o}{m}\right)^{1/2} - \left(\frac{m-1}{m} d_o\right)^{1/2} \cong 0.23 Z'^{0.4} \tag{4.1.2}$$

$$y = (d'^{1/2}_B - d^{1/2}_o) \tag{4.1.3}$$

$$\bar{d}'_B = \bar{d}_B + d_o + \left(4\frac{m-1}{m}\right)^{1/2} \bar{d}_B d_o^{1/2} \cong (d_o^{1/2} + 0.23 Z'^{0.4})^2 \tag{4.1.4}$$

$$\bar{d}_B = \frac{k_3^2}{m(m-1)k^2} Z^{2s} \tag{4.1.5}$$

d_o is the initial bubble diameter (at the distributor) and Z' is the height above the distributor. The model contains four adjustable parameters k, k_3, m and s. The corresponding values of these constants were estimated from the results of bubble mean properties obtained from several studies. The estimated values of k, k_3, m and s were 2.226 (in $m^{0.5}\ s^{-1}$), 5.174 (in $m^{0.6}\ s^{-1}$), 10 and 0.4 respectively.

Subsequently, the model was modified to consider the effect of bed diameter as a constraint to bubble growth. The density function in term of the bed diameter dependent bubble size, d_{BD}, was derived as follows

$$f''(d_{BD}) = \frac{f'(d'_B)}{\int_{d_o}^{D_T} f'(d'_B)\mathrm{d}d'_B} \tag{4.1.6}$$

and yields

$$f''(d_{BD}) = \frac{1}{2}\left\{\frac{\Gamma(m+1)}{\Gamma(m-1)}\right\}^{(m+1)/2} \cdot \frac{x^{m+1}}{\tilde{y}^{m+2} d_{BD}^{1/2}} \cdot \frac{\exp\left(-\left\{\frac{\Gamma(m+1)}{\Gamma(m-1)}\right\}^{1/2} \cdot \frac{x}{\tilde{y}}\right)}{[\Gamma(m+1) - \gamma(m+1,a)]} \tag{4.1.7}$$

where

$$\tilde{y} = (d_{BD}^{1/2} - d_o^{1/2}) \tag{4.1.8}$$

$$a = \left(\frac{\Gamma(m+1)}{\Gamma(m-1)}\right)^{1/2} \frac{x}{(D_T^{1/2} - d_o^{1/2})} \cong \frac{2.215 Z^{\wedge 0.4}}{(D_T^{1/2} - d_o^{1/2})} \tag{4.1.9}$$

and γ denotes an incomplete gamma function. The cumulative bubble diameter distribution was derived as

$$F''(d_{BD}) = \left\{\frac{\Gamma(m+1) - \gamma(m+1,b)}{\Gamma(m+1) - \gamma(m+1,b)}\right\} \tag{4.1.10}$$

where

$$b = \left(\frac{\Gamma(m+1)}{\Gamma(m-1)}\right)^{1/2} \frac{x}{(D_{BD}^{1/2} - d_o^{1/2})} \tag{4.1.11}$$

The effect of the bed diameter is observed to be notable if

$$a \cong \frac{2.215 Z^{\wedge 0.4}}{(D_T^{1/2} - d_o^{1/2})} > 3 \tag{4.1.12}$$

Furthermore, the expression for the average bubble diameter was derived from the density function as

$$\bar{d}_{BD} = \left[d_o^{1/2} + 0.23Z^{\wedge 0.4} - 0.023Z^{\wedge 0.4} \left\{ \frac{0.74Z^{\wedge 0.4}}{D_T^{1/2} - d_o^{1/2}} - 1 \right\} \right]^2 \qquad (4.1.13)$$

Accurate prediction of the initial bubble size is vital in any model. It provides the initial conditions and accounts for the effect of different types of distributor plate. Miwa et al. (1972) proposed that the initial bubble sizes may be evaluated from

(a) perforated plate

$$d_o = 0.872\{A_d(U_O - U_{mf})/n_d\}^{2/5} \qquad (4.1.14)$$

(b) porous plate

$$d_o = 0.376(U_O - U_{mf})^2 \qquad (4.1.15)$$

These expressions for the initial bubble diameters were derived based upon the assumption that all the excess gas, (U_O-U_{mf}), is directed to the formation of bubbles. However, based on continuity considerations over the cross-sectional area of the bed, the distribution of the gas flow in a fluidized bed may be separated into three components (Grace and Harrison, 1969; Clift and Grace, 1985). The total gas flow is balanced by the flow required to maintain the emulsion at minimum fluidization condition, Q_E, the visible bubble flow, Q_B, and the bubble through-flow, Q_T.

$$Q_{total} = Q_E + Q_B + Q_T$$

$$U_O = (1 - \varepsilon_B)k_1 U_{mf} + \varepsilon_B U_B + \varepsilon_B k_1 K_T U_{mf} \qquad (4.1.16)$$

Equation (4.1.16) suggests that only a fraction of the gas flow, Q_B, contributes to the formation of visible bubble phase in the fluidized bed. If this analysis applies to all sections in the bed, then for consistency the effect of the bubble throughflow should also be taken into consideration in the formation of the initial bubble size

at the distributor. The value of k_1 can be taken as unity if porosity of the emulsion phase is maintained at minimum fluidization conditions. Considering the initial bubbles to be spherical, the bubble throughflow can be taken as three times the minimum fluidization velocity (Davidson and Harrison, 1963), that is K_T equals to 3. Upon simplification, equation (4.1.16) reduces to

$$Q_B = A_d(U_O - U_{mf}[1 + 2\varepsilon_B]) \tag{4.1.17}$$

Alternate expressions for prediction of the initial bubble size may be deduced if the visible gas flowrate, Q_B, instead of excess gas flowrate is considered responsible for bubble formation. For a porous plate, the initial bubble diameter can be calculated from

$$d_o = 0.376(U_O - U_{mf}[1 + 2\varepsilon_B])^2 \tag{4.1.18}$$

In equation (4.1.18), the evaluation of the initial bubble size requires *a priori* knowledge of the ε_B and this value may be estimated by rearranging equation (4.1.16) as.

$$\varepsilon_B = \frac{U_O - U_{mf}}{U_B + k_1(K_T - 1)U_{mf}} \tag{4.1.19}$$

where U_B can be approximated by a correlation proposed by Davidson and Harrison (1963)

$$U_B = (U_O - U_{mf}) + 0.71\sqrt{g\,d_o} \tag{4.1.20}$$

The value of d_o is calculated by solving both equations (4.1.18) and (4.1.19) simultaneously.

4.1.2 Comparison of Model Calculations with Experimental Data

The experimental results for the bubble size distribution were compared with the theoretical prediction by the model equation (4.1.7). The prediction of the model based on the existing adjustable constants was observed to be poor. One

of the reasons of discrepancy is probably due to the fact that those constants were estimated for bubbles in a three-dimensional bed. Consequently, new values for the adjustable constants were estimated from the experimental results by employing a Chi-Square Goodness-of-Fit test. The values of m and s were unchanged but new value of k_3 was evaluated.

Unfortunately, a range of values of k_3 was implied from the test. It was found to vary from 3.5 to 6 $m^{0.6} s^{-1}$ depending on the bed height and fluidizing conditions. Clearly, the mathematical model possesses some shortcomings for predicting bubble size in a two-dimensional bed. Thus, the following section will highlight and discuss the discrepancy and deviation found in the comparisons. It is not the intention of this work to propose additional modification of or alteration to the existing theoretical model.

The effect of various fluidizing conditions and bed heights on the distribution of bubble size were investigated and compared with the theoretical model. **Figures 4.1.1a** and **b** show that the effect of gas velocity on the distribution is not significant. Interestingly, Chiba et al. (1975) have reported a similar observation for the higher gas velocities. However, the model over-predicts the bubble size at a higher gas rate. This is partly because of the over-prediction of initial bubble size as the excess gas velocity is increased. Furthermore, the model only considers the growth of bubble size by coalescence and neglects the effect of bubble splitting. It has also been suggested that the gas leakage at the bed wall may be prominent in a two-dimensional bed (Werther, 1978). Hence, such phenomenon may hinder the continuous growth of bubble size with increasing gas rate.

Figures 4.1.2a-d illustrate the growth of bubble size with bed height for powder size of 2.09×10^{-4} m. The extent of dispersion of the distribution increases progressively with bed height. Despite this, the proportion of smaller bubbles

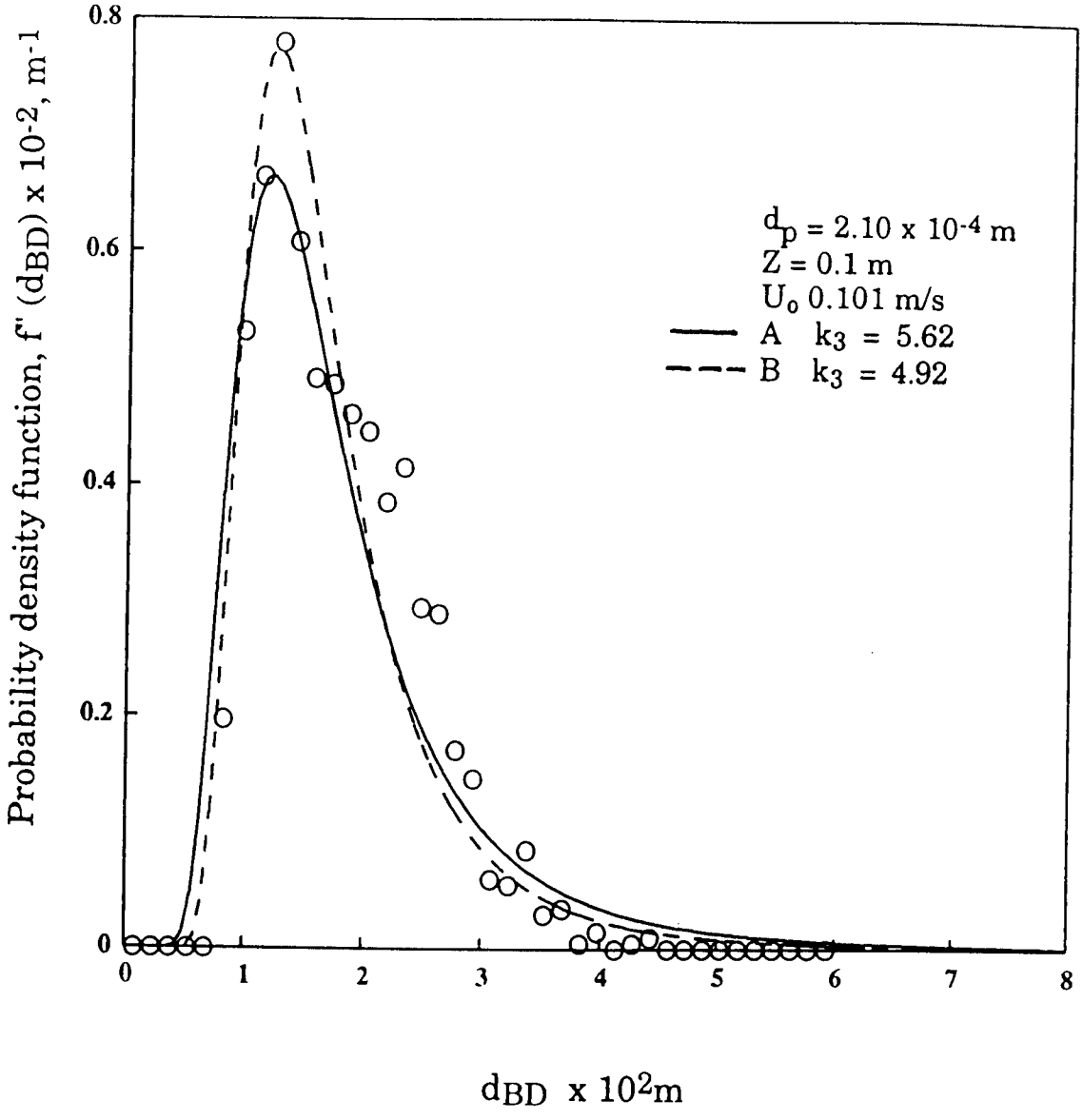

FIGURE 4.1.1a: Comparison of the model prediction for the bubble diameter density distribution with experimental data at different gas velocities
Curve A: d_o by equation 4.1.18
Curve B: d_o by equation 4.1.15

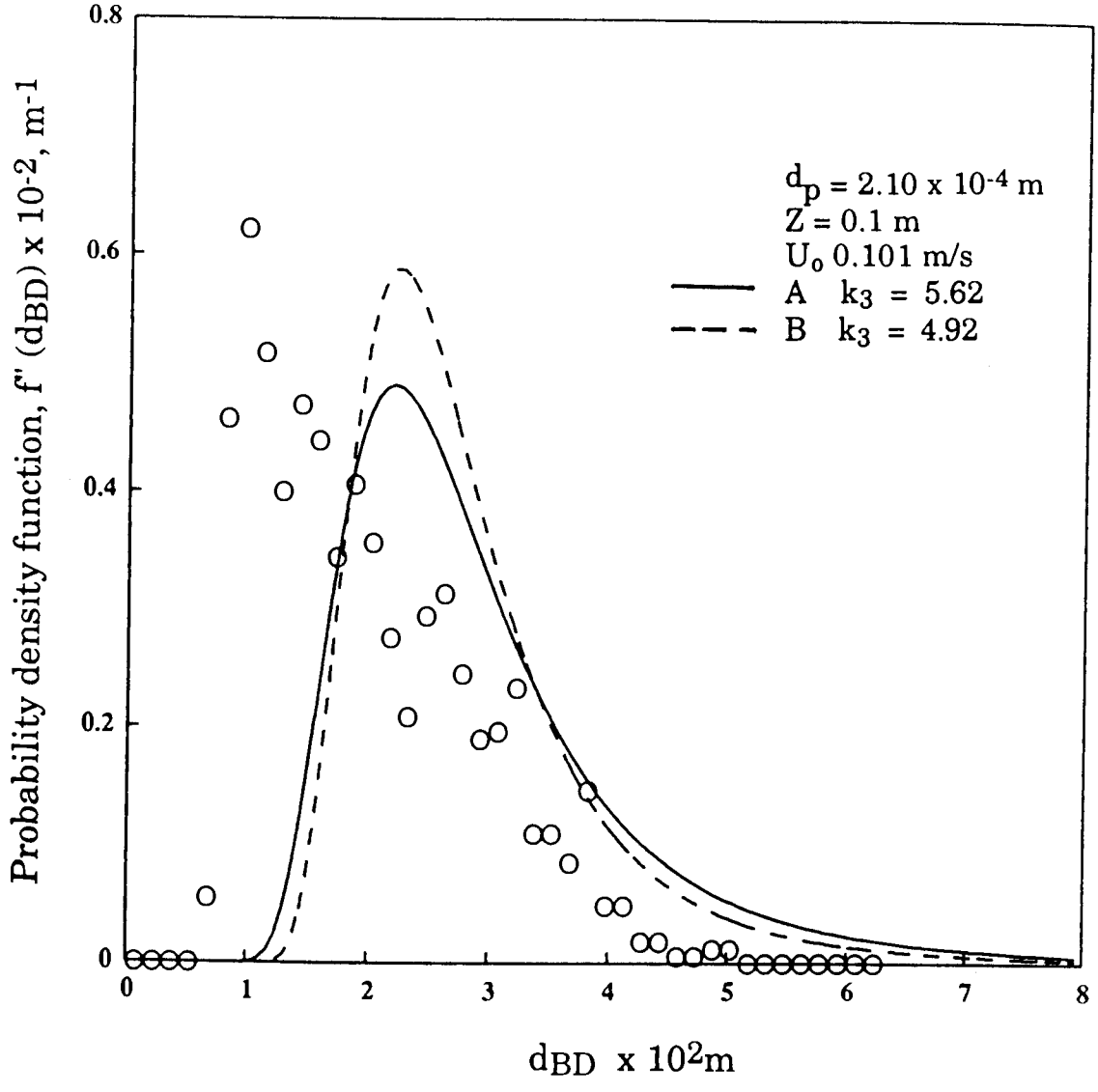

FIGURE 4.1.1b: Comparison of model prediction with experimental data

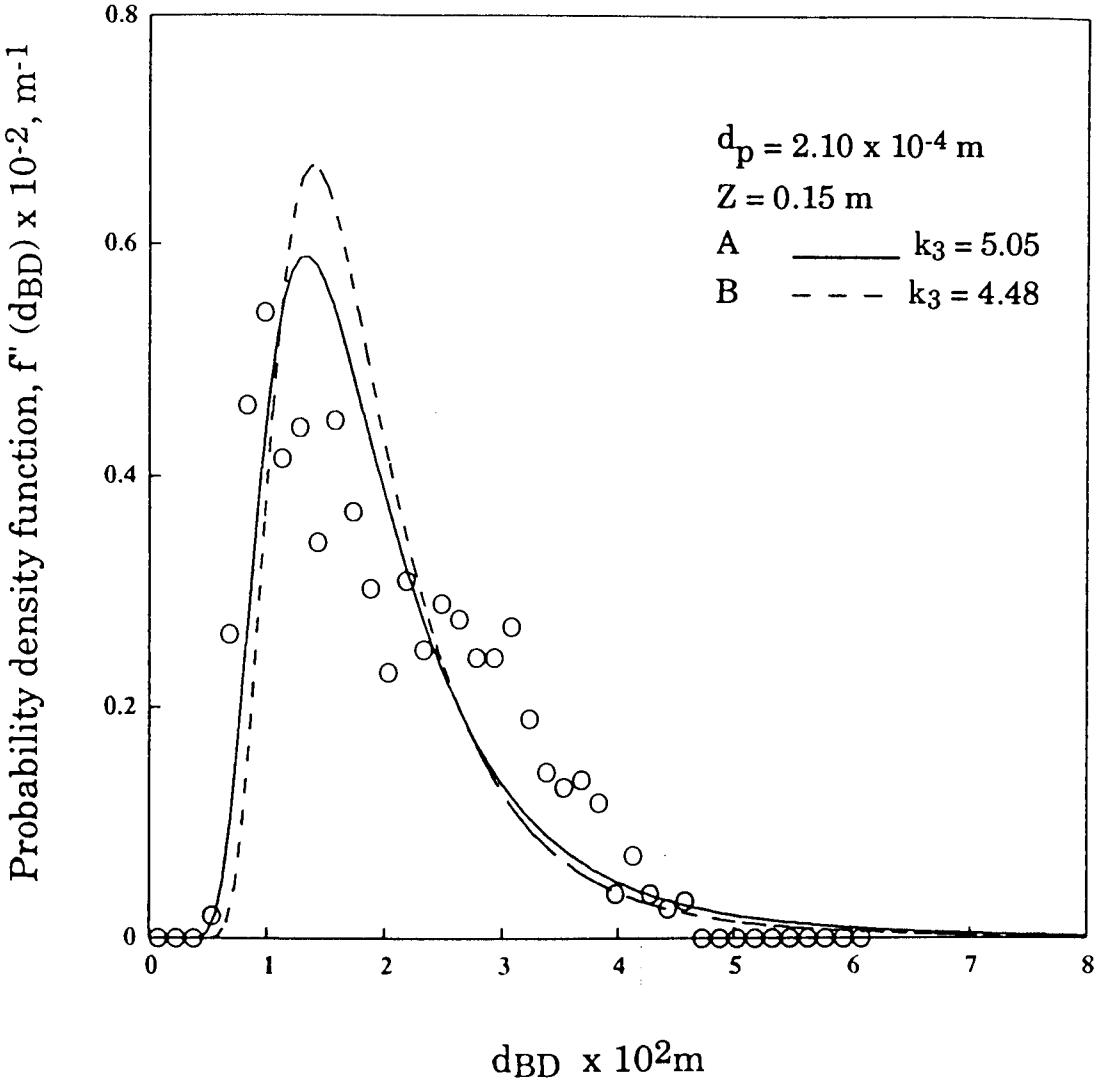

FIGURE 4.1.2a: Comparison of the model prediction for the bubble diameter distribution with experimental data at various bed heights.
Curve A: d_o by equation 4.1.18
Curve B: d_o by equation 4.1.15

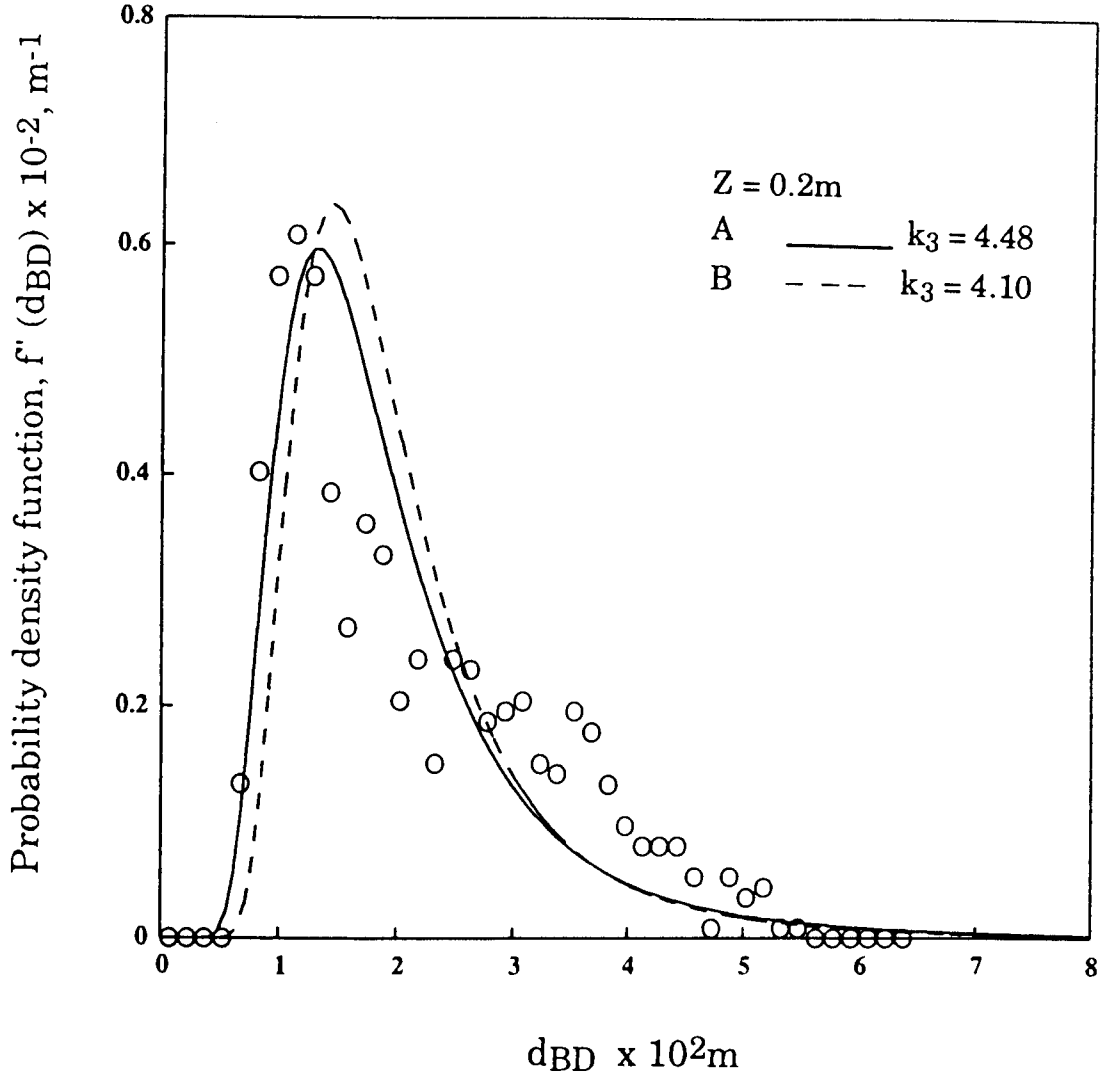

FIGURE 4.1.2b: Comparison of model prediction with experimental data.

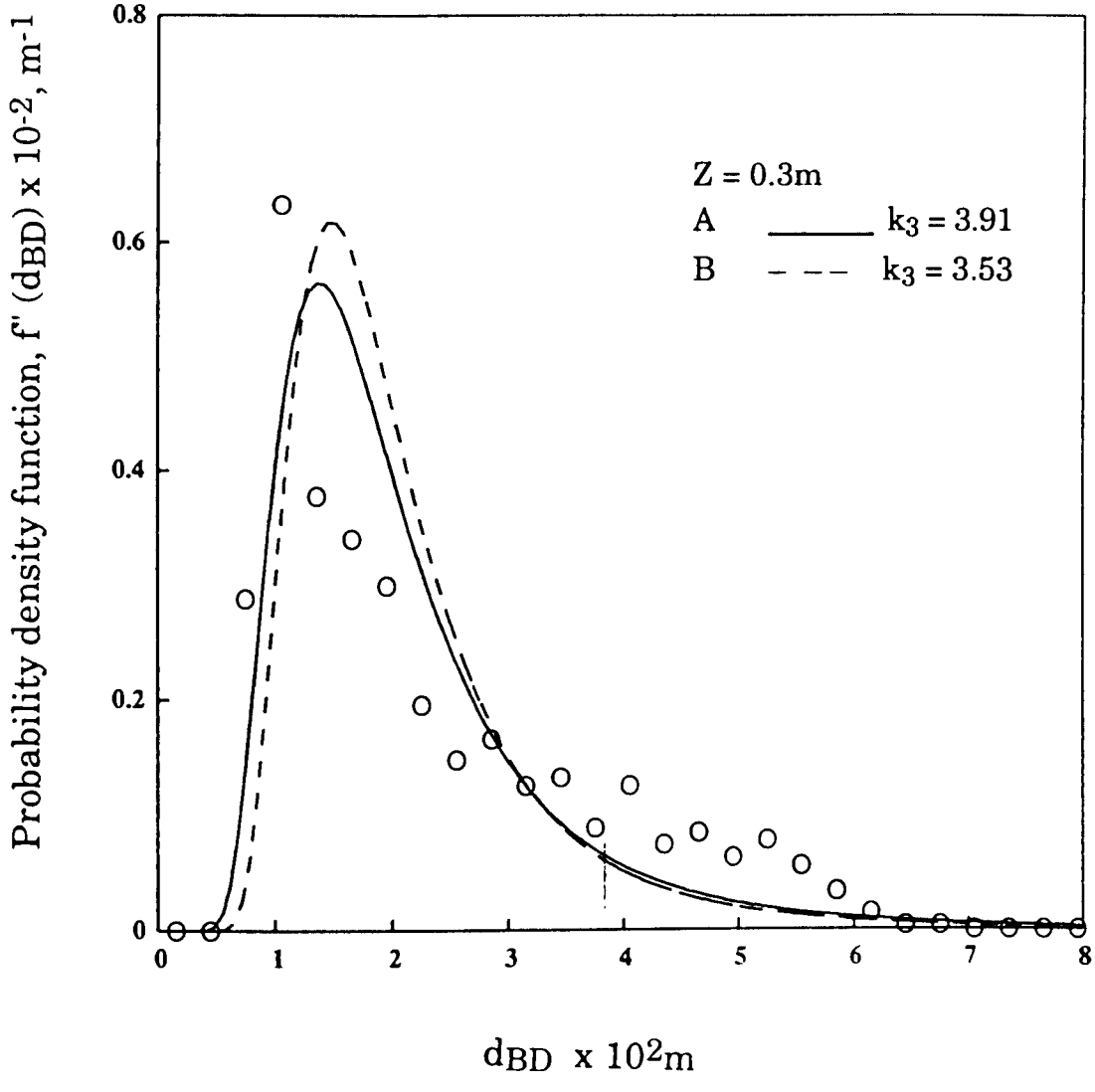

FIGURE 4.1.2c: Comparison of model prediction with experimental data.

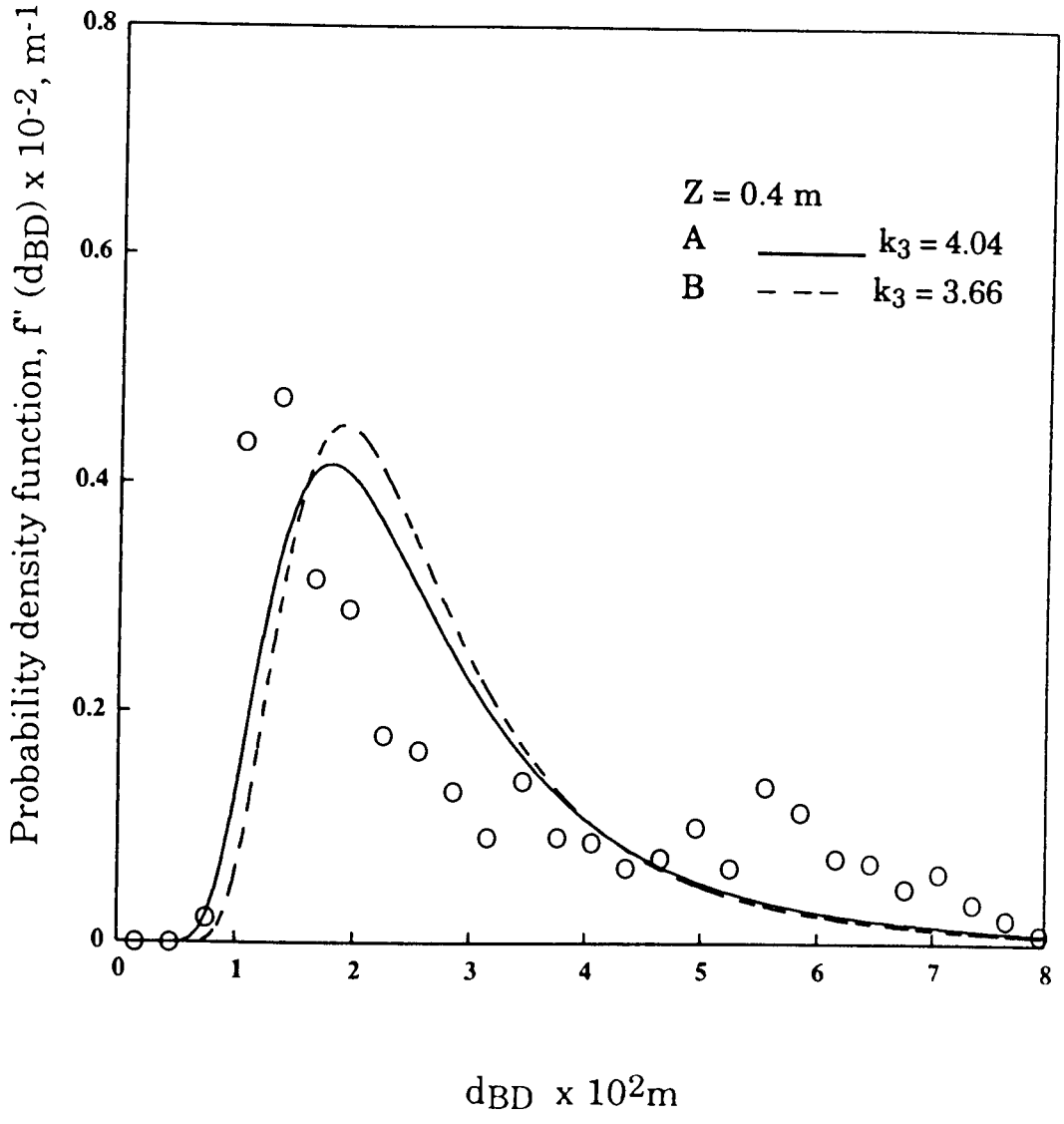

FIGURE 4.1.2d: Comparison of model prediction with experimental data.

remains substantial. It is not entirely certain if these smaller bubbles result from the breakage of the larger bubbles. However, it is highly improbable that such small bubbles will travel up the bed without coalescing with other bubbles. From the model prediction, it is observed that the value of k_3 decreases accordingly with increasing height of the bed. This behaviour highlights the inadequacy of the model in describing the growth mechanisms of the bubbles. A similar trend was also seen in the experiments conducted on a different powder size. These results are summarized as **Figures 4.1.3a** and **b**. **Figures 4.1.1** to **4.1.3** also display a comparison of predictions using the initial bubble size model proposed by Miwa et al. (1975) with the more complex model presented as equation (4.1.18). The effect appears to be minor and probably does not warrant the use of the more complex expression.

Adequate comparison of the experimental data for the bubble size distribution with other sources is not possible given the paucity of the experimental results available in the literature. Hence, the average bubble size must be used for comparison with various empirical correlations. The results are shown in **Figures 4.1.4a** and **b**. The empirical correlations used in the comparisons are given in **Table 4.1**. Large deviation in the prediction of the bubble size is observed for the correlations by Rowe and Yacono (1975) and Werther (1978). These correlations are developed for three-dimensional beds and appear inappropriate for two-dimensional or thin beds. The prediction of Chiba et al. (1973) for a two-dimensional bed shows good agreement with the experimental data. Similarly, the prediction derived from the population balance model - equation (4.1.13) - proposed by Agarwal (1987) gives reasonable fit. However, the equation by

TABLE 4.1. EMPIRICAL CORRELATIONS FOR AVERAGE BUBBLE SIZE.

Reference	Correlation	Comment
Chiba et al (1973)	$\overline{d}_B = d_O\left\{\frac{(2^{5/4}-1)(Z-Z_o)}{d_O}+1\right\}^{2/5}$	2 - D
Rowe and Yacono(1975)	$d_B = \frac{(U_O-U_{mf})^{1/2}(Z-Z_o)^{3/4}}{g^{0.25}}$	3 - D
Werther (1978)	$d_B = 0.00853[1+27.2(U_O-U_{mf})]^{\frac{1}{3}} \times[1+6.84(Z+Z_o-d_O)]^{1.21}$	3 - D
Mori and Wen (1975)	$d_B = D_{BM}-(D_{BM}-d_O)\exp\left(-\frac{0.3Z}{D_T}\right)$ $D_{BM} = 1.57\{A_t(U_O-U_{mf})\}^{2/5}$	3 - D

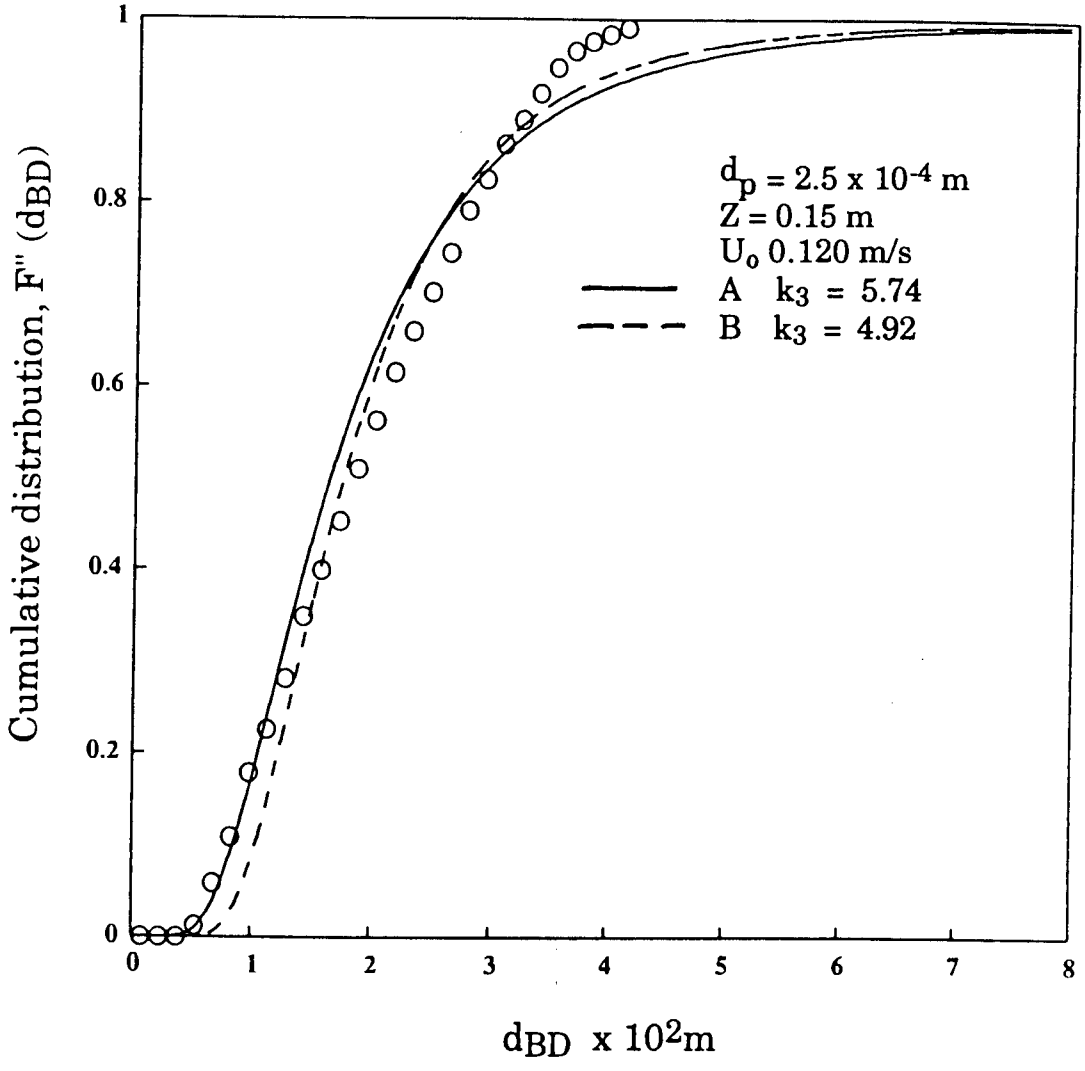

FIGURE 4.1.3a: Comparison of model prediction for the cumulative distribution of bubble size with experimental data at various bed heights.
Curve A: d_o by equation 4.1.18
Curve B: d_o by equation 4.1.15

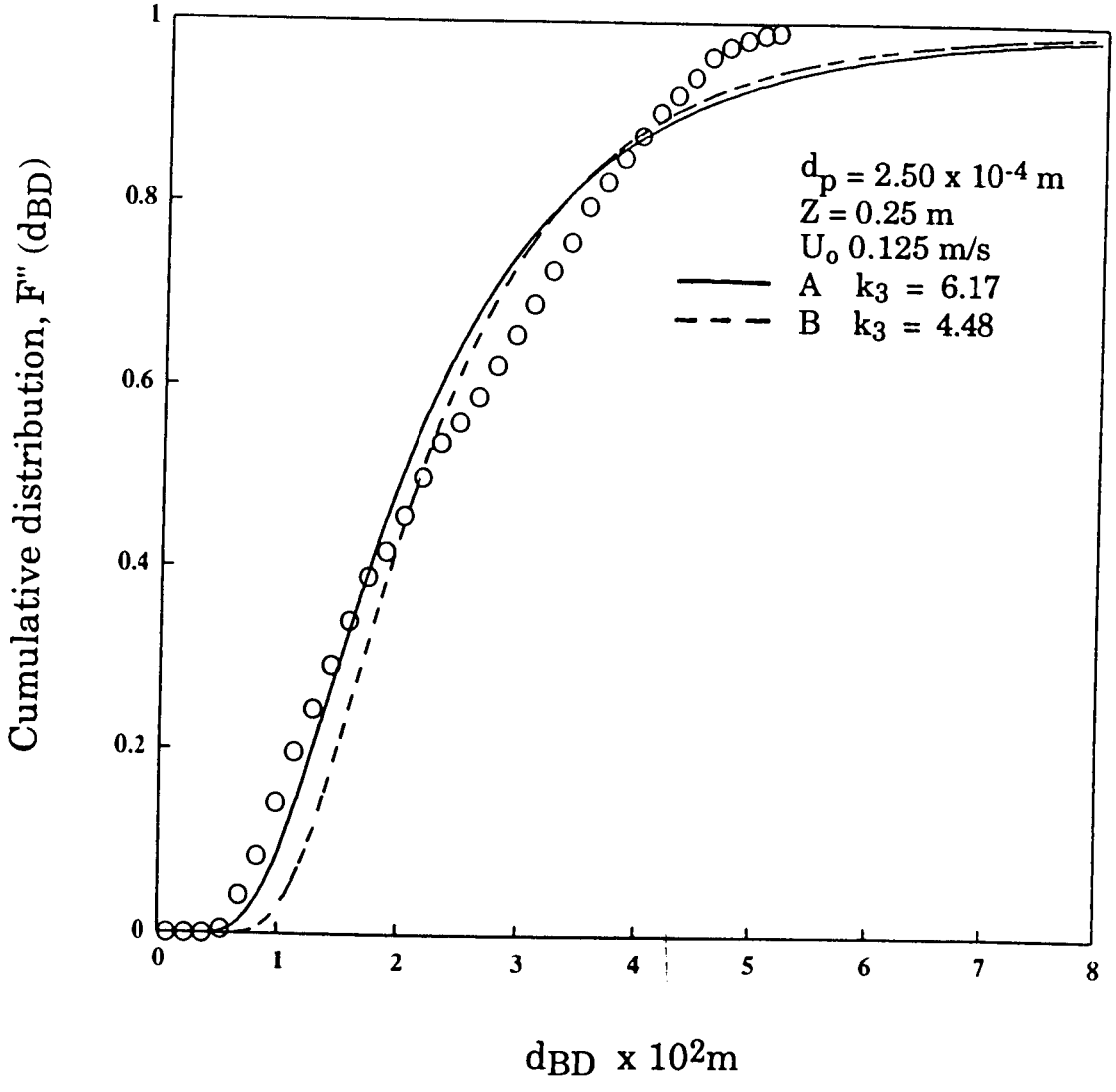

FIGURE 4.1.3b: Comparison of model prediction with experimental data

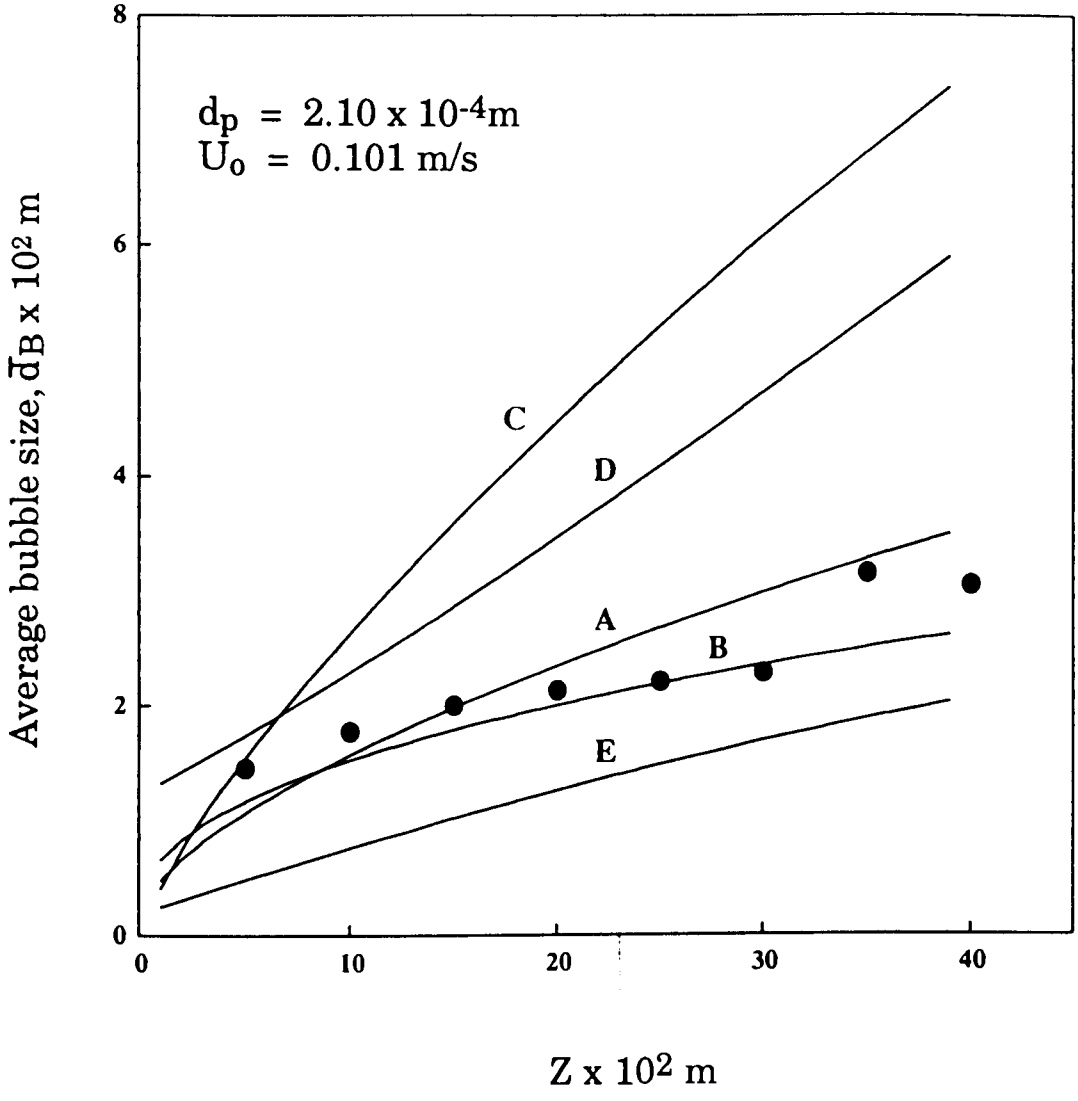

FIGURE 4.1.4a: Comparison of average bubble size $\bar{d}_B$ with various empirical correlations as a function of bed height. Curves A: by Agarwal (1987): B: Chiba et al (1975); C: Rowe and Yocono (1975); D: Werther (1978); E: Mori and Wen (1975).

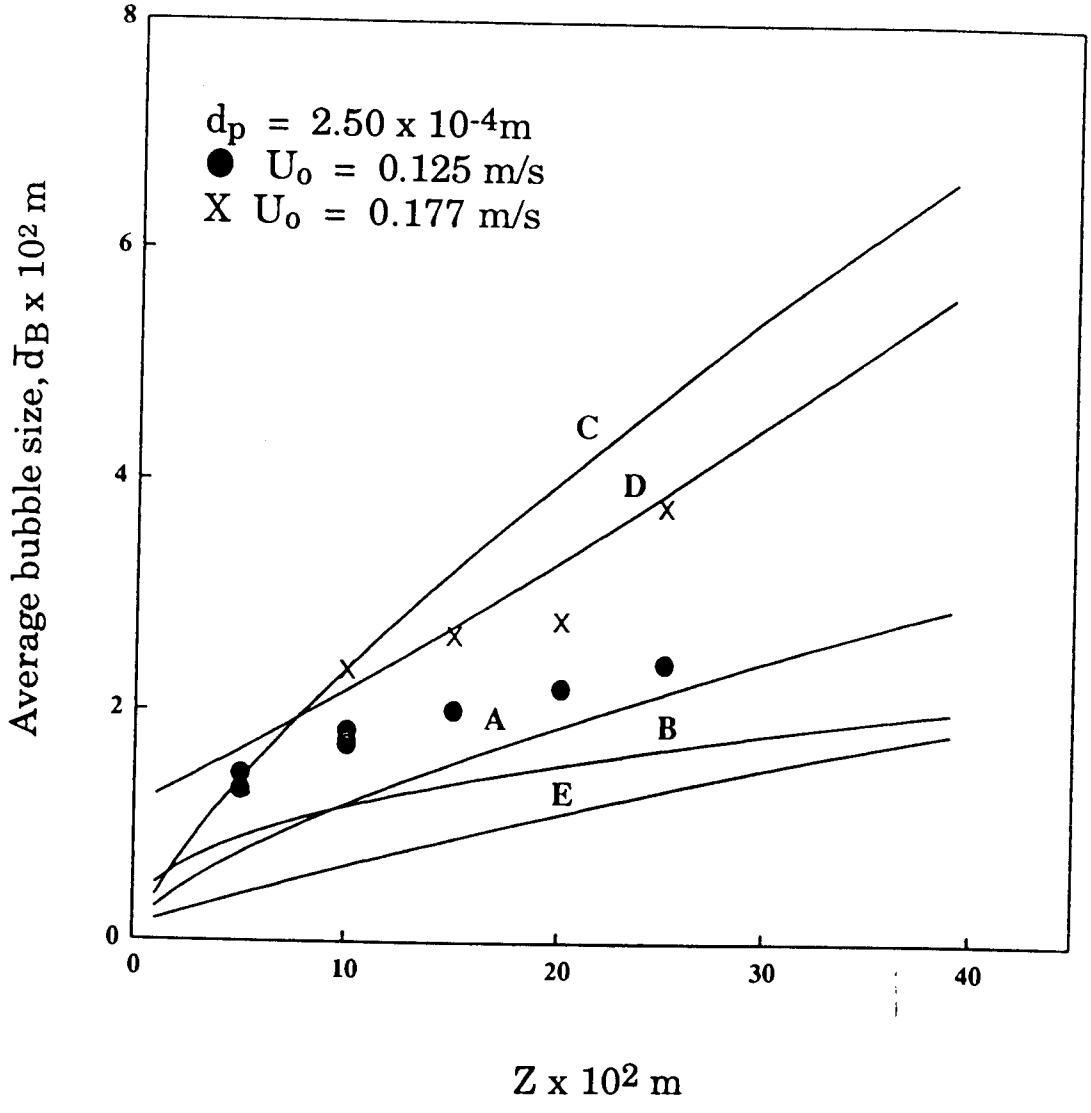

FIGURE 4.1.4b: Comparison of experimental data with empirical correlations for average bubble size.

Mori and Wen (1975) underpredicts the average bubble size. This may be a consequence of the uncertainty in the evaluation of the maximum bubble size, $d_{B,max}$.

Figures 4.1.5 presents the variation of the average bubble size with excess gas velocity. Again, the effect of the gas velocity on the average bubble diameter is observed to be insignificant. In contrast, the prediction by Chiba et al. (1973), Mori and Wen (1975), and Agarwal (1987) propose a stronger dependency of average bubble size on the excess gas velocity whereas predictions by Rowe and Yacono (1976) and Werther (1978) indicate a lesser effect. The behaviour observed in the experimental result may be attributed to the effect of bubble throughflow and minor gas leakage at the walls.

The variation of the average bubble shape parameters, S and α with height above the distributor are also considered. From **Figures 4.1.6**, it is clear that no appreciable changes of bubble shape factor and aspect ratio occurs with changing bed height. The average shape factor varies from 0.8 to 0.9 and the average aspect ratio ranges from 1 to 1.2. Therefore, it is sufficient to construe that the shape of the bubbles remain reasonably constant throughout the fluidized bed.

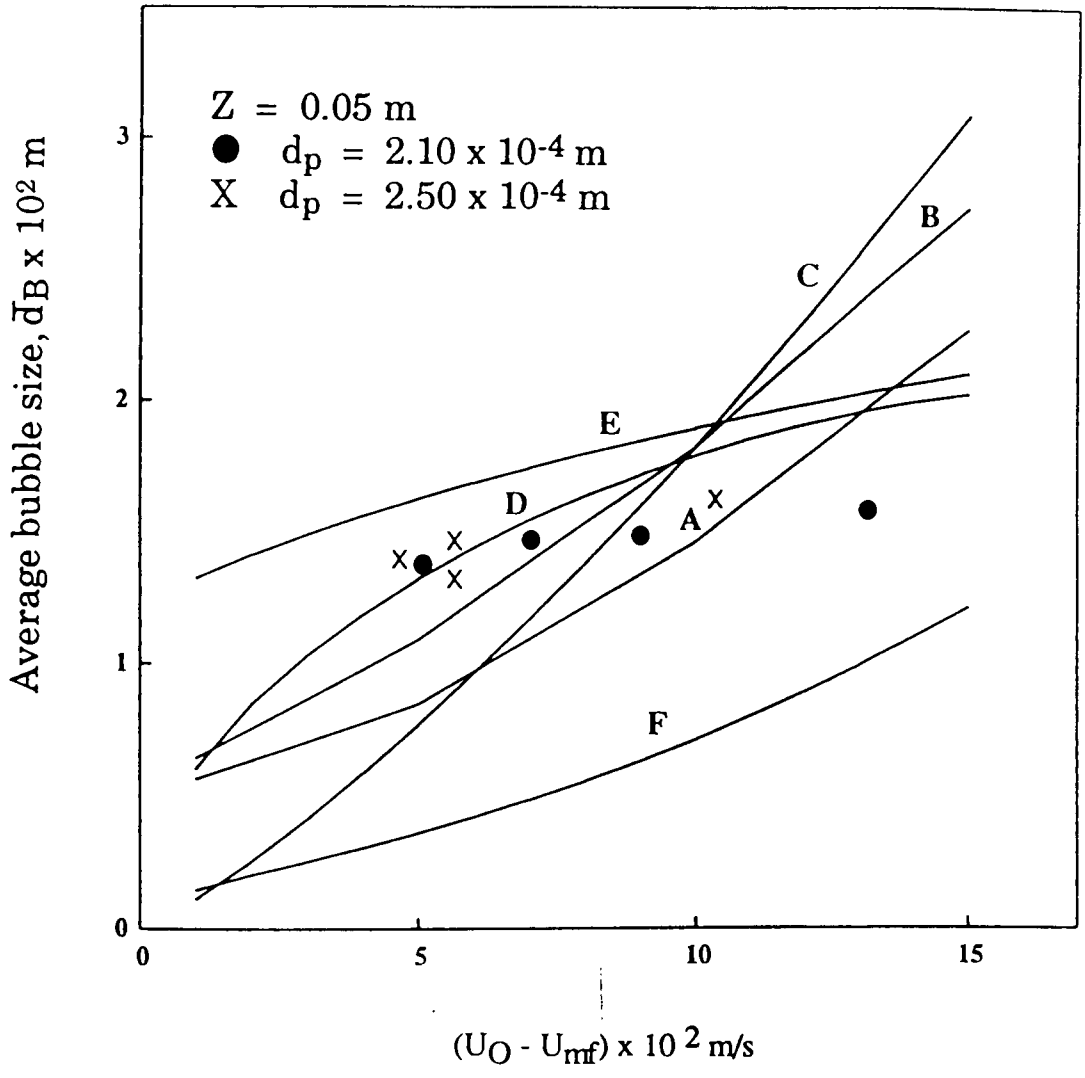

FIGURE 4.1.5: Comparison of average bubble size $\bar{d}_B$ with various empirical correlations as a function of gas velocity: Curves A: by Agarwal (1987). d_o by equation 4.1.18: B: Agarwal (1987) d_o by equaton 4.1.15; C: Chiba et al (1975); D: Rowe and Yocono (1975); E: Werther (1978); F: Mori and Wen (1975).

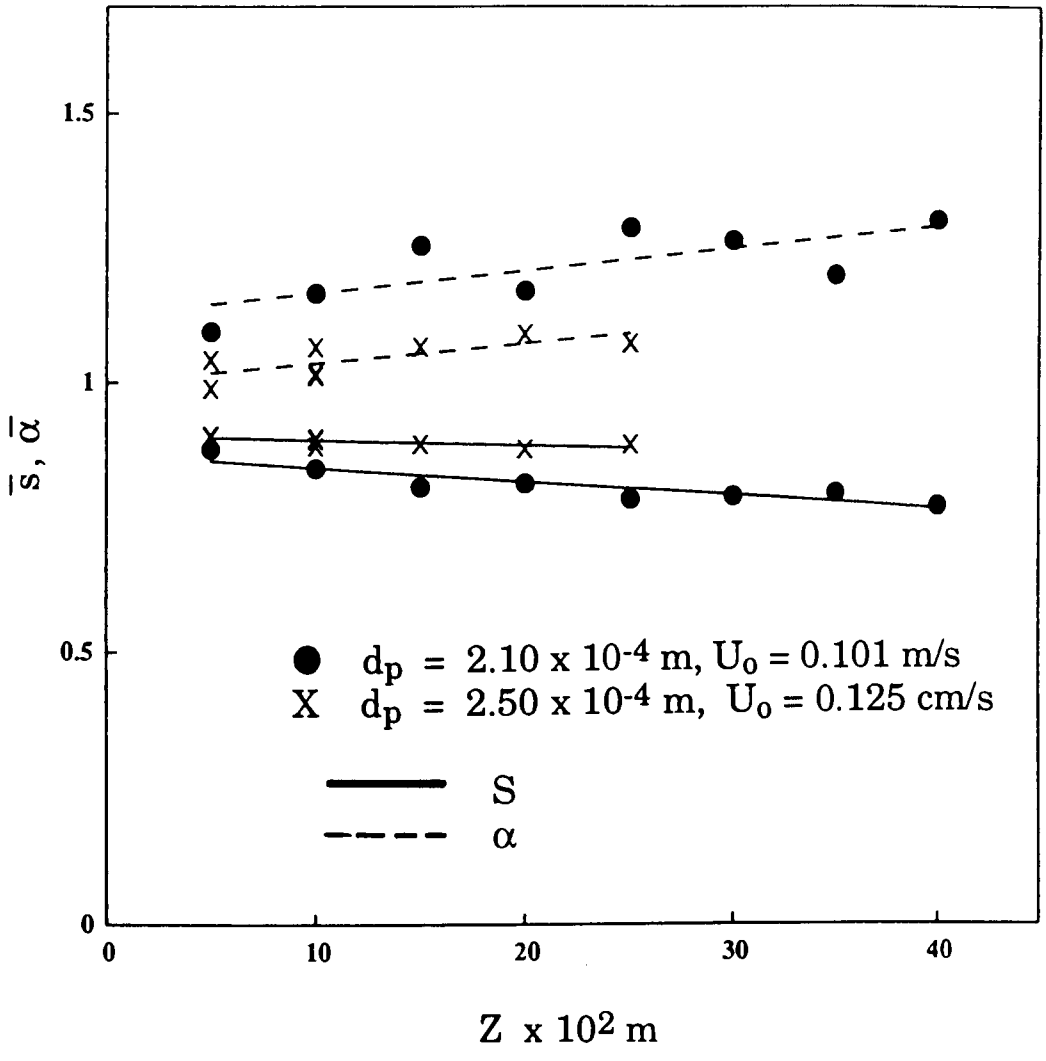

FIGURE 4.1.6: The plot of average bubble shape factor and aspect ratio with different bed heights.

4.1.3 Conclusions

A new method for non-intrusive sensing and measurement of important bubble characteristics was developed based upon the principles of digital image analysis.

The experimental measurements for bubble size distributions were compared with predictions from a population balance model using coalescence as the dominant growth mechanism. This comparison has highlighted some discrepancies and further work on modelling bubble growth is required. Average bubble size measurements compare favourably with the correlation of Chiba et al. (1973) for two-dimensional beds.

Given the simplicity of the method, it is ideal for the calibration of most types of submersible probes. Further work in this direction is described in the following sections.

4.2 CONVERSION OF BUBBLE PIERCED LENGTH TO BUBBLE SIZE

Bubble parameters in three-dimensional beds are often measured using submersible probes. Since the central axis of the rising bubble need not coincide with the vertical axis of the submerged probe, such probes measure only the pierced length and not the bubble diameter. In this section, using the methods described in sections 3.2.1 and 3.2.2, pierced length, maximum horizontal and vertical dimensions, circumference and cross-sectional area for individual bubbles intercepted at an 'imaginary' probe have been measured simultaneously. Several assumptions have been made in the literature regarding the bubble shape. These assumptions and the experimental data on bubble pierced lengths are used, in the framework provided by geometrical probability theory, to predict distributions of bubble size parameters. Comparison of theoretical predictions with measurements then enables the assessment of the applicability of geometrical probability methods for converting measured distributions of pierced lengths to bubble size distributions. Though these methods were first used by Werther (1974a,b), the results presented here, for the first time, verify their applicability experimentally.

4.2.1 Theoretical Analysis

It is assumed that each bubble in the population is described by its horizontal dimension, R (= $d_H/2$), and that the bubble population possesses uniform shape characteristics. The probability of measuring a pierced length, y, is the conditional probability, P(y|R), of measuring that pierced length from a bubble characterized by R integrated over the possible range of bubble sizes. Mathematically,

$$P(y) = \int_R P(y \mid R)P(R)dR \qquad (4.2.1)$$

where P(R) is the probability density function of the horizontal dimension of the bubbles detected at the probe.

To deduce P(R) from experimental data on P(y), the conditional probability P(y|R) must be determined. Let P(r|R) denote the conditional probability of detecting a bubble of size R with its centre at a distance r from the probe tip. If the shape is specified for a bubble characterized by R the functional relationship between y and r is monotonic and P(y|R) can also be expressed (Melsa and Sage, 1973) as

$$P(y \mid R) = P(r \mid R) \left| \frac{dr}{dy} \right| \tag{4.2.2}$$

Functional relationships for (dr/dy) for possible bubble shapes have been tabulated (Clark and Turton, 1988). Further,

$$P(r \mid R)\Delta R = \frac{\begin{array}{c}\text{number of bubbles (R) inter-}\\ \text{secting the probe with centres}\\ \text{at distance r from the probe}\\ \text{tip}\end{array}}{\begin{array}{c}\text{total number of the bubbles}\\ \text{(R) intersecting the probe}\end{array}} \tag{4.2.3}$$

To obtain a general expression for P(r|R), the number density function of the bubble centres at a height Z above the distributor and distance λ from the central axis of the bed is denoted as $P(Z,\lambda,R)$.

For a cylindrical bed, using the definition given by equation (4.2.3),

$$P(r \mid R) = \frac{\int_0^{2\pi} P(Z,\lambda,R) r \, d\theta}{\int_0^{R} \int_0^{2\pi} P(Z,\lambda,R) r \, d\theta \, dr} \tag{4.2.4}$$

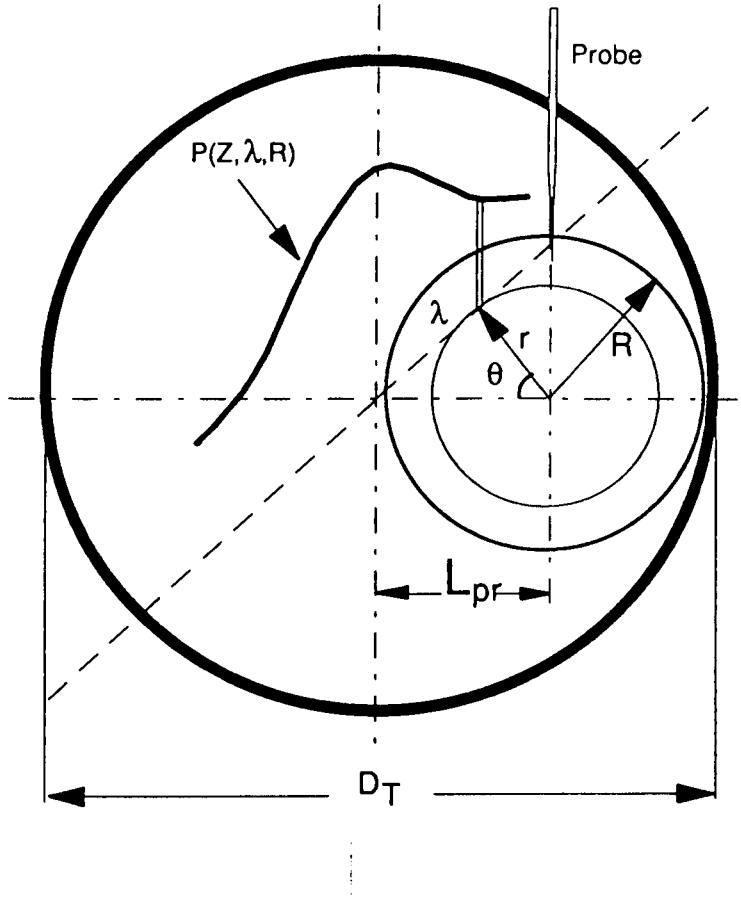

FIGURE 4.2.1: Geometry of a probe in a cylindrical bed.

The relation between r, λ, and the distance of the probe from the central axis of the bed, L_{pr}, can be determined from geometry (**Figure 4.2.1**) as

$$\lambda^2 = (r \sin\theta)^2 + (L_{pr} - r\cos\theta)^2 \qquad (4.2.5)$$

The assumption of homogeneous bubbling within the probe detection region in the cylindrical vessel implies that P(Z,λ,R) is constant leading, in agreement with Clark and Turton (1988), to

$$P(r \mid R) = \frac{2r}{R^2} \qquad (4.2.6)$$

Equation (4.2.6) will not apply to the thin/two-dimensional geometry of interest in this investigation. For this case, assuming the bubble size to be larger than the thickness of the bed, the angular variation need not be considered. The homogeneous bubbling assumption will then lead to, in agreement to with Sung and Burgess (1987)

$$P(r \mid R) = \frac{1}{R} \qquad (4.2.7)$$

The general form of P(r|R), equation (4.2.4), will permit consideration of non-homogeneous bubbling provided a suitable function for the bubble centre density function, P(Z,λ,R), is available. The homogeneous bubbling assumption has been retained in much of what follows.

4.2.2 Computational Procedures

Typical experimental distributions for the pierced length and other bubble size parameters have been shown in **Figure 3.2.6**. For computational ease in the transformation of bubble pierced length distribution, P(y), a continuous Gamma function

$$P(y) = \frac{b^{a+1} y^a}{\Gamma(a+1)} \exp(-by) \qquad (4.2.8)$$

was fitted through the discrete experimental measurements. The parameters, a and b, of the fitted distribution were determined from the mean, $\mu_{y,ex}$, and standard deviation, $\sigma_{y,ex}$, of the experimental data (Burgess and Calderbank, 1975) according to

$$b = \frac{\mu_{y,ex}}{\sigma^2_{y,ex}} \quad ; \quad a = \left(\frac{\mu_{y,ex}}{\sigma_{y,ex}}\right)^2 - 1 \tag{4.2.9}$$

For illustration, the fitted function is also shown in **Figure 3.2.6.**

The pierced length distribution can be used to estimate the local bubble size distribution, in conjunction with an assumed shape for the bubble population, using the backward transform technique established by Clark and Turton (1988). The continuous integral of equation (4.2.1) is approximated by a summation of a series of finite values consisting of the products of P(y|R), P(R) and ΔR:

$$P(y_i) \cong \sum_{j=0}^{m-1} P(y_i \mid R_j) P(R_j) \Delta R \tag{4.2.10}$$

where the pierced lengths are divided into *m* divisions such that

$$y_i = \frac{y_{\max}}{m}\left(m - \left(i + \frac{1}{2}\right)\right) \quad 0 \le i \le m-1 \tag{4.2.11}$$

and

$$R_j = \frac{R_{\max}}{m}(m-j); \quad \Delta R = \frac{R_{\max}}{m} \qquad 0 \le j \le m-1 \tag{4.2.12}$$

y_{max} is taken to be the maximum values measured in the system and R_{max} may be calculated from the given geometry

$$R_{\max} = \frac{y_{\max}}{\alpha(1+\eta)} \tag{4.2.13}$$

where

$$\eta = \sqrt{1 - \sin^2(\theta_w/2)} \tag{4.2.14}$$

By expanding the series for all possible y_i values and recognizing that a pierced length y_i can only come from a bubble of radius R_i or greater, a matrix of triangular form is then generated. Each series may be easily solved in a sequential manner to give the value of $P(R_j)$ required. Computer algorithm can be readily programmed to perform this task. From the calculated values of P(R), distributions in terms of other bubble geometrical parameters (only for monotonic function) may also be obtained, for instance

$$P(d_E) = P(R) \left| \frac{dR}{d d_E} \right| \tag{4.2.15}$$

The bubble shape also specifies the geometrical relation between the horizontal and other dimensions (d_V, d_E and C_P) of the bubble. These relations are summarized in **Table 4.2** and the nomenclature used is illustrated in **Figure 4.2.2**. Thus, distributions of other bubble dimensions can also be predicted once P(R) has been evaluated. It is clear that the comparison of predicted distributions of the several bubble size parameters with experimentally obtained data enables a comprehensive examination of the applicability of the geometrical probability approach and the assumed bubble shape.

In the literature, bubbles are commonly assumed to be spherical, spherical cap, ellipsoidal or hemispherical in shape. The simplest approach is to assume the bubble shape as spherical. Experimental observations (Rowe and Partridge, 1965) indicate that the bubbles are spherical with particle-wake region occupying the lower part of the sphere. Alternatively, an ellipsoidal shape may be assumed for the oblate bubbles with a constant aspect ratio α (Werther, 1974a, b; Chiba et al., 1973). For bubbles with a relatively flat base, a hemispherical bubble geometry may also be considered (Sung and Burgess, 1987). To evaluate the applicability of these assumptions, several bubble shapes were considered in the calculations.

TABLE 4.2. GEOMETRICAL RELATIONSHIPS FOR VARIOUS SHAPES.

Shape	area-equivalent diameter (d_E)	Circumference (C_P)
spherical	$2R$	$2\pi R$
ellipsoidal	$2R\sqrt{\alpha}$	$4a'E\left(\kappa,\frac{\pi}{2}\right)$ $E\left(\kappa,\frac{\pi}{2}\right)=\int_0^{\frac{\pi}{2}}\sqrt{1-\kappa\sin^2\phi}\,d\phi$ $\kappa=\frac{\sqrt{a'^2-b'^2}}{a'}$
spherical cap	$R\sqrt{\frac{4}{\pi}\left(\pi-\left(\frac{\theta_w}{2}-\frac{\sin\theta_w}{2}\right)\right)}$	$\left(1-\frac{\theta_w}{2\pi}\right)2\pi R+2R\sin\left(\frac{\theta_w}{2}\right)$
hemispherical	$\sqrt{2}R$	$\pi R+2R$

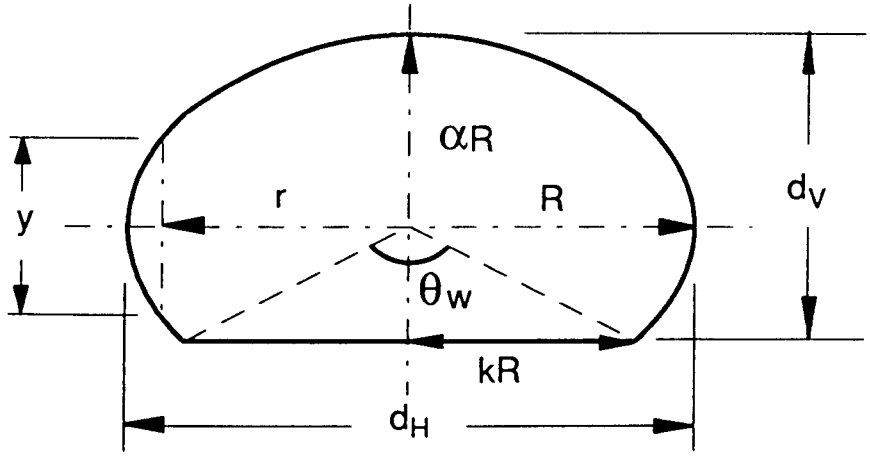

FIGURE 4.2.2: Geometry for the greater section of an ellipsoid

TABLE 4.3. BUBBLE SHAPES AND SHAPE PARAMETERS

Notation	Shape	Parameter	
		α	θ_w
a	spherical	1.0	0°
b	ellipsoidal	0.77	0°
c	spherical cap	1.0	120°
d	hemispherical	1.0	180°
e	ellipsoidal *	0.77	0°
	*(Werther's method)		

For the spherical cap bubble shape, the wake angle θ_w is expected to vary with the type of particles and size; for the present calculations, θ_w has been taken to be 120°. The bubble shapes and the corresponding shape parameters employed in the calculations are summarized in **Table 4.3.**

Further, estimation of bubble size distribution using Werther's method (Werther, 1974a,b) is also considered. In contrast to the backward transformation, Werther derived a relatively simple expression for the prediction of cumulative number density distribution in term of bubble vertical diameter d_V

$$F(d_V) = 1 - \left(\frac{P(y)}{P(d_{V,\min})}\right)\left(\frac{d_{V,\min}}{y}\right) \qquad d_{V,\min} \le y \le d_{V,\max} \qquad (4.2.16)$$

where $d_{V,min}$ is calculated as the pierced length corresponding to the maximum in the slope (with respect to the origin) of the P(y) versus y plot. However, the density distribution of $f(d_V)$ as derived from $F(d_V)$ should be distinguished from $P(d_V)$: the former represents the distribution of the bubble size in the *system* (that is, across the entire horizontal surface (three-dimensional) or line (two-dimensional) of the fluidized bed) whereas the latter depicts the distribution of the bubble size *touching (or measured by)* the probe. Thus, P(R) (or $P(d_V)$) is influenced by the size of the individual bubbles since larger bubbles have greater probability of being detected at the probe. P(R) and the system density distribution of bubble sizes, f(R) in three-dimensional bed, are related according to

$$P(R)dR = \frac{\pi R^2 f(R)dR}{\int_R \pi R^2 f(R)dR} \qquad (4.1.17)$$

It is apparent that f(R) is not equal to P(R) except for mono-sized bubbles. Also, since the second moment of bubble size R (that is, the denominator in equation (4.2.17) has a finite value, the following relationship is established

$$P(R) \propto R^2 f(R) \qquad (4.2.18a)$$

and for two-dimensional bed,

$$P(R) \propto R f(R) \qquad (4.2.18b)$$

Using this relationship, the values of f(R) estimated from equation (4.2.16) were converted to P(R) for comparison with the distributions calculated using the backward transformation method.

4.2.3 Distributions of Bubble Size Parameters

Typical comparisons of the predicted distributions with the experimental data at lower bed heights are shown in **Figure 4.2.3a-d**. These data were obtained using the 2.10×10^{-4} m sized powder as the bed material with a superficial gas velocity of 0.1013 m s^{-1} at a height of 0.1 m above the distributor at the central axis of the bed. The theoretical predictions assuming different bubble shapes are also plotted; the notation used for the predicted curves is given in **Table 4.3**. The comparisons reveal several interesting features:

- It is clear that curve **d**, generated assuming the hemispherical bubble shape, is incompatible with data. The agreement is comparatively better with curves **a** and **c** which assume spherical and spherical cap (with $\theta_w = 120^0$) bubble shapes respectively. The hemispherical bubble shape implies a wake angle $\theta_w = 180^0$ whereas the spherical bubble shape implies $\theta_w = 0^0$. It appears then that the bubble wake angle, if the spherical cap bubble shape is to be accepted, lies between 0 and 120^0. These numbers are consistent with the observations of Chiba et al. (1973). The wake angle could be treated as an adjustable parameter in our calculations. However, due to uncertainties discussed later in this section, such calculations appear unwarranted at this

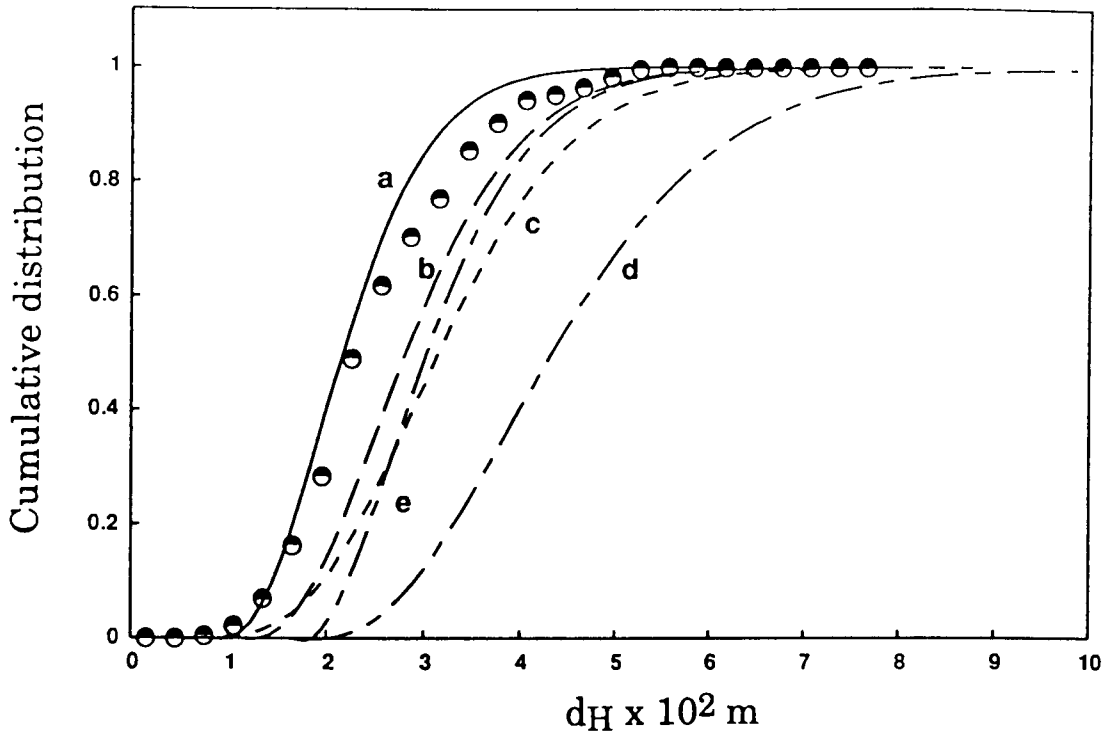

FIGURE 4.2.3a: Comparison of the predicted distributions of various bubble parameters (d_H, d_V, d_E, C_P) with experimental data at lower bed height using various bubble shape models.
a: spherical; b: ellipsoidal, $\alpha = 0.77$; c: spherical cap, $\theta w = 120°$; d: hemispherical and e: ellipsoidal, $\alpha = 0.77$, Werther's method. $d_p = 2.12 \times 10^{-4}$ m, Z = 0.1 m, $U_0 = 0.101$ m/s, $2 L_{pr}/D_T = 0.0$

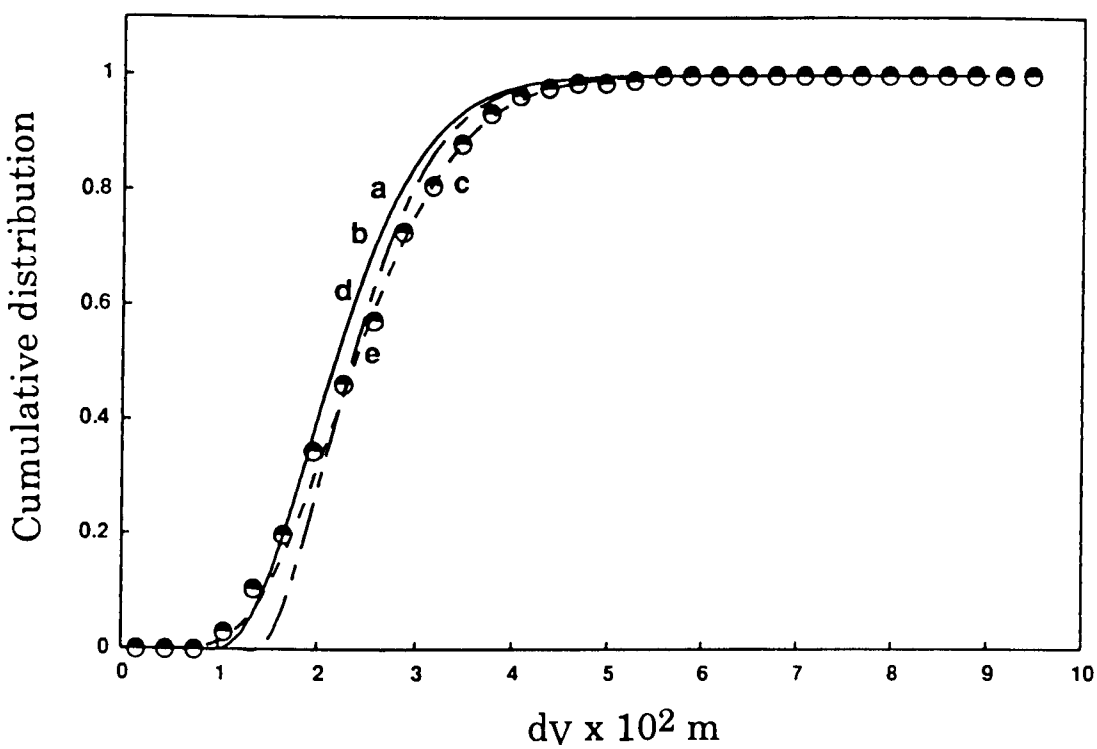

FIGURE 4.2.3b: Comparisons of predicted distributions with experimental data.

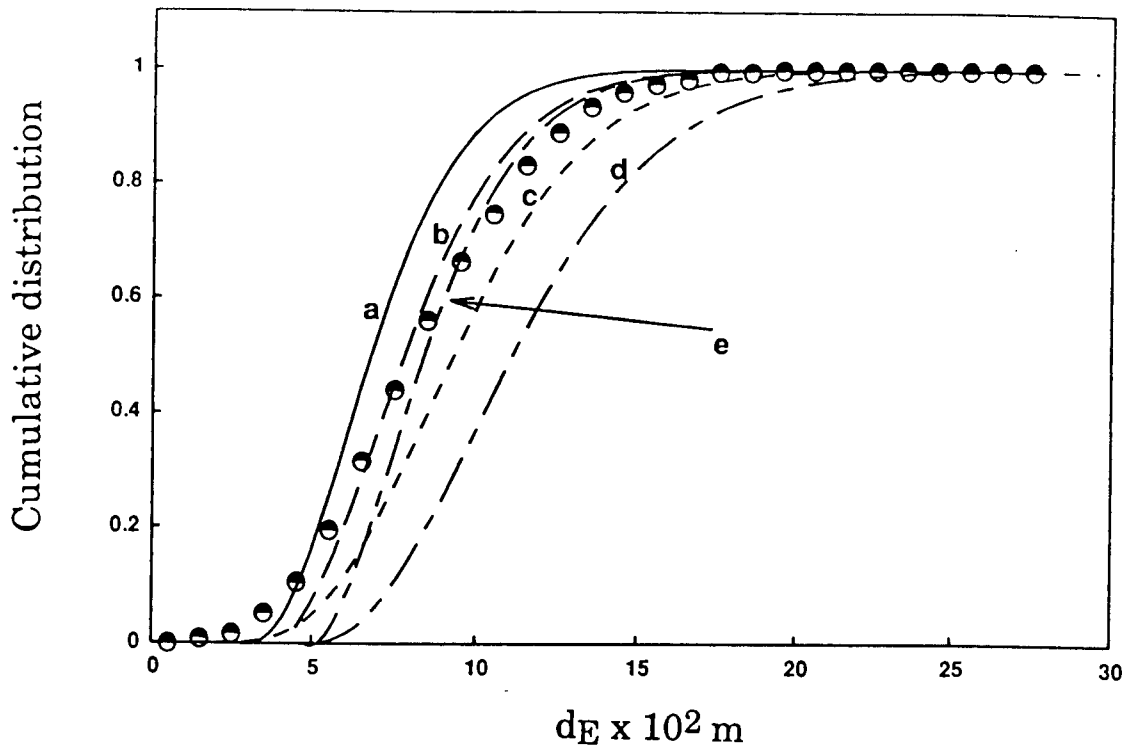

FIGURE 4.2.3c: Comparison of predicted distributions with experimental data

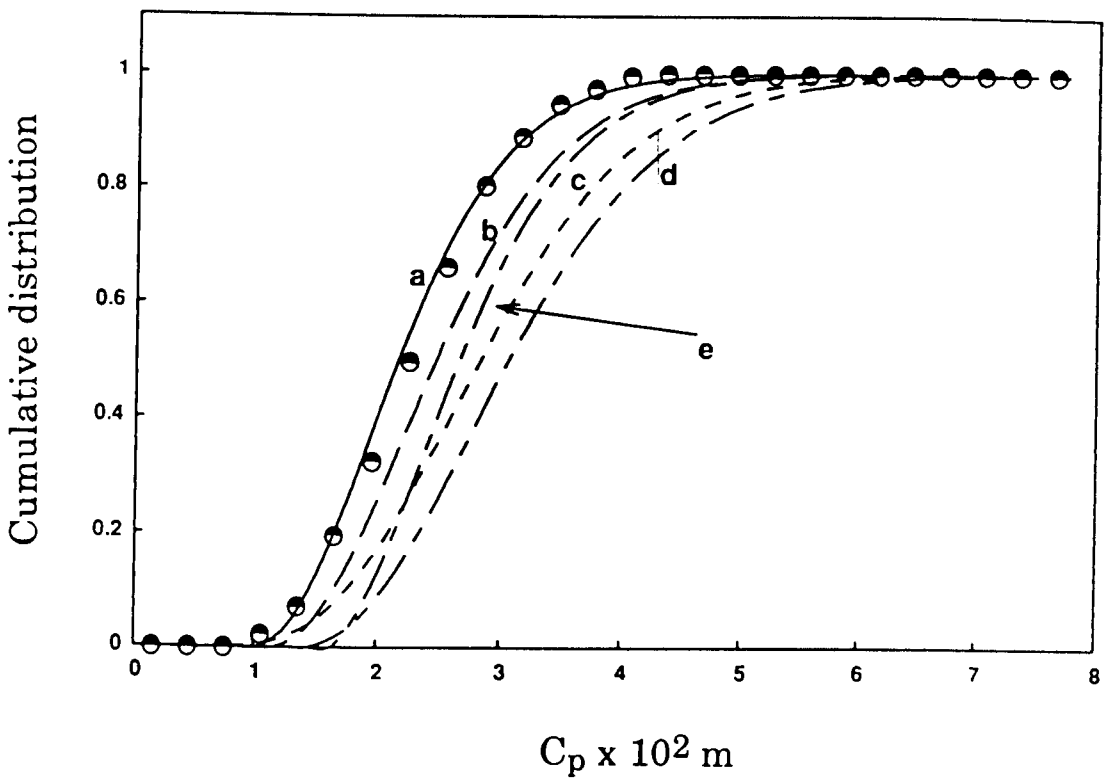

FIGURE 4.2.3d: Comparison of predicted distributions with experimental data

stage.

• Curves **b** and **e** are both obtained assuming ellipsoid bubbles with an aspect ratio, α, of 0.77. However, the prediction using Werther's method, curve **e**, has a different minimum bubble size compared to the backward transform calculations shown by curve **b**. During the course of computations, it was found that P(R) becomes negative for small values of R at the final stages of the calculations. This instability depends on the interval of bubble size (hence number of iterations) over which the calculations are performed. Similar behaviour was noted for calculations using Werther's method. Werther noted that, in his method, the selection of $d_{V,min}$ was somewhat arbitrary; however, this was tolerated as it had no effect on the distribution of remaining bubble sizes $d_V > d_{V,min}$. The backward transform algorithm does provide better agreement with experimental data in this case; a more complete comparison is discussed subsequently.

• The comparison also reveals that the predictions for the vertical diameter are identical for spherical, hemispherical and ellipsoidal bubble shapes. Given the geometry, equation (4.2.1) may also be expressed in term of vertical dimension d_V rather than R. Mathematically, the expressions relating $P(d_V)$ and P(y) for a spherical cap bubble with an arbitrary wake angle θ_w can be obtained using

$$p(r \mid R)\left|\frac{dr}{dy}\right| = \frac{\psi(y\psi-\eta)}{\sqrt{1-(y\psi-\eta)^2}} \qquad (4.2.19a)$$

$$\eta = \sqrt{1-\sin^2(\theta_w/2)} \qquad \psi = (1+\eta/d_V) \qquad (4.2.19b)$$

Similarly, for an ellipsoidal bubble with an arbitrary aspect ratio, α,

$$p(r \mid R)\left|\frac{dr}{dy}\right| = \frac{y}{d_V^2\sqrt{1-(y/d_V)^2}} \qquad (4.2.20)$$

It may be noted that equation (4.2.20) is independent of α; that is, ellipsoidal and spherical (α) bubble shapes will predict identical vertical diameters. It can be verified that for the hemispherical($\theta_w = 180^0$) bubble shape, equations (4.2.19) and (4.2.20) yield identical expressions. The difference between various bubble shapes is evident for other size measures.

- For the prediction of the maximum horizontal and vertical bubble dimensions and the area-equivalent diameter, the spherical bubble shape assumption appears superior. On the other hand, the ellipsoidal bubble assumption provides better agreement for the prediction of the bubble circumference. This apparent anomaly arises from the fact that the bubble shape is irregular and the circumference is inevitably larger than the more compact smooth shapes assumed for the purpose of theoretical analyses. This irregularity of bubble shape would have manifested in the measured projected area, A; however, these effects are dampened by the square root calculation in the conversion to the equivalent diameter, d_E.

The experimental data, in general, are encompassed by the predictions assuming spherical, curve **a**, and ellipsoidal (α = 0.77), curve **b**, bubbles. Qualitatively similar results were obtained for the other experimental conditions employed in this investigation.

4.2.4 Overall Statistical Analysis

Fairly extensive data have been collected during the course of this investigation. To provide an overall assessment of the predictions from geometrical probability, based on various shape characteristics, the predicted mean and the standard deviation of the distributions of the various size measures were compared

with the corresponding experimental values. The scatter plots of the predicted and experimental values for the means and standard deviations are shown in **Figures 4.2.4** to **4.2.7**. The average errors (deviation) of the mean values and standard deviations between the predicted and the experimental values for various models were also estimated and the results are tabulated in **Tables 4.4a** and **b**.

The qualitative consistency of the comparison between experiment and theory, discussed in detail for the size distributions shown in **Figures 4.2.3a-d**, is evident in these results. It can be ascertained that the hemispherical bubble shape leads to the maximum average error in the estimation of the means (43.6%) as well as standard deviations (63.5%)of the size distributions. The errors in the estimation of the mean and the standard deviation of the distribution of the vertical dimension, $F(d_V)$, is identical for spherical, ellipsoidal and hemispherical bubble shapes. The ellipsoidal bubble shape provides the best comparison with the experimental data on bubble circumference. In the estimation of the means of the distributions, calculations using Werther's method lead to lower absolute values for d_V and C_P whereas the backward transform calculations lead to lower errors in the estimations for d_H and d_E. The opposite trend is obtained in the estimation of the standard deviations of the distributions. The results from both calculation procedures are in reasonable agreement.

The assumption of a spherical bubble shape leads to the minimum error in the estimation of the mean as well as the standard deviation.

4.2.5 Approximate Relation between Bubble Pierced Length and Bubble Diameter Distributions

The use of geometrical probability in the conversion of the distribution of bubble pierced length to those of several bubble size measures has been discussed in the preceding sections. It appears useful to explore the possibility of establishing

TABLE 4.4a. OVERALL ERRORS ANALYSIS ON THE MEAN VALUES.

Shape Type	Absolute error, $\delta\mu$ (%)				
	d_H	d_V	d_E	C_P	Average
a	7.3	10.4	0.9	15.4	8.5
b	20.4	10.4	12.9	2.8	11.6
c	45.9	6.2	40.1	25.8	29.5
d	85.4	10.4	40.1	38.4	43.6
e	24.6	7.4	16.8	0.5	12.3

TABLE 4.4b OVERALL ERRORS ANALYSIS ON THE STANDARD DEVIATION.

Shape Type	Absolute Error, $\delta\sigma$ (%)				
	d_H	d_V	d_E	C_P	Average
a	5.1	16.0	28.4	10.7	15.1
b	36.4	16.0	46.3	2.7	25.4
c	65.8	0.5	81.8	32.9	45.3
d	110.1	16.0	81.6	46.2	63.5
e	25.4	22.7	34.5	5.6	22.1

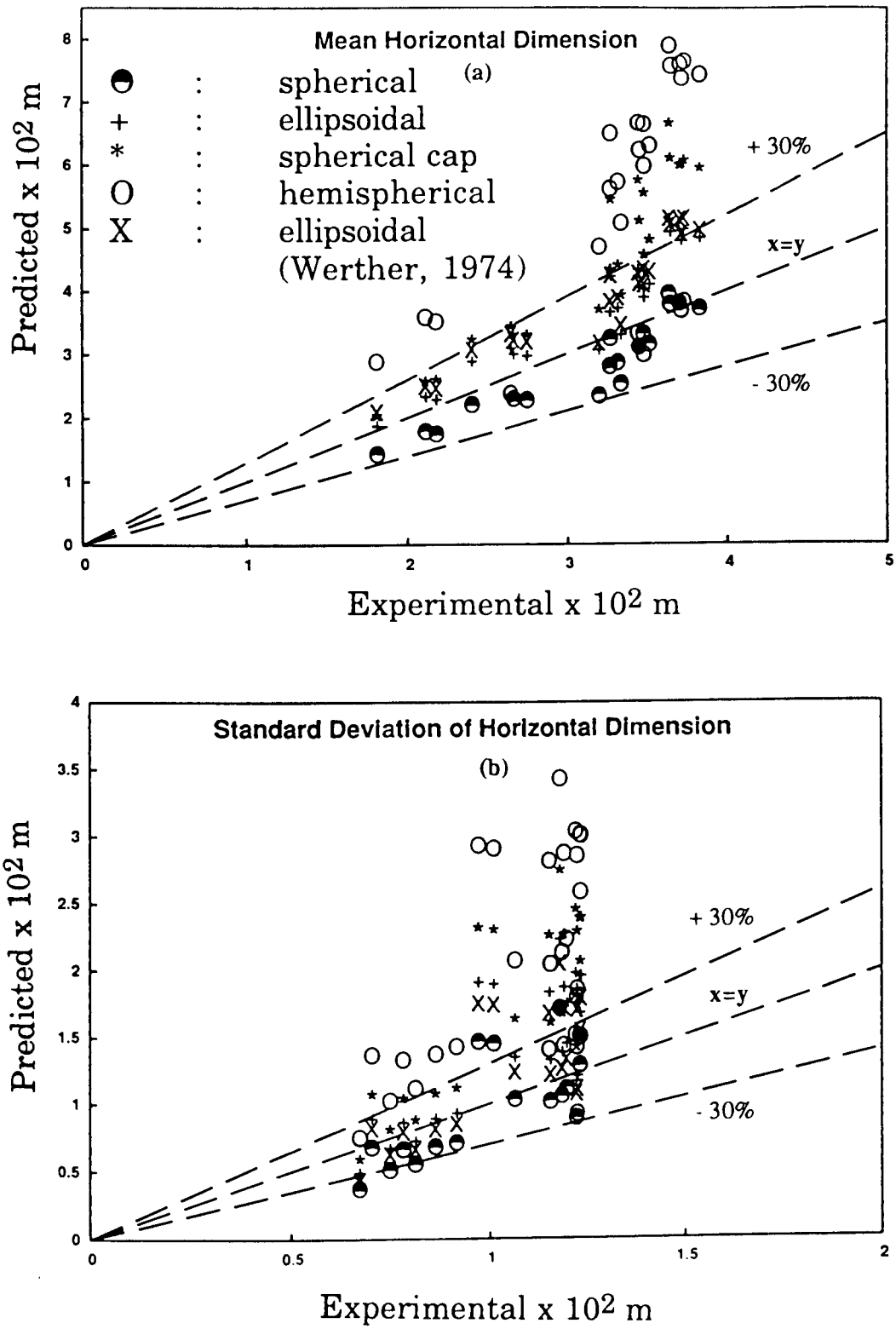

FIGURE 4.2.4: Comparison of predicted (a) mean and (b) standard deviation of bubble horizontal dimension, d_H, using various bubble shape models, with the experimental data

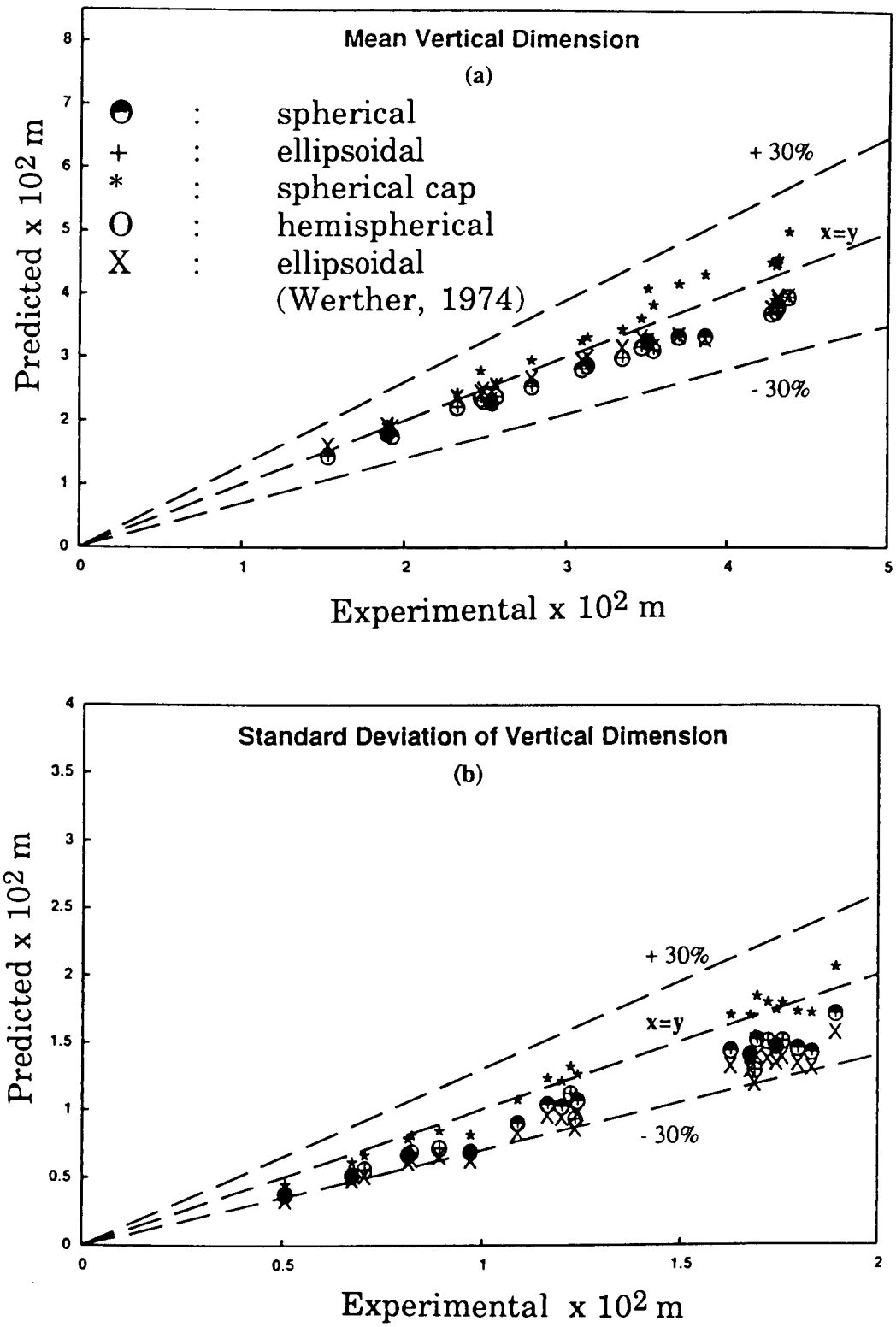

FIGURE 4.2.5: Comparison of predicted (a) mean and (b) standard deviation of bubble vertical dimension, d_V, using various bubble shape models, with the e erimental data

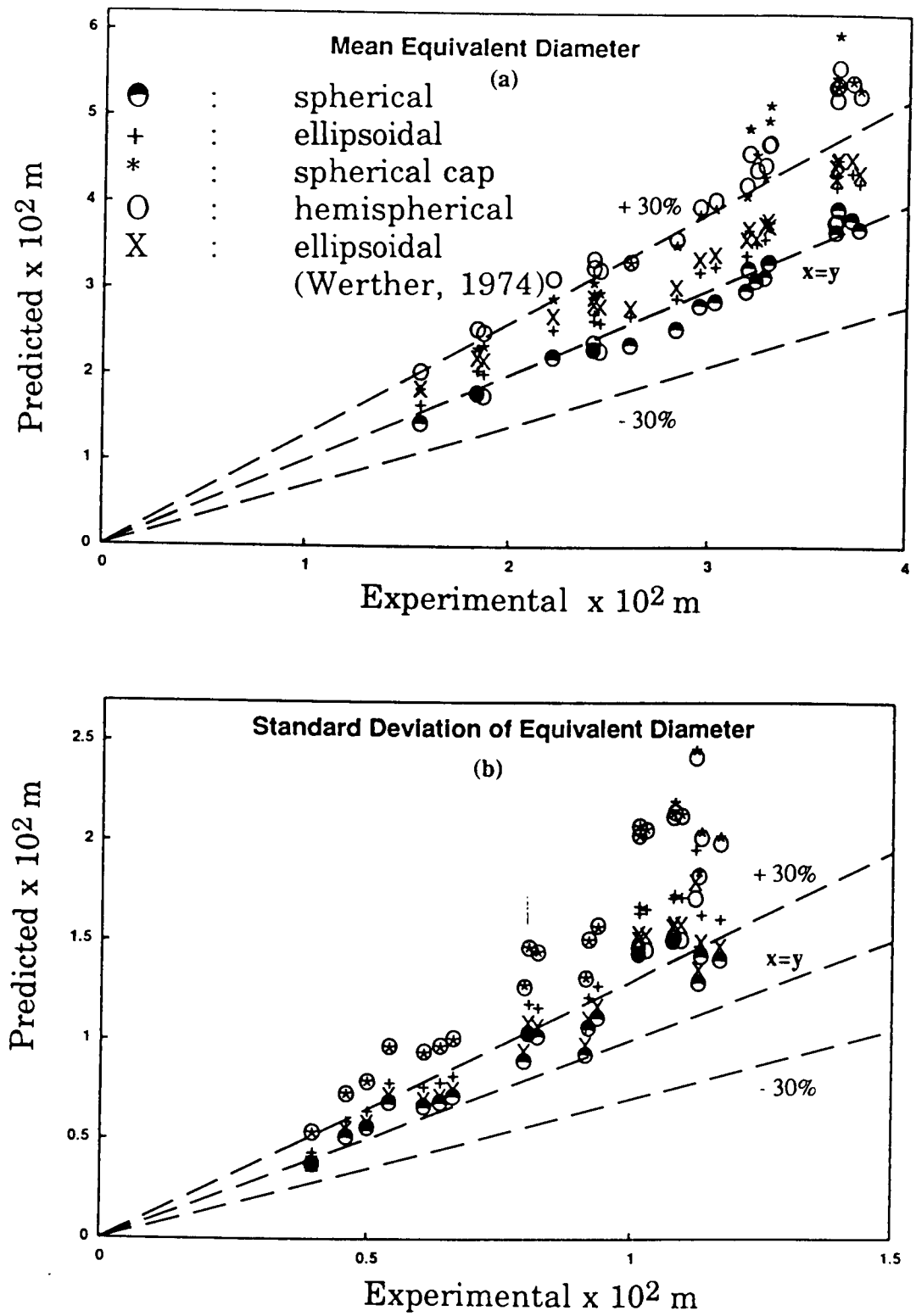

FIGURE 4.2.6: Comparisons of the predicted (a) mean and (b) standard deviation of bubble equivalent diameter, d_E, using various bubble shape models, with the experimental data.

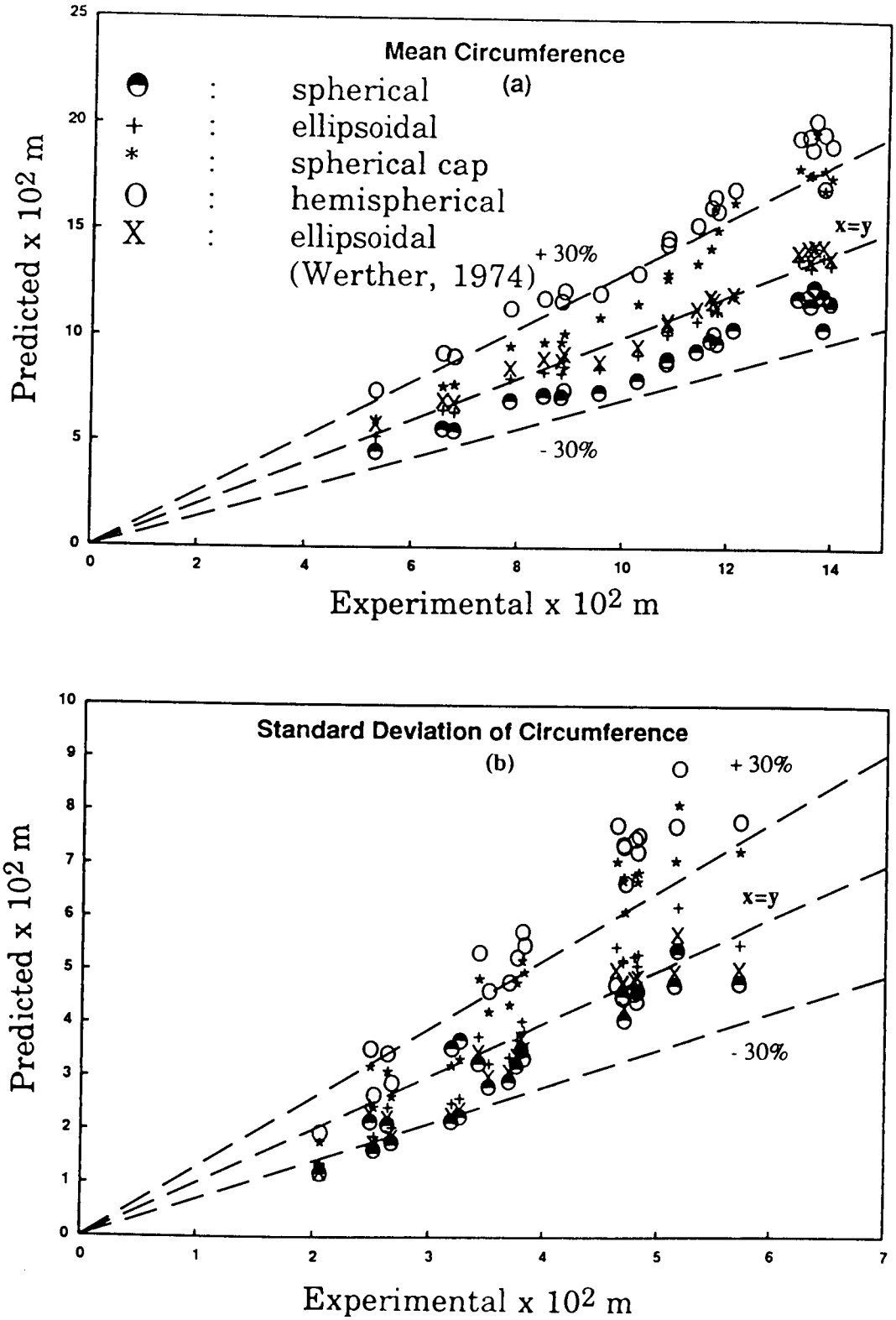

FIGURE 4.2.7: Comparisons of the predicted (a) mean and (b) standard deviation of bubble equivalent circumference, C_P, using various bubble shape models, with the experimental data.

simpler, though empirical, methods for the transformation. Inspection of the experimental data confirms that the size distributions can be fitted by Gamma functions of the form given by equation (4.2.8). The distributions of bubble size measures can be obtained if expressions for the parameters of the Gamma distribution are available. Several expressions have been proposed in the literature to relate the average values of the bubble pierced length and bubble diameter, **Table 2.2**. The plot of the experimental mean of bubble diameters in terms of d_H, d_V and d_E versus bubble pierced length, y, is shown in **Figure 4.2.8**. The agreement between the experimental data and correlations appears to be reasonable. To establish the relation between the mean and the standard deviation of the size distributions, a regression analysis was performed; the results are summarized in **Table 4.5**. The results show strong correlation between the standard deviation and mean property. A simple linear regression model $\sigma = A_0 + A_1 \mu$ was used and the corresponding coefficients have been estimated. Chiba et al. (1973) also observed that the variance of the bubble size distribution was uniquely correlated with the mean bubble size. The relationship $\sigma = A_0 \mu^{A_1}$ was used and the estimated values for coefficients A_0 and A_1 using a wide range of particle sizes and types were 0.245 and 1.535 respectively. However, an exception was observed for micro spherical catalyst particles (89 μm) where the coefficients A_0 and A_1 were 0.110 and 1.955 respectively. Chiba et al. (1975) suggested that the bubble size distribution may be expressed by a logarithmic normal distribution for most particles. Such empirical approaches provide simpler procedures for the estimation of bubble size distribution from the measured pierced length values in the regime of the regression analysis. In general, the geometrical probability approach is clearly preferable.

TABLE 4.5. CORRELATION BETWEEN THE EXPERIMENTAL MEAN AND STANDARD DEVIATION OF VARIOUS BUBBLE DIMENSIONS.

	$\sigma = A_0 + A_1 \mu$		
Bubble Dimension	A_0	A_1	**Corr. Coeff.**
Pierced length, y	-0.340	0.620	0.976
Horizontal dimension, d_H	0.143	0.288	0.853
Vertical dimension, d_V	-0.204	0.468	0.951
Equivalent diameter, d_E	-0.157	0.346	0.929

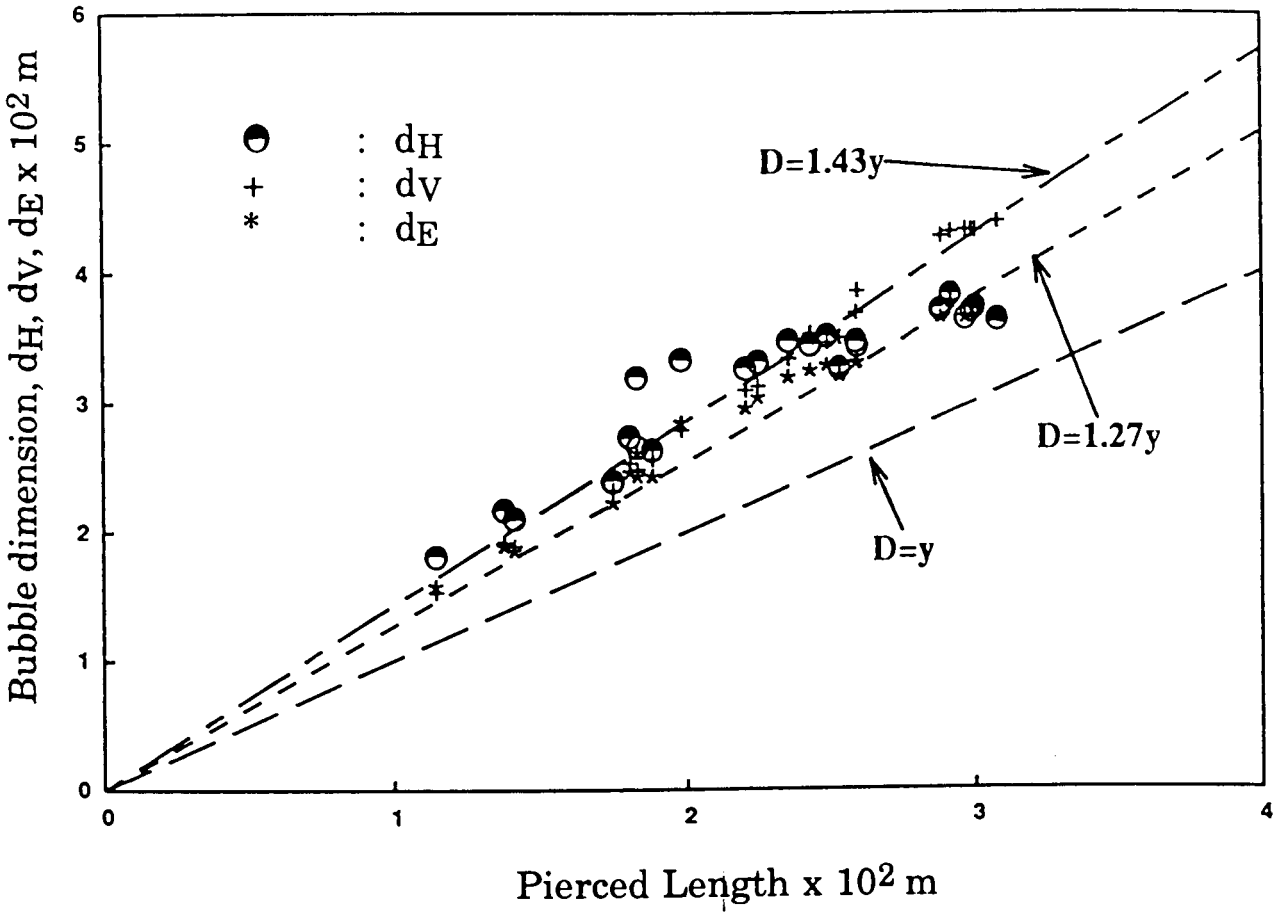

FIGURE 4.2.8: Comparisons between the mean values of different bubble dimensions (d_H, d_V, d_E) and mean bubble pierced length, y.

4.2.6 Requirements for Refinements in Theory

The results described above indicate that the geometrical probability approach, when used with the spherical bubble shape assumption, provides a reasonable method for the calculation of the distributions of bubble size measures from experimental data on the pierced lengths measured at a probe. There are two further refinements in theory which would strengthen the results reported in this study.

Firstly, the theory assumes lateral homogeneity in bubbling. To test this assumption, experiments were conducted at different lateral positions in the bed. In **Figures 4.2.9a** and **b**, the experimental cumulative distributions for the bubble pierced length, y, and the vertical dimension, d_v, are plotted for lateral positions $2L_{pr}/D_T$ of 0.0, 0.4 and 0.8 at a height of 0.25 m above the distributor. These data have been obtained using the 2.5×10^{-4}m powder fluidized at a gas velocity of 0.133 m s^{-1}. The inspection of these plots indicates that both size distributions are identical at $2L_{pr}/D_T = 0.0$ and 0.4, that is near the centre of the bed. This behaviour is consistent with the homogeneous bubbling assumption. On the other hand, the distributions of y and d_v at $2L_{pr}/D_T = 0.8$ are markedly different from those at $2L_{pr}/D_T = 0.0$ and 0.4. These data confirm the existence of lateral non-homogeneity in bubbling near the walls of the vessel. This behaviour is in qualitative agreement with earlier literature results for two and three-dimensional beds (Grace and Harrison, 1968; Werther, 1974a,b). At present, the functionality of $P(Z,\lambda,R)$, which describes the lateral non-homogeneity, has not been established and further work is necessary.

The theory also assumes uniform shape for the entire bubble population. However, due to the effect of complex interactions between neighbouring bubbles in the swarm, bubbles have been observed to occur in several forms and shapes

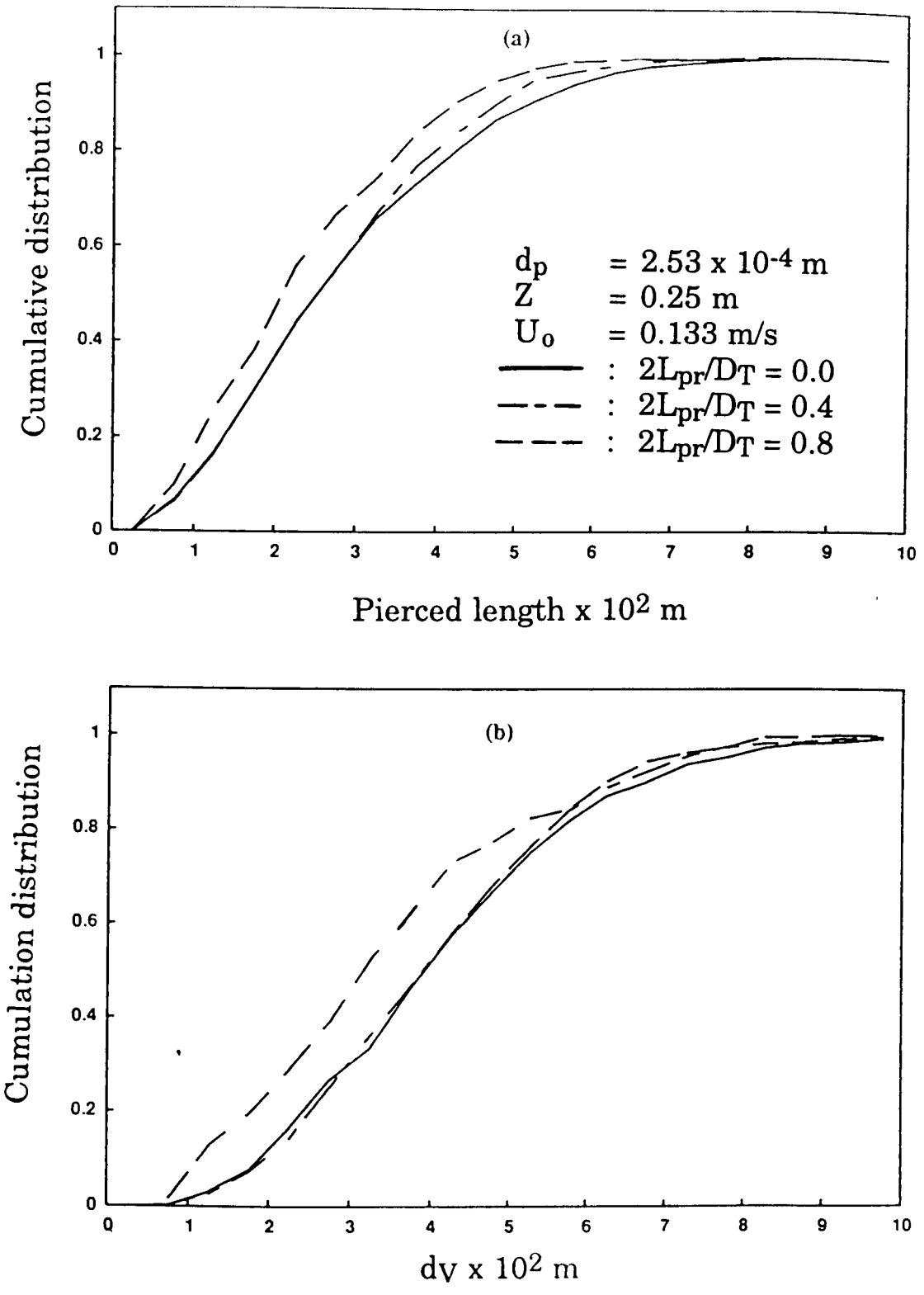

FIGURE 4.2.9: Experimental cumulative distributions for (a) pierced length, y, and (b) vertical dimension dv measured at different lateral positions, $2L_{pr}/D_T$ in the bed

(Hatano et al., 1986; Hatate et al., 1985). A typical measurement of the distribution of the bubble aspect ratio (d_V/d_H) is shown in **Figure 3.2.4c**. The means of the distributions are close to one - that is, the spherical bubble shape. However, it is clear that the assumption of uniform bubble shape characteristic is not correct. The transformation method described in the theory must allow the possibility of bubble characterization by more than one independent size characteristics. The derivation of an appropriate expression - instead of equation (4.2.1) - is possible. The concept of statistical sampling from a multivariate population has been discussed by Kendall and Stuart (1977). In the following example, with the extension of an additional size characteristic, the distribution of bubble pierced length is characterized by a joint probability of bubble centre, horizontal and vertical dimension. Alternatively, the vertical dimension may be interpreted by the aspect ratio. Thus

$$P(y) = \int_{\alpha} P(y, R \mid \alpha) P(\alpha) d\alpha$$

$$= \int_{\alpha} \int_{R} P(y \mid R, \alpha) P(R \mid \alpha) dR P(\alpha) d\alpha \qquad (4.2.21)$$

If R and α are independent, then P(R|α) equals P(R). Also

$$P(y \mid R, \alpha) = P(r \mid R, \alpha) \left| \frac{dr}{dy} \right| \qquad (4.2.22)$$

and

$$P(r \mid R, \alpha) = \frac{\int_0^{2\pi} P(Z, \lambda, R, \alpha) r d\theta}{\int_0^{R} \int_0^{2\pi} P(Z, \lambda, R, \alpha) r d\theta dr} \qquad (4.2.23)$$

Given experimental information of P(y) and P(α), the values of P(R) may be obtained numerically. The backward transformation technique can not be applied directly to this case and more sophisticated algorithms are required.

However, inclusion of one more size characteristics demands an additional stage of integration. The solution requires a more sophisticated algorithm than the backward transformation method. It is thought that the effect of non-homogeneity in bubbling needs to be considered in more detail before the additional computational efforts in the implementation of the more sophisticated algorithm can be justified.

4.2.7 Conclusions

The distributions of the bubble pierced length as well as other bubble size measures were measured experimentally by employing digital image analysis methods. The experimental results show that bubble size distribution can not be obtained directly from the pierced length distribution. However, reasonably reliable inferences can be made using geometrical probability approach. Results of comparison, for bubble size distributions as well as overall statistical analyses, suggest that simulations using spherical or ellipsoidal (α=0.77) models provide satisfactory agreement between experiment and theory. Lateral non-homogeneity in bubbling as well as the non-uniformity in bubble shapes have been detected experimentally. Further work is necessary to include these refinements in the theory.

These results will significantly enhance confidence in the use of intrusive probes (measuring only the pierced length distributions) to determine the size distributions of bubbles or droplets dispersed in a medium. Two further considerations need a more detailed appraisal:

- the ability of two-element probes to measure bubble velocity and pierced length unequivocally; and
- the possibility of alteration in the local behaviour of the dispersed phase due to the presence of the in bed probe.

The first issue is addressed in detail in the following section.

4.3 THE ANGLE OF BUBBLE RISE AND SUBMERSIBLE PROBE SIGNAL INTERPRETATION METHODS

Submersible probes used to measure bubble characteristics in three-dimensional beds often have two sensing elements to detect the presence (or absence) of the rising bubble void. Such probes measure the velocity of a bubble as the ratio of the probe tip separation and the time (delay time) taken for bubble interface to travel from the lower to the upper probe tip. The assumptions implicit in this measurement method are that the shape of the interface or the bubble does not deform substantially and that the bubble rises vertically (in alignment with the vertical probe axis). The former assumption may be valid if the distance between the probe tips is small. In this section, the implications of the latter assumption are examined both theoretically as well as experimentally. The image analysis techniques developed to measure the bubble velocity, described in **section 3.2.3**, also permit assessment of the relation between bubble size, shape and velocity in freely bubbling beds. For comparison, measurements have also been obtained for bubbles injected - singly or continuously from a single orifice - into a bed maintained at minimum fluidization conditions.

4.3.1 Theoretical Analysis

Consider an ideal circular (two-dimensional) shape bubble of radius R rising with a velocity $V_{B,\theta}$ at an angle θ_B with respect to the vertical axis as shown in **Figure 4.3.1a**. The vertical probe (with tip separation t_s) intercepts the bubble interface at a distance r from the central axis of the bubble. The bubble pierced lengths measured at the upper and lower tips are y_U and y_L respectively. From geometry, **Figure 4.3.1b**, the following relationship is established:

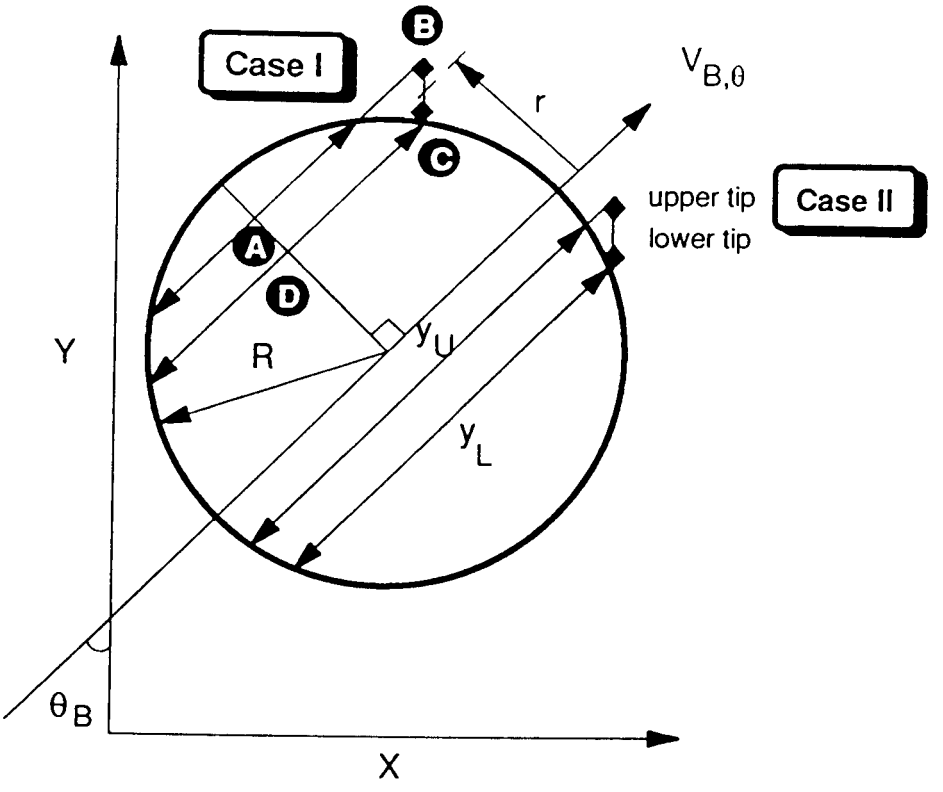

(a)

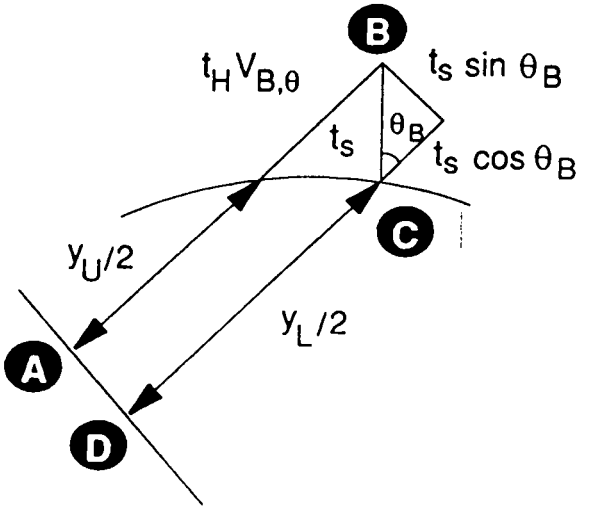

(b)

FIGURE 4.3.1: (a) Interpretation of probed signal for bubble moving at an angle θ_B

(b) Geometrical relationship of signals measured by the upper and lower probe.

$$y_U/2 + t_H V_{B,\theta} = y_L/2 + t_s \cos\theta_B \qquad (4.3.1a)$$

where t_H is the delay time for the interface to reach the upper tip. Rearrangement of equation (4.3.1a) yields

$$t_H = \frac{y_L/2 - y_U/2 + t_s \cos\theta_B}{V_{B,\theta}} = \frac{t_s}{V_{B,m}} \qquad (4.3.1b)$$

where $V_{B,m}$ is the inferred velocity assuming the bubble rises vertically past the probe. Therefore, the deviation of the velocity inferred by the dual-element probe, $V_{B,m}$, from the true velocity, $V_{B,\theta}$, can be expressed as

$$\frac{V_{B,m}}{V_{B,\theta}} = \frac{t_s}{y_L/2 - y_U/2 + t_s \cos\theta_B} \qquad (4.3.1c)$$

Referring to **Figure 4.3.1a**, two cases arise: case **I** where the pierced length measured by the lower probe, y_L is greater than the that measured by upper probe, y_U, whereas in case **II**, the converse is true. It can be shown from geometry that the difference in the pierced lengths at the two tips of the probe is

$$\Delta y = \frac{y_L}{2} - \frac{y_U}{2} = \pm\left\{\sqrt{R^2 - \left(r - t_s \frac{\sin\theta_B}{2}\right)^2} - \sqrt{R^2 - \left(r + t_s \frac{\sin\theta_B}{2}\right)^2}\right\} \qquad (4.3.2a)$$

Clearly, the variables influencing the ratio of inferred and actual velocity, $(V_{B,m}/V_{B,\theta})$, are the bubble radius R, the off-center distance r, and the angle of bubble incidence θ_B. Equation (4.3.2a) can then be written in terms of dimensionless length parameters $\beta = R/t_s$, $\tau = r/R$ and $\eta = \Delta y/t_s$ as

$$\eta = \pm\beta\left\{\sqrt{1 - \left(\tau - \frac{\sin\theta_B}{2\beta}\right)^2} - \sqrt{1 - \left(\tau + \frac{\sin\theta_B}{2\beta}\right)^2}\right\} \qquad (4.3.2b)$$

Consequently, equation (4.3.3) can be rewritten as

$$\frac{V_{B,m}}{V_{B,\theta}} = \frac{1}{\eta + \cos\theta_B} \qquad for \qquad (\eta + \cos\theta_B) > 0 \qquad (4.3.3)$$

Parametric studies with equation (4.3.3) revealed that $(V_{B,m}/V_{B,\theta})$ was more sensitive to τ and θ_B in comparison with β; computations for a bubble having radius ten times larger than the tip separation distance ($\beta = 10$) as functions of θ and τ are shown in **Figure 4.3.2**. The results indicate that in case **II**, the inferred velocity is always greater than the true velocity for all angles and increases with increasing value of angle of incidence θ_B. The extent of deviation is considerable if the off-center distance r is large. However, in case **I**, the inferred velocity may be over- or under-estimated depending on the angle of incidence and the off-center distance.

Though the above analysis is only for a simple bubble shape, its implication is critical for velocity measurement (and the consequent deduction of bubble size) using a dual-element probe. Given the geometry of a two-element probe, it is not possible to measure either the angle of incidence or the off-center distance which are of importance as shown above. Clearly, the measurements from a dual-element probe are questionable theoretically. It remains to establish the magnitude and the nature of the deviation of the angle of bubble rise from the vertical in practice.

4.3.2 Bubble Deformation

Whether submerged probes, dual-element or multiple-tipped, alter the local state of fluidization or not has been debated in the literature (Gunn and Al-Doori, 1985; Sung and Burgess, 1987; Rowe and Masson, 1981; Geldart and Kelsey, 1972; Rowe and Masson, 1980). In a fluidized bed, there is a continuous exchange of material (gas as well as solid) between the bubble and emulsion phases and the non-rigid bubble-emulsion interface could deform even in the absence of a submerged probe. An estimate of this deformation was made by measuring the local size and shape change between two successive image fields. The extent of

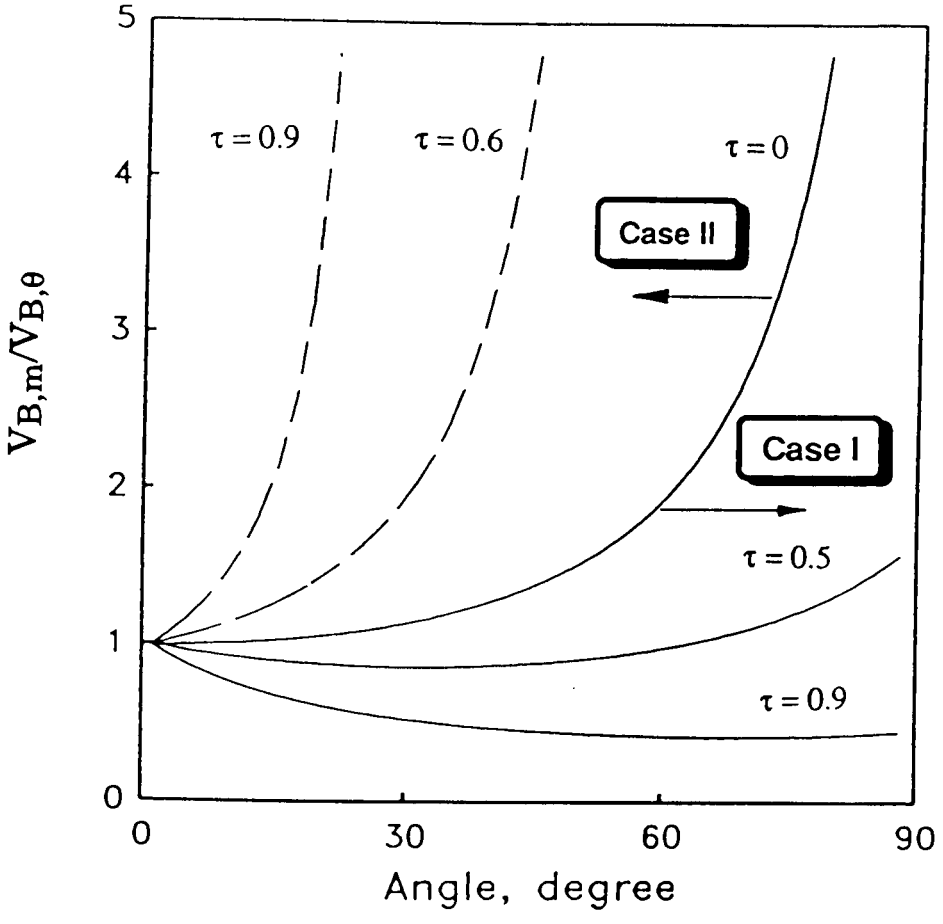

FIGURE 4.3.2: Typical parametric results (for $\beta = 10$) on the ratio of inferred and actual velocity ($V_{B,m}/V_{B,\theta}$) as a function of angle of incidence, θ_B, and off-centre distance, $\tau = r/R$.

change or deviation, δ, between fields was defined as

$$\delta = \left| 1 - \frac{F_2}{F_1} \right| \times 100 \qquad (\%) \qquad (4.3.4)$$

where F_1 and F_2 are the measurable variables in first and second image field respectively. Typical cumulative distributions for the extent of change in size and shape are shown in **Figure 4.3.3.** The change in the size d_E and shape factor S was found to be relatively small - that is, more than 50 % of the bubble population experienced less than 5 % deviation. However, the aspect ratio α changed considerably due to shape elongation from impending coalescence.

The measured changes are, at the present stage, indicative only since they also reflect possible limitations in the thresholding algorithms used in size/shape measurements. The data presented in the following have been screened to discard all measurements showing more than 5 to 10 % change between successive image fields.

An estimate of whether the interface velocity is the bubble velocity (as assumed in measurements using submersible probes) can, nevertheless, be made from these measurements. The changes measured by our technique occur between two successive image fields, that is, over 1/50 s. Consider a submerged probe with tips 4×10^{-3} mm apart. These measurements then represent the change, assuming that the probes do not induce any additional deformation, for bubbles with a velocity of about 0.2 m s^{-1}. Though the rate of bubble deformation needs to be measured to make any quantitative statement, it does appear that interface velocity can be taken as the bubble velocity for smaller probe tip separations and/or faster bubbles.

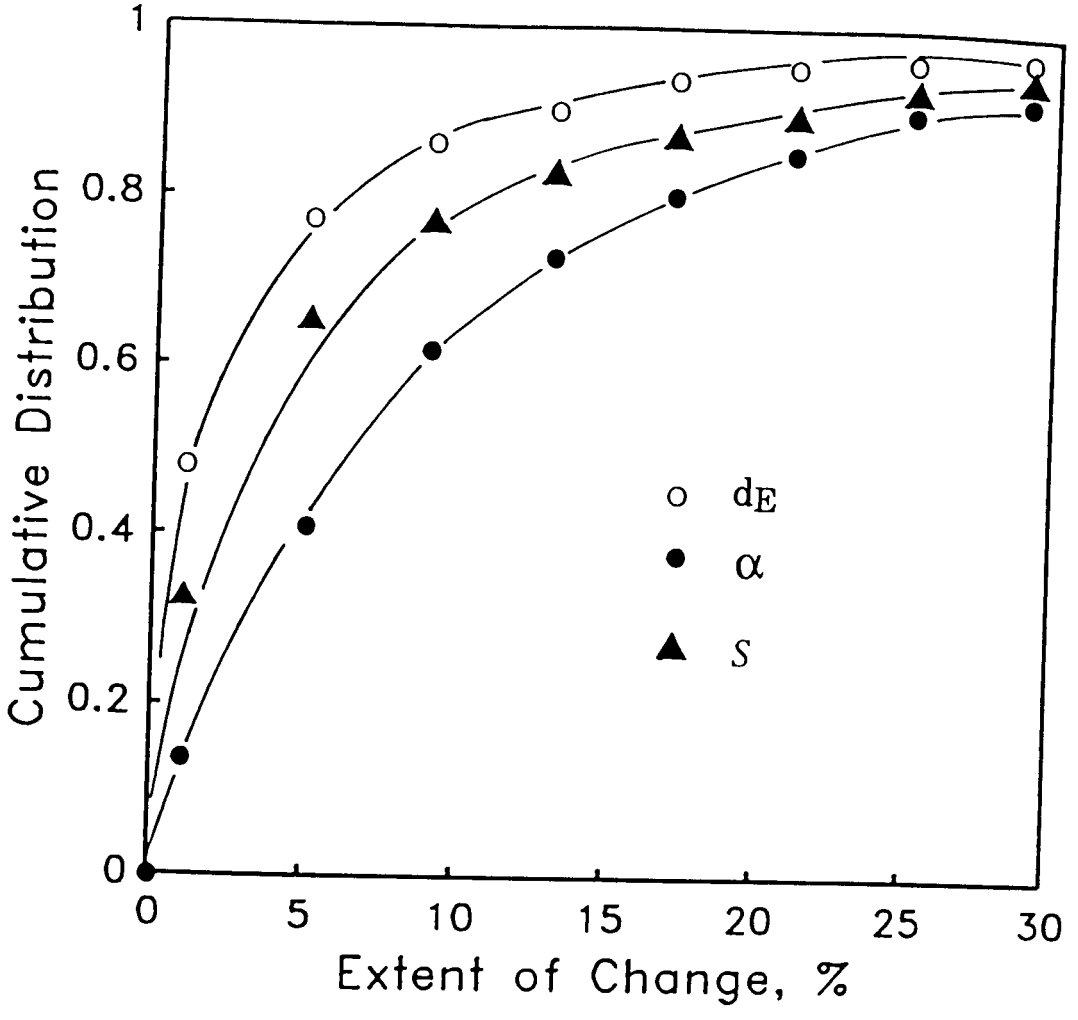

FIGURE 4.3.3: Extent of change and deformation for local bubble size (d_E), aspect ratio (α) and shape factor (S) between two image fields 1/50 s apart; experimental conditions:
$Z/H_F = 0.55$, $2L_{pr}/W = 0.0$, $U_o/U_{mf} = 2.84$

4.3.3 Measurements of Bubble Velocity

Experimental results demonstrating the effect of key variables on the distributions of absolute bubble velocity, $V_{B,s}$, are plotted in **Figures 4.3.4a-c.** Measurements at two heights ($Z/H_F = 0.28$; $Z/H_F = 0.55$) for $U_0 = 2.84U_{mf}$ along the central vertical axis of the bed clearly show, **Figure 4.3.4a**, that the average bubble velocity increases with height above the distributor. In **Figure 4.3.4b**, the effect of superficial gas velocity is examined by plotting measurements for U_O/U_{mf} of 1.4, 1.75 and 2.28 at $Z/H_F = 0.55$ along the central vertical axis of the bed. It is clear that both the mean and the standard deviation of the bubble velocity distribution increase with superficial velocity through the bed. The results examining the effect of horizontal position within the bed, **Figure 4.3.4c**, provide evidence of the lateral inhomogeneity in bubbling at the same height above the bed distributor.

Measured bubble velocities are mostly greater than 0.2 m s^{-1} indicating that a submersible probe with 4x 10^{-3} m tip separation would be likely to see smaller bubble deformation in comparison with the results in **Figure 4.3.3.**

4.3.4 Effect of Non-Vertical Bubble Rise on Measurements using Two-element Probes

The experimental data for the measured angles of incidence (or bubble rise) - in the form of a probability density function - for several probe locations and operating conditions are plotted in **Figure 4.3.5.** The range of the angle of incidence was found to be ±60° from most experiments. It is observed that, though the distributions of bubble sizes and velocities differ for these operating conditions, the density functions for the angle of bubble rise are remarkably similar. For comparison, the limited experimental data (Gunn and Al-Doori, 1987) are also

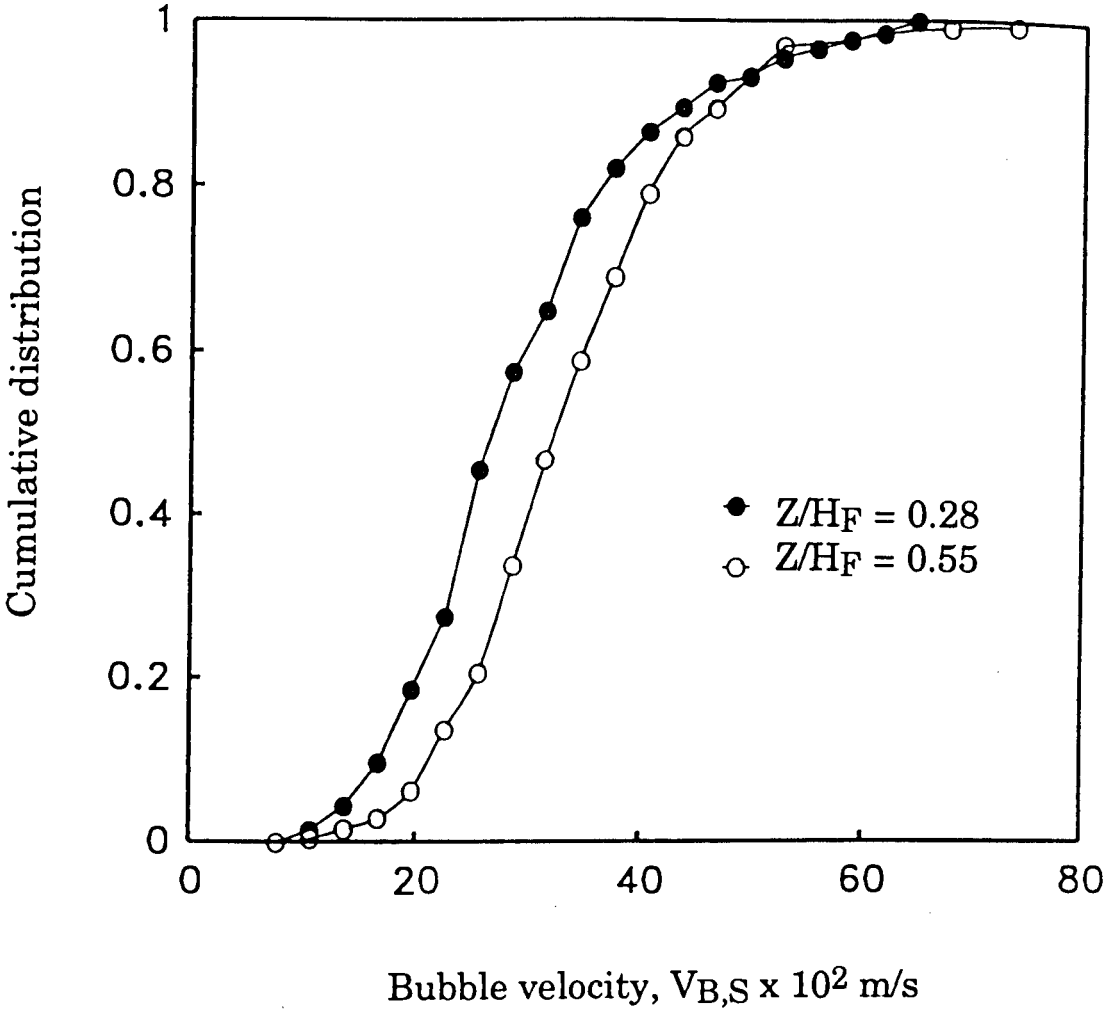

FIGURE 4.3.4a: Cumulative distributions of bubble velocity at different bed heights; experimental conditions: $2L_{pr}/W = 0.0$, $U_o/U_{mf} = 2.84$

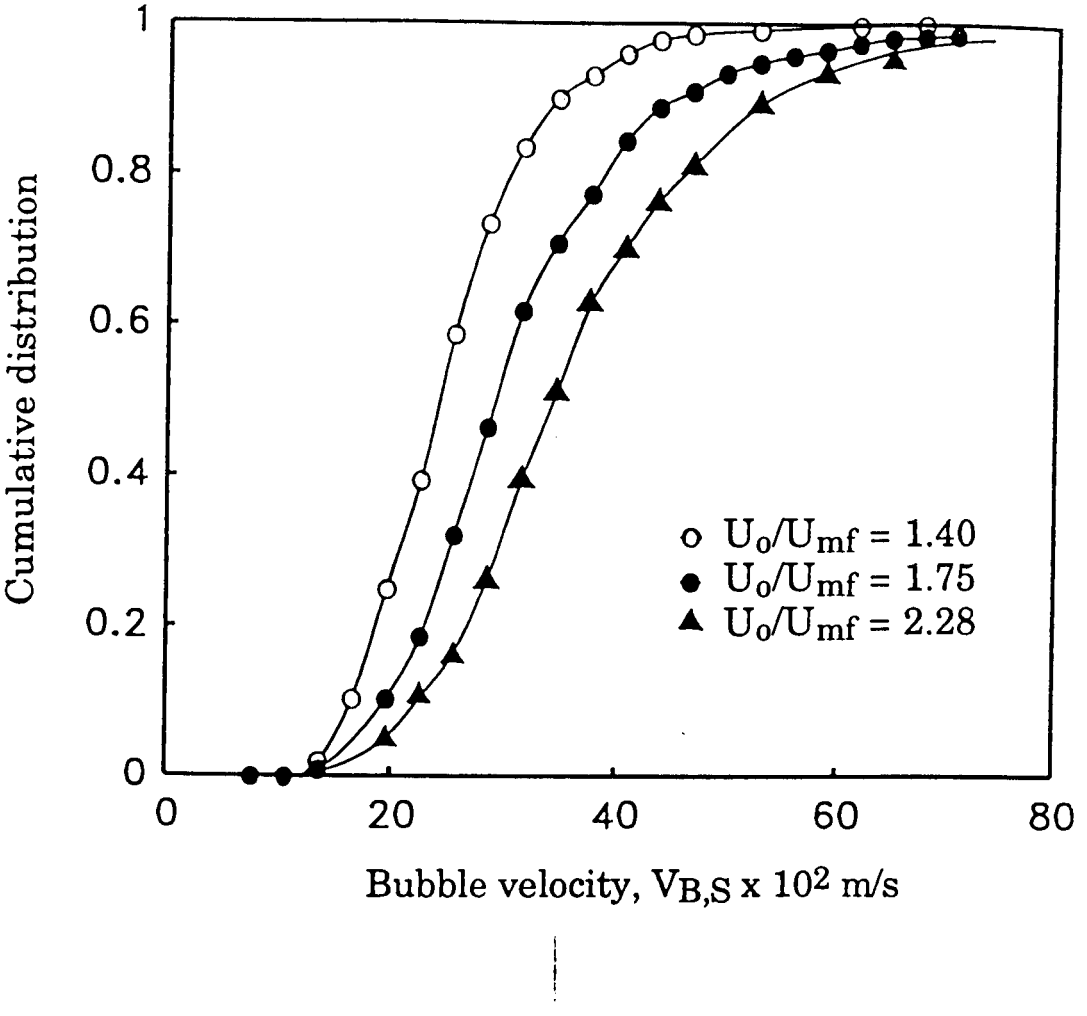

FIGURE 4.3.4b: Cumulative distributions of bubble velocity at different superficial gas velocities; experimental conditions:
$Z/H_F = 0.55$, $2L_{pr}/W = 0.0$, $U_o/U_{mf} = 2.84$

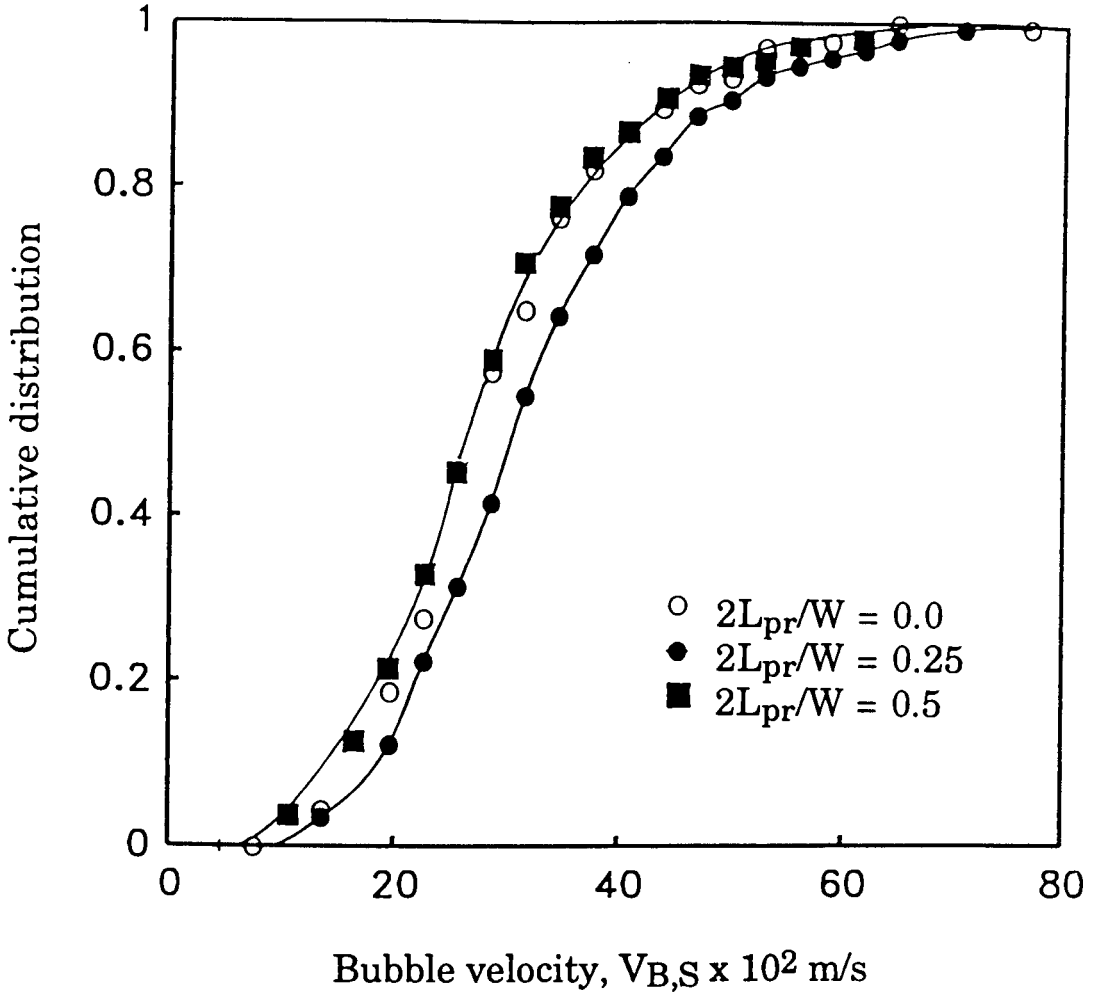

FIGURE 4.3.4c: Cumulative distributions of bubble velocity at different lateral bed positions; experimental conditions: $Z/H_F = 0.55$, $U_o/U_{mf} = 2.84$

plotted in **Figure 4.3.5**; their measurements are very similar. All these data can be conveniently represented by a Normal density function with a mean corresponding to vertical bubble rise ($\theta_B = 0$) and a standard deviation of 14°. Further research is necessary to provide a theoretical explanation for this interesting result.

The experimental results in **Figure 4.3.5** along with the theoretical computations plotted in **Figure 4.3.2** confirm that the bubble velocity measured by the two-element probe can be significantly different from the actual bubble velocity especially for higher values of τ. Since the measured velocity is subsequently used for the determination of bubble pierced length and size, experimental results reported using two-element submersible probes have to be viewed at best as qualitative.

4.3.5 Effect of Bubble Selection Criteria on Multiple-tipped Probe Measurements

As noted earlier, additional elements are incorporated in more sophisticated probe designs (Burgess and Calderbank, 1975; Burgess et al. 1981; Sung and Burgess, 1987) to detect and reject non-vertically rising bubbles. It has not been established, however, whether velocity and size distributions of vertically rising bubbles accurately reflect the distributions for the entire bubble population. To address this issue, the experimental data were screened to identify the bubbles with an angle of incidence lying between $\theta_B = \pm 5°$. From **Figure 4.3.5**, this fraction represents about 16 % of the entire bubble population. The size (area equivalent diameter, d_E) and velocity distributions for these screened bubbles are compared with corresponding distributions for the entire population in **Figures 4.3.6a-d** for several probe locations and operating conditions. It is clear from this comparison that multiple-tipped submersible probes will provide a satisfactory measurement of bubble characteristics in a gas fluidized bed.

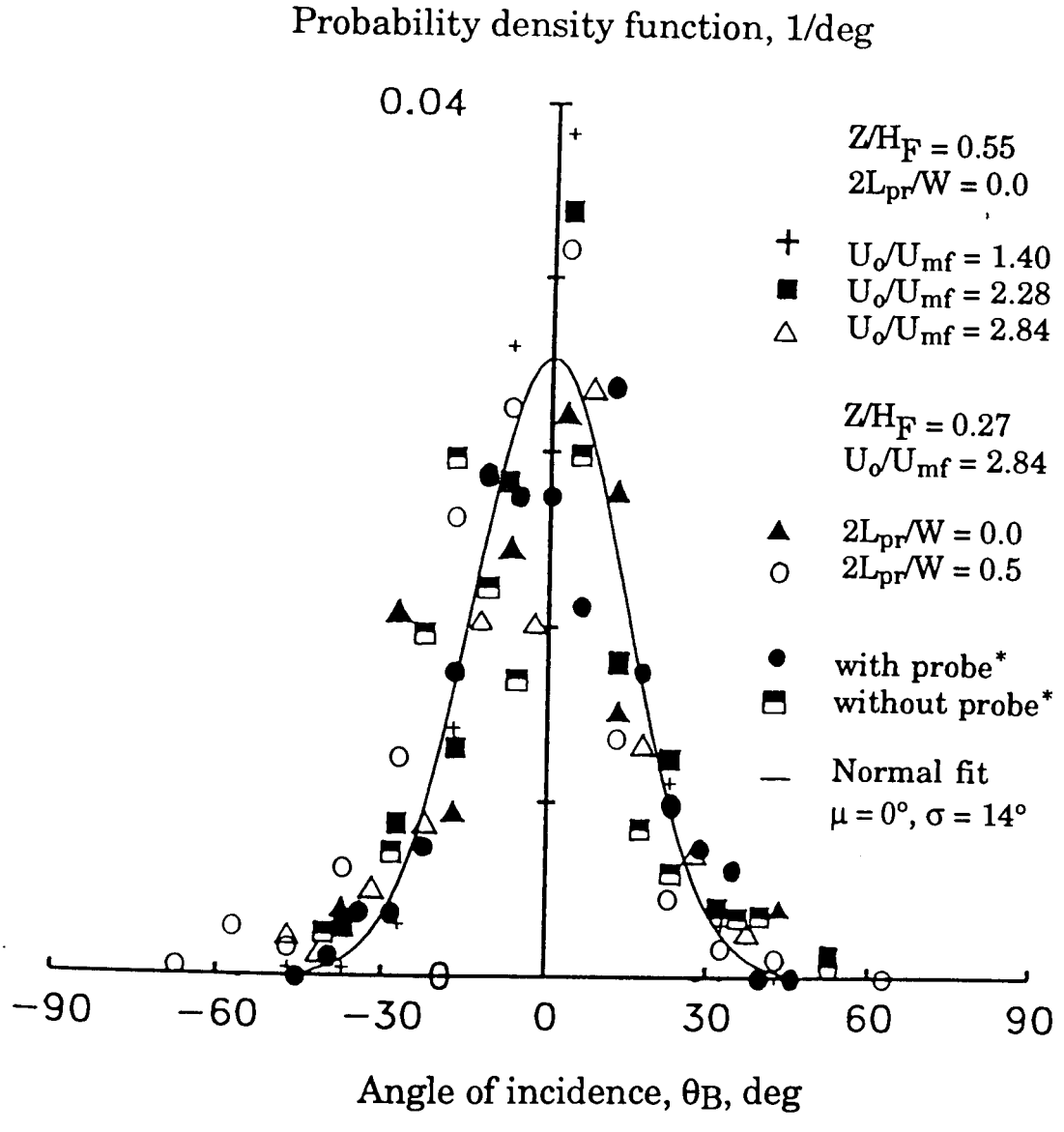

FIGURE 4.3.5: Distribution of the angle of incidence θ_B of the rising bubbles measured at various experimental conditions and compared with the experimental results of Gunn and Al-Doori (1987)*

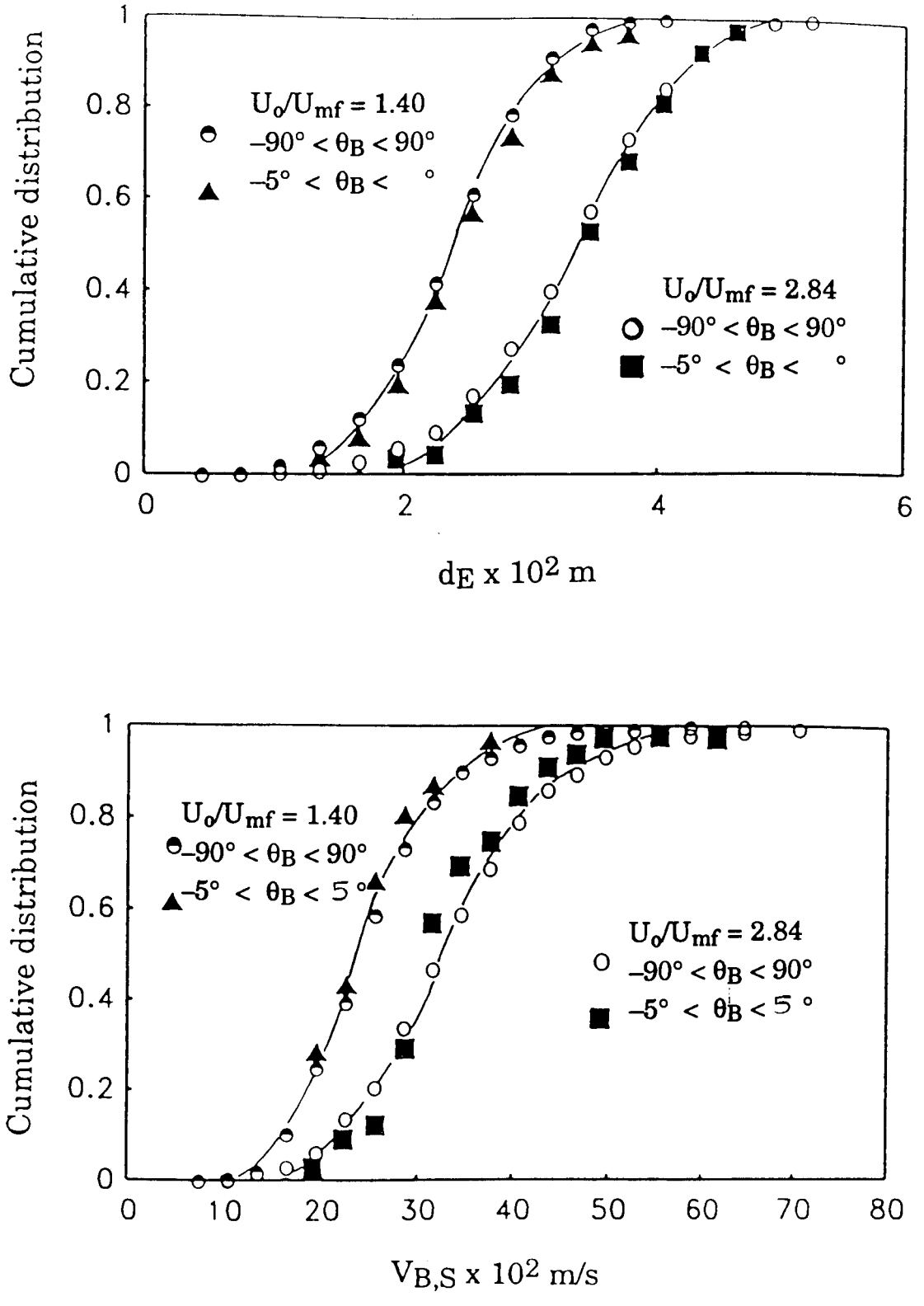

FIGURE 4.3.6: (a) Size and (b) velocity distribution for the entire population and those rising vertically at different gas velocity (Z/H_F = 0.55, 2 L_{pr}/W = 0.0)

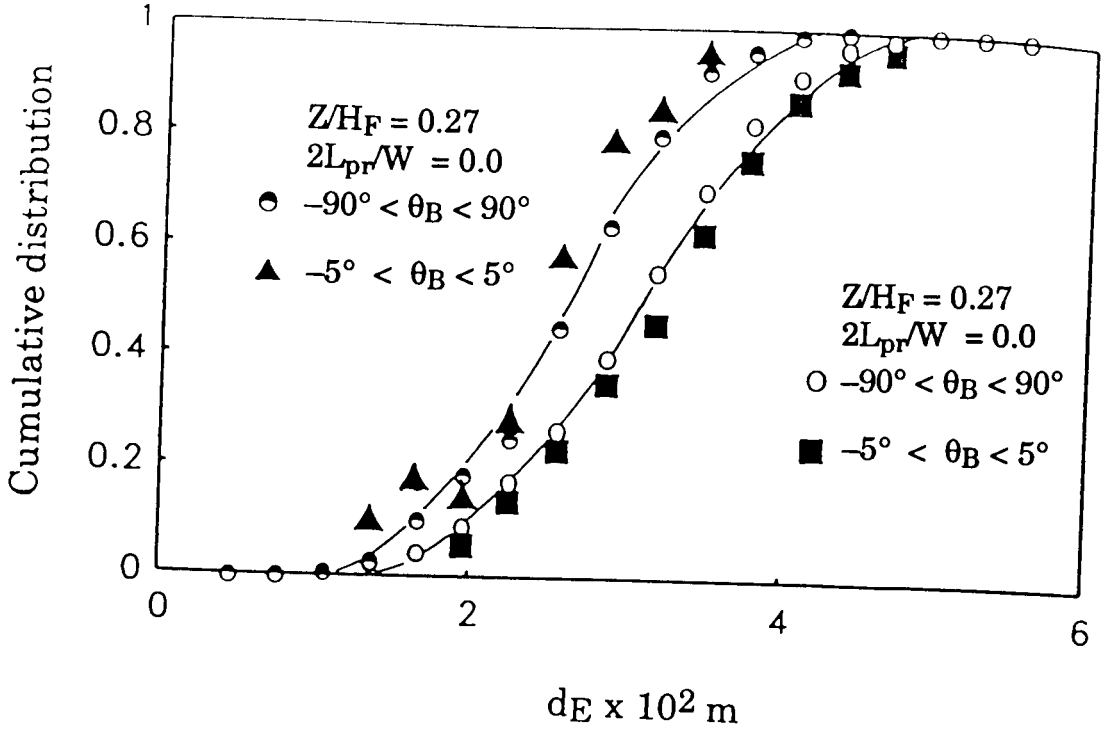

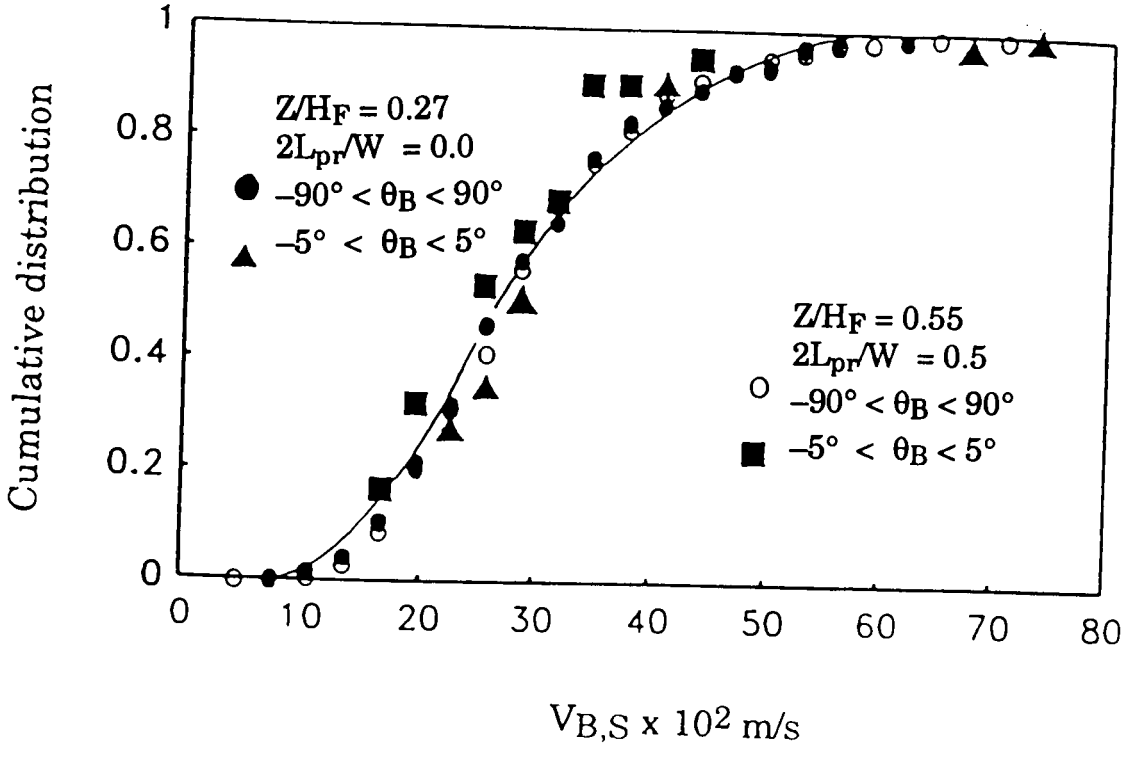

FIGURE 4.3.6: (c) Size and (d) velocity distribution for the entire population and those rising vertically at different heights (U_o/U_{mf} = 2.84)

4.3.6 Relationship Between Bubble Velocity and Size

The velocity of a single bubble, U_{Br}, rising in an incipient fluidized bed is related to its size, d_B, according to

$$U_{Br} = K_B\sqrt{g\,d_B} \tag{4.3.5}$$

The velocity for the bubbles rising in swarms, U_B, in a freely bubbling bed is most often calculated using (Davidson and Harrison, 1963)

$$U_B = U_O - U_{mf} + K_B\sqrt{g\,d_B} \tag{4.3.6}$$

The simultaneous measurement of bubble velocity and size enables us to assess the applicability of these expressions. Since submersible probes measure the vertical dimension of the bubble, the results are presented with d_B taken as d_V. It has been verified that similar results are obtained for other bubble size measures (d_B and d_H). In the first instance, the density functions for the rising velocity coefficient K_B were evaluated using equation (4.3.5) from the data for freely bubbling beds, **Figure 4.3.7a**. The range of the coefficients is seen to vary from 0.2 to 1.4 with a mean value of about 0.5. There is no appreciable difference in the coefficient distributions for bubbles measured at two different superficial velocity despite of a noticeable variation in the velocity distributions as shown in **Figure 4.3.4b**; similar plots were obtained for other operating conditions and probe locations. Separate experiments were also performed with bubbles injected continuously in incipient fluidized bed for comparison with results for freely bubbling beds. The density functions for the rising velocity coefficient for continuously injected bubbles - the data for two volumetric flow rates have also been plotted in **Figure 4.3.7a** - were seen to be in excellent agreement with freely bubbling bed results. Measurements were also performed, using frame-by-frame

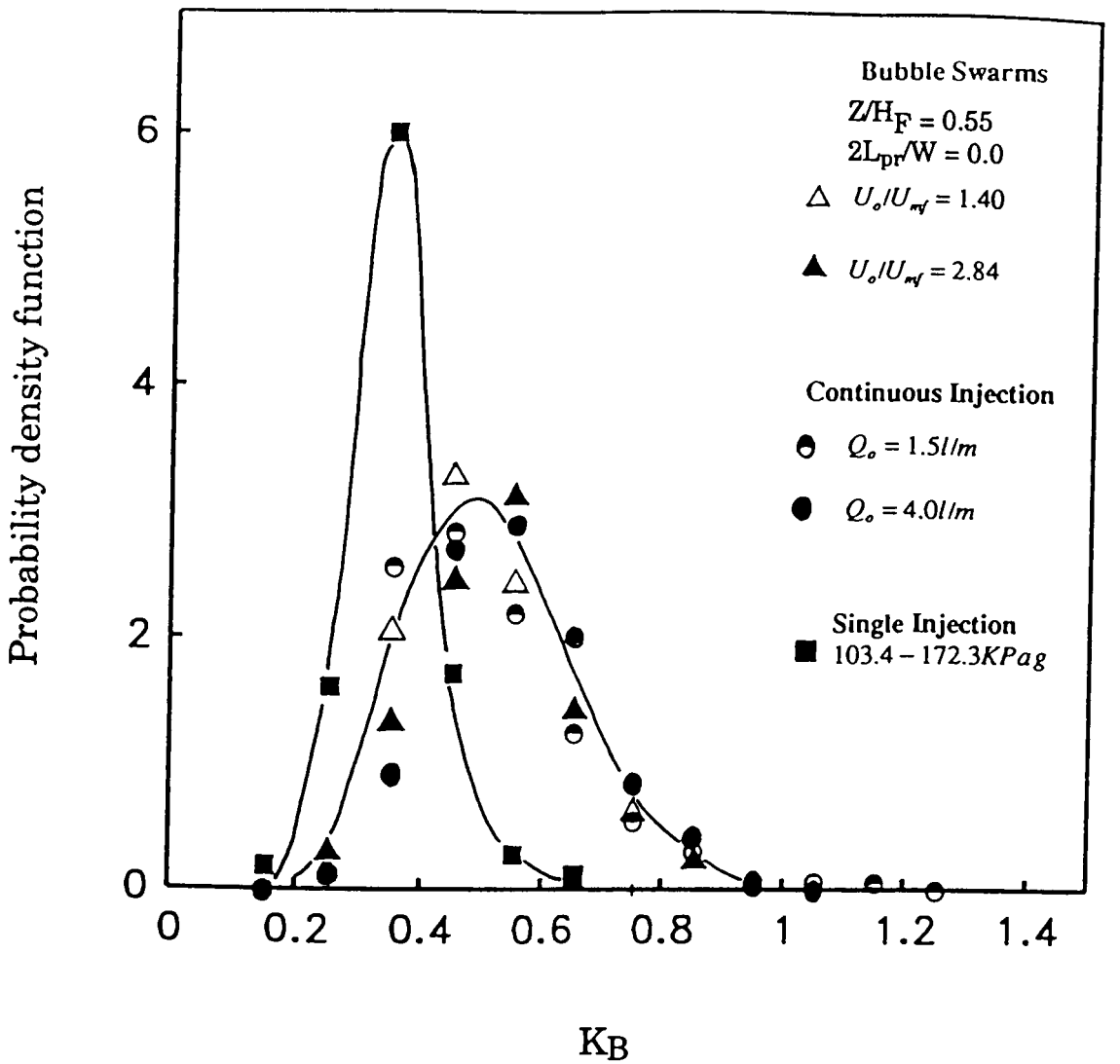

FIGURE 4.3.7a: Distribution of the coefficient of bubble rise velocity K_B (based on d_V) for bubble swarms and injected bubbles (continuous and single) calculated from the simple bubble velocity and size relationship, equation (4.3.5)

analysis of expriments recorded on video tape, on single bubbles injected in incipient fluidized beds to obtain data in the absence of bubble-bubble interactions. The density function for the rising velocity coefficient, also plotted in **Figure 4.3.7a**, is seen to have significantly lower mean and standard deviation. The variation in K_B values about the mean for the single bubble experiments is attributed to instantaneous jerky motion with periodical acceleration and shape change of the rising bubble. For bubble swarms in freely bubbling beds and for continuously injected bubbles in an incipient fluidized bed, this effect is compounded with the effects of interactions between bubbles leading to a broader density function and a higher mean K_B value.

The experimental data for freely bubbling beds were subsequently re-analysed to determine the density function for the rise velocity coefficient using equation (4.3.6); the results are compared with the single bubble data in **Figure 4.3.7b**. Though the standard deviation is still higher for the freely bubbling bed data, the mean value is in good agreement with that for the single bubble experiments. The inclusion of the $(U_O - U_{mf})$ term for freely bubbling beds does approximate bubble-bubble interaction effects in the calculation of the mean bubble velocity as concluded by Clift and Grace (1985) in a recent review.

4.3.7 Effect of Bubble Shape on Velocity

Hatano et al. (1986) concluded that the shape of the bubble - aspect ratio - has significant influence on the bubble velocity, and bubbles were classified into three different types, namely, spherical cap, elongated and slug. It was found that the rising velocity coefficient for the bubbles having larger aspect ratio had a higher value; for example, aspect ratio of 1.54 gave a rising velocity coefficient of 1.7.

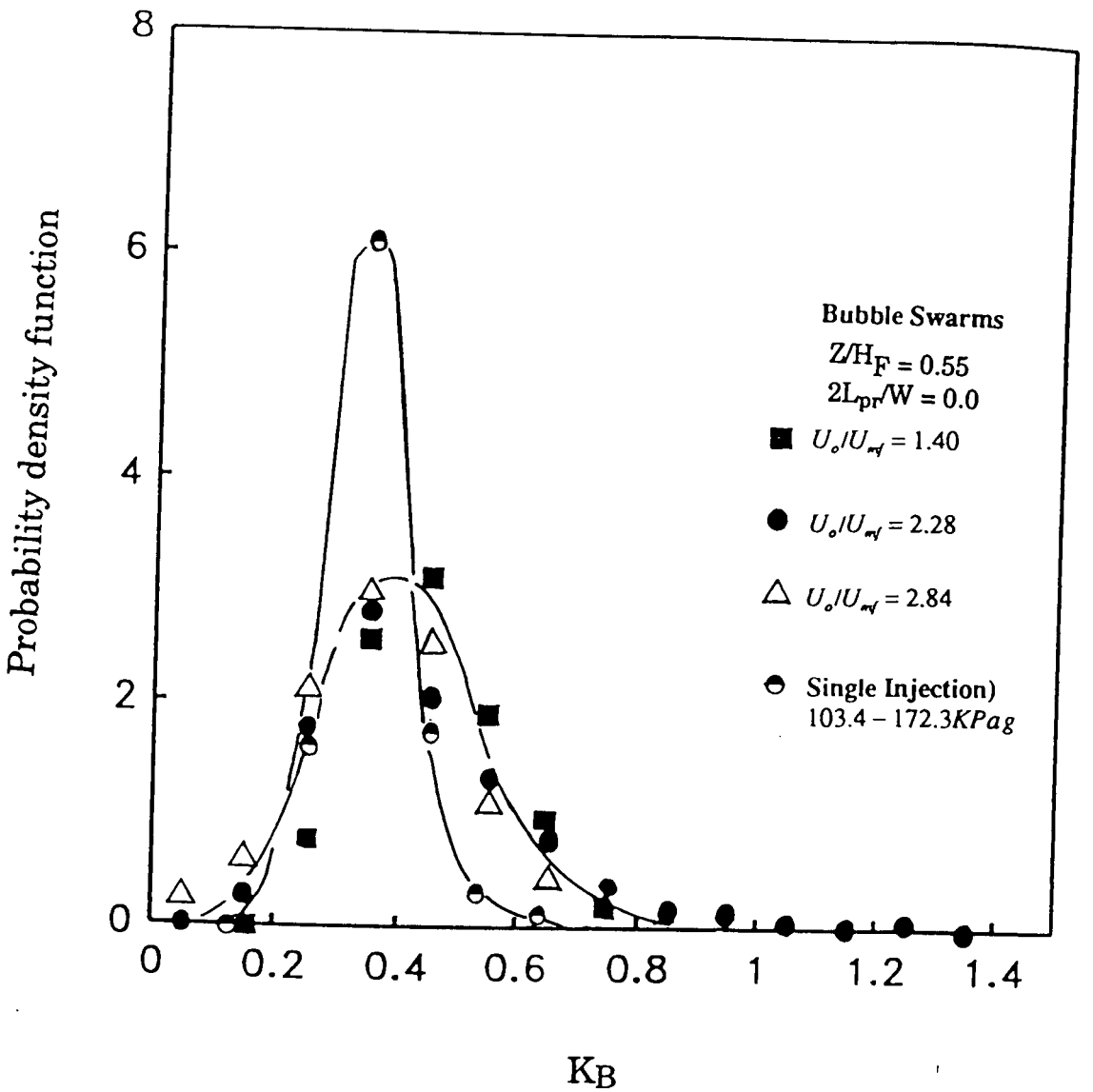

FIGURE 4.3.7b: Distribution of the coefficient of rise velocity K_B (based on d_V) for bubble swarms calculated from equation 4.3.6 with the inclusion of $(U_o - U_{mf})$ and compared with the K_B obtained for a single bubble injection experimental calculated from (4.3.5)

To examine the effect of aspect ratio on velocity, bubbles with $\alpha > 1$ were separated from the measured bubble populations. Typical cumulative velocity distributions, **Figure 4.3.8a**, show that bubbles having aspect ratios greater than 1 have a larger mean velocity. The corresponding scatter plot is shown in **Figure 4.3.8b**. For comparison, experimental data on single injected bubbles were analysed in a similar fashion - the results are also plotted in **Figure 4.3.8b**. The single bubble data indicate that the comparatively very few bubbles with $\alpha > 1$ have the same rising velocity coefficient as bubbles with $\alpha < 1$. These results suggest that in freely bubbling beds impending coalescence leads to higher aspect ratios as well as higher bubble velocities.

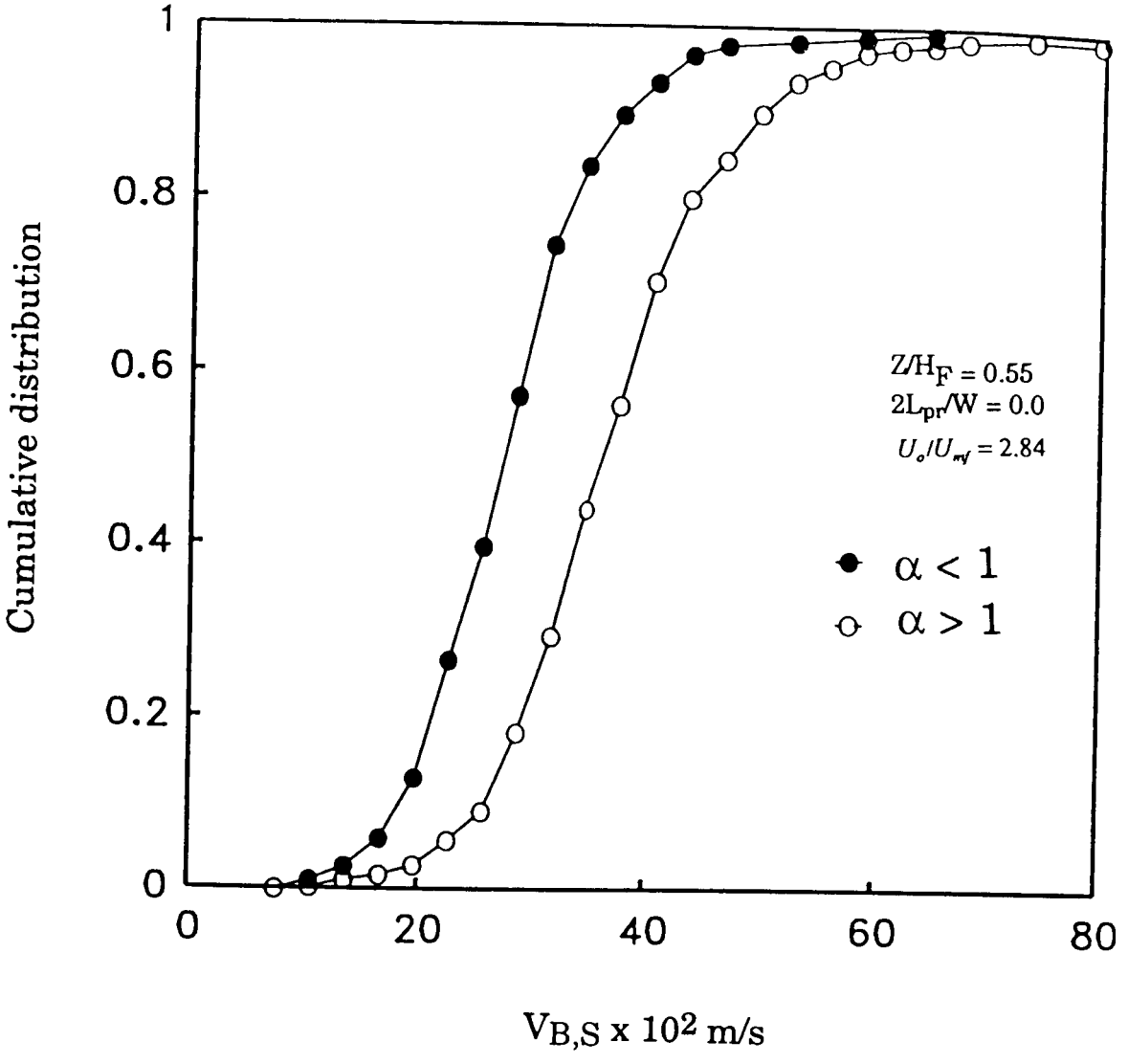

FIGURE 4.3.8a: Distribution of the coefficient of bubble velocity $V_{B,S}$ for bubbles having different aspect ratio

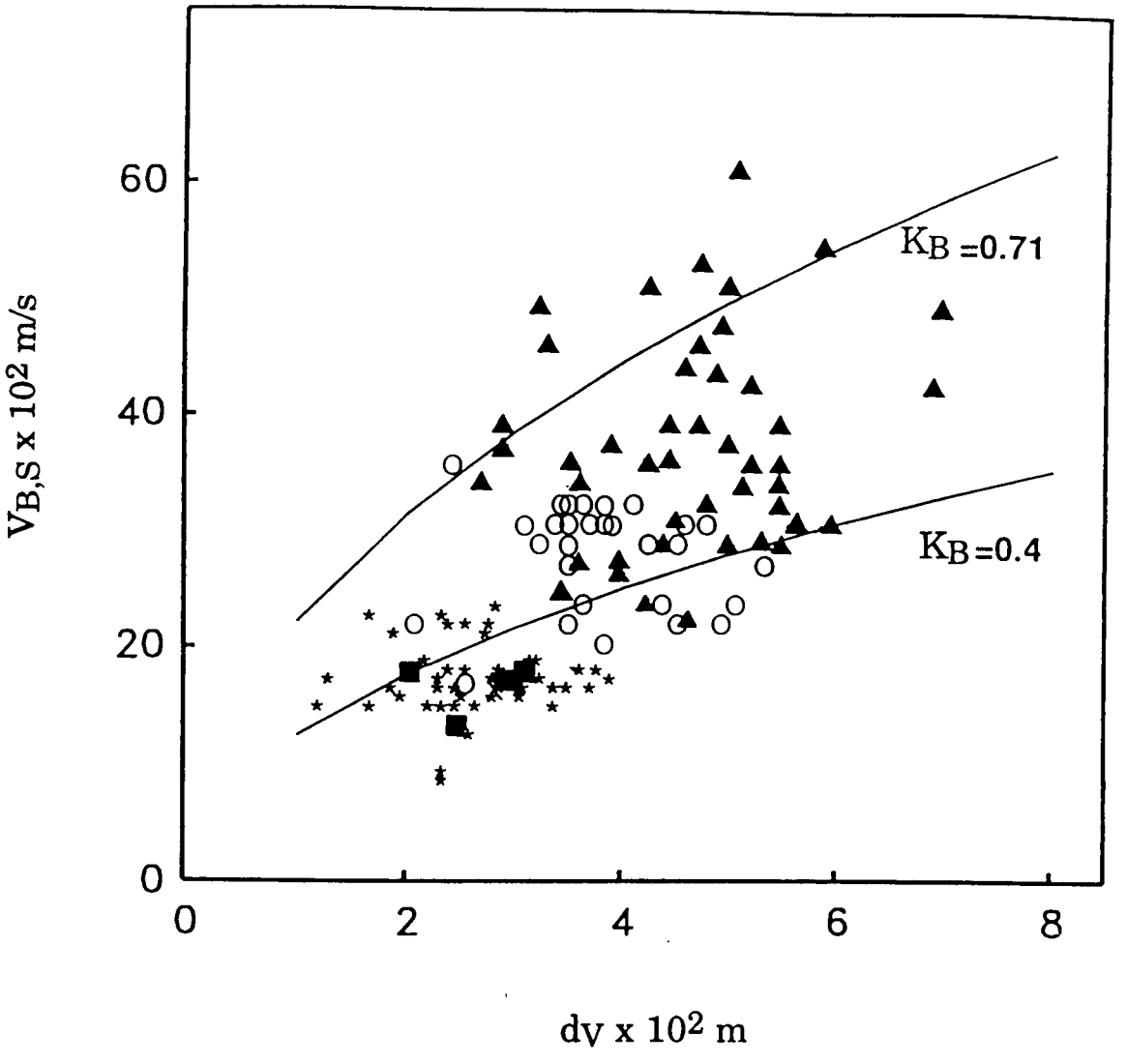

FIGURE 4.3.8b: Scatter plotvelocity $V_{B,S}$ vs size d_V for different aspect ratio α; bubble swarms: (o : $\alpha < 1$; ▲ : $\alpha > 1$) ; single injection (* : $\alpha < 1$; ■ : $\alpha > 1$)

4.3.8 Conclusions

The experimental results indicate that the angle of rise of bubbles deviates significantly from the vertical. Surprisingly, the density functions of the rise angle do not appear to depend strongly on the position in the bed and superficial gas velocity for the range of conditions considered. Since the existing signal analysis procedures for two-element submersible probes are based on vertical bubble rise, these results indicate that available results from such probes can not be considered as quantitative. Multiple-element probes detect and reject non-vertically rising bubbles. Analysis of the data establishes that such rejection does not bias the measurements of bubble characteristics and consequently such probes should be preferred.

Bubble size/shape have also been measured simultaneously using the global thresholding technique described in **section 3.2.1**. These measurements enable assessment of the relationship between bubble size/shape and velocity. For comparison with results for freely bubbling beds, separate experiments have been performed with bubbles (single as well as chains) injected in incipiently fluidized beds. The results indicate that the density functions for the rising velocity coefficient from freely bubbling beds are virtually identical for different locations in the bed and operating conditions considered in this investigation. These density functions are also in very good agreement with those from continuously injected bubbles in incipient beds. The single injected bubbles have lower mean and standard deviation. The inclusion of the excess gas velocity term in the equation for bubble velocity leads to good agreement between the mean of the rising velocity coefficient density function for bubbles injected singly and in freely bubbling beds; the standard deviation for freely bubbling beds, however, remains higher.

Chapter 5

RESULTS and DISCUSSION:

SOLIDS MIXING and SEGREGATION

5.1 MIXING OF UNIFORM SOLIDS

It is well recognized that the mixing of solids in gas fluidized beds is induced by the motion of bubbles: solids, in the form of bubble wakes, are carried up by bubbles, and the dense phase solids are simultaneously displaced downwards elsewhere. Periodic disposal and replenishment of wake fragments as the bubble rises through the bed also occurs. Various mathematical models have been proposed in the literature. Assessment and refinement of the more detailed models is hampered by the scarcity of experimental data on the simultaneous characterization of bubble flow and solids mixing. In this section, the experimental results obtained using the techniques described in **section 3.2.4** have been used to assess the three-phase countercurrent backmixing model.

5.1.1 Theory

Model equations : The three-phase counter-current back-mixing model assumes that the movement of gas and solids in the fluidized bed can be described in terms of three separate phases :

- an upward moving gas phase which is free of particles;
- a phase consisting of upward moving gas and particles (bubble wake and cloud regions); and
- a phase of downward moving particles and interstitial gas (the gas may be moving up or down depending on velocities of particles and the local slip velocities). This phase is also referred to as the dense or emulsion phase in the following.

Consider a material balance on the tracer in the upward moving wake (and drift) phase, **Figure 5.1.1a.** This phase occupies $f_W\varepsilon_B$ fraction of the total bed cross-sectional area and moves up at a velocity equal to the bubble velocity U_B carrying up C_W fraction of the tracer material. From the material balance, the concentration of the tracer in the upward moving phase, C_W, at time t and at a given height, Z, above the distributor, can be expressed as:

$$f_W\varepsilon_B\frac{\partial C_W}{\partial t} = -\frac{\partial(f_W\varepsilon_B U_B C_W)}{\partial Z} - k_W f_W\varepsilon_B(C_W - C_E) \qquad (5.1.1)$$

where f_W is the wake fraction, ε_B is the bubble fraction and k_W is the wake exchange coefficient.

A similar analysis, considering **Figure 5.1.1b**, for tracer concentration, C_E, in the phase of downward moving particles leads to

$$(1-\varepsilon_B - f_W\varepsilon_B)\frac{\partial C_E}{\partial t} = \frac{\partial((1-\varepsilon_B - f_W\varepsilon_B)U_S C_E)}{\partial Z} + k_E(1-\varepsilon_B - f_W\varepsilon_B)(C_W - C_E) \qquad (5.1.2)$$

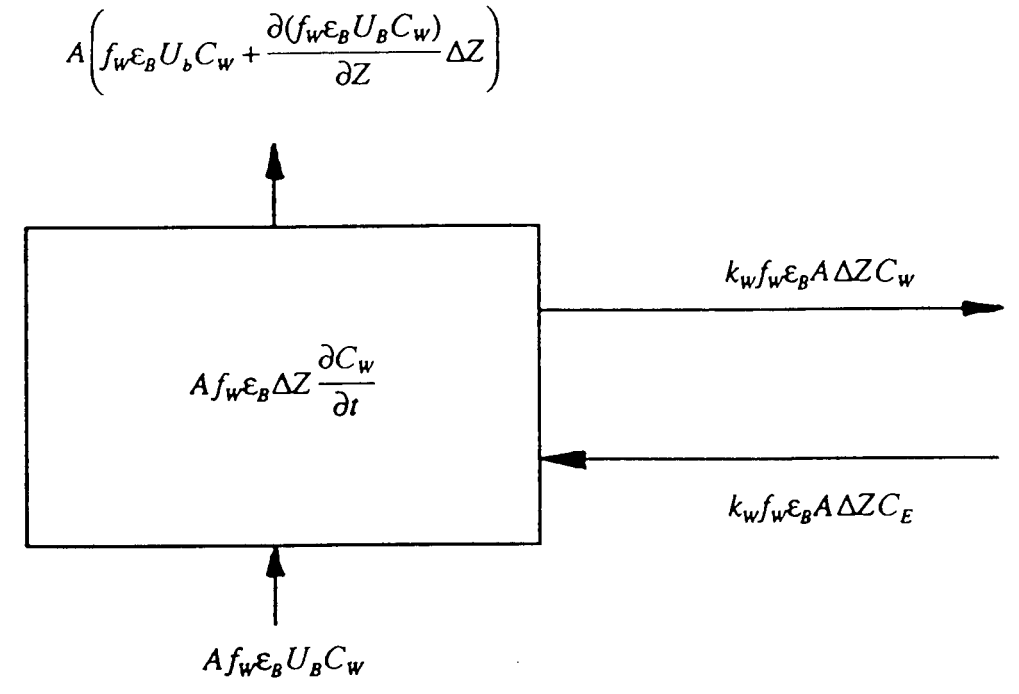

a

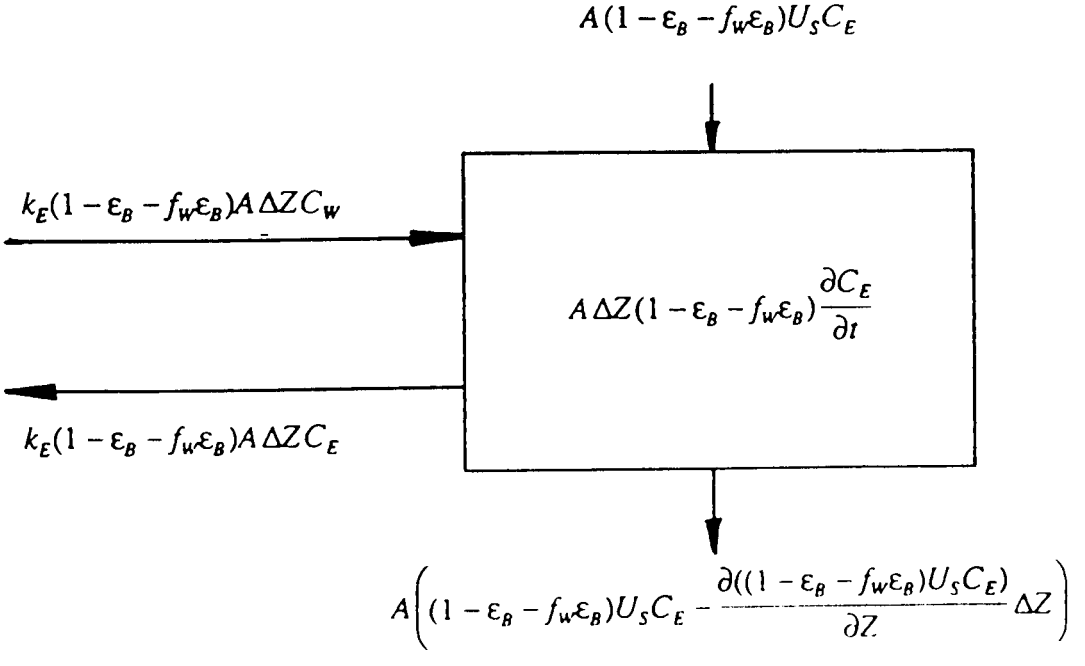

b

FIGURE 5.1.1: Material balance on the tracer in (a) the upward moving wake (and drift) phase; (b) in the downward moving dense phase.

where U_S is the velocity of the dense phase and k_E is the exchange coefficient which is related to k_W according to

$$k_E = \frac{k_W f_W \varepsilon_B}{1 - \varepsilon_B - f_W \varepsilon_B}$$

Equation (5.1.1) may be rewritten as

$$f_W \varepsilon_B \frac{\partial C_W}{\partial t} = -\left(\frac{\partial f_W}{\partial Z} \varepsilon_B U_B C_W + f_W \frac{\partial \varepsilon_B}{\partial Z} U_B C_W + f_W \varepsilon_B \frac{\partial U_B}{\partial Z} C_W + f_W \varepsilon_B U_B \frac{\partial C_W}{\partial Z} \right) - k_W f_W \varepsilon_B (C_W - C_E) \tag{5.1.3}$$

If bubble properties are assumed to be independent of height within the bed - through use of height-averaged parameters or otherwise - then equation (5.1.3) reduces to

$$\overline{f_W \varepsilon_B} \frac{\partial C_W}{\partial t} = -\overline{f_W \varepsilon_B U_B} \frac{\partial C_W}{\partial Z} - \overline{k_W f_W \varepsilon_B} (C_W - C_E) \tag{5.1.4}$$

Under a similar assumption, equation (5.1.2) reduces to

$$\overline{(1 - \varepsilon_B - f_W \varepsilon_B)} \frac{\partial C_E}{\partial t} = \overline{(1 - \varepsilon_B - f_W \varepsilon_B) U_S} \frac{\partial C_E}{\partial Z} + \overline{k_E (1 - \varepsilon_B - f_W \varepsilon_B)} (C_W - C_E) \tag{5.1.5}$$

Equations (5.1.4) and (5.1.5) have been employed in previous investigations using the three-phase counter-current back-mixing model. The experimental results obtained permit assessment of a less restrictive assumption according to which the bubble properties vary, but only slowly, with height above the distributor. According to this assumption, the material balance for the upward moving phase can be written, from equation (5.1.3), as

$$f_W \varepsilon_B \frac{\partial C_W}{\partial t} = -f_W \varepsilon_B U_B \frac{\partial C_W}{\partial Z} - k_W f_W \varepsilon_B (C_W - C_E) \tag{5.1.6}$$

Similarly, for the downward moving phase

$$(1-\varepsilon_B-f_W\varepsilon_B)\frac{\partial C_E}{\partial t}=(1-\varepsilon_B-f_W\varepsilon_B)U_S\frac{\partial C_E}{\partial Z}+k_E(1-\varepsilon_B-f_W\varepsilon_B)(C_W-C_E) \quad (5.1.7)$$

Equations (5.1.6) and (5.1.7) employ local height dependent bubble properties instead of constant or height averaged values used in equations (5.1.4) and (5.1.5). The total axial tracer concentration, $C(Z,t)$, at a given height above the distributor was evaluated from the model using the following expression

$$C(Z,t)=\frac{f_W\varepsilon_B C_W+(1-\varepsilon_B-f_W\varepsilon_B)C_E}{1-\varepsilon_B} \quad (5.1.8)$$

Numerical implementation : These equations were solved numerically following the scheme of Sitnai (1981). For the upward moving phase,

$$f_{W,i}\varepsilon_{B,i}\frac{dC_{W,i}}{dt}\cong-\left(f_{W,i}\varepsilon_{B,i}U_{B,i}\frac{C_{W,i}-C_{W,i-1}}{\Delta Z}\right)-k_{W,i}f_{W,i}\varepsilon_{B,i}(C_{W,i}-C_{E,i}) \quad (5.1.9)$$

for cells $i=2$ *to* M. Since there is no material leaving the system, all the material in the downward moving stream is recirculated into the upward moving phase. The discretized equation for the bottom cell, $i=1$, is consequently derived as

$$f_{W,1}\varepsilon_{B,1}\frac{dC_{W,1}}{dt}\cong-\left(f_{W,1}\varepsilon_{B,1}U_{B,1}\frac{C_{W,1}-C_{E,1}}{\Delta Z}\right)-k_{W,1}f_{W,1}\varepsilon_{B,1}(C_{W,1}-C_{E,1}) \quad (5.1.10)$$

For the downward moving phase, the discretized form for cell $i=1$ *to* $(M-1)$ is

$$(1-\varepsilon_{B,i}-f_{W,i}\varepsilon_{B,i})\frac{dC_{E,i}}{dt}\cong f_{W,i}\varepsilon_{B,i}U_{B,i}\frac{C_{E,i+1}-C_{E,i}}{\Delta Z}+k_{W,i}f_{W,i}\varepsilon_{B,i}(C_{W,i}-C_{E,i}) \quad (5.1.11)$$

and the difference equation for the top cell, $i=M$, is

$$(1-\varepsilon_{B,M}-f_{W,M}\varepsilon_{B,M})\frac{dC_{E,M}}{dt}\cong f_{W,M}\varepsilon_{B,M}U_{B,M}\frac{C_{W,M}-C_{E,M}}{\Delta Z}+k_{W,M}f_{W,M}\varepsilon_{B,M}(C_{W,M}-C_{E,M}) \quad (5.1.12)$$

5.1.2 Model Parameters

Before calculations can be carried out using the model, it is necessary to specify several parameters: the bubble phase parameters - d_B, U_B, and ε_B; the downward velocity of the dense phase, U_S; the wake fraction, f_W, and the wake exchange coefficient, k_W. In this investigation, as described in the following, the bubble phase parameters were established through independent measurements for the two-dimensional fluidized bed under consideration.

Bubble size : To model growth of circular bubbles in the two-dimensional fluidized bed, an approach parallel to that developed by Darton et al. (1977) for spherical bubbles in three-dimensional beds was adopted. Thus, the height dependent bubble size, d_B, was expressed as

$$d_B = \left(\frac{8(U_O - U_{mf})(2^{3/4} - 1)}{\pi \lambda_B g^{1/2}} Z + d_0^{3/2} \right)^{2/3} \qquad (5.1.13a)$$

where the initial bubble diameter, d_0, is given by

$$d_0 = \{8(U_O - U_{mf}) A_{C0} / \pi \lambda_B g^{1/2}\}^{2/3} \qquad (5.1.13b)$$

A_{C0} is the initial bubble catchment area (5.6 x 10^{-5} m^2 for a porous distributor). From experimental measurements on bubble size and velocity, the proportionality constant λ_B which describes the distance a bubble travels in a stream before coalescing with the adjacent stream to form a single new stream of larger bubbles, was found to be ~ 2. Comparison of the predicted bubble sizes with the experimental data for the local as well as level average bubble size using the above equation is shown in **Figure 5.1.2.**

Bubble velocity : Following Davidson and Harrison (1963), the bubble velocity was expressed as

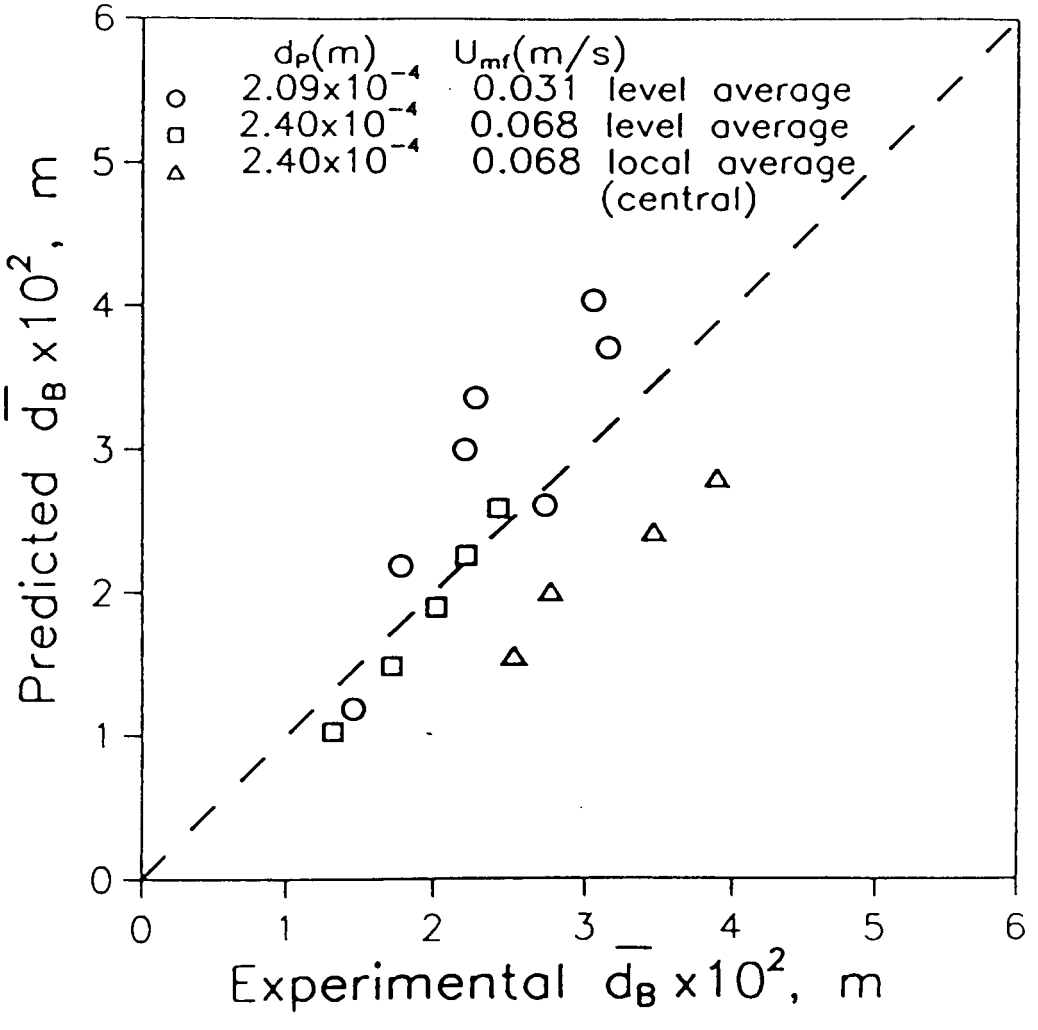

FIGURE 5.1.2: Comparison of experimentally measured bubble size with prediction using equation (5.1.13).

$$U_B = U_O - U_{mf} + K\sqrt{g\,d_B} \tag{5.1.14}$$

From results described in **Section 4.3,** $K_B = 0.4$ for the two-dimensional bed used in this investigation.

Bubble fraction : Clift and Grace (1985) have reviewed the several reasons why the measured visible gas flow deviates from the prediction of the simple two-phase theory. The major causes are: (a) an increase in interstitial gas flow in the dense phase (Khattab et al., 1988); and (b) high gas through-flow (Valenzuela and Glicksman, 1985) due to bubble shape, concentration and interaction. The particles used in this investigation fall in the Geldart B category; for such particles, the gas flow in the dense phase is expected to be close to that required for minimum fluidization (Valenzuela and Glicksman, 1985). Consequently, a gas balance considering the presence of the bubble, wake and dense phases (to be consistent with the three-phase model of the fluidized bed) and accounting for the through-flow in the bubbles was written as:

$$\varepsilon_B = \frac{U_O - U_{mf}}{U_B - (1 + f_W - K_T)U_{mf}} \tag{5.1.15}$$

where K_T is the through-flow factor. Time averages of the experimentally measured bubble fraction at different heights within the bed were used to estimate the bubble through-flow factor using the above equation, **Figure 5.1.3a**. The probability density function of the experimentally estimated factor, $(1 + f_W - K_T)$, at various bed heights for a range of fluidization gas velocities using the three particle size fractions, was plotted as shown in **Figure 5.1.3b**. The average through-flow factor, K_T, was estimated as 3.52. A wide variation was found for the smallest particle size, that is, $d_P = 2.40 \times 10^{-4}$ m. This average value of K_T is higher than the theoretical prediction of 2 for an isolated circular bubble (Davidson

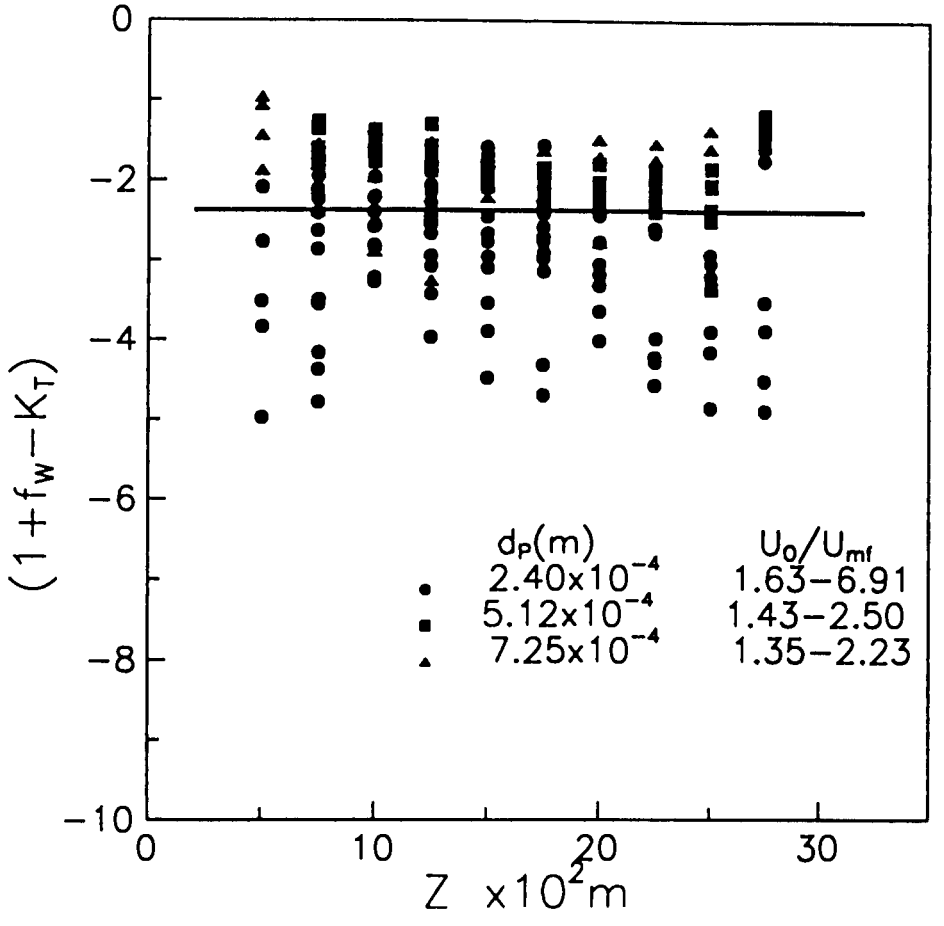

FIGURE 5.1.3a: Time averages of the experimentally measured bubble throughflow factor as a function of bed height.

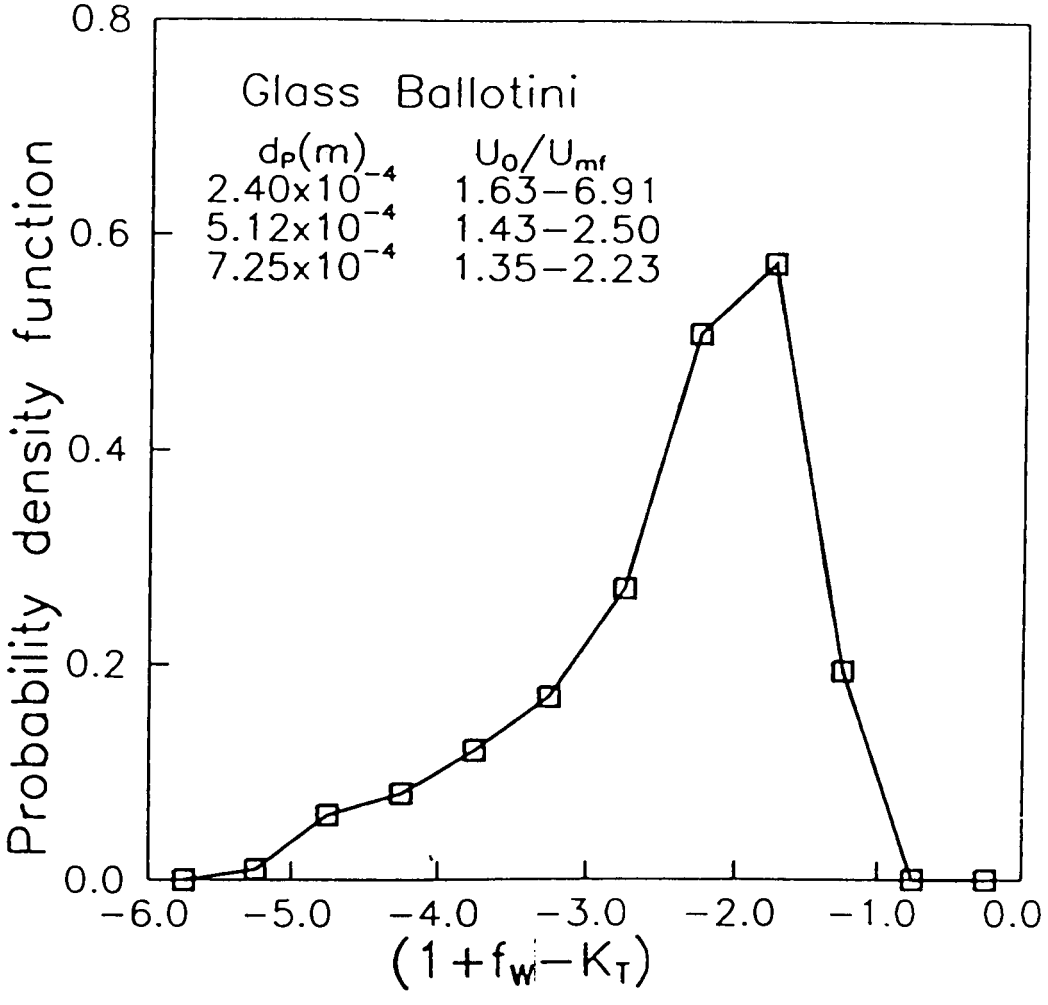

FIGURE 5.1.3b: Probability density function of $(1 + f_W - K_T)$ inferred from experimentally measured time-averaged bubble fraction at different heights, superficial velocities and particles sizes.

and Harrison, 1963) rising in an incipient fluidized bed. The result is, then, in agreement with Clift and Grace (1985) who suggested that the bubble through-flow will be higher for a freely bubbling bed compared with that for a single bubble. However, recent experimental measurements (Hilligardt and Werther, 1986) of the ratio of the through-flow velocity to the velocity of the gas in the dense phase in a freely bubbling bed were close to that predicted by the isolated bubble theory. Consequently, an independent estimate for the height averaged bubble fraction was made by measuring the bed expansion. These values of $\varepsilon_{B,Expt} = (H_E - H_F)/H_E$ calculated from the bed expansion data compare reasonably well with those obtained from height averaging of equation (5.1.15) $\overline{\varepsilon_B}$ based on image analysis results, **Table 5.1.**

Dense Phase Velocity : For a batch fluidized bed, the velocity of the phase with downward moving particles may be written as

$$U_S = \frac{f_W \varepsilon_B U_B}{1 - \varepsilon_B - f_W \varepsilon_B} \tag{5.1.16}$$

Exchange Coefficient : Models for exchange of solids between the phases of the fluidized bed, resulting in expressions for the wake exchange coefficient of the solids, have been proposed by Yoshida and Kunii (1968) and Chiba and Kobayashi (1977). The interchange of solids between these phases is assumed to result from the flow of solids into and out of the wake with the solids moving down in the thin cloud region leaving the wake at the same rate they enter. The model proposed by Yoshida and Kunii was adapted, considering a two-dimensional bubble, to obtain:

$$k_{WY} = \frac{4U_{mf}(1 - \varepsilon_{mf})}{\pi \varepsilon_{mf} f_W (1 - \varepsilon_B) d_B} = \frac{A_{WY}}{d_B} \tag{5.1.17}$$

It should be noted that equation (5.1.17) is derived for fast bubbles. Chiba and Kobayashi (1977) derived an expression for the exchange assuming that fluidized particles flow around a two-dimensional bubble as would an inviscid fluid. Considering the solids within the cloud region, they obtained

$$k_{WC} = \frac{4U_{mf}}{\pi\varepsilon_{mf}d_B} = \frac{A_{WC}}{d_B} \tag{5.1.18}$$

It should be noted that the exchange coefficients derived from both approaches vary directly with U_{mf} and inversely with bubble size.

Theoretical responses for the axial tracer concentration, $C(Z,t)$, were obtained using local height-dependent model parameters. The theoretical predictions were compared with experimental data obtained using bed particles of size d_P = 7.25 x 10^{-4} m (U_{mf} = 0.35 ms^{-1}) fluidized at U_O/U_{mf} = 1.75. The tracer (20 %, that is, x = 0.2) was initially located near the top of the bed (q = 0.8). The wake fraction, f_W, of 0.2 was estimated to give the best fit for the tracer arrival or breakthrough time (at different heights at which the simultaneous measurements were made) and, hence, the solids circulation rate. The values for the exchange coefficients were calculated from equations (5.1.17) and (5.1.18) as A_{WY} = 5.22 ms^{-1} and A_{WC} = 1.114 ms^{-1} respectively. The results of the simulation are shown in **Figure 5.1.4a** and **b** at two heights above the distributor. The predicted concentration responses using these exchange coefficients do not agree with the experimental data which show the presence of an oscillation at the higher height within the bed, **Figure 5.1.4b**. The calculated exchange coefficients are clearly too large. Separate simulations were carried out assuming that the bubble size was constant - the height-averaged bubble diameters were used in these calculations. Comparison with experimental data showed that the exchange coefficients were under-predicted close to the distributor and overpredicted near the top

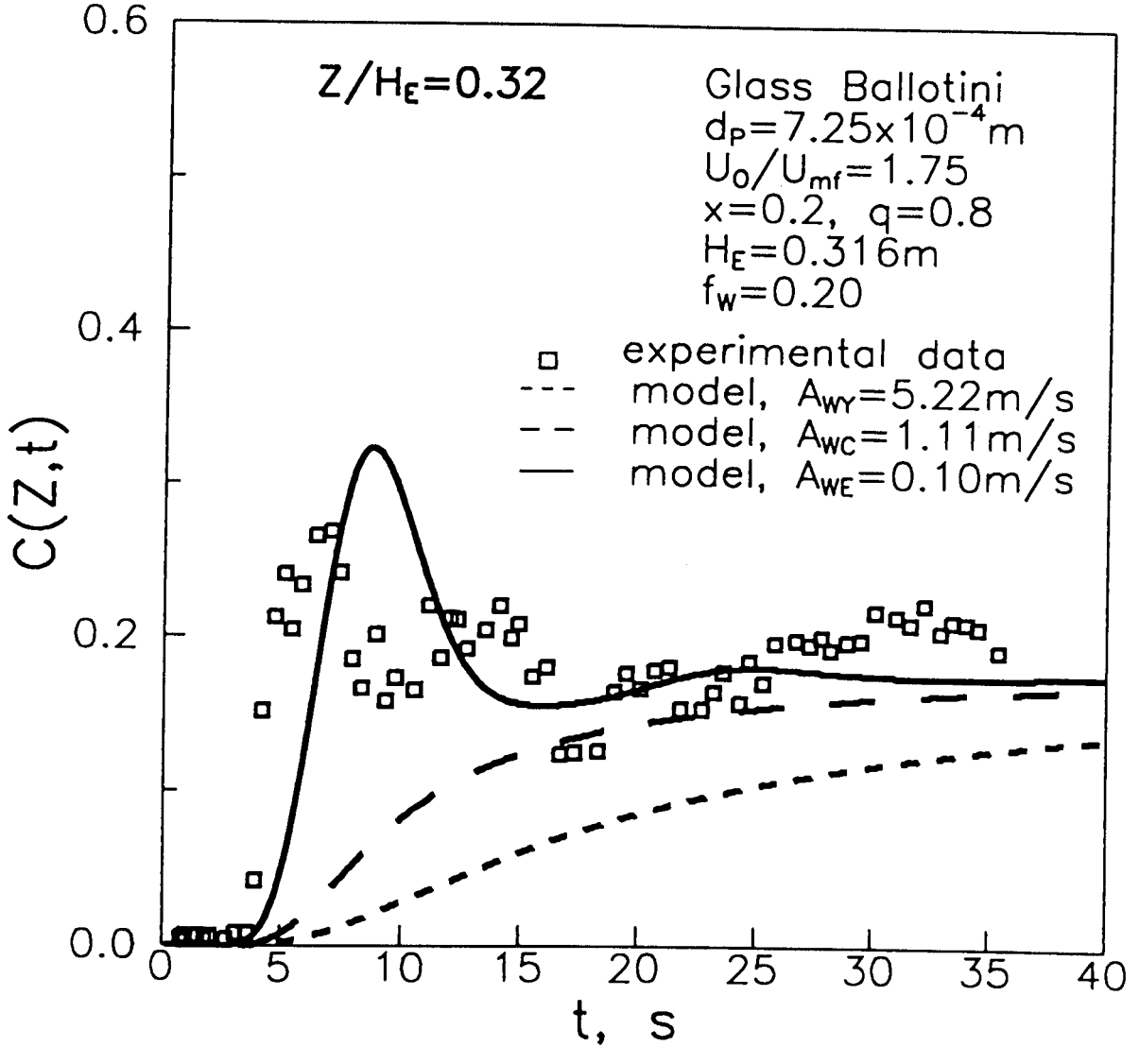

FIGURE 5.1.4a: Predictions of axial concentration response of solids tracer using values of exchange coefficient calculated by various solids exchange models and comparison with the experimental data.

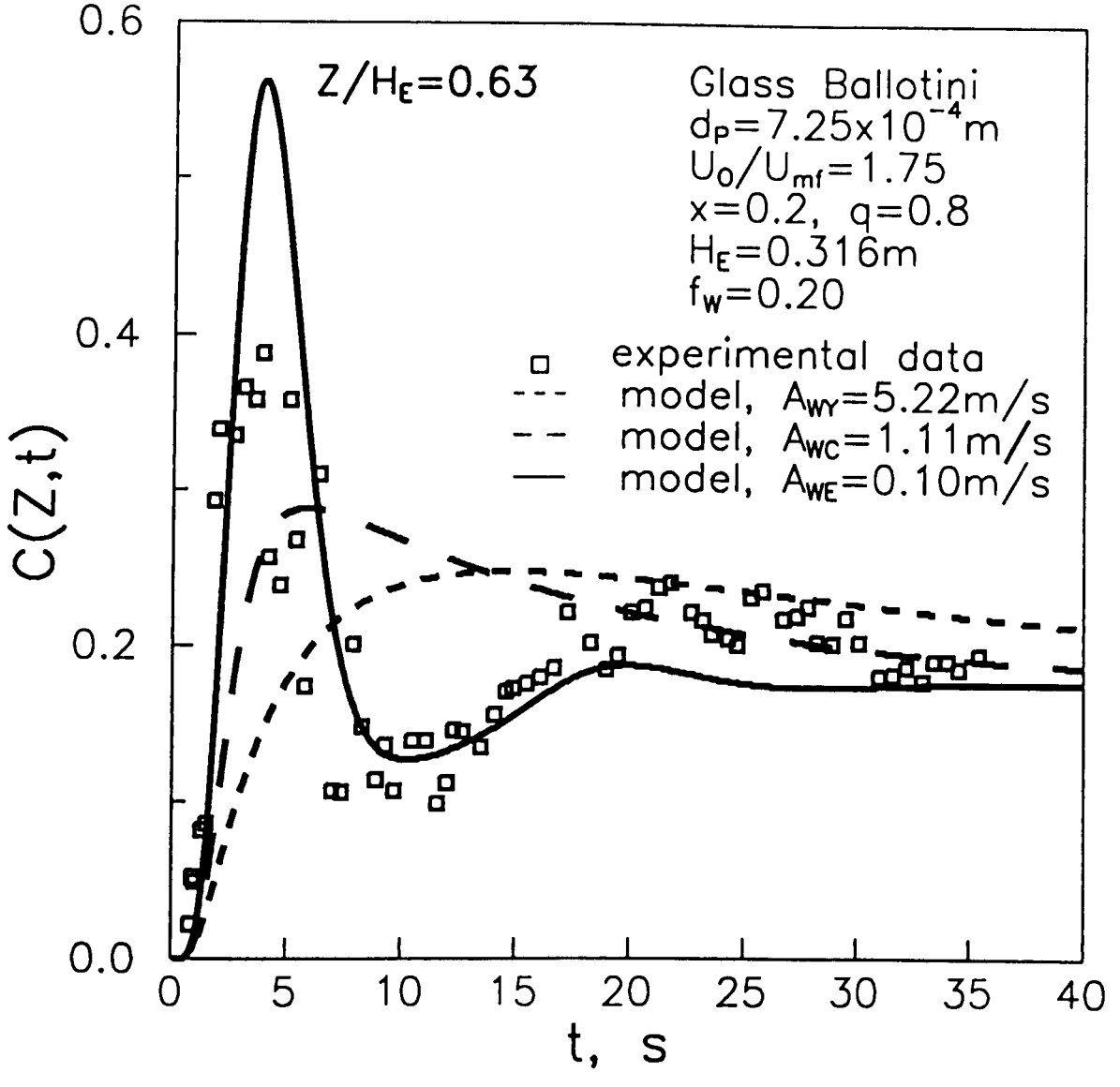

FIGURE 5.1.4b: Predictions of axial concentration response of solids tracer using values of exchange coefficient calculated by various solids exchange models and comparison with the experimental data.

of the bed. These observations, possible only because the experimental technique permits simultaneous data collection at different heights, indicated that the exchange coefficient should have an inverse bubble size dependence. Consequently, in the absence of a more detailed model, the exchange coefficients were written, in keeping with the bubble size dependence in equations (5.1.17) and (5.1.18), as

$$k_{WE} = \frac{A_{WE}}{d_B} \tag{5.1.19}$$

where A_{WE}, assumed to be a constant, was determined from the experimental data. It was found that A_{WE} = 0.1 ms^{-1} predicted the oscillation and recycle peaks as shown in **Figure 5.1.4a** and **b**. Evidently, the models of Yoshida and Kunii and that of Chiba and Kobayashi over-predict the exchange coefficient by an order of magnitude. Consequently, for further comparison of model predictions with experimental data, equation (5.1.19) was used to estimate the wake exchange coefficient by treating A_{WE} as an adjustable parameter to be estimated from the oscillation and recycle peaks in the solids mixing data.

5.1.3 Results of Model Comparison with Experimental Data

Using the approach described above - that is, equations (5.1.13) to (5.1.16) for hydrodynamic parameters and with wake fraction estimated from the tracer arrival time - A_{WE} was determined for the range of experimental conditions investigated.

The data obtained for d_P = 2.4 x 10^{-4} m for three different superficial gas velocities U_O/U_{mf} = 1.91, 2.21, 2.5 and 4.63 are plotted, respectively, in **Figures 5.1.5a-d**. For these runs, the amount of the tracer was 20 % of the bed material and the tracer was located initially near the top of the bed. In each of these figures,

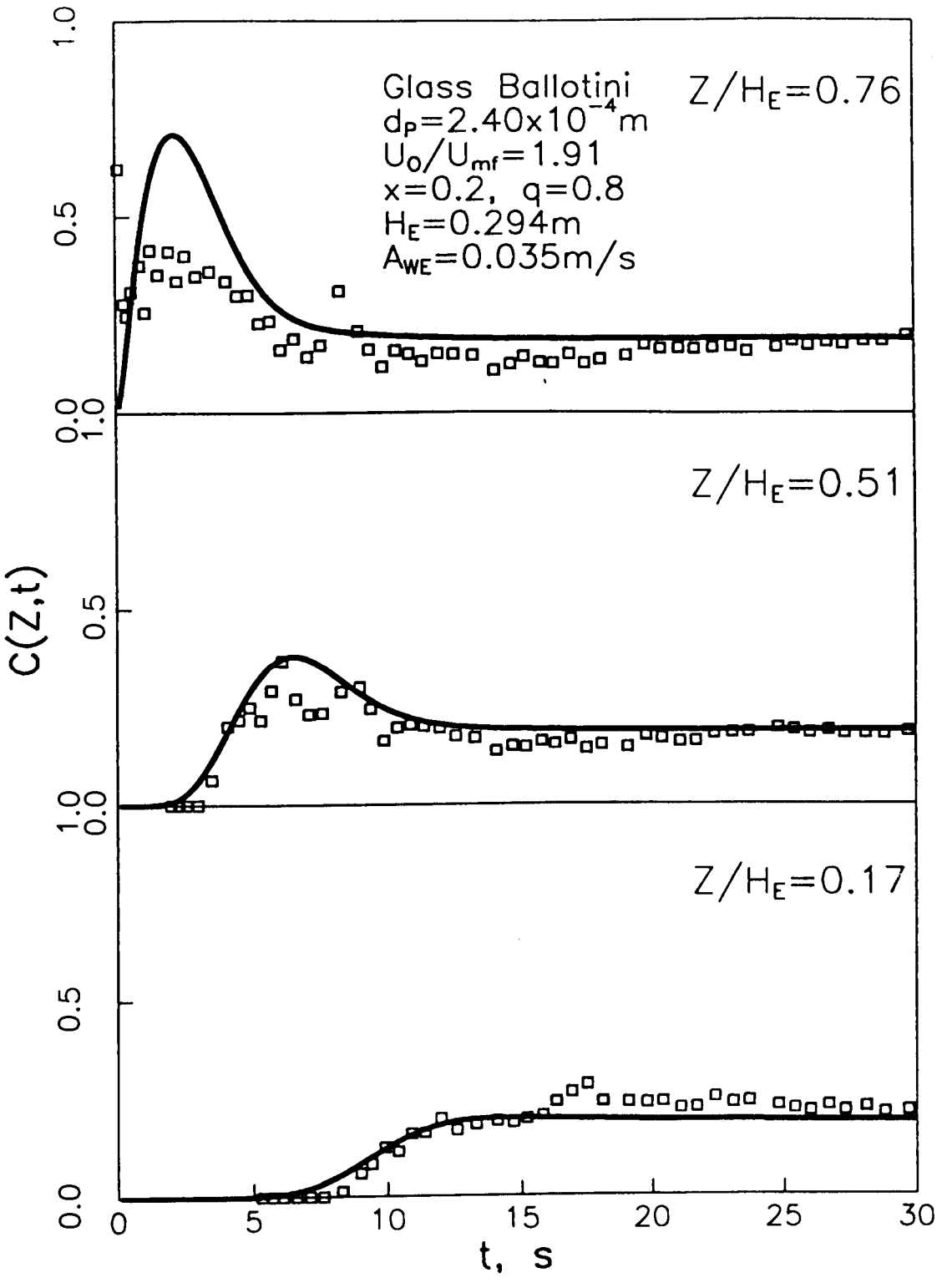

FIGURE 5.1.5a Comparison of model predictions with experimental data for $d_p = 2.40 \times 10^{-4}$ m and $U_o/U_{mf} = 1.91$.

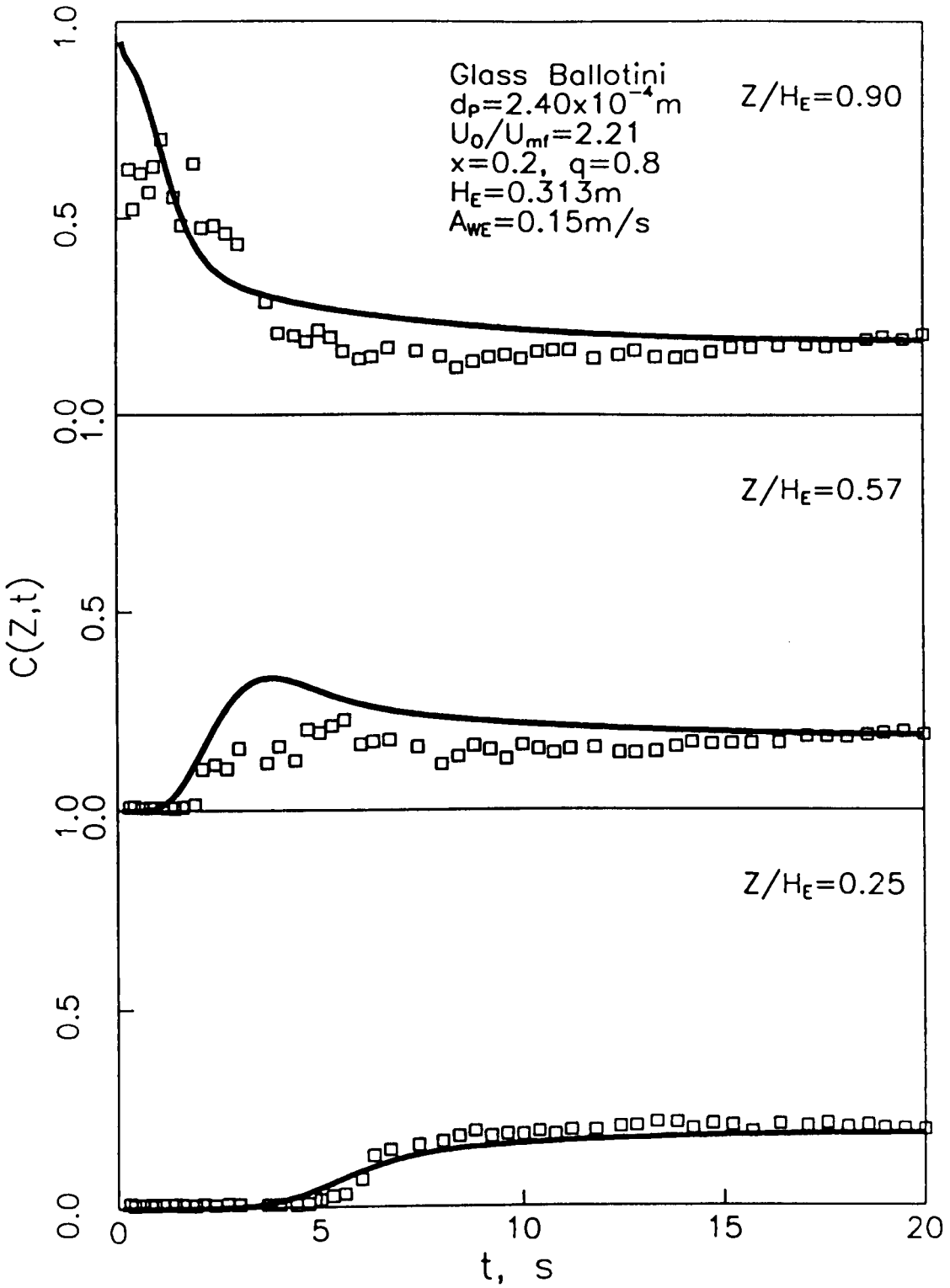

FIGURE 5.1.5b Comparison of model predictions with experimental data for $d_p = 2.40 \times 10^{-4}$ m and $U_o/U_{mf} = 2.21$.

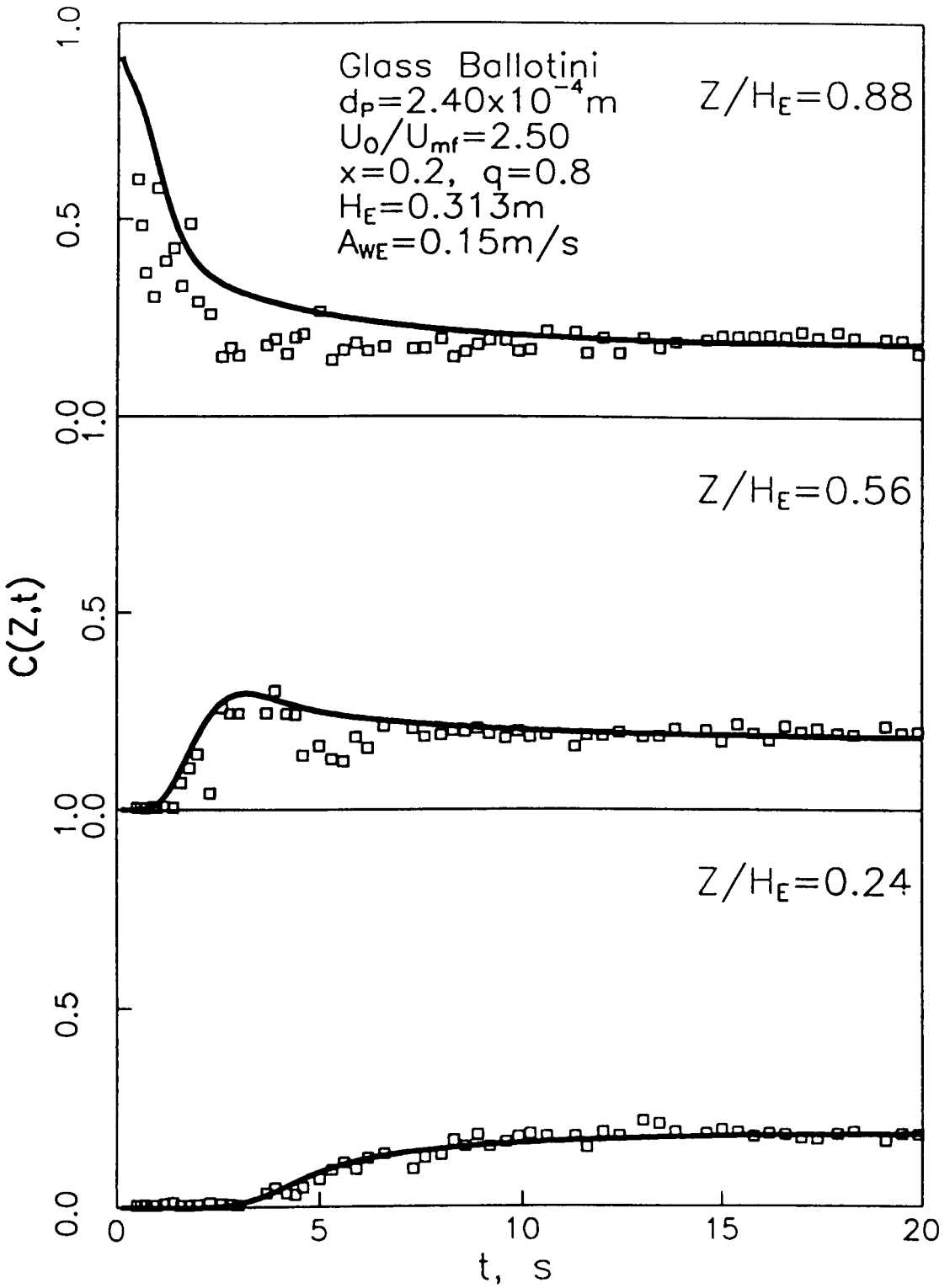

FIGURE 5.1.5c Comparison of model predictions with experimental data for $d_p = 2.40 \times 10^{-4}$ m and $U_o/U_{mf} = 2.50$.

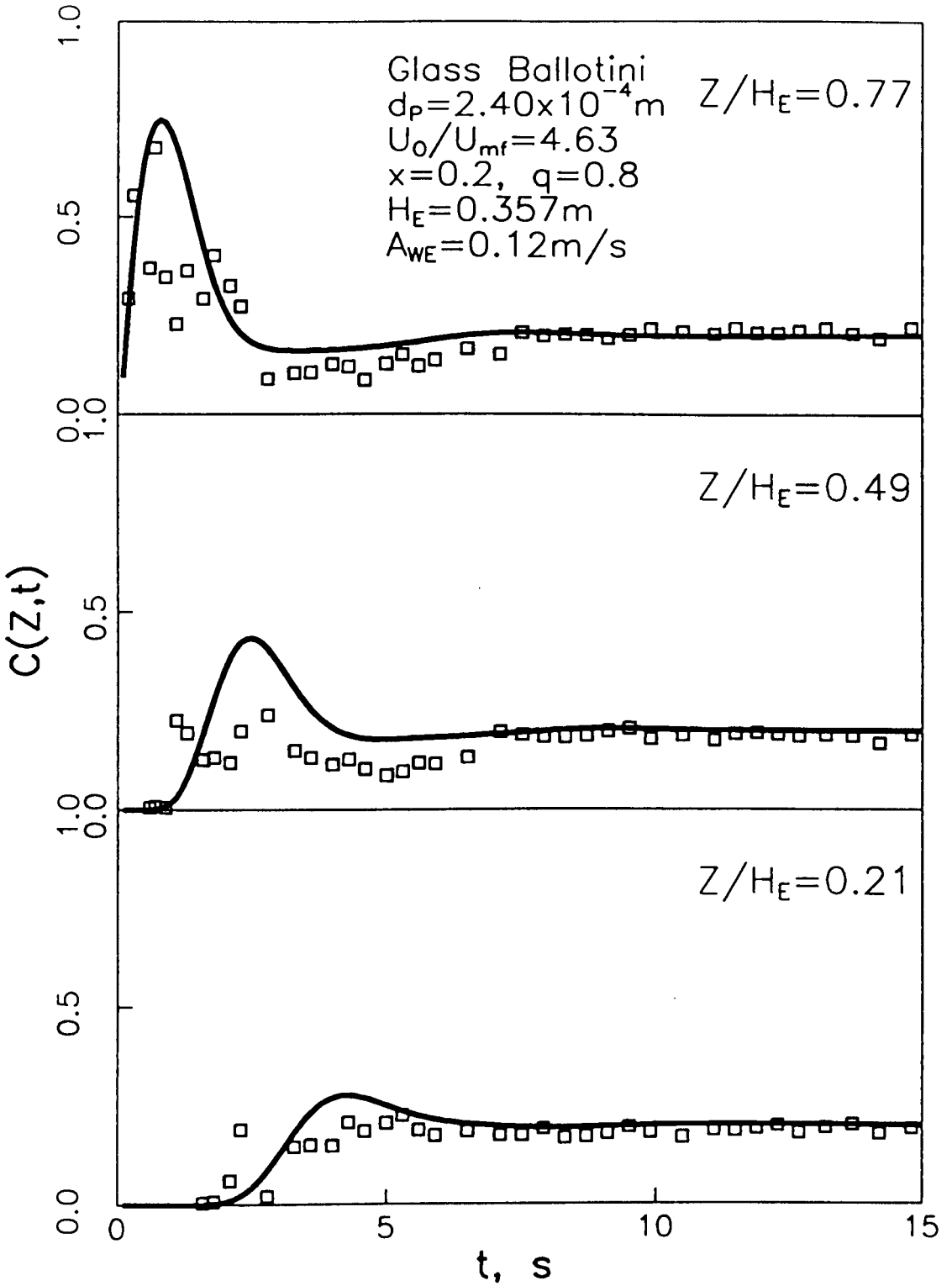

FIGURE 5.1.5d Comparison of model predictions with experimental data for $d_p = 2.40 \times 10^{-4}$ m and $U_o/U_{mf} = 4.63$

simultaneous measurements of the concentration as a function of time have been presented at three different heights within the bed to provide an overall picture of the mixing process. The model calculations have also been plotted. As may be seen, reasonable agreement can be obtained at different heights in the bed with an appropriate choice of A_{WE}; however, A_{WE} does appear to be a function of U_O/U_{mf}.

In **Figure 5.1.6**, data and model calculations are plotted for $d_P = 5.12 \times 10^{-4}$ m for $U_O/U_{mf} = 2.21$ at three different heights. The data show prominent oscillations or recycling of the tracer in the bed. For the largest particle size used in this investigation, $d_P = 7.25 \times 10^{-4}$ m, the results plotted in **Figure 5.1.7** for $U_O/U_{mf} = 1.75$ show even more obvious oscillations in tracer concentration with time at different heights within the bed. These oscillations imply small exchange coefficients. On the other hand, the models of Yoshida and Kunii (1968) and Chiba and Kobayashi (1977) predict that the exchange coefficient increases with increase in minimum fluidization velocity; the data do not support this prediction. It should be noted that the time duration of oscillations is of the order of 5 to 10 seconds; it is likely that experiments conducted using bed slumping and sectioning can miss such oscillations.

Separate experiments were conducted for $d_P = 2.4 \times 10^{-4}$ m and $U_O/U_{mf} = 2.21$ to examine the effect of initial conditions on solids mixing patterns. For these runs, the tracer was initially located close to the middle (q = 0.4) and at the distributor (q = 0.0). These data showed an altered pattern for the solids mixing depending on the initial condition. Nevertheless, good agreement was obtained between the experiments and model calculations using the appropriate initial condition, **Figure 5.1.8a-b**, with A_{WE} obtained from experimental data for tracer located initially at $q = 0.8$ (**Figure 5.1.5b**). This agreement enhances the confi-

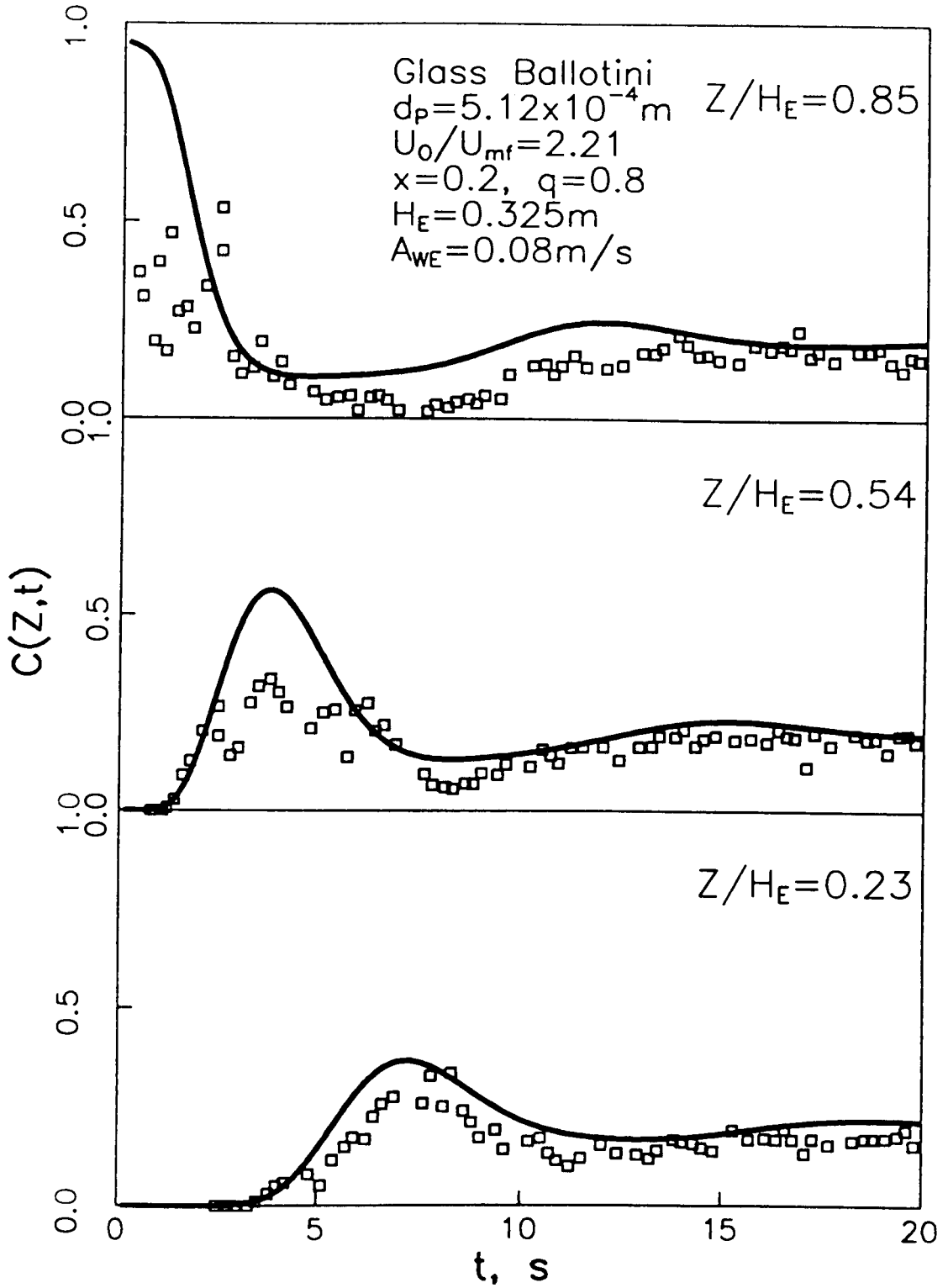

FIGURE 5.1.6: Comparison of model prediction with experimental data for $d_p = 5.12 \times 10^{-4}$ m and $U_o/U_{mf} = 2.2$.

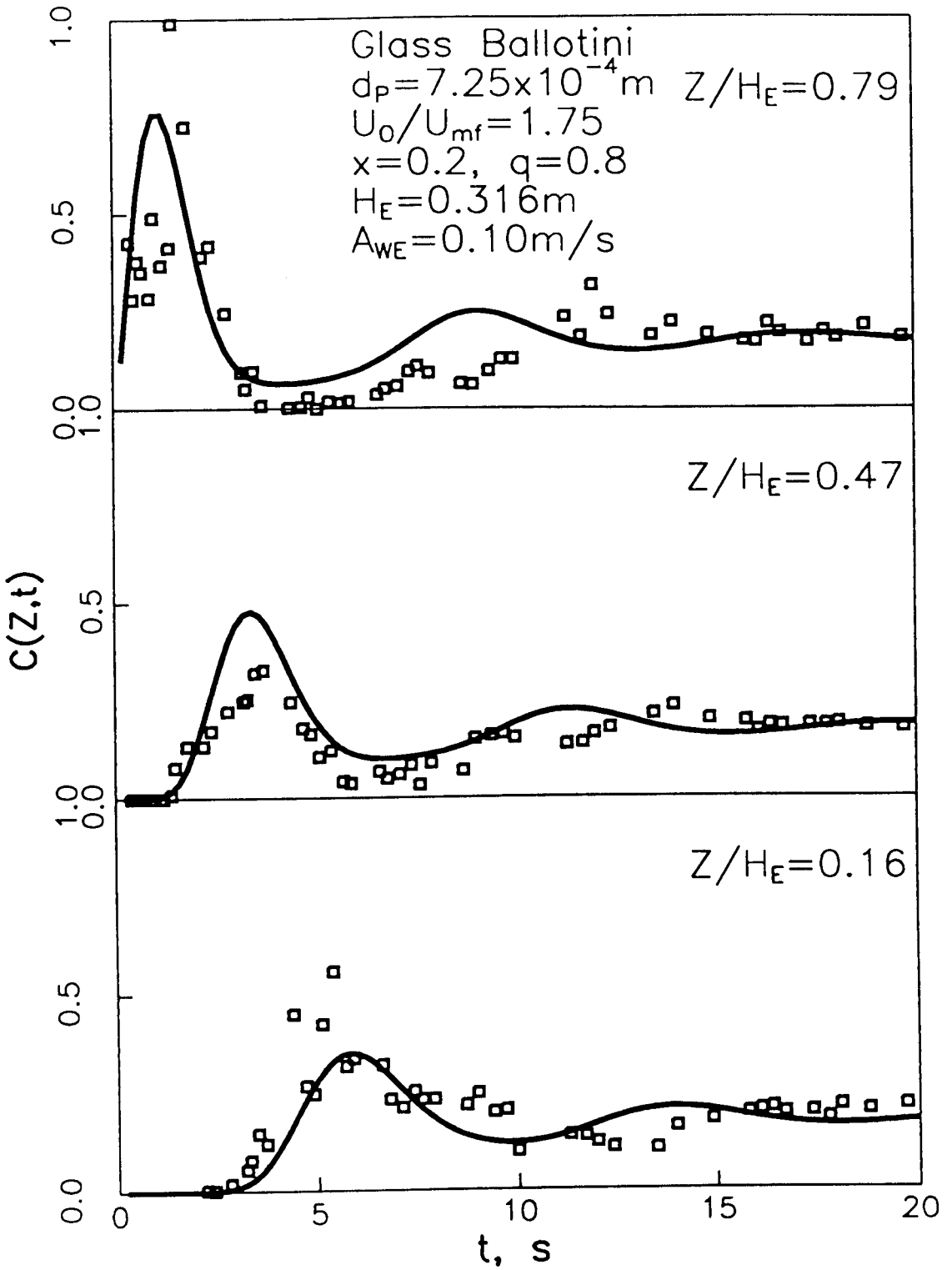

FIGURE 5.1.7: Comparison of model prediction with experimental data for $d_p = 7.25 \times 10^{-4}$ m and $U_o/U_{mf} = 1.75$

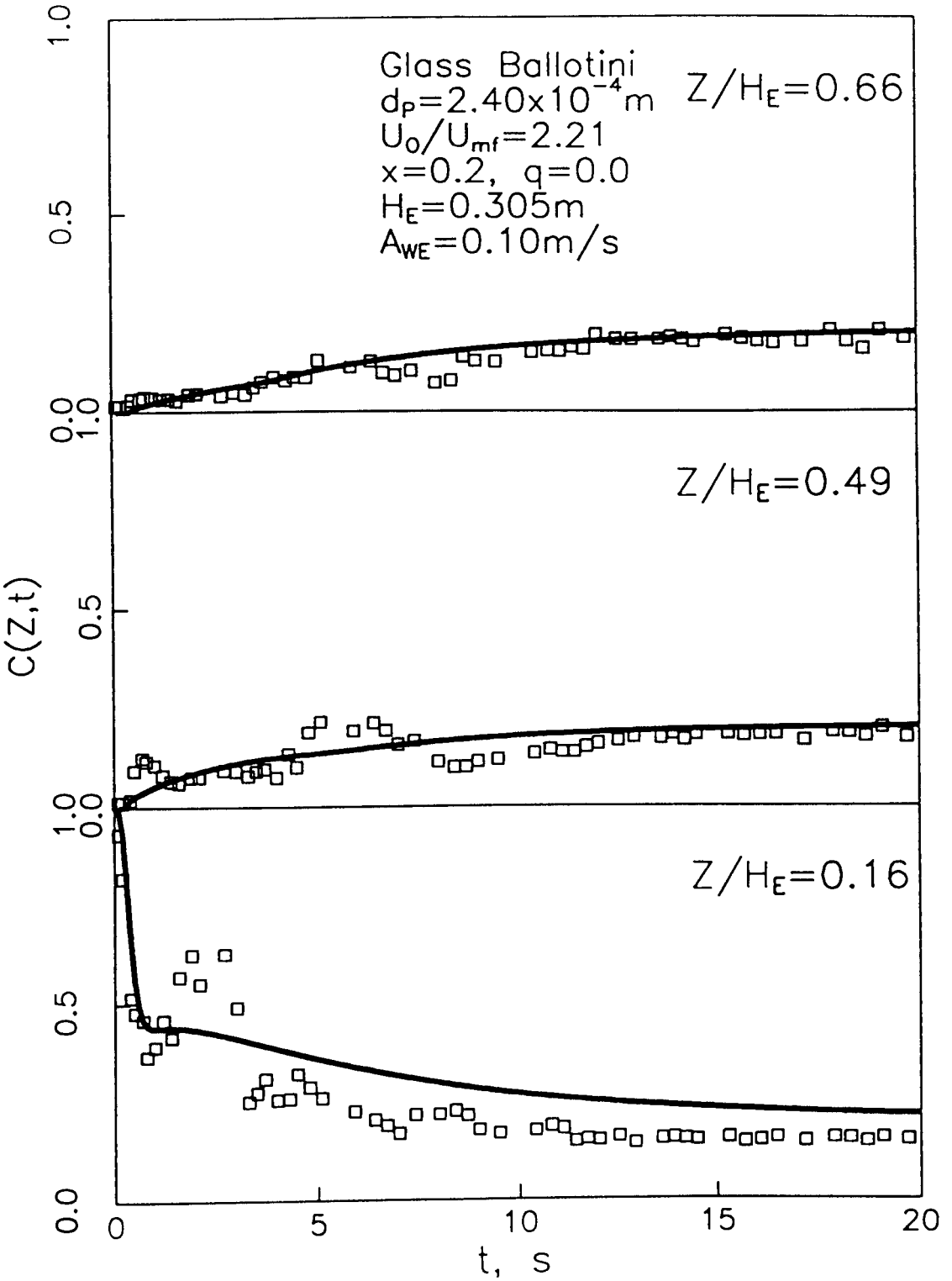

FIGURE 5.1.8a: Comparison of model prediction with experimental data: influence of intitial tracer location; d_p = 2.4 x 10^{-4} m and U_o/U_{mf} = 2.21; q = 0.0.

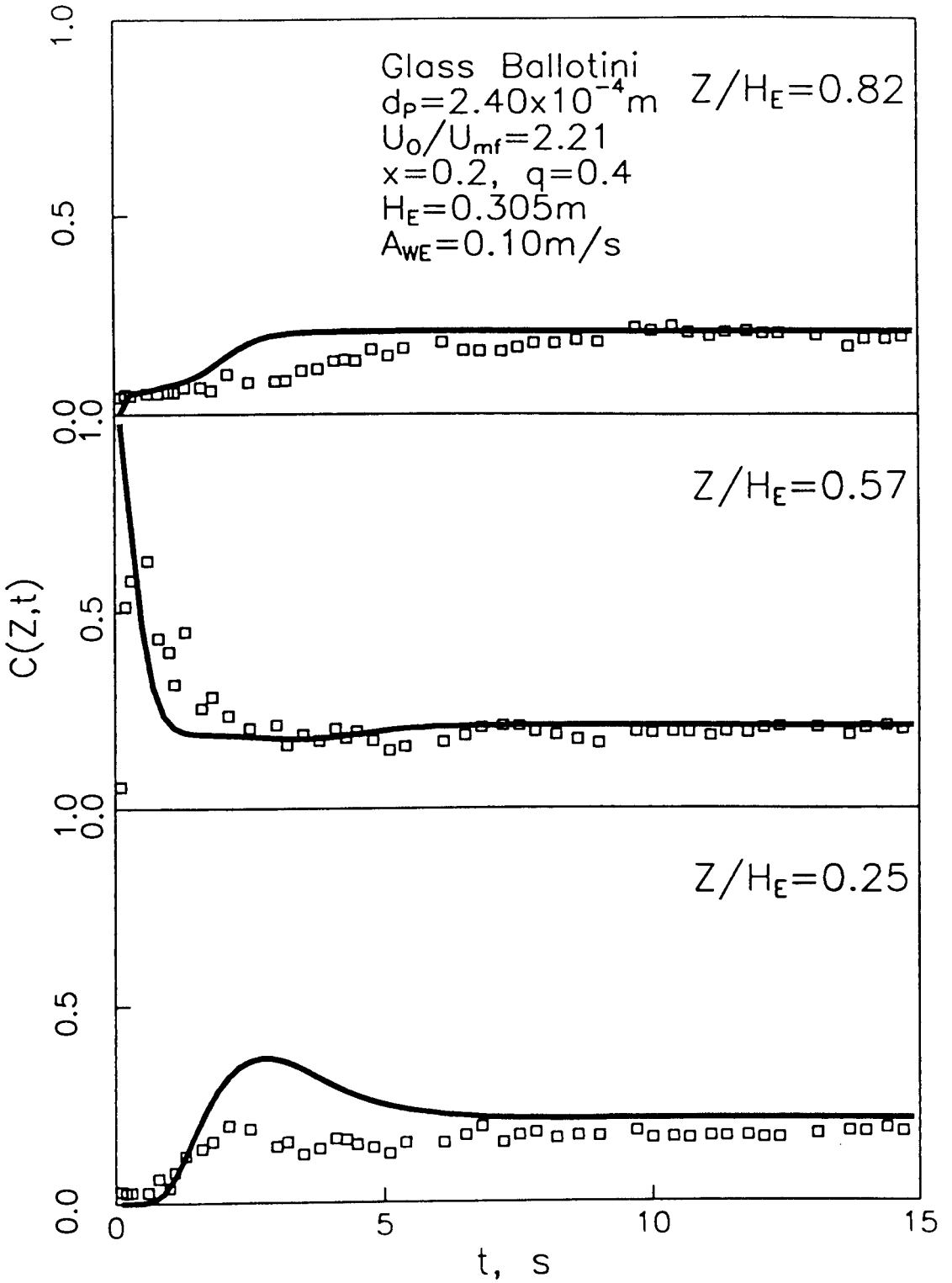

FIGURE 5.1.8b: Comparison of model prediction with experimental data: influence of intitial tracer location; $d_p = 2.4 \times 10^{-4}$ m and $U_o/U_{mf} = 2.21$; $q = 0.4$.

dence in the chosen values of A_{WE}.

The results of model calculations for the range of experiments conducted are summarized in **Table 5.1**. The values of the wake fraction, f_W, estimated from the tracer arrival time have been included. It will be noticed that for $d_P = 2.4 \times 10^{-4}$ m, the estimated values of the wake fraction are higher than what may be expected. The model of Gwyn et al. (1970) does not include the influence of solids drift induced by bubble motion. This effect is also not included in equation (5.1.16). It was considered convenient to lump solids motion through wake transport as well as drift in the wake fraction. The wake fraction measured from tracer arrival time will undoubtedly reflect both these mechanisms. Cranfield (1978) found that the transport of the solids in coarse particle systems ($d_P > 5.5 \times 10^{-4}$ m) is mainly due to the bubble-induced drift. In beds of smaller particles, motion of the solids was caused by both bubble-induced drift and wake. The combined machanisms of solids transport, then, are responsible for the higher values of the wake fraction (more correctly defined, in this context, as the fraction of the particles displaced upwards by the bubble) estimated for $d_P = 2.4 \times 10^{-4}$ m.

An important point to keep in mind while considering comparison between model calculations and experimental data is that the bubble parameters used in the calculations are time-averaged values whereas the mixing data are time-dependent. The mixing measured experimentally, in time frames of the order of seconds, will reflect the actual bubbling patterns which will surely have a random component superimposed on the time-averaged behaviour. To consider this aspect, replication tests were performed. These tests show that the initial movement of the tracer was influenced by the size and direction of the motion of

TABLE 5.1. SUMMARY OF MODELLING RESULTS ON MIXING OF UNIFORM SOLIDS

Input parameters						Estimated parameters		Evaluated parameters (average)				
d_P [m]	H_F [m]	U_O/U_{mf} [-]	$\varepsilon_{B,Expt}$ [-]	x [-]	q [-]	f_W [-]	A_{WE} [m/s]	$\overline{d_B}$ [m]	$\overline{U_B}$ [m/s]	$\overline{\varepsilon_B}$ [-]	$\overline{U_S}$ [m/s]	$\overline{k_W}$ [1/s]
2.40 x 10^{-4} m ($U_{mf} = 0.068 m/s$)	0.25	1.63	0.12	0.2	0.8	0.456	0.03	0.0151	0.194	0.130	0.0140	2.40
		1.91	0.15	"	"	0.374	0.035	0.0197	0.234	0.165	0.0184	2.16
		2.21	0.18	"	"	0.400	0.10	0.0242	0.273	0.198	0.0296	5.03
		2.50	0.20	"	"	0.396	0.15	0.0283	0.309	0.227	0.0402	6.45
		3.56	0.27	"	"	0.233	0.14	0.0423	0.426	0.302	0.0472	4.12
		4.63	0.30	"	"	0.193	0.12	0.0552	0.535	0.359	0.0645	2.68
		6.91	0.30	"	"	0.162	0.14	0.0758	0.740	0.450	0.1125	2.30
		2.21	0.18	0.2	0.4	0.400	0.10	0.0242	0.273	0.198	0.0296	5.03
		"	"	0.2	0.0	"	"	"	"	"	"	"
		"	"	0.1	0.9	"	"	"	"	"	"	"
		"	"	0.3	0.7	"	"	"	"	"	"	"
5.12 x 10^{-4} m ($U_{mf} = 0.24 m/s$)	0.25	1.43	0.094	0.2	0.8	0.150	0.07	0.0266	0.303	0.118	0.0062	3.17
		1.68	0.153	"	"	0.100	0.05	0.0375	0.401	0.166	0.0081	1.61
		1.94	0.194	"	"	0.129	0.09	0.0480	0.495	0.212	0.0176	2.28
		2.21	0.231	"	"	0.150	0.08	0.0582	0.586	0.252	0.0310	1.68
		2.50	0.254	"	'	0.152	0.12	0.0684	0.681	0.289	0.0446	2.15
7.25 x 10^{-4} m ($U_{mf} = 0.35 m/s$)	0.243	1.35	0.147	0.2	0.8	0.240	0.03	0.0304	0.336	0.108	0.0099	1.19
		1.54	0.194	"	"	0.150	0.035	0.0420	0.442	0.150	0.0119	1.01
		1.75	0.231	"	"	0.200	0.10	0.0536	0.548	0.192	0.0216	2.27
		2.00	0.258	"	"	0.176	0.06	0.0663	0.666	0.237	0.0440	1.11
		2.23	0.286	"	"	0.231	0.14	0.0783	0.778	0.273	0.0547	2.20

the first few bubbles as well as the random nature of bubbling, **Figure 5.1.9a** and **b**. It is clear that the overall solids mixing pattern in the replicate tests is very similar.

The experimental measurements of tracer concentration as function of time can be used to obtain data on the arrival time of the tracer at different axial positions within the bed. In **Figure 5.1.10a-c**, such data have been plotted for the three bed particle sizes investigated for different values of U_O/U_{mf}. Straight lines were drawn, by regression, through such data for each superficial velocity as shown in this figure. The slope of the straight line yields the height-averaged downward velocity of the dense phase, $\overline{U_S}$, for the experimental run. Similar results were obtained for other particle sizes. These measurements are compared with the predictions of the height-averaged form of equation (5.1.16) in **Figure 5.1.11**. It is seen that the agreement between observed and predicted (using the estimated value of f_W) dense phase velocity is good (within ± 30%). Though straight lines have been drawn in **Figure 5.1.10a-c** to estimate $\overline{U_S}$, the arrival velocity at different heights within the bed is not uniform, particularly for lower superficial velocities, and it is thought that the results at individual positions within the bed show the influence by the random aspects of bubble flow.

In **Figure 5.1.12**, the values of A_{WE} determined from the solids mixing experiments are plotted as a function U_O/U_{mf}. It is seen that for $d_P = 2.4 \times 10^{-4}$ m, A_{WE} increases virtually linearly below $U_O/U_{mf} \sim 3$. Particularly interesting is that, in this region, there is no particle size effect with values of A_{WE} for other particle sizes ($d_P = 5.12 \times 10^{-4}$ m, $U_{mf} = 0.24$ ms^{-1} ; $d_P = 7.25 \times 10^{-4}$ m, $U_{mf} = 0.35$ ms^{-1}) also clumping around the data for the smallest particle size ($d_P = 2.4 \times 10^{-4}$ m, $U_{mf} = 0.068$ ms^{-1}). For greater values of U_O/U_{mf}, A_{WE} calculated from data for $d_P = 2.4 \times 10^{-4}$ m seems to be constant at about 0.14-0.15 ms^{-1}. Limitations in the

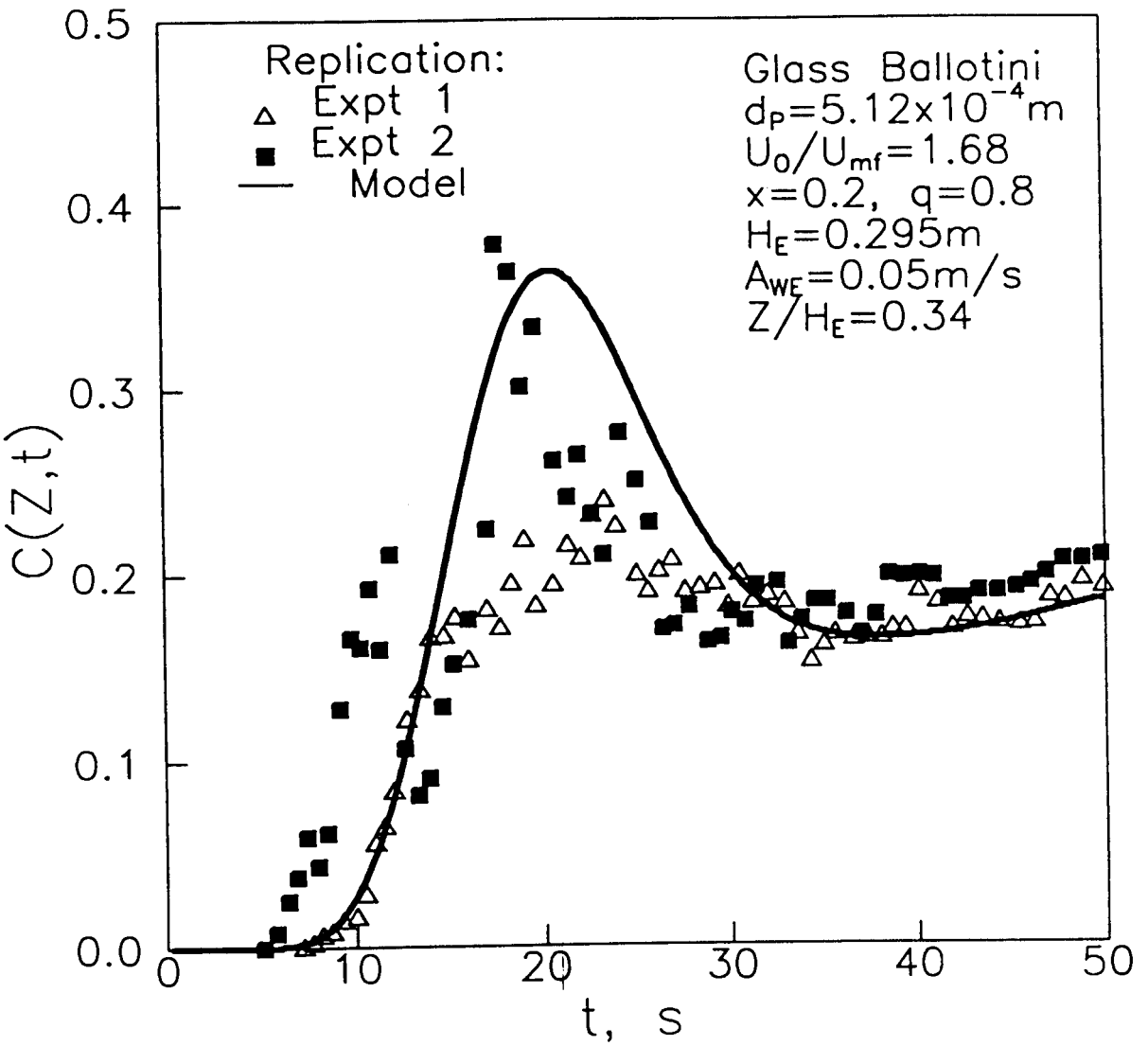

FIGURE 5.1.9a: Replicate tests

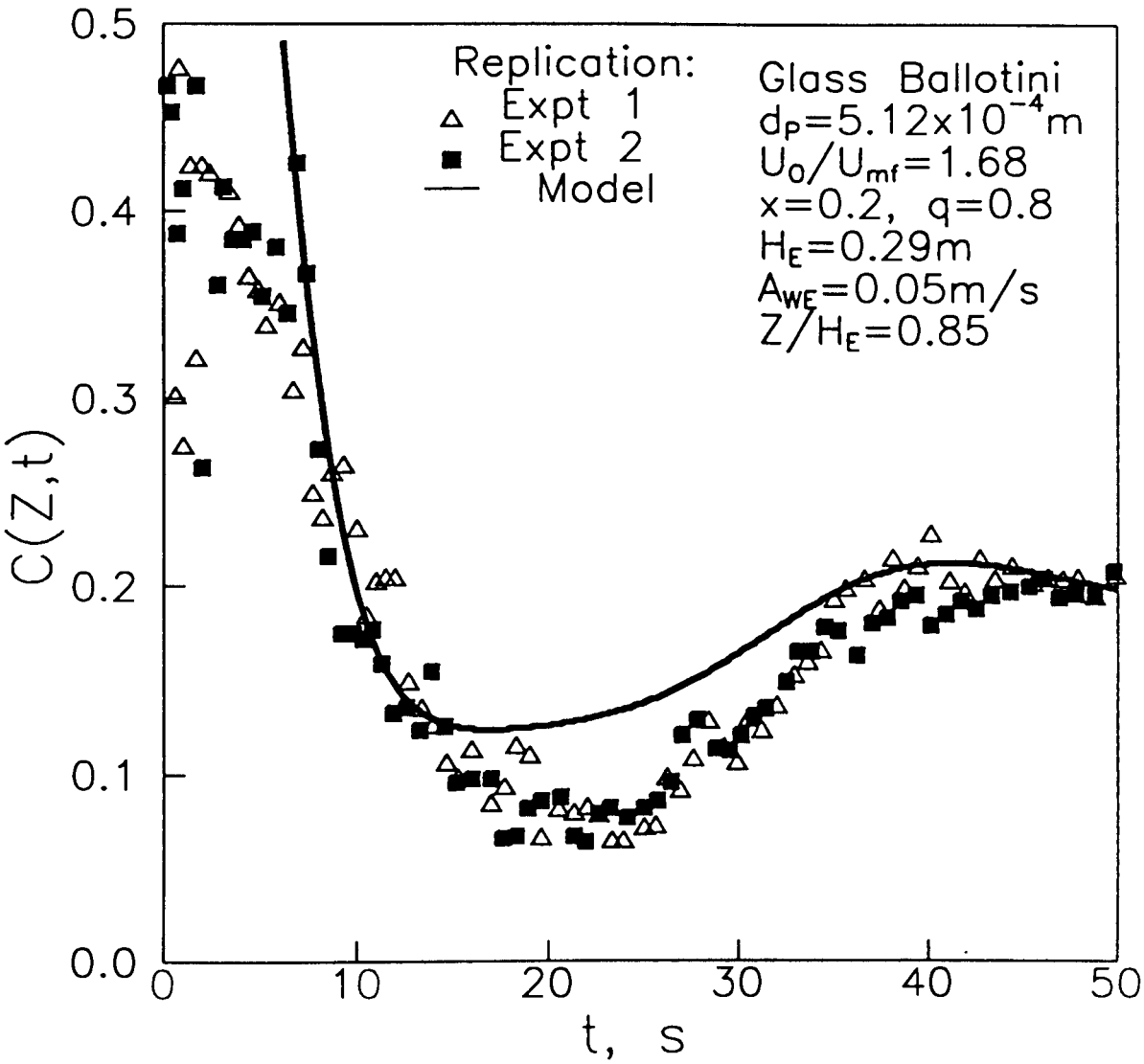

FIGURE 5.1.9b: Replicate tests

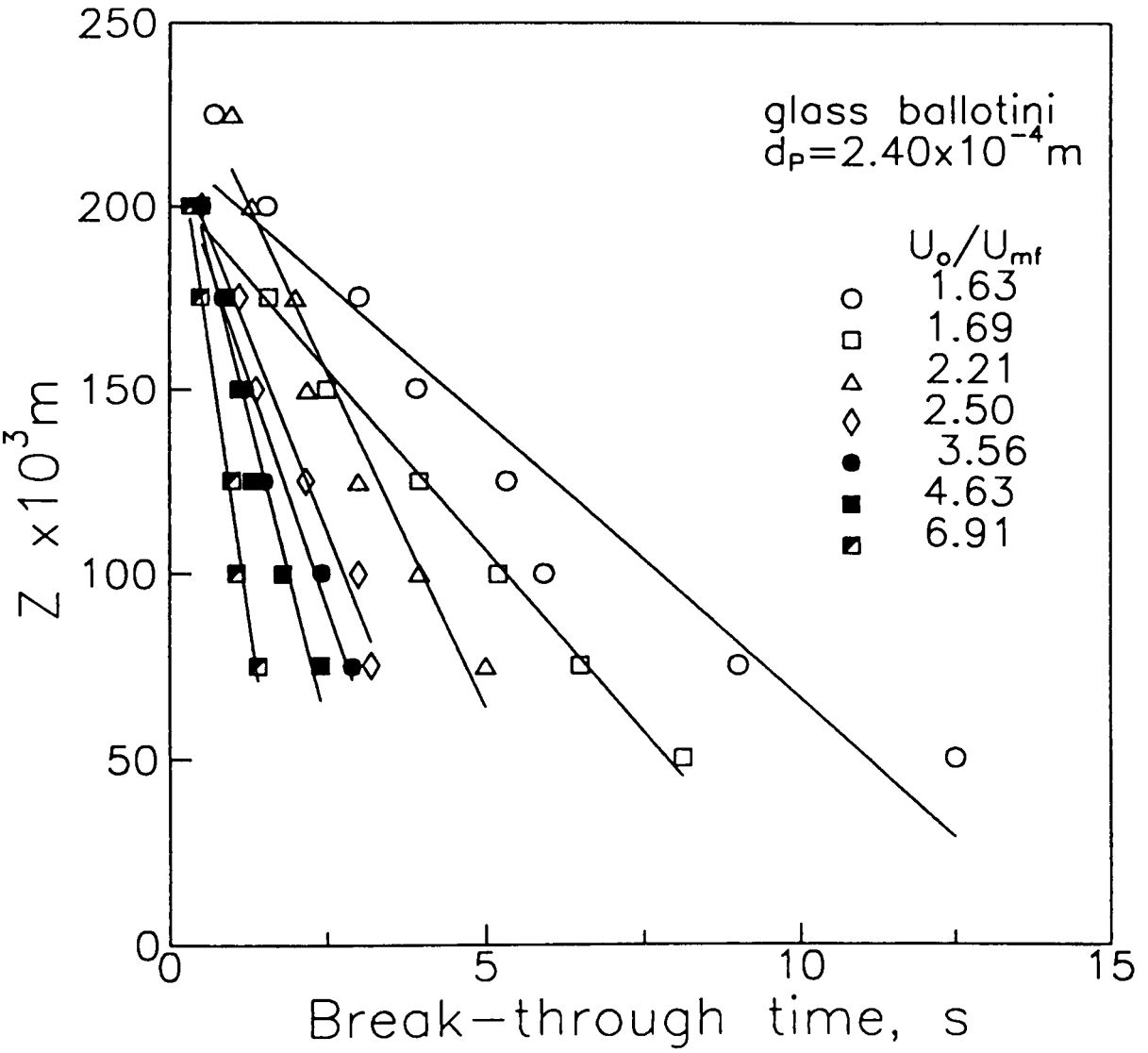

FIGURE 5.1.10a: Estimation of the average downward solids velocity, $\overline{U}_s$, from tracer arrival (break-through) time measurement: $d_p = 2.4 \times 10^{-4}$ m

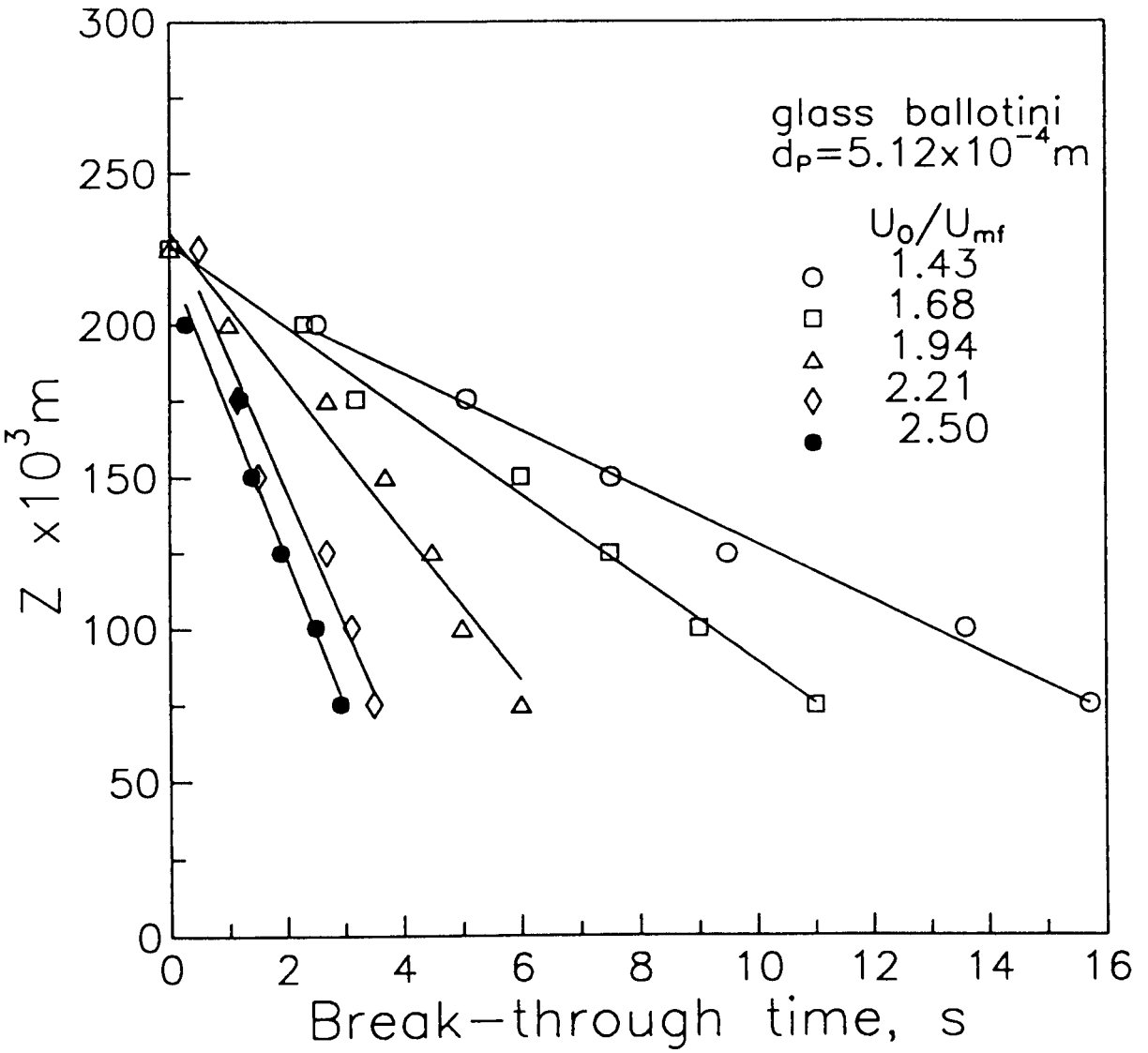

FIGURE 5.1.10b: Estimation of the average downward solids velocity, $\overline{U}_s$, from tracer arrival (break-through) time measurement: $d_p = 5.12 \times 10^{-4}$ m

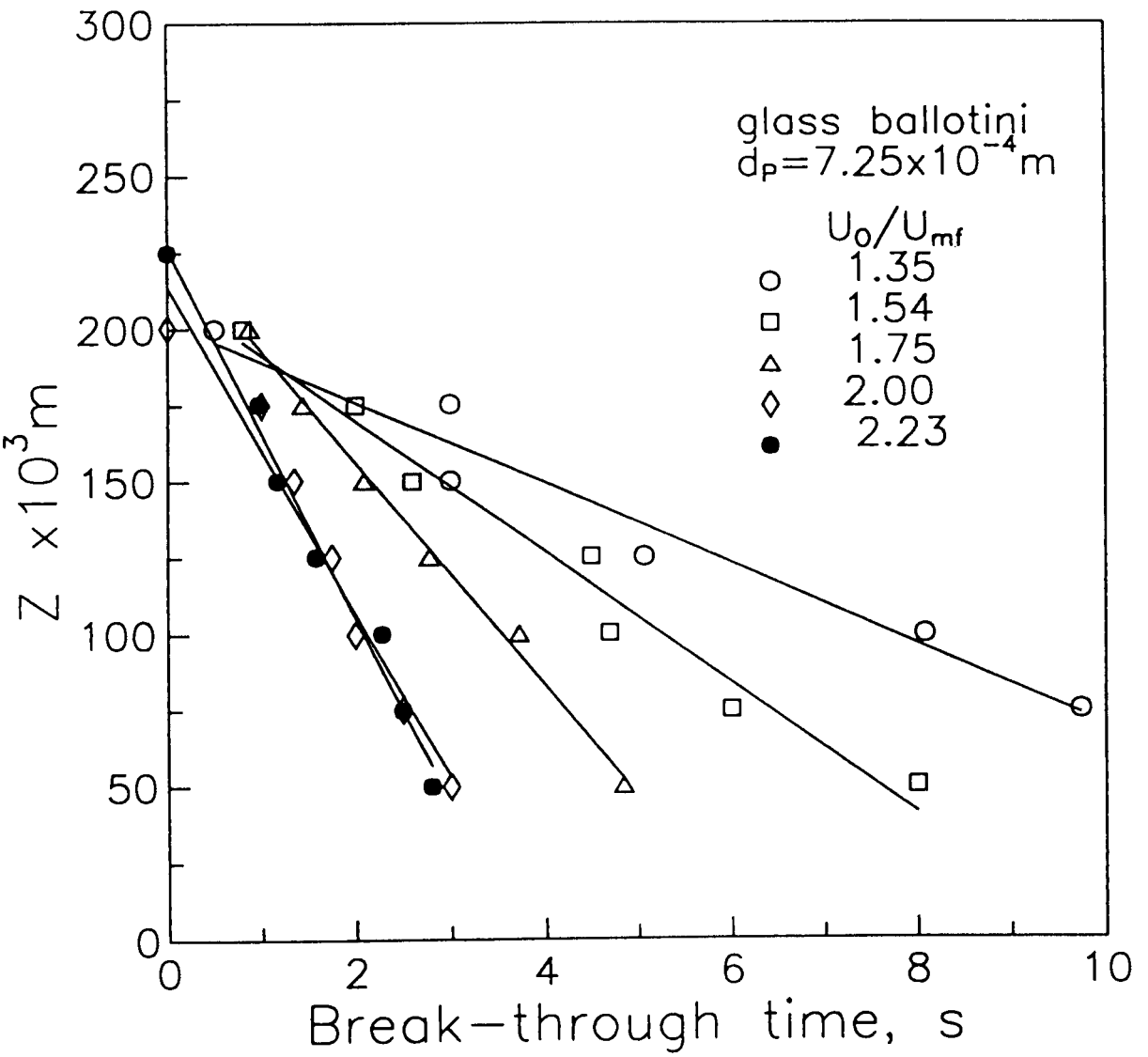

FIGURE 5.1.10c: Estimation of the average downward solids velocity, $\overline{U}_s$, from tracer arrival (break-through) time measurement: $d_p = 7.25 \times 10^{-4}$ m

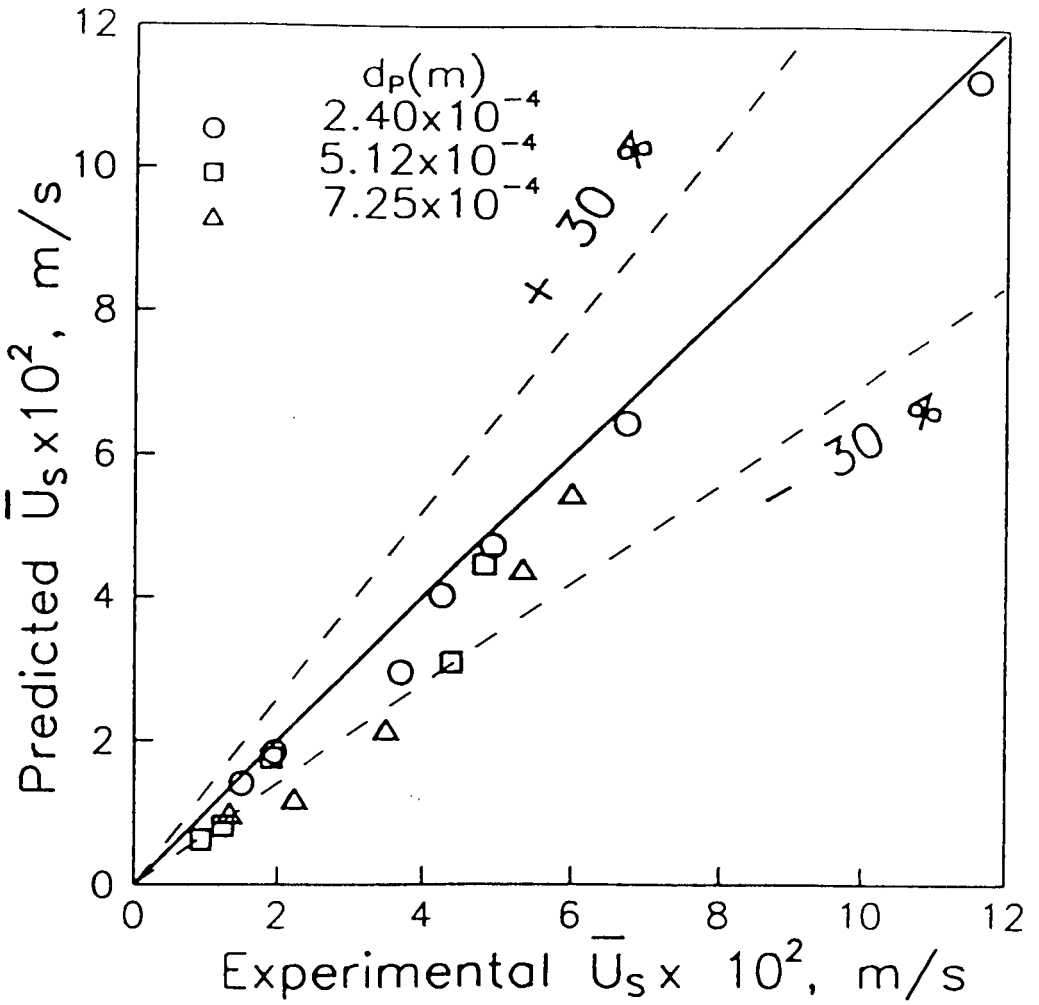

FIGURE 5.1.11: Comparison of the measured average dense phase solids velocity $\bar{U}_S$ with model calculation by equation (5.1.16).

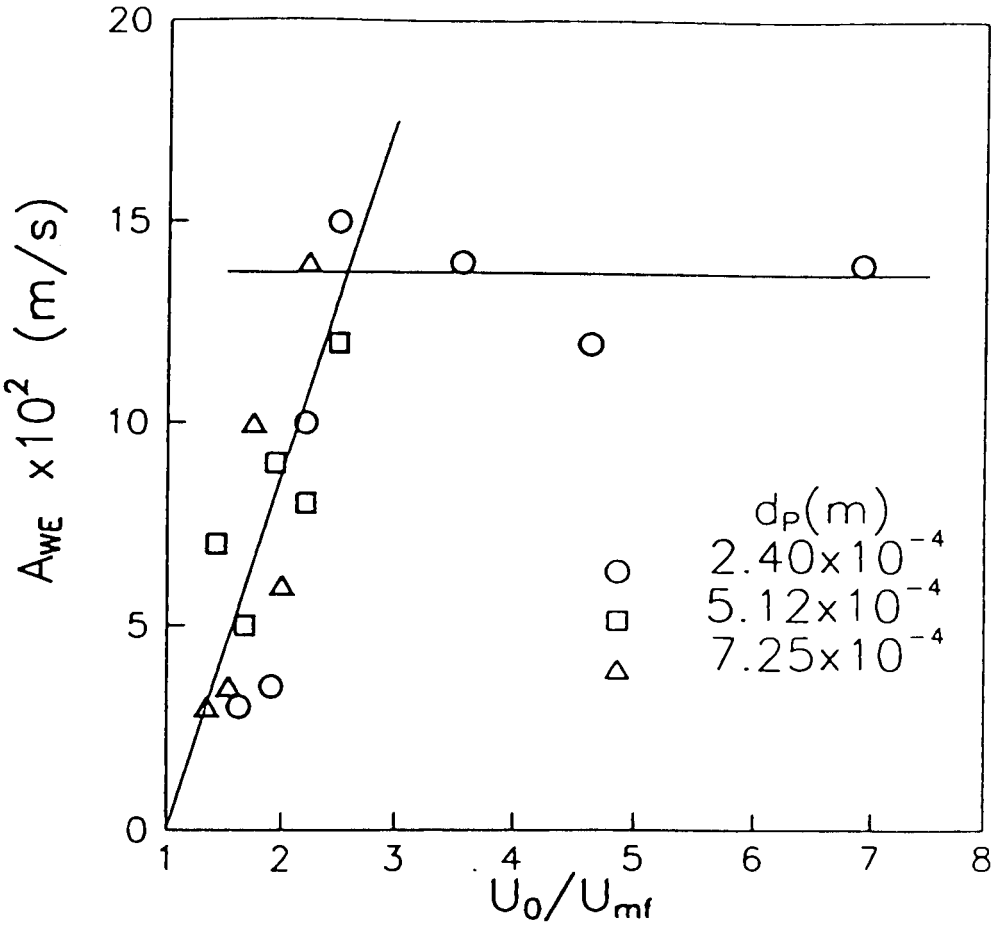

FIGURE 5.1.12: Plots of the estimated exchange constant A_{WE} with U_o/U_{mf} for different bed particle sizes.

experimental apparatus, at present, prevent collection of data for the larger particle sizes at higher values of U_O/U_{mf}. Such data are needed to establish whether the limit of A_{WE} = 0.14-0.15 ms^{-1} holds for other particle sizes as well.

In **Figure 5.1.13**, the values of the wake exchange coefficient obtained from our experiments are plotted as function of bubble diameter for comparison with the predictions of Yoshida and Kunii (1968) and Chiba and Kobayashi (1977). The hatched region represents our data set for all the particle sizes; it should be noted that for any particle size, according to the results plotted in **Figure 5.1.13**, k_W depends on bubble diameter, d_B, as well as U_O/U_{mf}. The predictions of Yoshida and Kunii, and Chiba and Kobayashi, are different straight lines on this plot depending on the particle size through U_{mf}. It is clear that their models are unable to predict our data.

It is now interesting to consider the data on the wake exchange coefficients for single bubbles injected in an incipient fluidized two-dimensional bed reported by Chiba and Kobayashi. The experiments were performed using bed (glass beads) and tracer (crushed silica gel) particles with a minimum fluidization velocity of 0.0215 ms^{-1}. Their data on the exchange coefficient, k_W (it appears that the y-axis of their Figure 7 should read $\pi\varepsilon_{mf}k_W/4U_{mf}$ instead of k_W as it has been shown in the paper) have also been plotted in **Figure 5.1.13**. If k_W increases with U_O/U_{mf} and does not depend on the particle size, as our experimental results described above indicate, then their measurements from single injected bubbles, should form the lower bound values for k_W. It can be seen from **Figure 5.1.13** that their data are, indeed, in line with these experimental results.

5.1.4 Discussion

The results obtained in this investigation show that the models available in the literature to estimate the wake exchange coefficient are inadequate. These

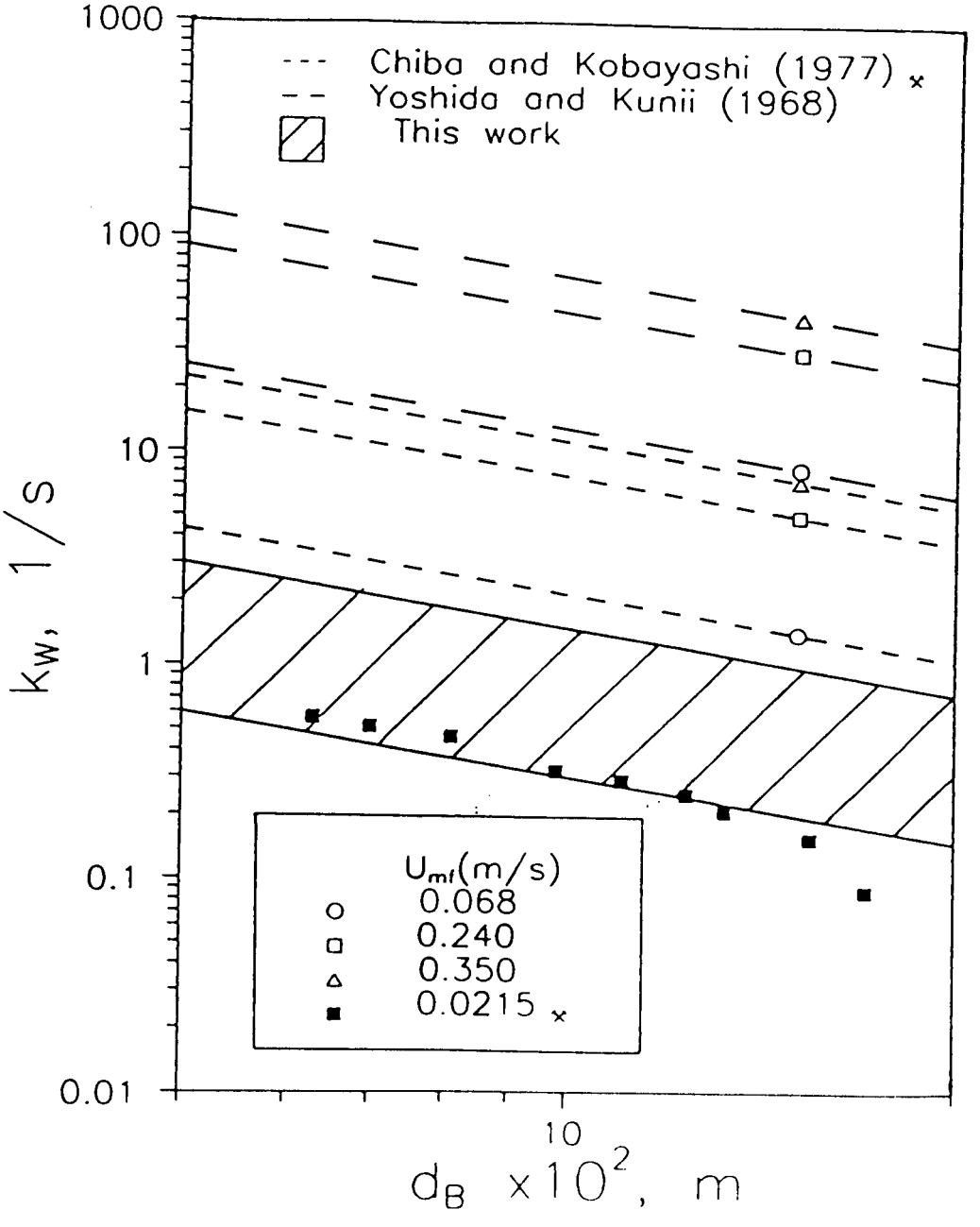

FIGURE 5.1.13: Plots of exchange coefficient k_W estimated from the present model analysis as a function of bubble size d_B and compared with the values calculated from solids exchange models by (Chiba and Kobayashi, 1977; and Yoshida and Kunii, 1968).

models suggest that k_W will increase with U_{mf}. Results obtained there, from experiments with different particle sizes, do not support this dependence. Further, these results also show that the wake exchange coefficient increases with U_O/U_{mf} for $U_O/U_{mf} < 3$; the models developed for isolated bubbles are unable to predict such dependence. If the model derivations are examined, it can be seen that U_{mf} appears in the equations from the postulate that the wake exchange involves solids moving around the bubble periphery within the bubble cloud region. Clearly, these models will not describe mixing behaviour in systems with slow bubbles. Solids motion around the edge of the bubble is not understood and the region around the bubble where the particles move may not be related to the thickness of the gas cloud. Improved understanding of solids mixing in bubbling beds will depend substantially on fundamental advances made in describing particle flow around, and through (raining), the bubble.

If the wake exchange coefficient is chosen in the form of equation (5.1.19), and A_{WE} is treated as an adjustable parameter, then the three-phase counter-current back-mixing model does provide reasonable agreement with experimentally observed solids mixing trends. In particular, the model is able to follow the oscillations and recycle peaks observed in the tracer concentration resulting from the gross circulation of solids. This behaviour appears to become increasingly more important in fluidized beds of larger particles. It is also important to experimentally measure the bubble fraction for input to model calculations as the currently available procedures for the estimation of visible bubble flow require further refinement to acquire predictive capabilities.

It is also important to consider the applicability of the results obtained in the two-dimensional bed to three-dimensional beds. The model calculations have been carried out using bubble phase parameters applicable to and measured

independently for the two-dimensional bed. It appears reasonable to suggest that the three-phase counter-current back-mixing model should apply to three-dimensional beds as well with appropriate choice of parameters. The bubble diameter (Darton et al., 1977) and velocity (Davidson and Harrison, 1963) for three-dimensional beds can be estimated with ease. The bubble fraction should be estimated from experiments as discussed earlier. It is thought that the results on the wake exchange coefficient obtained from the two-dimensional bed studies will apply to three-dimensional beds at least qualitatively: in terms of the absence of particle size effects and the dependence on U_O/U_{mf}. Quantitative agreement will depend on the magnitude of the difference between motion of solids around the edge of the bubble in two- and three-dimensional beds.

5.1.5 Conclusions

The solids mixing data obtained for uniform solids show oscillations in tracer concentration resulting from the gross circulation of the solids. These oscillations become increasingly prominent with increase in bed particle size.

The experimental data have been interpreted using the three-phase counter-current back-mixing model. The bubble phase parameters required for model calculations were also measured and interpreted in terms of appropriate models. The comparison of model calculations and experimental data shows that the models for the prediction of the wake exchange coefficient currently available in the literature (Yoshida and Kunii, 1968; Chiba and Kobayashi, 1977) are not adequate. In particular, the wake exchange coefficient appears to increase with U_O/U_{mf} for $U_O/U_{mf} < 3$ and the values, in this region, are independent of the particle size. The models, on the other hand, predict that the wake exchange coefficient should increase with increase in the minimum fluidization of the bed particles. In line with results obtained in this investigation, the experimental measurements of

Chiba and Kobayashi, for injected bubbles in a two-dimensional fluidized bed of particles smaller than those used in this investigation, were found to in excellent agreement with the lower bound of present measurements.

5.2 SEGREGATION IN BINARY FLUIDIZED SYSTEMS

Most fluidized beds contain mixed species. This may be because two or more solid components are fed into the bed or because the solids change in size and/or density during their conversion in the reactor. Segregation will then occur in most practical applications of fluidization.

It is recognized that segregation, like mixing, is a consequence of bubble motion. Though several mathematical models have been proposed in the literature, the emphasis has been on the prediction of the steady state behaviour. This, in part, is due to the very limited data on the time dependent behaviour of the segregation phenomenon. In this section, experimental measurements of the spatial (axial) and temporal variation of the jetsam concentration, obtained using the methods described in **sections 3.2.4** and **3.2.5**, have been used to evaluate the unsteady state versions of the more accepted models reported in the literature.

5.2.1 Theory

Model Equations : The mechanisms by which the particles segregate through the temporarily disturbed regions near rising bubbles have been modelled by Gilibaro and Rowe (1974) and Yoshida et al. (1980).

Gilibaro and Rowe (1974) defined a settlement rate, k_S, as the net downward flux of settling particle relative to the bulk of the bed. Naimer et al. (1982) related the settlement or segregation rate to bubble characteristics and the average segregation distance, Y_{GR}, measured by Tanimoto et al. (1980). On the other hand, Yoshida et al. (1980) viewed the segregation process to be a consequence of the shedding of jetsam from the wake phase into the dense phase. An adjustable

parameter R_Y was introduced in the solids exchange term to account for this effect. R_Y is unity if the system is homogeneous and zero if the system is strongly segregating. It was pointed out that R_Y may be a function of the physical properties of the particle, operating conditions and the concentrations of the particle species.

In the following theoretical study, the unsteady state material balances resulting from the Gibilaro-Rowe (G-R) model have been solved numerically. It should be noted that the axial diffusion term included in their formulation has been omitted following the recommendation of Nienow and Chiba (1985). Also, the relation between settlement rate and bubble behaviour suggested by Naimer et al. (1982) has been adopted. Thus

$$k_S = \frac{3}{4} Y_{GR} U_B \frac{\varepsilon_B}{1-\varepsilon_B} \tag{5.2.1}$$

Though steady state solutions of the G-R model, with or without the use of constant bubble properties, are available in the literature, modelling results on the variation of the axial concentration with time have not been reported.

Solutions of the Yoshida model have also been obtained for comparison. Though Yoshida et al. (1980) presented parametric results from the solution of the unsteady material balance equations, their computations were made assuming a constant bubble size.

For both the models, the possibility of the formation of a defluidized layer has been considered.

The material balances for the jetsam component over an incremental cell are illustrated in **Figure 5.2.1a** and **b**. Accordingly,

G-R Model:

Wake phase:

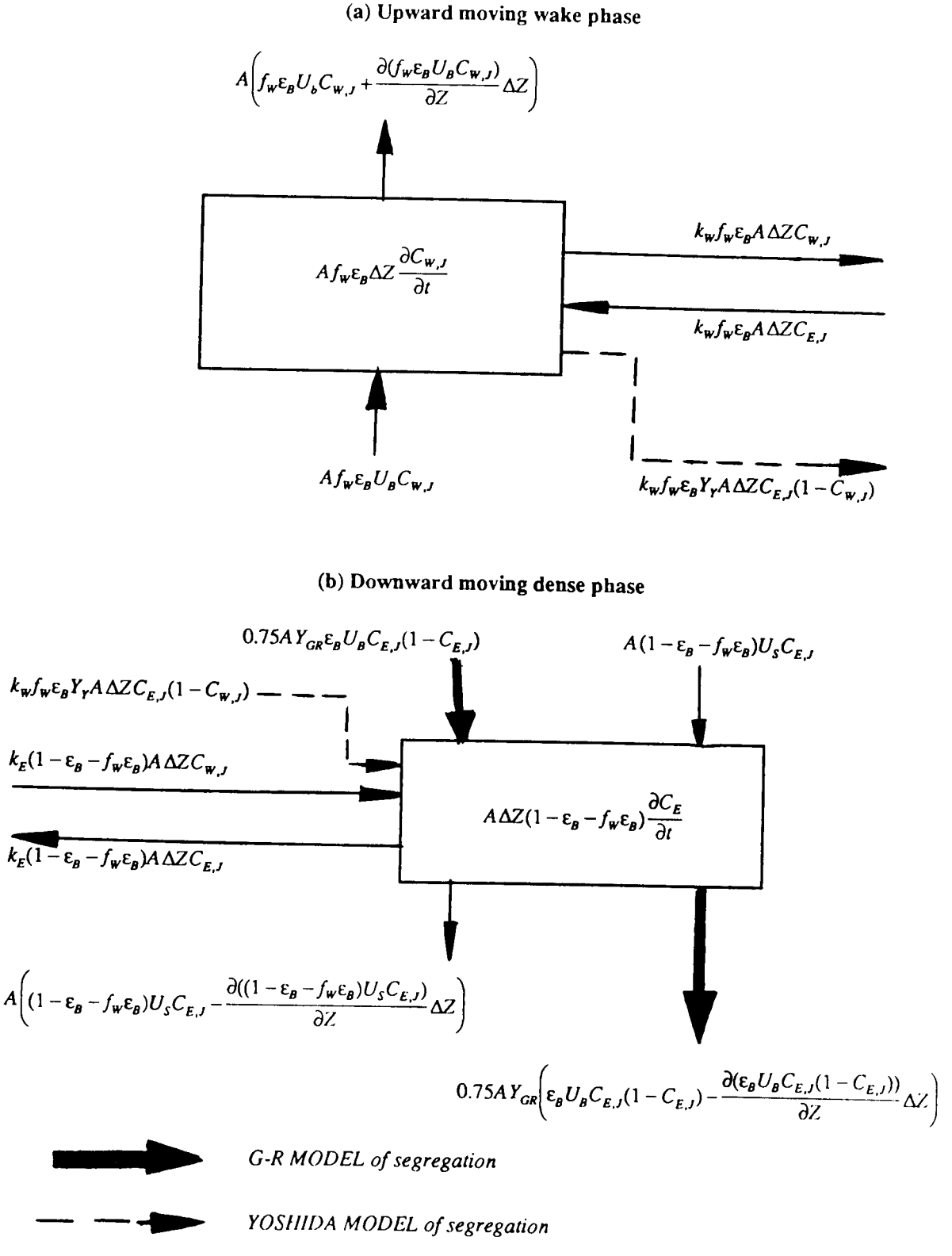

FIGURE 5.2.1: Material balance on the jestam in (a) the upward moving wake (and drift) phase; (b) in the downward moving dense phase.

$$f_W \varepsilon_B \frac{\partial C_{W,J}}{\partial t} = -\frac{\partial (f_W \varepsilon_B U_B C_{W,J})}{\partial Z} - k_W f_W \varepsilon_B (C_{W,J} - C_{E,J}) \qquad (5.2.2)$$

Dense phase:

$$(1-\varepsilon_B - f_W \varepsilon_B)\frac{\partial C_{E,J}}{\partial t} = \frac{\partial ((1-\varepsilon_B - f_W \varepsilon_B) U_S C_{E,J})}{\partial Z} + k_E (1-\varepsilon_B - f_W \varepsilon_B)(C_{W,F} - C_{E,J})$$

$$+\frac{\partial (0.75 Y_{GR} \varepsilon_B U_B C_{E,J}(1-C_{E,J}))}{\partial Z} \qquad (5.2.3)$$

Yoshida Model

Wake phase:

$$f_W \varepsilon_B \frac{\partial C_{W,J}}{\partial t} = -\frac{\partial (f_W \varepsilon_B U_B C_{W,J})}{\partial Z} - k_W f_W \varepsilon_B (C_{W,J} - C_{E,J}) - k_W f_W \varepsilon_B Y_Y C_{E,J}(1 - C_{W,J})$$

(5.2.4)

Dense phase:

$$(1-\varepsilon_B - f_W \varepsilon_B)\frac{\partial C_{E,J}}{\partial t} = \frac{\partial ((1-\varepsilon_B - f_W \varepsilon_B) U_S C_{E,J})}{\partial Z} + k_E (1-\varepsilon_B - f_W \varepsilon_B)(C_{W,J} - C_{E,J})$$

$$+ k_E (1-\varepsilon_B - f_W \varepsilon_B) Y_Y C_{E,J}(1 - C_{W,J}) \qquad (5.2.5)$$

where the extent of segregation is defined by $Y_Y (= 1 - R_Y)$.

The axial average concentration of the jetsam is calculated as

$$C(Z,t) = \frac{f_W \varepsilon_B C_{W,J} + (1-\varepsilon_B - f_W \varepsilon_B) C_{E,J}}{1-\varepsilon_B} \qquad (5.2.6)$$

Numerical implementation: The differential material balance equations can be rewritten using the finite difference approach as described in **section 5.1.1**. Several approximations, based on how the second term on the right hand side of equation (5.2.2) is treated, were considered:

slow change in bubble variables : In **section 5.1.1**, the change of the bubble properties with respect to height within the bed was assumed to be slow. Consequently,

$$\frac{\partial(f_W \varepsilon_B U_B C_{W,J})}{\partial Z} \cong f_W \varepsilon_B U_B \frac{\Delta C_{W,J}}{\Delta Z} \tag{5.2.7}$$

where f_W, ε_B and $U_B$are the local bubble properties. The difference between this approximation and that which uses height-averaged values has been discussed earlier.

ordinary difference : A more direct approach is to approximate the differential variable as

$$\frac{\partial(f_W \varepsilon_B U_B C_{W,J})}{\partial Z} \cong \frac{\Delta(f_W \varepsilon_B U_B C_{W,J})}{\Delta Z} \tag{5.2.8}$$

complete difference : If the minimum fluidization velocities of the jetsam and flotsam components are considerably different, then the bubble properties will experience significant changes with height within the bed and with the local bed composition during the course of segregation. This variation will be more prominent in the regions close to the distributor or at the upper interface of the defluidized layer. These variations were thought to be responsible for the numerical instabilities encountered when the approximations described above were used.

Clearly, the approximation scheme can be improved if the change of the bubble properties with height in the bed was treated in detail. For the purposes of this study, due to the lack of detailed knowledge, the wake fraction, f_W, was assumed to be independent of height within the bed. Since the bubble fraction, ε_B, and the bubble velocity, U_B, are related by equation (5.1.15), the differential term can be expressed as:

$$\frac{\partial(f_W \varepsilon_B U_B C_{W,J})}{\partial Z} \cong f_W \frac{\partial(\varepsilon_B U_B)}{\partial Z} C_{W,J} + f_W \varepsilon_B U_B \frac{\partial C_{W,J}}{\partial Z} \qquad (5.2.9a)$$

where

$$\varepsilon_B U_B = \frac{U_O - U_{mf}}{U_B + k' U_{mf}} U_B \quad ; \quad k' = -(1 + f_W - K_T) \qquad (5.2.9b)$$

and $\partial(\varepsilon_B U_B)/\partial Z$ can be derived analytically as follows

$$\frac{\partial(\varepsilon_B U_B)}{\partial Z} = \frac{U_O - U_{mf}}{\left(1 + k' \frac{U_O}{U_{mf}}\right)^2} \frac{k' U_{mf}}{U_B^2} \frac{\partial U_B}{\partial Z} \qquad (5.2.10a)$$

where, for the two-dimensional bed under consideration,

$$\frac{\partial U_B}{\partial Z} = \frac{8(2^{3/4} - 1)(U_O - U_{mf})}{3\pi \lambda_B d_B} \qquad (5.2.10b)$$

It should be noted that U_{mf} in the above equations refers to the minimum fluidization velocity of the mixture of particles with local bed composition.

A similar approach was extended for the differential term due to segregation as used in the G-R model,

$$\frac{\partial(0.75 Y_{GR} \varepsilon_B U_B C_{E,J}(1 - C_{E,J}))}{\partial Z} = 0.75 Y_{GR} \left(\frac{\partial(\varepsilon_B U_B)}{\partial Z} C_{E,J}(1 - C_{E,J}) + \varepsilon_B U_B (1 - 2C_{E,J}) \frac{\partial C_{E,J}}{\partial Z} \right) \qquad (5.2.11)$$

Discretized differential equations: The bed was divided into M cells in the axial direction for both the wake and the dense phases. The discretized differential equation of the jetsam concentration in wake phase for cell ($i = 2 \rightarrow M$) was expressed as follows

G-R Model:

Wake phase:

$$f_W \varepsilon_{B,i} \frac{dC_{W,J,i}}{dt} \cong -\left(f_W \varepsilon_{B,i} U_{B,i} \frac{C_{W,J,i} - C_{W,J,i-1}}{\Delta Z} \right) - f_W C_{W,J,i} \eta_i$$
$$- k_{W,i} f_W \varepsilon_{B,i} (C_{W,J,i} - C_{E,J,i}) \qquad (5.2.12)$$

where η_i is the corresponding *ith* term of $\partial(\varepsilon_B U_B)/\partial Z$. Since there is no material leaving the system, all the material in the downward moving stream is recirculated into the upward moving phase. The discretized equation for the bottom cell, $i = 1$, was consequently derived as

$$f_W \varepsilon_{B,1} \frac{dC_{W,J,1}}{dt} \cong -\left(f_W \varepsilon_{B,1} U_{B,1} \frac{C_{W,J,1} - C_{E,J,1}}{\Delta Z} \right) - f_W C_{W,J,1} \eta_1$$
$$- k_{W,1} f_W \varepsilon_{B,1} (C_{W,J,1} - C_{E,J,1}) \qquad (5.2.13)$$

Dense phase:

The discretized form for the dense phase for cell $i = 2 \rightarrow M - 1$ was expressed as

$$(1 - \varepsilon_{B,i} - f_W \varepsilon_{B,i}) \frac{dC_{E,J,i}}{dt} \cong f_W \varepsilon_{B,i} U_{B,i} \frac{C_{E,J,i+1} - C_{E,J,i}}{\Delta Z} + f_W C_{E,J,i} \eta_i$$
$$+ k_{W,i} f_W \varepsilon_{B,i} (C_{W,J,i} - C_{E,J,i})$$
$$+ 0.75 Y_{GR} \left(\eta_i C_{E,J,i} (1 - C_{E,J,i}) + U_{B,i} \varepsilon_{B,i} (1 - 2C_{E,J,i}) \frac{C_{E,J,i+1} - C_{E,J,i}}{\Delta Z} \right) \qquad (5.2.14)$$

Segregation can not extend beyond the boundary imposed by the distributor at the bottom of the bed. Consequently, the differential equation for cell $i = 1$ was written as

$$(1-\varepsilon_{B,1}-f_W\varepsilon_{B,1})\frac{dC_{E,J,1}}{dt}\cong f_W\varepsilon_{B,1}U_{B,1}\frac{C_{E,J,1+1}-C_{E,J,1}}{\Delta Z}+f_WC_{E,J,1}\eta_1$$
$$+k_{W,1}f_W\varepsilon_{B,1}(C_{W,J,1}-C_{E,J,1})$$
$$+0.75Y_{GR}\left(\eta_1C_{E,J,1}(1-C_{E,J,1})+U_{B,1}\varepsilon_{B,1}(1-2C_{E,J,1})\frac{C_{E,J,1+1}-C_{E,J,1}}{\Delta Z}+U_{B,1}\varepsilon_{B,1}C_{E,J,1}(1-C_{E,J,1})\right) \quad (5.2.15)$$

and for cell $i = M$

$$(1-\varepsilon_{B,M}-f_W\varepsilon_{B,M})\frac{dC_{E,J,M}}{dt}\cong f_W\varepsilon_{B,M}U_{B,M}\frac{C_{W,J,M}-C_{E,J,M}}{\Delta Z}+f_WC_{E,J,M}\eta_M$$
$$+k_{W,M}f_W\varepsilon_{B,M}(C_{W,J,M}-C_{E,J,M})$$
$$+0.75Y_{GR}\left(\eta_MC_{E,J,M}(1-C_{E,J,M})+U_{B,M}\varepsilon_{B,M}(1-2C_{E,J,M})\frac{C_{E,J,M+1}-C_{E,J,M}}{\Delta Z}-U_{B,M}\varepsilon_{B,M}C_{E,J,M}(1-C_{E,J,M})\right) \quad (5.2.16)$$

Yoshida Model:

Wake phase:

For cell $i = 2 \rightarrow M$:

$$f_W\varepsilon_{B,i}\frac{dC_{W,J,i}}{dt}\cong-\left(f_W\varepsilon_{B,i}U_{B,i}\frac{C_{W,J,i}-C_{W,J,i-1}}{\Delta Z}\right)-f_WC_{W,J,i}\eta_i$$
$$-k_{W,i}f_W\varepsilon_{B,i}(C_{W,J,i}-C_{E,J,i})$$
$$-k_{W,i}f_W\varepsilon_{B,i}Y_YC_{E,J,i}(1-C_{W,J,i}) \quad (5.2.17)$$

and the bottom cell $i = 1$

$$f_W\varepsilon_{B,1}\frac{dC_{W,J,1}}{dt}\cong-\left(f_W\varepsilon_{B,1}U_{B,1}\frac{C_{W,J,1}-C_{E,J,1}}{\Delta Z}\right)-f_WC_{W,J,1}\eta_1$$
$$-k_{W,1}f_W\varepsilon_{B,1}(C_{W,J,1}-C_{E,J,1})$$
$$-k_{W,1}f_W\varepsilon_{B,1}Y_YC_{E,J,1}(1-C_{W,J,1}) \quad (5.2.18)$$

Dense phase:

For cell $i = 1 \rightarrow M-1$

$$(1-\varepsilon_{B,i}-f_W\varepsilon_{B,i})\frac{dC_{E,J,i}}{dt} \equiv f_W\varepsilon_{B,i}U_{B,i}\frac{C_{E,J,i+1}-C_{E,J,i}}{\Delta Z}+f_WC_{E,J,i}\eta_i$$
$$+k_{W,i}f_W\varepsilon_{B,i}(C_{W,J,i}-C_{E,J,i})$$
$$+k_{W,i}f_W\varepsilon_{B,i}Y_YC_{E,J,i}(1-C_{W,J,i}) \qquad (5.2.19)$$

for cell $i = M$

$$(1-\varepsilon_{B,M}-f_W\varepsilon_{B,M})\frac{dC_{E,J,M}}{dt} \equiv f_W\varepsilon_{B,M}U_{B,M}\frac{C_{W,J,M}-C_{E,J,M}}{\Delta Z}+f_WC_{E,J,M}\eta_M$$
$$+k_{W,M}f_W\varepsilon_{B,M}(C_{W,J,M}-C_{E,J,M})$$
$$+k_{W,M}f_W\varepsilon_{B,M}Y_YC_{E,J,M}(1-C_{W,J,M}) \qquad (5.2.20)$$

5.2.2 Model Parameters

Bubble parameters : It was assumed that the gas bubbles in the binary mixture behave similarly to those in a fluidized bed of uniform particles. The bubble size, d_B; velocity, U_B; and the bubble fraction, ε_B, were calculated using equations (5.1.13 to 5.1.15) with U_{mf} for the uniform particles replaced by the minimum fluidization velocity of the binary mixture corresponding to the local composition, $U_{mf,c}$. For the purposes of the parametric study, $U_{mf,c}$ and composition were related using the expression proposed by Cheung et al. (1974)

$$U_{mf,c} = U_{mf,F}(U_{mf,J}/U_{mf,F})^{C_J^2} \qquad (5.2.21)$$

It was assumed that when the local concentration reached a level such that the operating velocity became less than the local minimum fluidization velocity, the layer corresponding to the discrete cell under consideration defluidized. This, then, resulted in the moving of the porous destributor to the upper interface of the defluidized layer, that is, to the next upward cell.

Exchange coefficient : Exchange coefficient, ζ_i, based on the results described in **section 5.1.3** were calculated using

$$k_W = \frac{A_{WE}}{d_B};$$

$$A_{WE} = 7.5\left(\frac{U_O}{U_{mf}} - 1\right) \quad for \quad \frac{U_O}{U_{mf}} \leq 3$$

$$A_{WE} = 15.0 \quad for \quad \frac{U_O}{U_{mf}} > 3$$

(5.2.22)

Segregation rate parameter : For solution of the G-R model equations, the dimensionless segregation distance, Y_{GR}, has to be specified. Tanimoto et al. (1980) measured the net distance moved down by agglomerates of jetsam particles in fluidized beds of different flotsam particles. They correlated their experimental results empirically in terms of the density and size ratios of the jetsam and flotsam particles according to

$$Y_{GR} = 0.45\left(\frac{\rho_J}{\rho_F}\right)\left(\frac{d_J}{d_F}\right)^{1/3} \quad -for\ two-dimensional\ bed \qquad (5.2.23a)$$

$$Y_{GR} = 0.6\left(\frac{\rho_J}{\rho_F}\right)\left(\frac{d_J}{d_F}\right)^{1/3} \quad -for\ three-dimensional\ bed \qquad (5.2.23b)$$

Recently Kozanoglu and Levy (1992) have proposed another correlation for the segration coefficient

$$Y_{KL} = 0.0063\frac{d_J - d_F}{d_F} + 0.0426\frac{\rho_J - \rho_F}{\rho_F} \qquad (5.2.24)$$

It should be noted that the values of the segregation coefficient predicted from the correlations of Tanimoto et al.(1980) are significantly larger than those obtained form equation (5.2.24). Beeckmans et al. (1987) have criticized the use of equations (5.2.23a,b) arguing that the segregation velocities predicted are significantly higher than those measured experimentally. However, Naimer et al.

(1982) observe that jetsam moves down in clumps following the passage of the rising bubble. Clearly, the matter is far from being resolved. For the purposes of the parametric study, Y_{GR} was treated as a variable. Further, following equations (5.2.23) and (5.2.24), Y_{GR} was assumed to depend only on the physical properties of the particles comprising the binary system; that is, it was assumed to be independent of the superficial gas velocity.

For solution of the Yoshida model equations, Y_Y was treated as a variable with $0 < Y_Y < 1$ and assumed, like Y_{GR}, to depend only on the physical properties of the particles comprising the binary system.

5.2.3 Parametric Studies

Selected results from the parametric study are presented in **Figures 5.2.2** to **5.2.7**. All these compulations have been made assuming that mass fraction of jetsam in the system is 20%. The results are discussed in terms of the key variables; other model parameters used are indicated in the captions of the figures.

Typical results from calculations using the Gibilaro-Rowe model are shown in **Figure 5.2.2**. In **Figure 5.2.2a**, the jetsam concentration, bubble size and bubble fraction calculations are shown as a function of time at several heights within the bed. It can be seen that the jetsam concentration increases at the lowest levels much faster than at the higher heights. The concentration reaches a plateau value of about 0.7 which is the composition with a minimum fluidization velocity equal to the operating superficial gas velocity. The layer at the bottom of the bed, though richer in jetsam, does contain flotsam due to entrapment (Yang and Keairns, 1982). As the lower levels within the bed get richer in jetsam, the local minimum fluidization velocity changes leading to smaller bubble sizes and smaller bubble fractions as shown in this figure. When the jetsam concentration reaches the

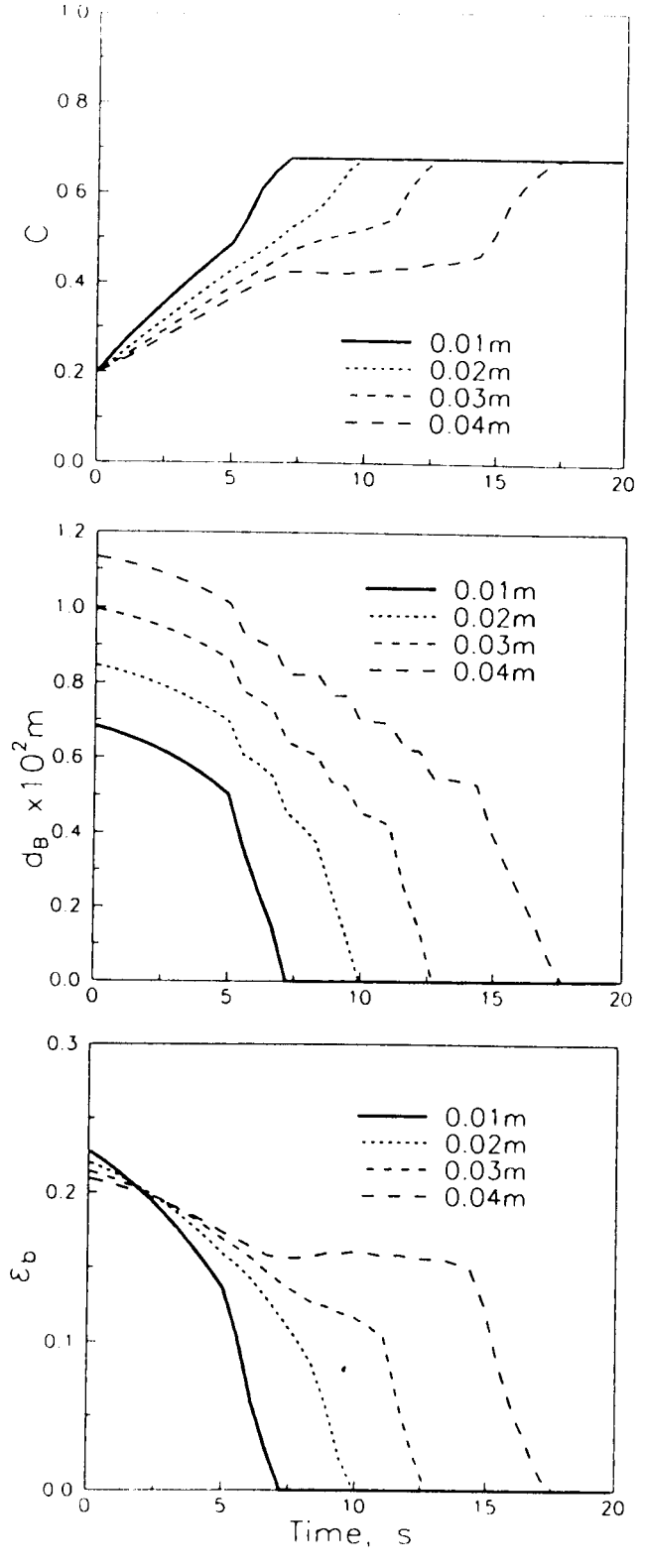

FIGURE 5.2.2a: Simulated response of (i) jetsam concentration; (ii) bubble size and (iii) bubble fraction as a function of time at different bed heights using G-R model (model parameters: U_0 = 0.15m/s; d_J/d_F = 3.0; ρ_J/ρ_F = 1.0, $U_{mf,J}/U_{mf,F}$ = 5.6, Y_{GR} = 0.65, f_W = 0.35)

plateau value (~ 0.7), U_O becomes equal to the local $U_{mf,c}$, the bubble size and fraction approach values of zero and, consequently, the region is assumed to defluidize.

In **Figure 5.2.2b**, calculations are presented for the axial jetsam concentration profile at different times starting from the initially well-mixed condition. It can be seen that the height of the defluidized layer increases with time and the upper portion of the bed gets leaner in jetsam. A more detailed picture of how the height of the defluidized layer increases with time is shown in **Figure 5.2.2c**. From this figure, it can be seen that, for the model parameters used in these calculations, a steady state is achieved after about 25 s and the height of the defluidized layer at this time is about 0.05 m.

Similar calculations using the Yoshida model are presented in **Figure 5.2.3.** For the parameters used in these calculations, a defluidized layer is not predicted. It can be seen from inspection of **Figure 5.2.3a** that the jetsam concentration, bubble size and the bubble fraction reach steady values at different heights at different times ranging from about 10 to 15 s. The axial jetsam concentration profile plotted for different times in **Figure 5.2.3b** shows that the jetsam concentration leading to defluidization is not reached even at the lowest height within the bed. Also, a global steady state, that is for the whole bed, in axial concentration is reached after about 20 s starting from the initially well mixed condition.

The influence of the superficial velocity on the transient response of the jetsam concentration at Z = 0.05 m using the G-R model is shown in **Figure 5.2.4a**. It is seen that the jetsam concentration in the defluidized layer increases as the superficial gas velocity is increased. An extremely important point, to be discussed in context of comparison with experimental data in a later section, is that higher superficial gas velocity leads to a more rapid attainment of steady state; for the

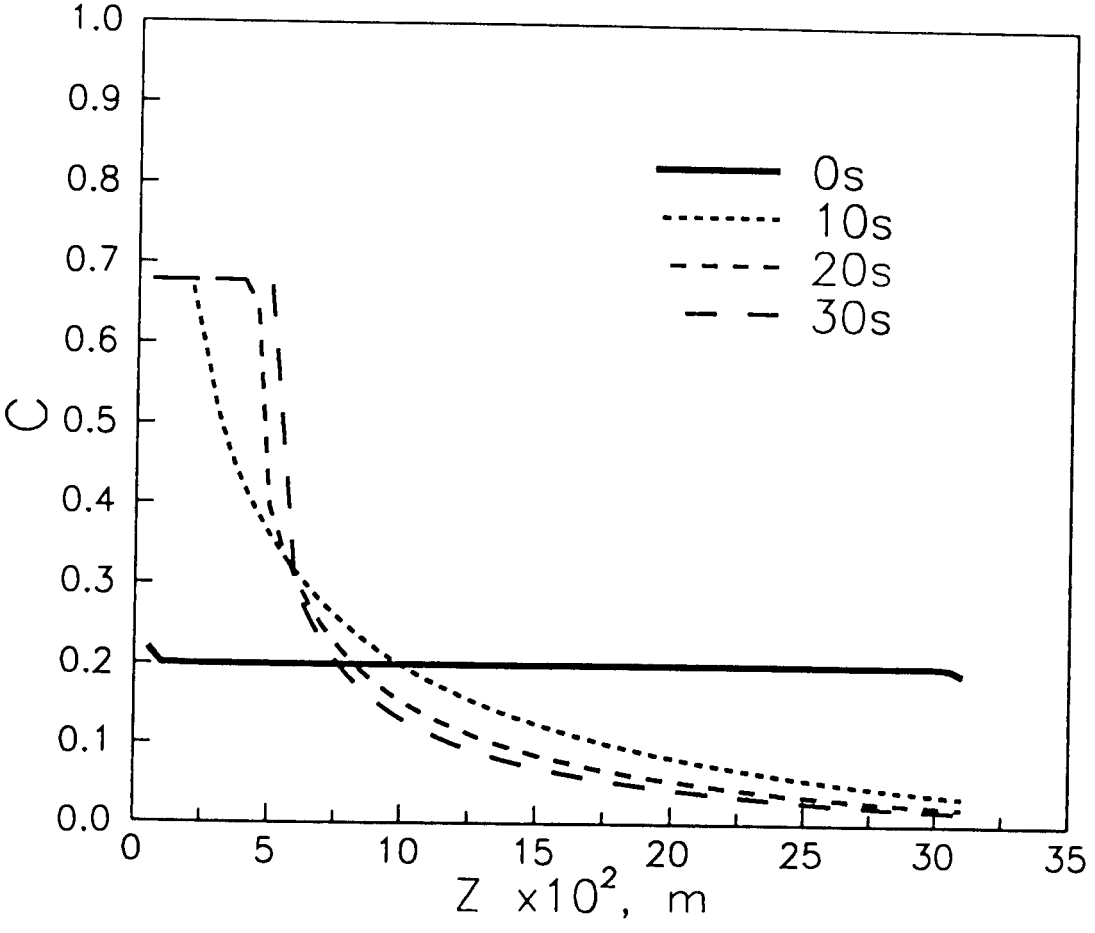

FIGURE 5.2.2b: Simulated response of jetsam concentration as a function of height within the bed at different times using G-R model (model parameters: U_o = 0.15m/s; d_J/d_F = 3.0; ρ_J/ρ_F = 1.0, $U_{mf,J}/U_{mf,F}$ = 5.6, Y_{GR} = 0.65, f_W = 0.35)

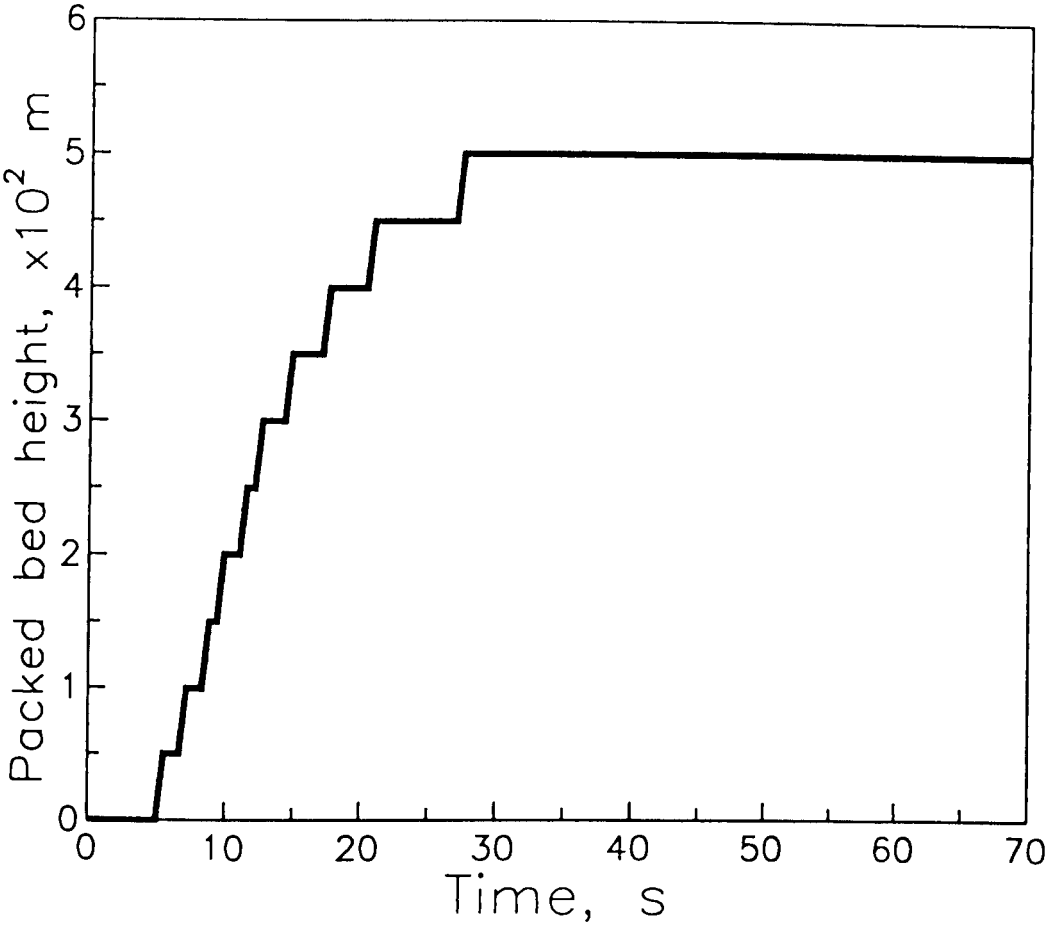

FIGURE 5.2.2c: Predicted height of the defluidized layer as a function of time using G-R model (model parameters: U_o = 0.15m/s; d_J/d_F = 3.0; ρ_J/ρ_F = 1.0, $U_{mf,J}/U_{mf,F}$ = 5.6, Y_{GR} = 0.65, f_W = 0.35)

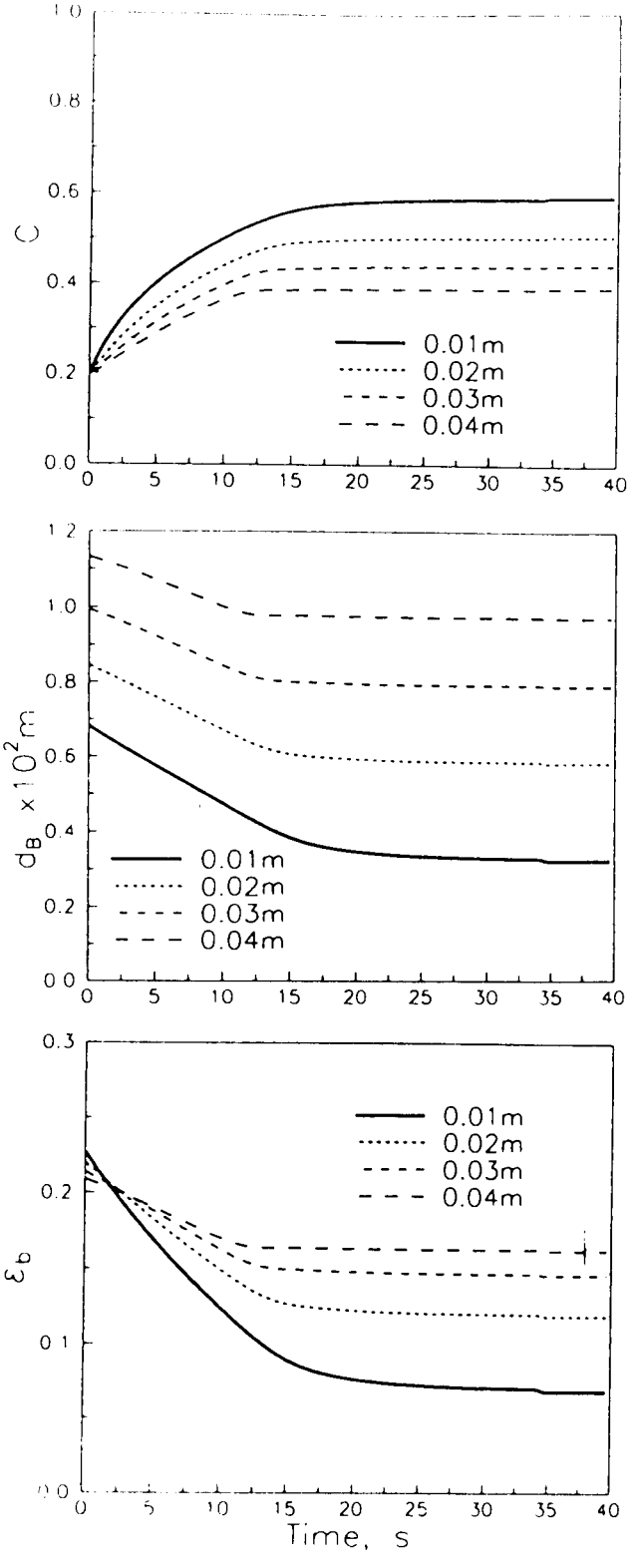

FIGURE 5.2.3a: Simulated response of (i) jetsam concentration; (ii) bubble size and (iii) bubble fraction as a function of time at different bed heights using Yoshida model (model parameters: U_o = 0.15m/s; d_J/d_F = 3.0; ρ_J/ρ_F = 1.0, $U_{mf,J}/U_{mf,F}$ = 5.6, Y_Y = 0.6, f_W = 0.35)

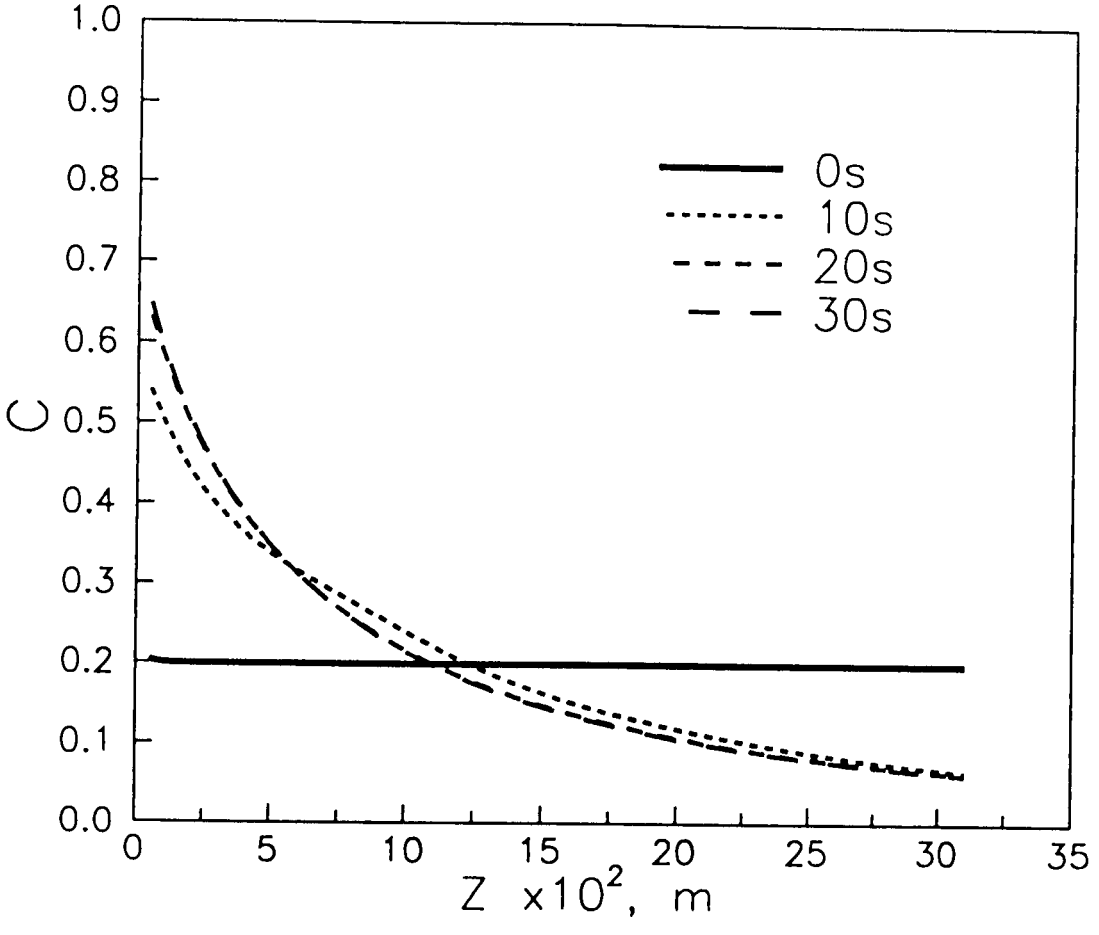

FIGURE 5.2.3b: Simulated response of jetsam concentration as a function of height within the bed at different times using Yoshida model (model parameters: U_o = 0.15m/s; d_J/d_F = 3.0; ρ_J/ρ_F = 1.0, $U_{mf,J}/U_{mf,F}$ = 5.6, Y_Y = 0.6, f_W = 0.35)

conditions used, this time is about 12 s for U_O = 0.1 m/s and about 2 s for U_O = 0.3 m/s. It should be noted that the attainment of the local steady state (at the specific height under consideration) does not necessarily imply that global steady state has been reached. In **Figure 5.2.4b**, the axial concentration profiles are plotted for t = 60 s. Calculations shown in **Figure 5.2.4a**, show that higher superficial velocities lead to smaller heights of the defluidized layer containing higher fraction of jetsam. A combination of these phenomena could lead to higher or lower jetsam concentration in the upper regions of the bed with increasing superficial gas velocities. The heights of the defluidized layer with time for the different superficial velocities are plotted in **Figure 5.2.4c**, these results essentially reinforce the conclusions drawn from the earlier calculations.

The influence of superficial gas velocity on the calculations using the Yoshida model are shown in **Figures 5.2.5a-c**. The calculations of the transient jetsam concentration at Z = 0.05 for different superficial gas velocities reveal that the concentration of the jetsam in the defluidized layer can increase as well as decrease with increasing superficial gas velocities. In agreement with the trends observed using the G-R model, the attainment of the local steady state is more rapid as the superficial velocity is increased. Calculations for the axial jetsam concentration profile, **Figure 5.2.5b**, indicate that a defluidized layer is formed only at the lowest superficial gas velocity of 0.1 m/s. The progression of this interface with time is shown in **Figure 5.2.5c**.

The influence of the dimensionless segregation parameter, Y_{GR}, on the calculations using the G-R model is shown in **Figures 5.2.6a-c**. In **Figure 5.2.6a**, the results, for the transient jetsam concentration at Z = 0.05 m are plotted. It can be seen that higher values of Y_{GR} lead to a more rapid formation of the defluidized layer (and attainment of local steady state). The concentration of the jetsam in

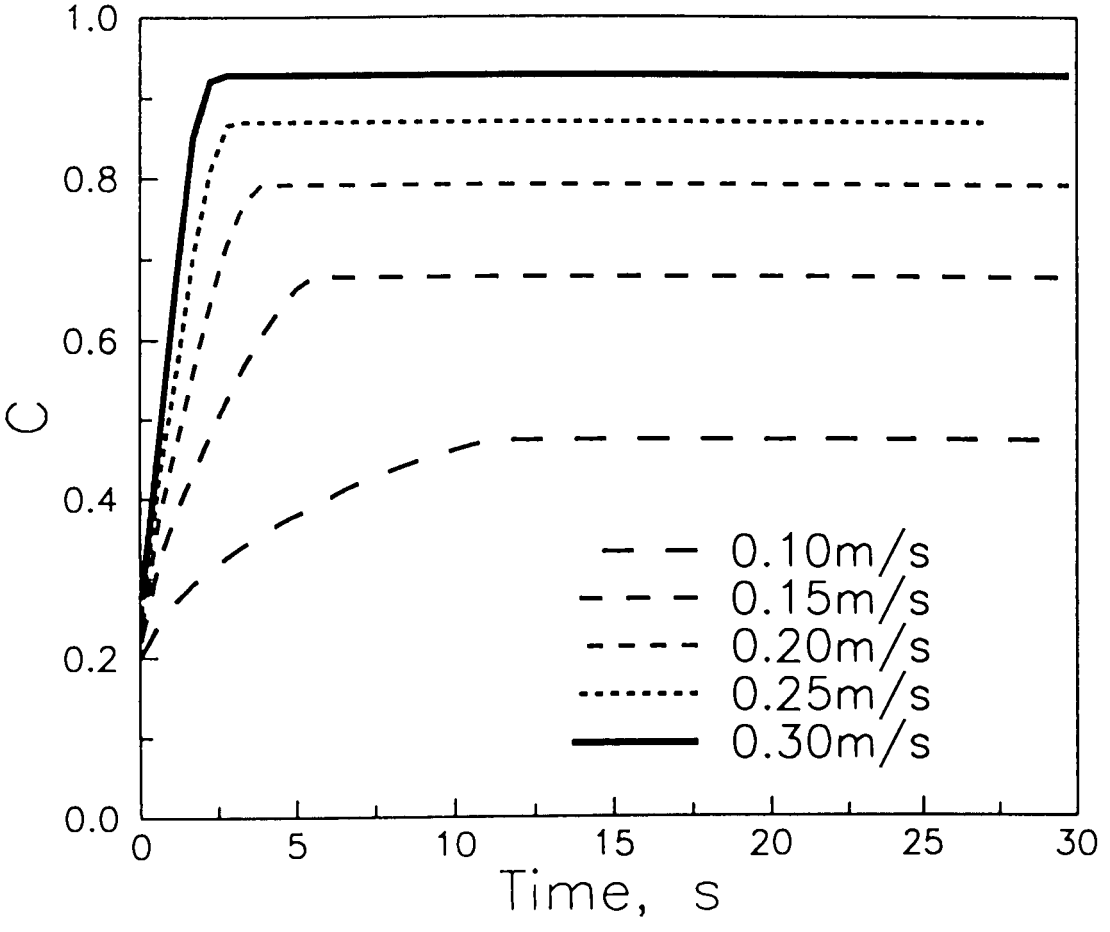

FIGURE 5.2.4a: Influence of superficial gas velocity on the transient response of jetsam concentration at Z = 0.05m using G-R model (model parameters: U_o = variable; d_J/d_F = 3.0; ρ_J/ρ_F = 1.0, $U_{mf,J}/U_{mf,F}$ = 5.6, Y_{GR} = 0.65, f_W = 0.35)

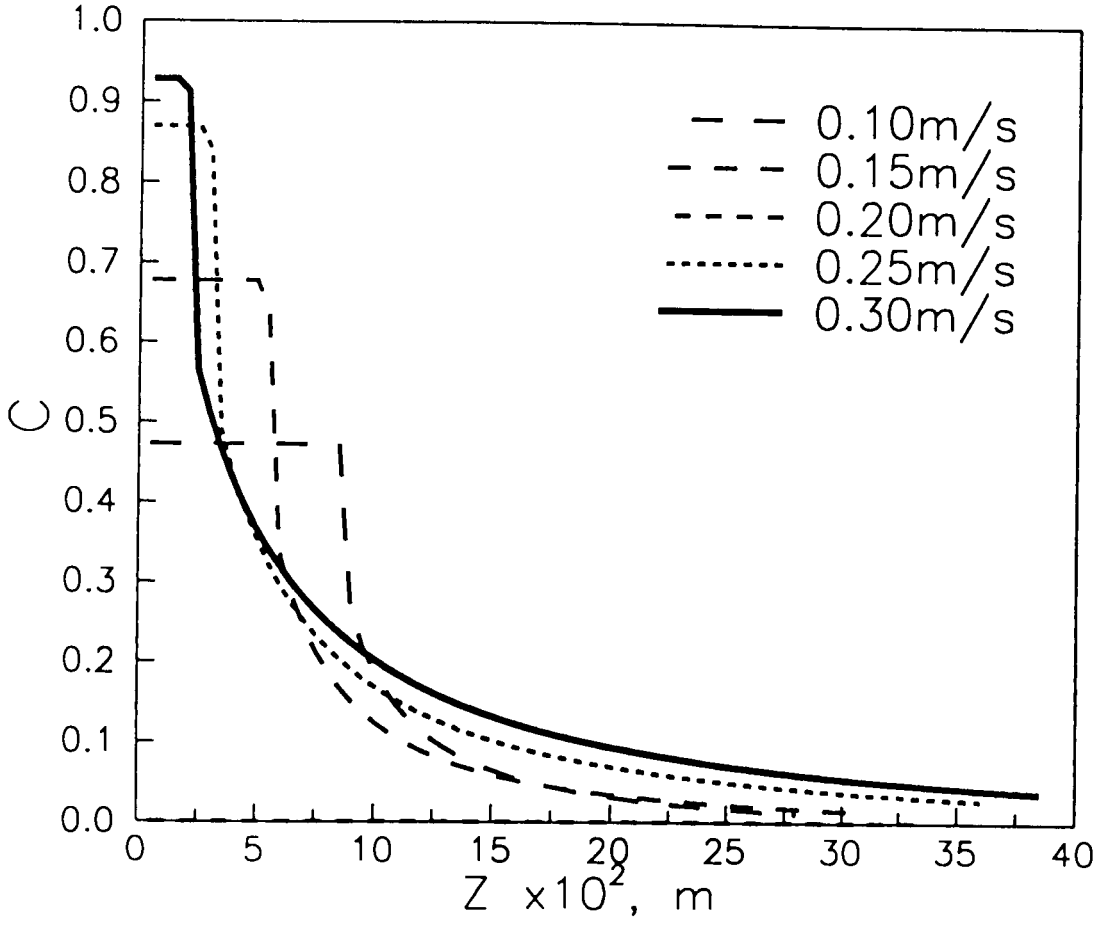

FIGURE 5.2.4b: Influence of superficial gas velocity on the axial jetsam concentration profile at t = 60s using G-R model (model parameters: U_o = variable; d_J/d_F = 3.0; ρ_J/ρ_F = 1.0, $U_{mf,J}/U_{mf,F}$ = 5.6, Y_{GR} = 0.65, f_W = 0.35)

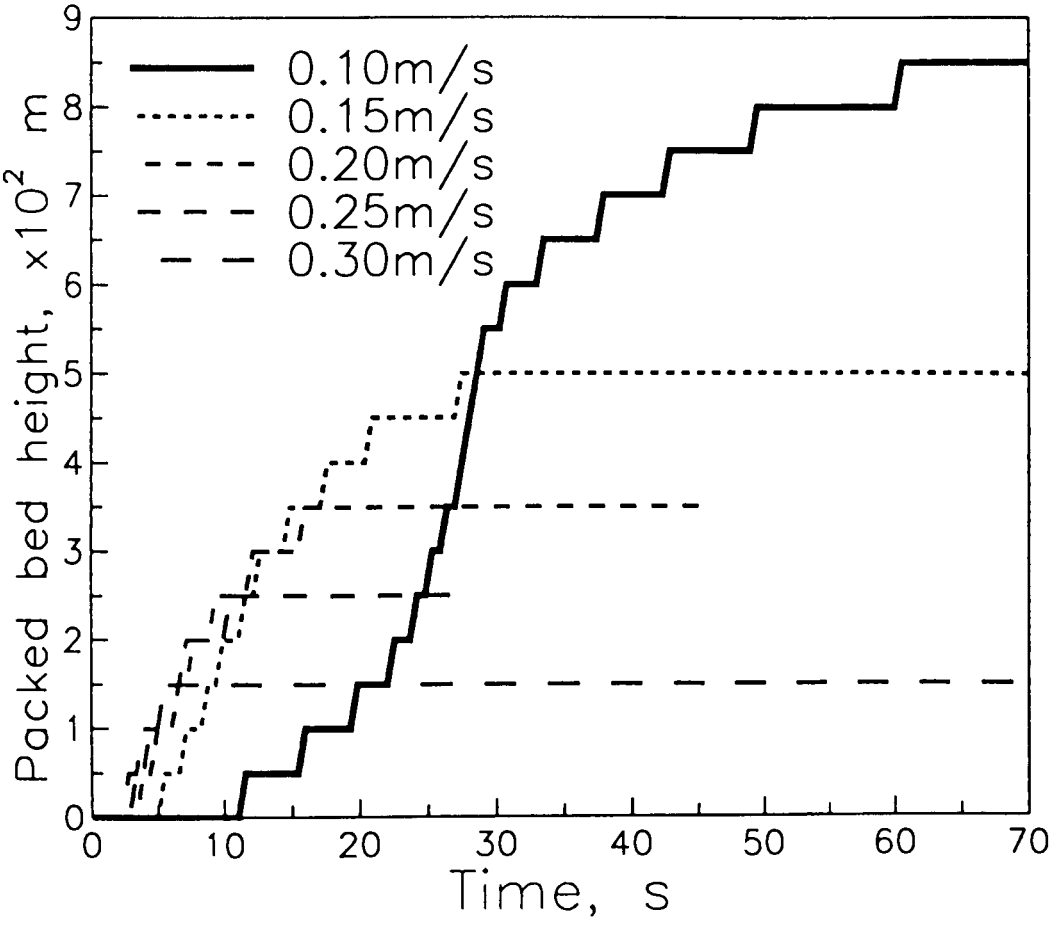

FIGURE 5.2.4c: Influence of superficial gas velocity on the predicted height of the defluidized layer as a function of time using G-R model (model parameters: U_o = variable; d_J/d_F = 3.0; ρ_J/ρ_F = 1.0, $U_{mf,J}/U_{mf,F}$ = 5.6, Y_{GR} = 0.65, f_W = 0.35)

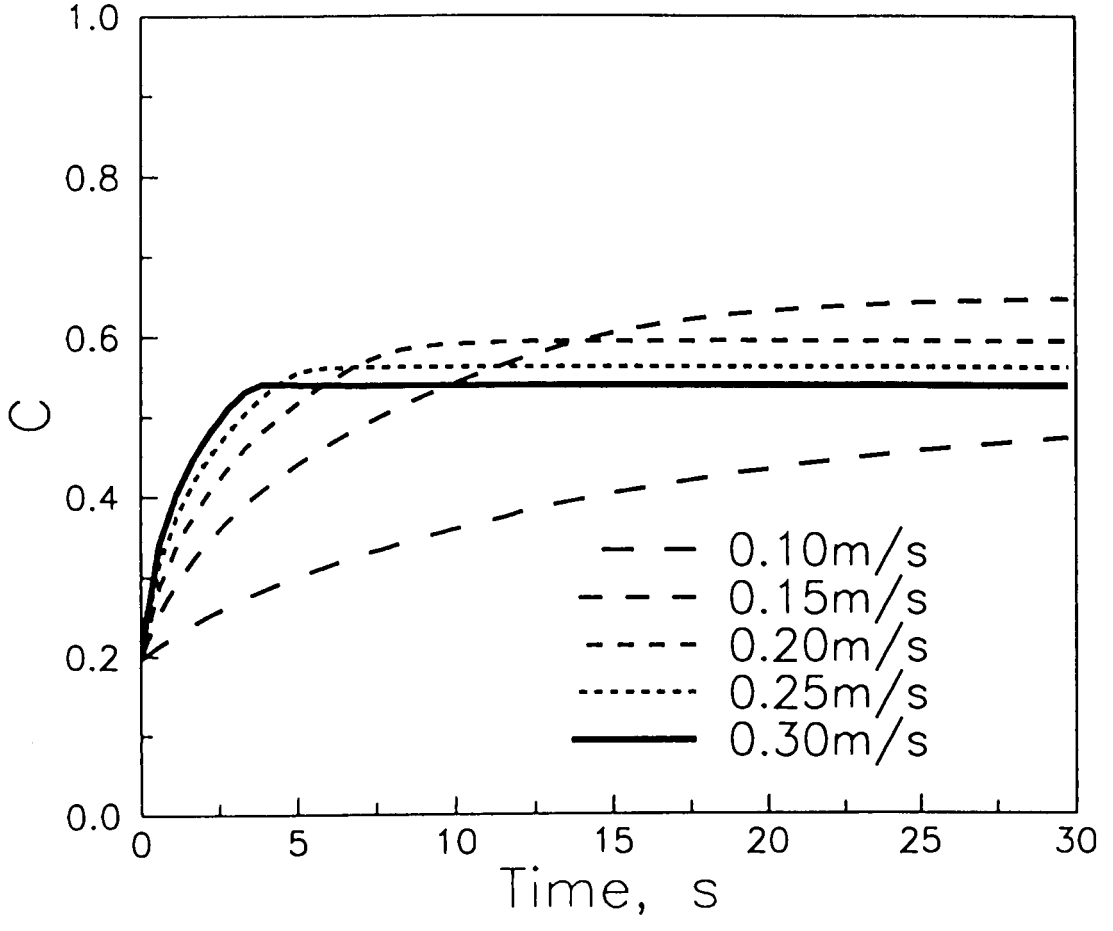

FIGURE 5.2.5a: Influence of superficial gas velocity on the transient response of jetsam concentration at Z = 0.05m using Yoshida model (model parameters: U_o = variable; d_J/d_F = 3.0; ρ_J/ρ_F = 1.0, $U_{mf,J}/U_{mf,F}$ = 5.6, Y_Y = 0.6, f_W = 0.35)

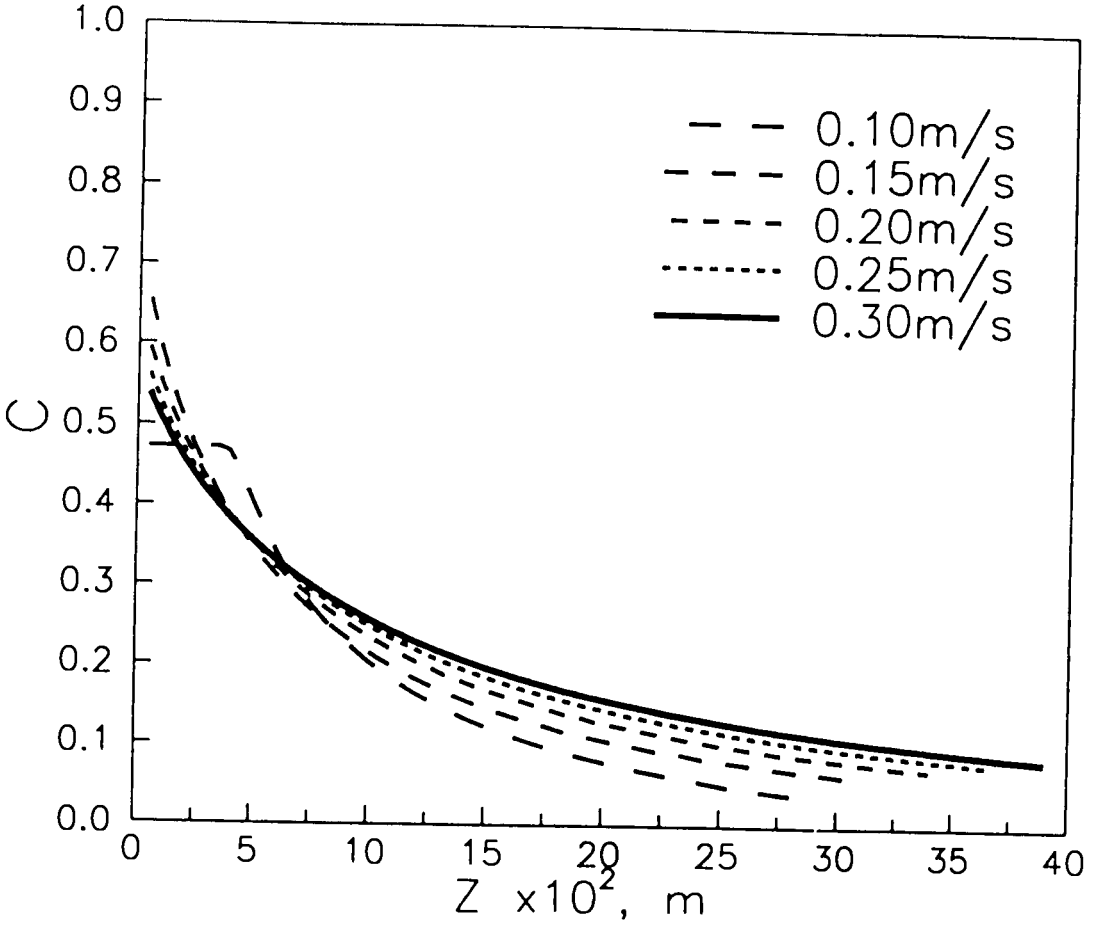

FIGURE 5.2.5b: Influence of superficial gas velocity on the axial jetsam concentration profile at t = 60s using Yoshida model (model parameters: U_o = variable; d_J/d_F = 3.0; ρ_J/ρ_F = 1.0, $U_{mf,J}/U_{mf,F}$ = 5.6, Y_Y = 0.6, f_W = 0.35)

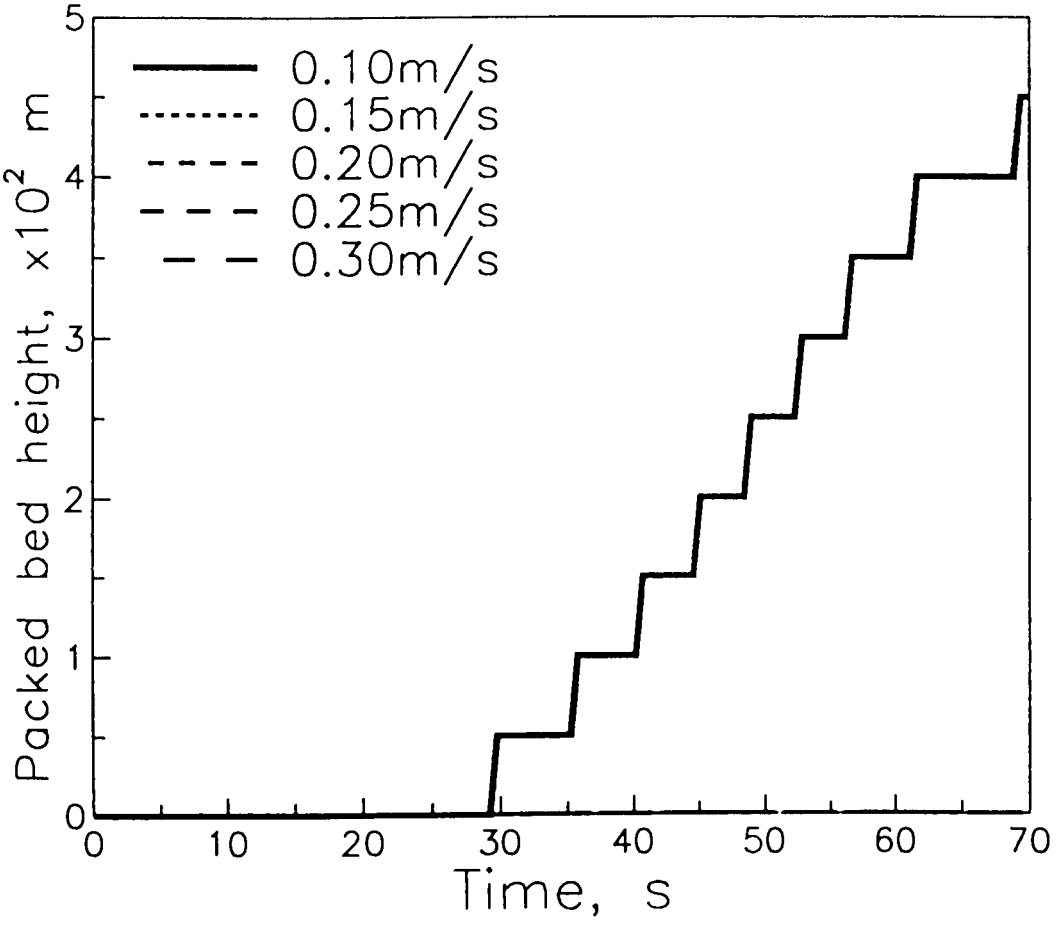

FIGURE 5.2.5c: Influence of superficial gas velocity on the predicted height of the defluidized layer as a function of time using Yoshida model (model parameters: U_o = variable; d_J/d_F = 3.0; ρ_J/ρ_F = 1.0, $U_{mf,J}/U_{mf,F}$ = 5.6, Y_Y = 0.6, f_W = 0.35)

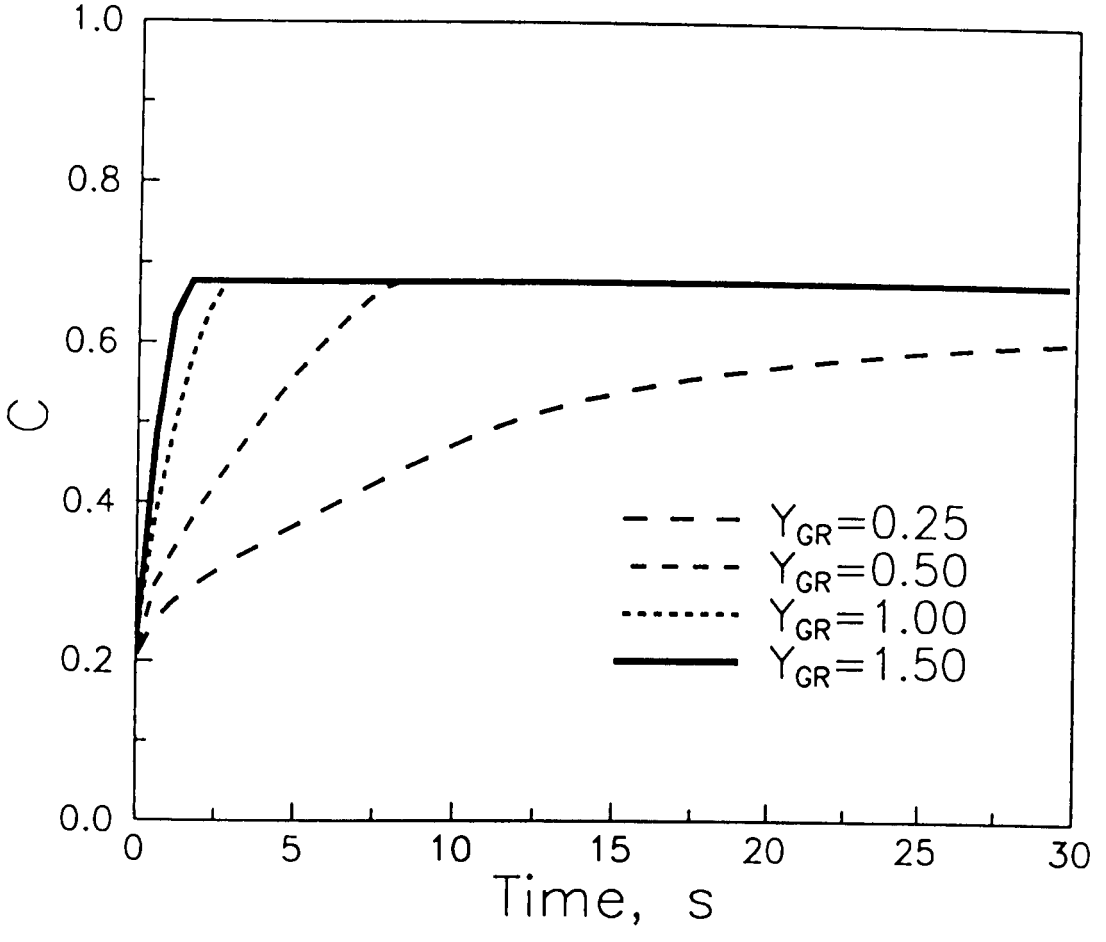

FIGURE 5.2.6a: Influence of segregation rate parameter on the transient response of jetsam concentration at Z = 0.05m using G-R model (model parameters: U_o = 0.15m/s; d_J/d_F = 3.0; ρ_J/ρ_F = 1.0, $U_{mf,J}/U_{mf,F}$ = 5.6, Y_{GR} = variable, f_W = 0.35)

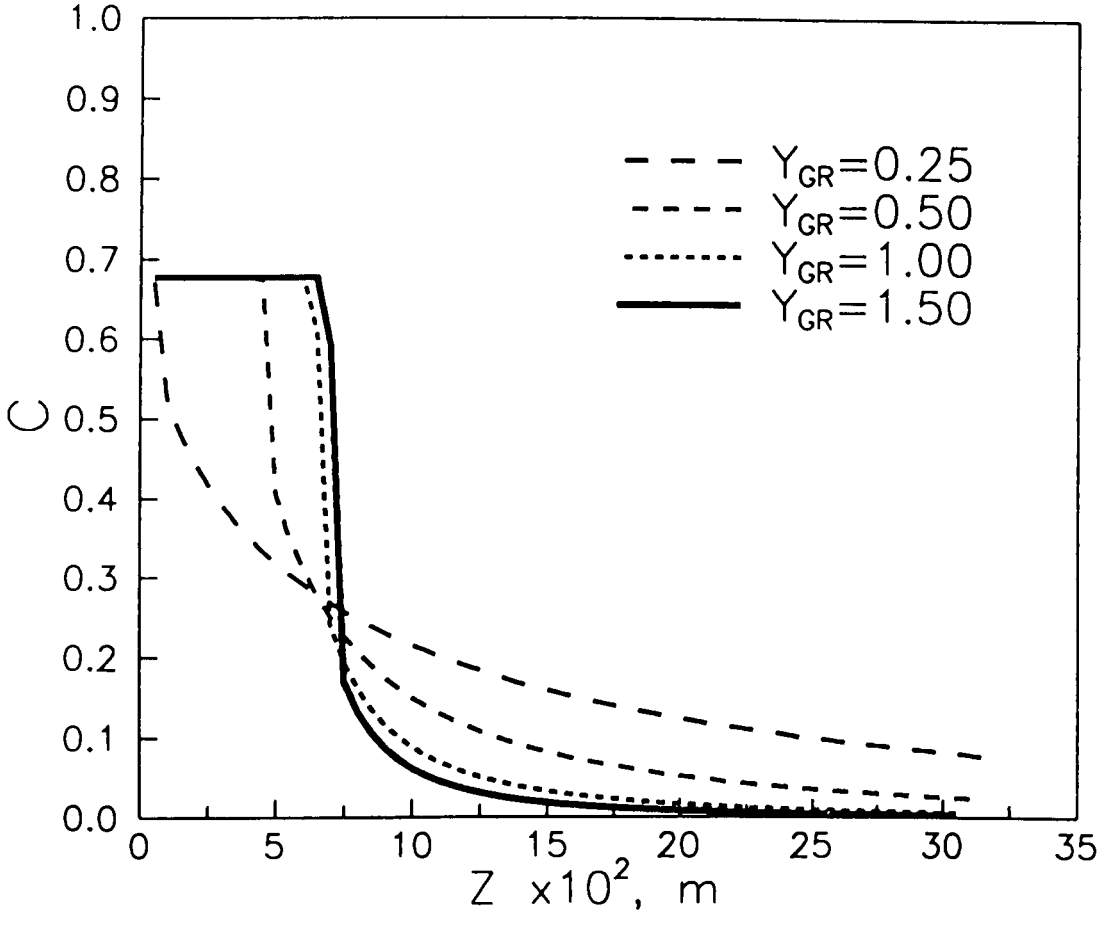

FIGURE 5.2.6b: Influence of segregation rate parameter on the axial jetsam concentration profile at t = 60s using G-R model (model parameters: U_o = 0.15m/s; d_J/d_F = 3.0; ρ_J/ρ_F = 1.0, $U_{mf,J}/U_{mf,F}$ = 5.6, Y_{GR} = variable, f_W = 0.35)

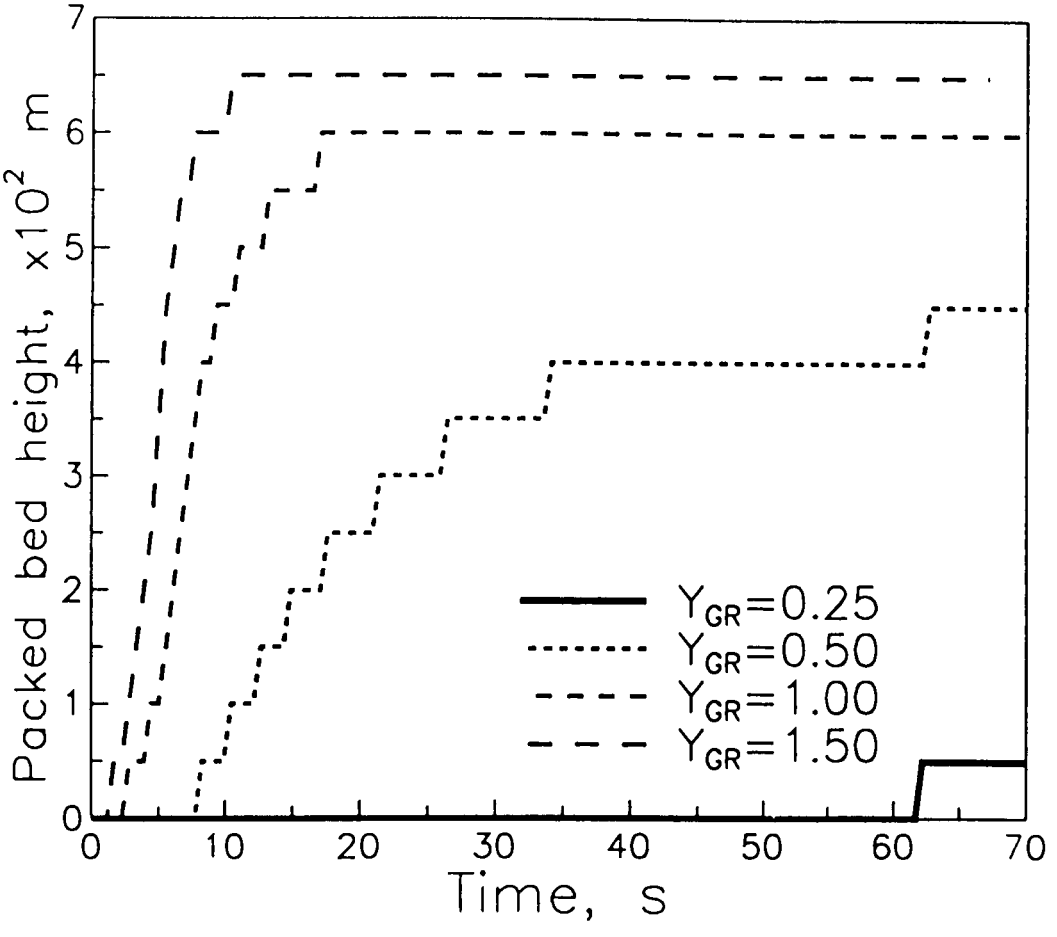

FIGURE 5.2.6c: Influence of segregation rate parameter on the predicted height of the defluidized layer as a function of time using G-R model (model parameters: U_o = 0.15m/s; d_J/d_F = 3.0; ρ_J/ρ_F = 1.0, $U_{mf,J}/U_{mf,F}$ = 5.6, Y_{GR} = variable, f_W = 0.35)

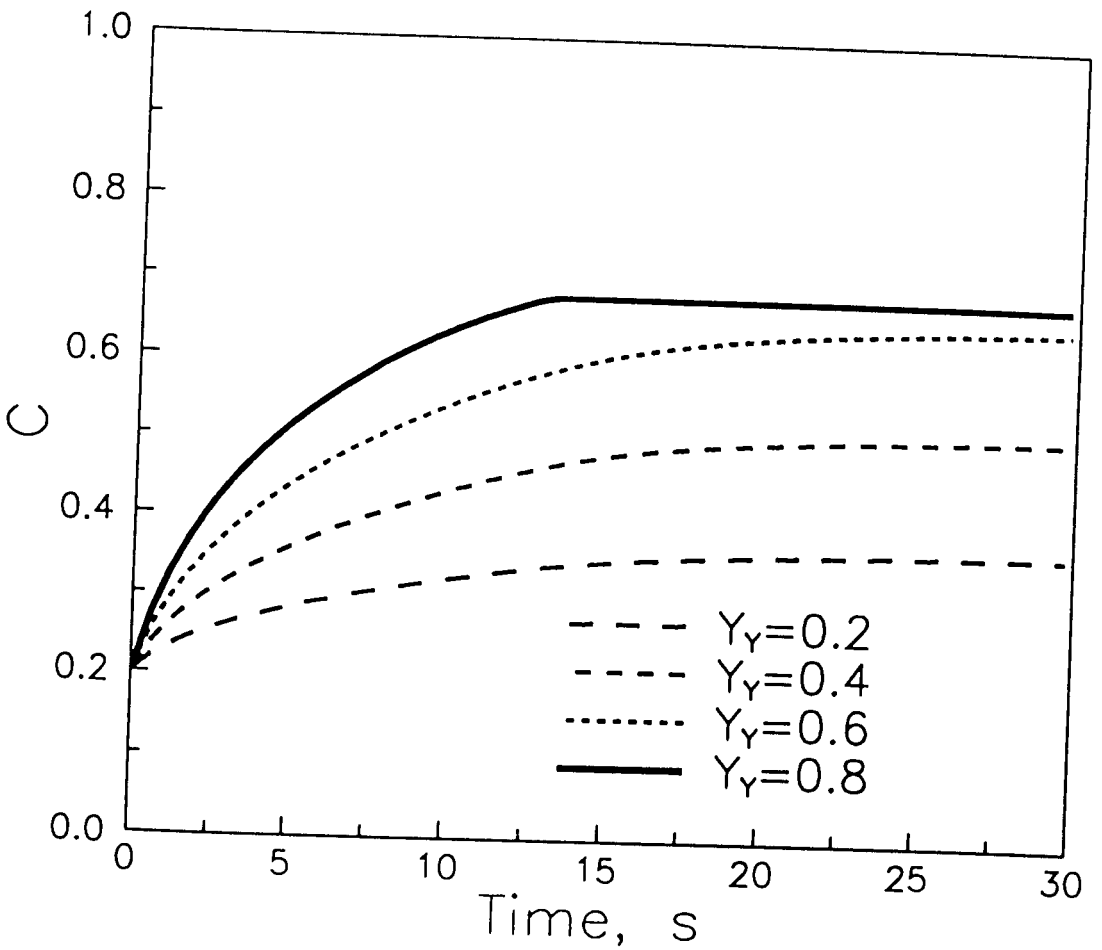

FIGURE 5.2.7a: Influence of segregation rate parameter on the transient response of jetsam concentration at Z = 0.05m using Yoshida model (model parameters: U_o = 0.15m/s; d_J/d_F = 3.0; ρ_J/ρ_F = 1.0, $U_{mf,J}/U_{mf,F}$ = 5.6, Y_Y = variable, f_W = 0.35)

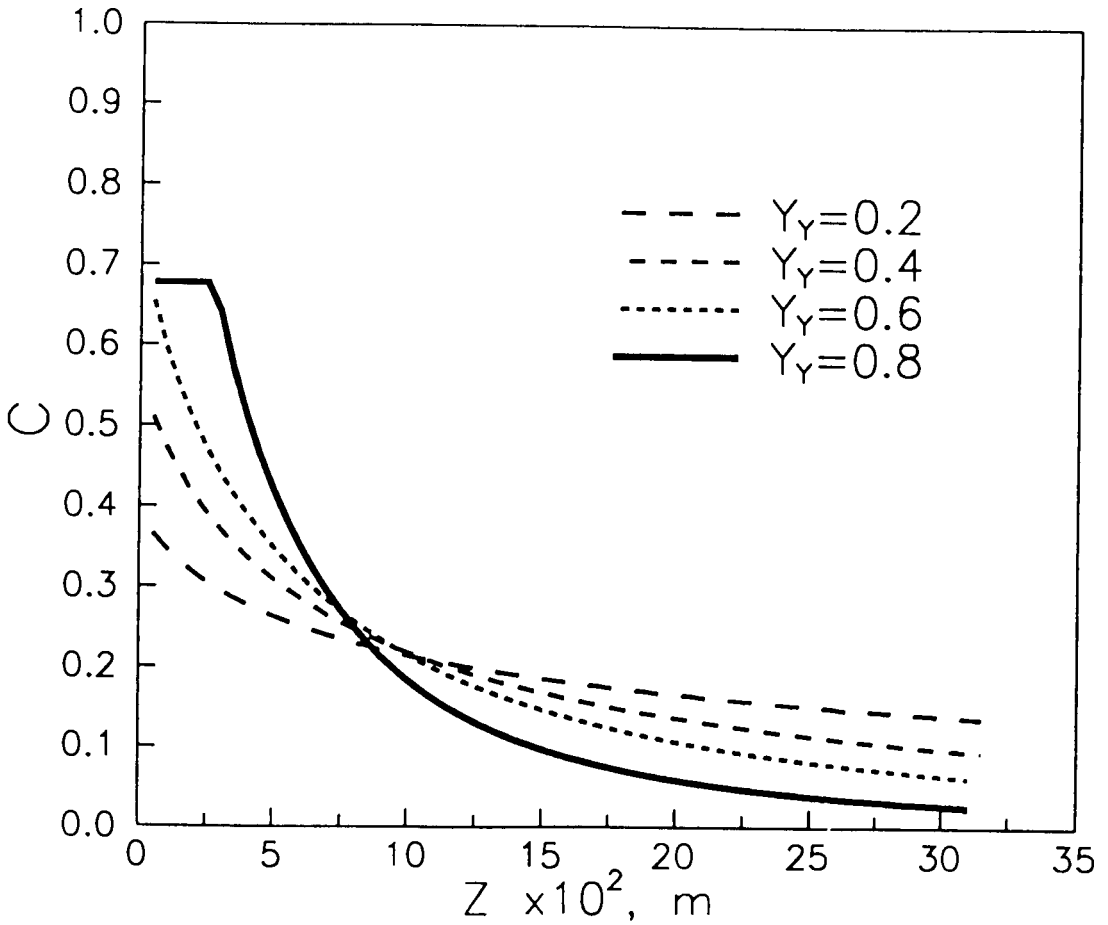

FIGURE 5.2.7b: Influence of segregation rate parameter on the axial jetsam concentration profile at t = 60s using Yoshida model (model parameters: U_o = 0.15m/s; d_J/d_F = 3.0; ρ_J/ρ_F = 1.0, $U_{mf,J}/U_{mf,F}$ = 5.6, Y_Y =variable, f_W = 0.35)

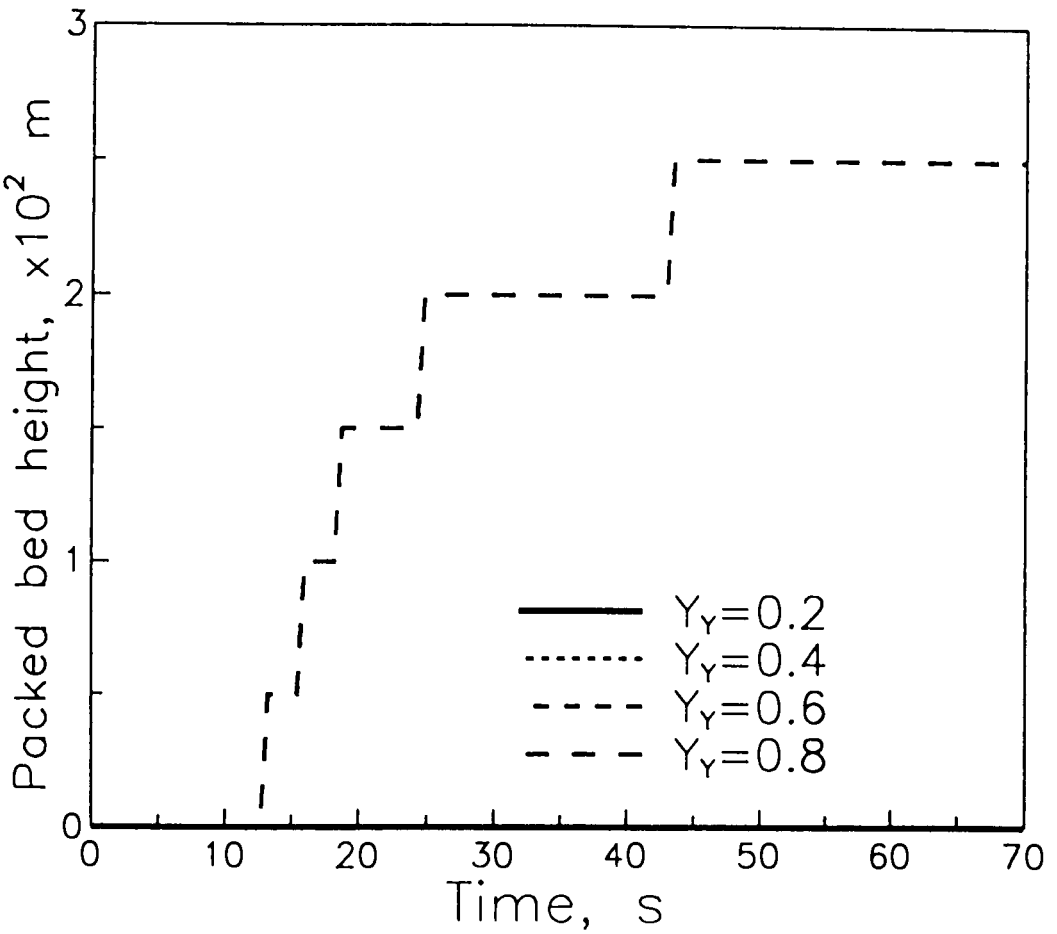

FIGURE 5.2.7c: Influence of segregation rate parameter on the predicted height of the defluidized layer as a function of time using Yoshida model (model parameters: U_o = 0.15m/s; d_J/d_F = 3.0; ρ_J/ρ_F = 1.0, $U_{mf,J}/U_{mf,F}$ = 5.6, Y_Y = variable, f_W = 0.35)

the defluidized layer is, of course, independent of Y_{GR}. The axial concentration profiles at t = 60 s, plotted in **Figure 5.2.6b**, show that higher values of Y_{GR} lead to a higher height for the defluidized layer as well as lower jetsam concentrations in the upper region of the fluidized bed. Further, the sharpness of the interface increases with Y_{GR}. These conclusions are reinforced considering results for the variation of the height of the defluidized layer with time plotted in **Figure 5.2.6c**.

Similar calculations, showing the influence of Y_Y on calculations for the jetsam concentration using the Yoshida model are shown in **Figures 5.2.7a-c**. These figures show that increase in Y_Y leads to more rapid attainment of local steady state conditions. Further, the formation of a defluidized layer is predicted only for $Y_Y = 0.8$.

From the parametric calculations, it was concluded that the two models predict qualitatively the same behaviour in terms of the influence of various parameters on the axial and temporal jetsam concentration profiles.

5.2.4 Comparison with Experimental Results

Minimum fluidization velocity of binary mixtures : The experimentally measured minimum fluidization velocities of the binary mixtures used in this investigation are plotted as a function of the jetsam mass fraction in **Figures 5.2.8a** and **b**. The measurements were made using the fast-defluidization technique described by Nienow and Chiba (1985). The results for the equi-density systems considered (Sets A and B, **Table 3.5**) are plotted in **Figure 5.2.8a** whereas the results for particles with differing densities and sizes (Sets C and D, **Table 3.5**) are shown in **Figure 5.2.8b**. For comparison with these data, the correlation of Cheung et al. (1974) - equation (5.2.21) - is also plotted in these figures. It is clear that the Cheung equation predicts data for the equi-density systems well, **Figure**

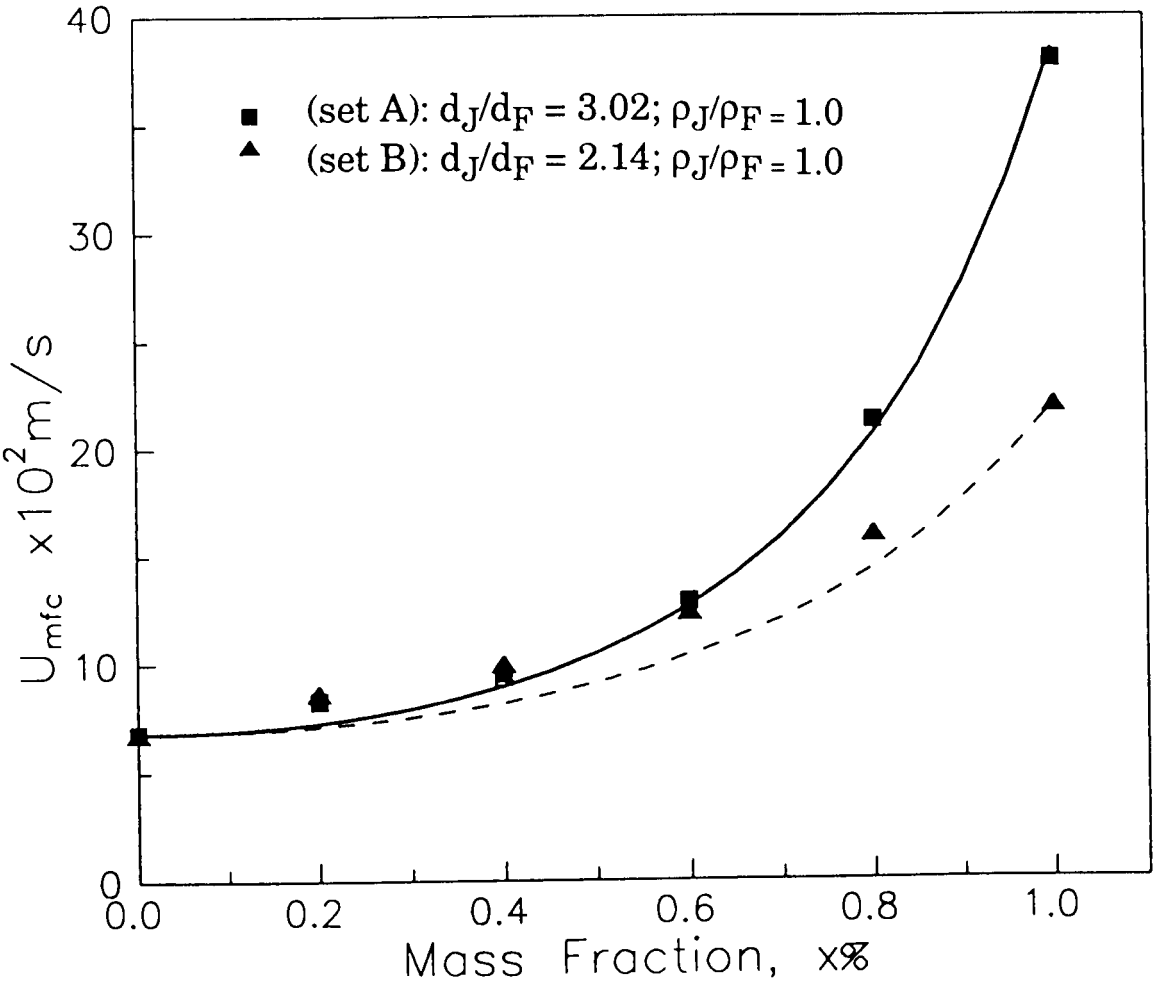

FIGURE 5.2.8a: Experimentally measured minimum fluidization velocity as a function of jetsam mass fraction in binary mixtures of equi-density particles

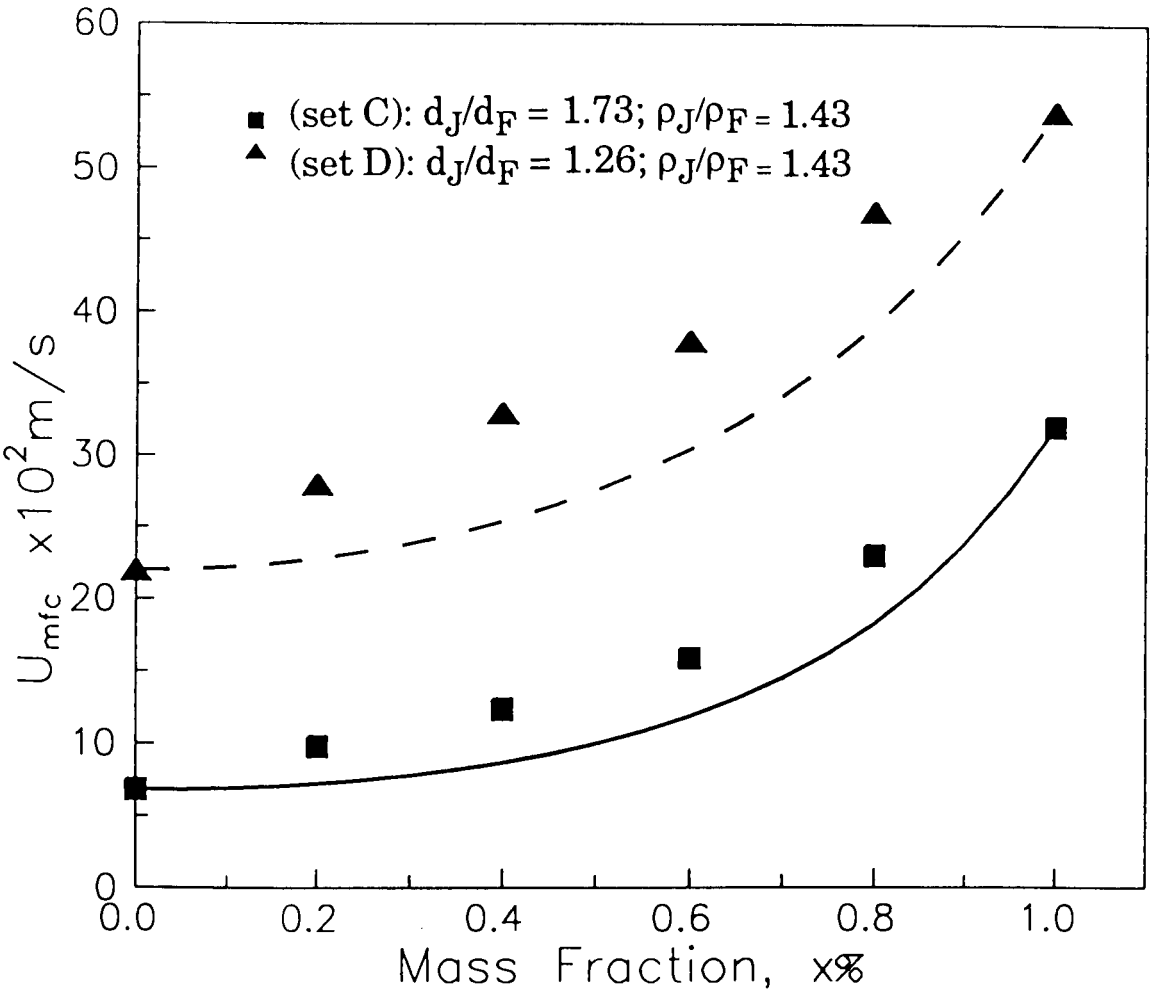

FIGURE 5.2.8b: Experimentally measured minimum fluidization velocity as a function of jetsam mass fraction in binary mixtures of particles of differing densities and sizes

5.2.8a; this observation is in agreement with previous comparisons (Nienow and Chiba, 1985). For particles of differing densities and sizes, the Cheung equation under-predicts the minimum fluidization velocities of the mixtures as shown in **Figure 5.2.8b**, this, too, is in accord with reported work (Nienow and Chiba, 1985).

Jetsam concentration profiles : The experimental measurements on the segregation behaviour of the binary systems considered, **Table 3.5**, are presented in **Figures 5.2.9** to **5.2.14**. The data for Set A particles fluidized using a superficial gas velocity of U_O = 0.155 m/s are presented in **Figures 5.2.9a-c**. The transient jetsam concentrations at different heights within the bed are shown in **Figure 5.2.9a**. These data are qualitatively similar to predictions of G-R and Yoshida models shown in **Figures 5.2.2a(i)** and **5.2.3.a(i)** respectively. The variation of the measured bubble fraction as a function of time at different heights within the bed is shown in **Figure 5.2.9b**. These results, too, are in qualitative agreement with predictions plotted from the two models in **Figures 5.2.2a(iii)** and **5.2.3a(iii)** respectively. The axial jetsam concentration profiles at different times, **Figure 5.2.9c**, are also in qualitative agreement with model calculations shown in **Figures 5.2.2b** and **5.2.3b**. The data for Set C particles with U_O = 0.152 m/s plotted in **Figures 5.2.10a-c** show similar trends. It would appear from such comparisons that, for a given superficial velocity, the theoretical models, with appropriate choice of parameters, can be made to fit the experimental data.

Discrepancy between model calculations and experimental data is brought forth when the concentration versus time data at different superficial velocities are considered as shown in **Figure 5.2.11a**. These data, at Z = 0.02 m, were obtained using Set A particles. From these data, it is clear that a higher superficial velocity leads to a slower attainment of steady state concentrations at the axial

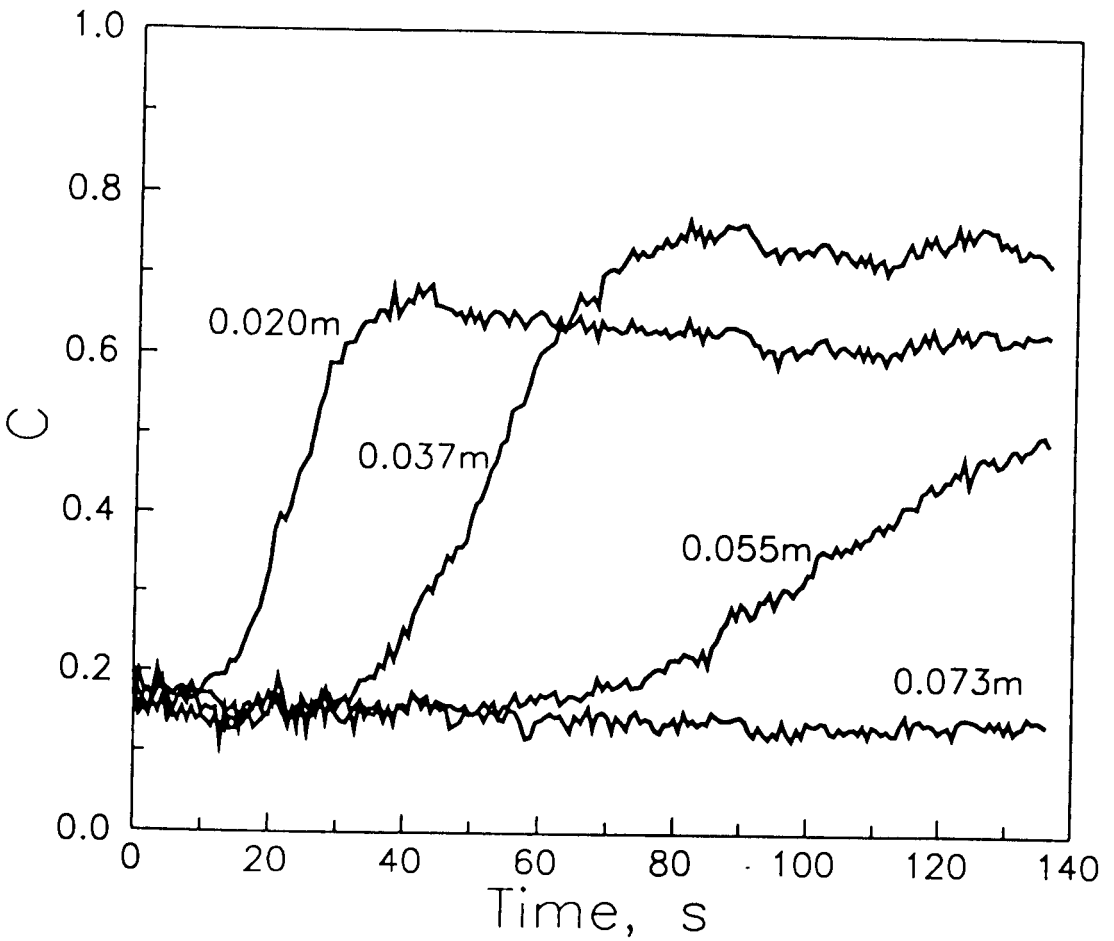

FIGURE 5.2.9a: Experimental response of jetsam concentration as a function of time at different bed heights for U_o = 0.155m/s; particle properties (set A): d_J/d_F = 3.02; ρ_J/ρ_F = 1.0, $U_{mf,J}/U_{mf,F}$ = 5.6

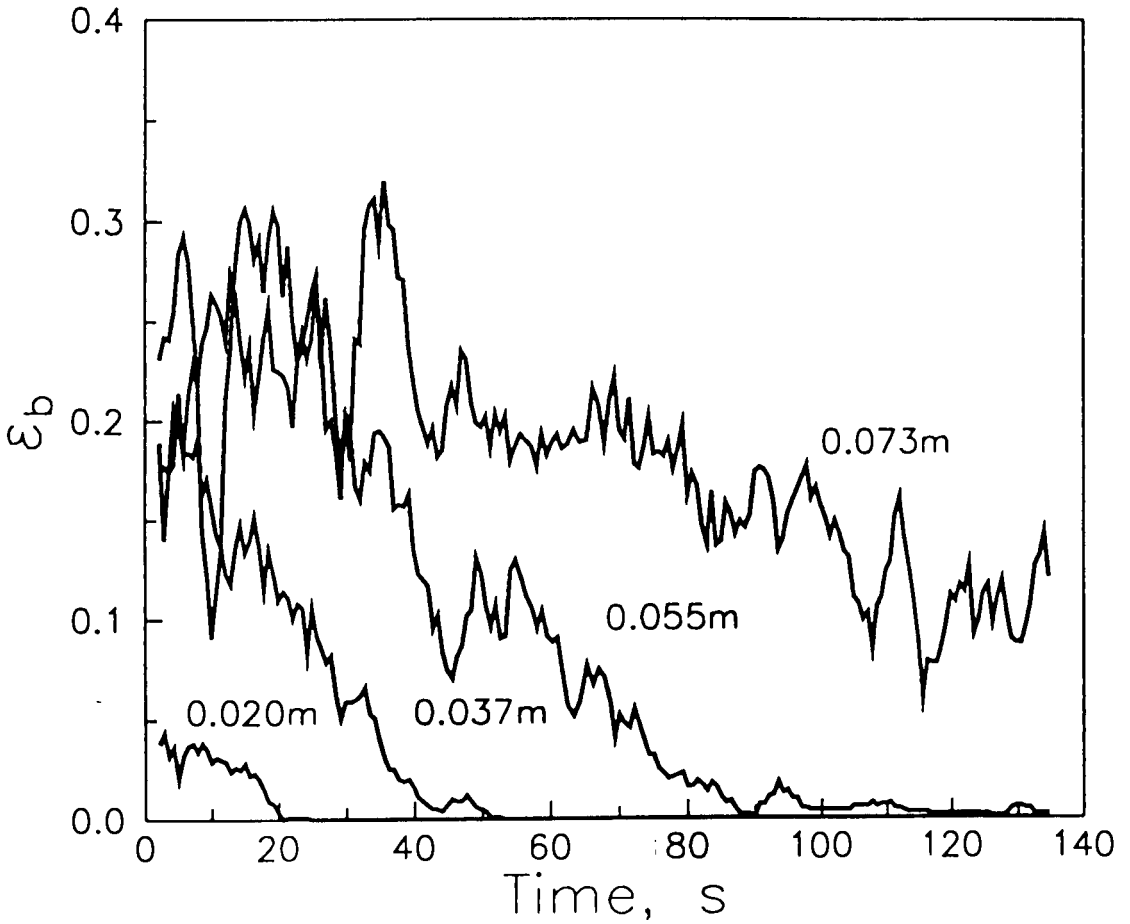

FIGURE 5.2.9b: Experimental response of bubble fraction as a function of time at different bed heights for U_o = 0.155m/s; particle properties (set A): d_J/d_F = 3.02; ρ_J/ρ_F = 1.0, $U_{mf,J}/U_{mf,F}$ = 5.6

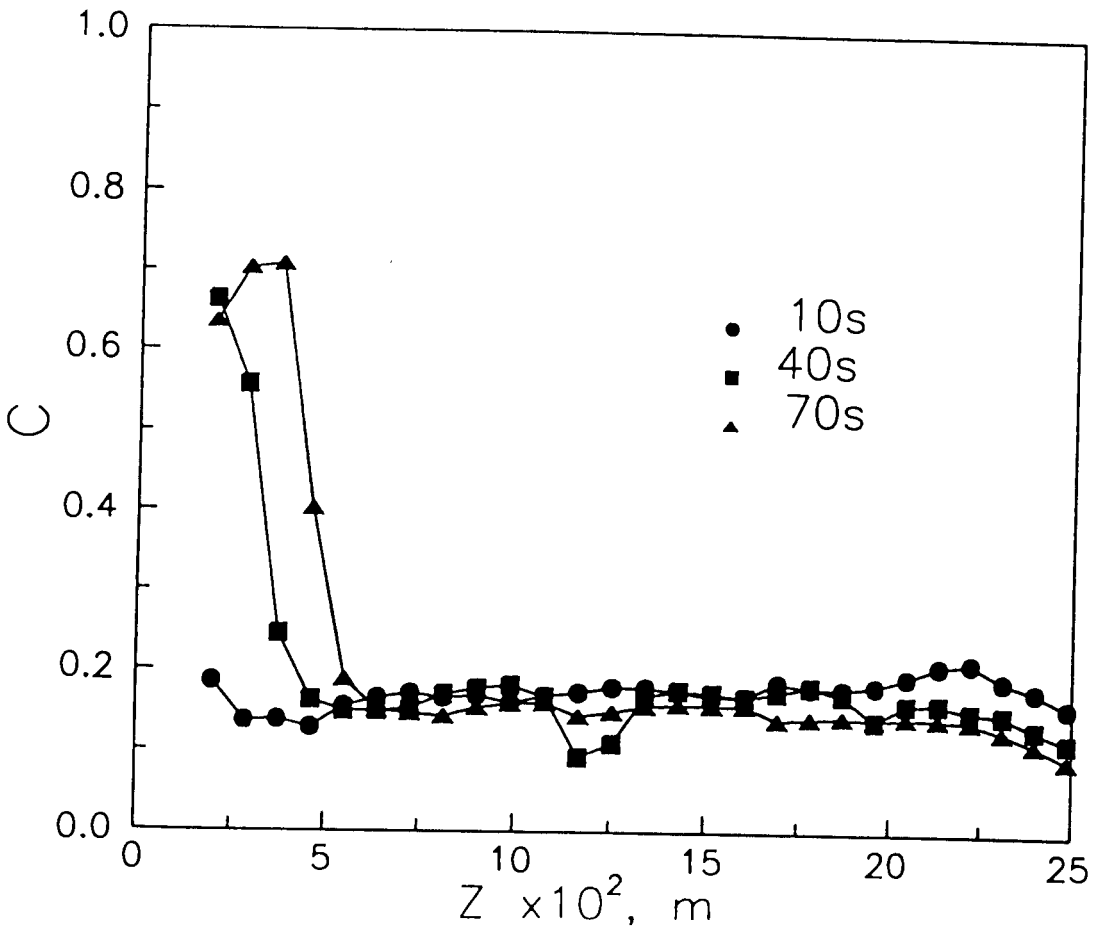

FIGURE 5.2.9c: Experimental axial jetsam concentration profile at different times for U_o = 0.155m/s; particle properties (set A): d_J/d_F = 3.02; ρ_J/ρ_F = 1.0, $U_{mf,J}/U_{mf,F}$ = 5.6

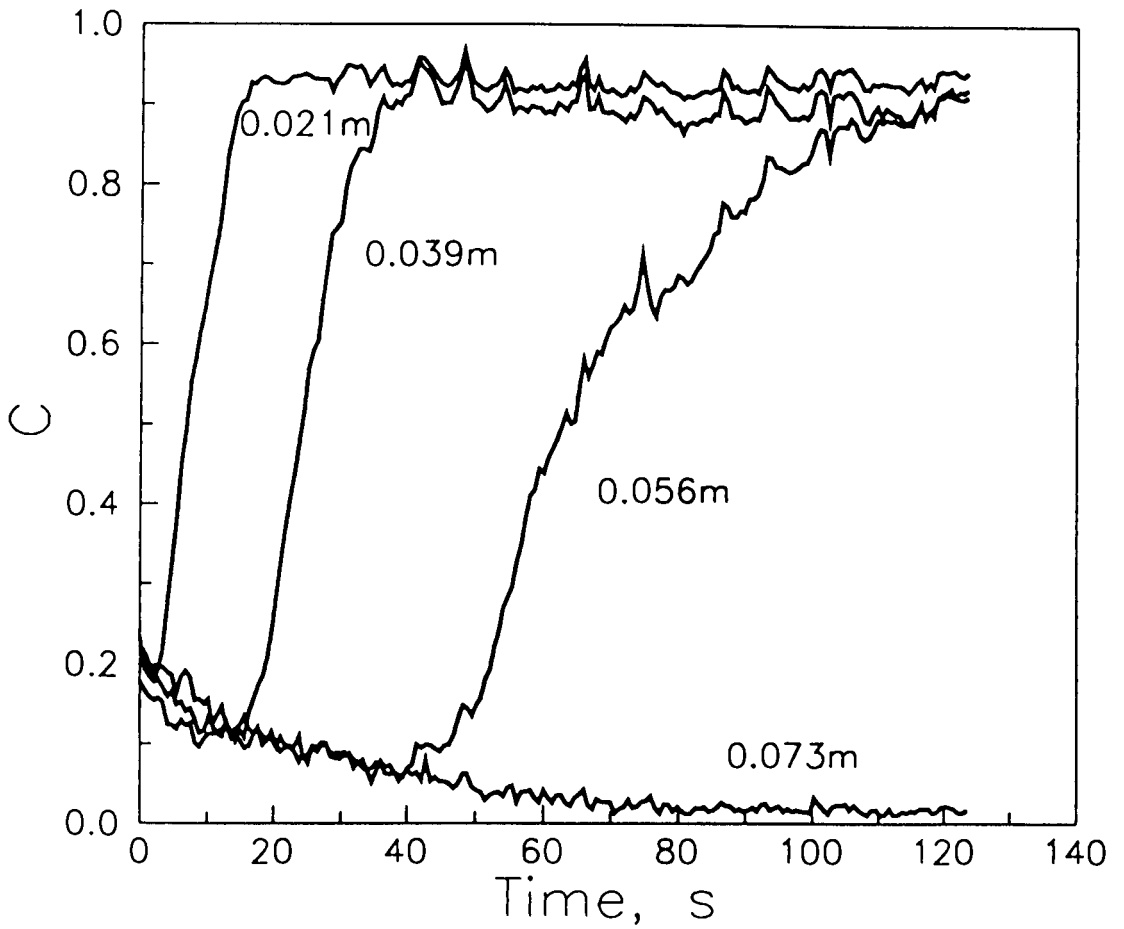

FIGURE 5.2.10a: Experimental response of jetsam concentration as a function of time at different bed heights for U_o = 0.152m/s; particle properties (set C): d_J/d_F = 1.73; ρ_J/ρ_F = 1.43, $U_{mf,J}/U_{mf,F}$ = 4.7

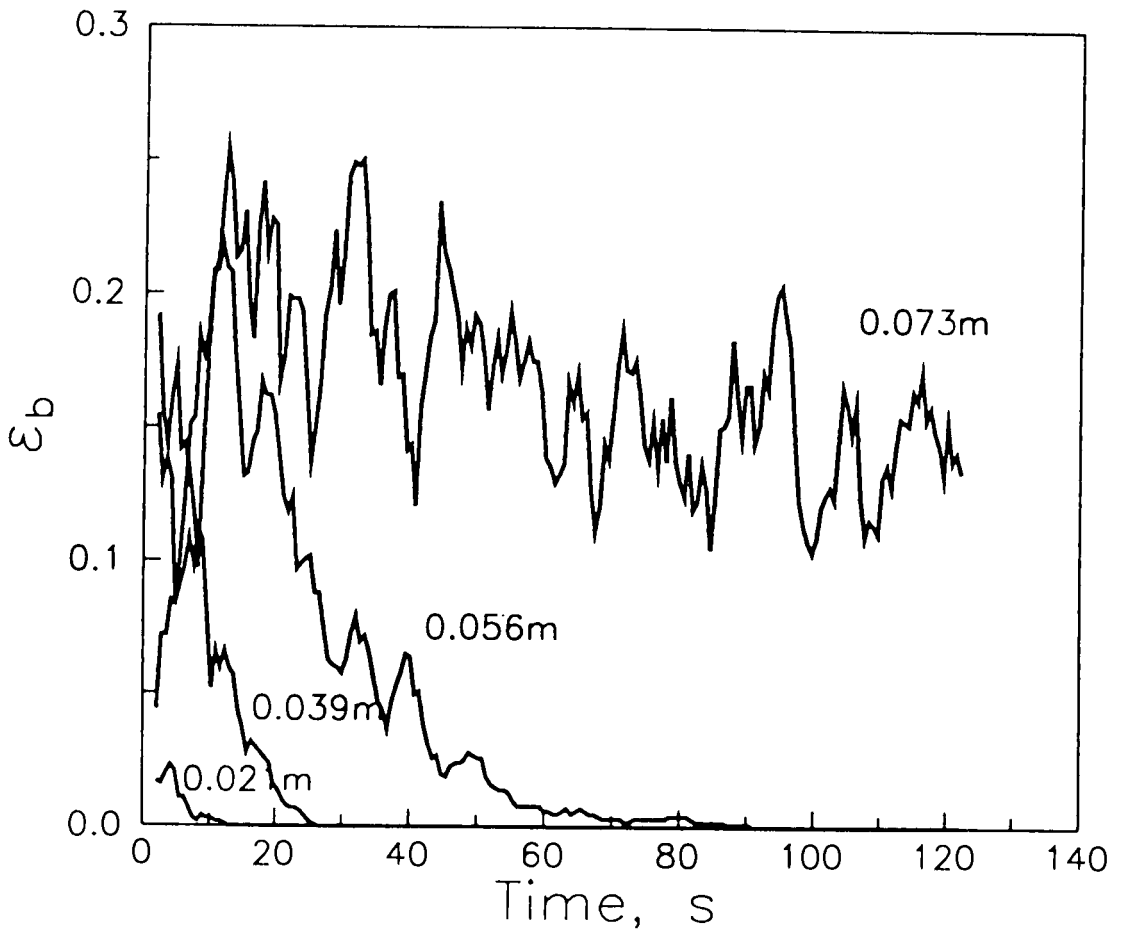

FIGURE 5.2.10b: Experimental response of bubble fraction as a function of time at different bed heights for U_0 = 0.152m/s; particle properties (set C): d_J/d_F = 1.73; ρ_J/ρ_F = 1.43, $U_{mf,J}/U_{mf,F}$ = 4.7

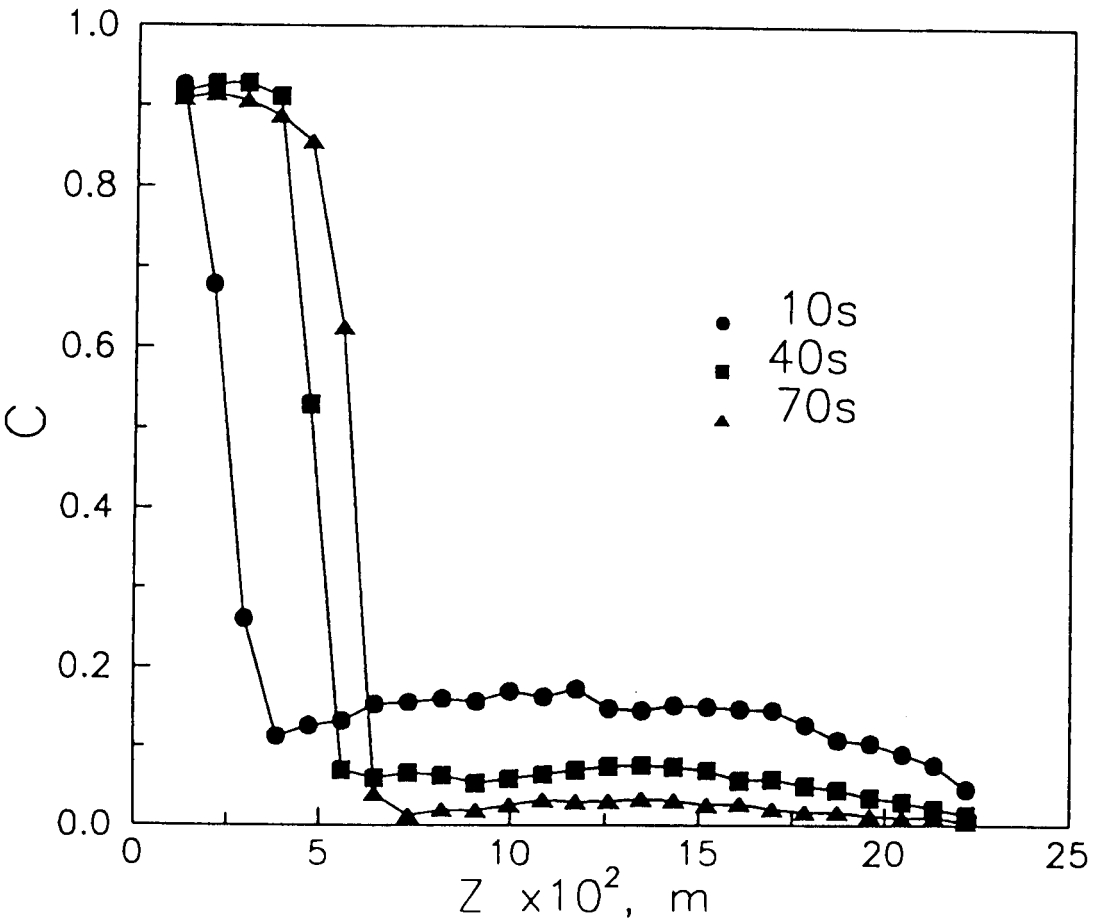

FIGURE 5.2.10c: Experimental axial jetsam concentration profile at different times for U_o = 0.152m/s; particle properties (set C): d_J/d_F = 1.73; ρ_J/ρ_F = 1.43, $U_{mf,J}/U_{mf,F}$ = 4.7

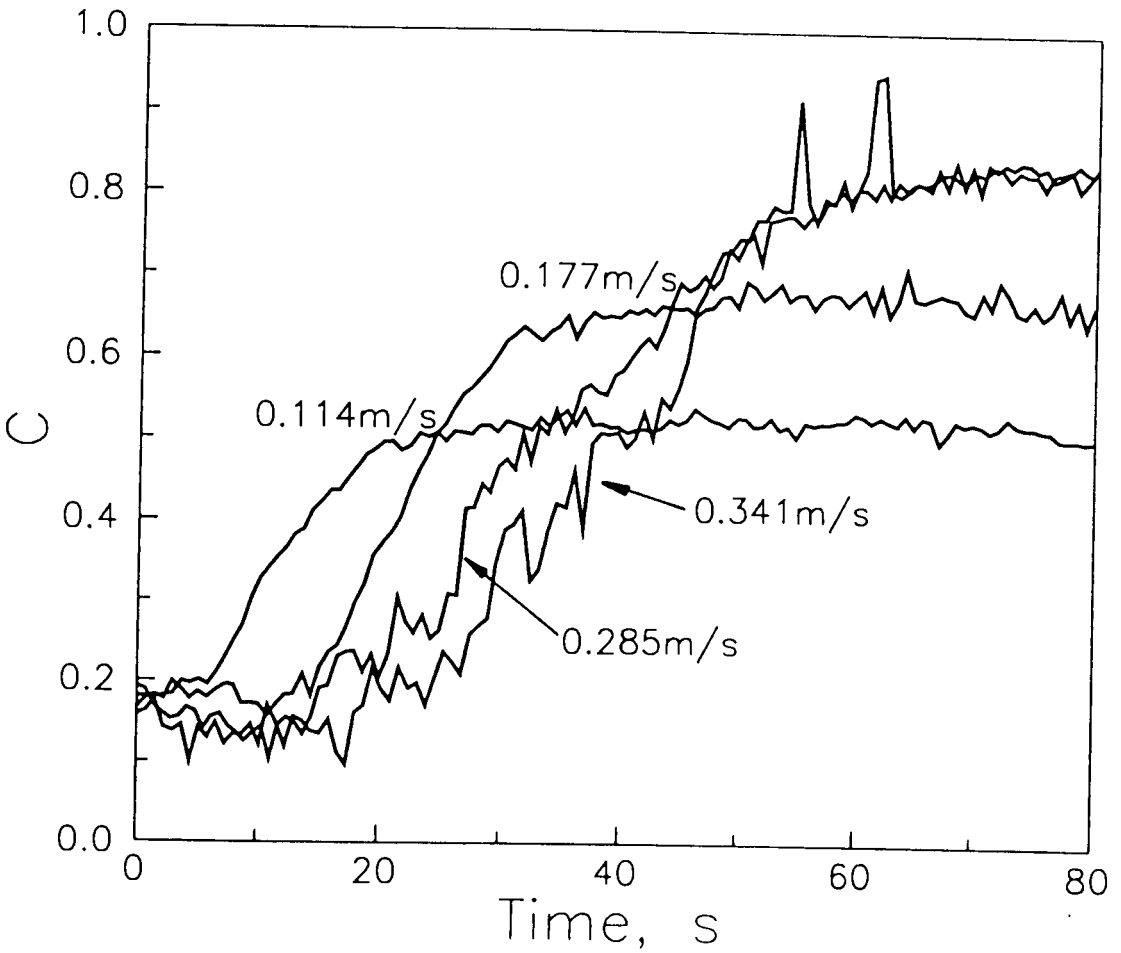

FIGURE 5.2.11a: Experimental response of jetsam concentration as a function of time for different superficial velocities at Z = 0.02m; particle properties (set A): $d_J/d_F = 3.02$; $\rho_J/\rho_F = 1.0$, $U_{mf,J}/U_{mf,F} = 5.6$

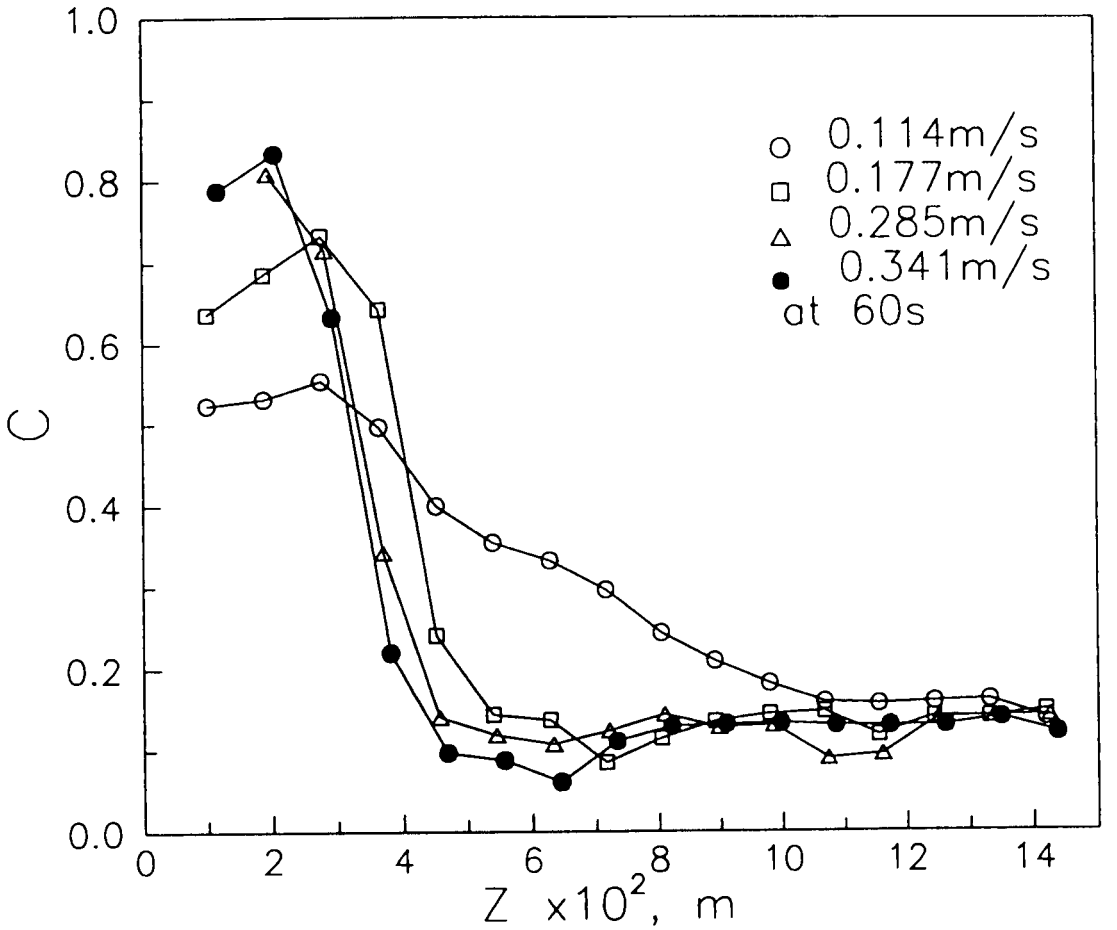

FIGURE 5.2.11b: Experimental axial jetsam concentration profile for different superficial velocities at t=60s particle properties (set A): $d_J/d_F = 3.02$; $\rho_J/\rho_F = 1.0$, $U_{mf,J}/U_{mf,F} = 5.6$

level under consideration. This trend is completely opposite to that predicted by the two models, **Figures 5.2.4a** and **5.2.5a**, as discussed earlier. On the other hand, the measured axial concentration profiles at different superficial velocities, **Figure 5.2.11b**, bear qualitative resemblance to theoretical calculations shown in **Figures 5.2.4b** and **5.2.5b**.

Experimental data obtained with other binary systems examined - Sets C and D, plotted in **Figures 5.2.12** and **5.2.13** respectively - reinforce the same conclusions; that is, though the theoretical models are in qualitative agreement with axial jetsam concent ration profiles at different superficial gas velocities, the data for the variation of concentration with time show the opposite trend in terms of rate of approach to equilibrium at any particular axial level.

A further mismatch between experiment and theoretical trends was observed for data obtained using Set B particles. In **Figure 5.2.14a**, the experimental measurements for U_o = 0.166 m/s show that the bed remained well-mixed for about 100 s before enrichment in jetsam concentration commenced at the lower levels leading to the formation of a defluidized layer after about 200 s. Similar results were obtained for other superficial gas velocities. Both theoretical models are unable to predict such behaviour.

The experimental results suggest that at higher superficial gas velocities, the mixing is stronger at any specific axial level; the segregation propensity is lower in comparison. From physical grounds, the experimental results appear to be reasonable and the discrepancies between experimental and theoretical trends can not be ascribed to the two-dimensional bed being used. The theoretical calculations - with the links used between segregation rate and bubbling parameters - on the contrary lead to higher local segregation rates when the superficial gas velocity through the bed is increased.

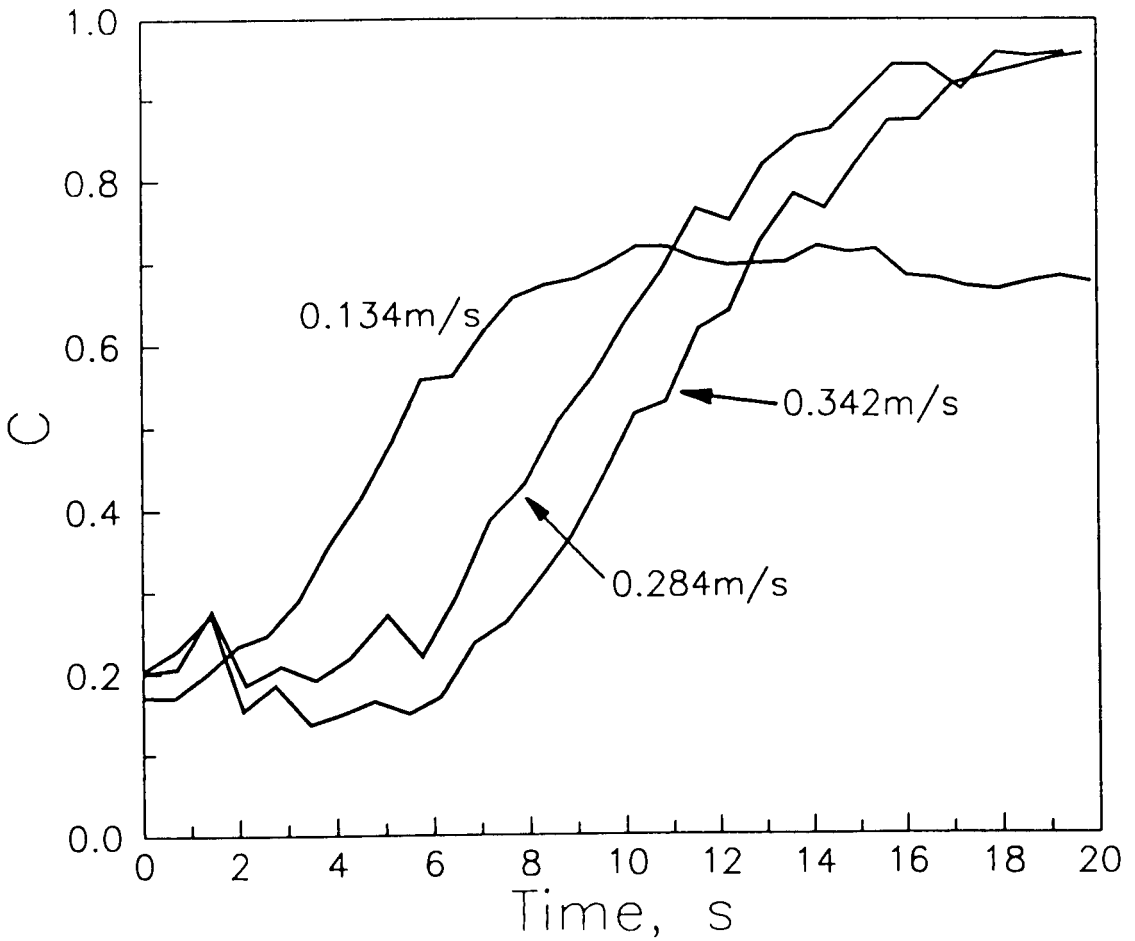

FIGURE 5.2.12a: Experimental response of jetsam concentration as a function of time for different superficial velocities at Z = 0.019m; particle properties (set C): $d_J/d_F = 1.73$; $\rho_J/\rho_F = 1.43$, $U_{mf,J}/U_{mf,F} = 4.7$

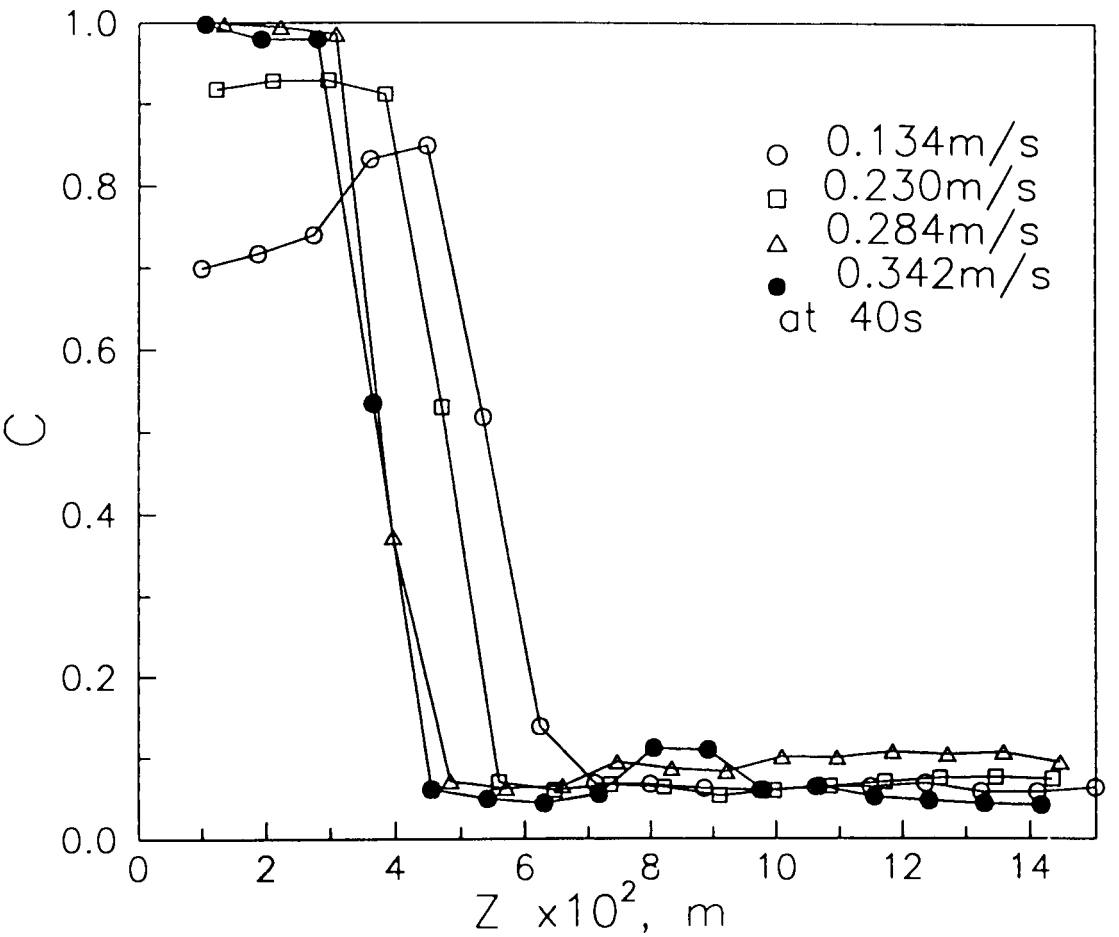

FIGURE 5.2.12b: Experimental axial jetsam concentration profile for different superficial velocities at t=40s particle properties (set C): $d_J/d_F = 1.73$; $\rho_J/\rho_F = 1.43$, $U_{mf,J}/U_{mf,F} = 4.7$

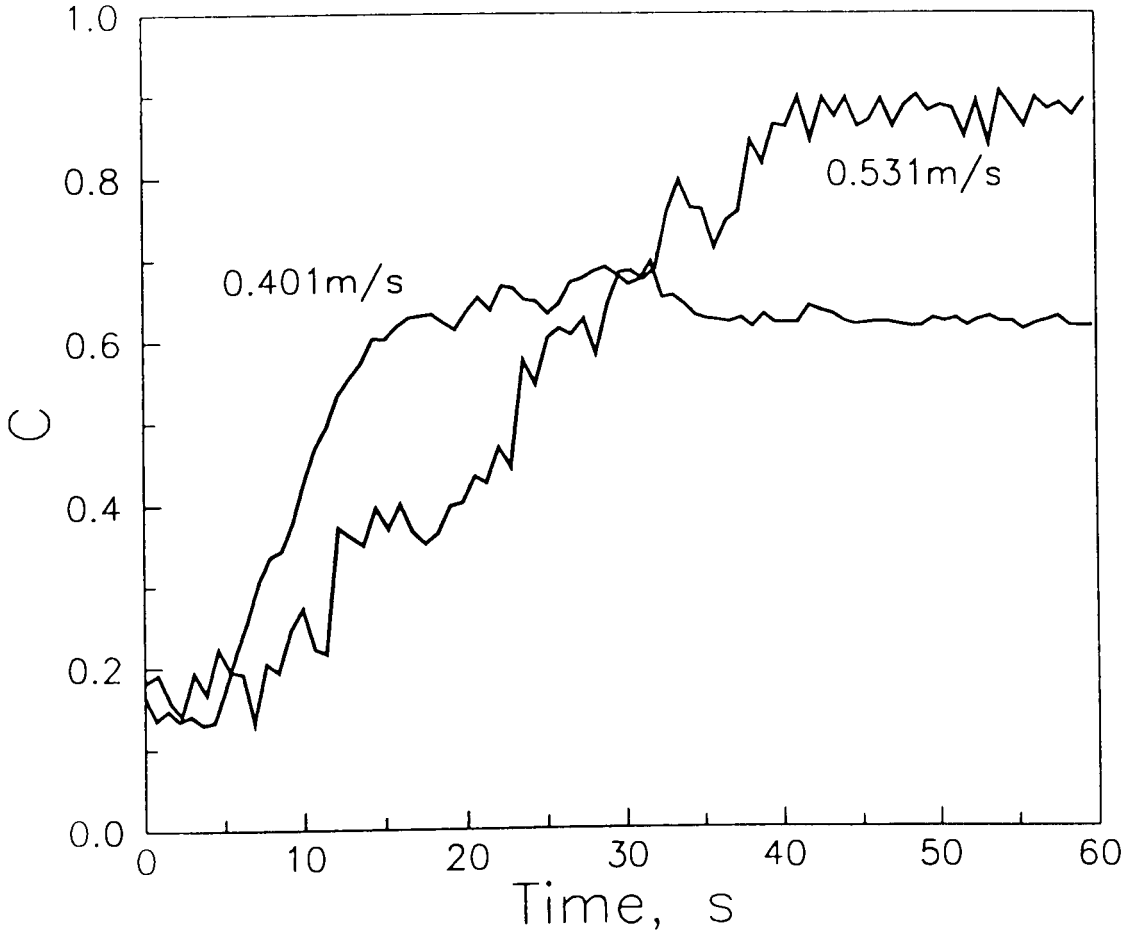

FIGURE 5.2.13a: Experimental response of jetsam concentration as a function of time for different superficial velocities at Z = 0.02m; particle properties (set D): d_J/d_F = 1.26; ρ_J/ρ_F = 1.43, $U_{mf,J}/U_{mf,F}$ = 2.45

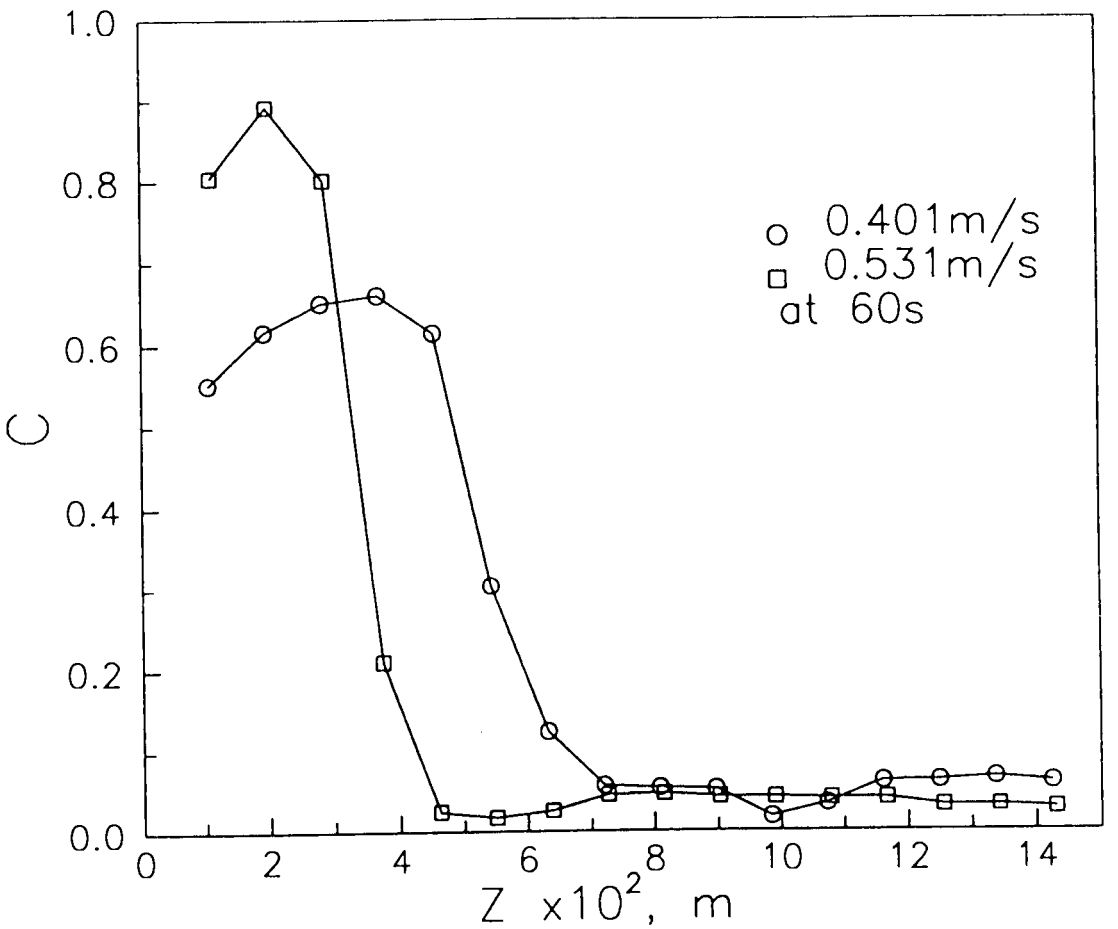

FIGURE 5.2.13b: Experimental axial jetsam concentration profile for different superficial velocities at t=60s particle properties (set D): $d_J/d_F = 1.26$; $\rho_J/\rho_F = 1.43$, $U_{mf,J}/U_{mf,F} = 2.45$

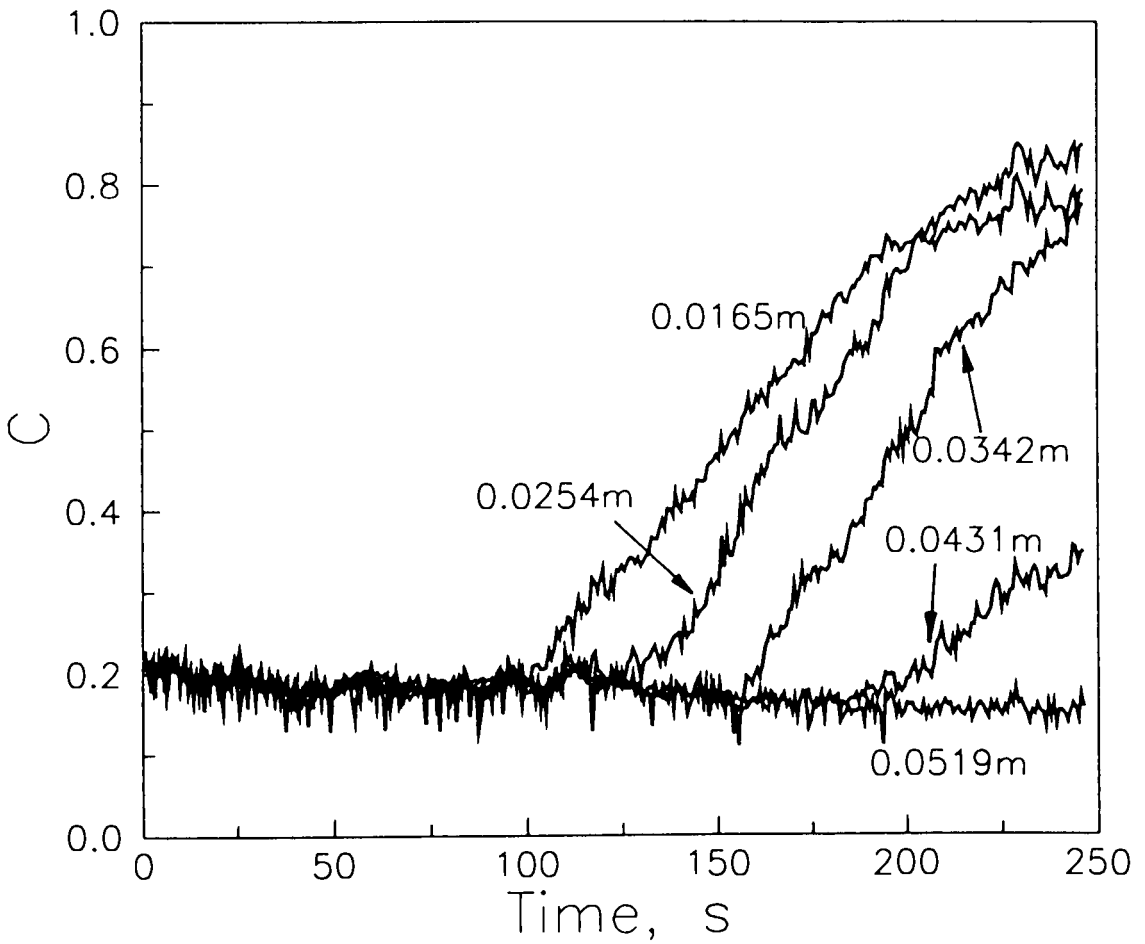

FIGURE 5.2.14a: Experimental response of jetsam concentration as a function of time at different bed heights for U_0 = 0.166m/s; particle properties (set B): d_J/d_F = 2.14; ρ_J/ρ_F = 1.0, $U_{mf,J}/U_{mf,F}$ = 3.23

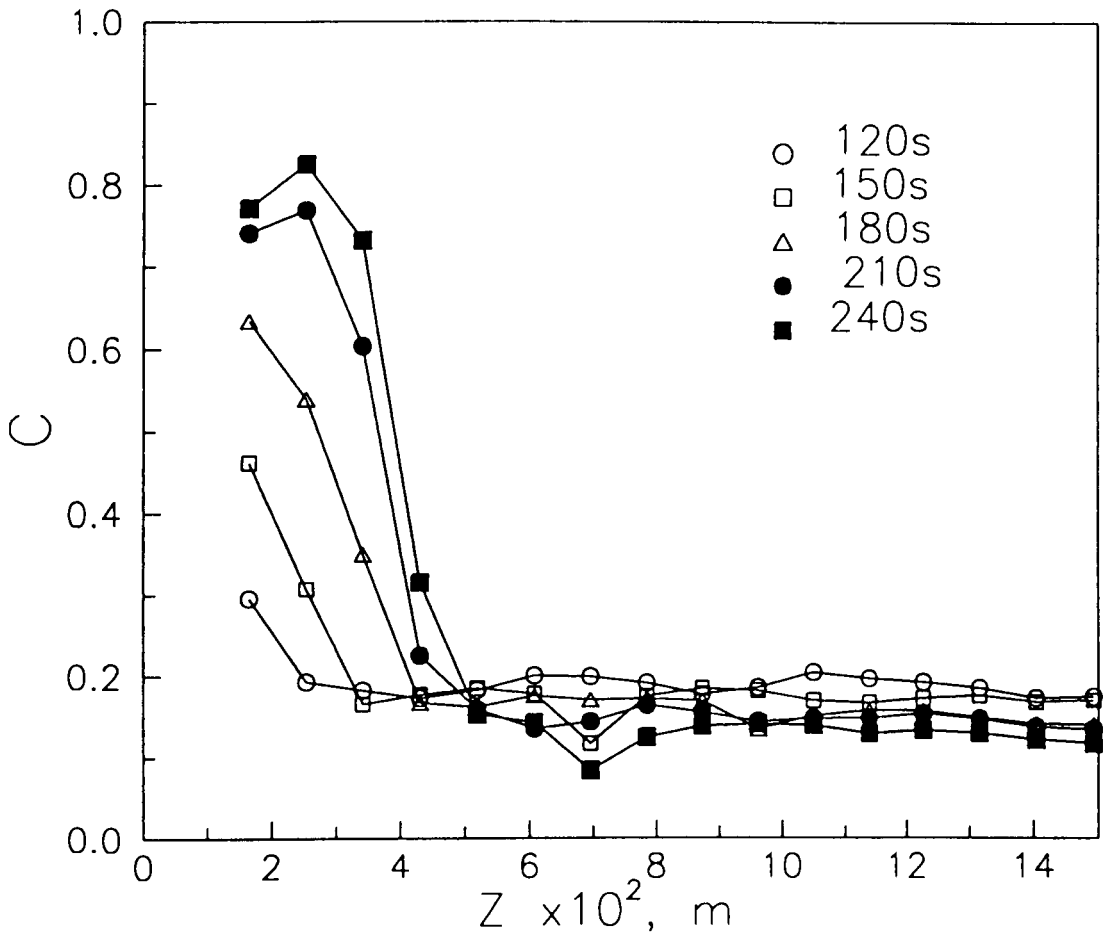

FIGURE 5.2.14b: Experimental axial jetsam concentration profile at different times for U_o = 0.166m/s; particle properties (set B): d_J/d_F = 2.14; ρ_J/ρ_F = 1.0, $U_{mf,J}/U_{mf,F}$ = 3.23

The mismatches brought forth by this investigation have not been uncovered in earlier work because of (i) the lack of detailed experimental data on the spatial (axial) and temporal evolution of jetsam concentration in the bed; and (ii) the emphasis on measurements of the axial jetsam concentration profiles for various systems at steady state.

Given that the G-R and Yoshida models are unable to reproduce the experimental trends successfully, there are two options which may be considered. The first option is to retain these models and assume that the Y_{GR} (or Y_Y) parameters contain a superficial velocity dependence as well. In that case Y_{GR}must be called a segregation propensity and not a segregation distance; this is because the segregation propensity must decrease even though the net distance moved by jetsam may increase with higher superficial velocities. In the course of this investigation, some simple functions were tested. However, they were unable to produce good agreement for all experimental conditions considered. In absence of theoretical guidelines, it was not considered judicious to pursue this line further. The other option is to consider other models to represent segregating fluidized beds. Two candidates currently available are:

. the model proposed by Sitnai (1981) which recognises that the existence of a separate wall phase of solids which exchanges particles from the central core region;

. the model of Kozanoglu and Levy (1992) which assumes the existence of four wake phases with different exchange characteristics.

Whether these models reflect the physical mechanisms actually involved in segregation or provide additional adjustable parameters for data fitting requires further evaluation.

Height of the defluidized layer: According to Chiba and Nienow (1983), the height of the defluidized layer depends on the concentration of the particle species as well as the superficial velocity. Yang and Keairns (1982) have made the interesting qualitative observation that the fluidizing velocity does not have a strong influence on the total time required to reach equilibrium for a particular mixture of particles. To verify their observations, and to explore the influence of time and superficial velocity on the height of the defluidized layer, two dimensionless groups $Z^* = Z_P/Z_{P,S}$ and $t^* = t/t_{P,S}$ were defined where $Z_{P,S}$ is the equilibrium height of the defluidized layer which is attained at time $t_{P,S}$. Clearly, $0 < Z^* < 1$ and $0 < t^* < 1$. From experimental measurements, plots of Z^* versus t^* were prepared for the binary systems considered; the results are presented in **Figures 5.2.15a-d**. These results suggest that the superficial velocity does not have a very strong influence on the rate of approach to equlibrium in terms of the dimensionless variables. Weakly segregating systems (Set B particles) appear to remain well mixed for a longer duration initially and reach the equilibrium defluidized layer height in comparatively shorter fraction of time, t^*. Strongly segregating systems, on the other hand, start forming a defluidized layer quickly; however, subsequently they take a comparatively larger fraction of t^* to reach equilibrium. These experimental data can be represented by a one-parameter equation of the type commonly used to represent vapour-liquid equilibrium data

$$Z^* = \frac{\alpha_{AB} t^*}{1 + (\alpha_{AB} - 1) t^*} \tag{5.2.25}$$

where the parameter α_{AB}, analogous to relative volatility, is a measure of the segregation propensity.

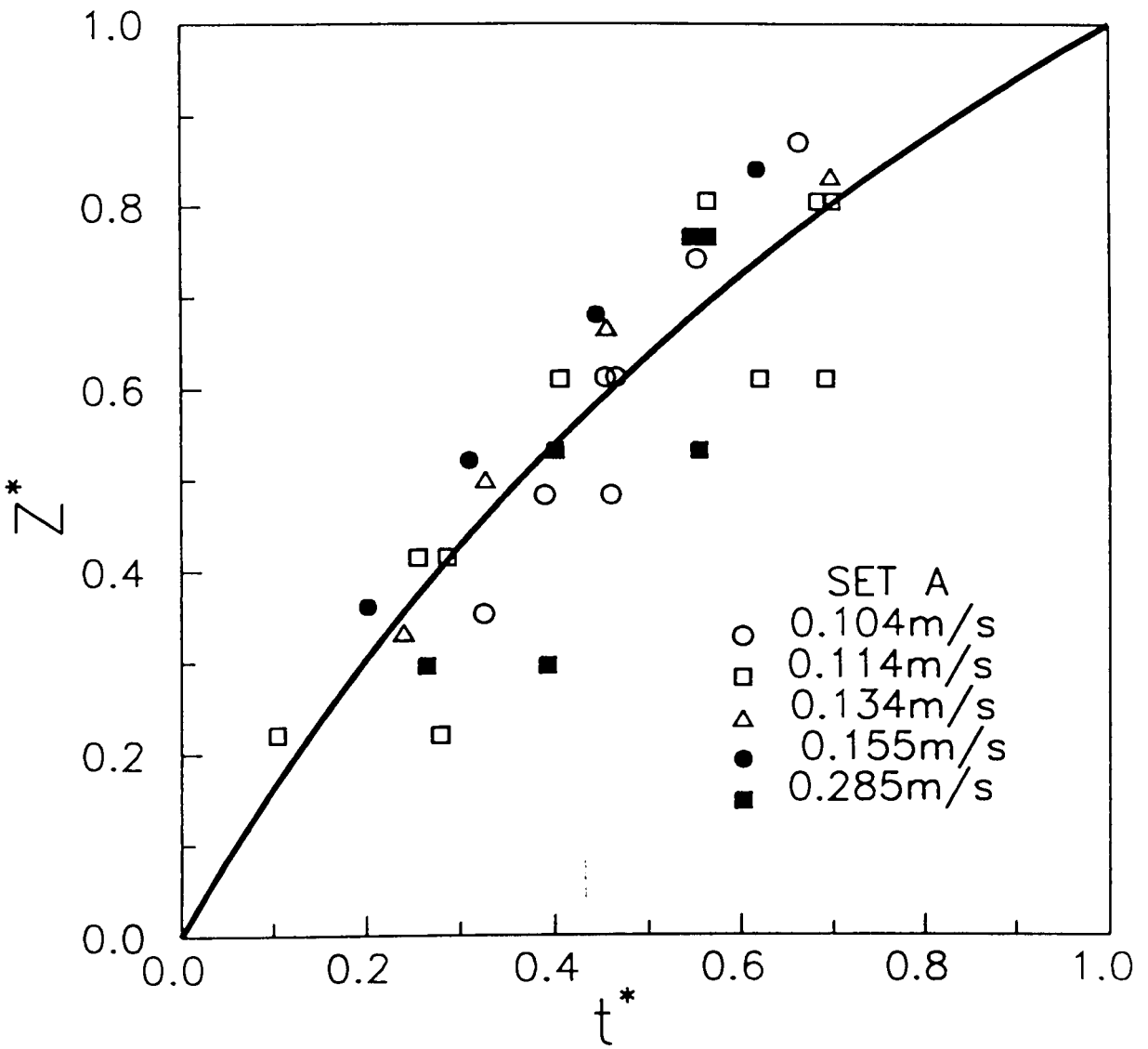

FIGURE 5.2.15a: Dimensionless height of the defluidized layer, Z*, as a function of dimensionless time, t*, for Set A (d_J/d_F = 3.02; ρ_J/ρ_F = 1.0, $U_{mf,J}/U_{mf,F}$ = 5.6) particles.

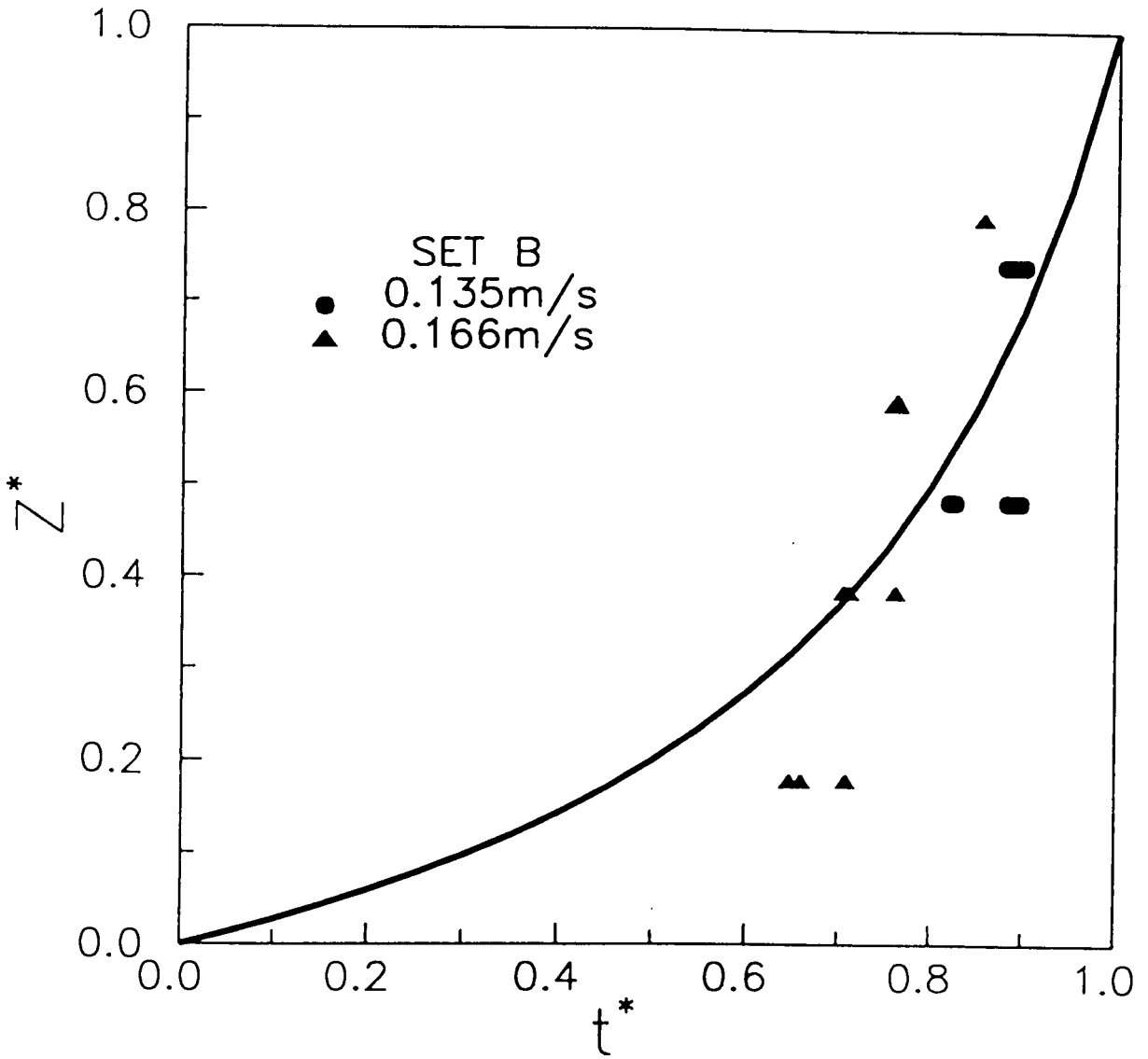

FIGURE 5.2.15b: Dimensionless height of the defluidized layer, Z*, as a function of dimensionless time, t*, for Set B (d_J/d_F = 2.14; ρ_J/ρ_F = 1.0, $U_{mf,J}/U_{mf,F}$ = 3.23) particles.

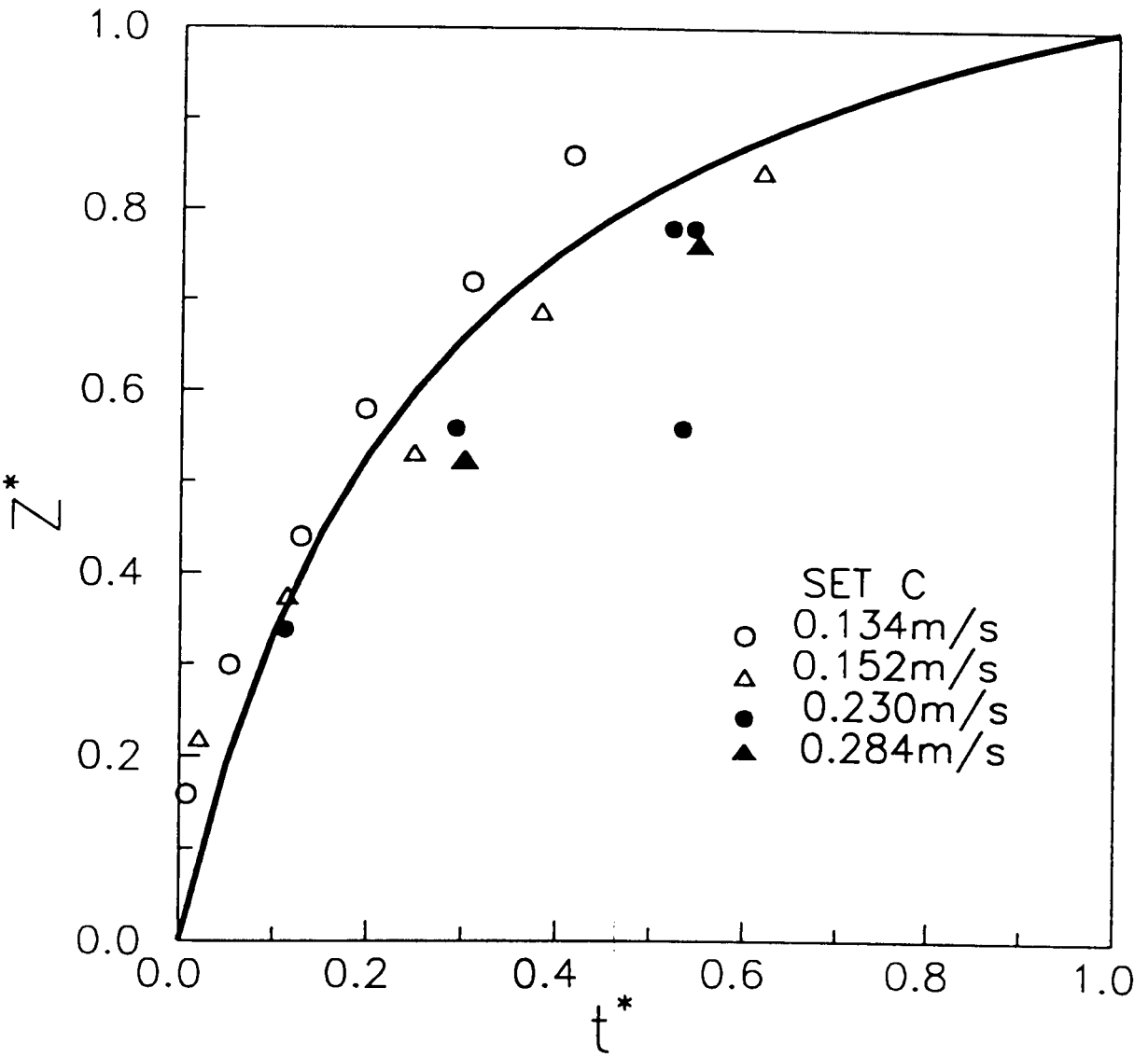

FIGURE 5.2.15c: Dimensionless height of the defluidized layer, Z*, as a function of dimensionless time, t*, for Set C (d_J/d_F = 1.73; ρ_J/ρ_F = 1.43, $U_{mf,J}/U_{mf,F}$ = 4.7) particles.

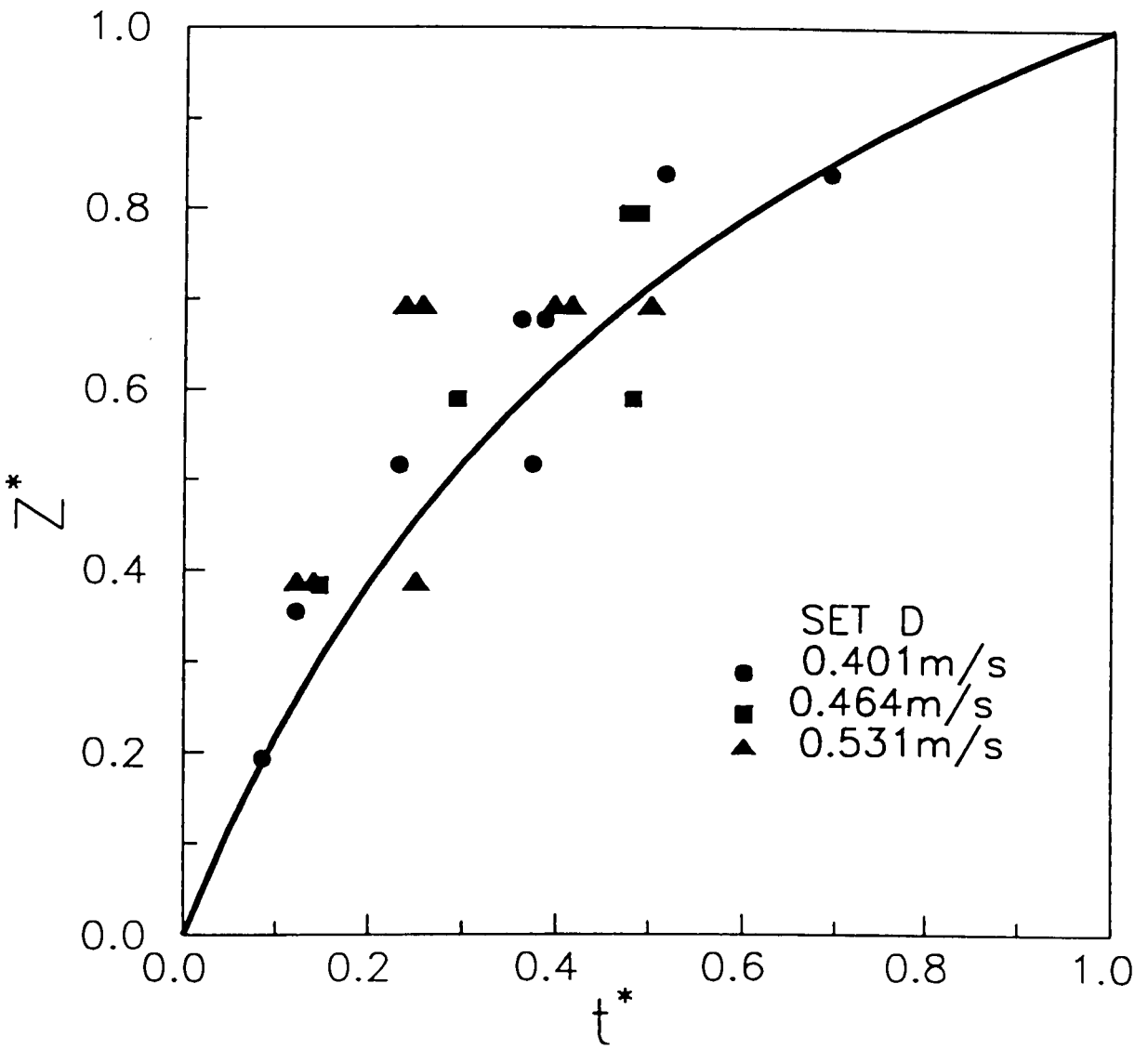

FIGURE 5.2.15d: Dimensionless height of the defluidized layer, Z*, as a function of dimensionless time, t*, for Set D (d_J/d_F = 1.26; ρ_J/ρ_F = 1.43, $U_{mf,J}/U_{mf,F}$ = 2.45) particles.

Equation (5.2.25) with appropriate values of α_{AB} has been plotted, along with the data, in **Figures 5.2.15a-d**. A higher value of α_{AB} represents a stronger tendency to segregate. The binary systems considered in this investigation can be arranged in order of increasing segregation tendency as follows

$$SetB(\alpha_{AB} = 0.25) < SetA(\alpha_{AB} = 1.75) < SetD(\alpha_{AB} = 2.5) < SetC(\alpha_{AB} = 4.5)$$

Interestingly, for these binary systems, Y_{GR} values calculated from equations (5.2.23) indicate the same order.

The equilibrium height of the defluidized layer, $Z_{P,S}$, and the time required to reach this height, $t_{P,S}$, will undoubtedly depend on the superficial gas velocity. In **Figure 5.2.16** $t_{P,S}$ has been plotted as a function of $(U_O - U^*_{mf,c})$ where $U^*_{mf,c}$ is calculated using the average concentration of the jetsam in the bed in equation (5.2.21), that is

$$U^*_{mf,c} = U_{mf,F}(U_{mf,J}/U_{mf,F})^{\bar{x}_J^2} \qquad (5.2.26)$$

For the binary system considered experimentally in this investigation, $\bar{x}_J \cong 0.2$.

In **Figure 5.2.17**, $Z_{P,S}$ has been plotted as a function of $(U_O - U^*_{mf,c})$. Surprisingly, the data for Sets A and C appear to fall on a single line. More data are required to establish whether this trend has a more general application. In **Figure 5.2.18**, experimental values of $Z_{P,S}$ has been plotted against $t_{P,S}$. The data suggest that linear relations may hold between these variables for different binary systems. Once again additional data are necessary to elaborate on the observed trends.

5.2.5 Conclusions

Unsteady material balance equations from the Gilibaro-Rowe and Yoshida models for segregating fluidized beds have been solved numerically. The

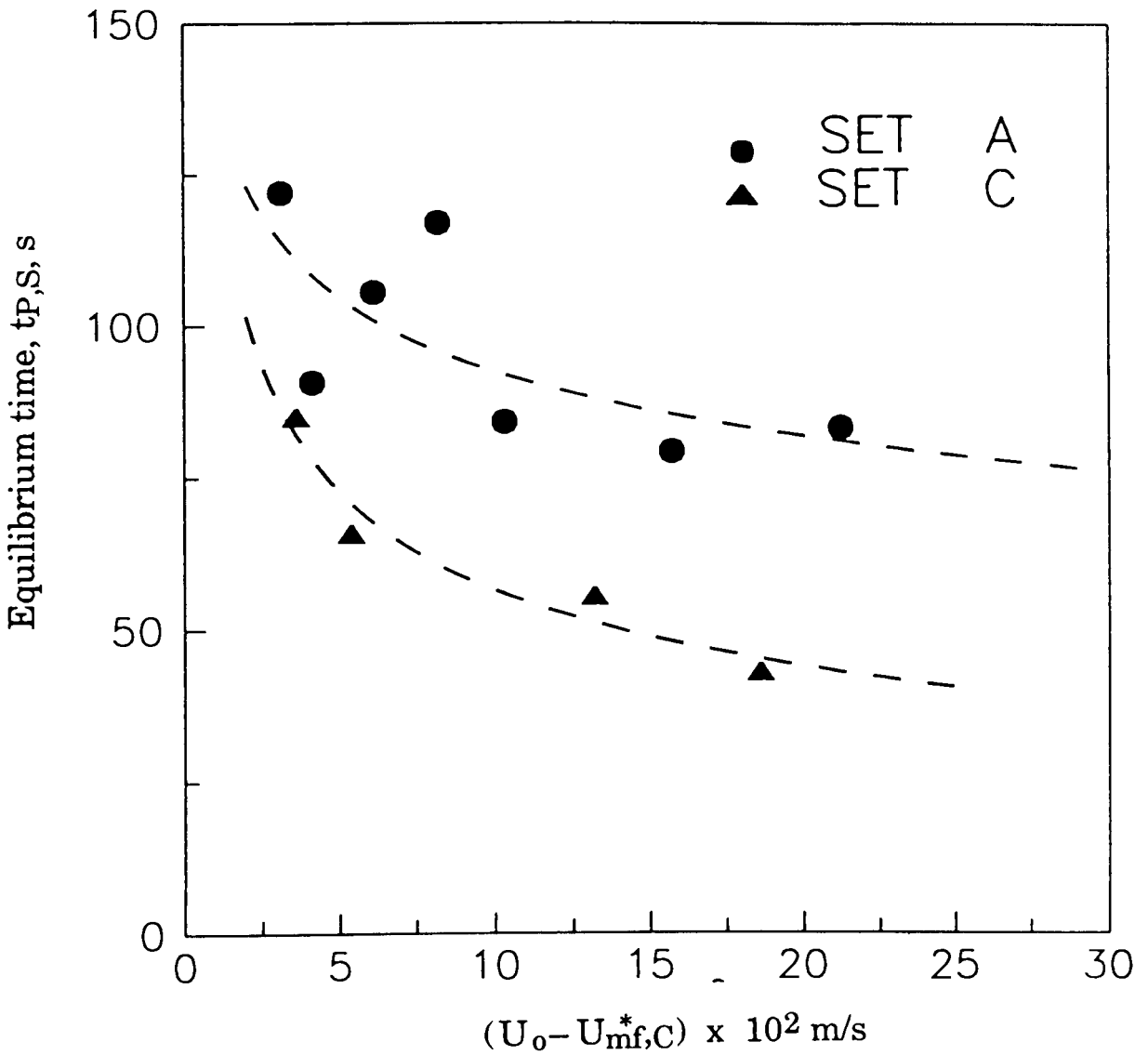

FIGURE 5.2.16: Time to reach the equilibrium defluidized layer height, $t_{P,S}$, as a function of the modified excess gas velocity, $(Uo-U^*_{mf,C})$, for Set A (d_J/d_F = 3.02; ρ_J/ρ_F = 1.0, $U_{mf,J}/U_{mf,F}$ = 5.6) and Set C (d_J/d_F = 1.73; ρ_J/ρ_F = 1.43, $U_{mf,J}/U_{mf,F}$ = 4.7) particles.

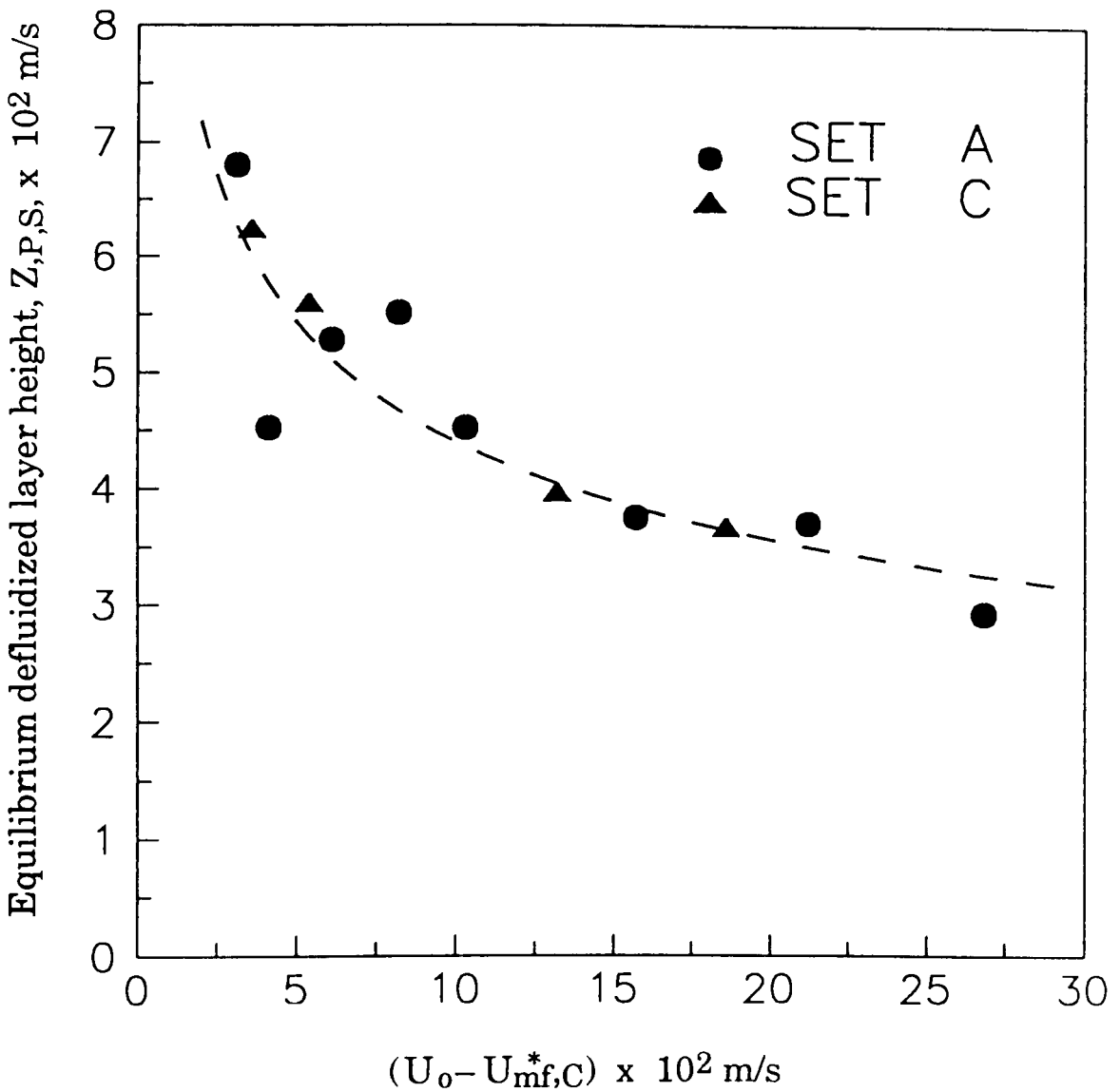

FIGURE 5.2.17: The equilibrium defluidized layer height, $Z_{P,S}$, as a function of the modified excess gas velocity, $(U_o - U^*_{mf,C})$, for Set A (d_J/d_F = 3.02; ρ_J/ρ_F = 1.0, $U_{mf,J}/U_{mf,F}$ = 5.6) and Set C (d_J/d_F = 1.73; ρ_J/ρ_F = 1.43, $U_{mf,J}/U_{mf,F}$ = 4.7) particles.

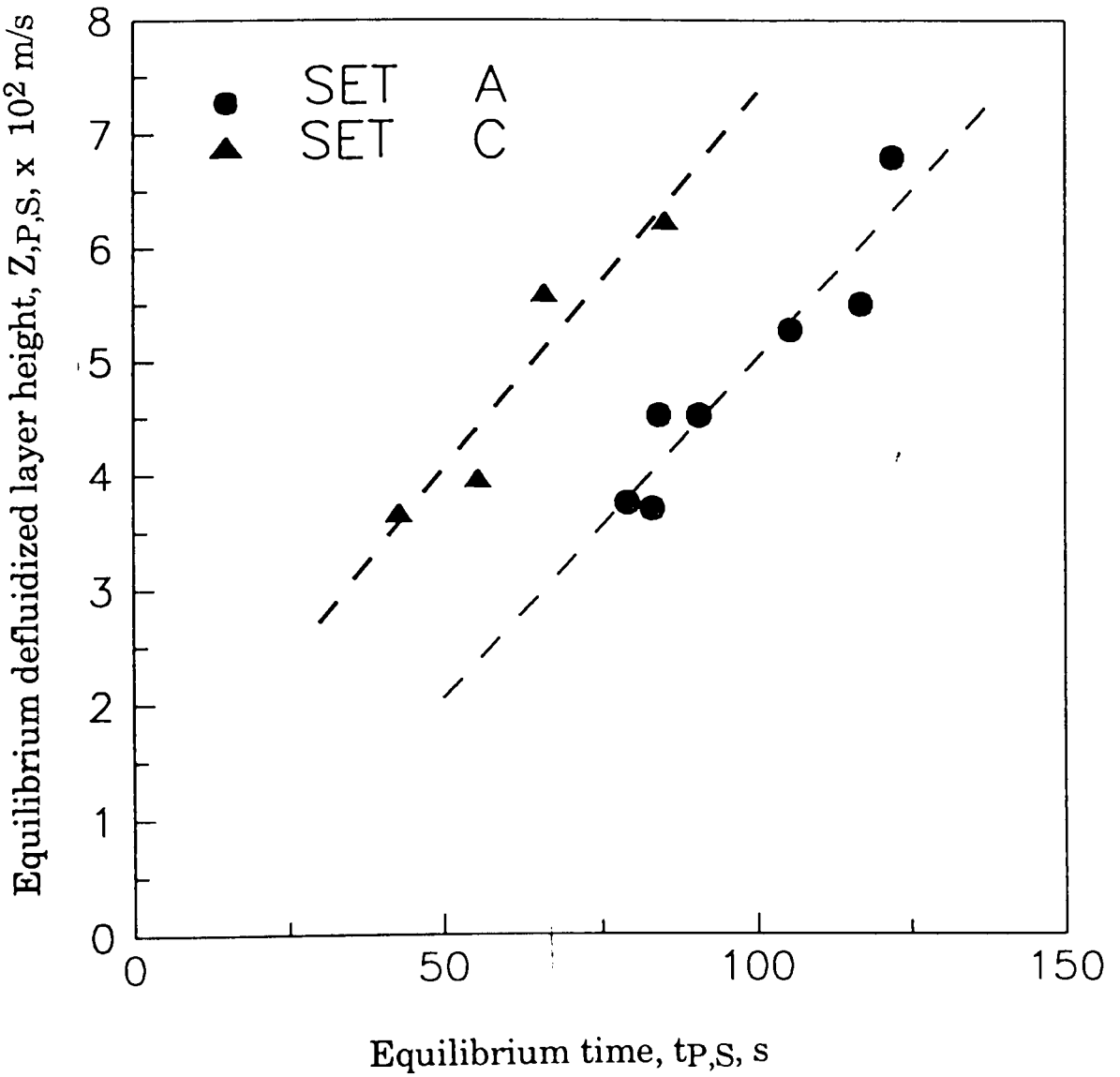

FIGURE 5.2.18: The equilibrium defluidized layer height, C as a function of the time required to reach equilibrium height, $t_{,P,S}$, for Set A (d_J/d_F = 3.02; ρ_J/ρ_F = 1.0, $U_{mf,\,J}/U_{mf,F}$ = 5.6) and Set C (d_J/d_F = 1.73; ρ_J/ρ_F = 1.43, $U_{mf,\,J}/U_{mf,F}$ = 4.7) particles.

possibility of the formation of a defluidized layer at the bottom of the bed has been taken into account. Comparison of model predictions with data indicates that though these models do reflect some features of the experiment, the influence of the superficial velocity on the temporal variation of the concentration at any specific height within the bed is not predicted. In fact, a trend completely opposite to that predicted is observed experimentally. If these models are to be used, then the segregation rate parameter must have a dependence on superficial velocity substantially different to that currently available in the literature.

Some preliminary empirical relations have been established for the movement of the defluidized layer with time. In particular, a promising new indicator for segregation propensity is proposed from analogy with vapour-liquid equilibrium data representation methods. Additional data are necessary before further generalization can be attempted.

5.3 MOTION OF A LARGE PARTICLE

In bubbling fluidized bed combustion, large coal particles - comprising about 1% of the total bed inventory - are fluidized along with smaller sulphur-sorbent particles. The density of the coal particles is less than that of the bed particles. This combination of the concentration, size and density results in the setting up of circulation pattern for a coal particle within the bed: a jerky upward movement under the influence of rising bubbles and a downward motion when associated with the dense phase (Nienow et al., 1978)

It appears important to characetrize this motion for improving the current understanding of combustion of coal in bubbling fluidized beds. In this section, the methods described in **section 3.2.6** have been utilized to detect and track a freely moving larger and lighter (or 'active') particle in fluidized beds of smaller particles. In addition, measurements have also been made for a macroscopic measure - residence phase probability - of the 'active' particle's association with the bubble phase.

5.3.1 Particle Motion and Circulation Pattern

5.3.1.1 Particle motion in one circulation

A complete circulation of an 'active' particle of density $\rho_A = 1141$ kgm^{-3} introduced at the top of the bubbling bed fluidized operated at a superficial gas velocity of 0.604 m s^{-1} has been shown in **Figure 3.2.19**. Visual observations, as well as experimental measurements, show that there are several recurrent 'active' particle motion patterns. Further, certain patterns are predominant in different regions of the bed. The particle circulates in the bed by moving predominantly downward slowly near the vertical edges of the bed and rising upward in a jerky movement in the central region. Several characteristic patterns of particle motion were observed during the particle's ascent to the

top of the bed. The particle could execute a looping pattern along the edge of the an upward moving bubble or fall through the roof of the bubble - in both these cases the particle ends up moving downwards. Further, the particle was also seen to travel a significant distance upward in the bubble wake before being shed off. The motion was especially fast when there was a bubble trailing the wake of the leading bubble. It is clear that bubbles cause particle motion; however, it appears that certain bubbles induce a greater upward motion than the others. The results in **Figure 3.2.19** illustrate these patterns : the particle was seen spiralling in the same region (half way above the distributor in the central region of the bed) for some time resulting in approximately zero net vertical displacement before being carried up to the top of the bed very quickly. These observations are in qualitative agreement with Nienow et al. (1978) and Tanimoto et al. (1980).

To illustrate the quantitative information that can be obtained from experiment, the X and Y co-ordinates of the particle in **Figure 3.2.19** are plotted as a function of time shown in **Figures 5.3.1a** and **b.** The corresponding velocity components, $V_{A,x}$, $V_{A,y}$ of the particle were calculated from the slopes of X-Y displacements versus time plots, **Figures 5.3.1c** and **d**, and the calculated absolute velocity $V_{A,s}$ is plotted in **Figure 5.3.1e**. It can be seen from these results that the magnitudes of $V_{A,x}$ and $V_{A,y}$ range from 0.01 to 0.25 m s^{-1} and 0.025 to 0.5 m s^{-1} respectively. Further, the plots show significant greater lateral and axial displacements during the rising portion of the circulation compared to when the particle is descending down along the edge of the wall. The absolute velocity in the rising section is significantly greater than those in the sinking region. Considering Figure 2, the number of cells (surrounding the 'active' particle) having intensities greater than the threshold

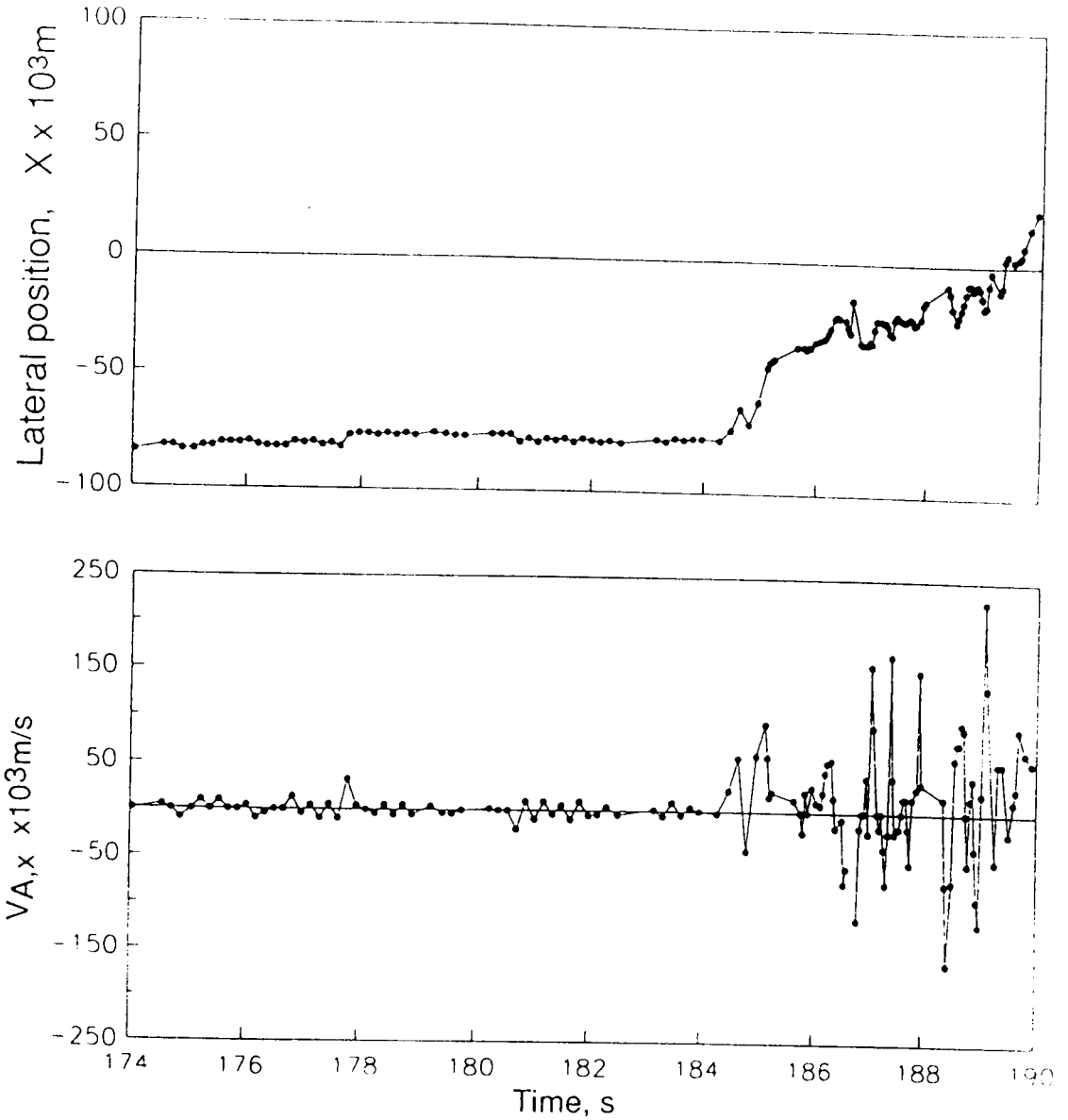

FIGURE 5.3.1: (a) Lateral position of the 'active' particle as a function of time

(b) Velocity component in the x-direction, $V_{A,x}$ as a function of time.

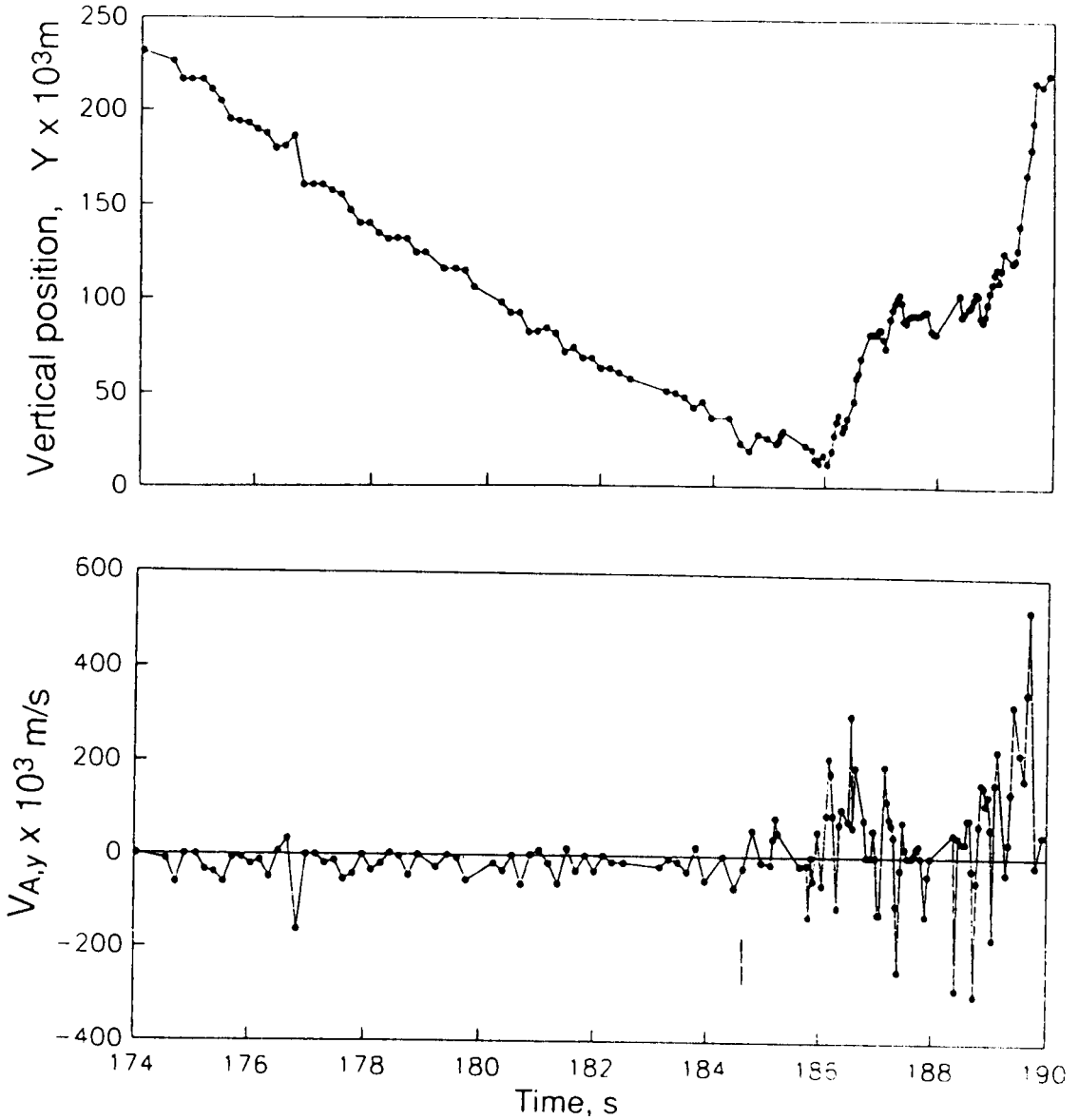

FIGURE 5.3.1: (c) Vertical position of the 'active' particle as a function of time

(d) Velocity component in the y-direction, $V_{A,y}$ as a function of time.

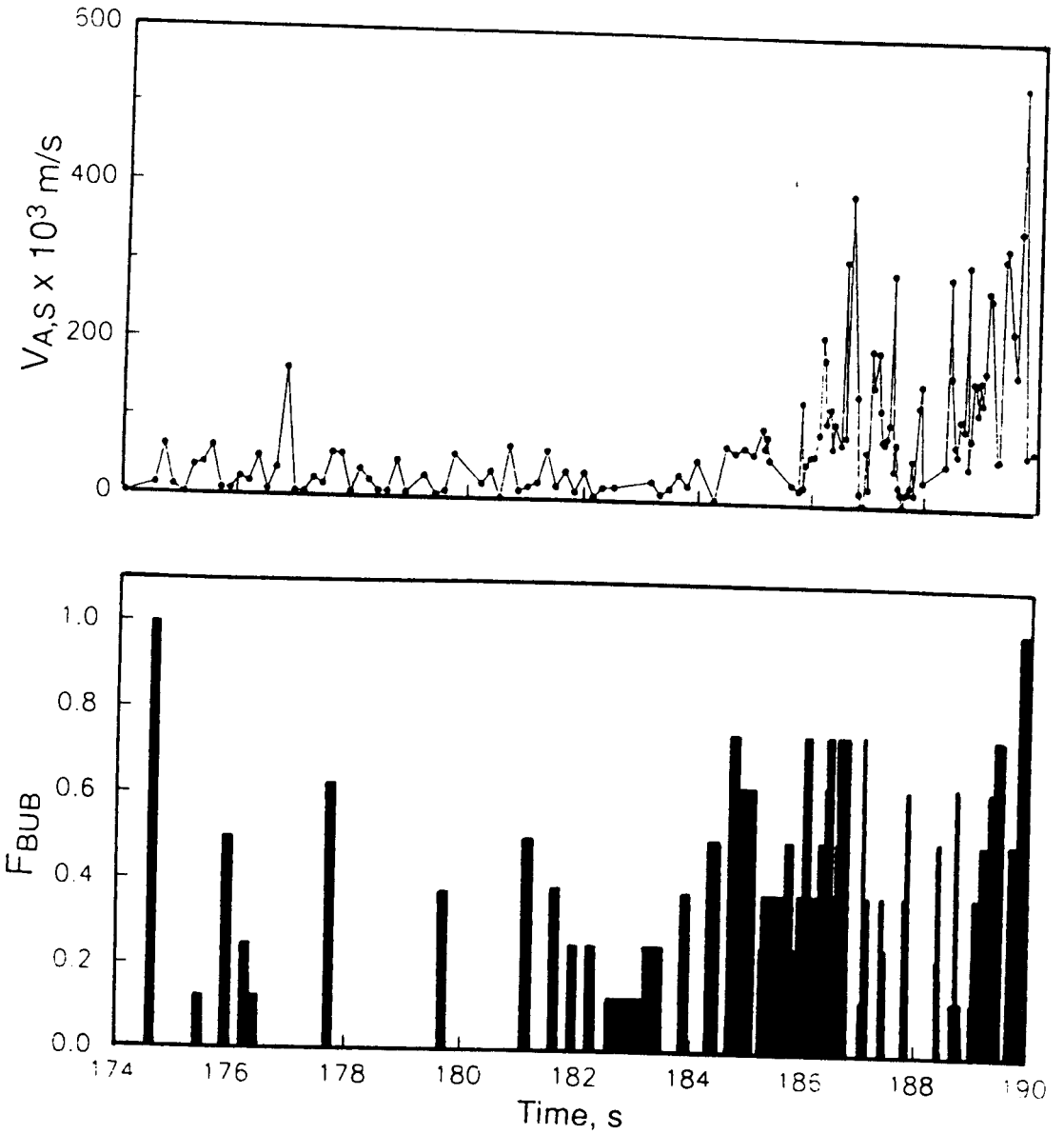

FIGURE 5.3.1: (e) Resultant velocity of the 'active' particle as a function of time
(f) Bubble-particle interaction as a function of time.

value (that is, in the bubble void) were determined. This number as a fraction of the total number of cells surrounding the active particle is a measure of bubble-particle interaction. This fraction, denoted as F_{BUB} is plotted as a function of time in **Figure 5.3.1f.** Simultaneous consideration of **Figures 5.3.1d-f** establishes clearly that the motion of the 'active' particle correlates very strongly with the presence of bubbles in its immediate vicinity.

5.3.1.2 Overall circulation pattern

The circulatory pattern of particle motion in the bed can be clearly illustrated with plot of Y versus time for a longer duration. **Figure 5.3.2** shows the rising and sinking patterns of the particle for a period of 150 s continuously. The circulation time ranges from approximately 8 to 22 s with a more dominant circulation time about 16 s. It is obvious that the circulation time is influenced by the depth to which the particle descends. Although the particle was seen more frequently to descend to a depth very close to the distributor, there were occasions where the particle was deflected back to the surface after only reaching down to a short distance. Such premature re-emergence of the particle to the surface occurs especially when the particle resides in the inner/central region of the bed in which a higher bubble frequency is encountered. The particle tends to sink down closer to the distributor when close to the vertical edge of the bed.

In addition, the average velocity vector of a specified region in the bed was calculated by averaging all the $V_{A,x}$ and $V_{A,y}$ components of that region. The average angular direction of particle motion was evaluated from $\tan^{-1}(\overline{V}_{A,x}/\overline{V}_{A,y})$ and was classified into one of the eight key directions with an angle of 45° between two intervals. A map of these vectors is shown in **Figure 5.3.3a.** These results, depicting the overall circulation pattern, substantiate the

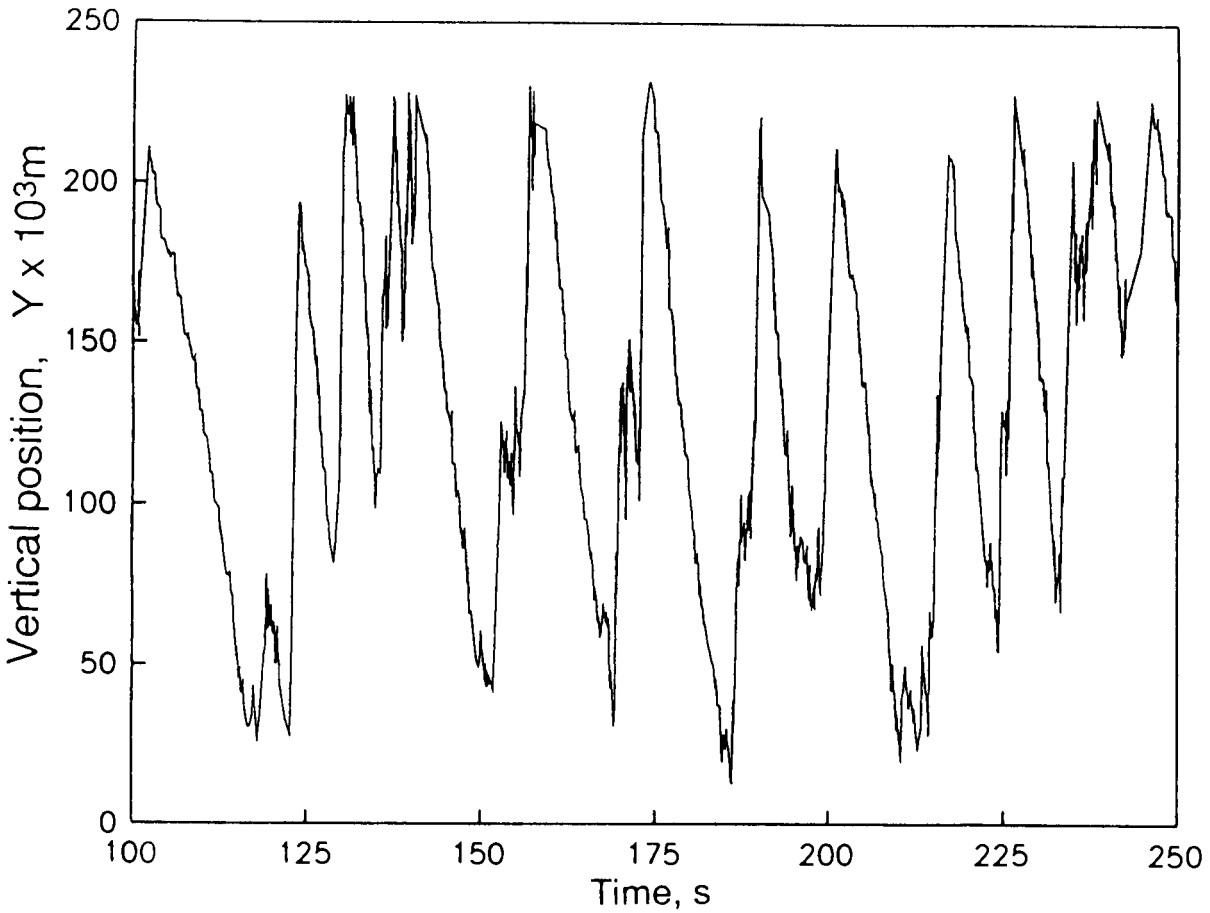

FIGURE 5.3.2: Circulation pattern of an 'active' particle in the fluidized bed

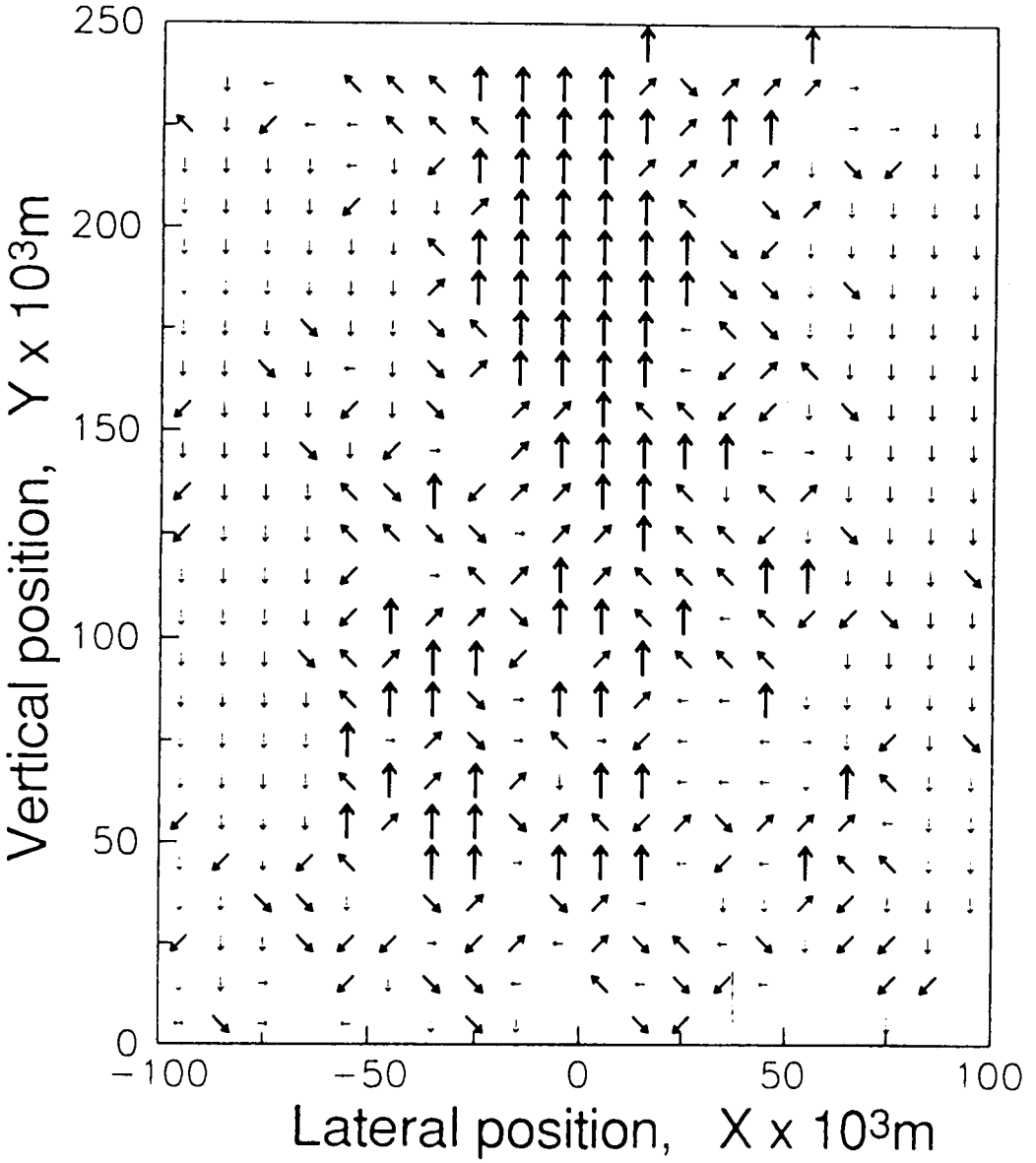

FIGURE 5.3.3a: Angular direction of 'active' particle motion.

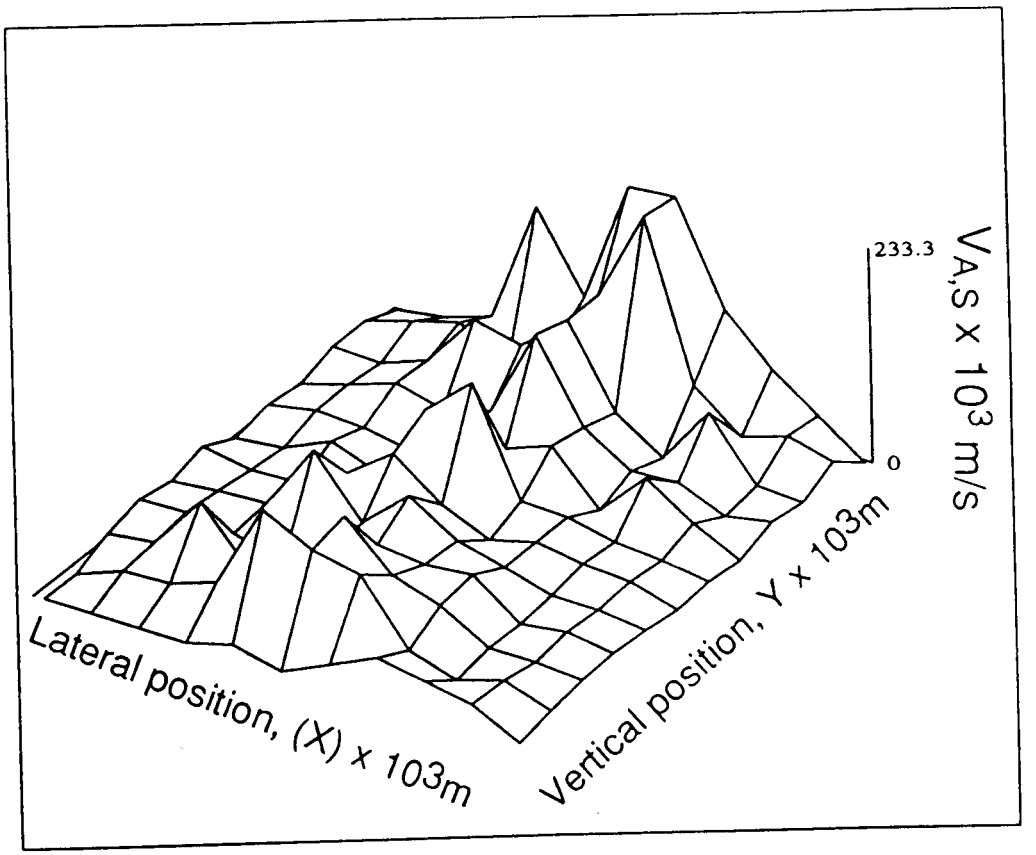

FIGURE 5.3.3b: Magnitude of 'active' particle velocity in various regions of the bed.

visual observations suggesting that the particle moves downward near the edge of the bed and rises through the central region. The pattern is very similar to the gross circulation pattern of the bed solids resulted from the wake-drift transport (Lin et al., 1985; Soo, 1986). The corresponding magnitudes of the velocity vectors, shown in **Figure 5.3.3b**, clearly indicate a higher magnitude for the particle velocity in the central region of the bed.

The plot of the height-averaged distribution for $\overline{V}_{A,y}$, **Figure 5.3.4a**, provides a convenient basis distinguishing characteristics of particle motion in the fluidized bed:

. the particle moves predominantly downward with a velocity, $V_{A,DW}$, in the wall region. This region extends about 20% of the bed width from either side of the wall; and

. the particle moves in downward and upward directions with velocities $V_{A,DC}$ and $V_{A,UC}$ respectively in the central region which occupies about 60% of the bed width.

The distributions of the particle velocity, $V_{A,s}$, in these regions are shown in **Figure 5.3.4b**. The mean and the spread of the velocities in both upward and downward directions in the central region are greater than those for the downward velocity in the wall region. On the other hand, the distributions for the particle velocities in both upward and downward directions are somewhat comparable. Experimental results obtained at different fluidizing conditions showed a similar trend.

5.3.1.3 Theory for 'active' particle velocity

Though substantial progress has been reported on the modelling of flow of the gas in a bubbling fluidized bed (Clift and Grace, 1985), prediction of

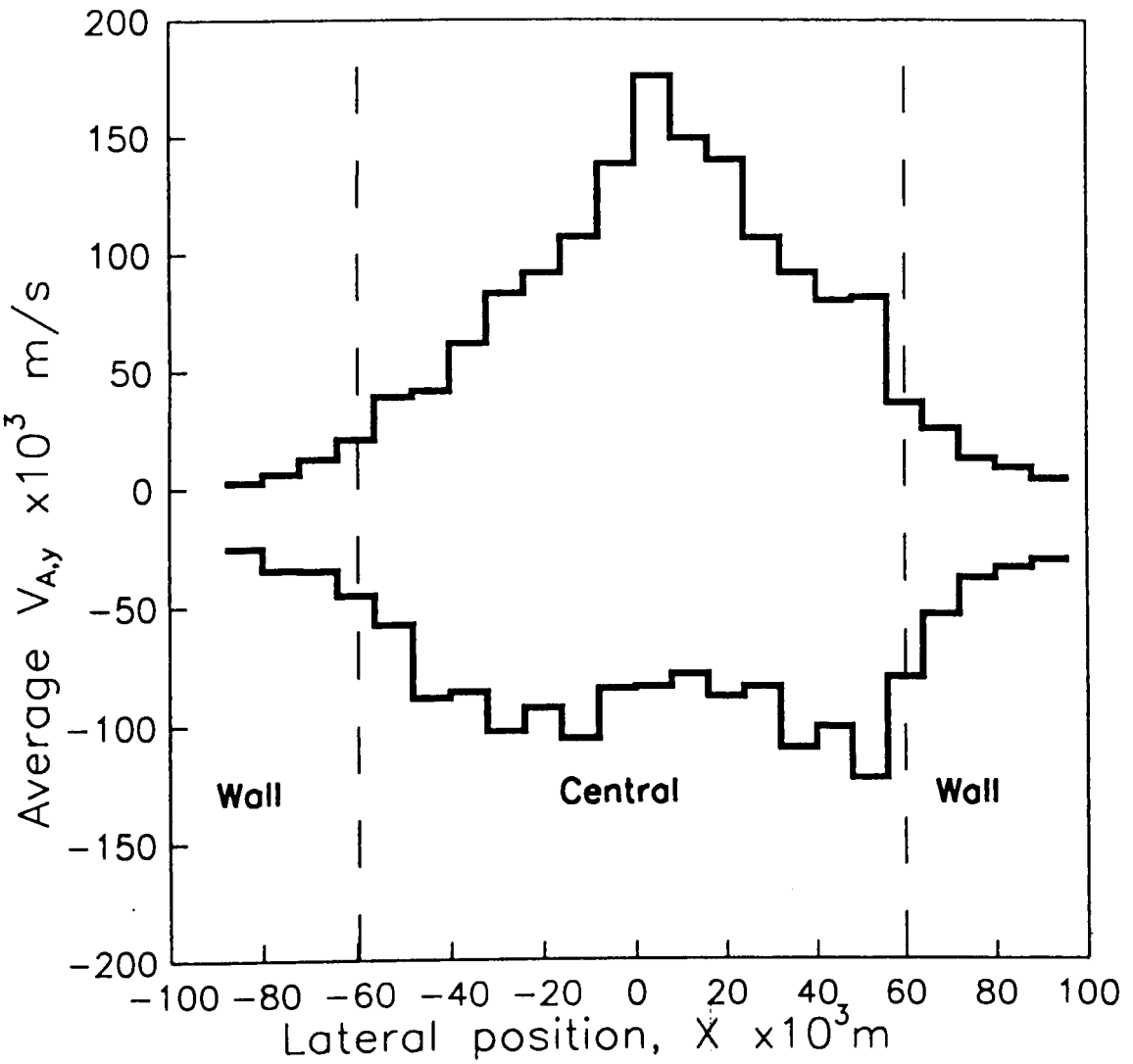

FIGURE 5.3.4a: Height-averaged velocity of the 'active' particle at different lateral positions.

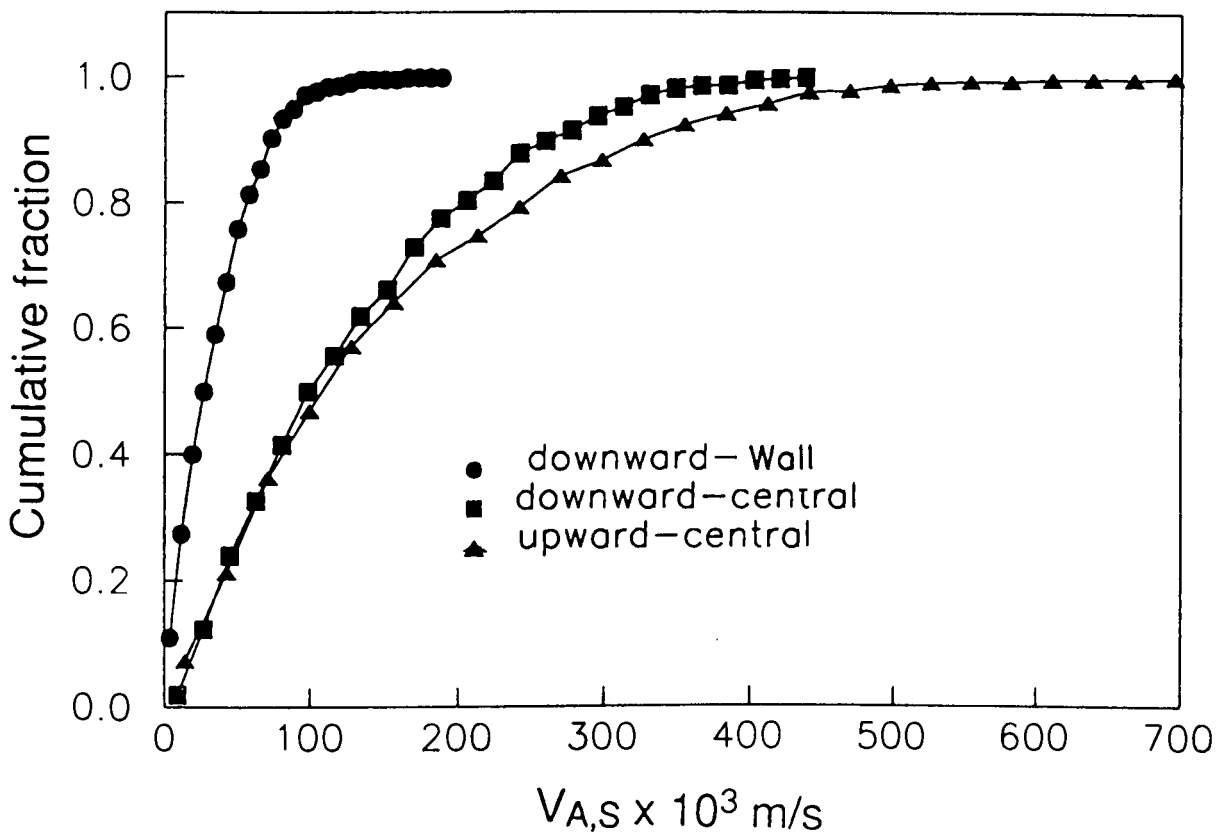

FIGURE 5.3.4b: The cumulative distributions of the height-averaged absolute particle velocity in different regions of the bed.

the solids flow still offers unsolved challenges. In the following we develop simple models, from semi-empirical considerations, to describe the motion of the 'active' particle.

Downward velocity of the 'active' particle in the wall region, $V_{A,DW}$: If there is no segregation between the 'active' and the bed particles when the 'active' particle resides completely in the dense phase (Rios et al., 1986; Agarwal, 1987), then the downward velocity of the 'active' particle in the wall region must be substantially the same as the downward velocity of the dense phase. To test this hypothesis, the dense phase velocity, U_S, was calculated as (Kunii and Levenspiel, 1969)

$$U_S = \frac{f_W \varepsilon_B U_B}{1 - \varepsilon_B - f_W \varepsilon_B} \tag{5.1.16}$$

The bubble fraction, ε_B, and the bubble rise velocity, U_B, were calculated using the appropriate equations (5.1.13-15). The results of the calculations with the wake fraction, f_W, taken as 0.2 are compared with experiment in **Figure 5.3.5a,b.** In **Figure 5.3.5a,** data are presented, and compared with theory, for the variation of $V_{A,DW}$ as a function of height within the bed. In **Figure 5.3.5b** the height-averaged measurements for $V_{A,DW}$ are plotted as a function of the excess gas velocity along with theoretical predictions. It can be seen that calculations compare favourably with experiment. These results are then in accord with Rios et al. (1986). Our experiemntal measurements show a stronger influence of the excess gas velocity, $(U_O - U_{mf})$. It should be noted that our measurements cover a wider range of the excess gas velocity; further, the trend is still in agreement with their theory.

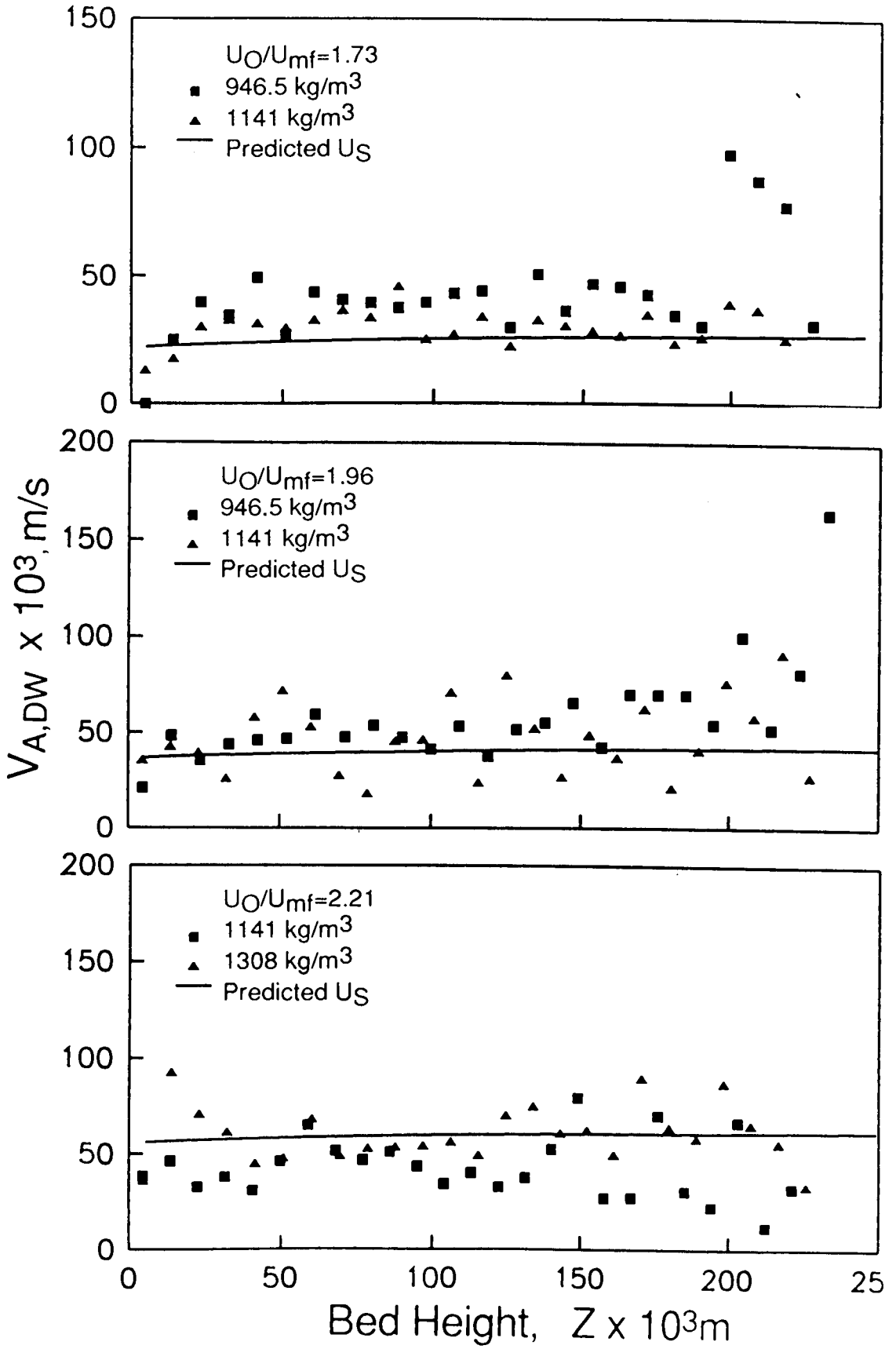

FIGURE 5.3.5a: The downward velocity of the 'active' particle in the wall region, $V_{A,DW}$, as a function of height: Comparison of experiment with theory.

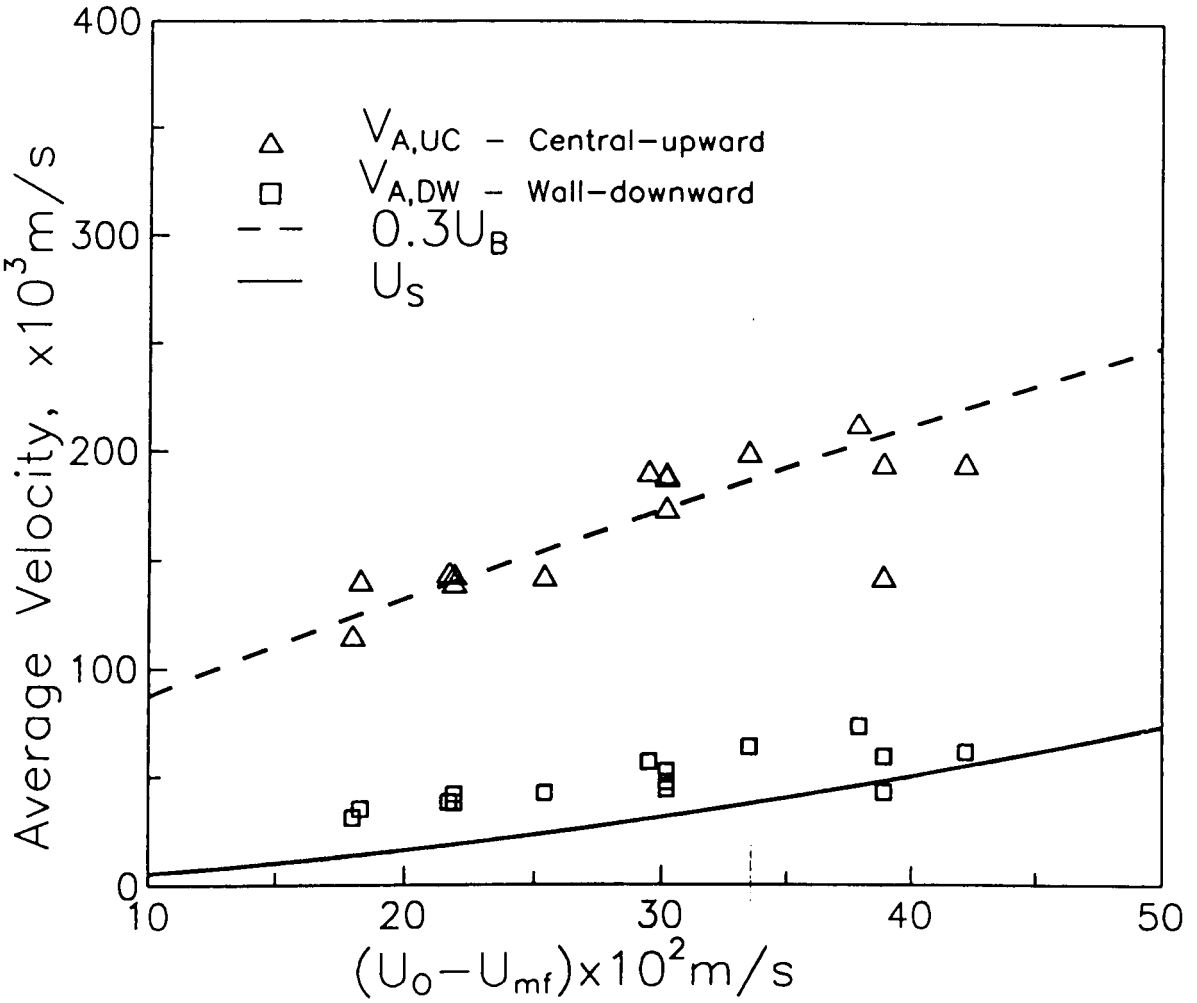

FIGURE 5.3.5b: Height-averaged velocity of the 'active' particles in two different regions of the bed as a function of excess gas velocity.

Upward velocity of the 'active' particle in the central region, $V_{A,UC}$:

Based on visual observations, Nienow et al. (1978) proposed that the height-averaged rise velocity of the 'active' particle, $\overline{U}_R$, can be written as

$$\overline{U}_R = 0.19(U_O - U_{mf})^{1/2} \qquad (5.3.1)$$

Nienow et al. (1978) further indicated that $\overline{U}_R$ was an order of magnitude lower than the bubble rise velocity. It should be noted that U_R differs in concept with the upward particle velocity, $V_{A,UC}$, measured in our experiments. U_R at any height above the distributor represents a time average of both upward and downward particle velocity components in the central region whereas $V_{A,UC}$ includes only the upward component. Hence our measurements are similar to those of Rios et al. (1986) who measured the upward velocity component of particle motion using an 'active' particle doped with radio-active tracer. They presented results on the variation of $V_{A,UC}$ with height above the distributor and concluded that $V_{A,UC}$ was about 30% of the bubble rise velocity.

To clarify the link between $V_{A,UC}$ and U_R, the net upward motion is visualized to result from the following steps:

. the particle executes a hesitating motion under the influence of rising bubbles. This motion is assumed to cause a zero net displacement as the 'active' particle waits for the 'right' bubble to arrive, lift and carry it; and

. once the 'right' bubble is encountered, the particle is carried up at the bubble velocity. After a certain time, the particle is shed from the wake of the bubble and rejoins the dense phase where it waits for another 'right' bubble to come along. This process is repeated until the 'active' particle reaches the top of the bed.

Now consider the time-averaged motion at any given location in the central region of the bed. The fraction of the occurrences corresponding to net upward motion in association with the bubble is denoted as K_R. Then, the fraction of upward hesitating motions (compensated by an equal number of downward hesitating motions and leading to net zero vertical displacement) is $(1-K_R)$. Therefore,

$$V_{A,UC} = (1-K_R)V_{A,HC} + K_R U_B \qquad (5.3.2a)$$

where $V_{A,HC}$ is the upward velocity of the particle during the hesitating motion. If it is assumed further that the upward and downward velocities during the hesitating motion are equal in magnitude (but opposite in direction) then

$$V_{A,UC} = (1-K_R)|V_{A,DC}| + K_R U_B \qquad (5.3.2b)$$

Rearrangement of equation (5.3.2b) yields an expression for estimating K_R from experimental measurements

$$K_R = \frac{V_{A,UC} - |V_{A,DC}|}{U_B - |V_{A,DC}|} \qquad (5.3.2c)$$

In **Figure 5.3.6** the experimental data are plotted with $V_{A,UC}$ and U_B as the y-axis and the corresponding $V_{A,DC}$ as the x-axis. These data lead to average values of $V_{A,UC}/V_{A,DC} = 1.2$ and $U_B/V_{A,DC} = 4.0 \pm 0.5$. Substitution of these numbers in equation (5.3.2c) yields $K_R = 0.07 \pm 0.01$. Further, the ratio of $V_{A,UC}/U_B$ can be determined easily as 0.3 which is in accord with the measurements of Rios et al. (1986) mentioned earlier.

The model for particle motion also leads to

$$U_R = K_R U_B \qquad (5.3.3)$$

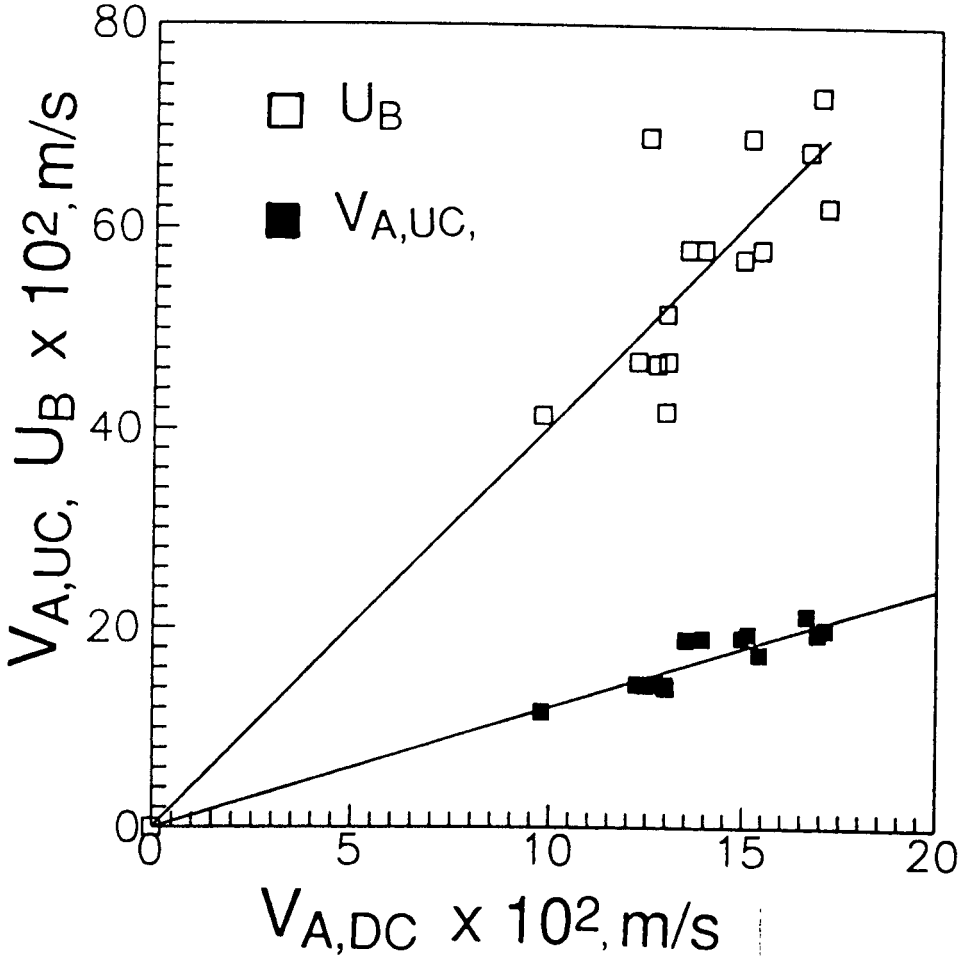

FIGURE 5.3.6: Plot of $V_{A,UC}$ and U_B as a function of $V_{A,DC}$

For comparison with the correlation of Nienow et al. (1978) given by equation (5.3.1), the velocity corresponding to the height-averaged bubble diameter (Darton et al., 1977) in a three-dimensional bed was calculated. Calculations using equation (5.3.3) with $K_R = 0.07 \pm 0.01$, shown in **Figure 5.3.7**, show satisfactory agreement with the higher value of K_R.

Downward velocity of the 'active' particle in the central region, $V_{A,DC}$:

The average downward velocity of the particle in the central region was found to be greater than the downward dense phase velocity but somewhat similar to the upward velocity in the same region. Visual observations indicated that these velocities were generally associated with the particle moving around the edge of a rising bubble or, less frequently, with the particle falling through the bubble roof. Considerable gaps remain in the current understanding of the motion of particles in the immediate vicinity of the bubble. Consequently, prediction of $V_{A,DC}$, in terms of bubble characteristics, appears difficult. Nevertheless, the measured values of $V_{A,DC}$ shed additional light on the measurements of the wake exchange coefficient in a bed of uniform particles reported in **section 5.1.3** as discussed in the following.

The exchange rate of the solids between the dense and wake phase is conventionally estimated assuming that the particles flowing within the bubble cloud region get into the wake and are well-mixed before leaving it (Yoshida and Kunii, 1968; Chiba and Kobayashi, 1977). Adaption of the Yoshida and Kunii model to a two-dimensional fast bubble leads to :

$$k_{WY} = \frac{4U_{mf}(1-\varepsilon_{mf})}{\pi\varepsilon_{mf} f_W (1-\varepsilon_B) d_B} = \frac{A_{WY}}{d_B} \qquad (5.1.17)$$

Similarly, the Chiba and Kobayashi model leads to

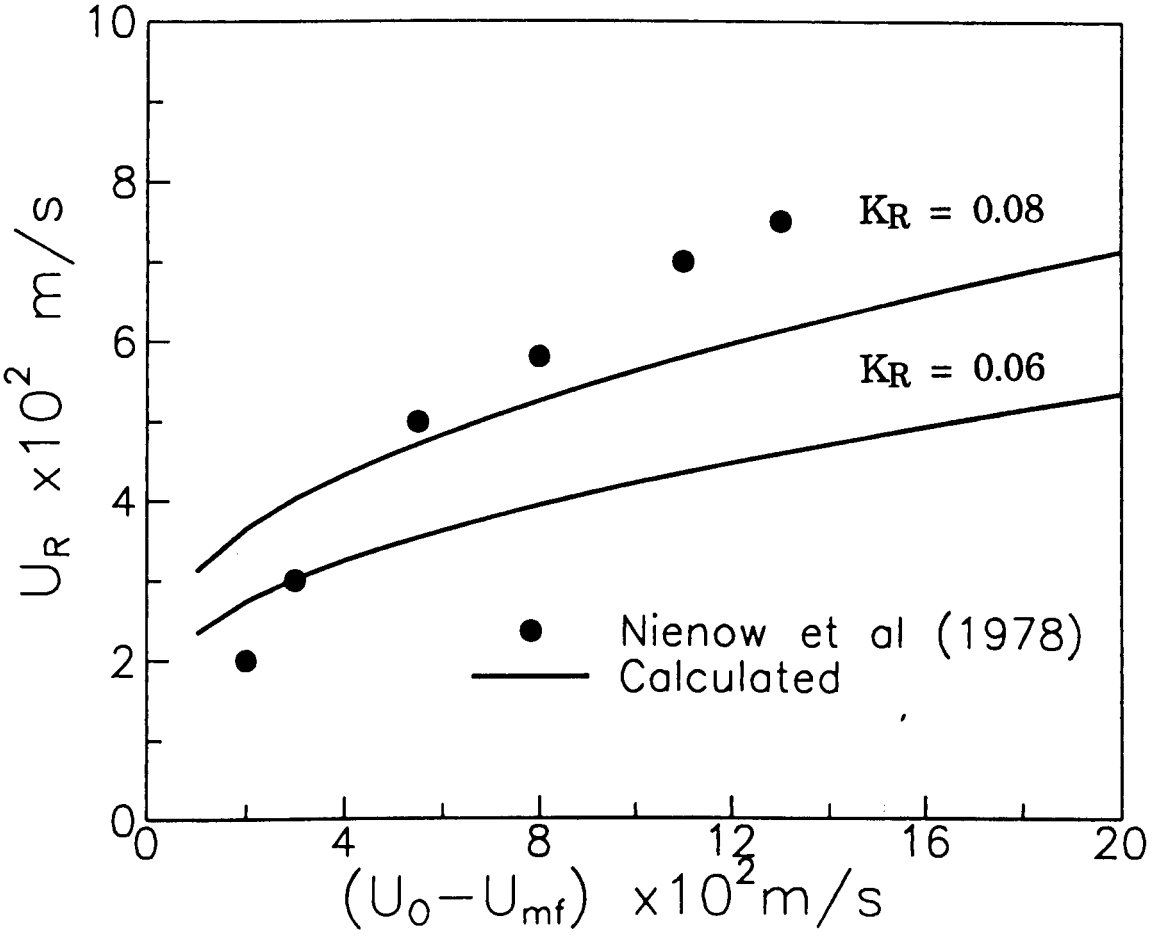

FIGURE 5.3.7: Comparison of the experimental data of Nienow et al. (1978) with calculations using equation (5.3.3)

$$k_{WC} = \frac{4U_{mf}}{\pi\varepsilon_{mf}d_B} = \frac{A_{WC}}{d_B} \tag{5.1.18}$$

Both these models for the wake exchange coefficient can be written as

$$k_{WE} = A_{WE}/d_B \tag{5.1.19}$$

The exchange coefficients derived from equations (5.1.17) and (5.1.18) vary directly with U_{mf} and inversely with bubble size. However, in our previous study on the mixing of uniform particles, section 5.1.3, the exchange constants A_{WY} and A_{WC} were found to be significantly larger than those determined from the fitting of the measured tracer concentration profiles using the three-phase countercurrent backmixing model. Further, the experimental exchange constants, A_{WE}, were also found to be a function of superficial gas velocity for a given particle type (constant U_{mf}); equations (5.1.17) and (5.1.18) do not predict such dependence.

In **Figure 5.3.8,** the measured values of $V_{A,DC}$ are plotted as a function of U_O/U_{mf}. The measured exchange constants in beds of uniformly sized particles, A_{WE}, have also been plotted. It is clear that both sets of data show a linear dependence on U_O/U_{mf} (for $U_O/U_{mf} < 3$ corresponding to $(U_O - U_{mf}) < 0.76\ \mathrm{m\,s^{-1}}$ for the 7.12×10^{-4} m glass ballotini bed particles under consideration).

A link between these measurements can be established using a simple model. It is assumed that the solids flowing in the region between a radius of $k_C d_B/2$ and the bubble boundary, $d_B/2$, enter the wake. The solids flux into and out of the bubble wake, $\dot{V}_W$, can then be estimated from the product of the downward velocity, V_P, of the bed particles and the cross-sectional area resulting from the thickness of the bed and the width of flow region,

$$\dot{V}_W = (k_C - 1)d_B t_T V_P \tag{5.3.4}$$

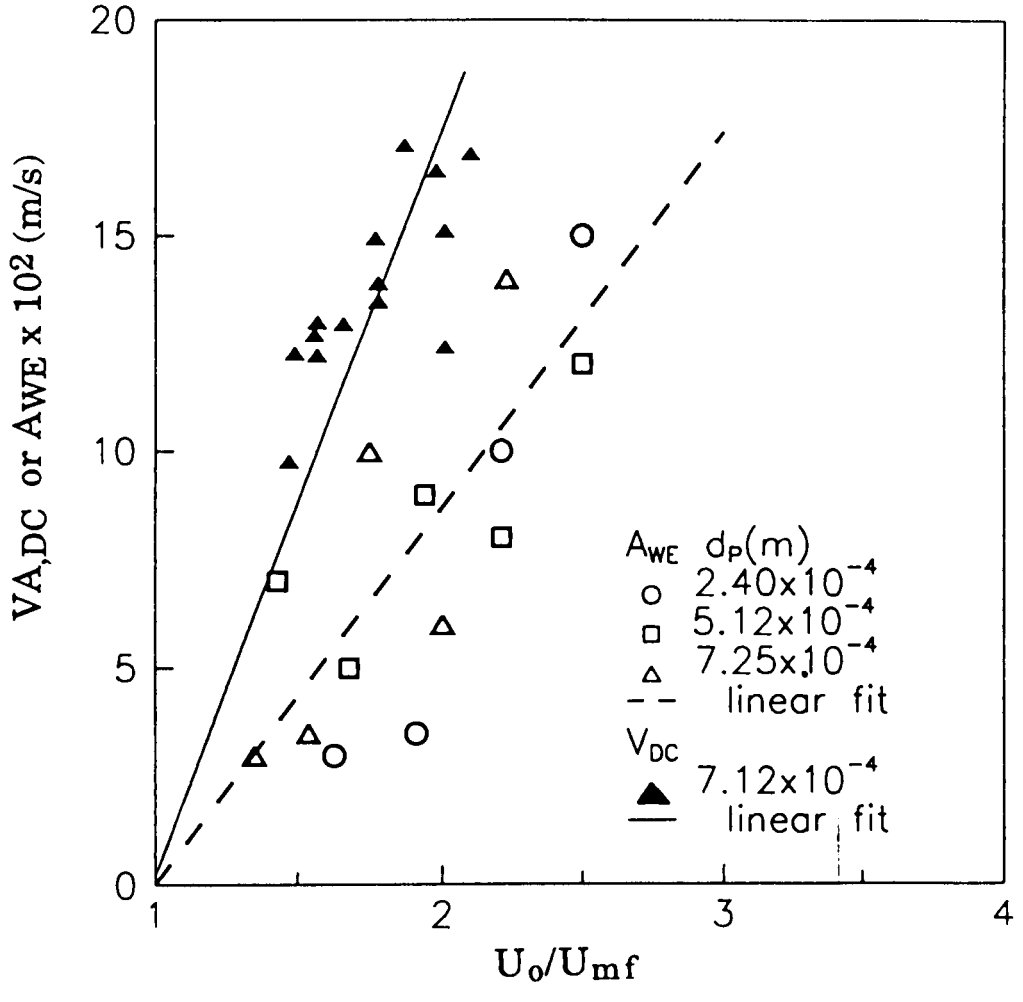

FIGURE 5.3.8: Downward velocity of the active particle in the central region, $V_{A,DC}$, and the wake exchange constant, A_{WE}, as a function of U_o/U_{mf}

It is also assumed that the 'active' particle can move down a net distance, $\bar{y}_s$, compared with the bulk bed particles following the passage of a bubble, **Figure 5.3.9**. Consequently,

$$V_{A,DC} = V_P + \bar{y}_s/t_B = V_P + Y_s U_B \tag{5.3.5}$$

where the bubble passage time, t_B, has been approximated as $t_B = d_B/U_B$ and the dimensionless segregation distance, Y_s, has been defined as $Y_s = \bar{y}_s/d_B$. The exchange coefficient can be written as

$$k_{WE} = \frac{\dot{V}_W}{V_W} \equiv \frac{(k_C - 1)d_B\ V_P}{\frac{\pi}{4} d_B^2 f_W} = \frac{A_{WE}}{d_B} \tag{5.3.6}$$

Combining equations (5.3.5) and (5.3.6),

$$A_{WE} = \frac{4(k_C - 1)}{\pi f_W} V_P = \frac{4(k_C - 1)}{\pi f_W}(V_{A,DC} - Y_s U_B) \tag{5.3.7}$$

Tanimoto et al. (1980) have presented measurements for Y_s (taken as Y_{GR} in **section 5.2**) where the segregating particle is heavier and larger than the bulk bed particles. For the case under consideration, though the 'active' particle is 10 times the size of the bed particles it is also considerably lighter. In the absence of detailed information, at present it is convenient to assume that $Y_s \equiv 0$. Now, if k_C is assumed to be constant then it can be concluded that A_{WE} should be proportional to $V_{A,DC}$ and should also vary with the superficial gas velocity.

From the slopes of $V_{A,DC}$ versus U_O/U_{mf} (0.1724 m s^{-1}) and A_{WE} versus U_O/U_{mf} (0.087 m s^{-1}), k_C was calculated to be approximately 1.08 using f_W = 0.20. This result implies that the region around the bubble from which the solids flow into the wake is 0.04 d_B in thickness. This thickness is considerably smaller than the thickness of the gas cloud from the Davidson (1963) and

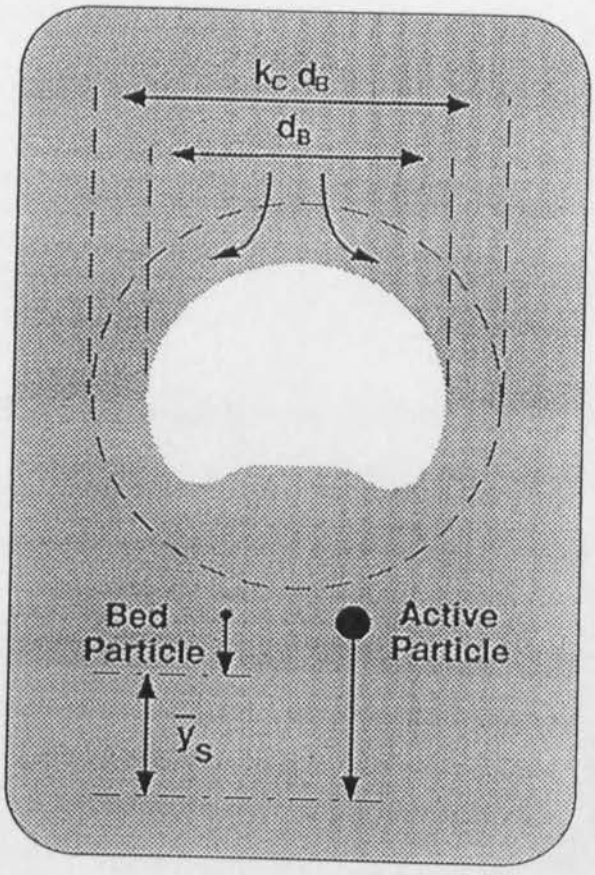

FIGURE 5.3.9: Schematic diagram of 'active' particle motion around a bubble.

Murray (1965) theories. This thickness is also smaller than the thickness of the region in which the solids are expected to move following the passage of a bubble (Singh et al., 1972; Gabor, 1972). The result indicates that only a fraction of the total solids flowing within the cloud region actually enter the wake.

There are some uncertainties in this analysis. The assumption that $Y_s \cong 0$ can be questioned. In addition, the assumption that the particles in the wake are well-mixed can be questioned as well. Kozanoglu and Levy (1990, 1992) suggest the presence of stagnant regions in the wake which will lead to lower exchange rates and, consequently, a lower value of k_C. Despite these uncertainties, the analysis does provide an explanation for the dependence of the wake exchange coefficient on the superficial gas velocity - the fundamental reasons why V_P and $V_{A,DC}$ vary with gas velocity require further investigation. At the very least, the measured variation of $V_{A,DC}$ with superficial gas velocity in a manner similar to the wake exchange coefficient inferred from tracer concentration data is thought to be independent corroboration for the results reported in **section 5.1.3**.

5.3.2 Phase Residence Probability

5.3.2.1 Experimental measurements

The phase with which the 'active' particle is associated within the bed was determined by measuring the average intensity of the neighbouring cells surrounding the particle. The number of the surrounding cells having intensity greater than threshold value (that is, in the bubble void), n_B, were determined. A particle was considered to be totally submerged in the dense phase if n_B was zero. In **Figure 5.3.10**, the cumulative fraction of events is plotted as a function

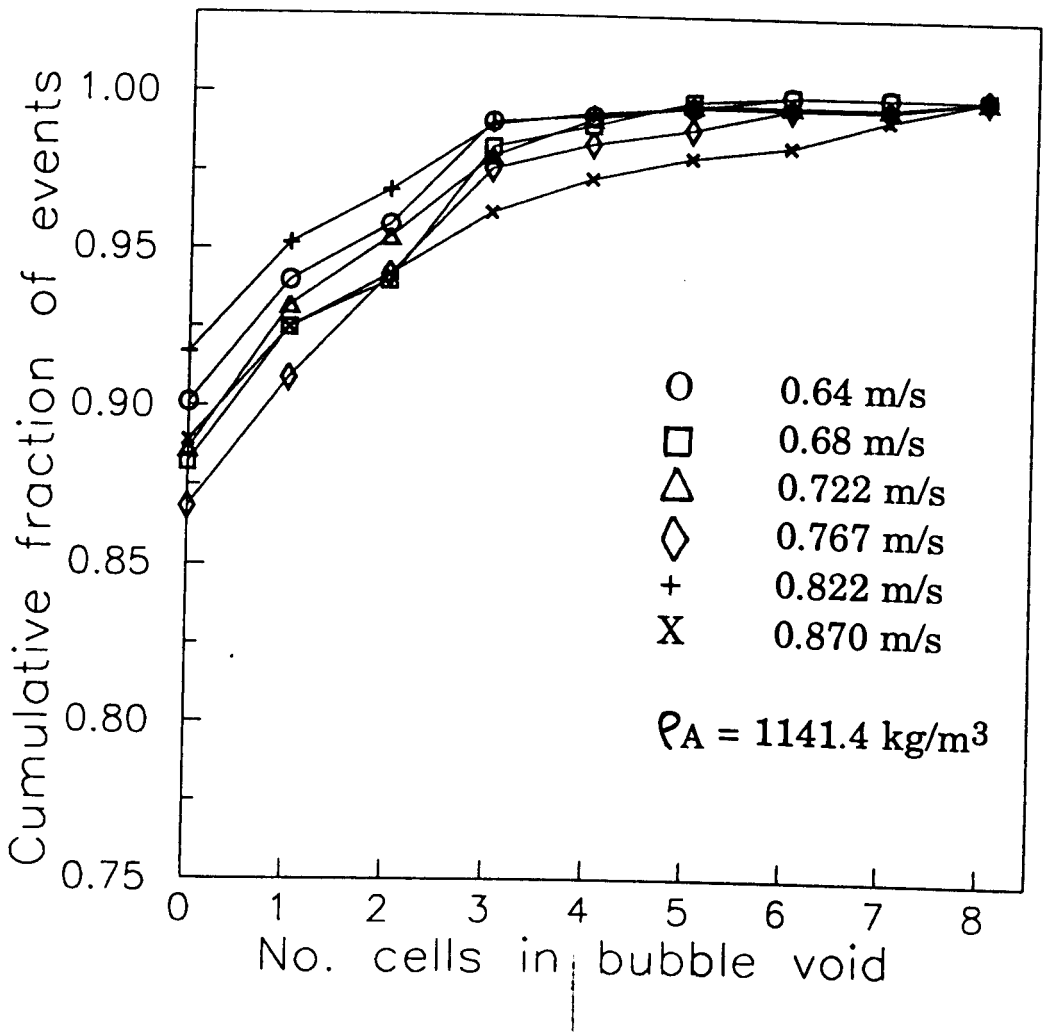

FIGURE 5.3.10: Cumulative faction of events as a function of the number cells surrounding the 'active' particle in the bubble void.

of n_B. It appears that the dense phase completely surrounds the 'active' particle for times ranging between 85 to 92%. For the rest of the time, the 'active' particle has some association with the bubble phase though the chance of its being present within the bubble phase entirely is very small. It was assumed that a particle resided in the dense phase if the number of surrounding cells in the bubble void is less than 25%, that is 2 of the 8 cells in **Figure 3.2.18.** Otherwise, the particle was considered to be in contact with the bubble phase. The probability of the 'active' particle residing in the dense phase, p, was then evaluated as

$$p = \frac{N_D}{N_T} \tag{5.3.8}$$

where N_D is the number of the events in which the 'active' particle was detected as present in the dense phase [p at $n_B \leq 2$] and N_T is the total number of events excluding all null decision events. Since the fluidized bed is considered as a two-phase system, the bubble phase residence probability is clearly $(1-p)$.

Experimentally measured values of the dense phase residence probability, p, of the 'active' particle are shown as a function of excess gas velocity in **Figure 5.3.11.** Clearly, the value of p decreases with increasing excess gas velocity because the 'active' particle associates increasingly with the bubble phase. The average value of p is measured to be about 0.92. In addition, the dependency of p on the density of the 'active' particle is very small. Thus, the 'active' particle spends about 10% of its time in association with the bubble phase for the experimental conditions considered in this investigation.

5.3.2.2 Theory for residence phase probability

Agarwal (1987) proposed a model for the residence phase probability which assumed that the 'active' particle experienced a series of captures and

sheddings while rising to the top of the bed. It was further assumed that there was no slip between the 'active' particle and the phase, bubble or dense, it was associated with. This model leads to

$$p = \frac{\overline{U_B}}{\overline{U_B} + \overline{U_D}} \tag{5.3.9}$$

The circulation pattern which emerges from our present measurements is that the downward velocity of the 'active' particle in the central region is significantly different from the dense phase velocity. Further, in the central region, only a fraction, K_R, of upward movements actually results in net upward displacement in association with the bubble; the fraction, $(1-K_R)$, of the upward movements is compensated by downward movements resulting in roughly zero net vertical displacement. The approach of Agarwal (1987) can be corrected and the dense phase residence probability determined using

$$p = \frac{X/U_S + X/U_R\psi}{X/U_S + X/U_R} \tag{5.3.10}$$

where X is the penetration depth of the 'active' particle in the fluidized bed. ψ is the fraction of the time spent by the particle in association with the dense phase during its sojourn in the central region and can be written as

$$\psi = (1-K_R)p_H \tag{5.3.11}$$

p_H is the fraction of time spent in association with the dense phase during the hesitating motions. Direct experimental determination of p_H, at this stage, appears difficult. Using equations (5.1.16), (5.3.10) and (5.3.11) it can be shown that

$$p = \frac{K_R((1-\varepsilon_B - f_w\varepsilon_B) - f_w\varepsilon_B p_H) + f_w\varepsilon_B p_H}{K_R(1-\varepsilon_B - f_w\varepsilon_B) + f_w\varepsilon_B} \tag{5.3.12}$$

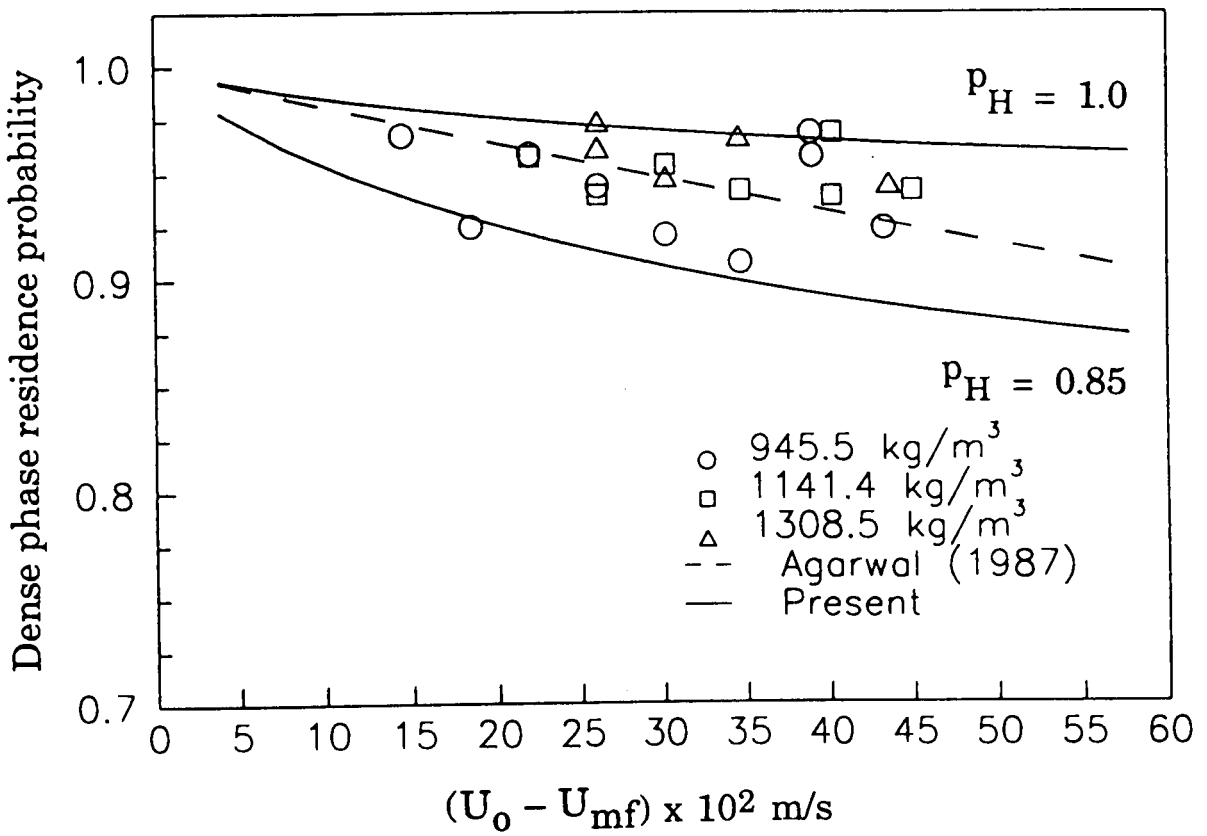

FIGURE 5.3.11: Dense phase residence probability as a function of excess gas velocity. Comparison of theory with experiment.

In **Figure 5.3.11**, calculations using equation (5.3.12) with K_R = 0.07 are compared with experimental data. The upper bound of the data corresponds to $p_H = 0.975$ and the lower bound to $p_H = 0.875$; an average value of $p_H = 0.9$ is recommended. This result implies that the active particle, even when not executing the net upward motion, is associated with the bubble phase for about 10% of the time. This is not specially surprising since the hesitating motions also are a direct consequence of bubbling activity. It is interesting to note that, in spite of differences in the mechanistic description, predictions from equation (5.3.9) compare well with experimental data in **Figure 5.3.11.**

5.3.2.3 Conclusions

Automated image analysis methods have been used to characterize the circulation pattern of the 'active' particle and to measure its velocity in the bubbling bed. The results show dominant 'active' particle motion patterns in various regions of the fluidized bed - descending near the edge of the wall and ascending in the central region. The downward velocity of the particle in the wall region is comparable to the calculated solids dense phase velocity. Extensive particle/bubble interaction was measured in the central rising region which leads to large upward and well as downward velocities. The average upward velocity of the particle was found to be about 0.3 U_B. The measured downward velocity in the central region - a consequence, mainly, of the 'active' particle moving around the bubble - provides a possible explanation for the dependency of the solids exchange constant on the fluidizing gas velocity.

This experimental technique has also been used to measure the phase residence probability of the 'active' particle. The measurements indicate that the 'active' particle is increasingly associated with the bubble phase of the fluidized bed as the excess gas velocity is increased.

Chapter 6

CONCLUSIONS AND RECOMMENDATIONS

A new method for non-intrusive sensing and measurement of important characteristics of bubbling fluidized beds has been developed based upon the principles of digital image analysis. The procedures developed provide several key elements which make this technique extremely attractive for such measurements and characterization. A high level of automation is introduced into the acquisition, processing and analysis of digitized images. The laborious manual effort and consequent tedium of previous studies have been dramatically alleviated. Automation of the analysis procedure means that a large number of images are captured for any data set. This should improve the statistical accuracy of any ensemble estimates produced. The use of gray-level thresholding improves the reliability for delineation of the phase boundary; edge detection is now objective and consistent. This is an important advantage where measurements in two-phase are necessary. The availability and continued development of image analysis software across several disciplines is another advantage.

In the research reported in this thesis, digital image analysis techniques have been used on two-dimensional fluidized beds to address the following problems :

- measurement of bubble size distributions;
- evaluation of geometrical probability methods for interpretation of pierced length signals obtained from dual-tipped submersible probes frequently employed for bubble characterization in three-dimensional beds;
- evaluation of the influence of non-vertical bubble rise on the interpretation methods, and designs, of submersible probes used in three-dimensional fluidized beds;
- measurement and interpretation of tracer concentration profiles in fluidized beds of uniform particles;
- measurement and interpretation of jetsam concentration profiles in segregating binary fluidized beds; and
- tracking of a larger and lighter (or 'active') particle in fluidized beds of smaller and heavier particles.

Given the versatility of the technique, it can be used readily to explore the influence of the presence of in-bed tubes on the behaviour of the bubble and solid phases. Extensions of the technique to other configurations of fluidized beds are also possible. In the following, the major conclusions from the study are summarized.

Bubble Size Distributions : The experimental measurements for bubble size distributions were compared with predictions from a population balance model using coalescence as the dominant growth mechanism. This comparison has highlighted some discrepancies and further work on modelling bubble growth is required. Average bubble size measurements compare favourably with the correlation of Chiba et al. (1973) for two-dimensional beds.

Given the simplicity of the method, it was considered ideal for the calibration of submersible probes and further work was undertaken in this direction.

Conversion of Bubble Pierced Lengths Measured at a Submersible Probe to Bubble Size Measures : The distributions of the bubble pierced length as well as other bubble size measures were measured experimentally. The experimental results showed that bubble size distribution can not be obtained directly from the pierced length distribution. However, reasonably reliable inferences can be made using geometrical probability approach. Results of comparison, for bubble size distributions as well as overall statistical analyses, suggested that simulations using spherical or ellipsoidal (α=0.77) models provide satisfactory agreement between experiment and theory. Lateral non-homogeneity in bubbling as well as the non-uniformity in bubble shapes have been detected experimentally. Further work is necessary to include these refinements in the theory.

These results will significantly enhance confidence in the use of intrusive probes (measuring only the pierced length distributions) to determine the size distributions of bubbles or droplets dispersed in a medium. Two further considerations need a more detailed appraisal:

- the ability of two-element probes to measure bubble velocity and pierced length unequivocally; and
- the possibility of alteration in the local behaviour of the dispersed phase due to the presence of the in bed probe.

Due to constraints of time, only the first issue could be addressed in detail; the conclusions from the study are outlined in the following.

Influence of the Angle of Bubble Rise on Bubble Velocity : This study was undertaken to determine whether the dual-tipped probe does measure bubble velocity and pierced length unequivocally. Theoretical analysis showed that the angle of bubble rise will influence the measurements made using submersible probes based on the conventional probe signal interpretation methods. The experimental results indicated that the angle of rise deviated significantly from the vertical. Surprisingly, the density functions of the rise angle did not appear to depend strongly on the position in the bed and superficial gas velocity for the range of conditions considered. Since the existing signal analysis procedures for two-element submersible probes are based on vertical bubble rise, these results show that available results from such probes can not be considered as quantitative. Multiple-element probes detect and reject non-vertically rising bubbles. Analysis of the data established that such rejection did not bias the measurements of bubble characteristics and consequently such probes should be preferred.

Bubble size/shape were also measured simultaneously using the global thresholding techniques. These measurements enabled assessment of the relationship between bubble size/shape and velocity. For comparison with results for freely bubbling beds, separate experiments were performed with bubbles (single as well as chains) injected in incipiently fluidized beds.

The results indicated that the density functions for the rising velocity coefficient from freely bubbling beds were virtually identical for different locations in the bed and operating conditions considered in this investigation. These density functions were also in very good agreement with those from continuously injected bubbles in incipiently fluidized beds. The density functions of the rise velocity coefficient for single injected bubbles had a lower mean and standard deviation. The inclusion of the excess gas

velocity term in the equation for bubble velocity led to good agreement between the mean of the rising velocity coefficient density function for bubbles injected singly and in freely bubbling beds; the standard deviation for freely bubbling beds, however, remained higher.

The possibility of alteration of the local behaviour of the dispersed phase due to the presence of submersible probes needs further study. Preliminary comparisons between measurements from two types of submersible probes - capacitance and fiber-optic - and image analysis were made. However, a complete study could not be undertaken because of time constraints.

Mixing of Uniform Solids : An effective and reliable method for the measurement of solids mixing in fluidized beds was developed. The advantage of this image analysis based technique included

- continuous data acquisition and fully automated data analysis;
- fast response;
- ability to measure the mixing behaviour while the bed is fluidized; and
- simultaneous measurement of mixing at different locations in the bed to enable unambiguous determination of model parameters.

The data obtained for the mixing of uniform solids showed oscillations in tracer concentration resulting from the gross circulation of the solids. These oscillations became increasingly more prominent with increase in bed particle size.

The experimental data were interpreted using the three-phase counter-current back-mixing model. The bubble phase parameters required for model calculations were also measured and interpreted in terms of appropriate models. The comparison of model calculations and experimental data showed that the models for the prediction of the wake exchange coefficient currently available in the literature (Yoshida and Kunii, 1968; Chiba

and Kobayashi, 1977) were not adequate. In particular, the wake exchange coefficient appeared to increase with U_o/U_{mf} for $U_o/U_{mf} < 3$ and the values, in this region, were independent of the particle size. The models, on the other hand, predicted that the wake exchange coefficient should increase with increase in the minimum fluidization of the bed particles. In line with these results, the experimental measurements of Chiba and Kobayashi, for injected bubbles in a two-dimensional fluidized bed of particles smaller than those used in this investigation, were found to in excellent agreement with the lower bound of our measurements.

It is expected that the results on the wake exchange coefficient obtained from the two-dimensional bed studies will apply to three-dimensional beds at least qualitatively in terms of the absence of particle size effects and the dependence on U_o/U_{mf}. Quantitative agreement will depend on the magnitude of the difference between motion of solids around the edge of the bubble in two- and three-dimensional beds. Additional theoretical work, supplemented by careful experiments, is necessary to investigate the motion of particles in the vicinity of the bubble to develop a predictive understanding of solids mixing in fluidized beds.

Segregation in Binary Fluidized Beds : Unsteady material balance equations from the Gilibaro-Rowe (1974) and Yoshida (1980) models for segregating fluidized beds were solved numerically. The possibility of the formation of a defluidized layer at the bottom of the bed was taken into account. Comparison of model predictions with data indicated that though these models did reflect some features of the experiment, the influence of the superficial velocity on the temporal variation of the concentration at any specific height within the bed was not predicted. In fact, a trend completely opposite to that predicted was observed experimentally. If these models are to be used, then the segregation rate parameter must have a dependence on superficial velocity substantially

different to that currently available in the literature. Further work in this direction is recommended. The influence of jetsam concentration was not explored in this experimental study; such measurements are recommended as well.

Some preliminary empirical relations were established for the movement of the defluidized layer with time. In particular, a promising new indicator for segregation propensity was proposed from analogy with vapour-liquid equilibrium data representation methods. Additional data are necessary before further generalization can be attempted.

Motion of a Larger and Lighter (or 'Active') Particle in Fluidized Beds of Smaller and Heavier Particles : Automated image analysis methods were used to characterize the circulation pattern of the 'active' particle and to measure its velocity in the bubbling bed. The results showed dominant 'active' particle motion patterns in various regions of the fluidized bed - descending near the edge of the wall and ascending in the central region. The downward velocity of the particle in the wall region was comparable to the calculated solids dense phase velocity. Extensive particle/bubble interaction was measured in the central rising region which led to large upward and well as downward velocities. The average upward velocity of the particle was found to be about 0.3 U_B. The measured downward velocity in the central region - a consequence, mainly, of the 'active' particle moving around the bubble - provided a possible explanation for the dependency of the solids exchange constant on the fluidizing gas velocity.

This experimental technique was also used to measure the phase residence probability of the 'active' particle. The measurements indicated that the 'active' particle was increasingly associated with the bubble phase of the fluidized bed as the excess gas velocity was increased. The results point to the necessity of including the motion of coal particles in future modelling of fluidized bed combustion.

NOMENCLATURE

a	parameter
a'	major axis of an ellipsoid, m.
A	area of a two-dimensional bubble, m^2
A_d	area of distributor, m^2
A_{C0}	bubble catchment area at the distributor, m^2
A_{WC}	exchange constant, ms^{-1}
A_{WE}	exchange constant, ms^{-1}
A_{WY}	exchange constant, ms^{-1}
A_0, A_1	variables.
b	parameter
b'	minor axis of an ellipsoid, m
C_R	correction factor for bubble size
C	concentration or volume fraction of the solids tracer, [-]
C_P	circumference, m
d_A	diameter of 'active' particle, m
d_B'	bubble diameter under unconstraint growth, m
d_B	bubble diameter, m
d_{DB}	bubbble diameter with growth constrained by presence of bed walls, m
d_E	area-equivalent diameter, m
d_F	flotsam particle size, m
d_H	maximum horizontal dimension, m

d_J	jetsam particle size of, m
d_0	initial bubble diameter, m
d_P	bed particle size, m
D_T	bed diameter or bed width in a 2-d bed, m
d_V	maximum vertical dimension, m
$d_{V,\min}$	minimum vertical dimension, m
E	elliptic integral
f	probability density function
F	cumulative distribution
f_W	wake fraction, [-]
F_1	measured bubble size/shape variable in the first image field
F_2	measured bubble size/shape variable in the second image field
g	acceleration due to gravity, m s^{-2}
H_E	expanded bed height, m
H_F	fixed bed height, m
I	mean gray scale of cell sample, [-]
k	adjustable parameter
k_1	constant for the bed expansion
k_3	adjustable parameter
k_E	dense or emulsion phase transfer coefficient based on the corresponding phase volume, s^{-1}
k_W	wake phase transfer coefficient based on the corresponding phase volume, s^{-1}

k_S	settlement rate, m s^{-1}
K_T	gas through-flow factor, [-]
K	constant
K_B	bubble rise velocity coefficient, dimensionless, [-]
K_R	fraction of occurences correspond to upward motion of 'active' particle in association with a bubble
L_{pr}	distance between probe tip and bed centre, m
m	adjustable parameter
n_B	number of the events in which the 'active' particle was detected as present in the bubble phase
n_T	total number of image frames analysed
n_d	number of holes in the perforated plate
p	the presence probability of the 'active' particle residing in the emulsion phase
q	initial location of the tracer discharge, [-]
Q	gas flowrate, m^3 s^{-1}
Q_T	bubble throughflow rate, m^3 s^{-1}
r	distance, m
R	radius of bubble, m
R_Y	dimensionless segregation parameter
s	adjustable parameter
S	shape factor (= $P/\pi d_e$)
t	time, s
t_S	separation between probe tips, m

t_B	bubble passage time, s
$t_{P,S}$	time required for reaching steady state conditions, s
t^*	dimensionless time required for reaching steady state conditions
t_T	bed thickness, m
t_H	delay time or the time required for the leading bubble interface to travel from the lower to the upper probe tip in a two-element probe, s
U_B	bubble velocity, m s^{-1}
U_{mf}	minimum fluidization velocity, m s^{-1}
$U_{mf,c}$	minimum fluidization velocity of a binary mixture, m s^{-1}
U_O	superficial gas velocity, m s^{-1}
U_{Br}	bubble rise velocity, m s^{-1}
$\overline{U_R}$	average rise velocity of the 'active' particle, m s^{-1}
U_S	average descent velocity of the dense phase, m s^{-1}
$V_{A,DC}$	downward velocity of the 'active' particle in the central region, m s^{-1}
$V_{A,DW}$	downward velocity of the 'active' particle in the wall region, m s^{-1}
$V_{A,HC}$	upward velocity of the 'active' particle during hesitating motion in the central region, m s^{-1}
$V_{A,S}$	absolute velocity of the 'active' particle, m s^{-1}
$V_{A,x}$	x-component of 'active' particle velocity, m s^{-1}
$V_{A,y}$	y-component of 'active' particle velocity, m s^{-1}
$V_{B,m}$	bubble rise velocity inferred by a conventional two-element probe, m s^{-1}
$V_{B,s}$	magnitude of the actual bubble velocity, m s^{-1}
$V_{B,x}$	x-component of bubble velocity, m s^{-1}

$V_{B,y}$	y-component of the bubble velocity, m s^{-1}
$V_{B,\theta}$	actual bubble rise velocity at an angle θ, m s^{-1}
W	width of the two-dimensional fluidized bed, m
X	position of 'imaginary' probe in a 2-D bed
x	fraction of tracer discharge, [-]
y	pierced length, m
y_L	pierced length at the lower tip of a two-element probe, m
y_U	pierced length at the upper tip of a two-element probe, m
Δy	difference in pierced lengths at the two tips of the probe, m
Y_{GR}	dimensionless segregation parameter
Y_{KL}	dimensionless segregation parameter
Y_Y	dimensionless segregation parameter
Z'	$Z' = Z + Z_o$, where $Z_o = 0$ for porous plate, m
Z	bed height from the distributor, m
Z_P	steady state height of defluidized layer, m
$Z_{P,S}$	height of defluidized layer at time t, m
Z^*	dimensionless height of the defluidized layer

Subscripts

B	bubble phase
BD	bubble diameter with the influence of bed diameter
E	emulsion (dense) phase
F	flotsam

J	jetsam
m	experimental measurement
max	maximum
min	minimum
nor	normalized quantity
TH	at threshold condition
total	total gas flow
W	wake phase

Superscript

—	average property

Greek symbols

α_{AB}	dimensionless segregation propensity
ε_B	bubble fraction
ρ_P	density of particle, kg/m^{-3}
ρ_A	density of 'active' particle, kg/m^{-3}
δ	variable
Γ	Gamma function $\Gamma(m+1) = \int_0^{\infty} a^m e^{-a} da$
γ	incomplete Gamma function $\gamma(m+1,a) = \Gamma(m+1)\left\{1 - e^{-a}\left(\sum_{i=0}^{m} \frac{a^i}{i!}\right)\right\}$
$\Delta A_{i,j}$	incremental cell area, m^{-2}
ε_{mf}	dense phase porosity at minimum fluidization, [-]

$\varepsilon_{B,Expt}$	bed expansion factor, $(H_E - H_F)/H_E$
λ_B	proportionality constant for the distance a bubble travels before coalescence, [-]
β	variable
η	variable
θ_B	angle of bubble rise or the angle of bubble incidence at a submerged probe, deg
τ	variable
α	aspect ratio
λ	radial distance from bed centre
μ	mean value
σ	standard deviation.
θ	angular variable (deg / rad)
ψ	variable
θ_w	wake angle (deg / rad)
ϕ	angular variable (rad)

REFERENCES

Agarwal, P.K., 1987, *The residence phase of active particles in fluidized beds of smaller inert particles*, **Chem Engng Sci**, 42, 2481-2483.

Agarwal, P.K., 1985, *Bubble characteristics in gas-fluidized beds*, **Chem Engng Res Des, 63**, 323-337.

Agarwal, P.K., 1986, *Single particle model for the evolution and combustion of coal volatiles*, **Fuel, 65**, 803-810.

Agarwal, P.K., 1987, *The effect of bed diameter on bubble growth and incipient slugging in gas fluidized beds*, **Chem Engng Res Des, 65**, 345-354

Agarwal, P.K. and La Nauze, R.D., 1989, *Transfer processes local to the coal particle: A review of drying, devolatilization and mass transfer in fluidized bed combustion*, **Chem Engng Res Des, 67**, 457-480.

Argyriou, D.T., List, H.L. and Shinnar, R., 1971, *Bubble growth by coalescence in gas fluidized beds*, **AIChE J, 17**, 122-130,

Atkinson C.M. and Clark, N.N., 1998, *Gas sampling from fluidized beds: A novel probe system*, **Powder Technol, 54**, 59-70.

Avidan, A. and Yerushalmi, J., 1985, *Solids mixing in an expanded top fluid bed*, **AIChE J, 31**, 835-841.

Babu, S.P., Leipziger, S, Less, B.S. and Weil, S.A., 1973, *Solids mixing in batch operated tapered and non-tapered gas fluidized beds*, **Chem Engng Prog Symp Ser, 66**, 49-57.

Bailie, R.C. 1967, *Double transport model for particle movement in a fluidized bed*, **Proc Intern Symp on Fluidization** (A.A.H. Drinkenburg, Ed), Netherlands University Press, Amsterdam, 322-333.

Beeckmans, J.M., Bergstrom, L. and Large, J.F., 1984, *Segregation mechanisms in gas fluidized beds*, **Chem Engng J, 28**, 1-11.

Beeckmans, J.M., Nilson, J. and Large, J.F., 1985, *Observations on the mechanisms of segregation in flotsam-rich, fully fluidized beds*, **Ind Engng Chem Fundam, 24**, 90-95.

Beeckmans, J.M. and Stahl, B., 1987, *Mixing and segregation kinetics in a strongly segregated gas-fluidized bed*, **Powder Technol, 53**, 31-38.

Bellgardt, D. and Werther, J., 1986, *A novel method for the investigation of particle mixing in gas-solids systems*, **Powder Technol, 48**, 173-180.

Berruti, F., Scott, D.S. and Rhodes, E., 1986, *Measuring and modelling lateral solids mixing in a three-dimensional batch gas-fluidized bed reactors*, **Can J Chem Engng, 64**, 48-55.

Bilbao, R., Lezaun, J., Menendez, M. and Ababades, J.C., 1988, *Model of mixing segregation of straw sand mixtures in fluidized beds*, **Powder Technol, 56,** 149-1551

Bilbao, R., Lezaun, J., Menendez. M. and Izquierdo, M.T., 1991, *Segregation of straw sand mixtures in fluidized beds in non-steady state*, **Powder Technol, 68,** 31-35

Burgess, J.M., Fane, A.G. and Fell, C.J.D., 1981, *Application of an electroresistivity probe technique to a two-dimensional fluidized bed*, **Trans Inst Chem Engng, 59**, 249-252.

Burgess, J.M. and Calderbank, P.H., 1975, *The measurement of bubble properties in two-phase dispersions - III. Bubble properties in a freely bubbling fluidized-bed*, **Chem Engng Sci, 30**, 1511-1518

Burgess, J.M. Fane, A.G., Fell, J.D., *Measurements and predictions of the mixing and segregation of solids in gas fluidized beds*, **2nd Pacific Chem Eng Con PACHEC '77 August 28-31,** 1405-1417

Burgess J. M. and Calderbank, P.H., 1975, *The measurement of bubble parameters in two-phase dispersions - I - The development of an improved probe technique*, **Chem Engng Sci, 30**, 743-750.

Castleman, K.R., 1976, **Digital Image Processing**, Prentice-Hall, Englewood Cliffs, p. 76.

Chan, I.H., Sishtla, C. and Knowlton, T.M., 1987, *The effect of pressure on bubble parameters in gas-fluidized beds*, **Powder Technol, 53**, 217-235.

Chen, J.L.P. and Keairns, D.L., 1975, *Particle segregation in a fluidized bed*, **Can J Chem Engng,** 53, 395-402.

Cheremisinoff, N.P., 1986, *Review of experimental methods for studying the hydrodynamics of gas-solid fluidised beds*, **Ind Engng Chem Proc Des Dev, 25**, 329-351

Cheung, L., Nienow, A.W. and Rowe, P.N., 1974, *Minimum fluidization velocity of a binary mixture of different sized particles*, **Chem Engng Sci, 29,** 1301-1303

Chiba, S., Chiba, T., Nienow, A.W. and Kobayashi, H., 1979, *The minimum fluidization velocity, bed expansion and pressure-drop profiles of binary particle mixtures*, **Powder Technol, 22,** 255-269

Chiba, S., Nienow, A.W., Chiba, T. and Kobayashi, H., 1980, *Fluidized binary mixtures in which denser component may be flotsam*, **Powder Technol, 26**, 1-10.

Chiba, T., and Kobayashi, H., 1982, *Effect of bubbling on solid segregation in gas fluidized beds*, **Proc China - Japan Symp on Fluidization**, 79-90.

Chiba, T., Terashima, K. and Kobayashi, H., 1975, *Lateral distribution of bubble sizes in two-dimensional gas fluidized beds*, **J Chem Engng Japan, 8**, 167-169.

Chiba, T. and Kobayashi, H., 1977, *Solid exchange between the bubble wake and the emulsion phase in a gas-fluidized bed*, **J Chem Engng Japan, 10**, 206-210.

Chiba, T. and Nienow, A.W., 1983, *Defluidization of large particles due to segregation*, in **Fluidization IV** (D. Kunii, and R. Toei, Eds), Engineering Foundation, New York, 195-202.

Chiba, T. Terashima, K and Kobayashi, H., 1973, *Bubble growth in gas fluidized beds*, **J Chem Engng Japan, 6**, 78-84.

Chyang, C-S., Kuo, C-C., Chen, M-Y., 1989, *Minimum fluidization velocity of binary mixtures*, **Can J Chem Engng, 67,** 344-347

Clark N.N. and Turton, R., 1988, *Chord length distributions related to bubble size distributions in multiphase flows*, **Int J Multiphase Flow, 14**, 413-424.

Clift R. and Grace, J.R., 1970, *Bubble interaction in fluidized beds*, **Chem Engng Prog Symp Ser, 66**, 14-27.

Clift R. and Grace, J.R., 1971, *Coalescence of bubbles in fluidized beds*, **AIChE Symp Ser, 67**, 23-33.

Clift R. and Grace, J.R., 1985, *Continuous bubbling and slugging*, in **Fluidization** (J.F. Davidson, R. Clift and D. Harrison, Eds), Academic Press, 73-131.

Cranfield, R.R., 1972, *A probe for bubble detection and measurement in large particles fluidized beds*, **Chem Engng Sci, 27,** 239-245.

Cranfield, R.R., 1978, *Solids mixing in fluidized beds of large particles*, **AIChE Symp Ser, 74**, 54-59.

Darton, R.C., La Nauze, R.D., Davidson, J.F., and Harrison, D., 1977, *Bubble growth due to coalescence in fluidized beds*, **Trans Instn ChemEngrs**, 55, 274-280.

Davidson J.F. and Harrison, D., 1963, **Fluidized Particles**, Cambridge University Press, London.

Daw, C.S. and Frazier, G.C., 1988, *A quantitative analysis of binary solids segregation in large-particle gas-fluidized beds*, **Powder Technol, 56**, 165-177.

de Groot, J.H., 1967, *Scaling up of gas fluidized bed reactors*, **Proc Intl Symp on Fluidization** (A.A.H. Drinkenburg, Ed), Netherlands University Press, Amsterdam, 348.

Donsi, G., Ferrari, G. and Formisani, B., 1988, *On the segregation mechanism of percolating fines in coarse particle fluidized beds*, **Powder Technol, 55**, 153-158.

Ekinci, E., Atakul, H., and Tolay, M., 1990, *Detection of segregation tendencies in a fluidized bed using temperature profiles*, **Powder Technol, 61,** 185-192

El-Sayed, D., El-Ayuty, I. and Stepanek, J.B., 1983, *Use of microwaves in the measurement of frequencies and amplitudes in liquid hold up fluctuations*, **Int J Multiphase Flow, 9,2,** 49-72

Esin, A. and Altun, M., 1984, *Correlation of axial mixing of solids in fluidized beds by a dispersion coefficient*, **Powder Technol, 39,** 241-244

Fan, L.T. and Chang, Y., 1979, *Mixing of large particles in two-dimensional gas fluidized beds*, **Can J Chem Engng, 57,** 88-97

Fox R.O. and Fan, L.T., 1987, *Stochastic modelling of chemical engineering system. Application of the generalized master equation to the bubble population in a bubbling fluidized bed*, **Chem Engng Sci, 42**, 1345-1358.

Gabor, J.D., 1967, *Wall effects on fluidized particle movement in a two-dimensional column*, **Proc Intl Symp on Fluidization**, (A.A.H. Drinkenburg, E), Netherlands University Press, 230-239.

Gabor, J.D., 1971, *Boundary effects on a bubble rising in a finite two-dimensional fluidized bed*, **Chem Engng Sci, 26,** 1247-1257

Gabor, J.D., 1972, *On the mechanics of fluidized particles movement*, **Chem Engng J, 4**, 118-126.

Garcia-Ochoa, F., Romero, A., Villar, J.C. and Bello, A., 1989, *A study of segregation in a gas-solid fluidized bed: Particles of different density*, **Powder Technol**, 58, 169-174.

Geldart, D, 1973, *Types of gas fluidization*, **Powder Technol, 7**, 285-292.

Geldart, D., 1969, *The size and frequency of bubbles in two- and three-dimensional gas fluidized beds*, **Powder Technol, 4**, 41-55.

Geldart, D. and Cranfield, R.R. 1972, *The gas fluidization of large particles*, **Chem Engng J, 3**, 211-231

Geldart D. and Kelsey, J.R., 1972, *The use of capacitance probes in gas-fluidized beds*, **Powder Technol, 6**, 45-50.

Gibilaro, L.G. and Rowe, P.N., 1974, *A model for a segregating gas fluidized bed*, **Chem Engng Sci,** 1403-1412.

Glicksman, L.R., Lord W.K. and Sakagami, M., 1987, *Bubble properties in large-particle fluidized beds*, **Chem Engng Sci, 42**, 479-491.

Gonzalez, R.C. and Wintz, P., 1987, **Digital Image Processing**, Addison-Wesley, 2nd edn., p.354.

Grace J.R. and Harrison, D., 1968, *The distribution of bubble within a gas-fluidized bed*, **Inst Chem Engrs Symp Ser, 30**, 105-113.

Grace J.R. and Harrison, D., 1969, *The behaviour of freely bubbling beds*, **Chem Engng Sci, 24**, 497-508.

Grewal, N.S. and Saxena, S.C., 1980, *Comparion of commonly used correlations for minimum fluidization velocity of small solid particles*, **Powder Technol, 26,** 229-234

Gunn D.J. and Al-Doori, H.H., 1985, *The measurement of bubble flows in fluidized beds by electrical probe*, **Int J Multiphase Flow, 11**, 535-551.

Gwyn, J.E., Moser, J.H., and Parker, W.A., 1970, *A three-phase model for gas-fluidized beds*, **Chem Engng Prog Symp Ser, 66**, 19-27.

Hatano, H., Khattab, I.A.H., Nakamura K. and Ishida, M., 1986, *Spatio-temporal measurement of bubble properties in free-bubbling fluidized beds*, **J Chem Engng Japan, 19**, 425-430.

Hatate.Y., King, D.F., Migita M. and Ikari, A., 1985, *Behaviour of bubble in a semi-cyclindrical gas-solid fluidized bed*, **J Chem Engng Japan, 18**, 99-104.

Hemati, M., Spieker, K., Laguerie, C., Alvarez, R. and Riera, F.A., 1990, *Experimental study of sawdust and coal particle mixing in sand or catalyst fluidized beds,* **Can J Chem Engng, 68,** 768-772

Hesketh, R.P. and Davidson J.F., 1991, *The effect of volatiles on the combustion of char in a fluidized bed,* **Chem Engng Sci, 46,** 3101-3113.

Hilligardt, K. and Werther, J., 1986, *Gas flow in and around bubbles in gas fluidized beds - local measurements and modelling considerations,* in Fluidization, **World Congress III of Chemical Engineering,** Tokyo, Japan, Vol III, 429-432.

Ishida, M., Shirai, T. and Nishiwaki, A., 1980, *Measurement of the velocity and direction of flow of solid particles in a fluidized beds,* **Powder Technol, 27,** 1-6.

Ishida, M. and Wen, C.Y., 1973, *Effect of solid mixing on non-catalytic solid-gas reactions in a fluidized bed,* **AICnt Symp Ser, 69,** 1-7

Jackson, R., 1970, *The present status of fluid mechanical theories of fluidization,* **Chem Engng Prog Symp Ser, 66,** 3-13

Kato, K and C.Y. Wen, 1969, *Bubble assemblage model for fluidized bed catalytic reactors,* **Chem Engng Sci, 24,** 1351

Kendall, M. and Stuart, A., 1977, **The Advanced Theory of Statistics,** Charles Griffin & Co, London, (4th eds).

Kendall, M.G. and Moran, P.A.P., 1963, **Geometrical Probability,** Charles Griffin and Co., London

Khattab, I.A., Kuroda, C. and Ishida, M., 1988, *Radial and vertical distributions of the interstitial gas velocity in a fluidized bed,* **J Chem Engng Japan, 21,** 282-287.

Kozanoglu, B. and Levy, E.K., 1991, *Transient mixing of homogeneous solids in a bubbling fluidized bed,* **AIChE Symp Ser, 67,** 58-69.

Kozanoglu, B. and Levy, E.K., 1992, *Mixing dynamics in a bubbling fluidized bed with binary solids,* in **Fluidization VII** (O.E. Potter and D.J. Nicklin, Eds) Engineering Foundation, New York, 141-149.

Kunii, D. and Levenspiel, O., 1969, **Fluidization Engineering,** Wiley, New York.

Lakshmanan, C.C. and Potter, O.E., 1987, *Cinematic modelling of solids mixing in fluidized beds,* **Ind Engng Chem Res, 26,** 292-296.

Lakshmanan, C.C. and Potter, O.E., 1990, *Numerical simulation of the dynamics of solids mixing in fluidized beds*, **Chem Engng Sci, 45**, 519-528.

Lewis, W.K., Gilliland, E.R. and Girouard, H., 1962, *Heat transfer and solids mixing in beds of fluidized solids*, **Chem Engng Prog Symp Ser, 58**, 87-97.

Lin, J.S., Chen, M.M. and Chao, B.T., 1985, *A novel radioactive particle tracking facility for measurement of solids motion in gas fluidized beds*, **AIChE J, 31**, 465-472.

Linjewile, T.M. And Agarwal, P.K., 1990, *Heat transfer behaviour and temperature of freely moving burning carbonaceous particles in fluidized beds*, **Twenty Third Symposium (International) on Combustion, Orleans.**

Linneweber, K.W., Blass E., 1983, *Measurement of local gas and solids hold up in three phase bubble columns*, **Ger. Chem Eng, 6**, 28-33.

Littman, H. and Homolka, G.A.J., 1970, *Bubble rise velocity in two-dimensional gas-fluidized beds from pressure measurements*, **Chem Engng Prog Symp Ser, 66**, 37-46.

Liu, Y. and Gidaspow, D., 1981, *Solids mixing in fluidized beds - A hydrodymanic approach*, **Chem Engng Sci, 36**, 539-547.

Loew, O., Schmutler, B. Resnick, W., 1979, *Particle and bubble behaviour and velocity in a large-particle bed with immersed obstacles*, **Powder Technol, 22**, 45-57.

May, W.G., 1959, *Fluidized-bed reactor studies*, **Chem Engng Prog, 55**, 49-57.

Melsa, J.L. and Sage, A.P., 1973, **An Introduction to Probability and Stochastic Processes**, Prentice Hall, Englewood Cliffs, NJ.

Miwa, K., Mori, S., Kato T. and Muchi, I., 1972, *Behaviour of bubbles in gaseous fluidized bed*, **Intl Chem Engng, 12**, 187-194.

Mori, S. and Wen, C.Y., 1975, *Estimation of bubble diameter in a gaseous fluidized beds*, **AIChE J, 211**, 109-115

Muramoto, T., Nakajima, M., Morooka, S. and Matsuyama, H., 1985, *Measurement of flow of solid particles in a gas fluidized bed*, **Chem Engng Commun, 35**, 193-201.

Murray, J.D., 1965, *On the mathematics of fluidization*, **J Fluid Mech, 22**, 57-80.

Naimer, N.S., Chiba, T. and Nienow, A.W., 1982, *Parameter estimation for a solids mixing/segregation model for gas fluidized beds*, **Chem Engng Sci, 37**, 1047-1057.

Nakamura, K. and Capes, G.E., 1977, *Correction for wall effect in point probe measurements of bubble size*, **Chem Engng Sci, 32**, 1339-1343.

Nienow, A.W., Naimer, N.S., and Chiba, T., 1987, *Studies of segregation/mixing in fluidized beds of different sized particles*, **Chem Engng Commun, 62**, 53-66.

Nienow, A.W., Rowe, P.N. and Cheung, L.Y.-L, 1978, *A quantitative analysis of mixing of two segregating powders of different density in a gas-fluidized bed*, **Powder Technol, 20**, 89-97.

Nienow, A.W., Rowe, P.N. and Chiba, T., 1978, *Mixing and segregation of a small proportion of large particles in gas fluidized beds of considerable smaller ones.* **AIChE Symp Ser, 74,** 45-53.

Nienow, A.W. and Cheesman, D.J., 1980, *The effect of shape on the mixing and segregation of large particles in a gas fluidized bed of small ores,* in **Fluidization III** (J.R. Grace and J.M. Matsen, Eds), 373-380.

Nienow, A.W. and Chiba, T., 1985, *Fluidization of dissimilar materials*, in **Fluidization** (J.F. Davidson, R. Clift and D. Harrison, Eds), Academic Press, London, 357-382.

Oki, K. Walawender, W.P. and Fan, L.T., 1977, *The measurement of local velocity of solid particles,* **Powder Technol, 18,** 171-178.

Park, W.H., Lee, N.G. and Capes, C.E., 1974, *Wall effects in point probe measurements of radial bubble distributions*, **Chem Engng Sci, 29**, 339-344.

Park W.H., Kang, W.K., Capes, C.E. and Osberg, G.L., 1969, *The properties of bubbles in fluidized beds at conducting particles as measured by an electroresistivity probe*, **Chem Engng Sci, 24**, 851-865.

Patrose, B. and Caram, H.S., 1982, *Optical fiber probe transit anemometer for particle velocity measurements in fluidized beds,* **AIChE J, 28,** 604-609.

Potter, O.E., 1971, in **Fluidization** (J.F. Davidson and D. Harrison, Eds), Academic Press, London, 293.

Prins, W., Siemons, R., Van Swaaij, W.P.M. and Radovanovic, M., 1989 *Devolatilization and ignition of coal particles in a two-dimensional bed*, **Combust Flame, 75**, 57-79.

Rice, R.W. and Brainovich, J.F., 1986, *Mixing/segregation in two- and three-dimensional fluidized beds: Binary systems of equidensity spherical particles*, **AIChE J, 32**, 7-16.

Rios, G.M. and Gibert, H., 1983, *Heat transfer between gas fluidized bed and big bodies: analysis and explanation of big body mobility effects*, in **Fluidization IV** (D. Kunii and R. Toei, Eds), Engineering Foundation, New York, 363-370.

Rios, G.M. and Tran, K.D. and Masson H., 1986, *Free object motion in a gas fluidized bed*, **Chem Engng Commun 47,** 247-272.

Rowe, P.N., 1971, *Experimental properties of bubbles,* in **Fluidization,** (J.F. Davidson and D. Harrison, Eds) **Academic Press**, 121-191.

Rowe, P.N., 1976, *Prediction of bubble size in a gas fluidised bed,* **Chem Engng Sci, 31** 285-288

Rowe, P.N., Nienow, A.W. and Agbim, A.J., 1972a, *A preliminary quantitative study of particle segregation in gas fluidized beds - Binary systems of near spherical particles*, **Trans Instn Chem Engrs, 50**, 324-333.

Rowe, P.N., Nienow, A.W. and Agbim, A.J., 1972b, *The mechanisms by which particles segregate in gas fluidized beds - Binary systems of near-spherical particles*, **Trans Instn Chem Engrs, 50**, 310-323.

Rowe, P.N., Partridge, B.A., Cheney, A.G., Henwood, G.A. and Lyall, E., 1965, *The mechanisms of solids mixing in fluidized beds*, **Trans Instn Chem Engrs, 43**, 271-286.

Rowe, P.N. and Nienow, A.W., 1976, *Particle mixing and segregation in gas fluidized beds. A review*, **Powder Technol,** Vol 15, 141-147.

Rowe, P.N. and Partridge, A., 1965, *An X-ray study of bubbles in fluidized beds*, **Trans Instn Chem Engrs, 43**, 157-175.

Rowe, P.N. and Yacono, C., 1975, *The distribution of bubble size in gas-fluidized beds*, **Trans Instn Chem Engrs, 53**, 59-60

Rowe P.N. and Everett, D.J., 1972, *Fluidized bed bubble viewed by X-ray, Part I - experimental details and interaction of bubble with solids surfaces*, **Trans Instn Chem Engrs, 50**, 42-54.

Rowe P.N. and Masson, H., 1980, *Fluidized bed bubbles observed simultaneously by probe and by X-rays*, **Chem Engng Sci, 35**, 1443-1447.

Rowe P.N. and Masson, H., 1981, *Interaction of bubbles with probes in gas fluidized beds*, **Trans Instn Chem Engrs, 59**, 177-185.

Saxena, S.C., Mathur A. and Sharma G.K., 1984, *Bubble dynamics and elutriation studies in gas fluidized beds,* **Chem Engng Commun, 29,** 35-61

Selim, M.S., Kothari, A.C. and Turian, R.M., 1983, *Sedimentation of binary suspensions,* **AIChE Symp Ser 79,** 103-108.

Seo, Y-C and Gidaspow, D., 1987, *And X-ray and γ-ray method of measurement of binary solids concentrations and voids in fluidized beds,* **Ind Engng Chem Res, 26,** 1622-1628.

Shah, B.H., Ramkrishna, D. and Borwanker, J.D., 1977, *Simulation of bubble populations in a gas fluidized bed,* **Chem Engng Sci, 32,** 1419-1425.

Singh, B., Fryer, C., and Potter, O.E., 1972, *Solids motion caused by a bubble in a fluidized bed,* **Powder Technol, 6,** 239-244.

Sitnai, O., 1981, *Solids mixing in a fluidized bed with horizontal tubes,* **Ind Engng Chem Process Des Dev, 20,** 533-538.

Soo, S.L., 1986, *Note on motions of phases in a fluidized bed,* **Powder Technol, 45,** 169-172.

Sung, J.S., 1987, *A theoretical and experimental study of segregation in gas fluidized beds,* **Ph.D. Thesis,** University of Queensland.

Sung, J.S., and Burgess, J.M., 1987, *A laser-based method for bubble parameter measurement in two-dimensional fluidized bed,* **Powder Technol, 49,** 165-175.

Sutherland, K.S., 1961, *Solids mixing studies in gas fluidized beds, part I: a preliminary comparison of tapered and non-tapered beds,* **Trans Instn Chem Engrs, 39,** 187-194.

Talmor, E. and Benenati, R.F., 1963, *Solids mixing and circulation in gas Fluidized beds,* **AIChE J 9,** 536-540.

Tanimoto, H., Chiba, S., Chiba, T. and Kobayashi, H., 1980, *Mechanism of solid segregation in gas fluidized beds,* in **Fluidization III** (J.R. Grace and J.M. Matsen, Eds), 381-388.

Tanimoto, H., Chiba, S. Chiba, T. and Kobayashi, H., 1981, *Jetsam descent induced by a single bubble passage in three-dimensional gas-fluidized beds,* **J Chem Engng Japan, 14,** 273-276.

Turton, R. and Clark, N.N., 1989, *Interpreting probe signals from fluidized beds,* **Powder Technol, 59,** 117-123

Valenzuela, J.A. and Glicksman, L.R., 1984, *An experimental study of solids mixing in a freely bubbling two-dimensional fluidized bed*, **Powder Technol, 38**, 64-72.

Valenzuela, J.A. and Glicksman, L.R., 1985, *Gas flow distribution in a bubbling fluidized bed*, **Powder Technol, 44**, 103-113.

van Deemter, J.J., 1967, *The counter-current flow model of a gas-solids fluidized bed*, **Proc. Intern. Symp. on Fluidization** (A.A.H. Drinkenburg, Ed), Netherlands University Press, Amsterdam, 334-347.

van Deemter, J.J. 1985, *Mixing*, in **Fluidization** (J.F. Davidson, R. Clift and D. Harrison, Eds), Academic Press, London, 331-355.

Verloop, J., de Nie, L.H. and Heertjes, P.M., 1968, *The residence time of solids in gas-fluidized beds*, **Powder Technol, 2**, 32-42.

Weimer, A.W., Gyure D.C. and Clough, D., 1985, *Application of gamma-radiation density gauge for determining hydrodynamic properties of fluidized beds*, **Powder Technol, 44**, 179-194.

Wen, C.Y., Krishnan, R., Khossravi, R. and Dutta, S., 1978, *Dead zone heights near the grid of fluidized beds*, in **Fluidization II**, (J.F. Davidson and D.L. Keairns, Eds), Cambridge University Press, London, 32-36.

Werther, J., 1974a, *Bubbles in gas-fluidized beds, Part I*, **Trans Instn Chem Engrs, 52**, 149-159.

Werther, J., 1974b, *Bubbles in gas-fluidized beds, Part II*, **Trans Instn Chem Engrs, 52**, 149-159.

Werther, J., 1977, *Bubble chains in large diameter gas fluidized beds*, **J Int Multiphase Flow J, 3**, 367-381.

Werther, J., 1978, *The influence of the distributor design on a bubble characteristics in large diameter gas fluidized beds*, in **Fluidization II** (J.F. Davidson and K.L. Keairns Eds.), Cambridge University Press, 7-12.

Werther J. and Molerus, O., 1973a, *The local structure of gas fluidized beds - I - A statistically based measuring system*, **Int J Multiphase Flow, 1**, 103-122.

Werther J. and Molerus, O., 1973b, *The local structure of gas fluidized beds - II - A spatial distribution of bubbles*, **Int J Multiphase Flow, 1**, 123-138.

Wittman, K., Wippern, D., Helmrich, H., and Schugerl, K., 1978, *Behaviour of the bubbles in a bench scale fluidized bed reactor with conversion of solid in continuous operation at various temperatures,* in **Fluidization II,** (J.F. Davidson and D.L. Keairns, Eds), Cambridge University Press, London, 173-178.

Yang, W.C. and Keairns, D.L., 1982, *Rates of partilce separation in a gas fluidized beds,* **Ind Eng Chem Fundam, 21,** 288-235.

Yasui, G. and Johanson, L.N., 1958, *Characteristics of gas pockets in fluidized beds,* **AIChE J, 4,** 445-452.

Yosef, B., Ginio, O., Mahlab D., Weitz, A., 1975, *Bubble size distribution measurement by doppler velocimeter,* **J Appl Physic, 46, 2,** 738-740

Yoshida, K., Kameyama, H. and Shimuzu, F. 1980, *Mechanism of particle mixing and segregation in gas fluidized beds,* in **Fluidization III** (J.R. Grace, and J.M. Matsen, Eds), Plenum Press, New York, 389-396.

Yoshida, K., Nakajima, K., Hamatani, N. and Shimizu, F., 1978, *Size distribution of bubbles in gas fluidized beds,* in **Fluidization II,** (J.F. Davidson, and D.L. Keairns, Eds), Cambridge University Press, London, 13-18.

Yoshida, K. 1982, *A new probe for measuring fluidized bed characteristics at high temperatures,* **Ind Eng Chem Fund, 21,** 83-85.

Yoshida. K. and Kunii, D., 1968, *Stimulus and response of gas concentration in bubbling fluidized beds,* **J Chem Engng Japan, 1,** 11-16.

Appendix A

PARTICLE SIZE DISTRIBUTION

The bed particles mainly consisted of glass ballotini were analysed for the size distribution using a Coulter LS Series Particle Size Analyzer. The cumulative distributions of the particle size were plotted.

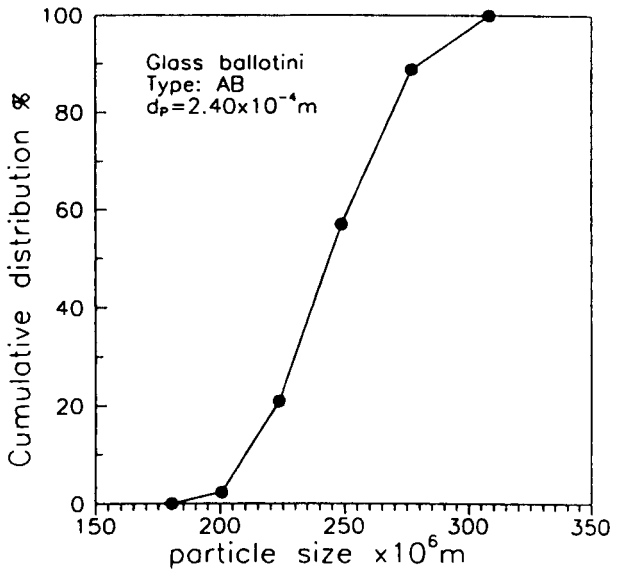

Figure A1: Cumulative size distribution for glass ballotini type AB

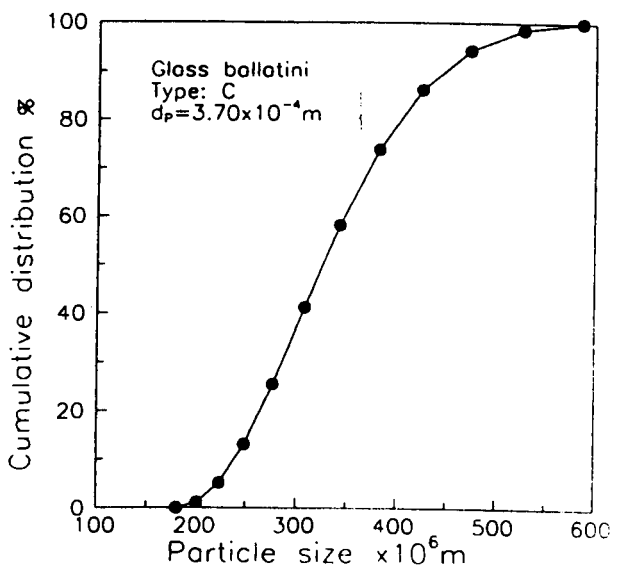

Figure A2: Cumulative size distribution for glass ballotini type C

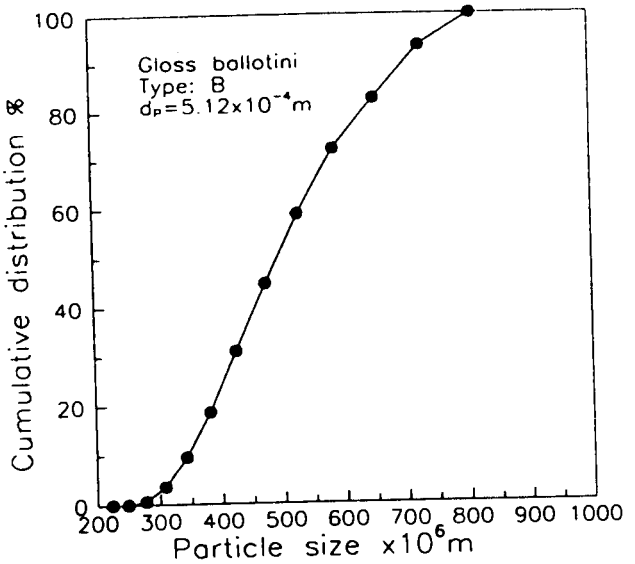

Figure A3: Cumulative size distribution for glass ballotini type B

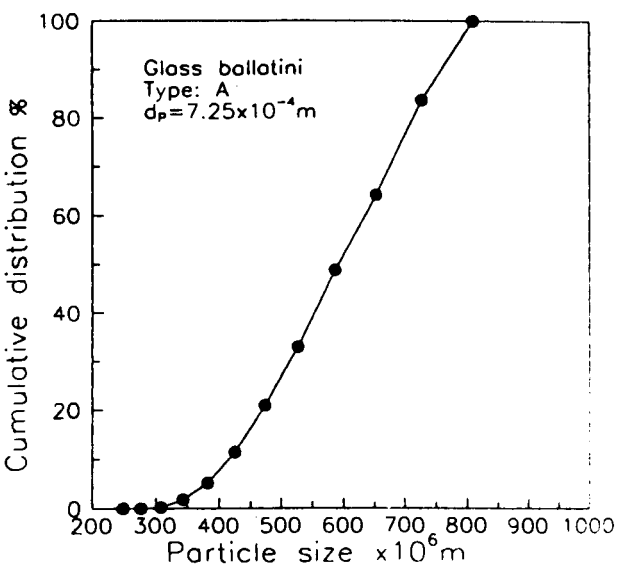

Figure A4: Cumulative size distribution for glass ballotini type A

Appendix B

MINIMUM FLUIDIZATION VELOCITY

The minimum fluidization velocities of the particles used were determined from the plots of bed pressure drop versus superficial gas velocity. As there were some variations of the size distribution of the particle obtained from the factory (manufacturer), the minimum fluidization of the particle were measured each time when there were changes in the batch. **Figure B1 and 2** show the variation of the measured U_{mf} values in both different batches under the same classification.

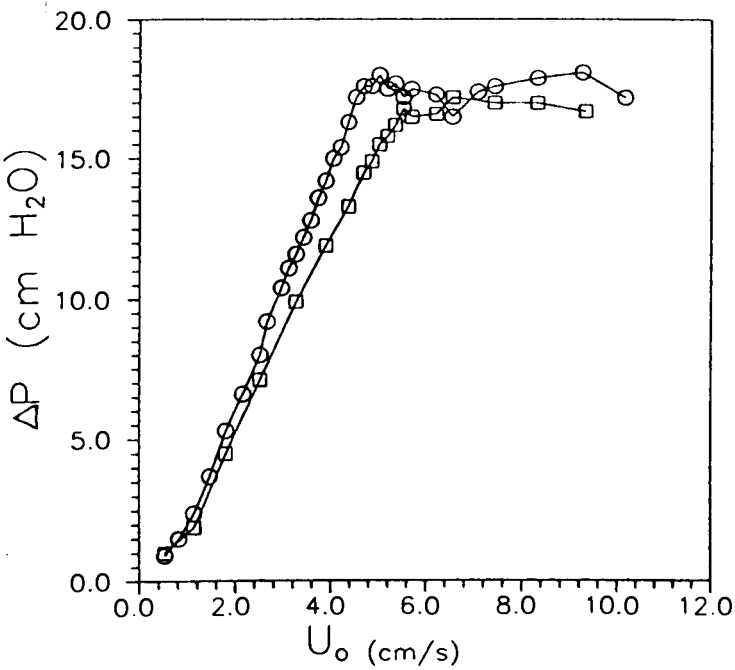

Figure B1: Minimum fluidization velocity determination for glass ballotini of one batch under classification type AB.

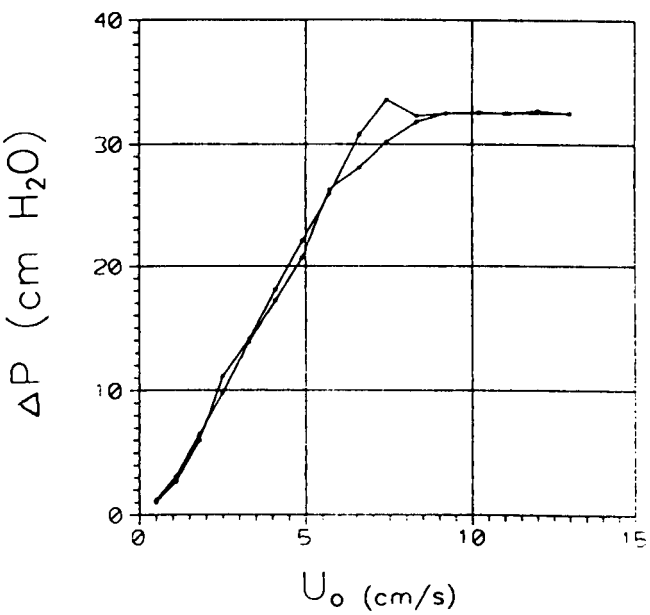

Figure B2: Minimum fluidization velocity determination for glass ballotini of another batch under classification type AB.

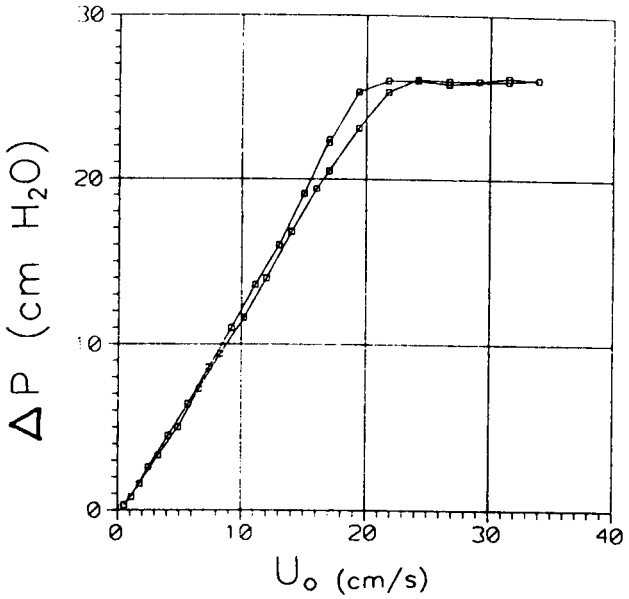

Figure B3: Minimum fluidization velocity determination for glass ballotini for type B.

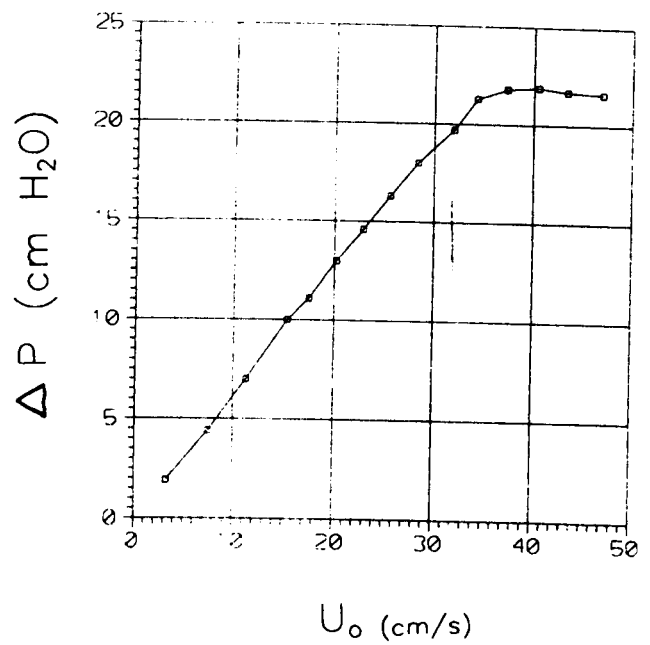

Figure B4: Minimum fluidization velocity determination for glass ballotini of one batch under classification A.

Appendix C

DERIVATION OF BUBBLE GROWTH MODEL OF DARTON (1977) IN A 2-D SYSTEM

A model describing the growth of bubble due to coalescence was proposed by Darton et al. (1977). The bubble growth model for the gas bubbles in a two-dimensional fluidized bed was derived following the similar approach.

A gas bubble in a fluidized bed is assumed to rise at a velocity U_B and the frequency with which they pass a fixed observer is $U_B/2a$ where a is the radius of the roughly circular region enclosing the bubble and its wake.

The volumetric flow due to the bubble is

$$Q = V_B U_B/2a \tag{C1}$$

and the volume of the bubble is V_B

$$V_B = \frac{\pi}{4} t_T d_B^2 \tag{C2}$$

$$U_B = K_B \sqrt{g\, d_B} \tag{C3}$$

where $K_B = 0.5$, and for circular bubble shape,

$$2a = d_B \tag{C4}$$

equation (C1) may be expressed as

$$Q = \frac{\pi}{4} t_T K_B g^{1/2} d_B^{3/2} \tag{C5}$$

and assuming the bubble flow is a result of excess gas

$$Q = (U_O - U_{mf}) A_C \tag{C6}$$

where the A_C is the catchment area from which gas is drawn into the bubble stream and is expressed as

$$A_C = D_C T \tag{C7}$$

equating equations (C5) and (C6) gives

$$D_C = \frac{\pi K_B g^{1/2}}{4(U_O - U_{mf})} d_B^{3/2} \tag{C8}$$

if each bubble size 'lives' for a distance $\lambda_B D_C$, where λ_B is constant, before coalescence between two adjacent streams gives a singles new stream of larger bubbles. Thus the height Z_N at the N stage of the coalescence is

$$Z_N = \lambda_B D_{C0} + \lambda_B D_{C1} + \ldots + \lambda_B D_{C(N-1)} \tag{C9}$$

$$Z_N = \frac{\pi K_B \lambda_B g^{1/2}}{4(U_O - U_{mf})} (d_{B0}^{3/2} + d_{B1}^{3/2} + \ldots + d_{B(N-1)}^{3/2}) \tag{C10}$$

assuming no loss or gain in bubble volume during coalescence

$$d_{Bn}^2 = 2^n d_{B0}^2 \tag{C11}$$

$$Z_N = \frac{\pi K_B \lambda_B g^{1/2}}{4(U_O - U_{mf})} d_{B0}^{3/2} \sum_{n=0}^{N-1} 2^{3n/4} \tag{C12}$$

From geometric series

$$\sum_0^n q^n = \frac{1-q^{n+1}}{1-q} \tag{C13}$$

and it can be shown that

$$Z_N = \frac{\pi K_B \lambda_B g^{1/2}}{4(U_O - U_{mf})(2^{3/4}-1)} (d_{BN}^{3/2} - d_{B0}^{3/2}) \tag{C14}$$

rearranging

$$d_{BN} = \left(\frac{4(U_O - U_{mf})(2^{3/4}-1)}{\pi K_B \lambda_B g^{1/2}} Z_N + d_{B0}^{3/2} \right)^{2/3} \tag{C15}$$

where

$$d_{B0} = \left(\frac{4(U_O - U_{mf}) A_{C0}}{\pi K_B \lambda_B g^{1/2}} \right)^{2/3} \tag{C16}$$

Appendix D

COMPUTER PROGRAMS AND CODES

Due to the large volume and size of the computer programs used in various sections of the studies, it not prossible to include all the codes of the computer programs developed. Hence, only some selected key features of the computer are included.

Listed programs and subroutines are:

- automated bubble size measurement
- automated particle tracking
- computer simulation for solids mixing and segregation

Automated bubble size measurement:
An extract of the subroutine for the measurement of bubble size parameters, circumference, and centroid.

```
$include:'itexpc.inc'

c.      Bubble/object parameters measurement routines
c._____
_____
c. The following routines are used to measure the size, circumference
c. centroid, pierced length and maximum and minimum size in both
c. horizontal and vertical directions.

c. The routines are:
c. SIZEONE
c. Sizing the one single object given a point in the object is known.
c. Object identification by intensity greater than threshold value.

c.   This is the major part of the subroutine for the measurement of the
c.   parameters. The corresponding routines, require certain parameters
c.   to be predefined, i.e. linear dimension calibration, incremental
c.   size for the trapezoidal sectioning of the object, starting point
c.   of the horizontal line which intersecting the objects and its lenght,
c.   vertical reference line and its corresponding height in real dimension
c.   with respect to a datum line, and the threshold value distinguishing
c.   the object and background. Note: identification of the object is
c.   based upon a global threshold value with object having gray scale
c.   larger than threshold. These parameters are defined and passed on
c.   through the common block /AA/

c.   The output of the measurement may be obtained through a common block
c.   /EE/. Hence, it is required to define this in the Main Program.

c. FOEDGE(x,y,thresh,x1,x2)
c. determine any two points (x1 and x2) intercepting the object boundary
c. along y=y at given a starting point at (x,y) inside the object.

c.
BOUND(subx,pos1,pos2,xmin,y_xmin,xmax,y_xmax,ymin,ymax)

c.
Y_MN(subx,pos1,ymin,ymax,x_ymin,x_ymax)
c.   required common block /AA/
c.   common /AA/
vermm,hormm,pixacc,piyacc,xref1,dxref,Yref,thresh,
c.   +stepsi,Height

c.
X_MN(ystart,intvy,xloc,xmin,xmax,y_xmin,y_xmax)
c.   also required common block /AA/

c. YDIRTN(xloc,yloc,y,dir,thresh,stepsi)

c. XDIRTN(xloc,yloc,x,dir,thresh,stepsi)

c. OBSIZE(xmin,y_xmin,xmax,y_xmax)
c.   also required common block /AA/
c.   where measured bubble parameters are declared in commom block
c.   common/EE/
Xposn,Yposn,Area,CL,xcord,ycord,xprobe,Plenght

c. NEARER(x,y,up,down,thresh,piyacc)



    Subroutine SIZEON()
c. Call this routine name to measure the object size parameters

    integer*2
xref1,dxref,Yref,thresh,pixacc,piyacc,stepsi
    integer*2
Nobub,Bubloc(20,2),pos1,pos2,subx,bub,ichk
    integer*2 xprobe,unit,Xmean,Ymean,int2
    integer*2
ymin,ymax,x_ymin,x_ymax,xmin,xmax,y_xmin,y_xmax
    integer*2
pymin,pymax,px_ymin,px_ymax,pxmin,pxmax,py_xmin,
   +py_xmax

    real*4
vermm,hormm,Xposn,Yposn,Area,CL,xcord,ycord
    real*4 Plenght,Height
```

```
c. need to specify the following common blocks
/AA/ and /EE/ in the MAIN
c. program
      common /AA/
vermm,hormm,pixacc,piyacc,xref1,dxref,Yref,th
resh,
     +stepsi,Height
      common/EE/
Xposn,Yposn,Area,CL,xcord,ycord,xprobe,Plen
ght

      common /CC/
ymin,ymax,x_ymin,x_ymax,xmin,xmax,y_xmin
,y_xmax
      common /DD/
pymin,pymax,px_ymin,px_ymax,pxmin,pxmax,
py_xmin,
     +py_xmax
      common /Fileunit/ unit
      common/CEN/ Xmean,Ymean
c. determining the two intercepting points on
the object boundary
      write(*,*)'pixacc, piyacc=', pixacc, piyacc
      call
FOEDGE(xprobe,Yref,thresh,pos1,pos2)
      write(*,*)'pos1, pos2', pos1, pos2
      subx=int2((pos2-pos1)/(pixacc*1.0))
      write(*,*) 'subx=', subx

c. if detected bubble section is too small, the
method by sectioning
c. may not work properly, so these bubbles will
be ignored.

      if (subx.gt.2) then
```

```
c. if this is true, it is required to determine the
possible maximum and
c. minimum boundary positions for the bubble

c. first, the horizontal detected length is
subdivided into a series of
c. sections and at each position, axial (vertical)
search in both
c. upward and downward directions are carried
out. This will give the
c. minimum and maximum vertical boundary
positions. Knowing these quantities
c. lateral (horizontal) search is performed to
determine the horizontal
c. boundary positions because in terms of
evaluation of the bubble size
c. maximum and minimum lateral positions are
required.

      call BOUND(subx,pos1,pos2)

      call OBSIZE(xmin,y_xmin,xmax,y_xmax)

      write(*,949)
 949
format(/1X,3X,'X',5X,'Y',4X,'Area',4X,'C_L',3
X,'Xmax',2X,'Ymax',
     +3X,'P_L')
      if (unit.ne.6) then
      write(6,950)
Xposn,Yposn,Area,CL,xcord,ycord,Plenght
      endif
      write(unit,950)
Xposn,Yposn,Area,CL,xcord,ycord,Plenght
 950  format(1X,2F6.1,F8.1,F7.1,3F6.1)

      else
      write(*,*)'*  Size is too small to measure.'
      endif
      return
      end


      Subroutine BOUND(subx,pos1,pos2)
      external Y_MN, X_MN

c. This routine search for the maximum and
minimum edge of the bubble
c. boundary, it is only required to specify two
intersection points at
c. the boundary along any horizontal reference
line Yref.
c. in addition, minimum and maximum vertical
boundary is known.

      integer*2
yupsub,UXN,UXM,YUXN,YUXM
      integer*2
ydnsub,DXN,DXM,YDXN,YDXM
      integer*2 YMN,YMX,XYMN,XYMX
      integer*2
ymin,ymax,x_ymin,x_ymax,xmin,xmax,y_xmin
,y_xmax
      integer*2 subx,pos1,pos2
      integer*2
pixacc,piyacc,xref1,dxref,Yref,thresh,stepsi
      real*4 Height,vermm,hormm
      common /AA/
vermm,hormm,pixacc,piyacc,xref1,dxref,Yref,th
resh,
     +stepsi,Height
      common /CC/
ymin,ymax,x_ymin,x_ymax,xmin,xmax,y_xmin
,y_xmax
```

```
c. Search upward and downward with respect to
Yref line

    call
Y_MN(subx,pos1,YMN,YMX,XYMN,XYMX)
    ymin=YMN
    x_ymin=XYMN
    ymax=YMX
    x_ymax=XYMX
    yupsub=int2((Yref-ymin)/(piyacc*1.0))
    ydnsub=int2((ymax-Yref)/(piyacc*1.0))

    if(yupsub.lt.2) then
c. if yupsub less than 2 then no horizontal
search at the upper section
c. can be made, hence keep the old values
    UXN=pos1
    UXM=pos2
    YUXN=Yref
    YUXM=Yref
    else
c. otherwise, search for the maximum and
minimum boundary locations
c. are necessary.
    call
X_MN(ymin,yupsub,x_ymin,UXN,UXM,YUX
N,YUXM)
    endif
c. Similarly situation for the lower section from
the Yref
    if(ydnsub.lt.2) then
    DXN=pos1
    DXM=pos2
    YDXN=Yref
    YDXM=Yref
    else
    call
X_MN(Yref,ydnsub,x_ymax,DXN,DXM,YDX
N,YDXM)
    endif
c. The minimum and maximum values of the
horizontal boundary location from
c. both upper and lower section are compared so
that the true minimum and
c. maximum values are determined.
    if (UXN.lt.DXN) then
    xmin=UXN
    y_xmin=YUXN
    else
    xmin=DXN
    y_xmin=YDXN
    endif
    if (UXM.gt.DXM) then
    xmax=UXM
    y_xmax=YUXM
    else
    xmax=DXM
    y_xmax=YDXM
    endif
    return
    end

    Subroutine FOEDGE(x,y,thresh,x1,x2)
c. determine any two points (x1 and x2)
intercepting the object boundary
c. along y=y at given a starting point at (x,y).
c. The point (x,y) has to be inside the object.
c. i.e. intensity greater than threshold value,
thresh.
c. note have change 'intensity' variable to
'intens' ie 6 characters
    integer*2
intens,x,y,thresh,x1,x2,left,right,RPIXEL
    left=-1
    right=1
    x1=x
    x2=x
c. search to the left
 10  if (x1.ge.0) then
    intens=RPIXEL(x1,y)
    if (intens.gt.thresh) then
    x1=x1+left
    goto 10
    else
    x1=x1+right
    endif
    endif
c. making sure that x1,x2 are within the object
boundary

c. search to the right
 20  if (x2.le.511) then
    intens=RPIXEL(x2,y)

    if (intens.gt.thresh) then
    x2=x2+right
    goto 20
    else
    x1=x1+left
    endif

    endif

    return
    end

    Subroutine
Y_MN(subx,pos1,ymin,ymax,x_ymin,x_ymax)
```

```
      external YDIRTN
      integer*2
subx,pos1,ymin,ymax,x_ymin,x_ymax,yu,yd,xlo
c
      integer*2
pixacc,piyacc,xref1,dxref,Yref,thresh,stepsi
      integer*2 up,dn,j,Yf
      real*4 vermm,hormm,Height

      common /AA/
vermm,hormm,pixacc,piyacc,xref1,dxref,Yref,th
resh,
     +stepsi,Height
      up=-1
      dn=1
      do 30 j=1,subx-1
      xloc=pos1+j*pixacc
      Yf=Yref
      call YDIRTN(xloc,Yf,yu,up,thresh,stepsi)
      call YDIRTN(xloc,Yf,yd,dn,thresh,stepsi)
      if(j.eq.1) then
      ymin=yu
      ymax=yd
      x_ymin=xloc
      x_ymax=xloc
      else
      if (yu.lt.ymin) then
      ymin=yu
      x_ymin=xloc
      elseif (yd.gt.ymax) then
      ymax=yd
      x_ymax=xloc
      endif
      endif
 30   continue
      return
      end

      Subroutine
X_MN(ystart,intvy,xloc,xmin,xmax,y_xmin,y_x
max)
      external XDIRTN
      integer*2
ystart,intvy,xmax,y_xmax,xmin,y_xmin
      integer*2
xR,xL,xloc,y,thresh,xref1,dxref,Yref,stepsi
      integer*2 pixacc,piyacc,right,left
      real*4 vermm,hormm,Height
      common /AA/
vermm,hormm,pixacc,piyacc,xref1,dxref,Yref,th
resh,
     +stepsi,Height
      right=1
      left=-1
      do 10 i=1,intvy
      y=ystart+i*piyacc
      call XDIRTN(xloc,y,xR,right,thresh,stepsi)
      call XDIRTN(xloc,y,xL,left,thresh,stepsi)
      if(i.eq.1) then
      xmax=xR
      xmin=xL
      y_xmin=y
      y_xmax=y
      goto 10
      endif
      if (xL.lt.xmin) then
      xmin=xL
      y_xmin=y
      elseif (xR.gt.xmax) then
      xmax=xR
      y_xmax=y
      endif
 10   continue
      return
      end

      Subroutine
YDIRTN(xloc,yloc,y,dir,thresh,stepsi)
      integer*2
xloc,y,stepsi,RPIXEL,thresh,yloc,pix,dir
      y=yloc
 10   pix=RPIXEL(xloc,y)
      if (y.le.0) then
      y=0
      return
      endif
      if(y.ge.511) then
      y=511
      return
      endif
      if ((pix.lt.thresh).and.(y.eq.yloc)) goto 20
      if(pix.gt.thresh) then
      y=y+stepsi*dir
      goto 10
      endif
      y=y-stepsi*dir
 20   return
      end

      Subroutine
XDIRTN(xloc,yloc,x,dir,thresh,stepsi)
      integer*2
xloc,yloc,x,stepsi,RPIXEL,thresh,pix,dir
      x=xloc
 10   pix=RPIXEL(x,yloc)
      if(x.le.0)then
      x=0
      return
      endif
      if(x.ge.511)then
      x=511
```

```
      return
      endif

      if ((pix.lt.thresh).and.(x.eq.xloc)) goto 20
      if(pix.gt.thresh) then
      x=x+stepsi*dir
      goto 10
      endif
      x=x-stepsi*dir
20    return
      end

      Subroutine
OBSIZE(xmin,y_xmin,xmax,y_xmax)
      external YDIRTN,LINE,NEARER
c. measurement of the bubble size
c. bubcir(i,1) contains the x position,
bubcir(i,2)=y upper position
c. bubcir(i,3)=y lower postion (along X=x)
c.
      integer*2
xmin,y_xmin,xmax,y_xmax,x,y,bubcir(512,3),i
ntvx
      integer*2
yup,ydown,up,dn,RPIXEL,igsc,int2
      integer*2
pixacc,piyacc,xref1,dxref,Yref,thresh,stepsi
      integer*2
xprobe,pcup,pcdown,ymini,ymaxi,Ymean,Xmea
n
      real*4
dA,Area,CL,y1,y2,dyup,dydown,DLup,DLdown
      real*4
Height,vermm,hormm,Xposn,Yposn,xcord,ycor
d,Plenght
      real*4 Ysum,Xsum
      common /AA/
vermm,hormm,pixacc,piyacc,xref1,dxref,Yref,th
resh,
     +stepsi,Height
      common/EE/
Xposn,Yposn,Area,CL,xcord,ycord,xprobe,Plen
ght
      common/CEN/ Xmean,Ymean

      intvx=int2((xmax-xmin)/(pixacc*1.0))
      if(intvx.lt.1) then
      write(*,*)'* Object too small - IGNORED'
      goto 40
      endif
      Area=0.0
      CL=0.0

      Ysum=0.0
      Xsum=0.0
      up=-1
      dn=1
      do 10 i=1,intvx+1
      if (i.eq.1) then
      bubcir(i,1)=xmin
      bubcir(i,2)=y_xmin
      bubcir(i,3)=y_xmin
      ymini=y_xmin
      ymaxi=y_xmin
      goto 30
      elseif (i.eq.(intvx+1)) then
      bubcir(i,1)=xmax
      bubcir(i,2)=y_xmax
      bubcir(i,3)=y_xmax
      goto 20
      endif
      x=xmin+(i-1)*pixacc
      y=int2((bubcir(i-1,2)+bubcir(i-1,3))/2.0)
      igsc=RPIXEL(x,y)
      if(igsc.lt.thresh) then
c. if the estimated starting point location lies in
the region where
c. intens less than the threshold, use NEARER
to search for the possible
c. locations and assuming that it is possible to
find the points
c. Note: NEARER doesn't handle the situation
which is otherwise
      call NEARER(x,y,bubcir(i-1,2),bubcir(i-
1,3),thresh,piyacc)
      endif

      call YDIRTN(x,y,yup,up,thresh,stepsi)
      call YDIRTN(x,y,ydown,dn,thresh,stepsi)
c. determine the minimum and maximum
vertical extremities
      if (yup.lt.ymini) ymini=yup
      if (ydown.gt.ymaxi) ymaxi=ydown
      if (yup.eq.ydown) then
      bubcir(i,1)=x
      bubcir(i,2)=bubcir(i-1,2)
      bubcir(i,3)=bubcir(i-1,3)
      goto 20
      endif
      bubcir(i,1)=x
      bubcir(i,2)=yup
      bubcir(i,3)=ydown
c. determine the vertical pierced lenght at
position (xprobe,Yref)
      if ((xprobe.ge.bubcir(i-
1,1)).and.(xprobe.lt.x)) then
      call
YDIRTN(xprobe,y,pcup,up,thresh,stepsi)
```

```
    call
YDIRTN(xprobe,y,pcdown,dn,thresh,stepsi)
    Plenght=(pcdown-pcup)*vermm
    call LINE(xprobe,pcup,xprobe,pcdown,255)
    endif


 20  y1=(bubcir(i-1,3)-bubcir(i-1,2))*vermm
    y2=(bubcir(i,3)-bubcir(i,2))*vermm
    dA=pixacc*hormm*(y1+y2)/2.0
    Area=Area+dA

    dyup=(bubcir(i,2)-bubcir(i-1,2))*vermm
    dydown=(bubcir(i,3)-bubcir(i-1,3))*vermm

DLup=(dyup**2+(hormm*pixacc)**2)**0.5

DLdown=(dydown**2+(hormm*pixacc)**2)**
0.5
    CL=CL+DLup+DLdown
    call LINE(bubcir(i-1,1),bubcir(i-
1,2),bubcir(i,1),bubcir(i,2),
   +0)
    call LINE(bubcir(i-1,1),bubcir(i-
1,3),bubcir(i,1),bubcir(i,3),
   +0)

 30  Ysum=Ysum+bubcir(i,2)+bubcir(i,3)
    Xsum=Xsum+bubcir(i,1)
 10  continue
    Ymean=int2(Ysum/(2.0*(intvx+1)))
    Xmean=int2(Xsum/((intvx+1)*1.0))
    Xposn=(Xmean-xref1)*hormm
    Yposn=(Yref-Ymean)*vermm+Height
    xcord=hormm*(xmax-xmin)
    ycord=vermm*(ymaxi-ymini)
 40  return
    end

    Subroutine
NEARER(x,y,up,down,thresh,piyacc)
    integer*2
iniy1,iniy2,up,down,thresh,RPIXEL,igsc1,igsc2
    integer*2 int2,x,y,n,ick,piyacc
    ick=0
c. search every 0.5piyacc division so that to
ensure that the point
c. within the bubble is found
    n=int2(2.0*(down-up)/(piyacc*1.0))
    do 10 i=1,n-1
    iniy1=up+i*piyacc
    igsc1=RPIXEL(x,iniy1)

    if(igsc1.ge.thresh) then
c. assuming that there is a point bounded by the
points 'up' and 'down'
    y=iniy1
    return
    endif
 10  continue
    return
    end


c.          End of bubble parameters
measurement routine
c.
```

•

An extract of the programs and subroutines for the particle detection and recognition algorithm used in the study of large and lighter particle in a fluidized bed.

```
$include:'itexpc.inc'

      subroutine
emulsion(x1,y1,dx,dy,ithrs,Gmean,Gstdv)
c. measure intensity in emulsion phase
      integer*2 dx,dy,ithrs,pixel,x,y,x1,y1
      logical*2 INSIDE
      character gsbloc(54000)
      real*8 sum1,sum2
      common /imgmem/ gsbloc
c. gsbloc data called somewhere else
      sum1=0.0
      sum2=0.0
      iemul=0
      ibub=0
      icount=0
      do 10 i=1,dy
      y=y1+(i-1)
      do 20 j=1,dx
      x=x1+(j-1)
      idata=(y-y1)*dx+(x-x1)+1
      if(INSIDE(x,y)) then


      Pixel=ICHAR(gsbloc(idata))

      if(pixel.lt.ithrs) then
      icount=icount+1
      ratio=(icount-1)/float(icount)
      sum1=sum1*ratio+Pixel/float(icount)
      sum2=sum2*ratio+Pixel*Pixel/float(icount)

      endif

      endif
 20   continue

 10   continue

      Gmean=sum1
      Gstdv=(sum2-Gmean**2)**0.5

      return
      end



      subroutine REFINE(Px,Py,ithrs)
c. refine the position of particle
      integer*2 dxp,dyp,ithrs,pixel,x,y,x1,y1,n,x2,y2
      integer*2
xstart,ystart,Pxmin,Pymin,Px,Py,dx,dy
      logical*2 INSIDE
      character gsbloc(54000)
      common /imgmem/ gsbloc
      common /PSIZE/ dxp,dyp
c. gsbloc data called somewhere else

      x1=Px-dxp
      y1=Py-dyp

      x2=Px+dxp
      y2=Py+dyp
      dx=x2-x1
      dy=y2-y1

      call getbloc(x1,y1,dx,dy)

      ifirst=0

      do 10 i=1,dyp,2
      ystart=y1+(i-1)

      do 20 j=1,dxp,2
      xstart=x1+(j-1)

      sum1=0.0
      icount=0

      do 30 i1=1,dyp
      y=ystart+(i1-1)

      do 40 j1=1,dxp
      x=xstart+(j1-1)


      if(INSIDE(x,y)) then
      idata=(y-y1)*dx+(x-x1)+1

      Pixel=ICHAR(gsbloc(idata))

      if(pixel.lt.ithrs) then
      icount=icount+1
      ratio=(icount-1)/float(icount)
      sum1=sum1*ratio+Pixel/float(icount)
```

```
      endif

      endif

 40   continue
 30   continue

      if(ifirst.eq.0) then
      Gmin=sum1
      Pxmin=xstart+dxp/2
      Pymin=ystart+dyp/2
      ifirst=1
      else

      if(sum1.lt.Gmin) then
      Gmin=sum1
      Pxmin=xstart+dxp/2
      Pymin=ystart+dyp/2
      endif

      endif

 20   continue
 10   continue

      Px=Pxmin
      Py=Pymin

      return
      end

      Subroutine
     QSEARCH(x1in,y1in,x2in,y2in,Px,Py,GSmin)
c. search for the possible particle positions
      integer*2
     x1in,y1in,x2in,y2in,dxp,dyp,Px,Py,Pxmin,Pymin
      integer*2 x,y,int2,dx,dy
      integer*2 pixel
      integer*2 dxstep,dystep
      real*4 GSmin,pave(512)
      logical*2 INSIDE,JUSTIN

      character gsbloc(54000)
      common /imgmem/ gsbloc

      common /PSIZE/ dxp,dyp
      common /criteria/ Fpsize,critcut,w1,w2,w3,w4
c. call data from getbloc

      dx=x2in-x1in
      dy=y2in-y1in
      dxstep=Fpsize*dxp
      dystep=Fpsize*dyp
      nx=dx/dxstep
      ny=dy/dystep



      icount=0
      ifirst=0

      do 10 i1=1,ny
      ystart=y1in+(i1-1)*dystep

      do 20 i2=1,nx
      pave(i2)=0.0
 20   continue

      do 30 i3=1,dystep
      y=ystart+(i3-1)

      do 40 i4=1,nx
      xstart=x1in+(i4-1)*dxstep

      do 50 i5=1,dxstep
      x=xstart+(i5-1)
      idata=(y-y1in)*dx+(x-x1in)+1
      pixel=ichar(gsbloc(idata))
      pave(i4)=Pave(i4)+Pixel
 50   continue
 40   continue
 30   continue

      do 60 i6=1,nx
      x=x1in+(i6-1)*dxstep+dxstep/2
      y=y1in+(i1-1)*dystep+dystep/2
      pave(i6)=pave(i6)/float(dxstep*dystep)

      if ( INSIDE(x,y) ) then

      if(ifirst.eq.0) then
      Pxmin=x
      Pymin=y
      Gmin=pave(i6)
      ifirst=1
      else
      if(pave(i6).lt.Gmin) then
      Pxmin=x
      Pymin=y
      Gmin=pave(i6)
```

```
      endif
      endif
      endif

60    continue

10    continue

      Px=Pxmin
      Py=Pymin
      Gsmin=Gmin

      return
      end


      Subroutine QGSMAP(Gsmap,Femap,ithrs)
c. obtain intensity map around the particle
      integer*2 dxp,dyp,Px,Py,PXmin,PYmin
      integer*2 x,y,int2,dx,dy,ithrs
      integer*2 pixel,ichar
      integer*2 dxstep,istep,dypstep,dxpstep
      real*4 Gsmap(3,3),Femap(3,3)
      logical*2 INSIDE

      character gsbloc(54000)
      common /imgmem/ gsbloc

      common /PSIZE/ dxp,dyp
      common /criteria/ Fpsize,critcut,w1,w2,w3,w4
      common /Iphase/ AvePI,StdPI, Modemul,
Modbub
      icount=0
      ifirst=0

      do 10 i1=1,3

      do 20 i2=1,3
      Gsmap(i1,i2)=0.0
      Femap(i1,i2)=0.0
20    continue


      do 30 i3=1,dyp

      do 40 i4=1,3

      do 50 i5=1,dxp
      icount=icount+1
      pixel=ichar(gsbloc(icount))
      if(pixel.lt.ithrs) then
      Gsmap(i1,i4)=Gsmap(i1,i4)+pixel
      Femap(i1,i4)=Femap(i1,i4) + 0.75
      endif
50    continue
40    continue
30    continue

      do 60 i6=1,3

      if((i1.eq.2).and.(i6.eq.2)) then
      frtn=dxp*dyp*0.75*0.3
      else
      frtn=dxp*dyp*0.75*0.5
      endif
      if(Femap(i1,i6).lt.frtn) then
      Gsmap(i1,i6)=Modbub*1.0
      else
      Gsmap(i1,i6)=Gsmap(i1,i6)*0.75/Femap(i1,i6)
      endif

60    continue

10    continue

      return
      end


      subroutine
QCONFIRM(Px,Py,idecision,GSmap)
c. modified Pconfirm
c. final confirm for the identified particle
      integer*2
Px,Py,dxp,dyp,x1,y1,x2,y2,xstart,ystart
      integer*2 x1in,y1in,x2in,y2in,x,y,dx,dy
      integer*2 dxcell,dycell,ithrs,istart
      integer*2 dxpcell,dypcell,dxx,dyy,inbub
      logical*2 INSIDE
      real*4 GSmap(3,3),Femap(3,3)
      real*4 Fpsize,critcut,w1,w2,w3,w4


      common /PSIZE/ dxp,dyp
      common /criteria/ Fpsize,critcut,w1,w2,w3,w4
      common /Iphase/ AvePI,StdPI, Modemul,
Modbub
      common /thrs/ ithrs
```

```
      x1in=Px-3*dxp
      y1in=Py-3*dyp
      x2in=Px+3*dxp
      y2in=Py+3*dyp
      dxcell=6*dxp
      dycell=6*dyp

      call getbloc(x1in,y1in,dxcell,dycell)
c     call BOXSHOW(x1in,y1in,x2in,y2in)

      istart=Modemul+(Modbub-Modemul)*2/3.0
      ikeep=istart

      call
     NTHSBUB(x1in,y1in,dxcell,dycell,istart,ithrs)
      if (ithrs.le.Modemul) ithrs=ikeep

      call
     Emulsion(x1in,y1in,dxcell,dycell,ithrs,ave,stdv)
      emul=ave
      estd=stdv
      call REFINE(Px,Py,ithrs)

      x1=Px-dxp*1.5
      y1=Py-dyp*1.5

      x2=Px+dxp*1.5
      y2=Py+dyp*1.5
      dx=3*dxp
      dy=3*dyp

      call getbloc(x1,y1,dx,dy)
c     call BOXSHOW(x1,y1,x2,y2)

      call QGSMAP(Gsmap,Femap,ithrs)
      AR=0.75
      frtn=0.3*dxp*dyp*AR

c
     write(*,*)'emul=',emul,'estd=',estd,'Gsmap22=',Gs
     map(2,2)
c     write(*,*)'Femap22=',Femap(2,2)
      idecision=0
      stdmod=estd**0.95

      call inbubp(Femap,inbub)

      if(inbub.eq.0) then
      scale=0.33
      else
      scale=-0.33
      endif

      setd1=scale*stdmod


     if((Femap(2,2).ge.frtn).and.(Gsmap(2,2).le.(emul-
     setd1)))
     >  then
      idecision=1
      inscnt=0

      do 10 i=1,3

      do 20 j=1,3
      dxx=0
      dyy=0
      if(i.eq.1) dyy=-1.5*dyp
      if(i.eq.3) dyy=1.5*dyp
      if(j.eq.1) dxx=-1.5*dxp
      if(j.eq.3) dxx=1.5*dxp

      x=Px+dxx
      y=Py+dyy

      if((i.eq.2).and.(j.eq.2)) then
      if(INSIDE(x,y)) then
      else
      idecision=0
      endif

      else

      if(INSIDE(x,y)) then
      inscnt=inscnt+1
      diff=Gsmap(i,j)-Gsmap(2,2)
      setd2=ABS(scale)*stdmod
      if(setd2.lt.5) setd2=5.0
      if(diff.le.setd2) then
      idecision=0
      endif

      endif
      endif
     20  continue
     10  continue

      endif

c     call BOXSHOW(x1,y1,x2,y2)
c     write(*,*)'inscnt=',inscnt
```

```
    if((idecision.eq.1).and.(inscnt.lt.5)) idecision=0

c     write(*,'(9F7.1/)') ((GSmap(i,j),j=1,3),i=1,3)

c     call BOXSHOW(x1in,y1in,x2in,y2in)

      return
      end


      subroutine inbubp(Femap,inbub)
c. check if in bubble
      integer*2 dxp,dyp,inbub
      real*4 Femap(3,3)
      common /PSIZE/ dxp,dyp
      inbub=0
      sum=0.0
      do 10 i=1,3
      do 20 j=1,3
      sum=sum+Femap(i,j)
 20   continue
 10   continue
      total=9.0*dxp*dyp*0.75
      ratio=sum/total
      if(ratio.lt.0.5) inbub=1

      return
      end



      function INEQ(a,a1,a2,b1,b2)
      integer*2 a,a1,a2,b1,b2,INEQ
c. usage: a1,a2 denominator, INEQ=value of line
on a

      if(a1.eq.a2) then

      INEQ=b1

      else

      INEQ=(b2-b1)*(a-a1)/float(a2-a1)+b1

      endif

      return
      end

      function INSIDE(x,y)
c.MODIFIED INSIDE with BEDAREA and PSIZE
c. check if inside the bed search area
      logical*2 INSIDE
      integer*2 x,y,INEQ
      integer*2
BXY(4,2),dxp,dyp,x1out,y1out,x2out,y2out
      integer*2 x1,y1,x2,y2

      common /BEDAREA/ x1out,y1out,x2out,y2out
      common /PSIZE/ dxp,dyp
      common /BAOI/ BXY
c. upper line

      x1=x1out+5*dxp
      y1=y1out+5*dyp

      x2=x2out-5*dxp
      y2=y2out-5*dyp
c. rough check if in BEDAREA = 5 particle size

if((x.ge.x1).and.(x.le.x2).and.(y.ge.y1).and.(y.le.y2
)) then

      INSIDE=.TRUE.

      else


if(y.gt.INEQ(x,BXY(1,1),BXY(2,1),BXY(1,2),BX
Y(2,2))) then

c. right line


if(x.lt.INEQ(y,BXY(2,2),BXY(3,2),BXY(2,1),BX
Y(3,1))) then

c. lower line


if(y.lt.INEQ(x,BXY(3,1),BXY(4,1),BXY(3,2),BX
Y(4,2))) then

c. left line


if(x.gt.INEQ(y,BXY(4,2),BXY(1,2),BXY(4,1),BX
Y(1,1))) then

            INSIDE=.TRUE.
```

```
        else

          INSIDE=.FALSE.

        endif

       else

       INSIDE=.FALSE.

       endif

 else

 INSIDE=.FALSE.

 endif

else

INSIDE=.FALSE.

endif

endif

return

end


    subroutine SALL(idecision,Px,Py,GSmap)
c. search for all clusters/cells in AOI
    parameter (mcell=10, mtcell=mcell*mcell)

    integer*2 xdiv,ydiv,xcell(mcell),ycell(mcell)
    integer*2 x1out,y1out,x2out,y2out,x,y,ithrs
    integer*2 x1,y1,x2,y2

    integer*2
x1in,y1in,x2in,y2in,dxcell,dycell,istart
    integer*2 dxp,dyp,Px,Py,RPIXEL,GS(mtcell)
    integer*2 Xpos(mtcell),Ypos(mtcell),icodecut
    integer*2
GSindx(mtcell),GSOUT(mtcell),GRINDX(mtcell)

    logical*2 INSIDE
    real*4 GSmap(3,3),Gpmean

    common /BEDAREA/ x1out,y1out,x2out,y2out
    common /XYCELL/ xdiv,ydiv,xcell,ycell
    common /PSIZE/ dxp,dyp
    common /Iphase/ AvePI,StdPI, Modemul,
Modbub
    common /codcut/ icodecut
    common /thrs/ ithrs
    call CODECUT(icodecut)

    dxcell=(x2out-x1out)/float(xdiv)
    dycell=(y2out-y1out)/float(ydiv)

    icount=0

    do 10 i=1,xdiv

    x1in=xcell(i)
    x2in=xcell(i)+dxcell

    do 20 j=1,ydiv

    y1in=ycell(j)
    y2in=ycell(j)+dycell

    call getbloc(x1in,y1in,dxcell,dycell)

c    call BOXSHOW(x1in,y1in,x2in,y2in)

    call
QSEARCH(x1in,y1in,x2in,y2in,Px,Py,GPmean)

c    call BOXSHOW(x1in,y1in,x2in,y2in)

    icount=icount+1

    Xpos(icount)=Px
    Ypos(icount)=Py

    GS(icount)=int2(GPmean)

 20  continue
 10  continue



    icell=icount

    call
IMYSORT(icell,GS,GSindx,GSOUT,GRINDX)

c. to speed up the analysis, we may specify not all
the cells will be
```

```
c. analysed. eg. may be only HALF the total
number of cells/clusters
c. iclust = the number of the first few clusters to be
analysed

      iclust=icell

      idecision=0

      do 40 ik=1,iclust

      Px=Xpos(GRINDX(ik))
      Py=Ypos(GRINDX(ik))
c. idecision=1 is yes, i.e there is a particle


      call Edgechk(Px,Py,icheck)
      if(icheck.eq.1) then
      iupper=Modemul+(Modbub-Modemul)/2

      if(GS(GRINDX(ik)).lt.iupper) then


      call QCONFIRM(Px,Py,idecision,GSmap)


      if(idecision.eq.1) goto 99

      endif
      endif

 40   continue

 99   return
      end


c. SORTING PROGRAM
**********************************************
**
      subroutine
IMYSORT(N,ARRIN,INDX,ARROUT,RINDX)
c. sort an array ARRIN of INTEGER numbers,
INDX gives the ranking of
c. the sorted number, a same rank is given for more
than one INDX elements
      integer*2
ARRIN(N),INDX(N),ARROUT(N),RINDX(N)
      irank=1
      iremain=N
      call IZERO(N,INDX,ARROUT,RINDX)

      call
FINDMIN(N,ARRIN,INDX,irank,iremain,ixmin)
 20   if(iremain.gt.0) then
      call
SAMERANK(N,ARRIN,INDX,irank,iremain,ixmi
n)
      if(iremain.gt.0) then
      irank=irank+1
      call
FINDMIN(N,ARRIN,INDX,irank,iremain,ixmin)
      goto 20
      endif
      endif
      call
SORTED(N,ARRIN,INDX,ARROUT,RINDX,iran
k)
      return
      end

      Subroutine
IZERO(N,INDX,ARROUT,RINDX)
      integer*2 INDX(N),ARROUT(N),RINDX(N)
      do 10 i=1,N
      INDX(i)=0
      ARROUT(i)=0
      RINDX(i)=0
 10   continue
      return
      end

      Subroutine
SAMERANK(N,ARRIN,INDX,irank,iremain,ixmi
n)
      integer*2 ARRIN(N),INDX(N)
      do 10 i=1,N
      if(INDX(i).eq.0) then
       if(ARRIN(i).eq.ixmin) then
       INDX(i)=irank
       iremain=iremain-1
       endif
      endif
 10   continue
      return
      end

      Subroutine
FINDMIN(N,ARRIN,INDX,irank,iremain,ixmin)
      integer*2 ARRIN(N),INDX(N)
      number=1
```

```
   do 10 i=1,N
   if(INDX(i).eq.0) then
    if(number.eq.1) then
     ixmin=ARRIN(i)
     i_d=i
     number=2
    else
     if(ARRIN(i).lt.ixmin) then
      ixmin=ARRIN(i)
      i_d=i
     endif
    endif
   endif
10  continue
   iremain=iremain-1
   INDX(i_d)=irank
   return
   end

   Subroutine
SORTED(N,ARRIN,INDX,ARROUT,RINDX,iran
k)
   integer*2
ARRIN(N),INDX(N),ARROUT(N),RINDX(N)
   m=0
   do 10 i=1,irank
   do 20 j=1,N
   if (INDX(j).eq.i) then
   m=m+1
   ARROUT(m)=ARRIN(j)
   RINDX(m)=j
   endif
20  continue
10  continue
   return
   end
c. SORTING PROGRAM
(end)**********************************
******



   subroutine
NTHSBUB(x1,y1,dx,dy,istart,thresh)
c. this routine find the intensity for the edge of the
bubble
c. need to supply a starting point
c. it search for the RHS 'foot' of a distribution
which lies on the LHS
c. of the so called inten
csity distribution for the bubble phase.
c.

c. determine the threshold from a block obtained by
"getbloc"
   integer*2 thresh,filno,istart,i,idegree
   integer*2 x1,x2,dx,y1,y2,dy
   integer*4 histaoi(256),histvals(256)
c. if the search continuosly find 5 successive
positive slopes, stop the search
   idegree=5



   call HISTOG(x1,y1,dx,dy,1,1,histaoi)

   do 5 i=1,256
   histvals(i)=histaoi(i)
5   continue
   filno=10
   call SMOOTH(histaoi,filno,histvals)

   icount=0
   thresh=istart
   i=thresh
30  if(histvals(i).ge.histvals(i-1)) then
   thresh=i-1
   i=thresh
   icount=0
   else
   icount=icount+1
   i=i-1
   endif

   if((icount.lt.idegree).and.(i.gt.0)) goto 30
   thresh=thresh+filno+idegree
   return
   end

   subroutine Edgechk(Px,Py,icheck)
c. check if the position is outside the boundary
   integer*2 Px,Py,x,y,dxx,dyy,dxp,dyp
   integer*2 xul
   logical*2 INSIDE

   common /PSIZE/ dxp,dyp
   inscnt=0
   icheck=1
   do 10 i=1,3

   do 20 j=1,3
   dxx=0
   dyy=0
```

```
      if(i.eq.1) dyy=-1.5*dyp
      if(i.eq.3) dyy=1.5*dyp
      if(j.eq.1) dxx=-1.5*dxp
      if(j.eq.3) dxx=1.5*dxp

      x=Px+dxx
      y=Py+dyy

      if((i.eq.2).and.(j.eq.2)) then

      if(lNSIDE(x,y)) then

      do 30 ii=1,2
      do 40 jj=1,2

      dxx=0
      dyy=0
      if(ii.eq.1) dyy=-0.5*dyp
      if(ii.eq.2) dyy= 0.5*dyp
      if(jj.eq.1) dxx=-0.5*dxp
      if(jj.eq.2) dxx= 0.5*dxp

      x=Px+dxx
      y=Py+dyy

      if(INSIDE(x,y)) then

      else

      icheck=0

      endif
   40 continue
   30 continue

      else

      icheck=0

      endif

      else

      if(INSIDE(x,y)) then
      inscnt=inscnt+1
      endif

      endif

   20 continue
   10 continue
      if(inscnt.lt.5) icheck=0
      return
      end



      Function JUSTIN(Px,Py)
c. check if the position is outside the boundary in
1/2 Px,Py
      integer*2 Px,Py,x,y,dxx,dyy,dxp,dyp
      integer*2 xul
      logical*2 INSIDE,JUSTIN

      common /PSIZE/ dxp,dyp
      JUSTIN=.TRUE.

      do 30 ii=1,2

      do 40 jj=1,2

      dxx=0
      dyy=0
      if(ii.eq.1) dyy=-0.5*dyp
      if(ii.eq.2) dyy= 0.5*dyp
      if(jj.eq.1) dxx=-0.5*dxp
      if(jj.eq.2) dxx= 0.5*dxp

      x=Px+dxx
      y=Py+dyy

      if(INSIDE(x,y)) then

      else

      JUSTIN=.FALSE.

      endif
   40 continue
   30 continue

      return
      end
```

```
      Program for simulation of solids mixing and
            segregation in fluidized bed
        implicit real*8 (A-H,O-Z)
c. Simulation of solids mixing and segregation in
fluidized bed
c. Prediction of average axial tracer concentration
(transient)
c, C = f(Z,t)
c. numerical solution using IMSL numerial library.
        parameter (Nmax=500)
        character*2 MH,DH
        character*12
 fout1,fout2,fout3,fout4,fout5,fout7,fout8
        character*12 fout9, fout10
        dimension
 PARAM(50),CZ(10),B(1,1),RWKSP(73000)
        dimension
 ZLOC(10),TLOC(10),DBLOC(10),EZ(10),Y(2*N
max)
        dimension
 Ebz(Nmax),Ct(Nmax,10),DB(Nmax),Us(Nmax)
        dimension CW(Nmax),CE(Nmax)
        dimension CA(Nmax)

        external DIVPAG,DSET,FCN,FCNJ,IWKIN

        common /WORKSP/RWKSP
        common /VARI/ U, Umf, Emf, fw, qx, xi, N
        common /ZEXP/ ZLOC,NZ
        common /TEXP/ TLOC,NT
        common /TIME/ Ttot,Dt,Dtwrit
        common /BUBF/ Ebz
        common /BUBD/ DB,Us,TK
        common /STAG/ NB
        common /DXSIZE/ DX
        common /PCONC/ CW,CE
        common /DEFLU/ IDEFLU
        common /MODEL/ Imodel, Ischem
        common /SSCHK/ SFAC
        common /HEADER/ MH

        pi=3.141592654
        g=981.0
        call IWKIN(73000)
c. reserve unit=9 for input



        call FBVAR

        do 10 i=1,50
        PARAM(i)=0.0
 10   continue


c. DIVPAG settings
        TOL=1.0D-6
        PARAM(4)=5000000
        PARAM(10)=1
        PARAM(12)=1
c. A maxtrix a constant = implicit or 2 if A depend
on t
        PARAM(19)=0

c       write(*,*)'Enter File header [Char=2], G=GR,
Y=YOS model'
c       write(*,*)'To run > 1 program Use different
header'
c       read(*,'(A)') MH
c       if(Imodel.eq.1) MH='GR'
c       if(Imodel.eq.2) MH='YS'


        if(IDEFLU.eq.0) DH='CF'
        if(IDEFLU.eq.1) DH='DF'


        fout1=MH//DH//'CAT.dat'
        fout2=MH//DH//'DBT.dat'
        fout3=MH//DH//'EBT.dat'
        fout4=MH//DH//'CWT.dat'
        fout5=MH//DH//'CET.dat'
        fout7=MH//DH//'HET.dat'
        fout8=MH//DH//'CAZ.dat'
        fout9=MH//DH//'CST.dat'

        OPEN (1,file=fout1,status='unknown')
        OPEN (2,file=fout2,status='unknown')
        OPEN (3,file=fout3,status='unknown')
        OPEN (4,file=fout4,status='unknown')
        OPEN (5,file=fout5,status='unknown')
        OPEN (7,file=fout7,status='unknown')
        OPEN (9,file=fout9,status='unknown')

        T=0.0
        NB=0
        icount=1
        IDO=1
        itime=0

        M=Ttot/Dt
        NTskip=int(Dtwrit/Dt)
```

```
      write(*,*)'processing'
      write(*,*)' '

      do 20 i=1,M

      TEND=i*Dt
      NEQ=2*(N-NB)


      write(*,200)  TEND
 200  format('+','Time=',F10.3,' s')

      call CTOY(Y)


      IDO=1

      call
DIVPAG(IDO,NEQ,FCN,FCNJ,B,T,TEND,TOL,P
ARAM,Y)
      call YTOC(Y)

      IDO=3

      call
DIVPAG(IDO,NEQ,FCN,FCNJ,B,T,TEND,TOL,P
ARAM,Y)


      call CFBVAR


c. extracting C vs t at specified height of Dcell size

      do 40 k=1,NZ

      Z = Zloc(k)

      call AVEPRO(Z,Cave,Eave)

      CZ(k)=Cave
      EZ(k)=Eave

 40   continue


c. extracting C vs Z data at different time



if((TEND.ge.TLOC(icount)).and.(icount.le.NT))
then

      do 60 j=1,N

      C1=((Ebz(j)*fw)*CW(j)+(1-Ebz(j)-
fw*Ebz(j))*CE(j))/(1-Ebz(j))
      Ct(j,icount)=C1

 60   continue

      icount=icount+1

      endif


c. check if steady state has reached

      sum=0.0

      do 80 j=1,N
      C1=((Ebz(j)*fw)*CW(j)+(1-Ebz(j)-
fw*Ebz(j))*CE(j))/(1-Ebz(j))
      sum=sum+ABS(C1-CA(j))
      CA(j)=C1
 80   continue

      if(itime.gt.0) then

      if(sum.le.(SFAC*N)) then
      write(*,*)'Approaching steady state condition'
      goto 99
      endif

      endif

      itime=1

c. only print out at required time interval

      if(iTskip.eq.0) then

      write(1,110) TEND, (CZ(k), k=1,NZ)
      write(2,110) TEND, (DB(k), k=1,NZ)
      write(3,110) TEND, (EBz(k), k=1,NZ)
      write(4,110) TEND, (CW(k), k=1,NZ)
      write(5,110) TEND, (CE(k), k=1,NZ)
      write(7,120) TEND, (N*DX), (NB*DX)
      write(9,110) TEND, (CA(k), k=1,NZ)
c     write(*,110) (TEND),(CZ(k), k=1,NZ)

      endif
```

```
      iTskip=iTskip+1
      if(iTskip.gt.NTskip) iTskip=0

  110 format(F7.3,8F8.4)
  120 format(F7.3,2F10.2)

      T=TEND

   20 continue


   99 close(1,status='keep')
      close(2,status='keep')
      close(3,status='keep')
      close(4,status='keep')
      close(5,status='keep')
      close(7,status='keep')
      close(9,status='keep')

      OPEN (1,file=fout8,status='unknown')

      do 70 j=1,N
      Z1=j*DX
      write(1,130) Z1,(Ct(j,k), k=1,NT)
   70 continue
  130 format(F7.2,8F8.4)
      close(1,status='keep')

      END


      subroutine AVEPRO(Z,Cave,Eave)
c. calculate avarage C for several cells
      implicit real*8 (A-H,O-Z)
      parameter (Nmax=500)

      dimension Ebz(Nmax),DB(Nmax),Us(Nmax)
      dimension CW(Nmax),CE(Nmax)


      common /VARI/ U, Umf, Emf, fw, qx, xi, N
      common /BUBF/ Ebz
      common /BUBD/ DB,Us,TK
      common /DXSIZE/ DX
      common /PCONC/ CW,CE
      common /SCell/ Dcell

      KZ = Z/DX
      KN = Dcell/DX

      if (KN.ge.1) then
c. for Dcell size larger than DX : lumped conc
      sumC=0.0
      sumE=0.0

      do 10 k = 1, KN

      j = KZ - KN/2 + k
      sumC=sumC + ((Ebz(j)*fw)*CW(j)+(1-Ebz(j)-
fw*Ebz(j))*CE(j))
      sumE=sumE + (1-Ebz(j))

   10 continue

      Cave=sumC/sumE
      Eave=1.0 - sumE/(1.0*KN)
      else
c. simple linear interpolation of the concentration

      j =KZ
      Z1=j*DX
      C1=((Ebz(j)*fw)*CW(j)+(1-Ebz(j)-
fw*Ebz(j))*CE(j))/(1-Ebz(j))
      E1=(Ebz(j))

      j =KZ+1
      Z2=j*DX
      C2=((Ebz(j)*fw)*CW(j)+(1-Ebz(j)-
fw*Ebz(j))*CE(j))/(1-Ebz(j))
      E2=Ebz(j)
      Cave=C1+(C2-C1)*(Z-Z1)/(Z2-Z1)

      Eave=E1+(E2-E1)*(Z-Z1)/(Z2-Z1)

      endif

      return
      end


      subroutine YTOC(Y)

      implicit real*8 (A-H,O-Z)
      parameter (Nmax=500)
      dimension Y(2*Nmax),CW(Nmax),
CE(Nmax)
      dimension
VUb(Nmax),VFR(Nmax),VWK(Nmax),VYS(Nma
x),VEBZ(Nmax)
```

```
      dimension Ub(Nmax),FR(Nmax),WK(Nmax),
     Ebz(Nmax)

      common /VARI/ U, Umf, Emf, fw, qx, xi, N
      common /STAG/ NB
      common /PROP/ Ub,FR,WK,YS
      common /BUBF/ Ebz
      common /VPROP/
     VUb,VFR,VWK,VYS,VEBZ,VBDZ
      common /PCONC/ CW,CE


      do 10 i=1,N

      if(i.gt.NB) then

      CW(i)=( Y(i-NB) )

      CE(i)=( Y((i-NB)+(N-NB)) )


      endif
   10 continue

      return
      end



      subroutine CTOY(Y)
c. changing of input array for the DE solver
      implicit real*8 (A-H,O-Z)
      parameter (Nmax=500)
      dimension Y(2*Nmax),CW(Nmax),CE(Nmax)
      dimension
     VUb(Nmax),VFR(Nmax),VWK(Nmax),VEBZ(Nm
     ax),Ebz(Nmax)
      dimension
     Ub(Nmax),FR(Nmax),WK(Nmax),VYS(Nmax),Y
     A(Nmax)
      dimension BDZ(Nmax),VBDZ(Nmax)

      common /VARI/ U, Umf, Emf, fw, qx, xi, N
      common /STAG/ NB
      common /PROP/ Ub,FR,WK,YS
      common /BUBF/ Ebz
      common /VPROP/
     VUb,VFR,VWK,VYS,VEBZ,VBDZ
      common /PCONC/ CW,CE
      common /YADJS/ YA
      common /BUBDZ/ BDZ

      do 10 i=1,N

      if(i.gt.NB) then

      Y(i-NB)=CW(i)
      Y((i-NB)+(N-NB))=CE(i)
      VUb(i-NB)=Ub(i)
      VFR(i-NB)=FR(i)
      VEBZ(i-NB)=Ebz(i)
      VWK(i-NB)=WK(i)
      VYS(i-NB)=YA(i)
      VBDZ(i-NB)=BDZ(i)
      endif

   10 continue
      return
      end



      function CLIMIT(C1)
      implicit real*8 (A-H,O-Z)
      common /VARI/ U, Umf, Emf, fw, qx, xi, N
      common /UMFR/ RUMF
      common /DEFLU/ IDEFLU
      common /CRITIC/ CC


      if(C1.le.0.0) C1=0.0
      if(C1.ge.CC) C1=CC

      CLIMIT=C1

      return
      end



      subroutine FCN(NEQ,T,Y,YPRIM)
c. input function for the differential equation for
solid tracer
c. material balance using DIVPAG subroutine of
IMSL library
      implicit real*8 (A-H,O-Z)
      parameter (Nmax=500)
      dimension Y(2*Nmax),YPRIM(2*Nmax)
      dimension
     VUb(Nmax),VFR(Nmax),VWK(Nmax)
```

```
      dimension
Ub(Nmax),FR(Nmax),WK(Nmax),VYS(Nmax),
VEBZ(Nmax)
      dimension VBDZ(Nmax)

      common /VARI/ U, Umf, Emf, fw, qx, xi, N
      common /PROP/ Ub,FR,WK,YS
      common /VPROP/
VUb,VFR,VWK,VYS,VEBZ,VBDZ
      common /DXSIZE/ DX
      common /MODEL/ Imodel, Ischem
      common /CRITIC/ CC
      common /SATURC/ CSAT

c. Using Gibilaro and Rowe (model 1) and Yoshida
(model 2)

c. I = 1 to N for upward movement of solids with
bubble phase
c. I = N+1 to 2N for downward movement in the
emulsion phase

c. upward movement
c. cell 1 - bottom
c. 3 mechanisms:

c. 1 : convective
c. 2 : exchange
c. 3 : segregation

c. 3 difference approximation schemes considered

      M=NEQ/2

c. ---------------------------------------------------
-------

c. ****************** Approximation scheme
1 ********************

c. ---------------------------------------------------
-------

      if(Ischem.eq.1) then

c. using local value - assuming slow change in
bubble properties

c. bottom cell

      i=1

      a1 = -1.0 * VUb(i) * ( Y(i) - Y(M+i) ) / DX
      a2 = -1.0 * VWK(i) * ( Y(i) - Y(M+i) )

      if(Imodel.eq.1) then

      a3 = 0.0

      elseif(Imodel.eq.2) then

      a3 = -1.0 * VWK(i) * VYS(i) * Y(M+i) * (
CSAT - Y(i) )

      endif

      YPRIM(i)= a1 + a2 + a3

c. cell 2 to M-1

      do 10 i=2,M-1

      a1 = -1.0 * VUb(i) * ( Y(i) - Y(i-1) ) / DX
      a2 = -1.0 * VWK(i) * ( Y(i) - Y(M+i) )

      if(Imodel.eq.1) then

      a3 = 0.0

      elseif(Imodel.eq.2) then

      a3 = -1.0 * VWK(i) * VYS(i) * Y(M+i) * (
CSAT - Y(i) )

      endif

      YPRIM(i)= a1 + a2 + a3

10    continue

c. top cell

      i=M

      a1 = -1.0 * VUb(i) * ( Y(i) - Y(i-1) ) / DX
      a2 = -1.0 * VWK(i) * ( Y(i) - Y(M+i) )

      if(Imodel.eq.1) then

      a3 = 0.0
```

```
    elseif(Imodel.eq.2) then

    a3 = -1.0 * VWK(i) * VYS(i) * Y(M+i) * (
CSAT - Y(i) )

    endif

    YPRIM(i)= a1 + a2 + a3


c. downward movement

c. cell 1

    i=1

    a1 = VFR(i) * VUb(i) * ( Y(M+i+1) - Y(M+i) )
/ DX
    a2 = VFR(i) * VWK(i) * ( Y(i) - Y(M+i) )

    if(Imodel.eq.1) then

    a3 =
VFR(i)*0.75*VYS(i)*VUb(i)*Y(M+i+1)*(CSAT-
Y(M+i))/DX

    elseif(Imodel.eq.2) then

    a3 = VFR(i) * VWK(i) * VYS(i) * Y(M+i) * (
CSAT - Y(i) )

    endif

    YPRIM(M+i)= a1 + a2 + a3

c. cell 2-M-1

    do 20 i=2,(M-1)

    a1 = VFR(i) * VUb(i) * ( Y(M+i+1) - Y(M+i) )
/ DX
    a2 = VFR(i) * VWK(i) * ( Y(i) - Y(M+i) )

    if(Imodel.eq.1) then

    a3a =
VFR(i)*0.75*VYS(i)*VUb(i)*Y(M+i+1)*(CSAT-
Y(M+i))/DX
    a3b = -
1.0*VFR(i)*0.75*VYS(i)*VUb(i)*Y(M+i)*(1.0-
Y(M+i-1))/DX

    a3 = a3a + a3b

    elseif(Imodel.eq.2) then

    a3 = VFR(i) * VWK(i) * VYS(i) * Y(M+i) * (
CSAT - Y(i) )

    endif

    YPRIM(M+i)= a1 + a2 + a3

 20  continue

c. top cell M

    i=M
    a1 = VFR(i) * VUb(i) * ( Y(i) - Y(M+i) ) / DX
    a2 = VFR(i) * VWK(i) * ( Y(i) - Y(M+i) )

    if(Imodel.eq.1) then
    a3a = 0.0

    a3b = -
1.0*VFR(i)*0.75*VYS(i)*VUb(i)*Y(M+i)*(CSAT
-Y(M+i-1))/DX

    a3 = a3a + a3b

    elseif(Imodel.eq.2) then

    a3 = VFR(i) * VWK(i) * VYS(i) * Y(M+i) * (
CSAT - Y(i) )

    endif

    YPRIM(M+i)= a1 + a2 + a3


c. ----------
-------

c. ********** Approximation scheme
2 **********

c. ----------
-------


    elseif(Ischem.eq.2) then
```

```
c. using ordinary difference method

c. bottom cell 1

      i=1


      a1a = -1.0 *  VUb(i) * Y(i) /DX
      a1b = VUb(i) * Y(M+i) /DX

      a1 = (a1a + a1b)

      a2 = -1.0 * VWK(i) * ( Y(i) - Y(M+i) )

      if (Imodel.eq.1) then

      a3 = 0.0

      elseif(Imodel.eq.2) then

      a3 = -1.0 * VWK(i) * VYS(i) * Y(M+i) * (
CSAT - Y(i) )

      endif

      YPRIM(i)= a1 + a2 + a3


c. cell 2 to M-1

      do 90 i=2,M-1


      a1a = (VEBZ(i-1)/VEBZ(i) )*  VUb(i-1) * Y(i-
1) /DX

      a1b = -1.0 *  VUb(i) * Y(i) /DX

      a1 = ( a1a + a1b )

      a2 = -1.0 * VWK(i) * ( Y(i) - Y(M+i) )


      if(Imodel.eq.1) then

      a3 = 0.0

      elseif(Imodel.eq.2) then

      a3 = -1.0 * VWK(i) * VYS(i) * Y(M+i) * (
CSAT - Y(i) )

      endif


      YPRIM(i)= a1 + a2 + a3


 90   continue


c. top cell

      i=M

      a1a = ( VEBZ(i-1) / VEBZ(i) )  *  VUb(i-1) *
Y(i-1) /DX

      a1b = -1.0 * VUb(i) * Y(i) /DX

      a1 = ( a1a + a1b )

      a2 = -1.0 * VWK(i) * ( Y(i) - Y(M+i) )

      if(Imodel.eq.1) then

      a3 = 0.0

      elseif(Imodel.eq.2) then

      a3 = -1.0 * VWK(i) * VYS(i) * Y(M+i) * (
CSAT - Y(i) )

      endif

      YPRIM(i)= a1 + a2 + a3


c. downward movement

c. cell 1

      i=1

      a1a = (VFR(i)* VEBZ(i+1)/ VEBZ(i)) *
VUb(i+1) * Y(M+i+1) /DX
      a1b = -1.0* VFR(i) *  VUb(i) * Y(M+i) /DX
```

```
      a1 = ( a1a + a1b )

      a2 = VFR(i) * VWK(i) * ( Y(i) - Y(M+i) )

      if(Imodel.eq.1) then

      a3 = 0.75 * VYS(i+1) *VUb(i+1)*VFR(i)*
(VEBZ(i+1)/VEBZ(i))

     > * Y(M+i+1) * ( CSAT - Y(M+i) ) / DX

      elseif(Imodel.eq.2) then

      a3 = VFR(i) * VWK(i) * VYS(i) * Y(M+i) * (
CSAT - Y(i) )

      endif

      YPRIM(M+i)= a1 + a2 + a3

c. cell 2-M-I

      do 100 i=2,(M-1)

      a1a = (VFR(i)* VEBZ(i+1)/ VEBZ(i)) *
VUb(i+1) * Y(M+i+1)
      a1b = -1.0* VFR(i) *  VUb(i) * Y(M+i)

      a1 = ( a1a + a1b ) / DX

      a2 = VFR(i) * VWK(i) * ( Y(i) - Y(M+i) )

c. check if fw to be removed

      if(Imodel.eq.1) then

      a3a = 0.75 * VYS(i+1)*VUb(i+1)* VFR(i)*
VEBZ(i+1)/VEBZ(i)*

     > Y(M+i+1) * (CSAT - Y(M+i)) /DX


      a3b = -1.0 * 0.75 * VYS(i)*VUb(i)* VFR(i) *

     > Y(M+i) * ( CSAT - Y(M+i-1)) /DX

      a3 = (a3a + a3b )

      elseif(Imodel.eq.2) then

      a3 = VFR(i) * VWK(i) * VYS(i) * Y(M+i) * (
CSAT - Y(i) )

      endif

      YPRIM(M+i)= a1 + a2 + a3


 100  continue

c. cell M

      i=M

      a1a = VFR(i) * VUb(i) * Y(i) /DX
      a1b = -1.0 * VFR(i) * VUb(i) * Y(M+i)/ DX

      a1 = (a1a + a1b)

      a2 = VFR(i) * VWK(i) * ( Y(i) - Y(M+i) )


      if(Imodel.eq.1) then

      a3a = 0.0

      a3b = -1.0 * 0.75 * VYS(i)*VUb(i)* VFR(i) *

     > Y(M+i) * ( CSAT - Y(M+i-1)) /DX

      a3 = (a3a + a3b )

      elseif(Imodel.eq.2) then

      a3 = VFR(i) * VWK(i) * VYS(i) * Y(M+i) * (
CSAT - Y(i) )

      endif

      YPRIM(M+i)= a1 + a2 + a3
```

```
c. ------------------------------------------------------------
-------

c. ******************* Approximation scheme
3 **********************

c. ------------------------------------------------------------
-------

     elseif(Ischem.eq.3) then

c. complete difference method
c. using local value + d(Ub Eb) dz terms

c. upward movement


c. bottom cell

     i=1

     a1 = -1.0 * VUb(i) * ( Y(i) - Y(M+i) ) / DX
     a2 = -1.0 * VWK(i) * ( Y(i) - Y(M+i) )
     b1 = -1.0 * Y(i) * fw* VBDZ(i) / (fw *
VEBZ(i) )

     if(Imodel.eq.1) then

     a3 = 0.0

     elseif(Imodel.eq.2) then

     a3 = -1.0 * VWK(i) * VYS(i) * Y(M+i) * (
CSAT - Y(i) )

     endif

     YPRIM(i)= a1 + a2 + a3 + b1

c. cell 2 to M-1

     do 510 i=2,M-1

     a1 = -1.0 * VUb(i) * ( Y(i) - Y(i-1) ) / DX
     a2 = -1.0 * VWK(i) * ( Y(i) - Y(M+i) )

     b1 = -1.0 * Y(i) * fw* VBDZ(i) / (fw *
VEBZ(i) )

     if(Imodel.eq.1) then

     a3 = 0.0

     elseif(Imodel.eq.2) then

     a3 = -1.0 * VWK(i) * VYS(i) * Y(M+i) * (
CSAT - Y(i) )

     endif

     YPRIM(i)= a1 + a2 + a3 + b1

 510  continue


c. top cell

     i=M

     a1 = -1.0 * VUb(i) * ( Y(i) - Y(i-1) ) / DX
     a2 = -1.0 * VWK(i) * ( Y(i) - Y(M+i) )

     b1 = -1.0 * Y(i) * fw* VBDZ(i) / (fw *
VEBZ(i) )

     if(Imodel.eq.1) then

     a3 = 0.0

     elseif(Imodel.eq.2) then

     a3 = -1.0 * VWK(i) * VYS(i) * Y(M+i) * (
CSAT - Y(i) )

     endif

     YPRIM(i)= a1 + a2 + a3 + b1



c. downward movement


c. cell 1

     i=1

     a1 = VFR(i) * VUb(i) * ( Y(M+i+1) - Y(M+i) )
/ DX
```

```
    a2 = VFR(i) * VWK(i) * ( Y(i) - Y(M+i) )

    b1 =  Y(M+i) * fw* VBDZ(i) * VFR(i) / (
fw*VEBZ(i) )

    if(Imodel.eq.1) then


    a3a = 0.75 * VYS(i) * VBDZ(i) * Y(M+i) * (
1.0 - Y(M+i) )
    > * VFR(i) / ( fw*VEBZ(i) )


    a3b = 0.75 * VYS(i) * VUb(i)*
(VFR(i)/fw)*(1.0 - 2.0*Y(M+i))*
    > ( Y(M+i+1) - Y(M+i) ) / DX


    a3c = 0.75*VYS(i)*VUb(i)*(VFR(i)/fw)*
Y(M+i)*(1.0 - Y(M+i))

    a3= a3a + a3b + a3c

    elseif(Imodel.eq.2) then

    a3 = VFR(i) * VWK(i) * VYS(i) * Y(M+i) * (
CSAT - Y(i) )

    endif


    YPRIM(M+i)= a1 + a2 + a3 + b1
```

c. cell 2-M-1

```
    do 520 i=2,(M-1)

    a1 = VFR(i) * VUb(i) * ( Y(M+i+1) - Y(M+i) )
/ DX
    a2 = VFR(i) * VWK(i) * ( Y(i) - Y(M+i) )

    b1 =  Y(M+i) * fw* VBDZ(i) * VFR(i) / (
fw*VEBZ(i) )


    if(Imodel.eq.1) then

    a3a = 0.75 * VYS(i) * VBDZ(i) * Y(M+i) * (
1.0 - Y(M+i) )
    > * VFR(i) / ( fw*VEBZ(i) )


    a3b = 0.75 * VYS(i) *
VUb(i)*(VFR(i)/fw)*(1.0 - 2.0*Y(M+i))*
    > ( Y(M+i+1) - Y(M+i) ) / DX

    a3= a3a + a3b

    elseif(Imodel.eq.2) then

    a3 = VFR(i) * VWK(i) * VYS(i) * Y(M+i) * (
CSAT - Y(i) )

    endif

    YPRIM(M+i)= a1 + a2 + a3 + b1

520  continue
```

c. top cell M

```
    i=M
    a1 = VFR(i) * VUb(i) * ( Y(i) - Y(M+i) ) / DX
    a2 = VFR(i) * VWK(i) * ( Y(i) - Y(M+i) )

    b1 =  Y(M+i) * fw* VBDZ(i) * VFR(i) / (
fw*VEBZ(i) )

    if(Imodel.eq.1) then

    a3a = 0.75 * VYS(i) * VBDZ(i) * Y(M+i) * (
1.0 - Y(M+i) )
    > * VFR(i) / ( fw*VEBZ(i) )

    a3b = 0.75 * VYS(i) * VUb(i)*
(VFR(i)/fw)*(1.0 - 2.0*Y(M+i))*
    > ( Y(M+i+1) - Y(M+i) ) / DX

    a3c = 0.75 * VYS(i)
*VUb(i)*(VFR(i)/fw)*Y(M+i)*(1.0 - Y(M+i))


    a3= a3a + a3b - a3c

    elseif(Imodel.eq.2) then

    a3 = VFR(i) * VWK(i) * VYS(i) * Y(M+i) * (
CSAT - Y(i) )

    endif

    YPRIM(M+i)= a1 + a2 + a3 + b1
```

```
      endif


      RETURN
      END




      subroutine FCNJ(NEQ,X,Y,DYPDY)
      implicit real*8 (A-H,O-Z)
      parameter (Nmax=500)
      dimension Y(2*Nmax),DYPDY(*)
      return
      end



      subroutine FBVAR
c. calculate initial bubble properties
      implicit real*8 (A-H,O-Z)
      parameter (Nmax=500)
      character*12 finp
      character*2 MH
      dimension
Ub(Nmax),Ebz(Nmax),WK(Nmax),FR(Nmax)
      dimension CW(Nmax),CE(Nmax)
      dimension
Zloc(10),TLOC(10),Z(Nmax),DB(Nmax),Us(Nma
x),YA(Nmax)
      common /VARI/ U, Umf, Emf, fw, qx, xi, N
      common /BEDH/ Hfix,Ebm
      common /ZEXP/ ZLOC,NZ
      common /TEXP/ TLOC,NT
      common /TIME/ Ttot,Dt,Dtwrit
      common /PROP/ Ub,FR,WK,YS
      common /BUBF/ Ebz
      common /BUBD/ DB,Us,TK
      common /EXCH/
EXFAC,power,EXLIM,EXINT
      common /UMFR/ RUMF
      common /DXSIZE/ DX
      common /LHS/ XLHS,YLHS
      common /DEFLU/ IDEFLU
      common /MODEL/ IMODEL, Ischem
      common /MSTATE/ Istate
      common /PCONC/ CW,CE
      common /PRATIO/ RRHO,RDP
      common /YADJS/ YA
      common /CYSVAL/ CYS
      common /Yoption/ iYoption
      common /YCpower/ alpha,beta,gamma
      common /YCval/ Yconst
      common /CTYPE/ ICtype
      common /CRITIC/ CC
      common /CRIFAL/ CCF
      common /SSCHK/ SFAC
      common /SATURC/ CSAT
      common /SCell/ Dcell
      common /HEADER/ MH
      common /BUBVEL/ IBUBVEL
      common /ICVOL/ CIVOL
      common /ECONST/ EC1, EC2
      g=981.0
c     *.inp file
      OPEN (9,file='gryos3.inp',status='old')

      rewind(9)
      write(*,*)'Reading input data file....'

c. BED MATERIAL: XM(mass of bed, kg);
RHO1/2(density of particle, kg/m3,
c. RHO1: tracer);  DP1/2(particle size, mu or mm).
      read(9,'(A)') MH
      read(9,*) XM
      read(9,*) RHO1
      read(9,*) RHO2
      read(9,*) DP1
      read(9,*) DP2

c. OPERATING CONDITIONS: U,Umf(cm/s);
Istate=0: seg, 1: fully mix;
c. Iform= 0: ideal input, =1: data file input

      read(9,*) U
      read(9,*) Umf, RUMF, FumfT, FumfF, EC1,
EC2
      read(9,*) Emf
      read(9,*) qx
      read(9,*) xi
      read(9,*) Istate, Iform

c. MODEL INPUTS:  Imodel(1:GR,  2:YOS);
c. Appx scheme 1: point Ub,  2: difference Ub
c. ICsat: 0 ( =1.0);  1 ( = CC).
c. IDEFLU( 0:No,  1:Yes ).
```

```
c. Ictype(0:Cave, 1:CW, 2:CE)
c. SFAC = residue erros check for steady state
c. EXFAC = now a slope for U/Umfc
c. different functionality for Y may be used
c. Ys (max value oe mean)
c. IYoption; 0:constant; 1:f(C) ramp to 1; 2: f(C)
ramp to CC;
c. 3: f(C) trianglular; 4: symmetrical bell;
c. 5: skewed bell (define alpha, beta, gamma = 1.0)
c. CYS = lowest C where Y > 0 applies only to
iYoption 1,2,3
c. IBUBVEL=1 (U-Umf);  2: no (U-Umf)

      read(9,*) Imodel, Ischem, ICsat
      read(9,*) IDEFLU, ICtype
      read(9,*) DX, SFAC
      read(9,*) fw, IBUBVEL
      read(9,*) TK
      read(9,*) EXFAC, EXINT, EXLIM
      read(9,*) power
      read(9,*) YS, iYoption, CYS, alpha, beta,
gamma

c. DURATION:  (in second)

      read(9,*) Ttot, Dt, Dtwrit

c. REQUIRED BED HEIGHTS FOR C(t):  (in cm)
NZ = 8 max

      read(9,*) NZ, Dcell
      read(9,*) (Zloc(i),i=1,NZ)

c. REQUIRED TIME FOR C(z):  (in second)
NT=8 max

      read(9,*) NT
      read(9,*) (Tloc(i),i=1,NT)

      close(9,status='keep')

c. check for conflicting case

      if(YS.eq.0.0) then
      if((Istate.eq.0).and.(IDEFLU.eq.0)) then
      write(*,*)'Homogeneous Mixing simulation'
      if(RUMF.ne.1.0) then
      write(*,*)'RUMF not equal 1.0;  so set to 1.0'
      RUMF=1.0
      endif
      else
      write(*,*)'Unidentified simulation mode for
homogeneous mixing'
      stop
      endif

      elseif(Ys.gt.0.0) then
      if((Istate.eq.0).and.(IDEFLU.eq.1)) then

      if(U.le.(RUMF*Umf)) then

      if(qx.eq.0) then
      write(*,*)'Packed bed at base, permanently
segregate'
      else
      write(*,*)'Tracer layer remains packed - unable
to fluidize'
      endif

      stop

      endif
      endif

      endif


      Area=20*0.9

      RRHO=RHO1/RHO2
      RDP =DP1/DP2

      YST=0.6*RRHO*RDP**0.333
      YSL=0.0063*(RDP-1.0)+0.0426*(RRHO-1.0)

c. FumfT and FUmfF >= 1.0

      UT = U/FumfT
      UF = U/FumfF

      if (UF.le. (Umf)) then
      write(*,*)'FumfF is too large ie. UF < Umf'
      write(*,*)'will change FumfF to 1.0'
      FumfF = 1.0
      endif

      if (RUMF.gt.1.0) then
c. cheung equation only for size difference

      if(RRHO.eq.1) then
      CCT=(log(UT/Umf)/log(RUMF))**0.5
```

```
      CCF=(log(UF/Umf)/log(RUMF))**0.5

      else
c. simple approximation will find some
correlations
c. change to exponential fit (simple) A exp ( B * x)
c. x in mass fraction
      CCT=(UT/Umf-1.0)/(RUMF-1.0)
      CCF=(UF/Umf-1.0)/(RUMF-1.0)

      XCCT = (log(UT/EC1)) / EC2
      XCCF = (log(UF/EC1)) / EC2

      CCT=XCCT/(XCCT + RRHO*(1.0 - XCCT) )
      CCF=XCCF/(XCCF + RRHO*(1.0 - XCCF) )

      endif

      if(CCT.ge.1.0) CCT=1.0
      if(CCF.ge.1.0) CCF=1.0
      else
      write(*,*)' note: Tracer has lower Umf'
      CCT=1.0
      CCF=1.0

      endif

      CC=CCT
      write(*,*) 'ICsat=', ICsat
      if (ICsat.eq.0) CSAT=1.0
      if (ICsat.eq.1) CSAT=CC

      write(*,*)'Critical C (theoretically)    =',CC

      write(*,*)'Critical C (in bubbling zone) =',
CCF

      if(iYoption.eq.5) then
      Yconst = Ypeak(alpha,beta,gamma)
      endif



      if(Iform.eq.0) then


      VS=XM*(xi/RHO1 + (1-xi)/RHO2 )
      YLHS=VS*1.0D6/(Area*DX*(1-Emf))

      CIVOL=xi/(xi + RRHO*(1.0 - xi) )

c. Initial N, assuming eb=0.2
      call ESTIN

c. For species balance

      XLHS=xi*XM*1.0D6/(RHO1*Area*DX*(1-
Emf))

c. LHS of Solids volume fraction:
c. For total balance

      call CINIT

      else

      call CIDATA

      YLHS=N*1.0*(1.0-0.2)
      XLHS=0.0

      do 5 i=1,N

      XLHS=XLHS+CE(i)*(1.0-0.2)

5     continue

      endif



      SDB=0
      SUb=0
      SEbz=0
      SFR=0
      SUs=0
      SWK=0

      call CFBVAR


      write(*,*)'(Tim)   YS=',YST
      write(*,*)'(Levy)  YS=',YSL
      write(*,*)'(Input) YS=',YS
      do 10 i=1,N

      Z(i) = i * DX
      SDB=SDB+DB(i)
      SUb=SUb+Ub(i)
      SEbz=SEbz+Ebz(i)
      SFR=SFR+FR(i)
      SUs=SUs+Us(i)
```

```
      SWK=SWK+WK(i)

10    continue

c. height averaged properties

      SDB=SDB/float(N)
      SUb=SUb/float(N)
      SEbz=SEbz/float(N)
      SFR=SFR/float(N)
      SUs=SUs/float(N)
      SWK=SWK/float(N)


OPEN(unit=1,file='gryosinf.dat',status='unknown')
      write(1,*)'   Z       DB       Ub       Ebz
Us
     >      Kw'
c. height average properties
      do 20 i=1,N

      write(1,600)
Z(i),DB(i),Ub(i),Ebz(i),Us(i),WK(i)

20    continue
600   format(5F10.4,G10.2)

      write(1,*) 'AVERAGE VALUES'
      write(1,600)
DX*N/2.0,SDB,SUb,SEbz,SUs,SWK


      close(1,status='keep')
      return
      end



      subroutine CFBVAR
c. calculate local bubble and fluidization conditions
      implicit real*8 (A-H,O-Z)
      parameter (Nmax=500)
      dimension
Ub(Nmax),Ebz(Nmax),WK(Nmax),FR(Nmax),YA
(Nmax)
      dimension
Zloc(10),Z(Nmax),DB(Nmax),Us(Nmax),
CW(Nmax),CE(Nmax)
      dimension BDZ(Nmax)

      common /VARI/ U, Umf, Emf, fw, qx, xi, N
      common /BEDH/ Hfix,Ebm
      common /ZEXP/ Zloc,NZ
      common /TIME/ Ttot,Dt,Dtwrit
      common /PROP/ Ub,FR,WK,YS
      common /BUBF/ Ebz
      common /BUBD/ DB,Us,TK
      common /EXCH/
EXFAC,power,EXLIM,EXINT
      common /UMFR/ RUMF
      common /STAG/ NB
      common /DXSIZE/ DX
      common /LHS/ XLHS,YLHS
      common /PCONC/ CW,CE
      common /DEFLU/ IDEFLU
      common /PRATIO/ RRHO,RDP
      common /YADJS/ YA
      common /CYSVAL/ CYS
      common /Yoption/ iYoption
      common /YCpower/ alpha,beta,gamma
      common /YCval/ Yconst
      common /CTYPE/ ICtype
      common /CRITIC/ CC
      common /CRIFAL/ CCF
      common /BUBVEL/ IBUBVEL
      common /BUBDZ/ BDZ
      common /ICVOL/ CIVOL
      common /ECONST/ EC1, EC2

      g=981.0
      Ump=RUMF*Umf


30    sumEB=0.0


      do 10 i=1,Nmax
c. have the option of C1 being CE or CW or
average

c. note used Ebz from last calculation

      if(ICtype.eq.0) then

      Cbed = Ebz(i) * fw * CW(i) + (1-Ebz(i)-
fw*Ebz(i)) * CE(i)

      elseif(ICtype.eq.1) then

      Cbed = CW(i)
```

```
      elseif(ICtype.eq.2) then

      Cbed = CE(i)

      endif

      CFAC=0.999
c. check for defluidization condition

      if((IDEFLU.eq.1).and.(Cbed.ge.(CFAC*CCF))
) then


      NB = i
      CW(i) = CC
      CE(i) = CC
      Z(i)  = i*DX
      DB(i) = 0.0
      Ub(i) = 0.0
      Ebz(i)= 0.0
      FR(i) = 0.0
      Us(i) = 0.0
      WK(i) = 1000
      YA(i) = 0.0
      BDZ(i)= 0.0
      else

c. calculating new bubble parameters basing on the
new C


c. Concentration effect on the Umf - Cheung et al.,
1978

      if ((Ys.eq.0.0).or.(RUMF.eq.1.0)) then

      CUMF=1.0

      else


      CUMF=Cbed

      endif

c. for equi-density
c. an intial assumption

      if(RRHO.eq.1.0) then

      UMFC= Umf*(RUMF)**(CUMF*CUMF)

      else

c. for equi-size (or relatively) with density effect

c     UMFC=Umf*(RUMF*CUMF+(1.0-CUMF))
c. fit with exponential equation for density effect
(experimental)

      UMFC=EC1 * Exp(EC2 * CUMF)

      endif

      Z(i) = i*DX
      Z0   = NB*DX
      ZF   = Z(i)-Z0

      DB(i) = dbdarton(U,UMFC,ZF)

      if(IBUBVEL.eq.1) then

      Ub(i) = ( U - UMFC ) + 0.4 * ( g * DB(i) ) **
0.5

      elseif(IBUBVEL.eq.2) then

      Ub(i) = 0.5 * ( g * DB(i) ) ** 0.5

      endif

c. calculate the change of the bubble properties
with height
      xlambda=2.0

      pi=3.141592654

      XKprim = -1.0 * (1.0 + fw - TK)

      PHI=0.4*8.0*(2.0**0.75 -1.0)/ (3.0 * pi
*xlambda)

      UC1=  (U-UMFC)**2.0 * XKprim * UMFC

      UC2= (1.0 + XKprim * UMFC/Ub(i) )**2.0

      BDZ(i) = UC1*PHI/(Ub(i)*Ub(i)*DB(i)*UC2)


      Ebz(i) = ( U - UMFC ) / ( Ub(i) - (1.0 + fw -
TK) * UMFC )
```

```
    FR(i) = fw * Ebz(i) / ( 1.0 - Ebz(i) - fw * Ebz(i)
)
    Us(i) = FR(i) * Ub(i)
c. introduce Uo/Umf effect   make EXFAC as
slope of AWE vs U/Umf

     if((U/UMFC).le.EXLIM) then
     AWE = EXFAC*U/UMFC - EXINT
     WK(i) = AWE / (DB(i)**power)
     else
     AWE = EXFAC*EXLIM - EXINT
     WK(i) = AWE / (DB(i)**power)
     endif
c. various functions for segregation parameters
c. introduce ramp function; define CYS=minimum
C with no segregation
c. symmetrical ramp function

     if(Ys.eq.0) then

     YA(i)=0.0

     else


     if (iYoption.eq.0) then

     YA(i) = YS

     elseif((iYoption.eq.1).or.(iYoption.eq.2)) then

      CUPPER=1.0

      if(iYoption.eq.2) CUPPER=CC

      if (Cbed.le.CYS) then

      YA(i)=0.0

      elseif ((Cbed.gt.CYS).and.(Cbed.le.(1.0-
CYS)) ) then

      YA(i) = YS * (Cbed - CYS) / (CUPPER -
2.0*CYS)

      else

      YA(i) = YS

      endif

     elseif(iYoption.eq.3) then

      if(Cbed.lt.0.5) then

      YA(i) = YS * Cbed

      else

      YA(i) = YS * (1.0 - Cbed)

      endif

     elseif(iYoption.eq.4) then

      zeta = 13.0 * (Cbed - 0.5)

      eta = 4.0 * (exp(-1.0*zeta)/ ((1 + exp(-
1.0*zeta)) ** 2.0))

      YA(i) = YS * eta

     elseif(iYoption.eq.5) then

c. Yconst cal in FBVAR

      CX = Cbed

      YA(i) = YS * Yeta(CX,alpha,beta,gamma)

      YA(i) = YA(i) / Yconst


     elseif(iYoption.eq.6) then

c. Y = f(U/Umf)


      YA(i) = YS * ( (U - UMFC) / (Ump - Umf) )
** gamma

     elseif(iYoption.eq.7) then

c. Y = f(U/Umf)


      YA(i) = YS *  (U/UMFC - 1.0)  ** gamma

c. other option (U-UMFC)

     endif
```

```
      endif

      endif

      if(YLHS.le.(sumEB + (1-Ebz(i) ) ) ) goto 99
      sumEB=sumEB+(1-Ebz(i))


   10 continue

c. the N is determined from total mass balance

   99 N=i

c     write(*,*)'new N and NB=', N, NB

      XRHS=0.0

      do 15 j=1,N

      if(j.le.NB) then

      C1 = CC

      else

      C1 = Ebz(j) * fw * CW(j) + (1.0-Ebz(j)-
fw*Ebz(j)) * CE(j)

      endif

      XRHS=XRHS+C1

   15 continue


      FAC=XLHS/XRHS


c     write(*,*)'Fac=',FAC


      do 20 j=1,N

      if(j.le.NB) then

      else

      C1=CW(j)*FAC
      CW(j)=CLIMIT(C1)

      C1=CE(j)*FAC
      CE(j)=CLIMIT(C1)

      endif

   20 continue

      if(ABS(1.0-FAC).gt.0.001) goto 30


      return
      end


      function Yeta(CX,alpha,beta,gamma)
c. peak function for Ys
      implicit real*8 (A-H,O-Z)

      Yeta = (CX**alpha * (1.0 -
CX)**beta)**gamma

      return

      end


      function Ypeak(alpha,beta,gamma)
c. in this case the peak is at the slope change

      implicit real*8 (A-H,O-Z)

      do 10 i=1,9999

      CX1=0.0001*(i-1)
      CX2=0.0001*(i)

      slope=Yeta(CX2,alpha,beta,gamma)-
Yeta(CX1,alpha,beta,gamma)

      if(slope.gt.0.0) ksign=1
      if(slope.eq.0.0) ksign=0
      if(slope.lt.0.0) ksign=-1

      if(i.eq.1) then

      ksign1=ksign

      else
```

```
      ksign2=ksign

      if(ksign1.ne.ksign2) then

      CX=(CX1+CX2)/2.0

      Ypeak=Yeta(CX,alpha,beta,gamma)

      goto 99

      else

      ksign1=ksign2

      endif

      endif


 10   continue

 99   return

      end


      subroutine ESTIN
c. use to estimate the initial N size from bubble
fraction.

      implicit real*8 (A-H,O-Z)
      parameter (Nmax=500)
      dimension
Ub(Nmax),Ebz(Nmax),WK(Nmax),FR(Nmax),YA
(Nmax)
      dimension
Zloc(10),Z(Nmax),DB(Nmax),Us(Nmax),
CW(Nmax),CE(Nmax)
      common /VARI/ U, Umf, Emf, fw, qx, xi, N
      common /BEDH/ Hfix,Ebm
      common /ZEXP/ Zloc,NZ
      common /TIME/ Ttot,Dt,Dtwrit
      common /PROP/ Ub,FR,WK,YS
      common /BUBF/ Ebz
      common /BUBD/ DB,Us,TK
      common /EXCH/
EXFAC,power,EXLIM,EXINT
      common /UMFR/ RUMF
      common /STAG/ NB
      common /DXSIZE/ DX
      common /LHS/ XLHS,YLHS
      common /PCONC/ CW,CE
      common /DEFLU/ IDEFLU
      common /PRATIO/ RRHO,RDP
      common /YADJS/ YA
      common /CYSVAL/ CYS
      common /Yoption/ iYoption
      common /CRITIC/ CC
      common /BUBVEL/ IBUBVEL
      common /ICVOL/ CIVOL
      common /ECONST/ EC1, EC2

      g=981.0

      Ump=RUMF*Umf

      sumEB=0.0
      NB=0
      CFAC=0.999
      do 10 i=1,Nmax


      if((IDEFLU.eq.1).and.(xi.ge.(CFAC*CC)) )
then

      NB=i

      Ebz(i)=0.0

      else


c. Concentration effect on the Umf - Cheung et al.,
1978

      if ((Ys.eq.0.0).or.(RUMF.eq.1.0)) then

      CUMF=1.0

      else

c. check for other density ***

      CUMF=CIVOL

      endif

c. for equi-density
c. an intial assumption
```

```
    if(RRHO.eq.1.0) then

    UMFC= Umf*(RUMF)**(CUMF*CUMF)

    else

c. for equi-size (or raltively) with density effect

c     UMFC=Umf*(RUMF*CUMF+(1.0-CUMF))

c. fit with exponential equation for density effect
(experimental)

     UMFC=EC1 * Exp (EC2 * CUMF)

     endif

     Z(i) = i*DX
     Z0  = NB*DX
     ZF  = Z(i)-Z0

     DB(i) = dbdarton(U,UMFC,ZF)

     if(IBUBVEL.eq.1) then

     Ub(i) = ( U - UMFC ) + 0.4 * ( g * DB(i) ) **
0.5

     elseif(IBUBVEL.eq.2) then

     Ub(i) = 0.5 * ( g * DB(i) ) ** 0.5

     endif

     Ebz(i) = ( U - UMFC ) / ( Ub(i) - (1.0 + fw -
TK) * UMFC )
     FR(i) = fw * Ebz(i) / ( 1.0 - Ebz(i) - fw * Ebz(i)
)
     WK(i) = EXFAC* U / UMFC /
(DB(i)**power)

     if(YLHS.le.(sumEB + (1-Ebz(i) ) ) ) goto 99
     sumEB=sumEB+(1-Ebz(i))

     endif

 10  continue

c. the N is determined from total mass balance

 99  N=i
c. estimate Dt from the maximum faster bubble at
least in the first instant
     Dt1=dx/(Ub(1))
     Dt2=dx/(Ub(N))
     Dt3=1/WK(1)
     Dt4=1/WK(N)
     Dt5=1/FR(1)*0.75* YS *Ub(1)
     Dt6=1/FR(N)*0.75* YS *Ub(N)
     write(*,*)'estimated  N and NB=', N, NB
     write(*,*)'residence time:'
     write(*,*)' ub 1-N, wk (1-N), Ys (1-N)'
     write(*,100) Dt1, Dt2, Dt3, Dt4, Dt5, Dt6
 100 format(6E12.2,' s')
     write(*,*)'input Dt :', Dt
     write(*,*)'change Dt in GRYOS3.INP'

     return
     end


     subroutine CINIT
c. initialization of concentration - ideal case
     implicit real*8 (A-H,O-Z)
     parameter (Nmax=500)
     dimension CW(Nmax),CE(Nmax)
     common /VARI/ U, Umf, Emf, fw, qx, xi, N
     common /PCONC/ CW,CE
     common /MSTATE/ Istate
     common /ICVOL/ CIVOL

     NI=(xi*N+0.0001)

     if ((xi+qx).le.1.0) then
     Na=qx*N
     Nb=(qx+xi)*N
     else
     write(*,*)'#  allocation of xi and q not correct'
     stop
     endif

     do 10 i=1,N

     if(Istate.eq.0) then

c. try to allow for non-pure layer

     if ((i.gt.Na).and.(i.le.Nb)) then
     CW(i)= 1.0
     CE(i)= 1.0
```

```
      else
      CW(i)= 0.0
      CE(i)= 0.0
      endif

      elseif(Istate.eq.1) then

      CW(i)= CIVOL
      CE(i)= CIVOL

      endif

 10   continue

      return
      end

      subroutine CIDATA
c. initial concentration from data file
      implicit real*8 (A-H,O-Z)
      parameter (Nmax=500)
      dimension CW(Nmax),CE(Nmax)
      common /VARI/ U, Umf, Emf, fw, qx, xi, N
      common /PCONC/ CW,CE
      common /MSTATE/ Istate
      common /DXSIZE/ DX
      open(9,file='cin.dat',status='old')
      read(9,*) DX
      write(*,*)'Dx=',DX
      N=0
 10   read(9,*,END=99) Y,CI
      N=N+1

      write(*,*) N,CI

      CW(N)= CI
      CE(N)= CI

      goto 10

 99   close(9,status='keep')
      return
      end


      function dbdarton(U,Umf,Z)
c. average bubble size by darton's method modified
for 2D
c. circular bubble shape

      implicit real*8 (A-H,O-Z)
      pi=3.141592654
      power=2/3.0
      thick=1.0
      UK=0.5
      SF=1.0
      xlambda=2.0

      XF=1.0

      if(U.gt.XF*Umf) then

      a=(4.0*SF/UK/(981**0.5)/pi)**power
      b=(U-Umf)**power
      c=(0.6818*Z/xlambda+0.56/thick)**power
      dbdarton=a*b*c

      else

      U=XF* Umf

      dbdarton=0.0


      endif


      return
      end

      function DbChiba(U,Umf,Z)
      implicit real*8 (A-H,O-Z)
      pi=3.141592654
      g=981.0
c. bubble size: Chiba, 2D
      thick=1.0
      CKb=0.5
      dbo= (4.0/(pi*g**0.5))**2.0 * ((U-
Umf)/thick/CKb)**2.0
      write(*,*) 'dbo=',dbo
      Zo=0.0
      DbChiba=dbo*((2.0**1.25-1.0)*(Z-
Zo)/dbo+1.0)**(0.4)
      return
      end
```